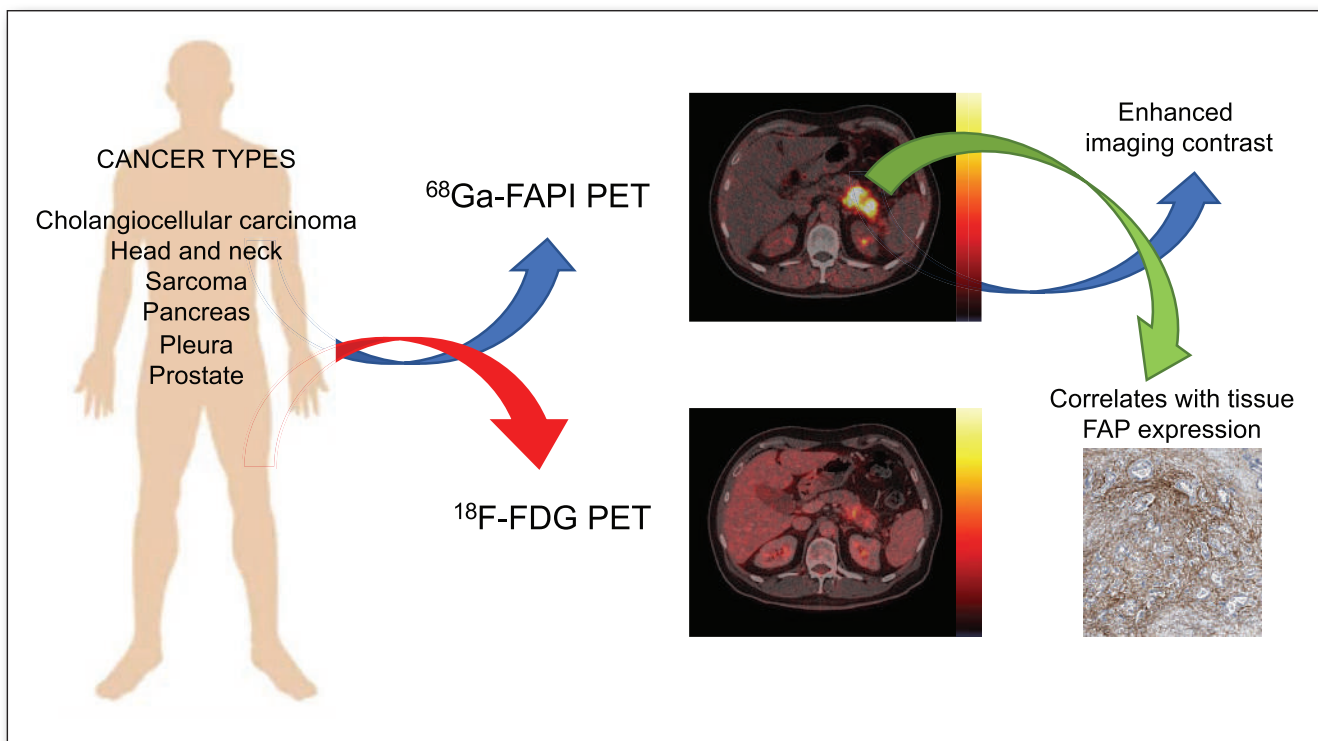


**FEATURED
ARTICLE**

Fibroblast-Activation Protein PET and Histopathology in a Single-Center Database of 324 Patients and 21 Tumor Entities. Nader Hirmas et al. See page 711.



^{177}Lu -FAP6-IP-DOTA: Exploring a promising fibroblast-activation protein-targeted radioligand for treatment of solid tumors.
Spencer Lindeman et al. See page 759.



Explore IAC Accreditation

IAC offers a **unique approach to accreditation** and is leading the field with **innovative, customized solutions** for your facility.

IAC is a nonprofit, nationally recognized accrediting organization, founded by medical professionals to advance appropriate utilization, standardization and quality of diagnostic imaging and intervention-based procedures.

- **Customer Service:** Facilities are busy caring for their patients and accreditation should not interfere with that. IAC clinical staff are available to guide applicant facilities through the accreditation process via phone, live chat or e-mail quickly and efficiently.
- **Quality & Safety Focused:** Offering a meaningful clinical peer review of case studies (with pathology) to evaluate diagnostic quality, report accuracy and report completeness, IAC is a partner in quality. IAC provides quality improvement-focused solutions such as the IAC QI Self-Assessment Tool, to help facilities optimize processes and improve patient safety and outcomes.
- **Continuous Improvement:** Accreditation must be thorough to truly affect the quality of care provided; however, IAC continues to explore ways to enhance the application process to make it simpler, more efficient and cost-effective to applicants including a base application fee reduction for facilities applying in 2023 and discounts on multiple site applications.

Join the more than 14,000 IAC-accredited facilities who consistently express the highest levels of satisfaction with IAC's customer service and resources. IAC offers accreditation for:

Vascular Testing
Echocardiography
Nuclear/PET
MRI . CT / Dental CT

Carotid Stenting
Cardiac Electrophysiology
Cardiovascular Catheterization
Vascular Interventional

IAC

Improving health care through accreditation®

intersocietal.org | 800.838.2110



IAC Offering 20% Reduction on Base Application Fees for 2023

To learn more or access our Online Fee Estimator, scan the QR code to the left or visit our website at intersocietal.org/iac/2023fees.

EDITOR'S PAGE

669 What Is Theranostics?

Wolfgang A. Weber, Henryk Barthel, Frank Bengel, Matthias Eiber, Ken Herrmann, and Michael Schäfers

HIGHLIGHTS

671 2022 SNMMI Highlights Lecture: General Nuclear Medicine

Andrei Iagaru

DISCUSSIONS WITH LEADERS

678 Looking at the Future of Prostate Cancer Treatment: A Conversation Between Michael Morris, Jeremie Calais, and Johannes Czernin

Michael J. Morris, Jeremie Calais, and Johannes Czernin

HOT TOPICS

682 The Emergence of Somatostatin Antagonist-Based Theranostics: Paving the Road Toward Another Success?

Alessio Imperiale, Abhishek Jha, Leah Meuter, Guillaume P. Nicolas, David Taieb, and Karel Pacak

STATE OF THE ART

685 Clinical Translation of Targeted α -Therapy: An Evolution or a Revolution?

Benedikt Feuerercker, Clemens Kratochwil, Hojjat Ahmadzadehfar, Alfred Morgenstern, Matthias Eiber, Ken Herrmann, and Kelsey L. Pomykala

CONTINUING EDUCATION

693 Amino Acid PET in Neurooncology

Norbert Galldiks, Philipp Lohmann, Gereon R. Fink, and Karl-Josef Langen

EDITORIAL

701 An Opinion on ChatGPT in Health Care—Written by Humans Only

Jens Kleesiek, Yonghui Wu, Gregor Stiglic, Jan Egger, and Jiang Bian

ONCOLOGY

Clinical

704 ^{64}Cu Treatment Planning and ^{67}Cu Therapy with Radiolabeled [$^{64}\text{Cu}/^{67}\text{Cu}$]MeCOSar-Octreotide in Subjects with Unresectable Multifocal Meningioma: Initial Results for Human Imaging, Safety, Biodistribution, and Radiation Dosimetry

Dale L. Bailey, Kathy P. Willowson, Matthew Harris, Colin Biggin, Alireza Aslani, Nigel A. Lengkeek, Jon Stoner, M. Enid Eslick, Harry Marquis, Michelle Parker, et al.

THERANOSTICS

Clinical

711 ■ FEATURED ARTICLE OF THE MONTH. Fibroblast-Activation Protein PET and Histopathology in a Single-Center Database of 324 Patients and 21 Tumor Entities

Nader Hirmas, Rainer Hamacher, Miriam Sraib, Marc Ingenwerth, Lukas Kessler, Kim M. Pabst, Francesco Barbato, Katharina Lueckerath, Stefan Kasper, Michael Nader, et al.

717 Initial Results of ^{68}Ga -FAPI-46 PET/MRI to Assess Response to Neoadjuvant Chemotherapy in Breast Cancer

Philipp Backhaus, Matthias C. Burg, Inga Asmus, Michaela Pixberg, Florian Büther, Hans-Jörg Breyholz, Randy Yeh, Stefanie B. Weigel, Patricia Stichling, Walter Heindel, et al.

724 Noninvasive Assessment of Human Epidermal Growth Factor Receptor 2 (HER2) in Esophagogastric Cancer Using ^{89}Zr -Trastuzumab PET: A Pilot Study

Melissa A. Lumish, Steven B. Maron, Viktoriya Paroder, Joanne F. Chou, Marinela Capanu, Steven Philemond, Joseph A. O'Donoghue, Heiko Schöder, Jason S. Lewis, Serge K. Lyashchenko, et al.

731 Is ^{18}F -FDG PET Needed to Assess ^{177}Lu -PSMA Therapy Eligibility? A VISION-like, Single-Center Analysis

Robert Seifert, Tugce Telli, Boris Hadaschik, Wolfgang P. Fendler, Phillip H. Kuo, and Ken Herrmann

738 Unspecific ^{18}F -PSMA-1007 Bone Uptake Evaluated Through PSMA-11 PET, Bone Scanning, and MRI Triple Validation in Patients with Biochemical Recurrence of Prostate Cancer

Robert Seifert, Tugce Telli, Marcel Opitz, Francesco Barbato, Christoph Berliner, Michael Nader, Lale Umutlu, Martin Stuschke, Boris Hadaschik, Ken Herrmann, et al.

744 A Pilot Study of ^{68}Ga -PSMA11 and ^{68}Ga -RM2 PET/MRI for Biopsy Guidance in Patients with Suspected Prostate Cancer

Heying Duan, Pejman Ghanouni, Bruce Daniel, Jarrett Rosenberg, Alan Thong, Christian Kunder, Carina Mari Aparici, Guido A. Davidzon, Farshad Moradi, Geoffrey A. Sonn, et al.

Basic

751 Targeted α -Therapy Using ^{225}Ac Radiolabeled Single-Domain Antibodies Induces Antigen-Specific Immune Responses and Instills Immunomodulation Both Systemically and at the Tumor Microenvironment

Thomas Ertveldt, Ahmet Krasniqi, Hannelore Ceuppens, Janik Puttemans, Yana Dekempeneer, Kevin De Jonghe, Wout de Mey, Quentin Lecocq, Yannick De Vlaeminck, Robin Maximilian Awad, et al.

759 ■ FEATURED BASIC SCIENCE ARTICLE. Fibroblast Activation Protein-Targeted Radioligand Therapy for Treatment of Solid Tumors

Spencer D. Lindeman, Ramesh Mukkamala, Autumn Horner, Pooja Tudi, Owen C. Booth, Roxanne Huff, Joshua Hinsey, Anders Hovstadius, Peter Martone, Fenghua Zhang, et al.

RADIOBIOLOGY/DOSIMETRY**Clinical****767 Toward Single-Time-Point Image-Based Dosimetry of ¹⁷⁷Lu-PSMA-617 Therapy**

Julia Brosch-Lenz, Astrid Delker, Friederike Völter, Lena M. Unterrainer, Lena Kaiser, Peter Bartenstein, Sibylle Ziegler, Arman Rahmim, Carlos Uribe, and Guido Böning

775 Biodistribution, Dosimetry, and Pharmacokinetics of ⁶⁸Ga-CBP8: A Type I Collagen–Targeted PET Probe

David Izquierdo-Garcia, Pauline Désogère, Mariane Le Fur, Sergey Shubaev, Iris Y. Zhou, Ian Ramsay, Michael Lanuti, Onofrio Catalano, Ciprian Catana, Peter Caravan, et al.

Basic**782 Dosimetric Variability Across a Library of Computational Tumor Phantoms**

Lukas M. Carter, Simone Krebs, Harry Marquis, Juan C. Ocampo Ramos, Edmond A. Olguin, Emilia O. Mason, Wesley E. Bolch, Pat B. Zanzonico, and Adam L. Kesner

CARDIOVASCULAR**Clinical****791 Long-Term Prognostic Value of ⁸²Rb PET/CT-Determined Myocardial Perfusion and Flow Reserve in Cancer Patients**

Josef J. Fox, Audrey Mauguen, Kimiteru Ito, Dipti Gupta, Alice Yu, Thomas H. Schindler, H. William Strauss, and Heiko Schöder

PULMONARY**Clinical****797 Molecular Imaging of Pulmonary Inflammation in Users of Electronic and Combustible Cigarettes: A Pilot Study**

Reagan R. Wetherill, Robert K. Doot, Anthony J. Young, Hsiaoju Lee, Erin K. Schubert, Corinde E. Wiers, Frank T. Leone, Robert H. Mach, Henry R. Kranzler, and Jacob G. Dubroff

MOLECULAR IMAGING**Clinical****803 Detection of Early Esophageal Neoplastic Barrett Lesions with Quantified Fluorescence Molecular Endoscopy Using Cetuximab-800CW**

Ruben Y. Gabriëls, Lisanne E. van Heijst, Wouter T.R. Hooghiemstra, Anne M. van der Waaij, Gursah Kats-Ugurlu, Arend Karrenbeld, Dominic J. Robinson, Anna Tenditnaya, Vasilis Ntziachristos, Dimitris Gorpas, et al.

Translational**809 Imaging Diverse Pathogenic Bacteria In Vivo with ¹⁸F-Fluoromannitol PET**

Spenser R. Simpson, Alexandria E. Kesterson, Justin H. Wilde, Zoraiz Qureshi, Bijoy Kundu, Mark P. Simons, and Kiel D. Neumann

NEUROLOGY**Clinical****816 Utility of Amino Acid PET in the Differential Diagnosis of Recurrent Brain Metastases and Treatment-Related Changes: A Meta-analysis**

Timo Schlürmann, Birgit Waschulzik, Stephanie Combs, Jens Gempt, Benedikt Wiestler, Wolfgang Weber, and Igor Yakushev

INVITED PERSPECTIVE**822 Tau PET Visual Reads: Research and Clinical Applications and Future Directions**

David N. Soleimani-Meigooni and Gil D. Rabinovici

PHYSICS AND INSTRUMENTATION**825 A Multicenter Study on Observed Discrepancies Between Vendor-Stated and PET-Measured ⁹⁰Y Activities for Both Glass and Resin Microsphere Devices**

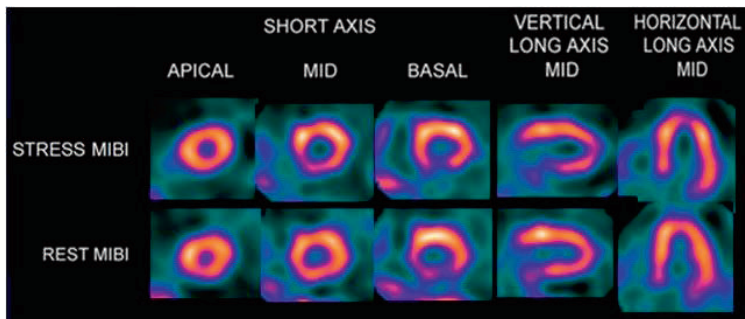
Silvano Gnesin, Justin K. Mikell, Maurizio Conti, John O. Prior, Thomas Carlier, Thiago V.M. Lima, and Yuni K. Dewaraja

DEPARTMENTS**8A This Month in JNM**



Myocardial Perfusion Function and Risk Stratification^{1,2}

- **First technetium-labeled myocardial perfusion imaging agent providing physicians prognostic information for patient management decisions related to coronary artery disease^{1,3}**
- **Used in over 10 million patients since 1991³**



INDICATIONS AND USAGE FOR CARDIOLITE®

Myocardial Imaging: Cardiolite® (Kit for the Preparation of Technetium Tc99m Sestamibi for Injection), is a myocardial perfusion agent that is indicated for detecting coronary artery disease by localizing myocardial ischemia (reversible defects) and infarction (non-reversible defects), in evaluating myocardial function and developing information for use in patient management decisions. Cardiolite® evaluation of myocardial ischemia can be accomplished with rest and cardiovascular stress techniques (e.g. exercise or pharmacologic stress in accordance with the pharmacologic stress agent's labeling).

CONTRAINDICATIONS:

None known.

IMPORTANT SAFETY INFORMATION:

Cardiolite® has been rarely associated with acute severe allergic and anaphylactic events of angioedema and generalized urticaria. In some patients the allergic symptoms developed on the second injection during Cardiolite® imaging. The most frequently reported adverse events include headache, chest pain/angina, ST segment changes on ECG, nausea, and abnormal taste and smell.

Infrequently, death has occurred 4 to 24 hours after Tc99m Sestamibi use and is usually associated with exercise stress testing (See Section 5.2). Pharmacologic induction of cardiovascular stress may be associated with serious adverse events such as myocardial infarction, arrhythmia, hypotension, bronchoconstriction and cerebrovascular events.

WARNINGS AND PRECAUTIONS:

In studying patients in whom cardiac disease is known or suspected, care should be taken to assure continuous monitoring and treatment in accordance with safe, accepted clinical procedure.

Caution should be exercised and emergency equipment should be available when administering Cardiolite®.

Before administering Cardiolite® patients should be asked about the possibility of allergic reactions to either Cardiolite® or Miraluma®. Miraluma® is an identical compound used in breast imaging.

The contents of the vial are intended only for use in the preparation of Technetium Tc99m Sestamibi and are not to be administered directly to the patient without first undergoing the preparative procedure.

Please see Brief Prescribing Summary on the following page.

Please see Full Prescribing information at www.cardiolite.com





Kit for the Preparation of
Technetium Tc99m Sestamibi for Injection

FOR DIAGNOSTIC USE

BRIEF SUMMARY

Please see Full Prescribing Information available at <https://www.lantheus.com/assets/Cardiolite-US-PI-513121-0619mktg.pdf> for complete information.

INDICATION AND USAGE

Myocardial Imaging: CARDIOLITE[®], Kit for the Preparation of Technetium Tc99m Sestamibi for Injection, is a myocardial perfusion agent that is indicated for detecting coronary artery disease by localizing myocardial ischemia (reversible defects) and infarction (non-reversible defects), in evaluating myocardial function and developing information for use in patient management decisions. CARDIOLITE[®] evaluation of myocardial ischemia can be accomplished with rest and cardiovascular stress techniques (e.g., exercise or pharmacologic stress in accordance with the pharmacologic stress agent's labeling).

It is usually not possible to determine the age of a myocardial infarction or to differentiate a recent myocardial infarction from ischemia.

Breast Imaging: MIRALUMA[®], Kit for the Preparation of Technetium Tc99m Sestamibi for Injection, is indicated for planar imaging as a second line diagnostic drug after mammography to assist in the evaluation of breast lesions in patients with an abnormal mammogram or a palpable breast mass.

MIRALUMA[®] is not indicated for breast cancer screening, to confirm the presence or absence of malignancy, and it is not an alternative to biopsy.

CONTRAINDICATIONS

None known

WARNINGS AND PRECAUTIONS

Warnings

In studying patients in whom cardiac disease is known or suspected, care should be taken to assure continuous monitoring and treatment in accordance with safe, accepted clinical procedure. Infrequently, death has occurred 4 to 24 hours after Tc99m Sestamibi use and is usually associated with exercise stress testing.

Pharmacologic induction of cardiovascular stress may be associated with serious adverse events such as myocardial infarction, arrhythmia, hypotension, bronchospasm and cerebrovascular events. Caution should be used when pharmacologic stress is selected as an alternative to exercise; it should be used when indicated and in accordance with the pharmacologic stress agent's labeling.

Technetium Tc99m Sestamibi has been rarely associated with acute severe allergic and anaphylactic events of angioedema and generalized urticaria. In some patients the allergic symptoms developed on the second injection during CARDIOLITE[®] imaging. Patients who receive CARDIOLITE[®] or MIRALUMA[®] imaging are receiving the same drug. Caution should be exercised and emergency equipment should be available when administering Technetium Tc99m Sestamibi. Also, before administering either CARDIOLITE[®] or MIRALUMA[®], patients should be asked about the possibility of allergic reactions to either drug.

General Precautions

The contents of the vial are intended only for use in the preparation of Technetium Tc99m Sestamibi and are not to be administered directly to the patient without first undergoing the preparative procedure.

Radioactive drugs must be handled with care and appropriate safety measures should be used to minimize radiation exposure to clinical personnel. Also, care should be taken to minimize radiation exposure to the patients consistent with proper patient management.

Contents of the kit before preparation are not radioactive. However, after the Sodium Pertechnetate Tc99m Injection is added, adequate shielding of the final preparation must be maintained. The components of the kit are sterile and non-pyrogenic. It is essential to follow directions carefully and to adhere to strict aseptic procedures during preparation.

Technetium Tc99m labeling reactions depend on maintaining the stannous ion in the reduced state. Hence, Sodium Pertechnetate Tc99m Injection containing oxidants should not be used.

Technetium Tc99m Sestamibi should not be used more than six hours after preparation.

Radiopharmaceuticals should be used only by physicians who are qualified by training and experience in the safe use and handling of radionuclides and whose experience and training have been approved by the appropriate government agency authorized to license the use of radionuclides.

Stress testing should be performed only under the supervision of a qualified physician and in a laboratory equipped with appropriate resuscitation and support apparatus.

The most frequent exercise stress test endpoints sufficient to stop the test reported during controlled studies (two-thirds were cardiac patients) were:

Fatigue	35%
Dyspnea	17%
Chest Pain	16%
ST-depression	7%
Arrhythmia	1%

ADVERSE REACTIONS

Adverse events were evaluated in 3741 adults who were evaluated in clinical studies. Of these patients, 3068 (77% men, 22% women, and 0.7% of the patient's genders were not recorded) were in cardiac clinical trials and 673 (100% women) in breast imaging trials. Cases of angina, chest pain, and death have occurred. Adverse events reported at a rate of 0.5% or greater after receiving Technetium Tc99m Sestamibi administration are shown in the following table:

Body System	Table 2.0 Selected Adverse Events Reported in > 0.5% of Patients Who Received Technetium Tc99m Sestamibi in Either Breast or Cardiac Clinical Studies*			
	Breast Studies	Cardiac Studies	Total	
	Women n = 673	Women n = 685	Men n = 2361	Total n = 3046
Body as a Whole	21 (3.1%)	6 (0.9%)	17 (0.7%)	23 (0.8%)
Headache	11 (1.6%)	2 (0.3%)	4 (0.2%)	6 (0.2%)
Cardiovascular	9 (1.3%)	24 (3.5%)	75 (3.2%)	99 (3.3%)
Chest Pain/Angina	0 (0%)	18 (2.6%)	46 (1.9%)	64 (2.1%)
ST segment changes	0 (0%)	11 (1.6%)	29 (1.2%)	40 (1.3%)
Digestive System	8 (1.2%)	4 (0.6%)	9 (0.4%)	13 (0.4%)
Nausea	4 (0.6%)	1 (0.1%)	2 (0.1%)	3 (0.1%)
Special Senses	132 (19.6%)	62 (9.1%)	160 (6.8%)	222 (7.3%)
Taste Perversion	129 (19.2%)	60 (8.8%)	157 (6.6%)	217 (7.1%)
Parosmia	8 (1.2%)	6 (0.9%)	10 (0.4%)	16 (0.5%)

*Excludes the 22 patients whose gender was not recorded.

In the clinical studies for breast imaging, breast pain was reported in 12 (1.7%) of the patients. In 11 of these patients the pain appears to be associated with biopsy/surgical procedures.

The following adverse reactions have been reported in ≤ 0.5% of patients: signs and symptoms consistent with seizure occurring shortly after administration of the agent; transient arthritis, angioedema, arrhythmia, dizziness, syncope, abdominal pain, vomiting, and severe hypersensitivity characterized by dyspnea, hypotension, bradycardia, asthenia, and vomiting within two hours after a second injection of Technetium Tc99m Sestamibi. A few cases of flushing, edema, injection site inflammation, dry mouth, fever, pruritis, rash, urticaria and fatigue have also been attributed to administration of the agent.

DRUG INTERACTIONS

Specific drug-drug interactions have not been studied.

OVERDOSAGE

The clinical consequences of overdosing with CARDIOLITE[®] are not known.

PATIENT COUNSELING INFORMATION

CARDIOLITE[®] and MIRALUMA[®] are different names for the same drug. Patients should be advised to inform their health care provider if they had an allergic reaction to either drug or if they had an imaging study with either drug.

Lactation: Interruption of breastfeeding after exposure to Technetium Tc99m Sestamibi is not necessary, however, a lactating woman should be advised to consider restricting close contact with her breast fed infant to a maximum of 5 hours in the 24 hour period after Technetium Tc99m Sestamibi administration in order to minimize radiation exposure.

To report SUSPECTED ADVERSE REACTIONS, contact Lantheus Medical Imaging, Inc. at 1-800-362-2668 or FDA at 1-800-FDA-1088 or www.fda.gov/medwatch.

Distributed by:
Lantheus Medical Imaging[®]
331 Treble Cove Road, N. Billerica, Massachusetts 01862 USA
For Ordering Tel: Toll Free: 800-299-3431
All Other Business: 800-362-2668
(For Massachusetts and International call 978-667-9531)



LANTHEUS[™]

The Official Publication of **SNMMI**

Publications Committee

TODD E. PETERSON, PhD, FSNMMI
Chair

CAROLYN J. ANDERSON, PhD, FSMMMI
PAIGE B. BENNETT, MD
JOYITA DUTTA, PhD
MICHAEL M. GRAHAM, PhD, MD, FACP, FACR,
FSNMMI
HOSSEIN JADVAR, MD, PhD, FACNM,
FSNMMI
STEVEN M. LARSON, MD, FACNM
HEINRICH R. SCHELBERT, MD, PhD, FSNMMI
HEIKO SCHÖDER, MD, MBA, FSNMMI
DAVID M. SCHUSTER, MD
JESSICA WILLIAMS, CNMT, RT(N),
FSNMMI-TS
HARVEY A. ZIESSMAN, MD, FSNMMI

Ex officio

JOHANNES CZERNIN, MD, FSNMMI
MUNIR GHESANI, MD, FACNM, FACP
ARNOLD M. STRASHUN, MD, FSNMMI
KATHY S. THOMAS, MHA, CNMT,
PET, FSNMMI-TS
HENRY F. VANBROCKLIN, PhD, FSNMMI

Associate Director of Communications
SUSAN ALEXANDER

Senior Copyeditor
SUSAN NATH

Senior Publications & Marketing Service Manager
STEVEN KLEIN

Editorial Production Manager
PAULETTE MCGEE

Editorial Project Manager
MARK SUMIMOTO

Director of Communications
REBECCA MAXEY

CEO
VIRGINIA PAPPAS

MISSION STATEMENT: *The Journal of Nuclear Medicine* advances the knowledge and practice of molecular imaging and therapy and nuclear medicine to improve patient care through publication of original basic science and clinical research.

JNM (ISSN 0161-5505 [print]; ISSN 2159-662X [online]) is published monthly by SNMMI, 1850 Samuel Morse Drive, Reston, VA 20190-5316. Periodicals postage is paid at Herndon, VA, and additional mailing offices. Postmaster, send address changes to *The Journal of Nuclear Medicine*, 1850 Samuel Morse Drive, Reston, VA 20190-5316. The costs of publication of all nonsolicited articles in *JNM* were defrayed in part by the payment of page charges. Therefore, and solely to indicate this fact, these articles are hereby designated "advertisements" in accordance with 18 USC section 1734.

DISCLOSURE OF COMMERCIAL INTEREST: Johannes Czernin, MD, editor-in-chief of *The Journal of Nuclear Medicine*, has indicated that he is a founder of Sofie Biosciences and holds equity in the company and in intellectual property invented by him, patented by the University of California, and licensed to Sofie Biosciences. He is also a founder and board member of Trethera Therapeutics and holds equity in the company and in intellectual property invented by him, patented by the University of California, and licensed to Triangle. He also serves on the medical advisory board of Actinium Pharmaceuticals and on the scientific advisory boards of POINT Biopharma, RayzeBio, and Jubilant Pharma and is a consultant for Amgen. No other potential conflicts of interest were reported. Manuscripts submitted to *JNM* with potential conflicts are handled by a guest editor.

EDITORIAL COMMUNICATIONS should be sent to: Editor-in-Chief, Johannes Czernin, MD, *JNM* Office, SNMMI, 1850 Samuel Morse Drive, Reston, VA 20190-5316. Phone: (703) 326-1185; Fax: (703) 708-9018. To submit a manuscript, go to <https://submit-jnm.snmjournals.org>.

BUSINESS COMMUNICATIONS concerning permission requests should be sent to the publisher, SNMMI, 1850 Samuel Morse Drive, Reston, VA 20190-5316; (703) 708-9000; home page address: jnm.snmjournals.org. Subscription requests and address changes should be sent to Membership Department, SNMMI at the address above. Notify the Society of change of address and telephone number at least 30 days before date of issue by sending both the old and new addresses. Claims for copies lost in the mail are allowed within 90 days of the date of issue. Claims are not allowed for issues lost as a result of insufficient notice of change of address. For information on advertising, contact Team SNMMI (Kevin Dunn, Rich Devanna, and Charlie Meitner; (201) 767-4170; fax: (201) 767-8065; TeamSNMMI@cunnasso.com). Advertisements are subject to editorial approval and are restricted to products or services pertinent to nuclear medicine. Closing date is the first of the month preceding the date of issue.

INDIVIDUAL SUBSCRIPTION RATES for the 2023 calendar year are \$633 within the United States and Canada; \$680 elsewhere. Make checks payable to the SNMMI. CPC IPM Sales Agreement No. 1415158. Sales of individual back copies from 1999 through the current issue are available for \$60 at <http://www.snmjournals.org/subscribe> (subscriptions@snmmi.org; fax: (703) 667-5134). Individual articles are available for sale online at <http://jnm.snmjournals.org>.

COPYRIGHT © 2023 by the Society of Nuclear Medicine and Molecular Imaging. All rights reserved. No part of this work may be reproduced or translated without permission from the copyright owner. Individuals with inquiries regarding permission requests, please visit <http://jnm.snmjournals.org/site/misc/permission.xhtml>. Because the copyright on articles published in *The Journal of Nuclear Medicine* is held by the Society, each author of accepted manuscripts must sign a statement transferring copyright (available for downloading at <http://jnm.snmjournals.org/site/misc/ifora.xhtml>). See Information for Authors for further explanation (available for downloading at <http://www.snmjournals.org/site/misc/ifora.xhtml>).

The ideas and opinions expressed in *JNM* do not necessarily reflect those of the SNMMI or the Editors of *JNM* unless so stated. Publication of an advertisement or other product mentioned in *JNM* should not be construed as an endorsement of the product or the manufacturer's claims. Readers are encouraged to contact the manufacturer with any questions about the features or limitations of the products mentioned. The SNMMI does not assume any responsibility for any injury or damage to persons or property arising from or related to any use of the material contained in this journal. The reader is advised to check the appropriate medical literature and the product information currently provided by the manufacturer of each drug to be administered to verify the dosage, the method and duration of administration, and contraindications.

EDITOR-IN-CHIEF

Johannes Czernin, MD
University of California at Los Angeles
Los Angeles, California

IMMEDIATE PAST EDITOR

Dominique Delbeke, MD, PhD
Vanderbilt University Medical Center
Nashville, Tennessee

ASSOCIATE EDITORS, CONTINUING EDUCATION

Hossein Jadvar, MD, PhD, MPH, MBA, FACNM, FSNMMI

University of Southern California
Los Angeles, California

Lale Kostakoglu, MD, MPH
University of Virginia Health System
Charlottesville, Virginia

ASSOCIATE EDITORS

Ramsey Derek Badawi, PhD

UC Davis Medical Center
Sacramento, California

Henryk Barthel, MD, PhD
Leipzig University
Leipzig, Germany

Frank M. Bengel, MD
Hannover Medical School
Hannover, Germany

Lisa Bodei, MD, PhD
Memorial Sloan Kettering Cancer Center
New York, New York

Irene Buvat, PhD
Université Paris Sud
Orsay, France

Jérémie Calais, MD
University of California at Los Angeles
Los Angeles, California

Sharmila Dorbala, MBBS
Brigham and Women's Hospital
Lexington, Massachusetts

Alexander E. Drzezga, MD
University Hospital of Cologne
Cologne, Germany

Jan Grimm, MD, PhD
Memorial Sloan Kettering Cancer Center
New York, New York

Ken Herrmann, MD, MBA
Universitätsklinikum Essen
Essen, Germany

Thomas A. Hope, MD
University of California, San Francisco
San Francisco, California

Jason S. Lewis, PhD
Memorial Sloan Kettering Cancer Center
New York, New York

David A. Mankoff, MD, PhD
University of Pennsylvania
Philadelphia, Pennsylvania

Heiko Schöder, MD
Memorial Sloan Kettering Cancer Center
New York, New York

Wolfgang Weber, MD
Technical University of Munich
München, Germany

SERIES EDITOR, FOCUS ON MI

Carolyn J. Anderson, PhD
University of Missouri
Columbia, Missouri

SERIES EDITOR, HOT TOPICS

Heinrich R. Schelbert, MD, PhD
University of California at Los Angeles
Los Angeles, California

CONSULTING EDITORS

Nancy Knight, PhD
University of Maryland School of Medicine
Baltimore, Maryland

Barry A. Siegel, MD
Mallinckrodt Institute of Radiology
St. Louis, Missouri

Arnold M. Strashun, MD
SUNY Downstate Medical Center
Scarsdale, New York

H. William Strauss, MD
Memorial Sloan Kettering Cancer Center
New York, New York

ASSOCIATE EDITORS (INTERNATIONAL)

Gerald Antoch, MD
Düsseldorf, Germany
Richard P. Baum, MD, PhD
Bad Berka, Germany

Ambros J. Beer, MD

Ulm, Germany
François Bénard, MD, FRCPC
Vancouver, Canada

Thomas Beyer, PhD
Vienna, Austria

Andreas K. Buck, MD, PhD
Würzburg, Germany

Ignasi Carrío, MD
Barcelona, Spain

June-Key Chung, MD
Seoul, Korea

Stefano Fanti, MD
Bologna, Italy

Markus Hacker, MD
Wien, Austria

Rodney J. Hicks, MD, FRACP
Melbourne, Australia

Michael S. Hofman, MBBS, FRACP
Melbourne, Australia

Ora Israel, MD
Haifa, Israel

Andreas Kjaer, MD, PhD, DMSc
Copenhagen, Denmark

Adriaan A. Lammertsma, PhD
Amsterdam, The Netherlands

Michael Lassman, PhD
Würzburg, Germany

Helmut R. Macke, PhD
Freiburg, Germany

Wim J.G. Oyen, MD, PhD
Milan, Italy

John O. Prior, MD, PhD
Lausanne, Switzerland

Osman Ratib, MD, PhD
Geneva, Switzerland

Mike Sathekge, MBChB, MMed, PhD
Pretoria, South Africa

Markus Schwaiger, MD
München, Germany

Andrew M. Scott, MD
Heidelberg, Australia

Nagara Tamaki, MD, PhD
Kyoto, Japan

Jia-He Tian, PhD
Beijing, China

Mei Tian, MD, PhD
Hangzhou, China

EDITORIAL CONSULTANTS

Martin S. Allen-Auerbach, MD
Los Angeles, California

Magnus Dahlbom, PhD
Los Angeles, California

Andrew Quon, MD
Los Angeles, California

Christiaan Schiepers, MD, PhD
Los Angeles, California

Daniel H. Silverman, MD, PhD
Los Angeles, California

Roger Slavik, PhD
Winterthur, Switzerland

EDITORIAL BOARD

Diane S. Abou, PhD
St. Louis, Missouri

Hojjat Ahmadzadehfari, MD
Dortmund, Germany

Valentina Ambrosini, MD, PhD
Bologna, Italy

Norbert Avril, MD
Cleveland, Ohio

Shadfar Bahri

Los Angeles, California
Jacques Barbet, PhD
Saint-Herblain, France

Bradley Jay Beattie, PhD
New York, New York

Matthias Richard Benz, MD
Los Angeles, California

Elie Besserer-Offroy, PhD, FACSc
Los Angeles, California

Pradeep Bhambhani, MD
Birmingham, Alabama

Angelika Bischof-Delaloye, MD
Lausanne, Switzerland

Christina Bluemel, MD
Würzburg, Germany

Ronald Boellaard, PhD
Groningen, The Netherlands

Nicolaas Bohnen, MD

Ann Arbor, Michigan
Wesley E. Bolch, PhD
Gainesville, Florida

Elias H. Botvinick, MD
San Francisco, California

Winfried Brenner, MD, PhD
Berlin, Germany

Richard C. Brunken, MD
Cleveland, Ohio

Ralph Buchert, PhD
Hamburg, Germany

Alfred Buck, MD
Menzingen, Switzerland

Denis B. Buxton, PhD
Bethesda, Maryland

Weibo Cai, PhD
Madison, Wisconsin

Federico Caobelli, MD
Basel, Switzerland

Giuseppe Carlucci, PhD
Los Angeles, California

Richard E. Carson, PhD
New Haven, Connecticut

Paolo Castellucci, MD
Bologna, Italy

Francesco Ceci, MD, PhD
Turin, Italy

Juliano J. Cerci
Curitiba, Brazil

Delphine Chen, MD
Seattle, Washington

Xiaoyuan Chen, PhD
Singapore

Simon R. Cherry
Davis, California

Arturo Chiti, MD
Rozzano, Italy

Peter M. Clark, PhD
Los Angeles, California

Christian Cohade, MD
Montreal, Canada

Ekaterina (Kate) Dadachova, PhD
Saskatoon, Canada

Issa J. Dahabreh, MD
Boston, Massachusetts

Heike Elisabeth Daldrup-Link, MD, PhD
Stanford, California

Farrokh Dehdashti, MD
St. Louis, Missouri

Robert C. Delgado-Bolton, MD, PhD
Logroño, Spain

Thorsten Derlin, MD
Hannover, Germany

Elisabeth G.E. de Vries, PhD
Groningen, The Netherlands

Marcelo F. Di Carli, MD
Boston, Massachusetts

David W. Dick, PhD
Iowa City, Iowa

Vasken Dilsizian, MD
Baltimore, Maryland

Jacob Dubroff, MD, PhD
Philadelphia, Pennsylvania

Janet F. Eary, MD
Bethesda, Maryland

W. Barry Edwards, PhD
Columbia, Missouri

Matthias Eiber, MD
Munich, Germany

David Eidelberg, MD
Manhasset, New York

Georges El Fakhri, PhD
Boston, Massachusetts

Peter J. Ell, MD
London, United Kingdom

Keigo Endo, MD
Nantan, Japan

Einat Even-Sapir, MD, PhD
Tel Aviv, Israel

Frederic H. Fahey, DSc
Boston, Massachusetts

Melpomeni Fani, PhD, MSc
Basel, Switzerland

Andrea Farolfi, MD
Bologna, Italy

Wolfgang Peter Fendler, MD
Essen, Germany

EDITORIAL BOARD, continued

James W. Fletcher, MD
Indianapolis, Indiana
Amy M. Fowler, MD, PhD
Madison, Wisconsin
Kirk A. Frey, MD, PhD
Ann Arbor, Michigan
Andrei Gafita
Los Angeles, California
Victor H. Gerbaudo, PhD, MSHCA
Boston, Massachusetts
Frederik L. Giesel, MD, PhD, MBA
Düsseldorf, Germany
Karolien Goffin, MD, PhD
Leuven, Belgium
Serge Goldman, MD, PhD
Brussels, Belgium
Stanley J. Goldsmith, MD
New York, New York
Martin Gotthardt, MD, PhD
Nijmegen, The Netherlands
Michael Graham, MD, PhD
Iowa City, Iowa
David Groheux, MD, PhD
Paris, France
Uwe A. Haberkorn, MD
Heidelberg, Germany
Mathieu Hatt, PhD, HDR
Brest, France
Wolf-Dieter Heiss, MD
Cologne, Germany
Karl Herholz, MD
Manchester, United Kingdom
Thomas F. Heston, MD
Las Vegas, Nevada
John M. Hoffman, MD
Salt Lake City, Utah
Carl K. Hoh, MD
San Diego, California
Jason P. Holland, DPhil
Zurich, Switzerland
Roland Hustinx, MD, PhD
Liege, Belgium
Andrei H. Iagaru, MD
Stanford, California
Masanori Ichise, MD
Chiba, Japan
Heather A. Jacene, MD
Boston, Massachusetts
Francois Jamar, MD, PhD
Brussels, Belgium
Jae Min Jeong, PhD
Seoul, Korea
John A. Katzenellenbogen, PhD
Urbana, Illinois
Zohar Keidar, MD, PhD
Haifa, Israel
Kimberly A. Kelly, PhD
Charlottesville, Virginia
Laura M. Kenny, MD, PhD
London, United Kingdom
Fabian Kiesling, MD
Aachen, Germany
E. Edmund Kim, MD, MS
Orange, California
Francoise Kraeber-Bodéré, MD, PhD
Nantes, France
Clemens Kratochwil, MD
Heidelberg, Germany
Kenneth A. Krohn, PhD
Portland, Oregon
Brenda F. Kurland, PhD
Pittsburgh, Pennsylvania
Constantin Lapa, MD
Augsburg, Germany
Suzanne E. Lapi, PhD
Birmingham, Alabama
Steven M. Larson, MD
New York, New York
Dong Soo Lee, MD, PhD
Seoul, Korea
Jeffrey Leyton, PhD
Sherbrooke, Canada
Xiang-Guo Li, PhD
Turku, Finland
Hannah M. Linden, MD
Seattle, Washington
Martin A. Lodge, PhD
Baltimore, Maryland
Katharina Lückerath, PhD
Los Angeles, California
Susanne Lütje, MD, PhD
Bonn, Germany

Umar Mahmood, MD, PhD
Boston, Massachusetts
H. Charles Manning, PhD
Nashville, Tennessee
Giuliano Mariani, MD
Pisa, Italy
Chester A. Mathis, PhD
Pittsburgh, Pennsylvania
Alan H. Maurer, MD
Philadelphia, Pennsylvania
Jonathan McConathy, MD, PhD
Birmingham, Alabama
Alexander J.B. McEwan, MD
Edmonton, Canada
Yusuf Menda, MD
Iowa City, Iowa
Philipp T. Meyer, MD, PhD
Freiburg, Germany
Matthias Miederer, MD
Mainz, Germany
Erik Mittra, MD, PhD
Portland, Oregon
Christine E. Mona, PhD
Los Angeles, California
Dae Hyuk Moon, MD
Seoul, Korea
Jennifer Murphy, PhD
Los Angeles, California
Helen Nadel, MD, FRCPC
Stanford, California
Matthias Nahrendorf, MD, PhD
Boston, Massachusetts
Yuji Nakamoto, MD, PhD
Kyoto, Japan
David A. Nathanson, PhD
Los Angeles, California
Nghi C. Nguyen, MD, PhD
Dallas, Texas
Sridhar Nimmagadda, PhD
Baltimore, Maryland
Egbert U. Nitzsche, MD
Aarau, Switzerland
Daniela E. Oprea-Lager, MD, PhD
Amsterdam, The Netherlands
Medhat M. Osman, MD, PhD
Saint Louis, Missouri
Christopher J. Palestro, MD
New Hyde Park, New York
Miguel Hernandez Pampaloni, MD, PhD
San Francisco, California
Neeta Pandit-Taskar, MD
New York, New York
Ashwin Singh Parikh, MBBS, MD
Saint Louis, Missouri
Michael E. Phelps, PhD
Los Angeles, California
Gerold Porenta, MD, PhD
Vienna, Austria
Sophie Poty, PhD
Montpellier, France
Edwin (Chuck) Pratt, PhD, MS Eng
New York, New York
Daniel A. Pryma, MD
Philadelphia, Pennsylvania
Valery Radchenko, PhD
Vancouver, Canada
Caius G. Radu, MD
Los Angeles, California
Isabel Rauscher, MD
Munich, Germany
Nick S. Reed, MBBS
Glasgow, United Kingdom
Mark Rijpkema, PhD
Nijmegen, The Netherlands
Steven P. Rowe, MD, PhD
Baltimore, Maryland
Mehran Sadeghi, MD
West Haven, Connecticut
Orazio Schillaci, MD
Rome, Italy
Charles Ross Schmidlein, PhD
New York, New York
David M. Schuster, MD
Atlanta, Georgia
Travis Shaffer, PhD
Stanford, California
Sai Kiran Sharma, PhD
New York, New York
Anthony F. Shields, MD, PhD
Detroit, Michigan
Barry L. Shulkin, MD, MBA
Memphis, Tennessee

Yu Shyr, PhD
Nashville, Tennessee
Albert J. Sinusas, MD
New Haven, Connecticut
Riemer H.J.A. Slart, MD, PhD
Groningen, The Netherlands
Piotr Slomka, PhD, FACC
Los Angeles, California
Simon John Christoph Soerensen, MD
Stanford, California
Ida Sonni, MD
Los Angeles, California
Michael G. Stabin, PhD
Richland, Washington
Lisa J. States, MD
Philadelphia, Pennsylvania
Sven-Erik Strand, PhD
Lund, Sweden
Rathan M. Subramaniam, MD, PhD, MPH
Dunedin, New Zealand
John Sunderland, PhD
Iowa City, Iowa
Suleman Surti, PhD
Philadelphia, Pennsylvania
Julie Sutcliffe, PhD
Sacramento, California
David Taieb, MD, PhD
Marseille, France
Laura H. Tang, MD, PhD
New York, New York
Ukihide Tateishi, MD, PhD
Tokyo, Japan
James T. Thackeray, PhD
Hannover, Germany
Mathew L. Thakur, PhD
Philadelphia, Pennsylvania
Alexander Thiel, MD
Montreal, Canada
Daniel L.J. Thorek, PhD
St. Louis, Missouri
David W. Townsend, PhD
Singapore
Timothy Turkington, PhD
Durham, North Carolina
Gary A. Ulaner, MD, PhD
Irvine, California
David Ulmert, MD, PhD
Los Angeles, California
Lena M. Unterrainer, MD, MHBA
Munich, Germany
Christopher H. van Dyck, MD
New Haven, Connecticut
Douglas Van Nostrand, MD
Washington, District of Columbia
Patrick Veit-Haibach, MD
Toronto, Canada
Nerissa Viola-Villegas, PhD
Detroit, Michigan
John R. Votaw, PhD
Atlanta, Georgia
Richard L. Wahl, MD
St. Louis, Missouri
Anne Marie Wallace, MD
La Jolla, California
Martin A. Walter, MD
Geneva, Switzerland
Rudolf A. Werner, MD
Wuerzburg, Germany
Andreas G. Wibmer, MD
New York, New York
Anna M. Wu, PhD
Duarte, California
Randy Yeh, MD
New York, New York
Hyewon (Helen) Youn, PhD
Seoul, Korea
Pat B. Zanzonico, PhD
New York, New York
Brian M. Zeglis, PhD
New York, New York
Robert Zeiser, MD
Freiburg, Germany
Hong Zhang, MD, PhD
Hangzhou, China
Hongming Zhuang, MD, PhD
Philadelphia, Pennsylvania
Sibylle I. Ziegler, PhD
Munich, Germany

ASSISTANT TO THE EDITOR

Joshua N. Wachtel
Los Angeles, California

Defining current and future theranostics:

Weber and colleagues look at elements in the success of PSMA theranostics and reflect on the potential for similar advances in combined diagnostics/therapeutics in other areas nuclear medicine. *Page 669*

Focus on general nuclear medicine: Iagaru offers highlights and insights on general nuclear medicine topics presented at the most recent SNMMI Annual Meeting. *Page 671*

Discussions with leaders: Czernin and colleagues talk with Michael J. Morris, MD, a leading expert in genitourinary oncology, on the current status and future potential for nuclear medicine in the diagnosis and treatment of prostate cancer. *Page 678*

Somatostatin-based theranostics: Imperiale and colleagues summarize advances in somatostatin receptor-targeted peptide receptor radionuclide therapy, a novel paradigm in theranostics with promise for revolutionizing diagnostic and therapeutic management of neuroendocrine tumors. *Page 682*

α -Radioligand therapy: Feuerercker and colleagues review important studies evaluating α -emitting targeted therapies as potential next-generation theranostics and report on 3 promising clinical applications administered systemically. *Page 685*

Amino acid PET in neurooncology: Galldikis and colleagues provide an educational overview of the added clinical value of amino acid PET in glioblastoma or brain metastases for differential diagnosis and assessment of tumor extent, treatment-related changes, and treatment response. *Page 693*

ChatGPT in health care: Kleesiek and colleagues look at the widespread interest in large language model-trained artificial intelligence applications, their potential in health care, and responsibilities for expert human involvement in shaping and monitoring these technologies. *Page 701*

$^{64/67}\text{Cu-SARTATE}$ imaging and therapy: Baille and colleagues report on first-in-humans use of ^{64}Cu and ^{67}Cu as a theranostic pair in patients with meningiomas, with advantageous methodology for normal-organ dosimetry. *Page 704*

FAPI PET for oncologic imaging: Hirmas and colleagues present an overview of a prospective, 3-y fibroblast-activation protein inhibitor registry study, with head-to-head comparison of tumor

uptake in $^{68}\text{Ga-FAPI}$ and $^{18}\text{F-FDG}$ PET, as well as FAP immunohistochemistry. *Page 711*

$^{68}\text{Ga-FAPI-46 PET/MRI}$ in breast cancer NAC: Backhaus and colleagues assess and validate the diagnostic performance of follow-up breast $^{68}\text{Ga-FAPI-46 PET/MRI}$ in classifying response status of local breast cancer and lymph node metastases after completion of neoadjuvant chemotherapy. *Page 717*

PET in HER2+ mECC: Lumish and colleagues describe the utility of ^{89}Zr -trastuzumab PET in elucidating variations in human epidermal growth factor receptor 2 expression in primary tumors and metastases in metastatic esophagogastric cancer. *Page 724*

PSMA only versus PSMA/FDG for treatment eligibility: Seifert and colleagues reanalyze data from patients who underwent both $^{18}\text{F-FDG}$ and PSMA PET for PSMA-targeted therapy eligibility to determine whether both studies are necessary to identify suitable candidates. *Page 731*

Unspecific bone uptake in $^{18}\text{F-PSMA-1007 PET}$: Seifert and colleagues explore the frequency of unspecific bone uptake and bone metastases separately for $^{18}\text{F-PSMA-1007}$ and $^{68}\text{Ga-PSMA-11}$ in biochemical recurrence of prostate cancer. *Page 738*

PSMA and GRPR PET-guided prostate biopsy: Duan and colleagues report on the potential of $^{68}\text{Ga-PSMA11}$ and $^{68}\text{Ga-RM2 PET/MRI}$ for biopsy guidance in patients with suspected prostate cancer. *Page 744*

Targeted α -therapy in melanoma: Ertveldt and colleagues detail studies on the mechanisms of immune activation in a melanoma model using α -targeted radionuclide therapy with ^{225}Ac -labeled single-domain antibodies. *Page 751*

$^{177}\text{Lu-FAP6-IP-DOTA}$ therapy: Lindeman and colleagues evaluate the performance of a fibroblast-activation protein-targeted radioligand conjugate in 4 tumor models, with potential for optimization in clinical treatment of solid tumors. *Page 759*

$^{177}\text{Lu-PSMA STP}$ dosimetry: Brosch-Lenz and colleagues assess differences in the time-integrated activity of single-time-point versus multiple-time-point image-based dosimetry protocols for $^{177}\text{Lu-PSMA-617}$ therapy. *Page 767*

Biodistribution and dosimetry of $^{68}\text{Ga-CBP8}$:

Izquierdo-Garcia and colleagues determine the biodistribution, dosimetry, and pharmacokinetics of this peptide-based, type I collagen-targeted probe in PET/MRI imaging of tissue fibrosis in healthy human subjects. *Page 775*

Tumor dosimetry phantoms: Carter and colleagues create computer-generated tumor models to assess the effects of tumor shape, size, and margin contour on absorbed dose for several clinically applied therapeutic radionuclides. *Page 782*

PET MFR and cancer survival: Fox and colleagues detail the prognostic capabilities of quantitative PET-derived myocardial flow reserve data for overall survival in a cohort of patients with known or suspected coronary artery disease. *Page 791*

$^{18}\text{F-NOS PET}$ and pulmonary inflammation: Wetherill and colleagues report on an $^{18}\text{F-NOS}$ PET study quantifying inducible nitric oxide synthase expression to characterize oxidative stress and inflammation in the lungs of electronic cigarette users, cigarette smokers, and controls. *Page 797*

NIR-FME detection of esophageal neoplasia: Gabriels and colleagues investigate the feasibility of an epidermal growth factor receptor-targeted tracer to improve near-infrared fluorescence molecular endoscopy detection of early-stage esophageal adenocarcinoma. *Page 803*

$^{18}\text{F-Fluoromannitol PET}$ and bacterial infection: Simpson and colleagues describe development of this novel radiopharmaceutical with the potential to specifically identify bacteria and monitor antibiotic efficacy in vivo. *Page 809*

PET in recurrent brain metastases: Schürmann and colleagues summarize evidence from a meta-analysis on the diagnostic utility of amino acid PET in differential diagnosis of recurrent brain metastases and treatment-related changes. *Page 816*

Tau PET visual reads: Soleimani-Meigooni and Rabinovici offer perspective on the evolution of visual interpretation of tau PET imaging. *Page 822*

PET-measured activity of microspheres: Gnesin and colleagues report on a multicenter, multi-PET-device study comparing manufacturer-declared ^{90}Y activity in vials with quantitative ^{90}Y PET/CT assessment of the same vials and comment on resulting implications for selective internal radiation therapy dosimetry. *Page 825*

What Is Theranostics?

Wolfgang A. Weber¹, Henryk Barthel², Frank Bengel³, Matthias Eiber¹, Ken Herrmann⁴, and Michael Schäfers⁵

¹Technical University of Munich, Munich, Germany; ²Leipzig University, Leipzig, German; ³Hannover Medical School, Hannover, Germany; ⁴Universitätsklinikum Essen, Essen, Germany; and ⁵University of Münster, Münster, Germany

The term *theranostics* has clearly become a buzzword. To a large extent, this is due to the success of prostate-specific membrane antigen (PSMA)-targeted radioligands. These ligands can be labeled with positron- or γ -emitting isotopes for imaging or with β - or α -emitting isotopes for therapy. The diagnostic or therapeutic targeting ligands are otherwise identical or similar. PSMA-targeted imaging and therapy have rapidly become a new clinical standard for prostate cancer management during the last 10 y, and applications in other diseases are being investigated. Sessions at nuclear medicine meetings are now often separated between PSMA imaging and non-PSMA imaging, and several PSMA radioligands have been approved for imaging and therapy of prostate cancer or are in late-stage development. In the wake of these clinical successes, an impressive number of new biotech companies have been founded that aim to develop new theranostic agents.

But what exactly has made PSMA theranostics so successful? In this editorial, we try to answer this question and reflect on what may be necessary to repeat the success of PSMA theranostics in other areas of nuclear medicine. In doing so, we argue that the concept of theranostics should not be limited to oncology but may be equally or even more successful for nuclear medicine applications in neurology, cardiology, and inflammatory and infectious diseases.

As a starting point, we define theranostics as a combination of molecularly targeted imaging and therapy in which imaging provides actionable information that enables new or more effective therapies. This definition is much broader than the commonly used definition of theranostics as a combination of radionuclide imaging therapy that uses the same (a similar) targeting molecule or as a combination of imaging and therapy that both use the same molecular target, as exemplified by PSMA-based theranostics (1). Nevertheless, we believe it is still specific enough to differentiate theranostics from other common uses of medical imaging.

Most oncologic imaging for tumor staging in fact does not meet our definition of theranostic imaging. These imaging studies stratify patient populations better but do not improve outcomes, because they merely shift patients from one prognostic group to another. This stage migration was described by Feinstein et al. in 1985 (2) and called the Will Rogers phenomenon in honor of the humorist–philosopher Will Rogers. Will Rogers, who was born in Oklahoma in 1879, supposedly once said that “When the Okies left Oklahoma and moved to California, they raised the average intelligence levels in both states.” Will Rogers was referring to the exodus of the Okies to California during the Great Depression in the 1930s. Feinstein et al. observed

that new imaging technologies, at that time CT and bone scans, shifted many patients with lung cancer to a higher TNM stage because these new technologies found more metastases than clinical examination and planar radiographs. The outcome of the patients who were shifted to a higher stage was better than that of patients in the same stage as defined by the older imaging technologies. This led to an improved outcome in each of the stage groups without changing the outcome of the whole patient group. Similar effects of new imaging technology on stage-specific patient outcomes have been reported for many other cancer types and other diseases.

Although oncologic CT and ^{18}F -FDG PET/CT mostly upstage patients and thereby only limit therapeutic options (3), the results of PSMA PET/CT can lead to new therapeutic options. This is most obvious in patients with metastatic castration-resistant prostate cancer. In this setting, high PSMA radioligand uptake indicates that PSMA radioligand therapy is a therapeutic option. However, PSMA PET scans can also provide actionable information in another setting. PSMA PET is highly specific for the detection of lymph node metastases of prostate cancer and can detect metastases much earlier than CT or MRI. Patients with biochemical recurrence after prostatectomy now frequently undergo radiotherapy of lymph node metastases identified on PSMA PET. The information from PSMA PET in this setting is actionable because of the high specificity of PSMA PET and because of the availability of a therapy that is guided by the imaging results, that is, stereotactic radiotherapy (4). Because of the lower sensitivity and specificity of CT and MRI, this radiotherapy was not feasible before the introduction of PSMA PET. Thus, the combination of PSMA PET and external-beam radiotherapy is also an example of theranostics according to our definition. In addition to radiotherapy, salvage lymph node dissection for PSMA-positive lymph node metastases is also being explored (5).

It is important to note here that the effectiveness of these local therapies in the setting of biochemical recurrence still needs to be proven by prospective clinical trials, but nevertheless, we would argue that one important reason for the success of PSMA PET imaging has been that it has enabled these new therapeutic options.

Our definition of theranostics is not limited to oncologic imaging and therapy. Another area of theranostics is the combination of β -amyloid imaging and antibody therapy. The amyloid antibody lecanemab has recently been approved by the Food and Drug



Wolfgang A. Weber

Administration, and some health insurances have already begun to reimburse lecanemab therapy (6). Before a patient can be treated with lecanemab, the presence of amyloid in the brain has to be determined. In most of the clinical studies of lecanemab, the presence of amyloid has been determined by amyloid PET. Thus, the results of the amyloid PET scan provide actionable information that results in a new therapy. Amyloid PET scans have so far been used relatively infrequently as purely diagnostic tools, but their use will now in all likelihood increase.

In addition to these 2 concrete examples of theranostics in a broader sense, there are several other such approaches in clinical use or development. In the fields of immunology and fibrosis, various novel radiopharmaceuticals for imaging are emerging in parallel to various targeted immunomodulatory or antifibrotic therapies. In the field of amyloidosis, novel, highly specific disease-modifying therapies are emphasizing the increasing need for companion diagnostic (imaging) biomarkers. Another example is dopamine transporter imaging and dopaminergic therapeutics in Parkinsonian syndromes. Moreover, under development are novel bacteria-selective radioligands that would enable differentiating sterile inflammation from infections. However, such approaches would also offer theranostic imaging characterizing individual bacterial strains to initiate specific and targeted antibiotic treatment and surgical resections. In oncology, ¹⁸F-fluoroestradiol has been Food and Drug Administration-approved for imaging of estrogen receptors and may be used to select patients for estrogen receptor-targeted therapies. Several clinical studies have suggested that imaging of human epidermal growth factor receptor 2 with radiolabeled antibodies may be superior to the analysis of expression of this receptor on biopsies for selecting patients for therapies directed toward it. Preclinically, imaging with ¹⁸F-labeled fibroblast activation protein inhibitor 74 has been used to image expression of fibroblast activation protein before chimeric antigen receptor T-cell therapy directed toward it.

We believe that it is more than semantics to call these approaches theranostic. Linking molecular imaging closely to a specific therapy provides a clear path to regulatory approval as a companion diagnostic. Once approved, it becomes significantly easier to run clinical trials of off-label uses in other indications.

In conclusion, theranostics is much more than switching of diagnostic and therapeutic isotopes. In fact, the concept of theranostics can and should be applied to imaging applications outside radioligand therapies and nuclear oncology. The therapeutic part of a theranostic pair does not have to be a radionuclide therapy but can be external-beam radiotherapy, surgery, medical therapy, or cellular therapy. Nevertheless, the underlying principle remains that the molecular imaging part of the theranostic pair provides actionable information. Obtaining this information requires that the results of the imaging study be highly specific and allow for clinical decision making. Following these principles may accelerate the regulatory approval of new molecular agents and broaden the use of molecular imaging in the clinic.

DISCLOSURE

No potential conflict of interest relevant to this article was reported.

REFERENCES

1. Langbein T, Weber WA, Eiber M. Future of theranostics: an outlook on precision oncology in nuclear medicine. *J Nucl Med*. 2019;60(suppl 2):13S–19S.
2. Feinstein AR, Sosin DM, Wells CK. The Will Rogers phenomenon: stage migration and new diagnostic techniques as a source of misleading statistics for survival in cancer. *N Engl J Med*. 1985;312:1604–1608.
3. Fischer B, Lassen U, Mortensen J, et al. Preoperative staging of lung cancer with combined PET-CT. *N Engl J Med*. 2009;361:32–39.
4. Bukavina L, Luckenbaugh AN, Hofman MS, et al. Incorporating prostate-specific membrane antigen positron emission tomography in management decisions for men with newly diagnosed or biochemically recurrent prostate cancer. *Eur Urol*. November 17, 2022 [Epub ahead of print].
5. Horn T, Krönke M, Rauscher I, et al. Single lesion on prostate-specific membrane antigen-ligand positron emission tomography and low prostate-specific antigen are prognostic factors for a favorable biochemical response to prostate-specific membrane antigen-targeted radioguided surgery in recurrent prostate cancer. *Eur Urol*. 2019;76:517–523.
6. US VA to cover Eisai, Biogen Alzheimer's treatment Leqembi. Reuters website. <https://www.reuters.com/world/us/us-veterans-health-administration-providing-coverage-eisais-alzheimers-treatment-2023-03-13/>. Updated March 14, 2023. Accessed March 29, 2023.

2022 SNMMI Highlights Lecture: General Nuclear Medicine

Andrei Iagaru

Stanford University School of Medicine, Stanford, California

The Highlights Lectures at the closing sessions of SNMMI Annual Meetings were originated and presented for more than 30 y by Henry N. Wagner, Jr., MD. Beginning in 2010, the duties of summarizing selected significant presentations at the meeting were divided annually among 4 distinguished nuclear and molecular medicine subject matter experts. The 2022 Highlights Lectures were delivered on June 14 at the SNMMI Annual Meeting in Vancouver, Canada. This month we feature the lecture by Andrei Iagaru, MD, Professor of Radiology–Nuclear Medicine at Stanford University School of Medicine (CA) and Chief of the Division of Nuclear Medicine and Molecular Imaging at Stanford HealthCare, who spoke on general nuclear medicine highlights from the meeting. Note that in the following presentation summary, numerals in brackets represent abstract numbers as published in The Journal of Nuclear Medicine (2022;63[Suppl 2]).

Key Words: general nuclear medicine; review; nuclear medicine practice

J Nucl Med 2023; 64:671–677

DOI: 10.2967/jnmed.123.265758

Welcome to my favorite part of the SNMMI Annual Meeting, the Highlights Lectures. I want to begin by briefly noting the outstanding work that has been done in nuclear medicine to address issues generated by the COVID-19 pandemic. Our community continues to contribute to the management of these patients through SPECT/CT, PET/CT, and novel imaging techniques. We are also an integral part of the larger effort to expand knowledge about the virus and its short- and long-term effects. A few of the notable presentations at this meeting include those by: Melhem and Keu from the Université de Montréal and the Hôpital Cité-de-la-Santé (Laval, both in Canada), who reported on “SPECT VQ and CTPA agreement for diagnosis of pulmonary embolism during the COVID-19 pandemic: a single-institution experience” [2793]; Khandelwal et al. from the Sanjay Gandhi Postgraduate Institute of Medical Sciences (Lucknow, India), who reported on “A prospective study to investigate the implementation of semiquantitative inflammatory load in post-COVID-19 lung disease to strategize therapy” [2326]; Wang et al. from the University of California–Davis, who reported on “Multiorgan metabolic changes in COVID-19 recovery measured with total-body dynamic ¹⁸F-FDG PET” [2329]; Maldonado et al. from University Hospital Quironsalud (Madrid, Spain), who reported on “Molecular imaging PET/CT in oncologic patients with unsuspected asymptomatic infection with SARS-CoV-2: the Spanish experience (Delta and Omicron variants)” [2330]; and Callaud and Bailly from Centre Hospitalier Universitaire

Tours and Centre Hospitalier Régional Orléans (both in France), who reported on “Time-reduction for simultaneous dual-isotope lung scintigraphy using 3D-ring CZT SPECT/CT” [2789]. Although time restrictions require that I move on to other topics, I want to congratulate these authors and researchers for the great work they are doing.



Andrei Iagaru, MD

CHANGING PERSPECTIVES IN NUCLEAR MEDICINE AND MOLECULAR IMAGING

The theme this year for this lecture is “How can we look at the same radiopharmaceutical or disease or scan and see things so differently?” This is somewhat analogous to the different perspectives that artists may take on their subjects. The same bowl of fruit would have been presented in radically different ways by, for example, Dalí and Picasso. What we do in nuclear medicine and molecular imaging is art in a different form. We are able to identify what happens in patients and to select tools from our armamentarium that allow us to provide increasingly detailed diagnoses. These tools vary and are continuously replaced by newer and more effective approaches, just as the ways in which we define and understand disease change with growing scientific understanding and experience. Let’s look at some examples from this year’s SNMMI Annual Meeting presentations.

PEDIATRIC IMAGING

My distinguished colleague at Stanford, Helen Nadel, MD, reminds us often that “imaging children is not like imaging small adults.” With adult patients, we often think of digital scanners as enabling faster exams and perhaps higher throughput—a perspective reflecting our work as busy clinicians. In pediatrics, digital scanners also offer the opportunity to reduce administered radiopharmaceutical dosage. Alves et al. from the Cincinnati Children’s Hospital Medical Center (OH) reported on the “Feasibility of reduced count acquisition of whole-body ¹⁸F-FDG PET in children and young adults imaged with a digital PET scanner” [2384]. The SNMMI Pediatric Imaging Council recognized Dr. Alves with their Majd–Gilday Young Investigator Award for this work. These researchers looked at various simulated acquisition times (60, 55, 50, 45, 40, and 30 s/bed) for pediatric patients who underwent imaging on a 5-ring 25-cm axial-field-of-view PET/CT system. Reconstructed images were scored on several criteria, including overall image quality, by pediatric radiologists. The resulting data indicated that no qualitative impact was observed down to almost 55 s/bed, suggesting the potential for faster scans with lower radiation (up to 67%) and for reduction or elimination of sedation/anesthesia in some patients. The authors summarized their finding that “for children and young adults

Received Mar. 20, 2023; revision accepted Mar. 20, 2023.
For correspondence or reprints, contact Andrei Iagaru (aiagaru@stanford.edu).
Published online Apr. 13, 2023.
COPYRIGHT © 2023 by the Society of Nuclear Medicine and Molecular Imaging.

receiving 0.12 mCi/kg injected activity of ^{18}F -FDG and imaged with a state-of-the-art extended-field-of-view digital PET/CT system, an acquisition time of 60 s/bed (or 0.8 mCi/kg injected activity imaged at 90 s/bed) shows no significant impact in image quality or quantitative measures.”

In a similar approach with a different scanner, Zhang et al. from the Ohio State University Wexner Medical Center (Columbus), the University of Pennsylvania (Philadelphia), and the University of Cincinnati (OH) reported on “Feasibility of low-dose ^{18}F -FDG PET in pediatric oncology” [2387]. This study evaluated low-dose PET via an intraindividual comparison using both data simulation and actual scan validation. Body mass index (BMI)-adapted ^{18}F -FDG administration was proposed and validated. This approach

showed a 30%–70% dose reduction for pediatric imaging and up to 92% reduction for infants and small children, without compromising image quality and SUV quantification. Figure 1 shows comparisons of whole-body ^{18}F -FDG PET in children with different BMI values. Lesions were identifiable across all reconstructed datasets, and equivalent image quality was maintained with robust semi-quantitative measurements. Pediatric patients deserve not only the lowest achievable dose from CT (about which we have heard much more) but also from PET, and it is clear that with advances in technology this can be achieved.

Is it possible to look at lymphoma and see things quite differently from different perspectives? Some imaging physicians believe that ^{18}F -FDG PET is the best approach. MR experts believe that

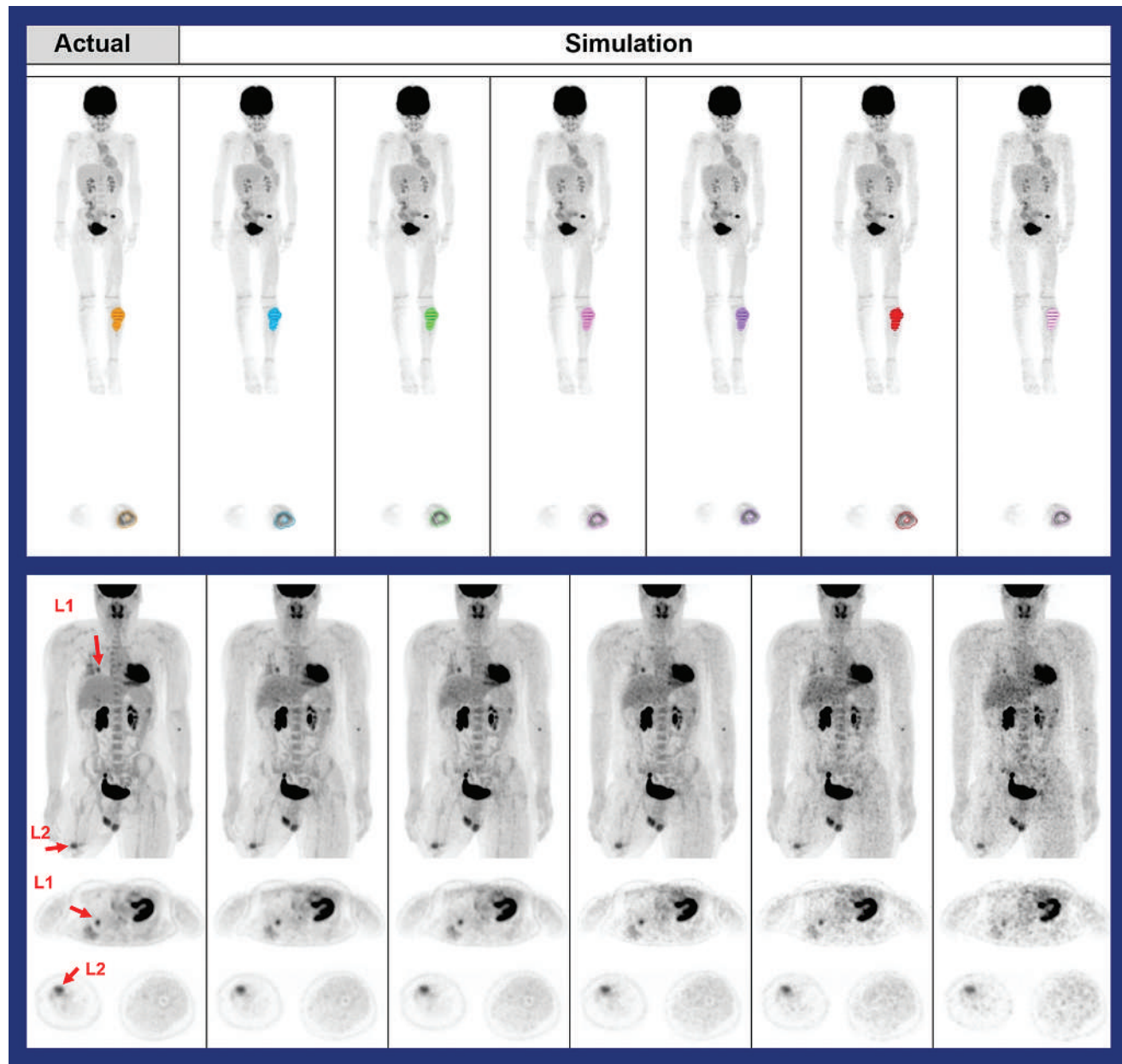


FIGURE 1. Feasibility of low-dose ^{18}F -FDG PET in pediatric oncology. Comparison of whole-body imaging in pediatric patients (BMI = 17, top row images, and 26, bottom row) at (far left) actual full-dose scan (180 s/bed) and (left to right) simulated reduced doses (range, 33%–92% reduction). Lesions are identifiable across all PET datasets, and equivalent image quality was maintained with robust SUV quantification achieved with substantial ^{18}F -FDG dose reduction.

diffusion-weighted (DW) imaging with MRI is best. Baratto et al. from Stanford University (CA), Children's Hospital of Philadelphia (PA), and Yale University (New Haven, CT) reported on these perspectives by “Comparing ^{18}F -FDG PET/MRI and DW MRI for staging and restaging of Langerhans cell histiocytosis (LCH) in children” [2386]. In the study, 23 children and young adults with biopsy-proven LCH underwent simultaneous ^{18}F -FDG PET/MRI with DW MRI ($n = 20$) or sequential ^{18}F -FDG PET/CT plus DW MRI ($n = 3$), including 23 baseline scans and 16 follow-up scans after chemotherapy. Comparing SUV semiquantitative data on PET and mean apparent diffusion coefficient map data from MR, they found highly similar accuracy, specificity, and sensitivity in staging and restaging LCH. This tells us that in order for PET/MRI to be more widely adopted in routine practice, we need to shorten the duration of these exams. Patients with multifocal LCH are usually very young and will require multiple follow-up imaging throughout their lives. PET/MRI in pediatric patients makes perfect sense, because substituting MRI for the CT removes one portion of the radiation dose and the high quality of the PET component lowers the other. This raises several questions: How do we make it faster? Do we really need all the MR sequences? If not, which ones are needed? These authors showed that it is possible to optimize PET/MR workflow in a way that can make it faster and perhaps more widely available and used.

What perspectives can PET and MRI provide in differentiating posttransplant lymphoproliferative disorder (PTLD) from lymphoma? Jayapal et al. from the Lucile Packard Children’s Hospital at Stanford School of Medicine (CA) reported on “Predictive patterns of pediatric PTLD on PET/MRI” [2786]. In this retrospective study, the authors identified unique patterns of whole-body ^{18}F -FDG PET/MRI metabolic activity in 38 children with PTLD. In 17 of the 21 (81%) patients with PTLD with abnormal PET/MRI but without transformation to lymphoma, a characteristic pattern of diffuse and symmetric uptake with involvement of symmetric lymph node stations was noted (Fig. 2). Asymmetry in this pattern seemed to predict transformation to lymphoma. As the authors concluded, “these findings may help the clinician in patient management to determine need for biopsy and therapy versus continued observation.” Management and treatment decisions diverge

significantly over time after transplantation depending on this diagnostic differentiation. Looking for this imaging symmetry provides a different and very useful perspective in this setting.

In the oncology world, we are familiar and experienced with sodium fluoride for evaluation of bony metastases. Unfortunately, we are not always reimbursed for these studies, so the use of sodium fluoride has diminished over time. Paravastu et al. from the National Institutes of Health (Bethesda, MD) and the Foundation for Research and Technology Hellas (Heraklion, Greece) reported on “Quantitative analysis of ^{18}F -NaF PET/CT imaging: evaluation of denosumab treatment in fibrous dysplasia” [2771]. These authors looked at potential utility of the tracer in predicting responses to treatment, and the resulting images were exquisite (Fig. 3). With data from SUV_{\max} , SUV_{mean} , and total lesion activity changes from baseline to 6 mo posttreatment in 8 patients with fibrous dysplasia, they showed that successful treatment with denosumab was associated with a marked reduction in bone turnover, as quantified by ^{18}F -NaF PET/CT. Findings like these have the potential to open new incentives for reintroduction of sodium fluoride in wider clinical use. As a community we should not be intimidated by repeated denials from the Centers for Medicare & Medicaid Services and should work together to obtain appropriate coverage that could benefit a range of patients.

Our perspectives on radiopharmaceuticals often depend on our practice settings. I am accustomed to seeing ^{18}F -FDOPA, for example, from the glioma/brain tumor/motion disorder viewpoint, because it is the main referral pattern at my institution. In pediatrics, the focus with this radiopharmaceutical is on congenital hyperinsulinism. Navarantha et al. from Children’s Hospital of Philadelphia (PA) asked “ ^{18}F -FDOPA PET imaging in congenital hyperinsulinism [CHI] for localization of a focal pancreatic lesion: do medications interfere with radiotracer uptake?” [2388]. Patients with CHI who are unresponsive to initial insulin secretion medication undergo genetic testing to predict the focal form, as well as ^{18}F -FDOPA PET imaging to localize focal pancreatic lesions. Current imaging protocols call for discontinuation of CHI medications for 2 d before the scan. Evaluating imaging and other results with a variety of relevant medications, the authors showed that the most common drugs administered to CHI patients do not seem to interfere with pancreatic uptake of ^{18}F -FDOPA. Even with glucagon, which produced differences in head-to-liver SUV ratios, no differences were noted in pancreatic uptake. This is important and useful information that we can all take home and use clinically if we have access to ^{18}F -FDOPA.

Sathya Murthi et al. from Manchester University Hospitals and the Christie Hospital (both in Manchester, UK, and part of the National Health Services Trust) reported on the “Role of ^{18}F -DOPA PET/CT in suspected CHI” [2392]. These authors compared uptake values of focal lesions detected with 2 different reconstruction techniques to identify the superior reconstruction method. After initial visual assessment by physicians, focal lesions were assessed by semiquantitative analysis of $\text{SUV}_{\text{ratio}}$ of focal disease (SUV_{\max} in lesion/ SUV_{mean} of pancreatic tissue) and by $\text{SUV}_{\text{ratios}}$ calculated using both ordered-subset expectation maximization

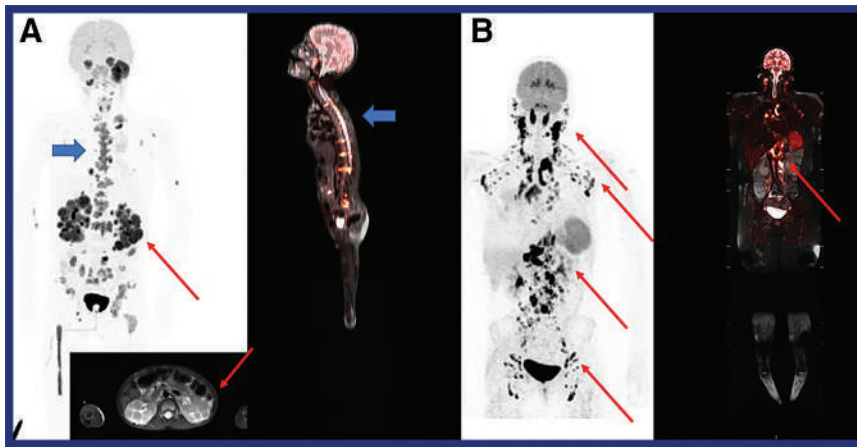


FIGURE 2. Predictive patterns of pediatric posttransplant lymphoproliferative disorder (PTLD) on PET/MRI. Asymmetry in lymph node involvement on PET/MRI correlated with progression to lymphoma. (A) 7-y-old boy after heart transplant with diffuse nonnodal and asymmetric pattern with renal, bone, and spinal cord lesions with B-cell lymphoma; and (B) 16-y-old girl after stem cell transplantation with symmetric nodal pattern of PTLD.

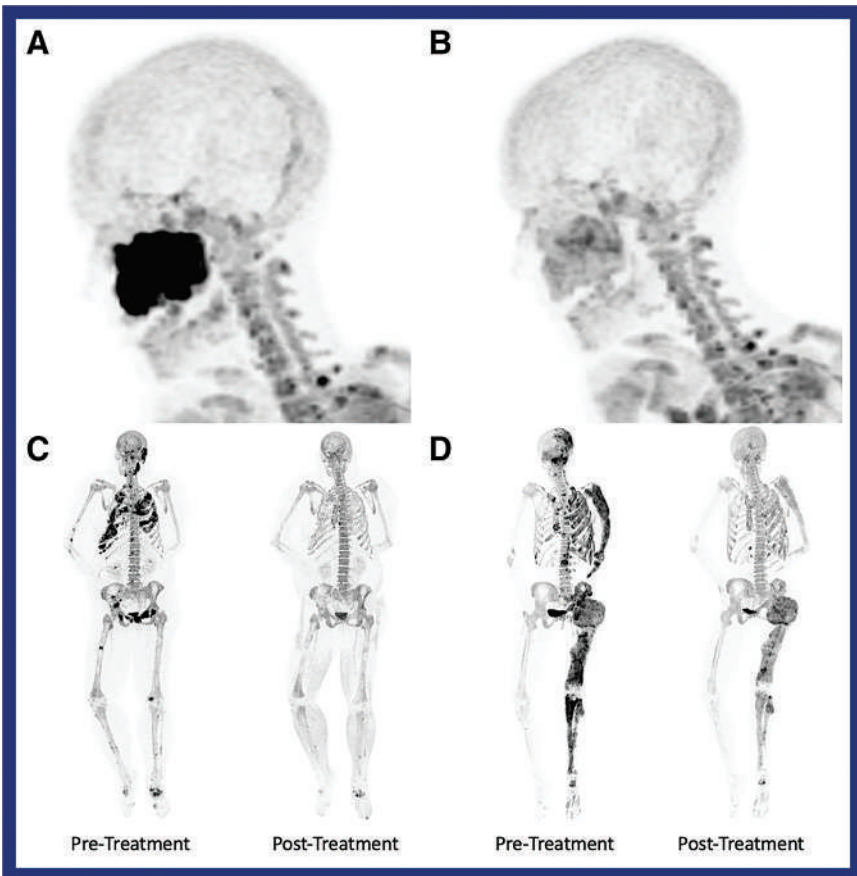


FIGURE 3. Quantitative analysis of ^{18}F -NaF PET/CT evaluation of denosumab treatment in fibrous dysplasia (FD). (A) Maxillary lesion in patient with monoostotic FD. (B) Marked improvement visualized by ^{18}F -NaF PET/CT after 6 mo treatment. (C and D) Representative images of treatment response on ^{18}F -NaF PET/CT in 2 patients with polyostotic FD.

(OSEM) and ultra-high definition (UHD) reconstructions. They concluded that ^{18}F -DOPA PET/CT with contrast-enhanced CT had high sensitivity in focal lesion detection (95.2%), resulting in successful surgical and clinical outcomes offering complete cure. They noted that this avoids potential long-term complications of total pancreatectomy. The finding that the UHD reconstruction method may be superior to OSEM reconstruction in this setting makes the case that we should not be reluctant to embrace new technologies that clearly improve patient care.

WIDENING PERSPECTIVES

Obesity is a well-recognized health risk. Nuclear medicine and molecular imaging tools have potential to provide meaningful information to these patients. Bini et al. from Yale University/Yale University School of Medicine (New Haven, CT) reported on “Liver and brain levels of 11 β -hydroxysteroid dehydrogenase type 1 (11 β -HSD1) enzyme in obesity: preliminary results from PET imaging studies” [2801]. 11 β -HSD1 catalyzes the conversion of inactive cortisone to active cortisol. In this study, 9 individuals (ages, 29–64 y) with a range of BMIs (22.6–34.4 kg/m²) underwent PET/CT imaging with arterial sampling after injection of ^{18}F -AS2471907, a novel PET tracer for 11 β -HSD1. The preliminary results suggested that obesity is associated with increased levels of 11 β -HSD1 in the liver

but decreased levels in the brain (although aging may increase brain 11 β -HSD1 levels). They noted that additional studies are needed to clarify the correlation of brain and liver 11 β -HSD1 with obesity. This has clear implications for obesity treatment strategies, including those associated with nonalcoholic fatty liver disease.

Obesity was also the focus of work by Muzik and Jiang from the Karmanos Cancer Institute at Wayne State University (Detroit, MI), who reported on “Decreased sympathetic innervation of cold-activated brown and white fat [BAT and WAT, respectively] in obese subjects using ^{11}C -HED PET imaging” [2238]. They investigated the relationship between sympathetic innervation and energy expenditure in both BAT and subcutaneous/visceral WAT in a group of obese and lean subjects during cold exposure. All patients underwent ^{11}C -HED and $^{15}\text{O}_2$ -water PET imaging at rest and after exposure to mild cold (16°C). In addition, ^{18}F -FDG images were obtained during the cold stress condition to assess the presence of activated BAT. Relative measurements of daily energy expenditure under both baseline and cold stress were obtained. They found that whole-body energy expenditure decreased in obese subjects during cold as a result of decreased sympathetic innervation (blood flow) in subcutaneous WAT, suggesting that the primary function of WAT in obese individuals is insulatory and not heat generating. This is an example of a new tracer that can be applied to a clinical question for which answers have

direct implications for both understanding the physiology of a widespread health challenge and for potential therapeutic interventions.

At this meeting we have heard about applications of fibroblast-activation protein inhibitor (FAPI) in almost every possible indication—it has gone from being a pan-cancer tracer to a pan-disease agent. Song et al. from Wuhan Union Hospital and Tongji Medical College of the Huazhong University of Science and Technology (both in Wuhan, China) reported on “Noninvasive visualization of liver fibrosis with ^{68}Ga -labeled FAPI” [2234]. The authors of this interesting study addressed an unmet need: identifying the presence of liver fibrosis early in the course of the disease so that we can consider ways to arrest or slow progression. In addition to reporting on serial ^{68}Ga -DOTA-FAPI-04 imaging in a mouse model of progressive liver fibrosis, the authors showed related imaging in humans. Figure 4 illustrates correlations between ^{68}Ga -DOTA-FAPI-04 uptake and histology in 5 example patients with escalating degrees of fibrosis. The authors concluded that this tracer “has the potential to display activated fibroblasts involved in the fibrotic process and to assess different stages of liver fibrosis... with promising applications in the accurate assessment and potential prediction of the prognosis of liver fibrosis.” The next question is whether, now that we have a tracer to assess progression in liver fibrosis, we can change the course of the disease? Perhaps we will hear more about this at future meetings. It is remarkable

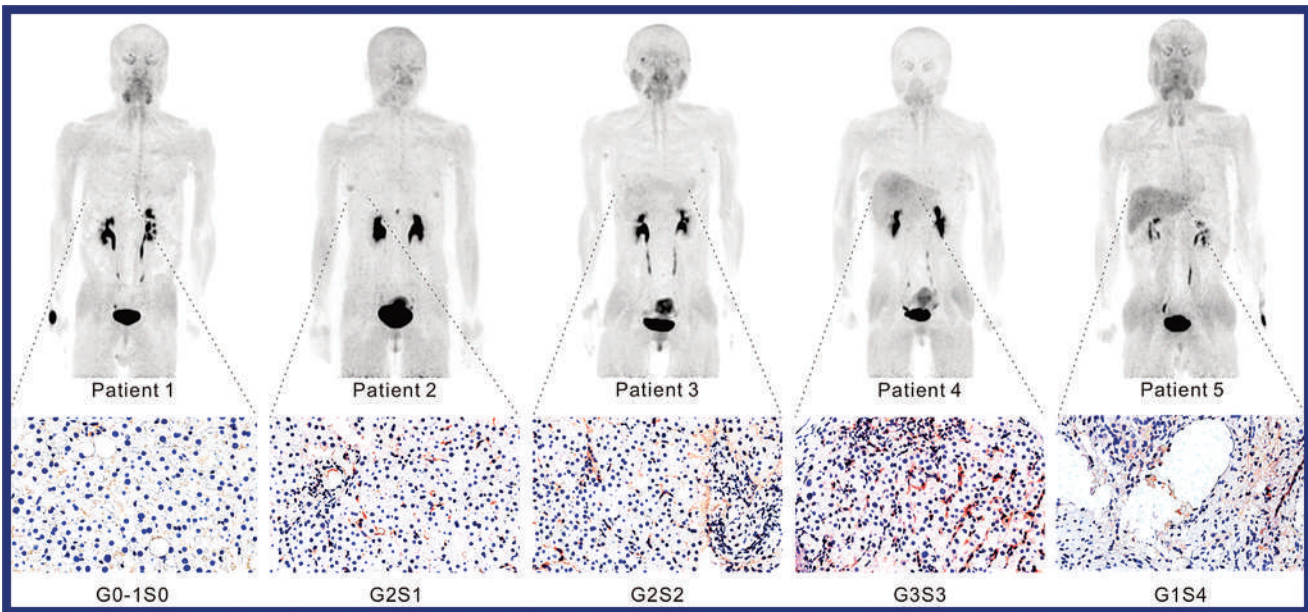


FIGURE 4. Noninvasive visualization of liver fibrosis with ^{68}Ga -DOTA-FAPI-04. Example correlations between ^{68}Ga -DOTA-FAPI-04 uptake and histology in 5 example patients with (left to right) escalating degrees of fibrosis.

that this tracer, developed for cancer imaging for which it was recognized as the 2019 SMMMI Image of the year, was again the focus of the 2022 Image of the Year, this time for predictive cardiac assessments. We are seeing it applied in an extraordinary number of other new applications by our community to improve patient care.

Wardak et al. from Stanford University/Stanford University School of Medicine (CA), Pliant Therapeutics (South San Francisco, CA), and Invicro, LLC (Boston, MA) reported on “Phase 2 drug target engagement study of PLN-74809 in patients with idiopathic pulmonary fibrosis (IPF) using a novel $\alpha_v\beta_6$ cystine knot PET imaging tracer” [2236]. The aim of this study was to evaluate the *in vivo* $\alpha_v\beta_6$ receptor occupancy of PLN-74809, an oral small-molecule dual-selective inhibitor of integrins $\alpha_v\beta_6$ and $\alpha_v\beta_1$, as assessed by

[^{18}F]FP-R₀1-MG-F PET/CT. This cystine knot radiopharmaceutical was originally developed for cancer. However, its target is not so much the cancer cells themselves as the tumor-associated fibrosis, making it a logical candidate for assessing pulmonary fibrosis. The authors compared kinetic modeling of uptake pre- and post-drug administration in IPF lungs to assess drug target engagement. They found that not only could target engagement of PLN-74809 with $\alpha_v\beta_6$ integrin receptors in the lungs of IPF patients be quantified using [^{18}F]FP-R₀1-MG-F PET/CT imaging (Fig. 5), but that PLN-74809 achieved a dose-dependent target engagement of up to 98% in the lungs of these patients. These preliminary data provide insights into the potential mechanism and clinical benefits of PLN-74809 as an antifibrotic therapeutic in IPF. This is also an example of the important role our field can play in working with the pharmaceutical industry to apply new markers to advance development of novel treatments.

Wilks et al. from Massachusetts General Hospital/Harvard Medical School (Boston, MA) reported on “PET imaging of neutrophil trafficking fungal infection” [2511]. Imaging infection and the immune system was the focus of much interest at this year’s meeting, again an area of unmet needs. These authors have designed a neutrophil precursor cell line that can be expanded *ex vivo* and transfused into neutropenic subjects to allow them to successfully combat fungal infections. In this study, they quantified the kinetics of these infused cells using PET imaging in healthy and neutropenic mice. With an ^{89}Zr -labeled agent, they were able to track exogenous neutrophils quantitatively and noninvasively in healthy, ablated, and fungal-infected mice for up to 7 d after infusion. Lower splenic uptake was observed in

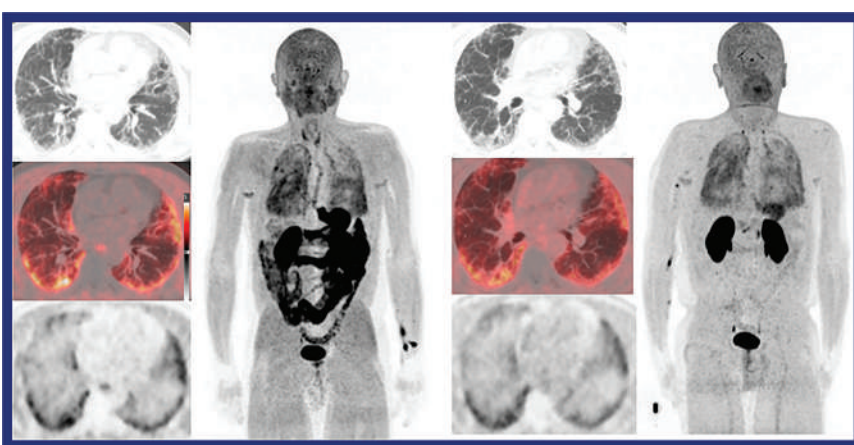


FIGURE 5. Imaging PLN-74809 in patients with idiopathic pulmonary fibrosis (IPF) with a novel $\alpha_v\beta_6$ cystine knot PET tracer. Example [^{18}F]FP-R₀1-MG-F PET/CT images acquired at baseline (left) and after administration of the antifibrotic drug (right). PET/CT enabled target engagement of PLN-74809 with $\alpha_v\beta_6$ integrin receptors in the lungs of IPF patients, showing dose-dependent target engagement of up to 98%.

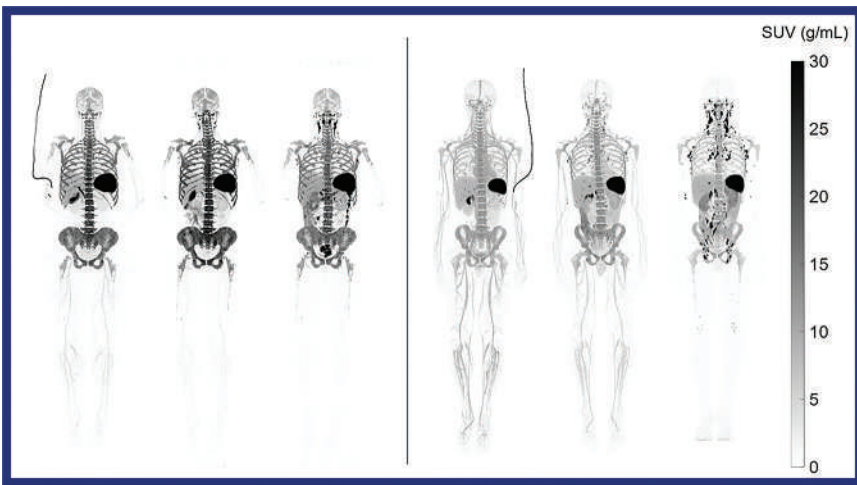


FIGURE 6. Imaging CD8⁺ T cells in patients recovering from COVID-19. ⁸⁹Zr-Df-crefmirlimab-berdoxam total-body PET with the uEXPLORER, showing SUV maximum-intensity projection images at (left to right in each image set) 30–90 min, 6–7 h, and 48–49 h in a post-COVID patient (left set) and a control subject (right set). High-definition tracking of T cell distribution in lymphoid organs was achieved, with a preliminary observation that recovering COVID-19 subjects had higher T cell mass than controls.

Candida-exposed animals, suggesting an active immune response to fungal infections. This work opens the door not only to enhanced understanding of the response of specific elements of the immune system to infections (fungal and bacterial) but also to development and optimization of neutrophil transfusion therapies in neutropenic patients. We look forward to seeing associated clinical data in the not-too-distant future.

Tremendous interest across all scientific and technical tracks at this meeting continued to focus on total-body PET imaging. In his Cassen Lecture, Simon Cherry, PhD, told us that it is only a matter of time until total-body PET is even faster, and the images his group is producing are truly remarkable. In one of these studies,

Omidvari et al. from the University of California Davis/University of California Davis Medical Center (Sacramento), Imperial College (London, UK), and ImaginAb (Inglewood, CA) reported on “Total-body imaging of CD8⁺ T cells in patients recovering from COVID-19: a pilot study using the uEXPLORER total-body PET” [2327]. Their goal was to obtain an *in vivo* quantitative measure of tissue distribution of CD8⁺ T cells by imaging with ⁸⁹Zr-Df-crefmirlimab-berdoxam, a minibody with high affinity to human CD8. In this pilot study, they aimed to quantify pathophysiologic changes in CD8⁺ T cell distribution in patients recovering from COVID-19 to illuminate the immunologic response and role of T cells in COVID-19 morbidity and immunity. The authors should be congratulated on the beautiful images they were able to acquire up to 48 h after submilli-curie (0.5 mCi) doses (Fig. 6). This imaging resulted in high definition of the expected distribution of T cells in lymphoid organs and derivation of high-quality Patlak parametric maps, along with a preliminary observation that recovering COVID-19 subjects in the study had higher T cell mass than controls. They concluded that “This study makes a compelling case to explore such *in vivo* functional aspects of T cells across a wide range of COVID-related conditions, vaccine response, and in clinical immunologic research in general, using the unique tools that total-body PET provides.”

Tumor-targeting bacteria are being investigated as therapeutic tools for solid tumors, and PET may have a role in the development and translation of these agents by providing data to confirm localization and proliferation of bacteria at the tumor site and to monitor off-target effects. Ordoñez et al. from T3 Pharmaceuticals AG (Basel, Switzerland) and Johns Hopkins University School of Medicine (Baltimore, MD) reported on “Imaging tumor-targeting bacteria using ¹⁸F-fluorodeoxysorbitol [¹⁸F-FDS] PET” [2510]. This is an interesting application of the concept of bacteria targeting. They evaluated in a murine model whether ¹⁸F-FDS PET could accurately monitor colonization of breast cancer tumors by a genetically modified strain of *Y. enterocolitica* (T3P-Y004) that is currently being evaluated for clinical trials. The researchers found that PET was able to differentiate sites of bacterial infection with low background in most organs, including the tumor site (Fig. 7). They concluded that “given that ¹⁸F-FDS is available for clinical use, bacteria-specific PET could be a valuable tool to support the development and implementation of tumor-targeting bacteria therapeutics.”

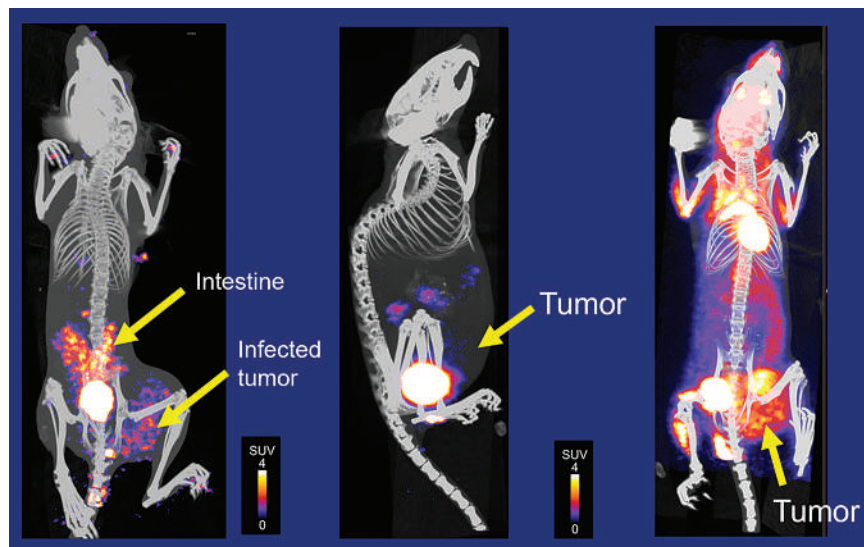


FIGURE 7. Imaging tumor-targeting bacteria in a mouse model using ¹⁸F-FDS PET. PET was able to differentiate sites of bacterial infection with low background in most organs, including the tumor site (left and right) compared with uninfected controls (middle), pointing to the potential for other applications of bacteria-specific PET to support development of tumor-targeting bacteria therapeutics.

From a very different but no less important global perspective, Giammarile et al. from the International Atomic Energy Agency (IAEA; Vienna, Austria) reported on “The IAEA Quality Management Audits

in Nuclear Medicine Practices (QUANUM) program: a practical tool for quality audits in nuclear medicine” [2776]. A key question as we leverage the power of aggregated data from clinical trials throughout the world is: How do we ensure that the quality of what we do and the protocols we use are similar and consistent? Through QUANUM, the IAEA supports implementation of effective quality systems while integrating all aspects of quality management into modern nuclear medicine services in its member states. The QUANUM program provides a tool to perform independent quality audits of nuclear medicine departments through comprehensive reviews of organizations and their clinical practice, as well as offering multidisciplinary team site visits. In their report, the IAEA authors described integration of the program in 73 nuclear medicine centers in 46 countries and detailed outcome analyses of the impact on practice quality. This is an important take home message for all of us: We need quality programs using protocols that can be reproduced from one institution to another, so that we all speak the same language about reports and images from our patients.

Another area increasingly emphasized by SNMMI and very important to all of our clinical practices and trials is that of diversity and representation. How do we make sure that the research we do is representative of the populations we serve? How do we encourage enrollment of patients who reflect the diversity of the areas in which we practice? Badawi et al. from the University of California Davis (Sacramento) reported on “Diversifying the subject cohorts in total-body PET research: a feasibility study” [2780]. In this pilot effort, the uEXPLORER group targeted trial recruitment of

healthy subjects from underrepresented racial/ethnic groups in their catchment area. They consulted with their community advisory board to review existing trial/treatment publicity material for inclusivity and arranged for TV and radio spots, advertisements, and news articles. The result was more than 155 inquiries, and the underrepresented recruitment goal was met. This study offers a template for outreach and recruitment in studies that aim to be more representative of the diversity of the local community.

CONCLUDING THOUGHTS

I will end with an editorial thought: my own perspective on all these perspectives. As the saying goes, “the stone age did not end because humans ran out of stones”; similarly, the age of photomultiplier tubes did not end for lack of photomultiplier tubes. It ended because industry, academia, and private practice put a great deal of effort into continued innovation and clinical adoption. I am confident that the end of the age of planar imaging in general nuclear medicine will not come about because of a lack of standard scanners. It will be because the technology has advanced, so that we do not need to do planar all the time—we will have protocols adapted to target the specific organ of interest or to survey the whole body. As a community, we should strive to be early adopters. We should not be so busy with what we do on a routine basis that we fail to see the benefits of new technologies. I believe that we will continue to see new and even more innovative ways through which general nuclear medicine contributes to the advancement of both our field and the wider world of medical knowledge and health care.

Looking at the Future of Prostate Cancer Treatment

A Conversation Between Michael Morris, Jeremie Calais, and Johannes Czernin

Michael J. Morris¹, Jeremie Calais², and Johannes Czernin³

¹Memorial Sloan Kettering Cancer Center, New York, New York; ²University of California at Los Angeles, Los Angeles, California; and ³David Geffen School of Medicine at UCLA, Los Angeles, California

Johannes Czernin, MD, editor in chief of *The Journal of Nuclear Medicine*, and Jeremie Calais, MD, MSc, his colleague at the University of California Los Angeles, talked with Michael J. Morris, MD, Member and Attending and Prostate Cancer Section Head at Memorial Sloan Kettering Cancer Center, and a professor in medicine at Weill Cornell Medicine (both in New York, NY). Dr. Morris received his medical degree from the Icahn School of Medicine at Mount Sinai in 1994, followed by a residency in medicine at Columbia Presbyterian Medical Center (both in New York, NY). He completed a fellowship in oncology at MSKCC. He specializes in treating patients with prostate cancer, with a focus on those who have or are at high risk of developing metastatic disease. He has established an international reputation in the field of bone- and tumor-directed radiopharmaceuticals and for multidisciplinary collaborative efforts in developing novel imaging biomarkers for prostate cancer. Dr. Morris is the medical director of the Prostate Cancer Clinical Trials Consortium, an initiative funded by the Department of Defense and Prostate Cancer Foundation and designed to increase patient access to clinical trials in the United States.

Dr. Czernin: Can you tell us a little bit about your training and how you became a leading prostate cancer expert?

Dr. Morris: My background is in medical oncology. I was trained here in New York City, where I also grew up. My original interest in oncology arose because there were and are so many unanswered questions for cancer and also for prostate cancer. When I started, we basically had hormonal therapy. Little was known about the disease biology. I became interested in prostate cancer in my first year of fellowship and, at that time, began developing relationships with 2 mentors. One was Steven M. Larson, MD, who was in charge of nuclear medicine at that time at Memorial, and the other was Howard Scher, MD, who was in charge of genitourinary oncology. Since prostate cancer at that point was nearly a nonimageable disease and the whole world of therapeutics was wide open, I have stayed in that niche for the rest of my career.

Dr. Calais: You have a specific interest in nuclear medicine techniques, both for imaging and therapy. Can you tell us how you got into that?

Dr. Morris: Steve Larson inceptioned my interest in imaging, and Howard Scher got me interested in drug and biomarker development. Prostate-specific membrane antigen (PSMA) was cloned by Warren Heston, PhD, shortly before my fellowship began, and through the years I've been part of efforts to develop antibody approaches, small-molecule targeting agents, and α - and β -therapies. Over the last 20 y this became a success story through exemplary worldwide collaborations.

Dr. Czernin: Can you comment on the changing role of bone scans with the emergence of PSMA and how you adapt your clinical practice to the different kinds of resulting information?

Dr. Morris: The bone scan index (BSI) was the brainchild of Steve Larson. It was the first time we could take a nonquantitative disease like prostate cancer and create the size or numeric information that is key to biomarker development in a prostate cancer context. The BSI also stimulated artificial intelligence (AI) applications, because doing this manually is incredibly work intensive. In turn, this also showed how AI could (even in what was then a primitive form) transform how we think about disease and turn the nonmeasurable into the measurable in a practical way. This constituted a set of intellectual landmarks that was and still is a good way of quantifying disease burden for the purposes of prognosis and response assessments.

Dr. Calais: Can you comment on the collaborations between Sloan and EXINI Diagnostics that helped to translate the BSI? Could the same approach be applied to PSMA?

Dr. Morris: I think that the international collaboration with EXINI (now part of Lantheus) demonstrated that academia-industry collaborations can be very fruitful, as long as both participants bring something to the table. EXINI was a small company, and frequently those relationships work best, because everyone is interested in moving quickly and nimbly and doing the research as expeditiously as possible. This does set the table for a future model for PSMA AI collaborations with industry. PSMA AI will become much more influential, because PSMA has much wider applications in illuminating disease biology, disease extent, and potentially in response and progression assessments. The challenge to AI in today's environment is working with a set of platforms that are willing to undergo the full biomarker qualification process from analytic validation to clinical qualification. But we don't have a mechanism to charge insurances for PSMA imaging for serial treatment response



Michael J. Morris, MD

Received Mar. 6, 2023; revision accepted Mar. 6, 2023.

For correspondence or reprints, contact Johannes Czernin (jczernin@mednet.ucla.edu).

Published online Apr. 13, 2023.

COPYRIGHT © 2023 by the Society of Nuclear Medicine and Molecular Imaging.
DOI: 10.2967/jnumed.123.265684

assessments. So, we need a third party at the table, not only the software developer and the investigators but someone to ensure funding of the serial scans.

Dr. Calais: *Imaging should be covered, but the additional dimension of the AI approach would need to be reimbursed as well, and companies need a viable business model as an incentive.*

Dr. Morris: Serial bone scans look at treatment effects and are considered standard of care, but PSMA imaging is not. You need a stakeholder to fund the serial scans that could be on a clinical trial, and a therapeutic sponsor could pay for the trial. Imaging funding could be sourced from an imaging co., or it could be national funding through NCI or some other source. That cost, of course, could be shared, because development of a PSMA-based response biomarker would actually benefit all stakeholders.

Dr. Czernin: *You used the BSI before, and now PSMA enters the diagnostic scene with very different staging information and stage migration. This is a predicament for the oncologists. Nevertheless, you need to collect this information, because it is very useful—but that's different from acting on the information. In the range of scenarios from primary prostate cancer to recurrence to castrate-sensitive and -resistant disease, how do you deal with the different PSMA imaging-based information?*

Dr. Morris: In the past, our problem was that we could never really see the distribution of disease. Now we have the imaging to see those areas, and we're thinking, "Oh my, what are we going to do with this previously unknown pelvic or distant disease?" But this is the problem we've been wanting—a scenario in which we don't need nomograms and models because we can actually see the disease much earlier now. We can develop therapeutics based on better imaging and knowing where the disease is and how to adjust our therapeutic strategies accordingly rather than with

Dr. Morris: We have the issue of PSMA heterogeneity. Can we identify characteristics of patients who may have low or heterogeneous PSMA expression? For those patients, other potential targets can and should be developed, both for therapy and for diagnostics. These include prostate-specific antigen (PSA)-like human kallikrein 2 and prostate stem cell antigen, which look quite promising. Fluorinated dihydrotestosterone has great potential as a biomarker for AR-targeted drugs. The δ -like ligand 3 has real promise in small-cell lung cancer and, thus, potentially in neuroendocrine prostate cancer. The neuroendocrine patient population has a truly unmet need, and the whole world of diagnostics and therapeutics should be applied to them, because we have so little to offer otherwise.

Dr. Czernin: *What about FDG?*

Dr. Morris: It's almost ironic that we're talking about FDG, because our group has always believed that it had validity and informative value. The field went through many years of considering FDG as a poor imaging modality for prostate cancer. Now several groups, such as that of Michael Hofman, MBBS, have shown its utility in the realm of therapeutics. All the metabolic tracers, including fluciclovine and choline, still have roles in poorly differentiated disease and in identifying disease that does not have a specific molecular therapeutic target for a therapeutic purpose in terms of treatment selection.

Dr. Calais: *Let's switch to a look at the big therapeutic trials that have been published recently using various radiopharmaceutical-based therapies. Can you give us an overview, and are you satisfied with the results?*

Dr. Morris: The VISION trial was a very important study for all of us. Had the results not been positive, it would have been devastating for the field. VISION showed that radioligand therapy

"In terms of risk reduction and absolute benefit in overall survival and improvement in quality of life, radioligand therapy stands on its own compared with other therapeutics. The harder question is whether we might amplify these benefits by applying it earlier in the disease course, and in combination with other treatments."

model-based probabilities. But you are absolutely right that we do have stage migration and, indeed, a complete redefinition of staging. Now we have all these subcategories of "nonvisualized on standard imaging but visualized by PSMA." In some prostate cancer stages this makes a huge difference, especially, for example, in high-risk, localized disease, because now we are, in essence, re-categorizing some of these patients as having metastatic disease. This raises several questions. Should we be addressing the primary cancer in that context? How do we define high- and low-volume disease? How do we best stratify patients? Some clinical trials will have to be redone to develop evidence-based treatment plans that incorporate PSMA imaging. It makes a difference for medical treatment and introduces the entire concept of metastasis-directed therapy for low-volume/lower risk patients. Other questions naturally follow. How is metastasis-directed therapy best achieved? Is it with androgen receptor (AR)-directed therapy alone? What is the appropriate disease volume to be defined as no longer oligometastatic but polymetastatic? All of these questions still need to be addressed. I think that PSMA imaging's stage migration allows us to identify disease now to ask those questions much more accurately and earlier.

Dr. Calais: *In addition to PSMA PET imaging, what other PET or SPECT tracers do you consider highly valuable?*

can work for our most advanced prostate cancer patients. The trial taught a very important lesson for developing PSMA-based or other therapeutics, underscoring that the imaging component is key to successfully developing a drug. VISION also demonstrated that radioligand therapy can be successfully tested in prostate cancer, clinically benefit patients, and earn regulatory approval. It sets the path for radioligand therapy's future development in this disease. Studies are now examining the value of radioligand therapy in chemotherapy-naïve metastatic castrate-resistant prostate cancer (CRPC) and in metastatic castration-sensitive disease, both phase III registration trials. VISION's success has opened the door for potential success for ^{225}Ac . So, I think the trial was important beyond lutetium PSMA-directed therapy, improving survival and quality of life in patients with metastatic CRPC.

Dr. Czernin: *The criticism would be that everyone relapses after a fairly short time and that no one has ever been cured. How can you improve response rates, and how do you address resistance?*

Dr. Morris: People who criticize VISION on the basis that the median survival benefit was around 4 mo are not really seeing what defines success in a patient population with so few months left to live. Pretty much every drug that has been considered a success in that patient population has had a 4-mo survival benefit. VISION

was conducted in patients after AR pathway inhibition and after chemotherapy and, in some cases, after 2 different regimens of each. And in this very advanced setting, the VISION trial still saw a 4-mo survival benefit. I never tell any patient, even with early metastatic disease, that I have a cure or that we know how to cure their disease. I'm not even sure that the "cure" word is really useful. We don't cure diabetes, we don't cure HIV, but we can have those patients live full, productive, satisfying, complete lives despite those chronic diseases. I am not sure I would set up the expectation that disease eradication is the definition of success for metastatic cancer or that failure to eradicate disease means we failed to do right by the patients. You raise a very important point, though, that we can and must do better. This will happen as a combination of better patient selection on the bases of their disease biology and underlying genetics, as well as better stratification, treatment combinations and sequencing, and better drugs, all of which should achieve better outcomes than those VISION showed with the drug alone in the last phases of the disease.

Dr. Calais: Let's discuss briefly the current production and supply chain issues of α - and β -radiopharmaceuticals and how this has already affected your clinical work and trials.

Dr. Morris: The field has had some significant supply issues for lutetium as well for actinium over the last several months. This is a big issue, because there is so much patient, physician, and investigator need for these drugs. We have wait lists, and we're just trying to keep up with them. The lack of drug availability is devastating to patients. In addition, as a field we need to build out expertise for the day when the drug is more readily available. How many centers have true multidisciplinary teams in which nuclear medicine, medical oncology, and radiation oncology are working hand-in-hand in clinics to best treat these patients? How many centers have the physical space in their nuclear medicine departments to treat a disease as common as prostate cancer? It's really a need to organize joint care for patients, upskilling the medical oncologists to understand nuclear medicine issues and nuclear medicine physicians to understand general medical oncology issues. This process will go through growing pains. In terms of transitioning to α -labeled therapies, we still have to go through a much longer drug development period than people think. There is much more to figure out in terms of drug supply, mitigating salivary gland toxicity, and understanding how to best do dosing and how much "drug" we are delivering to tumors.

Dr. Czernin: You talked about the need for qualified providers and sites. We probably need about 100 sites in the United States to provide adequate services, and we are far from that. But there's another issue that you mentioned, and that's insurance coverage. PSMA-targeted diagnostics and therapy are now included in the National Comprehensive Cancer Network guidelines, so coverage should be provided.

Dr. Morris: Insurers' guidelines do not synchronize with best practice. For example, for the biochemically relapsed patient population, some insurers insist on a bone scan or CT before a PSMA PET. Such a requirement exposes patients to unnecessary radiation, inconvenience, and expense. Insurers are also asking for PSA thresholds above those at which we believe patients should get salvage therapy. We need to reach out to the insurers' medical directors and understand how they arrive at these thresholds.

Dr. Calais: When you compare the actual production costs of radionuclide-based therapies with conventional androgen-deprivation

therapy (ADT), do you think they are worth it? Are they sustainable? ADT already does a decent job in this advanced-age population. Is the added benefit, compared with that of the standard of care, sufficient to justify the very high costs?

Dr. Morris: For patients like those in the VISION trial who are at the end of their lives, there is no cheaper alternative, other than hospice care. It costs money to prolong life, preserve quality of life, and maintain functionality. In terms of risk reduction and absolute benefit in overall survival and improvement in quality of life, radioligand therapy stands on its own compared with other therapeutics. The harder question might be whether if it were delivered earlier in the course of the disease, are we really making more than an incremental benefit relative to AR-directed therapy alone or chemotherapy? We don't have the data to answer that. Long-term toxicity might be an issue as well. Cancer care is extraordinarily expensive in the United States and is a huge cause of psychologic distress and bankruptcy. Part of the answer to these issues lies in what incentivizes our health care system. But within that system, this also touches on the question of whether we should be treating advanced cancer patients with therapies other than palliative measures. I think the answer is yes.

Dr. Czernin: You have already talked about quality theranostic centers and what they should look like. Did you do a demand assessment for these therapies at MSKCC? What kind of patient volumes do you anticipate?

Dr. Morris: Our demand right now is much higher than it will be in a year or so, because we've had patients waiting for approval and waiting for drug supply. So we have a very long wait list right now of patients who are just trying to survive long enough to get treatment. These patients are deteriorating with every week that passes. Some of them will not survive to get treatment, which is very sad. But I hope that the drug supply issue is resolved quickly so that we can hit a steady state, with patients receiving the treatment they need.

Dr. Calais: As you already pointed out, medical oncologists, radiation oncologists, surgeons, and radiologists are already communicating relatively well, but nuclear medicine is sometimes a new addition. Can you comment on your relationships with your nuclear medicine colleagues, what you think these should be, and what you like and don't like in these relationships?

Dr. Morris: My relationship with nuclear medicine has always been outstanding. But in many centers, nuclear medicine is not part of shared research or shared clinical care. We need multidisciplinary integration of all the people who are actually caring for the patients, not only the doctors but nurses, pharmacists, and radiation safety experts working together. We have just created a new virtual clinic where all of the stakeholders now review together once a week every single patient. Our clinical trials continue to run as multidisciplinary studies, but we've had to create a new infrastructure for routine clinical care. What nuclear medicine still needs is a model of continuity of care. Each patient should have 1 nuclear medicine doctor longitudinally, just as is true with medical oncology, urology, and radiation oncology. The medical oncologists need to learn more about radiopharmaceuticals, related dosages, safety issues—the whole routine. Similarly, the nuclear medicine physicians need to learn more about basic management of side effects beyond just their own treatments. Both sides need to up-train and to grow and develop practice patterns to optimize continuity of care for the patient.

Dr. Czernin: The quality of the clinical research has markedly improved. If you consider trials that need to be done for

diagnostics and therapeutics, what would be your number 1 and 2 priorities?

Dr. Morris: For diagnostics, the most important trial that needs to be done now is verifying PSMA as a response and progression biomarker. This would shorten drug development profoundly. Right now, we have to wait for either radiographic progression-free survival data by standard scans or overall survival data in order to get a drug approved. Therapeutically, it is probably not the iterative trials that we're talking about with this generation of drug. It is looking forward to moving into the α -emitters and validating them as the next generation of therapies.

Dr. Calais: *If we were to enter the 3 keywords “Morris,” “nuclear medicine,” and “future” into a PubMed search, what results would you want to see there for our readership?*

Dr. Morris: It's hard to predict the future, but whatever the future holds it will depend on collaboration. My message to the nuclear medicine research community is that there is a body of knowledge that nuclear medicine has and that medical oncology does not have. Conversely, there is a body of knowledge that the medical oncologists have that nuclear medicine lacks. The effort to develop radioligand therapy should be a much more jointly informed clinical and research effort than it currently is. And we need to better take care of patients together. But communication and collaboration are fundamental to the pathway that we will share in the future. The more we do that, the more productive we will be.

Dr. Calais: *Thank you very much for your time. It is really a pleasure to communicate and collaborate with you.*

The Emergence of Somatostatin Antagonist-Based Theranostics: Paving the Road Toward Another Success?

Alessio Imperiale^{*1,2}, Abhishek Jha^{*3}, Leah Meuter³, Guillaume P. Nicolas⁴, David Taieb⁵, and Karel Pacak³

¹Nuclear Medicine and Molecular Imaging, ICANS, Strasbourg University, Strasbourg, France; ²Molecular Imaging–DRHIM, IPHC, UMR-7178, CNRS/Unistra, Strasbourg, France; ³Eunice Kennedy Shriver NICHD, National Institutes of Health, Bethesda, Maryland; ⁴Division of Nuclear Medicine, Center for Neuroendocrine and Endocrine Tumors, University Hospital Basel, Basel, Switzerland; and ⁵La Timone University Hospital, CERIMED, Aix-Marseille University, Marseille, France

The value of in vivo peptide receptor targeting for imaging and treating oncologic patients is well accepted and implemented in clinical practice. A prime example is somatostatin receptor (SSTR)-targeted peptide receptor radionuclide therapy (PRRT), which relies on an image-and-treat approach (theranostics), a rapidly evolving clinical concept in patients with neuroendocrine tumors (NETs).

SSTR agonists are internalized after high-affinity ligand receptor binding and have historically been used for in vivo SSTR receptor targeting. This mechanism is considered an essential step in in vivo receptor targeting using SSTR agonists (Fig. 1). The evolving PET/CT technology and the optimization of radiopharmaceutical chelation for effective somatostatin analog development opened the door to [⁶⁸Ga]Ga-DOTA⁰-Tyr³-octreotate ([⁶⁸Ga]Ga-DOTATATE) PET/CT. In 2016, [⁶⁸Ga]Ga-DOTATATE received Food and Drug Administration approval for SSTR imaging, followed by [⁶⁸Ga]Ga-DOTATOC and [⁶⁴Cu]Cu-DOTATATE in 2019 and 2020, respectively. SSTR-based PRRT was explored by the phase 3 NETTER-1 trial, a first-in-humans prospective multicenter randomized clinical trial comparing [¹⁷⁷Lu]Lu-DOTATATE (4 cycles, 7.4 GBq/cycle) with high-dose octreotide in 229 patients with progressive low-grade midgut NETs.

The NETTER-1 trial significantly improved progression-free survival with [¹⁷⁷Lu]Lu-DOTATATE, with a hazard ratio of 0.18 (95% CI, 0.11–0.29; $P < 0.0001$) (1). However, 5 y after the last patient randomization, there was no statistically significant difference in median overall survival between the [¹⁷⁷Lu]Lu-DOTATATE arm (48 mo; 95% CI, 37.4–55.2) and the control arm (36.3 mo; 95% CI, 25.9–51.7) despite a clinically significant improvement of the quality of life and progression-free survival in the [¹⁷⁷Lu]Lu-DOTATATE arm (1). Concerning treatment safety, only 3 of 111 patients (3%) of the [¹⁷⁷Lu]Lu-DOTATATE arm showed treatment-related severe adverse events during long-term follow-up, and 2 patients (2%) developed myelodysplastic syndrome, one of whom died 33 mo after randomization. No new cases of myelodysplastic syndrome or acute myeloid leukemia were reported during long-term follow-up.

At present, the NETTER-2 trial is ongoing to determine whether [¹⁷⁷Lu]Lu-DOTATATE prolongs progression-free survival in grade 2 or 3 gastroenteropancreatic NETs as first-line treatment in combination with long-acting octreotide (NCT03972488). A recent metaanalysis including more than 1,200 patients treated by [¹⁷⁷Lu]Lu-DOTATATE (1–8 cycles, 3.7–10 GBq/cycle) revealed a disease control rate (proportion of complete response, partial response, minor response, and stable disease) of 74.1% (95% CI, 67.8%–80%) and a disease response rate (proportion of complete response, partial response, and minor response) of 29.1% (95% CI, 20.2%–38.9%) (2). This evidence contributed to the inclusion of [¹⁷⁷Lu]Lu-DOTATATE in the therapeutic algorithms proposed by leading international societies as an effective and safe treatment option for NETs. Recently, a novel SSTR-agonist radioligand, [⁶⁴Cu]⁶⁴Cu-SARTATE, was compared with [⁶⁸Ga]Ga-DOTATATE, showing higher uptake and retention resulting in high-contrast diagnostic images upward of 24 h (3). [⁶⁷Cu]Cu-SARTATE, the therapeutic counterpart of [⁶⁴Cu]Cu-SARTATE, is currently being evaluated (NCT04023331).

Over the years, novel data have emerged for SSTR antagonists. The application of SSTR antagonists was initially discouraged because of lack of internalization. Despite these initial considerations, it was later found that a higher percentage of SSTR antagonists than of agonists was bound in animal and human models. This can be attributed mainly to the functional interaction of SSTR antagonists with a larger variety of SSTR conformations, allowing binding of both activated and inactivated SSTRs (Fig. 1) (4,5). Slow dissociation of antagonist receptor binding and minimal internalization are also thought to play a role in tumor detection. Further, SSTR antagonists are more chemically stable and hydrophobic than SSTR agonists, with a consequent longer duration of action and stabilization in a lipid-rich environment (4).

From a theranostic point of view, the high target-to-background ratio and prolonged in vivo tumor binding obtained with radiolabeled SSTR antagonist have been of paramount importance in promoting the use of SSTR antagonists over SSTR agonists. Compared with [⁶⁸Ga]Ga-DOTATATE in NETs, both [⁶⁸Ga]Ga-NODAGA-LM3 and [⁶⁸Ga]Ga-DOTA-LM3 demonstrated a significantly higher detection of liver metastases (202 vs. 235, $P = 0.01$, and 196 vs. 261, $P = 0.02$, respectively) and overall lesions (339 vs. 395, $P = 0.002$, and 372 vs. 447, $P = 0.02$, respectively), with a higher tumor-to-liver ratio of matched lesions in both arms ($P = 0.00$). There was no significant difference in detection of primary tumors (17 vs. 19, $P = 0.16$, and 13 vs. 15, $P = 0.16$, respectively), lymph

Received Jan. 4, 2023; revision accepted Feb. 2, 2023.

For correspondence or reprints, contact Alessio Imperiale (a.imperiale@icans.eu).

*Contributed equally to this work.

Published online Feb. 9, 2023.

COPYRIGHT © 2023 by the Society of Nuclear Medicine and Molecular Imaging.

DOI: 10.2967/jnumed.123.265406

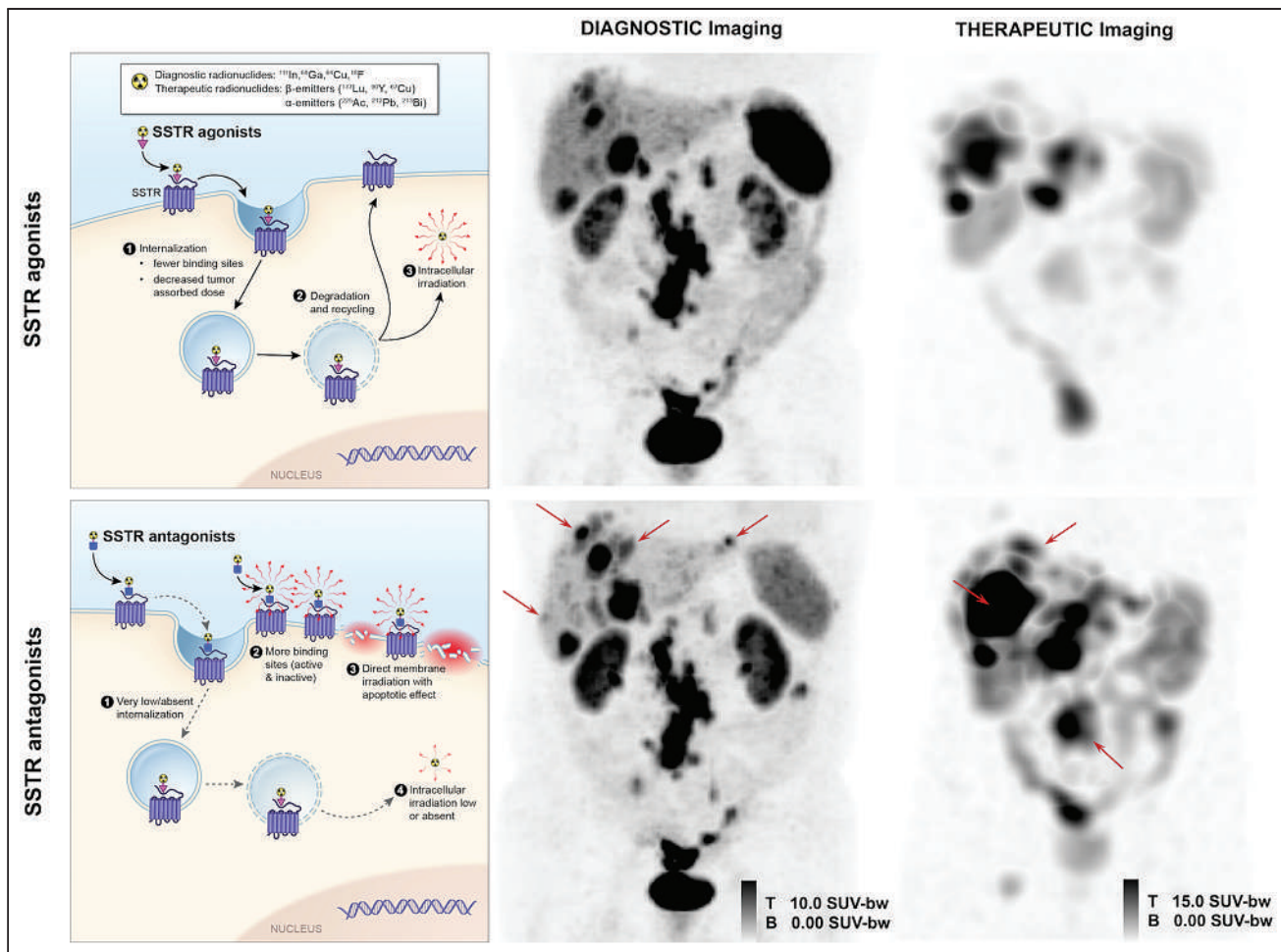


FIGURE 1. (Left) Mechanism of action of radiolabeled SSTR agonists and antagonists for theranostics application. SSTR agonists are internalized after binding to SSTR2, with consequent accumulation of radioactivity in cell. In contrast, SSTR antagonists bind more effectively to receptors on cell membrane, with near absence of internalization and direct membrane damage. (Middle) Head-to-head comparison between PET images (anterior maximum-intensity projection; SUV_{max} range, 0–10) of [⁶⁸Ga]Ga-DOTATOC (SSTR agonist) and [⁶⁸Ga]Ga-NODAGA-JR11 (SSTR antagonist) in patient with low-grade NET, showing more lesions (arrows, particularly in liver) for [⁶⁸Ga]Ga-NODAGA-JR11 than for [⁶⁸Ga]Ga-DOTATOC. (Right) Direct comparison of posttreatment SPECT images (anterior maximum-intensity projection; SUV_{max} range, 0–15) after [¹⁷⁷Lu]Lu-DOTATOC (cycle 1) and [¹⁷⁷Lu]Lu-DOTA-JR11 (cycle 2) performed within 10-wk interval. Tumor activity concentration at 24 h after injection is ~30% higher with antagonist (arrows) than with agonist even though administered activity of ¹⁷⁷Lu is ~50% less for antagonist than for agonist (3.9 vs. 7.4 GBq). B = bottom; bw = body weight; T = top.

node metastases (24 vs. 27, $P = 0.18$, and 29 vs. 32, $P = 0.18$, respectively), bone metastases (31 vs. 46, $P = 0.11$, and 126 vs. 126, $P = 1.00$, respectively), or other lesions (65 vs. 68, $P = 0.32$, and 8 vs. 13, $P = 0.10$, respectively) (6). In another comparative study, [⁶⁸Ga]Ga-DOTA-JR11 detected more liver (552 vs. 365, $P = 0.001$) but fewer bone (158 vs. 388, $P = 0.02$) metastases than ⁶⁸Ga-DOTATATE, but with comparable primary tumor detection (20 vs. 24, $P = 0.50$) and overall detection rate (835 vs. 875, $P = 0.15$) and with equal lymph node (43 vs. 43), pleural (51 vs. 51), and peritoneal (2 vs. 2) metastases (7). Similarly, in 12 gastroenteropancreatic NET patients, [⁶⁸Ga]Ga-NODAGA-JR11 demonstrated a significantly higher overall sensitivity (94% with 50 μ g and 88% with 15 μ g of [⁶⁸Ga]Ga-NODAGA-JR11) compared with [⁶⁸Ga]Ga-DOTATOC (15 μ g, 59.2%, $P < 0.001$, for both doses of [⁶⁸Ga]Ga-NODAGA-JR11) (8).

Radioligand SSTR antagonists have been documented to bind a higher percentage of SSTRs than do agonists (Fig. 1), increasing targeting even for tumors with low SSTR expression (4,5). This would be clinically important in high-grade NETs, poorly differentiated

neuroendocrine carcinoma, and certain non-NETs (breast carcinomas, renal cell carcinomas, and non-Hodgkin lymphomas) (9). For these reasons, there has been increasing interest in SSTR antagonists. In humans, 2 theranostic pairs of JR11 (i.e., [⁶⁸Ga]Ga-DOTA-JR11/[¹⁷⁷Lu]Lu-DOTA-JR11 and [⁶⁸Ga]Ga-NODAGA-JR11/[¹⁷⁷Lu]Lu-DOTA-JR11) have already been investigated (10,11). However, the safety profile of SSTR antagonists for PRRT requires further consideration and optimization. Severe hematotoxicity was observed compared with SSTR agonists at doses equivalent to or greater than that to red marrow. In a recent phase I clinical trial (12), 4 of 4 patients who received 2 cycles of [¹⁷⁷Lu]Lu-satoreotide-tetrahexan (also known as [¹⁷⁷Lu]Lu-DOTA-JR11) and an estimated bone marrow dose of at least 1.44 Gy developed grade 4 thrombocytopenia (and grade 3/4 neutropenia) and 57% developed grade 4 myelosuppression, but none of the patients with a bone marrow dose of 1.08 Gy or less experienced grade 4 thrombocytopenia or neutropenia. Therefore, the therapeutic protocol was revised to lower the bone marrow dose from 1.5 to 1 Gy and, subsequently, halve the dose in cycle 2. However, the hypothesis that the activity concentration in red

marrow is comparable to that in blood (11) could probably be reconsidered, as SSTR antagonists may have specific binding in red marrow, also supporting a dedicated dosimetry based on posttherapeutic SPECT/CT imaging.

[⁶⁸Ga]Ga-DOTA/NODAGA-LM3 and [¹⁷⁷Lu]Lu-DOTA-LM3 represent another attractive SSTR-antagonist-based theranostic pair with high tumor binding and preliminary favorable dosimetry (13). Furthermore, radiolabeling of SSTR antagonists with α -emitters would provide a joint benefit from the biologic characteristics of the antagonists and the physical properties of the α -emitters, with potential therapeutic advantages even in patients refractory to treatment with β -emitter-labeled somatostatin analogs.

In conclusion, published literature strongly suggests that SSTR antagonists are characterized by no cellular internalization but a strong binding capacity to SSTR receptors, suggesting a higher efficacy than SSTR agonists that undergo cellular internalization and have weaker SSTR binding. These unique characteristics of SSTR antagonists are now shifting clinical focus toward the use of radiolabeled SSTR antagonists to improve the diagnostic sensitivity (with some concerns at the bone level (7)) and therapeutic efficacy of SSTR-based PRRT. Although SSTR antagonists have been optimized at the diagnostic level, therapeutic applications must be further investigated. Decreasing administered activities, encouraging dosimetry, and increasing duration between PRRT cycles to limit hematotoxicity while preserving therapeutic efficacy should be further researched. Patients with multiple liver metastases and those with poorly differentiated NETs could be suitable candidates for promising new clinical investigations. Thus, SSTR antagonists currently represent a novel paradigm in theranostics that will undoubtedly revolutionize diagnostic and therapeutic management of NETs. We hope these discoveries will ultimately improve the clinical outcomes of patients with these rare tumors.

DISCLOSURE

This work was supported by the Intramural Research Program of the National Institutes of Health, Eunice Kennedy Shriver National Institute of Child Health and Human Development. No other potential conflict of interest relevant to this article was reported.

REFERENCES

1. Strosberg JR, Caplin ME, Kunz PL, et al. ¹⁷⁷Lu-Dotatate plus long-acting octreotide versus high-dose long-acting octreotide in patients with midgut neuroendocrine tumours (NETTER-1): final overall survival and long-term safety results from an open-label, randomized, controlled, phase-3 trial. *Lancet Oncol.* 2021;22:1752–1763.
2. Saravana-Bawan B, Bajwa A, Paterson J, McEwan AJB, McMullen TPW. Efficacy of ¹⁷⁷Lu peptide receptor radionuclide therapy for the treatment of neuroendocrine tumors: a meta-analysis. *Clin Nucl Med.* 2019;44:719–727.
3. Hicks RJ, Jackson P, Kong G, et al. Cu-SARTATE PET imaging of patients with neuroendocrine tumors demonstrates high tumor uptake and retention, potentially allowing prospective dosimetry for peptide receptor radionuclide therapy. *J Nucl Med.* 2019;60:777–785.
4. Jinj M, Zhang H, Waser B, et al. Radiolabeled somatostatin receptor antagonists are preferable to agonists for in vivo peptide receptor targeting of tumors. *Proc Natl Acad Sci USA.* 2006;103:16436–16441.
5. Fani M, Nicolas GP, Wild D. Somatostatin receptor antagonists for imaging and therapy. *J Nucl Med.* 2017;58(suppl 2):61S–66S.
6. Zhu W, Jia R, Yang Q, et al. A prospective randomized, double-blind study to evaluate the diagnostic efficacy of ⁶⁸Ga-NODAGA-LM3 and ⁶⁸Ga-DOTA-LM3 in patients with well-differentiated neuroendocrine tumors compared with ⁶⁸Ga-DOTATATE. *Eur J Nucl Med Mol Imaging.* 2022;49:1613–1622.
7. Zhu W, Cheng Y, Wang X, et al. Head-to-head comparison of ⁶⁸Ga-DOTA-JR11 and ⁶⁸Ga-DOTATATE PET/CT in patients with metastatic, well-differentiated neuroendocrine tumors: a prospective study. *J Nucl Med.* 2020;61:897–903.
8. Nicolas GP, Schreiter N, Kaul F, et al. Sensitivity comparison of ⁶⁸Ga-OPS202 and ⁶⁸Ga-DOTATOC PET/CT in patients with gastroenteropancreatic neuroendocrine tumors: a prospective phase II imaging study. *J Nucl Med.* 2018;59:915–921.
9. Cescato R, Waser B, Fani M, Reubi JC. Evaluation of ¹⁷⁷Lu-DOTA-sst2 antagonist versus ¹⁷⁷Lu-DOTA-sst2 agonist binding in human cancers in vitro. *J Nucl Med.* 2011;52:1886–1890.
10. Wild D, Fani M, Fischer R, et al. Comparison of somatostatin receptor agonist and antagonist for peptide receptor radionuclide therapy: a pilot study. *J Nucl Med.* 2014;55:1248–1252.
11. Krebs S, O'Donoghue JA, Biegel E, et al. Comparison of ⁶⁸Ga-DOTA-JR11 PET/CT with dosimetric ¹⁷⁷Lu-satoreotide tetraxetan (¹⁷⁷Lu-DOTA-JR11) SPECT/CT in patients with metastatic neuroendocrine tumors undergoing peptide receptor radionuclide therapy. *Eur J Nucl Med Mol Imaging.* 2020;47:3047–3057.
12. Reidy-Lagunes D, Pandit-Taskar N, O'Donoghue JA, et al. Phase I trial of well-differentiated neuroendocrine tumors (NETs) with radiolabeled somatostatin antagonist ¹⁷⁷Lu-satoreotide tetraxetan. *Clin Cancer Res.* 2019;25:6939–6947.
13. Baum RP, Zhang J, Schuchardt C, Muller D, Macke H. First-in-humans study of the SSTR antagonist ¹⁷⁷Lu-DOTA-LM3 for peptide receptor radionuclide therapy in patients with metastatic neuroendocrine neoplasms: dosimetry, safety, and efficacy. *J Nucl Med.* 2021;62:1571–1581.

Clinical Translation of Targeted α -Therapy: An Evolution or a Revolution?

Benedikt Feuerecker^{1–4}, Clemens Kratochwil⁵, Hojjat Ahmadzadehfar⁶, Alfred Morgenstern⁷, Matthias Eiber¹, Ken Herrmann^{3,8}, and Kelsey L. Pomykala⁹

¹Department of Nuclear Medicine, Technische Universität München, München, Germany; ²Department of Radiology, Technische Universität München, München, Germany; ³German Cancer Consortium, partner sites München, Heidelberg, and Essen, Germany; ⁴Department of Radiology, University Hospital, LMU München, München, Germany; ⁵Department of Nuclear Medicine, University Hospital Heidelberg, Heidelberg, Germany; ⁶Department of Nuclear Medicine, Klinikum Westfalen-Knappschaftskrankenhaus, Dortmund, Germany; ⁷European Commission, Joint Research Centre, Karlsruhe, Germany; ⁸Department of Nuclear Medicine, University Hospital Essen, Essen, Germany; and ⁹Institute for Artificial Intelligence in Medicine, University Hospital Essen, Essen, Germany

The field of radioligand therapy has advanced greatly in recent years, driven largely by β -emitting therapies targeting somatostatin receptor-expressing tumors and the prostate-specific membrane antigen. Now, more clinical trials are under way to evaluate α -emitting targeted therapies as potential next-generation theranostics with even higher efficacy due to their high linear energy and short range in human tissues. In this review, we summarize the important studies ranging from the first Food and Drug Administration-approved α -therapy, ^{223}Ra -dichloride, for treatment of bone metastases in castration-resistant prostate cancer, including concepts in clinical translation such as targeted α -peptide receptor radiotherapy and ^{225}Ac -PSMA-617 for treatment of prostate cancer, innovative therapeutic models evaluating new targets, and combination therapies. Targeted α -therapy is one of the most promising fields in novel targeted cancer therapy, with several early- and late-stage clinical trials for neuroendocrine tumors and metastatic prostate cancer already in progress, along with significant interest and investment in additional early-phase studies. Together, these studies will help us understand the short- and long-term toxicity of targeted α -therapy and potentially identify suitable therapeutic combination partners.

Key Words: targeted α -therapy; α -emitter; ^{225}Ac ; PSMA-617

J Nucl Med 2023; 64:685–692

DOI: 10.2967/jnumed.122.265353

The use of α -emitters has evolved over the past few years. They offer two advantages over treatments using β -emitters: first, α -radiation has a short range in tissues, resulting in irradiation of only a few cell diameters (<0.1 mm), allowing for selective treatment of cancer cells, and second, the high linear energy transfer of several megaelectron volts of α -radiation results in effective cell killing via DNA double-strand breaks (Fig. 1) (1). Therefore, close binding to the target is crucial to ensure therapeutic efficacy and safety.

To date, several clinical experimental α -treatments and an approved treatment for prostate cancer exist. ^{223}Ra -dichloride for treatment of bone metastases in castration-resistant prostate cancer was the first agent for which a survival benefit of 3 mo versus placebo was

proven in a prospective phase 3 randomized clinical trial. It paved the way for the clinical acceptance of targeted α -therapies (TATs) *in vivo* and is so far the only Food and Drug Administration-approved α -therapy (2,3). Additionally, for several other diseases, targets have been identified for α -therapy. Among them are bladder carcinoma showing overexpression of epidermal growth factor receptor (4), metastatic prostate cancer showing overexpression of prostate-specific membrane antigen, metastases of neuroendocrine tumors (NETs) with upregulated somatostatin receptors (5), glioma with substance P as a molecular target, and specific targets such as HuM195 in patients with leukemia (6).

Most of these TATs use either ^{213}Bi or ^{225}Ac as α -emitters, but many other radionuclides are currently discussed (^{149}Tb , ^{211}At , ^{212}Pb [for ^{212}Bi], $^{226/227}\text{Th}$, and ^{230}U) (7). Because of the short half-life of 46 min, ^{213}Bi -labeled agents have to be synthesized on site. In contrast, ^{225}Ac has 4 times more α -decays and a longer half-life (10 d), qualifying it as an attractive therapeutic nuclide-emitting energy of between 5.8 and 8.4 MeV (8). It has been proposed that because of the higher linear energy transfer of α -emitters, therapy resistance to β -emitters can be overcome. No relevant side effects were reported for local α -emitter application, such as in bladder cancer patients (4); however, systemic administration such as intravenous application with, for example, ^{223}Ra -dichloride have side effects, notably on bone marrow (2).

We present an overview of 3 promising clinical applications of TAT administered systemically, as well as future directions.

THE FRONT RUNNER: ^{223}RA -DICHLORIDE

Bone pain therapy using β -emitters for osteoblastic metastases has been established in the palliative setting for many years now. However, the only Food and Drug Administration-approved radiopharmaceutical with a positive impact on overall survival (OS) is the α -emitter ^{223}Ra (9). ^{223}Ra has a half-life of 11.4 d and decays into the stable daughter nuclide ^{207}Pb via 4 α -emissions (5.0–7.5 MeV). The median penetration range in soft tissue is 0.04–0.05 mm. Radium has physiologic similarities to calcium and selectively accumulates in bones, especially in areas with high bone metabolism such as marginal areas of bone metastases (10).

^{223}Ra -dichloride (Xofigo; Bayer) was Food and Drug Administration-approved in November 2013 for men with prostate cancer and bone metastases in whom the usual hormone blockade is no longer effective. The approval was based on the results of the

Received Dec. 22, 2022; revision accepted Feb. 10, 2023.

For correspondence or reprints, contact Kelsey L. Pomykala (kelsey.herrmann@uk-essen.de).

Published online Apr. 13, 2023.

COPYRIGHT © 2023 by the Society of Nuclear Medicine and Molecular Imaging.

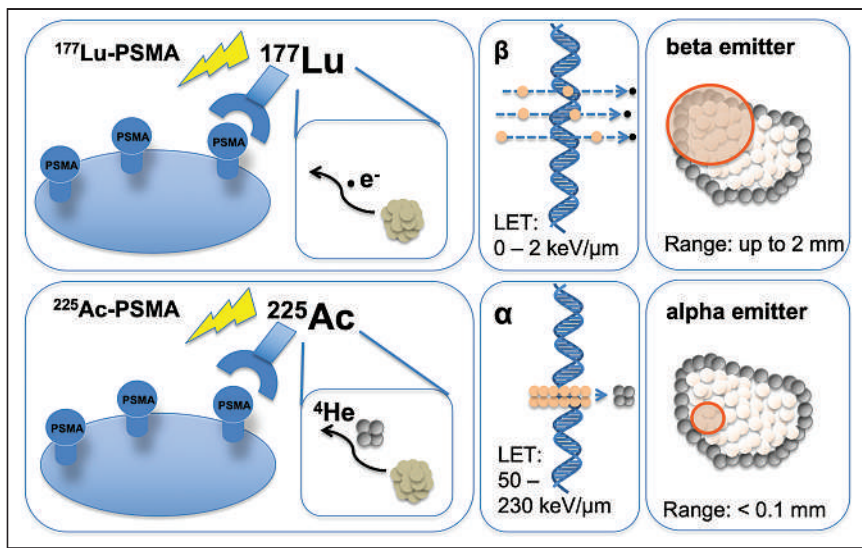


FIGURE 1. Comparison of radiobiologic effects of ^{225}Ac -PSMA and ^{177}Lu -PSMA. LET = linear energy transfer.

randomized, phase 3 ALSYMPCA trial (2). In this study, 921 patients who had received, were not eligible to receive, or declined chemotherapy with docetaxel and with at least 2 or more symptomatic bone metastases with no known visceral metastases were randomized 2:1 to receive 6 cycles of ^{223}Ra every 4 wk with the best standard of care or 6 infusions of placebo with the best standard of care. The OS was significantly longer in the ^{223}Ra group (14.9 vs. 11.3 mo; $P < 0.001$), the frequency of skeleton-related events was reduced, and the median time to a skeleton-related event was longer (15.6 vs. 9.8 mo; $P < 0.001$). No clinically significant differences in the frequency of grade 3 or 4 adverse events were observed between the groups (2). Nonhematologic toxicities are mild to moderate in intensity. The most common side effects are diarrhea, fatigue, nausea, vomiting, and bone pain, some of which are dose-related. These side effects are easily manageable with symptomatic and supportive treatments. Grade 3 and 4 thrombocytopenia was reported in 6% of patients on ^{223}Ra and in 2% of patients on placebo (2). ^{223}Ra is also accompanied by quality-of-life benefits (11).

Jiang et al. reported the 5-y real-world outcome of ^{223}Ra therapies for 228 patients. The median OS was 11.1 mo. The OS in

chemotherapy-naïve patients was significantly longer than in patients with a history of chemotherapy (12.3 vs. 8.1 mo; $P = 0.02$). No significant survival differences were observed between pre- and postabiraterone and prednisolone or enzalutamide patients. The fracture rate in the postabiraterone and prednisolone group was 24%, seemingly high (12).

Around the time of the ALSYMPCA trial, the hormone therapies abiraterone and enzalutamide were not part of the routine therapeutic approach, and therefore the feasibility of a therapy with ^{223}Ra before or after or even at the same time as these agents could not be studied at the time of approval of ^{223}Ra . The approval was changed in September 2018 because of the results of the ERA 223 study. In this prospective, phase 3 study, 806 patients were randomly assigned to receive ^{223}Ra ($n = 401$) or placebo ($n = 405$) in addition to abiraterone acetate plus prednisone or prednisolone. The study was prematurely unmasked because of the increased risk of fractures and a trend toward increased mortality in the group of patients who received ^{223}Ra in combination with abiraterone and prednisone. There was an increased incidence of fractures (29% vs. 11.4%) and a possible reduction in median OS (30.7 vs. 33.3 mo; $P = 0.13$) (13). Since then, according to the European Medicines Agency (14), ^{223}Ra therapy should be used only as monotherapy or in combination with a luteinizing hormone-releasing hormone analog for the treatment of patients with symptomatic bone metastases and no known visceral metastases, who have progressed after at least 2 prior lines of systemic therapy for metastatic castration-resistant prostate cancer (mCRPC) or are ineligible for any available systemic mCRPC treatment. It is also not recommended in patients with a low level of osteoblastic bone metastases or in patients with only asymptomatic bone metastases (15). The recommended regimen per the European Medicines Agency is 6 treatments of 55 kBq/kg every 4 wk.

An assessment of skeletal tumor burden on bone scintigraphy or PET before ^{223}Ra therapy is a valuable approach for the prognostication of OS and hematologic toxicity (16). In addition, tumor-specific prostate-specific membrane antigen imaging could be useful for selecting the most eligible patients (17).

There are limited data regarding the time interval between therapy with abiraterone and ^{223}Ra . Based on the half-lives of ^{223}Ra and abiraterone, it is recommended that subsequent treatment with ^{223}Ra be started no earlier than 5 d after the last administration of abiraterone. Subsequent systemic cancer therapy should be initiated no earlier than 30 d after the last dose of ^{223}Ra . Concurrent use of bisphosphonates or denosumab has been found to reduce the incidence of fractures in patients treated with ^{223}Ra (15).

In the case of disease progression after the initial 6 cycles of ^{223}Ra therapies, a rechallenge with a second course of 6 ^{223}Ra injections seems to be feasible, with minimal hematologic toxicity and sustained benefit in terms of OS (18).

α -PEPTIDE RECEPTOR RADIOTHERAPY: READY FOR PRIME TIME?

Somatostatin receptors are overexpressed in NETs and because of highly efficient *in vivo* agonist-induced internalization, they are

NOTEWORTHY

- After approvals of ^{177}Lu -DOTATATE and ^{177}Lu -vipivotide tetraxetan, TATs represent the next generation of theranostics.
- TATs offer advantages over other treatments due to their short range in tissues, allowing selective treatment of targeted cancer cells, and high linear energy transfer, leading to highly effective cell killing.
- ^{223}Ra -dichloride is approved for the treatment of bone metastases in castration-resistant prostate cancer; α -peptide receptor radiotherapy for the treatment of NETs and ^{225}Ac -PSMA therapies for prostate cancer are other promising clinical applications.
- These therapy models can be further investigated with new targets, as therapy combinations, and in patients with different stages of disease.

a perfect target for peptide receptor radiotherapy. Consecutively, ^{213}Bi -DOTATOC became the first somatostatin-receptor TAT demonstrating proof of mechanism in a clinical application: 8 patients without a sufficient response to previous β -peptide receptor radiotherapy demonstrated remarkable antitumor activity with α -peptide receptor radiotherapy (19). However, 2 y after therapy, patient glomerular filtration rate decreased significantly from an average of 115 mL/min to 83 mL/min (-30%). Also, the limited number of appropriate patients, challenging logistics related to the invasive arterial catheter placement and labeling procedure, and the costly demand of a gigabecquerel-sized $^{225}\text{Ac}/^{213}\text{Bi}$ generator on-site prevented broader clinical application.

^{225}Ac -DOTATOC was suggested to overcome these challenges (20). Preclinical results appeared promising, showing an added tumor size decrease sequencing cold DOTATOC, ^{177}Lu -DOTATOC, and ^{225}Ac -DOTATOC. Additionally, a maximum tolerable dose (applicable to mice) was determined, with tubular necrosis presenting the dose-limiting toxicity (20). The promising therapeutic range between antitumor activity and modest renal toxicity was recently confirmed by an independent study on mice (21). Preliminary dosimetry attempts—not published for ^{213}Bi - vs. ^{225}Ac -DOTATOC but for ^{213}Bi - vs. ^{225}Ac -PSMA-617 (a shuttle molecule with similar tracer pharmacokinetics)—done by the Heidelberg group demonstrated that in humans the longer effective half-life of ^{225}Ac -labeled small molecules in tumor versus kidney probably improves the therapeutic range of TAT (22). Nevertheless, neglecting microdosimetry, translocation effects of daughter nuclides and using average literature values for relative biological effectiveness, it was not possible to predict appropriate treatment activities for clinical application without additional empiric data. In 2015, the group presented its quasi-escalation experience with ^{225}Ac -DOTATOC (5). As demonstrated in Figure 2, antitumor activity could be observed at all dose levels; a maximum tolerable single-cycle dose of 40 MBq or 4-mo intervals with 25 MBq or 2-mo intervals with less than 18.5 MBq were suggested to be tolerable regarding acute hematologic toxicity. However, follow-up was too short to draw a final conclusion regarding chronic nephrotoxicity. In 2020, the first prospective clinical trial for ^{225}Ac -DOTATATE examined 32 patients with previous exposure to ^{177}Lu -DOTATATE who were treated with a 100 kBq/kg dose of ^{225}Ac -DOTATATE (23). Fifteen patients achieved partial remission, and 9 patients had stable disease. However, median follow-up was only 8 mo (range, 2–13 mo); thus, no conclusion

could be drawn about long-term tolerability. However, 5-y follow-up data for the Heidelberg cohort revealed a dose-dependent acute hematologic toxicity at single doses above 40 MBq or repeated doses greater than approximately 20 MBq ^{225}Ac -DOTATOC at 4-mo intervals. Treatment-related kidney failure occurred in 2 patients after a delay of greater than 4 y but was independent of administered radioactivity, and other clinical risk factors were important contributors (24).

Another α -emitter with appropriate decay characteristics for use in α -peptide receptor radiotherapy is ^{212}Pb (half-life, 10.6 h). In 2019, the preclinical characterization of ^{212}Pb -DOTAMTATE became available (25) and was well in line with the previous preclinical data obtained with ^{213}Bi - or ^{225}Ac -DOTATOC. A favorable outcome was observed, when the nontoxic cumulative dose of 1.7 MBq was fractionated into 3×0.6 MBq or 3×0.4 MBq in combination with chemotherapy. Another group has published preliminary results from the first-in-humans phase 1 dose escalation trial evaluating ^{212}Pb -DOTAMTATE in 20 patients with somatostatin receptor-positive NETs with no prior history of $^{177}\text{Lu}/^{90}\text{Y}/^{111}\text{In}$ peptide receptor radiotherapy (NCT03466216) (26). The study was a single-ascending-dose/multiple-ascending-dose trial using a $3 + 3$ dose-escalation scheme with an 8-wk dose-limiting toxicity period. The initial dose was 1.13 MBq/kg, and subsequent cohorts received an incremental 30% dose increase until a tumor response or a dose-limiting toxicity was observed. The maximum total dose per subject was 296 MBq in the single-ascending-dose cohort and 888 MBq in the multiple-ascending-dose cohort. Treatment was well tolerated, with the most common adverse events being nausea, fatigue, and alopecia. No serious treatment-emergent adverse events were related to the study drug, and no subjects required treatment delay or a dose reduction. Of the 10 subjects who received all 4 cycles, 8 (80%) demonstrated an objective, long-lasting radiologic response by RECIST 1.1 (26).

$^{225}\text{AC-PSMA-617 FOR THERAPY OF PROSTATE CANCER}$

Treatment of metastatic prostate cancer has been complemented by the use of α -emitters in the past few years. ^{225}Ac -PSMA-617 was first developed in vitro at the Joint Research Centre Karlsruhe in 2013 and 2014 (1). Kratochwil et al. first described a remarkable therapeutic effect of ^{225}Ac -PSMA-617 in patients with late-stage prostate cancer (Fig. 3) (27). The initial report included 2 patients who showed complete remission after exhausting conventional therapies, including chemotherapy and advanced hormone treatment.

The favorable pharmacologic properties and kinetics of PSMA-617 with fast tumor uptake, good internalization, long tumor retention, and rapid clearance of unbound ligand are desirable properties for the combination with an α -emitter (1). Because of the long half-life of several days and multiple α -emissions in the decay chain of ^{225}Ac , these pharmacokinetic properties are highly relevant to reduce potential clinical side effects. Almost all available studies used ^{225}Ac -PSMA-617 for treatment (Table 1). One study also investigated ^{225}Ac -PSMA-I&T (28) and demonstrated similar biochemical response rates, with any prostate-specific antigen (PSA) decline in 79% of patients, comparable to PSMA-617 ranging between 79% and 94% (Table 1). However, no data on clinical

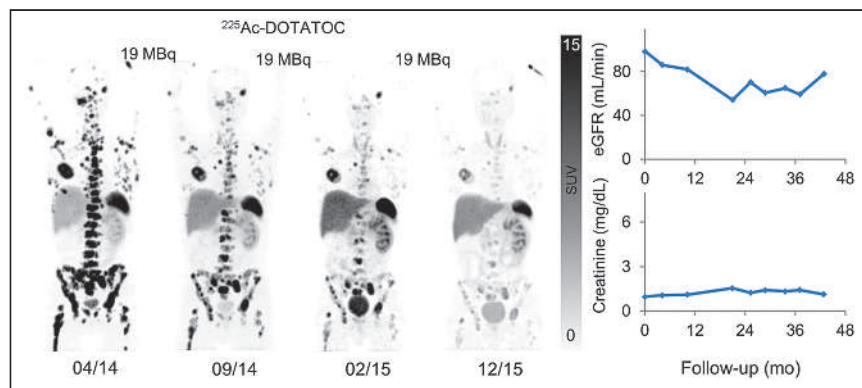


FIGURE 2. Patient with G2 (Ki-67, 5%) NET of right (resected) kidney received 3 cycles of 19 MBq of ^{225}Ac -DOTATOC. Maximum-intensity projections of ^{68}Ga -DOTATOC PET/CT done in advance, between cycles, and after last cycle demonstrate antitumor activity (left). Despite remaining solitary left kidney, cumulative 47 MBq of ^{225}Ac -DOTATOC did not lead to increase in serum creatinine (right, bottom) or estimated glomerular filtration rate (right, top) during 3 y of follow-up. eGFR = estimated glomerular filtration rate.

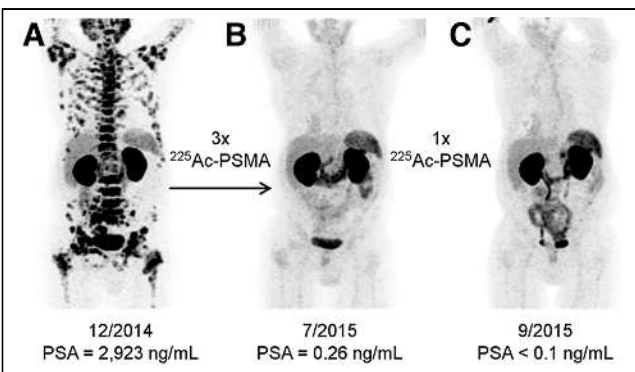


FIGURE 3. Initial promising results from Heidelberg group for patient with diffuse red bone marrow infiltration of mCRPC, which was considered contraindication for treatment with β -emitters. ^{68}Ga -PSMA-11 PET/CT scans demonstrating pretherapeutic tumor spread (A), restaging 2 mo after third cycle of ^{225}Ac -PSMA-617 (B), and restaging 2 mo after 1 additional consolidation therapy (C). (Reprinted from (27).)

progression-free survival (cPFS) and OS is currently available using ^{225}Ac -PSMA-I&T.

Dose Finding and Dosimetry Estimates

Subsequent studies focused on dose finding using between 50 and 200 kBq/kg activities of ^{225}Ac -PSMA-617 with the aim of finding a reasonable trade-off between therapeutic efficacy and side effects. For 8-week intervals, a reasonable trade-off was found to be a 100 kBq/kg activity of ^{225}Ac -PSMA-617 (29). At 50 kBq/kg, side effects were low but antitumor effects were insufficient, and at 200 kBq/kg, side effects increased significantly, with xerostomia as the dose-limiting toxicity (29). In this study, a dosimetry estimate showed that assuming a relative biological effectiveness of 5, 1 MBq of ^{225}Ac -PSMA-617 leads to mean doses of 2.3 Sv for salivary glands, 0.7 Sv for kidneys, and 0.05 Sv for red marrow that are composed of 99.4% α , 0.5% β , and 0.1% photon radiation, respectively (29). However, dosimetry of α -emitters is challenging, in part because of the short range of α -emitters in tissue and the complex decay schemes with multiple α -, β -, and γ -daughters with a broad range of energies and half-lives of the emitted nuclides. To date, no standardized means of imaging α -emitters exists (30).

Surrogate Markers of Response

The number of patients experiencing any PSA decline is in the range of 79%–94% (31–33). A maximum PSA decline of at least 90% was achieved in only 12% of the late-stage mCRPC patients (34) but in 40%–82% of patients in earlier stages (Table 1). Data on complete remission on PET are not available from all studies but are in the range of 0%–65% (Table 1). Median cPFS was between 4.1 and 15.2 mo, and the median OS was 7.7–18 mo (31,33–35). cPFS and OS, 4.1 and 7.7 mo, respectively, appear to be shorter in patients with late-stage mCRPC (e.g., median of 6 treatment regimens before ^{225}Ac -PSMA-617) compared with early- to intermediate-stage mCRPC patients (up to a median of 3 prior treatment regimens), with a cPFS of 7–15.2 mo and an OS of 12–18 mo, respectively.

Risk Factors

A study of advanced mCRPC patients, treated with ^{225}Ac -PSMA-617, found that those with high baseline immunohistochemical PSMA expression or DNA damage repair alterations tended to have longer OS (36). In a cohort of 72 patients, a PSA decline of at least

50% was significantly associated with OS and PFS in multivariate analysis after ^{225}Ac -PSMA-617 treatment (33). Additionally, previous ^{177}Lu -PSMA treatment was negatively correlated with PFS (33). In a study of 26 late-stage mCRPC patients, it is reported that liver metastases are associated with significantly shorter PSA PFS (median, 1.9 vs. 4.0 mo), cPFS (median, 1.8 vs. 5.2 mo), and OS (median, 4.3 vs. 10.4 mo) (34).

Xerostomia

Xerostomia has been reported to be a relevant side effect of ^{225}Ac -PSMA treatment. It seems to be more pronounced after intensive pretreatment. In late-stage mCRPC patients, xerostomia (grade 1/2) was reported in all patients, with 23% requesting stop of treatment to preserve quality of life (34). Kratochwil et al. (31) reported that 10% of patients discontinued treatment because of intolerable xerostomia. Sathenka et al. (33) reported grade 1/2 xerostomia in 85%–100% patients. Yadav et al. reported xerostomia of grade 1/2 in only 29% in an earlier-stage patient cohort (35). Khreich et al. reported that 20 patients who received a tandem therapy of ^{225}Ac -PSMA-617/ ^{177}Lu -PSMA-617 with 5.3 MBq (range, 1.5–7.9 MBq) of ^{225}Ac -PSMA and 6.9 GBq (range, 5.0–11.6 GBq) of ^{177}Lu -PSMA-617, had grade 1 (very mild) xerostomia in 8 of 20 patients (40%) and grade 2 (mild) in 5 of 20 (25%) (Fig. 1) (37). Xerostomia was reported as grade 1 (very mild) in 8 of 20 patients (40%) and grade 2 (mild) in 5 of 20 (25%) (37). In an attempt to maintain salivary gland function, Rathke et al. performed sialendoscopy on patients undergoing ^{225}Ac -PSMA-617 treatment (38). Despite sialendoscopy support with, for example, steroid injections, xerostomia was present after multiple cycles (38). Using monoclonal antibodies such as ^{225}Ac -J591 might reduce salivary gland uptake and hence xerostomia as previously reported, with only 8 of 32 (25%) patients showing grade 1 xerostomia (39). However, these antibodies have less renal excretion and may increase bone marrow toxicity.

Hematologic Side Effects

Compared with ^{177}Lu -PSMA, grade 3/4 hematologic toxicity seems to be higher for ^{225}Ac -PSMA. In a series of patients with late-stage mCRPC, hematologic grade 3/4 toxicities were reported in 35%, 27%, and 19% for anemia, leukopenia, and thrombocytopenia, respectively (34). In patients treated with ^{177}Lu -PSMA-radioligand therapy, the frequencies of grade 3/4 anemia, thrombocytopenia, and leukopenia were only 9%–10%, 2%–13%, and 3%–32%, respectively (40–43). However, the patients receiving ^{225}Ac -PSMA had been treated at a substantially later stage with a median of 6 prior treatments (34). Notably, the frequency of these adverse hematologic events was similar to that of investigational agents (44) or, for example, carboplatin/etoposide (45). Yadav et al. reported no grade 3/4 thrombocytopenia or leukopenia, but 1 of 28 patients had grade 3 anemia (35). Khreich et al. reported at least one grade 3/4 hematotoxicity in 25% of patients: 5% with grade 3 anemia, 10% with grade 3 leukopenia, and 10% with grade 4 anemia and thrombocytopenia each using a tandem therapy of ^{225}Ac -PSMA-617 and ^{177}Lu -PSMA (37).

^{225}Ac -PSMA-617/ ^{177}Lu -PSMA-617 Tandem Therapy

Up to 30% of mCRPC patients do not respond to ^{177}Lu -PSMA therapy (37). In patients with resistance to β -emitters, treatment with an α -emitter may still be effective. The combination of α - and β -emitters may allow for a lower dose of ^{225}Ac , reducing salivary gland toxicity. In 13 of 20 patients who received one course of ^{225}Ac -PSMA-617/ ^{177}Lu -PSMA-617 tandem therapy, biochemical response (PSA decline > 50%) and grade 1/2 xerostomia was observed (37). Rosar et al. reported partial response in 5 of 17 patients and stable

TABLE 1
Overview of Current Data on Compassionate Use of $^{225}\text{Ac-PSMA-617}$ RLT in Different Patient Cohorts: Effects of Treatment on PSA, Complete Remission in PET, and Median OS Are Summarized (34)

Cohort	Pretoria I	Pretoria II	Heidelberg	New Delhi	TUM	LMU	Pretoria III
	Chemo-naïve mHSPC/mCRPC	Early mCRPC	Intermediate mCRPC (7/40 after LuPSMA)	Early to intermediate	Late mCRPC (all after LuPSMA)	Early to intermediate mCRPC	mCRPC directly after ADT
<i>n</i>	17	73	40	28	26	18 (4 excluded because of incomplete follow-up)	53
$^{225}\text{Ac-PSMA-617}$	$^{225}\text{Ac-PSMA-617}$	$^{225}\text{Ac-PSMA-617}$	$^{225}\text{Ac-PSMA-617}$	$^{225}\text{Ac-PSMA-617}$	$^{225}\text{Ac-PSMA-617}$	$^{225}\text{Ac-PSMA-617}$	$^{225}\text{Ac-PSMA-617}$
Prior mCRPC lines	(no CTx, no second ADT, 3× LuPSMA)	1–2	Median, 3 (range, 1–7)	(15 prior LuPSMA, 13 no LuPSMA)	Median, 6 (range, 3–8) (all after LuPSMA)	Median, 3 (range, 2–4) 11/14 after LuPSMA	1 (ADT)
Any PSA ↓	94% (16/17)	83% (60/73)	93% (37/40)	79% (22/28)	88% (23/26)	79% (11/14)	96% (51/53)
Max. $\geq 50\%$ PSA ↓	88% (15/17)	70% (51/73)	75% (30/40)	39% (11/28)	65% (17/26)	50% (7/14)	91% (48/53)
Max. $\geq 90\%$ PSA ↓	82% (14/17)	58%* (42/73)	40%* (16/40)	14% (4/28)*	12% (3/26)	7% (1/14)*	NA
CR on PET	65% (11/17)	29% (21/73)	NA	2/22 (9%)	0%	NA	56% (30/54)
Median cPFS	NA	15.2 mo (est.)	7 mo	12 mo	4.1 mo	NA	22 mo [†] ; 4 mo [‡]
Median OS	NA	18 mo (est.)	>12 mo	17 mo	7.7 mo	NA	NA [†] ; 9 mo [‡]
Publication	(32)	(33)	(31)	(35)	(34)	(28)	(67)

*Extracted from waterfall plot.

[†]Patients with PSA decline $\geq 50\%$.

[‡]Patients with PSA decline < 50%.

TUM = Technische Universität München; LMU = Ludwig-Maximilians-Universität München; mHSPC = metastatic hormone-sensitive prostate cancer; ADT = androgen deprivation therapy; CTx = chemotherapy; max = maximum; NA = not available; CR = complete remission; est. = estimated.

disease in 7 of 17 patients, treated with tandem therapy after progression with ^{177}Lu -PSMA (46).

NEW TARGETS

In addition to hydroxyapatite, somatostatin receptors, and the prostate-specific membrane antigen, there are additional targets under investigation for their utility in TAT. One of the most prominent new targets is the fibroblast activation protein (FAP) that is overexpressed by cancer-associated fibroblasts in the stroma of several tumor entities as well as less frequently directly from tumor cells. FAP can be targeted with antibodies, peptides, and small molecules such as FAP inhibitors (FAPIs). FAP-targeted imaging has been explored in several malignancies, including glioma, nasopharyngeal carcinoma, gastric cancer, colorectal cancer, hepatocellular carcinoma, cholangiocarcinoma, soft-tissue sarcoma, pancreatic cancer, breast cancer, and prostate cancer (47). Research into the therapeutic application of FAPI radionuclides is still in the early stages. Breast cancer patients have been treated with ^{90}Y -FAPI-04 (48) and ^{177}Lu -DOTA.SA.FAPI (49), an ovarian cancer patient has been treated with ^{90}Y -FAPI-46 (50), and sarcoma and pancreatic cancer patients have been treated with ^{90}Y -FAPI-46 (50) and ^{177}Lu -FAPI-46.

As for TAT, ^{225}Ac -FAPI-46 has been used in pancreatic cancer mouse models and ^{153}Sm -FAPI-46 was used to treat a patient with soft-tissue sarcoma metastatic to the lung. In one study, 34 kBq of ^{225}Ac -FAPI-04 were injected into 6 PANC-1 xenograft mice, 3 wk after implantation with a tumor size of $0.98 \pm 0.66 \text{ cm}^3$ (51). Tumor size was compared with 6 control mice for up to 51 d. The mice who received ^{225}Ac -FAPI-04 showed significant tumor growth suppression compared with the control mice, without a significant change in body weight, with the equivalent dose in the tumor estimated to be $5.68 \pm 0.77 \text{ Gy/MBq}$. In another study, 3 kBq ($n = 3$), 10 kBq ($n = 2$), and 30 kBq ($n = 6$) of ^{225}Ac -FAPI-04 were injected into PANC-1 xenograft mice and tumor size and weight were compared with 7 control mice (52). The tumor growth was suppressed immediately after treatment with 10 kBq and 30 kBq, whereas the tumor-suppressive effects in the 3-kBq group were very mild. The tumor size of the 30-kBq group was significantly smaller than that in the control group on days 5–9 and day 25. The body weight in all groups showed a trend to decrease in the first week but recovered in the 3- and 10-kBq groups after day 7. Lastly, in a patient with fibrous spindle cell soft-tissue sarcoma metastatic to the lung, 3 cycles of 20 GBq of ^{153}Sm - and 8 GBq of ^{90}Y -FAPI-46 were well tolerated and achieved stable disease for 8 mo (53). In the future, ^{212}Pb -FAPI compounds will also be preclinically and potentially clinically explored.

Another target that is being investigated is human epidermal growth factor receptor type 2 (HER2), which is overexpressed in various cancers including breast, ovarian, bladder, pancreatic, and gastric. A preclinical study evaluated a HER2-targeting single-domain antibody labeled with ^{225}Ac , called ^{225}Ac -DOTA-2Rs15d, in mice with HER2-positive intraperitoneal ovarian cancer (54). Both a single dose of $86.84 \pm 8.97 \text{ kBq}$ of ^{225}Ac -DOTA-2Rs15d 7 d after tumor inoculation and 3 consecutive administrations of $86.84 \pm 8.97 \text{ kBq}$ of ^{225}Ac -DOTA-2Rs15d on days 7, 10, and 14 resulted in a significantly longer mean survival of 101 and 143 d, respectively, versus 56 d for mice receiving vehicle solution ($P < 0.0001$). Additionally, 3 consecutive doses of ^{225}Ac -DOTA-2Rs15d increased the mean survival (143 d) compared with a group receiving trastuzumab regimen (7.5 mg/kg loading dose, followed by 2 maintenance doses of 3.5 mg/kg) and a single dose of ^{225}Ac -DOTA-2Rs15d ($P < 0.0389$). There was histopathologic evidence of kidney toxicity after repeated doses of

^{225}Ac -DOTA-2Rs15d. The single-domain antibody 2Rs15d, also referred to as anti-HER2-VHH1, has also been labeled with ^{131}I and studied in HER2-positive breast cancer patients (NCT02683083, NCT04467515) (55).

Other targets including type I insulin-like growth factor (NCT03746431) (56), a transmembrane protein that is overexpressed in non-small cell lung, prostate, and breast cancers; neuropeptide receptor 1 (NCT05605522) (57), upregulated in colorectal and pancreatic cancers; and CD33 (NCT03867682) (58), found in myeloid tumor cells are being investigated in conjunction with ^{225}Ac .

COMBINATION THERAPY

TAT may also be advantageous in combination with other cancer treatments such as chemotherapy, immunotherapy, DNA repair inhibitors, and other radionuclide treatments. These types of regimens are already being readily studied in prostate cancer patients in combination with ^{177}Lu -PSMA treatment and can also be evaluated with TAT. For example, ^{225}Ac -PSMA-617 could also be studied in combination with androgen receptor signaling inhibitors or chemotherapy. Other innovative concepts include the concomitant administration of ^{225}Ac - and ^{177}Lu -PSMA-617 in mCRPC patients (59). HER2-targeted therapy can be studied in conjunction with trastuzumab. Additionally, studies of a combination of ^{177}Lu -DOTATATE and M3814 (an inhibitor of DNA-dependent protein kinase) for patients with pancreatic NETs (NCT04750954) and a combination of ^{223}Ra - dichloride and M3814 for patients with mCRPC (NCT04071236) are already under way; these concepts can also be studied with TAT. Future investigations can focus on combination therapies to evaluate possible synergistic effects.

CONCLUSION

The field of TAT is currently one of the most promising in innovative targeted cancer therapy. The question as to whether these new TATs are merely an evolution or small improvement of currently used therapies versus a revolution leading to a complete paradigm shift remains to be answered. Whereas several early- and late-stage clinical trials on NETs and metastatic prostate cancer are already under way, there is also a significant interest (and investment) by multiple well-funded early-phase biotechnical companies (60) dedicated to the further development of novel TAT concepts. Despite the profound excitement and incredible clinical potential, it is also important to emphasize the need to understand short- and long-term toxicity of TAT and identification of suitable therapeutic combination partners.

DISCLOSURE

Clemens Kratochwil is coinventor of patents for radiolabeled PSMA and FAP ligands; owns shares of FAPi Holding AG; indirectly received research support from Telix Pharmaceuticals; worked as a scientific advisor for Novartis Radiopharmaceuticals, Hoffmann-La Roche, and AdvanCell; and received speaker fees from Novartis. Hojjat Ahmadzadehfar reports fees from Bayer (speaker), Novartis/AAA (speaker), and IPSEN (speaker) and is an unpaid consultant for Novartis/AAA. Matthias Eiber reports fees from Blue Earth Diagnostics Ltd. (consultant, research funding), Novartis/AAA (consultant, speaker), Telix (consultant), Bayer (consultant, research funding), RayzeBio (consultant), Point Biopharma (consultant), Eckert-Ziegler (speaker), Janssen Pharmaceuticals (consultant, speakers bureau), Parexel (image review), and Bioclinica (image review).

outside the submitted work and a patent application for rhPSMA. Ken Herrmann reports personal fees from Bayer, Sofie Biosciences, SIRTEX, Adacap, Curium, Endocyte, BTG, IPSEN, Siemens Healthineers, GE Healthcare, Amgen, Novartis, ymabs, Aktis Oncology, Theragnostics, Pharma15, Debiopharm, AstraZeneca, and Janssen; nonfinancial support from ABX; grants from BTG; and other fees from Sofie Biosciences outside the submitted work. Kelsey Pomykala reports personal fees from ABX outside the submitted work. No other potential conflict of interest relevant to this article was reported.

REFERENCES

- Morgenstern A, Apostolidis C, Kratochwil C, Sathekge M, Krolicki L, Bruchertseifer F. An overview of targeted alpha therapy with ^{225}Ac tinium and ^{213}Bi bismuth. *Curr Radiopharm*. 2018;11:200–208.
- Parker C, Nilsson S, Heinrich D, et al. Alpha emitter radium-223 and survival in metastatic prostate cancer. *N Engl J Med*. 2013;369:213–223.
- Hoskin P, Sartor O, O’Sullivan JM, et al. Efficacy and safety of radium-223 dichloride in patients with castration-resistant prostate cancer and symptomatic bone metastases, with or without previous docetaxel use: a prespecified subgroup analysis from the randomised, double-blind, phase 3 ALSYMPCA trial. *Lancet Oncol*. 2014;15:1397–1406.
- Autenrieth ME, Seidl C, Bruchertseifer F, et al. Treatment of carcinoma in situ of the urinary bladder with an alpha-emitter immunoconjugate targeting the epidermal growth factor receptor: a pilot study. *Eur J Nucl Med Mol Imaging*. 2018;45:1364–1371.
- Kratochwil C, Bruchertseifer F, Giesel F, Apostolidis C, Haberkorn U, Morgenstern A. Ac-225-DOTATOC: an empiric dose finding for alpha particle emitter based radionuclide therapy of neuroendocrine tumors [abstract]. *J Nucl Med*. 2015; 56(suppl 3):1232.
- Rosenblat TL, McDevitt MR, Mulford DA, et al. Sequential cytarabine and alpha-particle immunotherapy with bismuth-213-lintuzumab (HuM195) for acute myeloid leukemia. *Clin Cancer Res*. 2010;16:5303–5311.
- Yang H, Wilson JJ, Orvig C, et al. Harnessing α -emitting radionuclides for therapy: radiolabeling method review. *J Nucl Med*. 2022;63:5–13.
- Sgouros G, Roeske JC, McDevitt MR, et al. MIRD pamphlet no. 22 (abridged): radiobiology and dosimetry of α -particle emitters for targeted radionuclide therapy. *J Nucl Med*. 2010;51:311–328.
- Parker C, Sartor O. Radium-223 in prostate cancer. *N Engl J Med*. 2013;369:1659–1660.
- Scholl C, Bundschuh RA, Hirzebruch S, et al. Radionuclide intake risks in the clinical administration of $^{223}\text{RaCl}_2$. *J Radiol Prot*. 2019;39:387–398.
- Nilsson S, Cislo P, Sartor O, et al. Patient-reported quality-of-life analysis of radium-223 dichloride from the phase III ALSYMPCA study. *Ann Oncol*. 2016; 27:868–874.
- Jiang XY, Atkinson S, Pearson R, et al. Optimising radium 223 therapy for metastatic castration-resistant prostate cancer: 5-year real-world outcome—focusing on treatment sequence and quality of life. *Clin Oncol (R Coll Radiol)*. 2020;32:e177–e187.
- Smith M, Parker C, Saad F, et al. Addition of radium-223 to abiraterone acetate and prednisone or prednisolone in patients with castration-resistant prostate cancer and bone metastases (ERA 223): a randomised, double-blind, placebo-controlled, phase 3 trial. *Lancet Oncol*. 2019;20:408–419.
- Ahmadvadefar H, Essler M, Rahbar K, Afshar-Oromieh A. Radionuclide therapy for bone metastases: utility of scintigraphy and PET imaging for treatment planning. *PET Clin*. 2018;13:491–503.
- EMA restricts use of prostate cancer medicine Xofigo. European Medicines Agency website. <https://www.ema.europa.eu/en/medicines/human/referrals/xofigo>. Published 2018. Accessed February 27, 2023.
- Fosbol MØ, Petersen PM, Kjaer A, Mortensen J. ^{223}Ra therapy of advanced metastatic castration-resistant prostate cancer: quantitative assessment of skeletal tumor burden for prognostication of clinical outcome and hematologic toxicity. *J Nucl Med*. 2018;59:596–602.
- Ahmadvadefar H, Azgomi K, Hauser S, et al. ^{68}Ga -PSMA-11 PET as a gate-keeper for the treatment of metastatic prostate cancer with ^{223}Ra : proof of concept. *J Nucl Med*. 2017;58:438–444.
- Sartor O, Heinrich D, Mariados N, et al. Re-treatment with radium-223: 2-year follow-up from an international, open-label, phase 1/2 study in patients with castration-resistant prostate cancer and bone metastases. *Prostate*. 2019;79:1683–1691.
- Kratochwil C, Giesel FL, Bruchertseifer F, et al. ^{213}Bi -DOTATOC receptor-targeted alpha-radionuclide therapy induces remission in neuroendocrine tumours refractory to beta radiation: a first-in-human experience. *Eur J Nucl Med Mol Imaging*. 2014;41:2106–2119.
- Miederer M, Henriksen G, Alke A, et al. Preclinical evaluation of the alpha-particle generator nuclide ^{225}Ac for somatostatin receptor radiotherapy of neuroendocrine tumors. *Clin Cancer Res*. 2008;14:3555–3561.
- Tafreshi NK, Pandya DN, Tichacek CJ, et al. Preclinical evaluation of [^{225}Ac]Ac-DOTA-TATE for treatment of lung neuroendocrine neoplasms. *Eur J Nucl Med Mol Imaging*. 2021;48:3408–3421.
- Kratochwil C, Schmidt K, Afshar-Oromieh A, et al. Targeted alpha therapy of mCRPC: dosimetry estimate of ^{213}Bi -PSMA-617. *Eur J Nucl Med Mol Imaging*. 2018;45:31–37.
- Ballal S, Yadav MP, Damle NA, Sahoo RK, Bal C. Concomitant ^{177}Lu -DOTA-TATE and capecitabine therapy in patients with advanced neuroendocrine tumors: a long-term-outcome, toxicity, survival, and quality-of-life study. *Clin Nucl Med*. 2017;42:e457–e466.
- Kratochwil C, Apostolidis L, Rathke H, et al. Dosing ^{225}Ac -DOTATOC in patients with somatostatin-receptor-positive solid tumors: 5-year follow-up of hematological and renal toxicity. *Eur J Nucl Med Mol Imaging*. 2021;49:54–63.
- Stallons TAR, Saidi A, Tworowska I, Delpassand ES, Torgue JJ. Preclinical investigation of ^{212}Pb -DOTAMTATE for peptide receptor radionuclide therapy in a neuroendocrine tumor model. *Mol Cancer Ther*. 2019;18:1012–1021.
- Delpassand ES, Tworowska I, Esfandiari R, et al. Targeted α -emitter therapy with ^{212}Pb -DOTAMTATE for the treatment of metastatic SSTR-expressing neuroendocrine tumors: first-in-humans dose-escalation clinical trial. *J Nucl Med*. 2022;63:1326–1333.
- Kratochwil C, Bruchertseifer F, Giesel FL, et al. ^{225}Ac -PSMA-617 for PSMA-targeted α -radiation therapy of metastatic castration-resistant prostate cancer. *J Nucl Med*. 2016;57:1941–1944.
- Zacherl MJ, Gildehaus FJ, Mittlmeier L, et al. First clinical results for PSMA-targeted α -therapy using ^{225}Ac -PSMA-I&T in advanced-mCRPC patients. *J Nucl Med*. 2021;62:669–674.
- Kratochwil C, Bruchertseifer F, Rathke H, et al. Targeted α -therapy of metastatic castration-resistant prostate cancer with ^{225}Ac -PSMA-617: dosimetry estimate and empiric dose finding. *J Nucl Med*. 2017;58:1624–1631.
- Sgouros G, Frey E, Du Y, Hobbs R, Bolch W. Imaging and dosimetry for alpha-particle emitter radiopharmaceutical therapy: improving radiopharmaceutical therapy by looking into the black box. *Eur J Nucl Med Mol Imaging*. 2021;49:18–29.
- Kratochwil C, Bruchertseifer F, Rathke H, et al. Targeted α -therapy of metastatic castration-resistant prostate cancer with ^{225}Ac -PSMA-617: swimmer-plot analysis suggests efficacy regarding duration of tumor control. *J Nucl Med*. 2018;59:795–802.
- Sathekge M, Bruchertseifer F, Knoesen O, et al. ^{225}Ac -PSMA-617 in chemotherapy-naïve patients with advanced prostate cancer: a pilot study. *Eur J Nucl Med Mol Imaging*. 2019;46:129–138.
- Sathekge M, Bruchertseifer F, Vorster M, et al. Predictors of overall and disease-free survival in metastatic castration-resistant prostate cancer patients receiving ^{225}Ac -PSMA-617 radioligand therapy. *J Nucl Med*. 2020;61:62–69.
- Feuerecker B, Tauber R, Knorr K, et al. Activity and adverse events of actinium-225-PSMA-617 in advanced metastatic castration-resistant prostate cancer after failure of lutetium-177-PSMA. *Eur Urol*. 2021;79:343–350.
- Yadav MP, Ballal S, Sahoo RK, Tripathi M, Seth A, Bal C. Efficacy and safety of ^{225}Ac -PSMA-617 targeted alpha therapy in metastatic castration-resistant prostate cancer patients. *Theranostics*. 2020;10:9364–9377.
- van der Doelen MJ, Mehra N, van Oort IM, et al. Clinical outcomes and molecular profiling of advanced metastatic castration-resistant prostate cancer patients treated with ^{225}Ac -PSMA-617 targeted alpha-radiation therapy. *Urol Oncol*. 2021;39:729.e7–729.e16.
- Khreich F, Ebert N, Ries M, et al. ^{225}Ac -PSMA-617/ ^{177}Lu -PSMA-617 tandem therapy of metastatic castration-resistant prostate cancer: pilot experience. *Eur J Nucl Med Mol Imaging*. 2020;47:721–728.
- Rathke H, Kratochwil C, Hohenberger R, et al. Initial clinical experience performing sialendoscopy for salivary gland protection in patients undergoing ^{225}Ac -PSMA-617 RLT. *Eur J Nucl Med Mol Imaging*. 2019;46:139–147.
- Tagawa ST, Sun M, Sartor AO, et al. Phase I study of ^{225}Ac -J591 for men with metastatic castration-resistant prostate cancer (mCRPC). *J Clin Oncol*. 2021;39(suppl):5015.
- Rahbar K, Ahmadvadefar H, Kratochwil C, et al. German multicenter study investigating ^{177}Lu -PSMA-617 radioligand therapy in advanced prostate cancer patients. *J Nucl Med*. 2017;58:88–90.
- Hofman MS, Violet J, Hicks RJ, et al. [^{177}Lu]-PSMA-617 radionuclide treatment in patients with metastatic castration-resistant prostate cancer (LuPSMA trial): a single-centre, single-arm, phase 2 study. *Lancet Oncol*. 2018;19:825–833.
- Heck MM, Tauber R, Schwaiger S, et al. Treatment outcome, toxicity, and predictive factors for radioligand therapy with ^{177}Lu -PSMA-I&T in metastatic castration-resistant prostate cancer. *Eur Urol*. 2019;75:920–926.
- Violet J, Sandhu S, Iravani A, et al. Long-term follow-up and outcomes of retreatment in an expanded 50-patient single-center phase II prospective trial of

- ¹⁷⁷Lu-PSMA-617 theranostics in metastatic castration-resistant prostate cancer. *J Nucl Med.* 2020;61:857–865.
44. Karzai F, Madan RA, Owens H, et al. A phase II study of the anti-programmed death ligand-1 antibody durvalumab (D; MEDI4736) in combination with PARP inhibitor, olaparib (O), in metastatic castration-resistant prostate cancer (mCRPC) [abstract]. *J Clin Oncol.* 2017;35(suppl):162.
45. Caubet M, Dobi E, Pozet A, et al. Carboplatin-etoposide combination chemotherapy in metastatic castration-resistant prostate cancer: a retrospective study. *Mol Clin Oncol.* 2015;3:1208–1212.
46. Rosar F, Hau F, Bartholomä M, et al. Molecular imaging and biochemical response assessment after a single cycle of [²²⁵Ac]Ac-PSMA-617/[¹⁷⁷Lu]Lu-PSMA-617 tandem therapy in mCRPC patients who have progressed on [¹⁷⁷Lu]Lu-PSMA-617 monotherapy. *Theranostics.* 2021;11:4050–4060.
47. Li M, Younis MH, Zhang Y, Cai W, Lan X. Clinical summary of fibroblast activation protein inhibitor-based radiopharmaceuticals: cancer and beyond. *Eur J Nucl Med Mol Imaging.* 2022;49:2844–2868.
48. Lindner T, Loktev A, Altmann A, et al. Development of quinoline-based theranostic ligands for the targeting of fibroblast activation protein. *J Nucl Med.* 2018;59:1415–1422.
49. Ballal S, Yadav MP, Kramer V, et al. A theranostic approach of [⁶⁸Ga]Ga-DOTA-SA.FAP_i PET/CT-guided [¹⁷⁷Lu]Lu-DOTA-SA.FAP_i radionuclide therapy in an end-stage breast cancer patient: new frontier in targeted radionuclide therapy. *Eur J Nucl Med Mol Imaging.* 2021;48:942–944.
50. Lindner T, Altmann A, Krämer S, et al. Design and development of ^{99m}Tc-Labeled FAPI tracers for SPECT imaging and ¹⁸⁸Re therapy. *J Nucl Med.* 2020;61:1507–1513.
51. Watabe T, Liu Y, Kaneda-Nakashima K, et al. Theranostics targeting fibroblast activation protein in the tumor stroma: ⁶⁴Cu- and ²²⁵Ac-Labeled FAPI-04 in pancreatic cancer xenograft mouse models. *J Nucl Med.* 2020;61:563–569.
52. Liu Y, Watabe T, Kaneda-Nakashima K, et al. Fibroblast activation protein targeted therapy using [¹⁷⁷Lu]FAPI-46 compared with [²²⁵Ac]FAPI-46 in a pancreatic cancer model. *Eur J Nucl Med Mol Imaging.* 2022;49:871–880.
53. Kratochwil C, Giesel FL, Rathke H, et al. [¹⁵³Sm]samarium-labeled FAPI-46 radioligand therapy in a patient with lung metastases of a sarcoma. *Eur J Nucl Med Mol Imaging.* 2021;48:3011–3013.
54. Rodak M, Dekempeneer Y, Wojewódzka M, et al. Preclinical evaluation of ²²⁵Ac-labeled single-domain antibody for the treatment of HER2pos cancer. *Mol Cancer Ther.* 2022;21:1835–1845.
55. D'Huysse M, Vos JD, Caveliers V, et al. Phase I trial of ¹³¹I-GMIB-Anti-HER2-VHH1, a new promising candidate for HER2-targeted radionuclide therapy in breast cancer patients. *J Nucl Med.* 2021;62:1097–1105.
56. Juergens RA, Zukotynski KA, Juneau D, et al. A phase I study of [²²⁵Ac]-FPI-1434 radioimmunotherapy in patients with IGF-1R expressing solid tumors [abstract]. *J Clin Oncol.* 2019;37:TPS3152.
57. Mahammad S, Duffy I, Simms R, et al. NTSR1 targeted alpha therapeutic [²²⁵Ac]-FPI-2059 induces regression in preclinical colorectal xenograft model. Fusion Pharmaceuticals website. <https://fusionpharma.com/wp-content/uploads/2021/10/FPI-2059-EANM-Presentation-Oct-2021.pdf>. Published 2020. Accessed February 27, 2023.
58. Garg R, Allen KJH, Dawicki W, Geoghegan EM, Ludwig DL, Dadachova E. ²²⁵Ac-labeled CD33-targeting antibody reverses resistance to Bcl-2 inhibitor venetoclax in acute myeloid leukemia models. *Cancer Med.* 2021;10:1128–1140.
59. Novruzov F, Mehdi E, Aliyeva G, et al. Tandem therapy versus single agent ¹⁷⁷Lu-PSMA and ²²⁵Ac-PSMA therapy of advanced stage metastatic castration resistant prostate carcinoma: clinical trial from Azerbaijan [abstract]. *J Nucl Med.* 2022;63(suppl 2):2548.
60. Bodei L, Herrmann K, Schöder H, Scott AM, Lewis JS. Radiotheranostics in oncology: current challenges and emerging opportunities. *Nat Rev Clin Oncol.* 2022;19:534–550.
61. Sathekge M, Bruchertseifer F, Vorster M, et al. mCRPC patients receiving ²²⁵Ac-PSMA-617 therapy in the post-androgen deprivation therapy setting: response to treatment and survival analysis. *J Nucl Med.* 2022;63:1496–1502.

Amino Acid PET in Neurooncology

Norbert Galldiks^{1–3}, Philipp Lohmann², Gereon R. Fink^{1,2}, and Karl-Josef Langen^{2–4}

¹Department of Neurology, Faculty of Medicine, University Hospital Cologne, University of Cologne, Cologne, Germany;

²Institute of Neuroscience and Medicine, Research Center Juelich, Juelich, Germany; ³Center for Integrated Oncology, Universities of Aachen, Bonn, Cologne, and Duesseldorf, Germany; and ⁴Department of Nuclear Medicine, RWTH University Hospital Aachen, Aachen, Germany

Learning Objectives: On successful completion of this activity, participants should be able to describe (1) advantages and limitations of anatomic MRI for brain tumor diagnostics; (2) the added clinical value of amino acid PET in glioblastoma patients or in patients with brain metastases for differential diagnosis, delineation of tumor extent, diagnosis of treatment-related changes, and assessment of treatment response; and (3) the differences in the information obtained by anatomical MRI and amino acid PET.

Financial Disclosure: Drs. Galldiks and Lohmann received honoraria for lectures from Blue Earth Diagnostics, and Dr. Galldiks received honoraria for advisory board participation from Telix Pharmaceuticals. The authors of this article have indicated no other relevant relationships that could be perceived as a real or apparent conflict of interest.

CME Credit: SNMMI is accredited by the Accreditation Council for Continuing Medical Education (ACCME) to sponsor continuing education for physicians. SNMMI designates each *JNM* continuing education article for a maximum of 2.0 AMA PRA Category 1 Credits. Physicians should claim only credit commensurate with the extent of their participation in the activity. For CE credit, SAM, and other credit types, participants can access this activity through the SNMMI website (<http://www.snmmlearningcenter.org>) through May 2026.

For decades, several amino acid PET tracers have been used to optimize diagnostics in patients with brain tumors. In clinical routine, the most important clinical indications for amino acid PET in brain tumor patients are differentiation of neoplasm from nonneoplastic etiologies, delineation of tumor extent for further diagnostic and treatment planning (i.e., diagnostic biopsy, resection, or radiotherapy), differentiation of treatment-related changes such as pseudoprogression or radiation necrosis after radiation or chemoradiation from tumor progression at follow-up, and assessment of response to anticancer therapy, including prediction of patient outcome. This continuing education article addresses the diagnostic value of amino acid PET for patients with either glioblastoma or metastatic brain cancer.

Key Words: FET; MET; FDOPA; fluciclovine

J Nucl Med 2023; 64:693–700

DOI: 10.2967/jnumed.122.264859

Contrast-enhanced anatomic MRI is the diagnostic method of choice for patients with primary (gliomas) and secondary (brain metastases) brain cancer because of excellent soft-tissue contrast, high spatial resolution, and widespread availability (1,2). Anatomic MRI is also an essential component of almost all clinical trials on brain tumor patients, based on its ability to generate surrogate endpoints (e.g., MRI findings consistent with complete or partial response or progressive disease) that can be correlated with progression-free and overall survival. On the other hand, its specificity for tumor tissue is suboptimal, resulting in challenges in distinguishing cancer from nonneoplastic lesions at initial presentation; delineating tumor extent, especially in nonenhancing tumors; and differentiating treatment-related changes from tumor relapse (1,3–8).

Received Jan. 16, 2023; revision accepted Mar. 10, 2023.
For correspondence or reprints, contact Norbert Galldiks (norbert.galldiks@uk-koeln.de).

Published online Apr. 13, 2023.

COPYRIGHT © 2023 by the Society of Nuclear Medicine and Molecular Imaging.

Irrespective of a continuously expanding number of advanced MRI sequences, other modalities—especially PET using multiple radiolabeled molecules—have been evaluated over the past few decades to overcome these limitations of anatomic MRI. In particular, the PET task force of the Response Assessment in Neuro-Oncology Working Group emphasized that the additional clinical value of amino acid PET for glioma patients, compared with anatomic MRI, is outstanding and justifies its widespread clinical use at all disease stages (9). In addition, the PET/Response Assessment in Neuro-Oncology Working Group has published recommendations for using amino acid PET in patients with brain metastases (10).

Although various new applications have been addressed recently using PET techniques (e.g., noninvasive grading in primary brain tumors characterized according to older classifications of the World Health Organization [WHO] (11), noninvasive prediction of molecular markers, diagnosis of malignant progression, and the prognostic value of PET in patients with newly diagnosed and untreated brain tumors), for neurooncologists and medical professionals involved in the care of patients with brain tumors, the following PET applications are of particular clinical interest: differentiation of neoplasms from nonneoplastic etiologies, delineation of tumor extent for further diagnostic and treatment management, differentiation of treatment-related changes such as pseudoprogression or radiation necrosis after radiation or chemoradiation from tumor relapse at follow-up, and prediction of response to anticancer therapy as evaluated by patient outcome. This continuing education article addresses the diagnostic value of amino acid PET for these clinically highly relevant indications in patients with either glioblastoma or metastatic brain cancer.

RADIOLABELED AMINO ACIDS

The most widely used amino acid tracers for PET to date are *O*-(2-¹⁸F-fluoroethyl)-L-tyrosine (¹⁸F-FET), ¹¹C-methyl-L-methionine (¹¹C-MET), and 3,4-dihydroxy-6-¹⁸F-fluoro-L-phenylalanine (¹⁸F-FDOPA). Their uptake is facilitated by large neutral amino acid transporters of the L-type (LAT) in gliomas and brain metastases (i.e., subtypes LAT1 and LAT2), which are regularly

overexpressed in both brain tumor types (1,12–15). Most early amino acid PET studies used ^{11}C -MET, but the short half-life of 20 min imposes logistic challenges, necessitating an on-site cyclotron (16,17). The advent of ^{18}F -labeled radiolabeled amino acids with a considerably longer half-life of 110 min allowed transport to other neurooncologic centers. For example, ^{18}F -FET was developed almost 25 y ago, and its use has multiplied (16,18,19), resulting in ^{11}C -MET replacement, especially in Europe (1). After being moved by LAT transporters into neoplastic tissue, ^{18}F -FET is not metabolized (20), whereas ^{11}C -MET shows incorporation into protein, participation in other metabolic pathways, or metabolic degradation (21).

^{18}F -FDOPA is another ^{18}F -labeled amino acid analog initially developed to evaluate dopamine synthesis in the basal ganglia and has also increasingly been used for imaging brain tumors (22). In the United States and Europe, ^{18}F -FDOPA is approved for characterizing presynaptic dopaminergic activity in patients with Parkinsonian syndromes, and in Europe ^{18}F -FDOPA has also been approved for imaging of brain tumors and various neuroendocrine tumors. Notably, physiologic uptake of ^{18}F -FDOPA in the striatum may hamper its use in evaluating tumor extent (1,23). On the other hand, uptake in the striatum can also be used as a reference for qualitative (visual) analysis of tumor uptake.

Acquisition of dynamic amino acid PET data (predominantly using the tracer ^{18}F -FET) allows characterization of the temporal pattern of tracer uptake by deriving a time–activity curve. Subsequently, qualitative and quantitative dynamic uptake parameters such as the configuration of time–activity curves, time to peak, and slope can be calculated for further data analysis to increase diagnostic performance, such as for diagnosis of treatment-related changes (24,25). Initial data suggest that the dynamic ^{18}F -FDOPA PET acquisition is also of value for differentiating glioma progression from treatment-related changes (26).

Although first used for brain tumor imaging in 1999 (27), the synthetic amino acid analog anti-1-amino-3- ^{18}F -fluorocyclobutane-1-carboxylic acid (^{18}F -fluciclovine) has gained clinical interest, particularly for imaging of primary and secondary brain tumors in recent years. Since this tracer was initially used primarily to diagnose prostate cancer recurrence (28), ^{18}F -fluciclovine was approved in the United States and Europe for evaluating recurrent prostate cancer (29), but the tracer also received orphan drug status for glioma imaging in the United States. Transport of ^{18}F -fluciclovine is mediated to some extent by LAT1 but predominantly by another neutral amino acid transporter, the neutral alanine, serine, cysteine transporter 2, which is not expressed at the luminal side of the blood–brain barrier (30). In general, significantly higher tumor-to-brain contrast is observed with ^{18}F -fluciclovine than with the established amino acid tracers (31), primarily because of the low transport of ^{18}F -fluciclovine through the intact blood–brain barrier. Like ^{11}C -MET, ^{18}F -FET, and ^{18}F -FDOPA, it appears that ^{18}F -fluciclovine accumulates also in nonenhancing gliomas and identifies infiltrating tumor areas that do not show contrast enhancement on MRI (32,33).

In general, all radiolabeled amino acids exhibit relatively low uptake in normal brain tissue, and brain tumors can easily be distinguished from the surrounding healthy-appearing brain tissue with high contrast. Of note, the use of ^{18}F -FDG—the most widely applied PET tracer in oncology—in distinguishing tumor tissue from normal tissue is limited by the physiologically increased rate of glucose metabolism in the cerebral cortex. Therefore, in recent

years, radiolabeled amino acids have become the preferred PET probes in neurooncology (1,9,10,34).

DIFFERENTIATION OF NEOPLASM FROM NONNEOPLASTIC ETIOLOGIES

In general, neoplastic lesions such as glioblastoma or brain metastases exhibit a considerably higher uptake of radiolabeled amino acids than do nonneoplastic lesions, a factor that may be considered for differential diagnosis. A metaanalysis including more than 450 patients from 13 ^{18}F -FET PET studies yielded a pooled sensitivity of 82% and specificity of 76% for diagnosing primary brain tumors (35). In that study, most patients had gliomas ($n = 338$; 84%) of various central nervous system (CNS) WHO grades. Eighteen patients had a nonglial brain tumor (5%). Across all tumor types, a mean tumor-to-brain ratio of 1.6 and a maximum tumor-to-brain ratio of 2.1 best separated primary neoplastic lesions from nonneoplastic lesions. A large single-center study including 393 patients observed comparable diagnostic performance (36). In that study, 68 patients were diagnosed with glioblastoma (17%). Of note, in that study, ^{18}F -FET uptake was evaluated only visually by a single nuclear medicine physician, and the results should be considered with caution (37). Another study of 174 patients with newly diagnosed cerebral lesions suggestive of brain tumors reported a high specificity (92%) but a lower sensitivity (57%) for the differentiation of neoplastic lesions from nonneoplastic lesions using ^{18}F -FET PET (38). On the other hand, a maximum tumor-to-brain ratio of more than 2.5 yielded a convincing positive predictive value of 98% for tumor tissue. For ^{11}C -MET PET, a series of 196 consecutive patients revealed that differentiation between gliomas and nontumoral lesions using a simple threshold was correct in 79% (39). Similar findings were recently observed in 101 pretreatment patients (40).

Thus, amino acid PET adds valuable information for differential diagnostics of suggestive CNS lesions for glial brain tumors, but neuropathologic tissue evaluation remains mandatory in most patients to provide a final diagnosis. Nevertheless, it should be kept in mind that mild but increased amino acid tracer uptake may also occur—although it is much less common—in nonneoplastic lesions (e.g., acute or subacute brain ischemia, brain abscess, inflammatory lesions related to active multiple sclerosis, or status epilepticus) (41–46). In addition, 20%–30% of patients with gliomas of CNS WHO grade 2 with an isocitrate dehydrogenase (IDH) gene mutation exhibit no amino acid uptake (42,43,47,48).

A subgroup of patients who had brain lesions without ^{18}F -FET uptake but with MRI findings suggestive of CNS WHO grade 2 gliomas (i.e., hyperintense T2/fluid-attenuated inversion recovery [FLAIR] signal without contrast enhancement) may even show photopenic defects on ^{18}F -FET PET with uptake visually lower than the healthy background uptake but harbor gliomas of higher CNS WHO grades (49). This phenomenon has also been described for the radiolabeled amino acids ^{11}C -MET and ^{18}F -FDOPA (50).

In most patients with metastatic brain cancer, even small brain metastases (maximal diameter, <5 mm) can easily be delineated by contrast-enhanced anatomic MRI. In addition, the increased expression of amino acid transporters in brain metastases is a compelling target for amino acid PET (13). For example, in 30 patients with 45 newly diagnosed brain metastases from cancer of different origins, approximately 90% of the lesions had a ^{18}F -FET uptake of 1.6 or more compared with the healthy-appearing contralateral hemisphere. In particular, in all lesions with a diameter larger than 1 cm, the ^{18}F -FET uptake was pathologically increased (51).

A similar dependence on lesion size was observed in patients with newly diagnosed brain metastases evaluated using ^{18}F -fluciclovine PET (52). Nevertheless, the most commonly used imaging modality for brain metastasis detection remains thin-slice contrast-enhanced MRI, which has the highest sensitivity for this application.

In contrast to extracranial cancer, the value of ^{18}F -FDG PET for brain metastasis detection appears to be limited. For example, a metaanalysis revealed ^{18}F -FDG PET to have a cumulative sensitivity of only 21% for diagnosis of brain metastases secondary to lung cancer (53).

DELINEATION OF TUMOR EXTENT

Regarding delineation of tumor extent in glioma patients, anatomic MRI is particularly limited in its ability to identify nonenhancing glioma subregions (1). Radiolabeled amino acids for PET can pass the intact blood-brain barrier (54,55). Predominantly in nonenhancing gliomas, several studies have spatially compared amino acid tracer uptake with neuropathologic findings obtained by stereotactic biopsy and shown that radiolabeled amino acids identify glioma extent more reliably than standard MRI (56–62). Furthermore, in patients with an MRI-based suspicion of a CNS WHO grade 2 glioma (typically a T2-hyperintense lesion without contrast enhancement on MRI), amino acid PET parameters obtained from both static and dynamic acquisitions correlated neuropathologically with the most malignant tumor parts (56–62)—a finding that is of considerable interest for prognostic evaluation and the planning of diagnostic and therapeutic interventions (e.g., biopsy and target volume definition for radiotherapy).

In terms of volumetric comparison of contrast enhancement with the tumor volume obtained by amino acid PET, previous studies of both newly diagnosed and recurrent IDH-wild-type glioblastomas suggested that there are significant differences in the size, overlap, and spatial correlation of tumor volumes (3,63,64), indicating that conventional contrast-enhanced MRI considerably underestimates the metabolically active tumor volume (Fig. 1). Consequently, efforts have been initiated to evaluate whether an amino acid PET-guided treatment may improve patient outcomes. Initial studies suggested that amino acid PET-based radiotherapy significantly affects patient survival (65,66).

In contrast to gliomas, the size and volume of brain metastases are usually well delineated on contrast-enhanced MRI because of fewer infiltrative growth characteristics on a submillimeter level (67). Thus, for biopsy or treatment planning, amino acid PET does

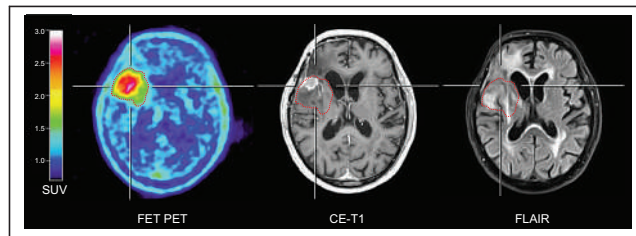


FIGURE 1. ^{18}F -FET PET, contrast-enhanced MRI, and FLAIR MRI of 89-y-old patient with recurrent IDH-wild-type glioblastoma. Metabolically active tumor as identified by increased uptake of ^{18}F -FET (threshold of 1.6 based on mean tumor-to-brain ratio) is outlined and projected onto MR images (red contour). Extent of metabolically active tumor on ^{18}F -FET PET exceeds contrast-enhancing tumor portion and shows considerable spatial discrepancies from area of FLAIR hyperintensities. CE = contrast-enhanced.

not add valuable information on extent, as reported for patients with newly diagnosed gliomas (58,68).

DIFFERENTIATION OF TUMOR RELAPSE FROM TREATMENT-RELATED CHANGES

After treatment for brain tumors, differentiation of treatment-related changes from actual tumor relapse remains challenging (1,4,8,69,70) and is of paramount clinical relevance, with considerable impact on clinical management. For example, a recent retrospective study of 189 patients found that amino acid PET changed clinical management in 53% of patients with suspected recurrent disease (71). Erroneous interpretation of treatment-related changes as tumor progression may lead to unnecessary and premature termination of an effective treatment option, with a subsequent potentially negative impact on survival. Furthermore, the efficacy of the subsequent treatment (72) may be overestimated, generating misleading results in studies evaluating recurrent treatment options (73).

In clinical routine, this differentiation is the most frequent indication for amino acid PET and is requested in almost 50% of glioma patients (74). In patients with predominantly IDH-wild-type glioblastoma, high diagnostic accuracy has repeatedly been shown for amino acid PET using ^{18}F -FET and ^{18}F -FDOPA in differentiating between tumor progression and treatment-related changes that occur early (i.e., pseudoprogression after chemoradiation plus temozolamide within the first 3 mo) or late (e.g., radiation necrosis, onset usually > 6 mo after radiotherapy completion) (24,69,75–82). In these studies, differentiation was correct 80%–90% of the time. For ^{11}C -MET PET, diagnostic performance appears to be slightly lower, with an accuracy of approximately 75% (83,84), most probably related to a higher affinity of ^{11}C -MET for inflammatory lesions (85). A recent prospective study evaluated ^{18}F -fluciclovine PET for diagnosing pseudoprogression and provided 90% sensitivity and 83% specificity for this clinically relevant indication (86). Importantly, PET findings were validated neuropathologically in that study in all patients ($n = 30$).

In patients with brain metastases, radiosurgery has become an indispensable and frequently used local treatment option (10,87). Depending on the irradiated lesion volume and radiation dose, an increased radiation necrosis rate has been reported in patients with brain metastases treated by radiosurgery (88). For differentiation of local radiation injury such as radiation necrosis from brain metastasis relapse after radiosurgery, PET using ^{18}F -FDOPA and ^{11}C -MET has consistently demonstrated high sensitivity and specificity of approximately 80% (Fig. 2) (83,89–92). Similarly, ^{18}F -FET PET parameters derived from static and dynamic acquisitions showed high sensitivity and specificity of 80%–90% for distinguishing radiation-induced changes after radiosurgery from recurrent brain metastases (25,93,94). A recent metaanalysis including 13 ^{11}C -MET, ^{18}F -FET, or ^{18}F -FDOPA PET studies with almost 400 patients highlighted the added clinical value of amino acid PET for differentiating treatment-related changes from brain metastasis relapse (95). In that study, pooled sensitivity and specificity were 82% and 84%, respectively.

In most of these studies, radiation-induced changes were distinguished from brain metastasis relapse solely on the basis of a single amino acid PET scan. A recent study evaluated serial amino acid PET scans and suggested that stable ^{18}F -FDOPA uptake over a long-term follow-up (median, 18 mo) identified radiation-induced changes with a relatively high accuracy of 94% (96). ^{18}F -FDOPA uptake did

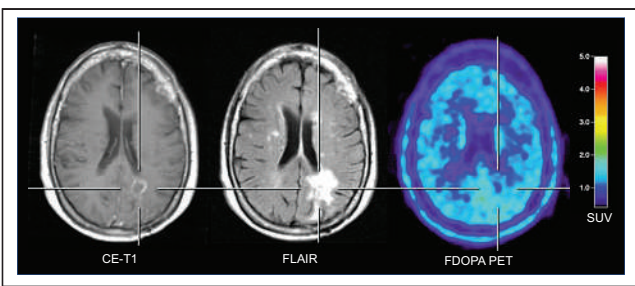


FIGURE 2. A 68-y-old woman with brain metastasis secondary to renal cell carcinoma who underwent anatomic MRI and ^{18}F -FDOPA PET. Twelve months after resection with postoperative radiosurgery, MRI suggested local tumor recurrence. In contrast, ^{18}F -FDOPA PET showed no increased metabolic activity (mean tumor-to-brain ratio, 1.0) indicating treatment-related changes such as radiation injury. Diagnosis was confirmed by subsequent neuroimaging 3 mo later, including amino acid PET and anatomic MRI, demonstrating unchanged imaging findings and stable clinical course without any therapeutic intervention. CE = contrast-enhanced.

not change significantly in radionecrotic lesions but did increase significantly over time in patients with brain metastasis relapse.

Checkpoint inhibitor immunotherapy as a systemic treatment option has considerable efficacy in patients with brain metastases, showing intracranial objective response rates of almost 60% (97,98). On the other hand, reactive changes on MRI may also occur after these systemic treatment options and can also be challenging to distinguish from brain metastasis relapse. For example, pseudoprogression related to inflammation triggered by immune system reactions may occur in patients with brain metastases treated with immune checkpoint inhibitors using antibodies against cytotoxic T-lymphocyte-associated antigen 4 (e.g., ipilimumab), programmed death protein 1 (e.g., pembrolizumab and nivolumab), or programmed cell death ligand 1 (e.g., atezolizumab). A pilot study highlighted the potential of amino acid PET using ^{18}F -FET to identify pseudoprogression in patients with melanoma brain metastases treated with blockade of cytotoxic T-lymphocyte-associated antigen 4 (99). A subsequent study confirmed the potential of amino acid PET in patients undergoing immune checkpoint inhibition; pseudoprogression was detected in a higher number of patients with brain metastasis secondary to lung cancer or melanoma (100).

ASSESSMENT OF TREATMENT RESPONSE

In glioma patients, changes in the extent of contrast enhancement on MRI are typically used as an indicator of complete or partial response or tumor progression (72,101). In addition, in patients treated with antiangiogenic agents for glioblastoma recurrence, an increase in signal hyperintensity on T2 or FLAIR MRI sequences was frequently used to diagnose nonenhancing tumor progression (72). Nevertheless, these signal changes are unspecific and may be related to perifocal edema, radiation injury, demyelination, inflammation, or ischemia, hampering the distinction from nonenhancing tumor (4,8,70). Alternative diagnostic methods such as amino acid PET have been evaluated to improve treatment response assessment. In glioblastoma patients, alkylating chemotherapy and antiangiogenic therapy are frequently applied systemic treatment options.

For ^{11}C -MET PET, a reliable response assessment to temozolomide and nitrosourea-based chemotherapy has been demonstrated primarily in glioblastoma patients at recurrence (102–105). Notably, metabolic responders on ^{11}C -MET PET had a significantly improved

outcome compared with metabolic nonresponders (102). Subsequently, ^{18}F -FET PET has been used to evaluate the effects of temozolomide in patients with CNS WHO grade 2 gliomas (106). In metabolic responders, ^{18}F -FET PET tumor volume reductions after treatment initiation were observed considerably earlier than volume reductions on FLAIR MRI. These findings were confirmed by subsequent ^{18}F -FET PET studies with more patients (107,108).

In patients with newly diagnosed IDH-wild-type glioblastoma, prospective studies assessed the predictive value of early ^{18}F -FET uptake changes 6–8 wk after postoperative chemoradiation with concomitant temozolomide relative to the baseline scan (109,110). ^{18}F -FET PET responders with a decrease in metabolic activity as assessed by tumor-to-brain ratios had significantly longer survival than patients with stable or increasing tracer uptake after chemoradiation. Similar findings were reported in newly diagnosed glioblastoma patients early after initiating adjuvant temozolomide chemotherapy, that is, after 2 cycles (111). An example for response assessment of temozolomide chemotherapy used in a patient with a progressive glioblastoma is shown in Figure 3.

According to current guidelines (112), lomustine-based chemotherapy is recommended for patients with CNS WHO grade 3 or 4 gliomas at recurrence, especially in Europe, where bevacizumab is not approved in most countries. A recent study evaluated the new occurrence of lesions on follow-up ^{18}F -FET PET scans showing pathologically increased metabolic activity remote from the tumor at baseline in mostly glioblastoma patients undergoing lomustine-based chemotherapy (113). In that study, the occurrence of these distant and metabolically active hot spots on ^{18}F -FET PET proved to be the strongest predictor for nonresponse.

Furthermore, amino acid PET has been particularly evaluated in the recurrence setting to assess response to antiangiogenic therapy such as bevacizumab (114). In addition, ^{18}F -FDOPA and ^{18}F -FET PET have been found useful for identifying pseudoresponse (115–119). Moreover, ^{18}F -FDOPA and ^{18}F -FET Pet also seem

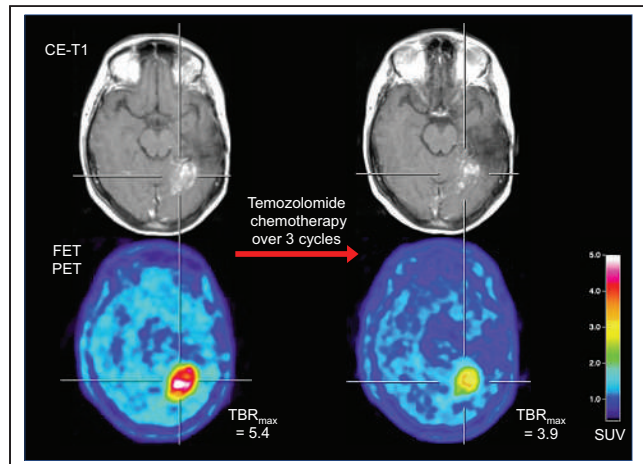


FIGURE 3. A 45-y-old woman with IDH-wild-type glioblastoma who underwent partial resection and radiotherapy with temozolomide plus lomustine chemotherapy as first-line treatment. Twenty-two months later, contrast-enhanced MRI and ^{18}F -FET PET were consistent with tumor progression (left). For treatment, temozolomide chemotherapy was initiated. After 3 cycles, clear decrease in maximum tumor-to-brain ratios ($\sim 28\%$) was observed, whereas MRI showed only slight decrease in contrast enhancement (right). Metabolic response was associated with progression-free survival of 6 mo after temozolomide initiation. CE = contrast-enhanced; TBR_{max} = maximum tumor-to-brain ratio.

helpful in predicting a favorable outcome in bevacizumab responders (118–120). A prospective study suggested that ¹⁸F-FET PET is useful for identifying metabolic responders to bevacizumab combined with lomustine in newly diagnosed IDH-wild-type glioblastoma patients early after treatment initiation (121). In that study, MRI changes according to the criteria of the Response Assessment in Neuro-Oncology Working Group (72) were not predictive of a favorable outcome, whereas ¹⁸F-FET PET parameters significantly predicted an overall survival of more than 9 mo.

Another anticancer therapy option with considerable efficacy in glioblastoma patients at recurrence is the multikinase inhibitor regorafenib, which is characterized by pronounced antiangiogenic activity (122). On the other hand, similar to glioma patients treated with standard chemoradiation using alkylating agents, equivocal MRI findings were also reported in glioma patients undergoing regorafenib treatment at recurrence (123–125). It has been suggested that amino acid PET using ¹⁸F-FET or ¹⁸F-FDOPA may help identify both treatment-related changes such as pseudoresponse or pseudoprogression and response to regorafenib (123–125).

The advent of immunotherapy using immune checkpoint inhibitors and targeted therapy has dramatically improved the treatment of extracranial cancer, especially in patients with skin, lung, or breast cancer. Moreover, recent trials have shown that patients with brain metastases may also benefit from these agents, especially when dual checkpoint blockade is applied (97,98). Similar to the response assessment in glioma patients, initial studies suggest that serial amino acid PET can potentially add valuable information to anatomic MRI for the assessment of immunotherapy effects. For example, a more recent study in 40 patients with more than 100 lung cancer or melanoma brain metastases treated with radiosurgery, checkpoint inhibitors, or combinations thereof evaluated whether ¹⁸F-FET PET may provide important diagnostic information on both response assessment and diagnosis of pseudoprogression (100). In that study, metabolic responders had significantly longer progression-free survival.

In addition to immune checkpoint blockade, targeted therapy using small molecules has demonstrated activity against brain metastases (126–128). The presence of predictive genetic alterations such as mutation of epidermal growth factor receptor, translocation of anaplastic lymphoma kinase or c-ROS oncogene 1, overexpression of human epidermal growth factor receptor 2, or mutation of BRAF V600E is considered an essential prerequisite for a response to targeted therapy options (129). Monitoring of metabolic activity reduction in patients with brain metastasis secondary to non-small cell lung cancer or melanoma treated with targeted therapies such as inhibitors of BRAF kinase or epidermal growth factor receptor as a sign of response appeared feasible using ¹⁸F-FET PET, whereas findings on anatomic MRI remained unchanged (10,130).

SUMMARY AND OUTLOOK

The current literature provides strong evidence that amino acid PET is of considerable clinical value for the most critical diagnostic indications in neurooncology. PET using amino acid tracers offers a variety of insights for the assessment of brain tumors, with the potential to overcome the limitations of anatomic MRI. The diagnostic improvement probably facilitates meaningful decision making and justifies more widespread use of this diagnostic tool (9,131). Furthermore, the necessary PET infrastructure is widely available, and the production of radiolabeled amino acids is well established, with costs comparable to other tracers

routinely used in clinical practice. Moreover, additional costs for amino acid PET can potentially be saved by the incurred costs of less reliable diagnostic imaging techniques (132–136).

Clinicians will find amino acid PET to be an especially robust and attractive approach for many indications, with the advantage of easy scan reading. Importantly, most studies using amino acid PET provide comparable results across different scanners, as is also a consequence of international and interdisciplinary efforts by major nuclear medicine and neurooncology societies regarding standardization of amino acid PET acquisition and evaluation in brain tumor imaging in adults and children (137,138).

Adding novel advanced MRI techniques (e.g., ultra-high-field 2-hydroxyglutarate spectroscopic MRI and chemical exchange saturation transfer imaging) to amino acid PET has the potential to provide a more profound evaluation of biologic characteristics in patients with glioblastoma or metastatic brain disease. The complementary information derived from these imaging techniques suggests differential biologic information warranting further evaluation (139).

A methodologic innovation that may significantly alleviate research in brain tumor patients is the increasing availability of hybrid PET/MRI scanners, which enable time-saving simultaneous acquisition of several PET and advanced MR parameters under the same physiologic or pathophysiologic conditions. In addition, hybrid PET/MRI provides practical advantages and is convenient for patients such as children and individuals with a poor clinical condition. On the other hand, initial research suggests that for frequently requested indications for amino acid PET in clinical routine, such as differentiating treatment-related changes from tumor relapse, there is no significant difference in diagnostic performance between simultaneous and sequential acquisitions of PET and MRI (140).

REFERENCES

- Langen KJ, Galldiks N, Hattingen E, Shah NJ. Advances in neuro-oncology imaging. *Nat Rev Neurol*. 2017;13:279–289.
- Pope WB, Brandal G. Conventional and advanced magnetic resonance imaging in patients with high-grade glioma. *Q J Nucl Med Mol Imaging*. 2018;62:239–253.
- Lohmann P, Stavrinou P, Lipke K, et al. FET PET reveals considerable spatial differences in tumour burden compared to conventional MRI in newly diagnosed glioblastoma. *Eur J Nucl Med Mol Imaging*. 2019;46:591–602.
- Dhermain FG, Hau P, Lanfermann H, Jacobs AH, van den Bent MJ. Advanced MRI and PET imaging for assessment of treatment response in patients with gliomas. *Lancet Neurol*. 2010;9:906–920.
- Brandsma D, Stalpers L, Taal W, Sminia P, van den Bent MJ. Clinical features, mechanisms, and management of pseudoprogression in malignant gliomas. *Lancet Oncol*. 2008;9:453–461.
- Hygino da Cruz LC Jr, Rodriguez I, Domingues RC, Gasparetto EL, Sorensen AG. Pseudoprogression and pseudoresponse: imaging challenges in the assessment of posttreatment glioma. *AJNR*. 2011;32:1978–1985.
- Yang I, Aghi MK. New advances that enable identification of glioblastoma recurrence. *Nat Rev Clin Oncol*. 2009;6:648–657.
- Kumar AJ, Leeds NE, Fuller GN, et al. Malignant gliomas: MR imaging spectrum of radiation therapy- and chemotherapy-induced necrosis of the brain after treatment. *Radiology*. 2000;217:377–384.
- Albert NL, Weller M, Suchorska B, et al. Response Assessment in Neuro-Oncology Working Group and European Association for Neuro-Oncology recommendations for the clinical use of PET imaging in gliomas. *Neuro Oncol*. 2016;18:1199–1208.
- Galldiks N, Langen KJ, Albert NL, et al. PET imaging in patients with brain metastasis: report of the RANO/PET group. *Neuro Oncol*. 2019;21:585–595.
- Louis DN, Ohgaki H, Wiestler OD, et al. The 2007 WHO classification of tumours of the central nervous system. *Acta Neuropathol (Berl)*. 2007;114:97–109.
- Youland RS, Kitange GJ, Peterson TE, et al. The role of LAT1 in ¹⁸F-DOPA uptake in malignant gliomas. *J Neurooncol*. 2013;111:11–18.
- Popin-Michault C, Bonnetaud C, Dufour M, et al. Study of LAT1 expression in brain metastases: towards a better understanding of the results of positron emission tomography using amino acid tracers. *PLoS One*. 2016;11:e0157139.

14. Wiriayasermkul P, Nagamori S, Tominaga H, et al. Transport of 3-fluoro-L-alpha-methyl-tyrosine by tumor-upregulated L-type amino acid transporter 1: a cause of the tumor uptake in PET. *J Nucl Med*. 2012;53:1253–1261.
15. Okubo S, Chen HN, Kawan N, Nishiyama Y, Haba R, Tamiya T. Correlation of L-methyl-[¹¹C]-methionine (MET) uptake with L-type amino acid transporter 1 in human gliomas. *J Neurooncol*. 2010;99:217–225.
16. Langen KJ, Hamacher K, Weckesser M, et al. O-(2-[¹⁸F]fluoroethyl)-L-tyrosine: uptake mechanisms and clinical applications. *Nucl Med Biol*. 2006;33:287–294.
17. Galldiks N, Law I, Pope WB, Arbizu J, Langen KJ. The use of amino acid PET and conventional MRI for monitoring of brain tumor therapy. *Neuroimage Clin*. 2016;13:386–394.
18. Wester HJ, Herz M, Weber W, et al. Synthesis and radiopharmacology of O-(2-[¹⁸F]fluoroethyl)-L-tyrosine for tumor imaging. *J Nucl Med*. 1999;40:205–212.
19. Langen KJ, Tonn JC, Weller M, Galldiks N. Letter to the Editor: “The role of imaging in the management of progressive glioblastoma. A systematic review and evidence-based clinical practice guideline” [J Neurooncol 2014; 118:435–460]. *J Neurooncol*. 2014;120:665–666.
20. Langen KJ, Jarosch M, Mühlensiepen H, et al. Comparison of fluorotyrosines and methionine uptake in F98 rat gliomas. *Nucl Med Biol*. 2003;30:501–508.
21. Singhal T, Narayanan TK, Jain V, Mukherjee J, Mantil J. ¹¹C-L-methionine positron emission tomography in the clinical management of cerebral gliomas. *Mol Imaging Biol*. 2008;10:1–18.
22. Becherer A, Karanikas G, Szabo M, et al. Brain tumour imaging with PET: a comparison between [¹⁸F]fluorodopa and [¹¹C]methionine. *Eur J Nucl Med Mol Imaging*. 2003;30:1561–1567.
23. Cicone F, Filiss CP, Minniti G, et al. Volumetric assessment of recurrent or progressive gliomas: comparison between F-DOPA PET and perfusion-weighted MRI. *Eur J Nucl Med Mol Imaging*. 2015;42:905–915.
24. Galldiks N, Stoeffels G, Filss C, et al. The use of dynamic O-(2-[¹⁸F]fluoroethyl)-L-tyrosine PET in the diagnosis of patients with progressive and recurrent glioma. *Neuro Oncol*. 2015;17:1293–1300.
25. Ceccon G, Lohmann P, Stoeffels G, et al. Dynamic O-(2-[¹⁸F]fluoroethyl)-L-tyrosine positron emission tomography differentiates brain metastasis recurrence from radiation injury after radiotherapy. *Neuro Oncol*. 2017;19:281–288.
26. Rozenblum L, Zaragori T, Tran S, et al. Differentiating high-grade glioma progression from treatment-related changes with dynamic [¹⁸F]FDOPA PET: a multicentric study. *Eur Radiol*. 2023;33:2548–2560.
27. Shoup TM, Olson J, Hoffman JM, et al. Synthesis and evaluation of [¹⁸F]-amino-3-fluorocyclobutane-1-carboxylic acid to image brain tumors. *J Nucl Med*. 1999;40:331–338.
28. Laudicella R, Albano D, Alongi P, et al. ¹⁸F-FACBC in prostate cancer: a systematic review and meta-analysis. *Cancers (Basel)*. 2019;11:1348.
29. Bognrud TV, Londalen A, Brandal P, et al. ¹⁸F-fluciclovine PET/CT in suspected residual or recurrent high-grade glioma. *Clin Nucl Med*. 2019;44:605–611.
30. Ono M, Oka S, Okudaira H, et al. Comparative evaluation of transport mechanisms of trans-1-amino-3-[¹⁸F]fluorocyclobutanecarboxylic acid and L-[methyl-¹¹C]-methionine in human glioma cell lines. *Brain Res*. 2013;1535:24–37.
31. Albano D, Tomasini D, Bonu M, Giubbini R, Bertagna F. ¹⁸F-fluciclovine (¹⁸F-FACBC) PET/CT or PET/MRI in gliomas/glioblastomas. *Ann Nucl Med*. 2020; 34:81–86.
32. Tsuyuguchi N, Terakawa Y, Uda T, Nakajo K, Kanemura Y. Diagnosis of brain tumors using amino acid transport PET imaging with ¹⁸F-fluciclovine: a comparative study with L-methyl-¹¹C-methionine PET imaging. *Asia Ocean J Nucl Med Biol*. 2017;5:85–94.
33. Wakabayashi T, Iuchi T, Tsuyuguchi N, et al. Diagnostic performance and safety of positron emission tomography using ¹⁸F-fluciclovine in patients with clinically suspected high- or low-grade gliomas: a multicenter phase IIb trial. *Asia Ocean J Nucl Med Biol*. 2017;5:10–21.
34. Galldiks N, Langen KJ, Albert NL, et al. Investigational PET tracers in neuro-oncology: what’s on the horizon? A report of the PET/RANO group. *Neuro Oncol*. 2022;24:1815–1826.
35. Dunet V, Rossier C, Buck A, Stupp R, Prior JO. Performance of ¹⁸F-fluoro-ethyl-tyrosine (¹⁸F-FET) PET for the differential diagnosis of primary brain tumor: a systematic review and metaanalysis. *J Nucl Med*. 2012;53:207–214.
36. Hutterer M, Nowosielski M, Putzer D, et al. [¹⁸F]-fluoro-ethyl-L-tyrosine PET: a valuable diagnostic tool in neuro-oncology, but not all that glitters is glioma. *Neuro Oncol*. 2013;15:341–351.
37. Langen KJ, Galldiks N. Reply to “[¹⁸F]-fluoro-ethyl-L-tyrosine PET: a valuable diagnostic tool in neuro-oncology, but not all that glitters is glioma” by Hutterer et al. *Neuro Oncol*. 2013;15:816–817.
38. Rapp M, Heinzel A, Galldiks N, et al. Diagnostic performance of ¹⁸F-FET PET in newly diagnosed cerebral lesions suggestive of glioma. *J Nucl Med*. 2013;54: 229–235.
39. Herholz K, Holzer T, Bauer B, et al. ¹¹C-methionine PET for differential diagnosis of low-grade gliomas. *Neurology*. 1998;50:1316–1322.
40. Yamaki T, Higuchi Y, Yokota H, et al. The role of optimal cut-off diagnosis in ¹¹C-methionine PET for differentiation of intracranial brain tumor from non-neoplastic lesions before treatment. *Clin Imaging*. 2022;92:124–130.
41. Floeth FW, Pauleit D, Sabel M, et al. ¹⁸F-FET PET differentiation of ring-enhancing brain lesions. *J Nucl Med*. 2006;47:776–782.
42. Pichler R, Dunzinger A, Wurm G, et al. Is there a place for FET PET in the initial evaluation of brain lesions with unknown significance? *Eur J Nucl Med Mol Imaging*. 2010;37:1521–1528.
43. Hutterer M, Nowosielski M, Putzer D, et al. [¹⁸F]-fluoro-ethyl-L-tyrosine PET: a valuable diagnostic tool in neuro-oncology, but not all that glitters is glioma. *Neuro Oncol*. 2013;15:341–351.
44. Sala Q, Metellus P, Taieb D, Kaphan E, Figarella-Branger D, Guedj E. ¹⁸F-DOPA, a clinically available PET tracer to study brain inflammation? *Clin Nucl Med*. 2014;39:e283–e285.
45. Hutterer M, Ebner Y, Riemenschneider MJ, et al. Epileptic activity increases cerebral amino acid transport assessed by ¹⁸F-fluoroethyl-L-tyrosine amino acid PET: a potential brain tumor mimic. *J Nucl Med*. 2017;58:129–137.
46. Ito K, Matsuda H, Kubota K. Imaging spectrum and pitfalls of ¹¹C-methionine positron emission tomography in a series of patients with intracranial lesions. *Korean J Radiol*. 2016;17:424–434.
47. Jansen NL, Graute V, Armbruster L, et al. MRI-suspected low-grade glioma: is there a need to perform dynamic FET PET? *Eur J Nucl Med Mol Imaging*. 2012; 39:1021–1029.
48. Wollring MM, Werner JM, Ceccon G, et al. Clinical applications and prospects of PET imaging in patients with IDH-mutant gliomas. *J Neurooncol*. December 29, 2022 [Epub ahead of print].
49. Galldiks N, Unterrainer M, Judov N, et al. Photopenic defects on O-(2-[¹⁸F]-fluoroethyl)-L-tyrosine PET: clinical relevance in glioma patients. *Neuro Oncol*. 2019; 21:1331–1338.
50. Zaragori T, Castello A, Guedj E, et al. Photopenic defects in gliomas with amino-acid PET and relative prognostic value: a multicentric ¹¹C-methionine and ¹⁸F-FDOPA PET experience. *Clin Nucl Med*. 2021;46:e36–e37.
51. Unterrainer M, Galldiks N, Suchorska B, et al. ¹⁸F-FET PET uptake characteristics in patients with newly diagnosed and untreated brain metastasis. *J Nucl Med*. 2017;58:584–589.
52. Øen SK, Johannessen K, Pedersen LK, et al. Diagnostic value of ¹⁸F-FACBC PET/MRI in brain metastases. *Clin Nucl Med*. 2022;47:1030–1039.
53. Li Y, Jin G, Su D. Comparison of gadolinium-enhanced MRI and ¹⁸FDG PET/PET-CT for the diagnosis of brain metastases in lung cancer patients: a meta-analysis of 5 prospective studies. *Oncotarget*. 2017;8:35743–35749.
54. Pauleit D, Stoeffels G, Schaden W, et al. PET with O-(2-[¹⁸F]fluoroethyl)-L-tyrosine in peripheral tumors: first clinical results. *J Nucl Med*. 2005;46:411–416.
55. Pirotte B, Goldman S, Massager N, et al. Comparison of ¹⁸F-FDG and ¹¹C-methionine for PET-guided stereotactic brain biopsy of gliomas. *J Nucl Med*. 2004;45: 1293–1298.
56. Kracht LW, Miletic H, Busch S, et al. Delineation of brain tumor extent with [¹¹C]L-methionine positron emission tomography: local comparison with stereotactic histopathology. *Clin Cancer Res*. 2004;10:7163–7170.
57. Pauleit D, Floeth F, Hamacher K, et al. O-(2-[¹⁸F]fluoroethyl)-L-tyrosine PET combined with MRI improves the diagnostic assessment of cerebral gliomas. *Brain*. 2005;128:678–687.
58. Pafundi DH, Laack NN, Youland RS, et al. Biopsy validation of ¹⁸F-DOPA PET and biodistribution in gliomas for neurosurgical planning and radiotherapy target delineation: results of a prospective pilot study. *Neuro Oncol*. 2013;15:1058–1067.
59. Roodakker KR, Alhusseinalkhudur A, Al-Jaff M, et al. Region-by-region analysis of PET, MRI, and histology in en bloc-resected oligodendroglomas reveals intratumoral heterogeneity. *Eur J Nucl Med Mol Imaging*. 2019;46:569–579.
60. Verburg N, Koopman T, Yaqub MM, et al. Improved detection of diffuse glioma infiltration with imaging combinations: a diagnostic accuracy study. *Neuro Oncol*. 2020;22:412–422.
61. Schön S, Cabello J, Liesche-Starnecker F, et al. Imaging glioma biology: spatial comparison of amino acid PET, amide proton transfer, and perfusion-weighted MRI in newly diagnosed gliomas. *Eur J Nucl Med Mol Imaging*. 2020;47:1468–1475.
62. Pauleit D, Floeth F, Hamacher K, et al. O-(2-[¹⁸F]fluoroethyl)-L-tyrosine PET combined with MRI improves the diagnostic assessment of cerebral gliomas. *Brain*. 2005;128:678–687.
63. Galldiks N, Ullrich R, Schroeter M, Fink GR, Jacobs AH, Kracht LW. Volumetry of [¹¹C]-methionine PET uptake and MRI contrast enhancement in patients with recurrent glioblastoma multiforme. *Eur J Nucl Med Mol Imaging*. 2010;37:84–92.
64. Suchorska B, Jansen NL, Linn J, et al. Biological tumor volume in ¹⁸F-FET-PET before radiochemotherapy correlates with survival in GBM. *Neurology*. 2015;84: 710–719.
65. Harat M, Blok M, Miechowicz I, Wiatrowska I, Makarewicz K, Malkowski B. Safety and efficacy of irradiation boost based on ¹⁸F-FET-PET in patients with newly diagnosed glioblastoma. *Clin Cancer Res*. 2022;28:3011–3020.

66. Laack NN, Pafundi D, Anderson SK, et al. Initial results of a phase 2 trial of ¹⁸F-DOPA PET-guided dose-escalated radiation therapy for glioblastoma. *Int J Radiat Oncol Biol Phys.* 2021;110:1383–1395.
67. Berghoff AS, Rajky O, Winkler F, et al. Invasion patterns in brain metastases of solid cancers. *Neuro Oncol.* 2013;15:1664–1672.
68. Munck AF Rosenschold P, Costa J, Engelholm SA, et al. Impact of [¹⁸F]-fluoroethyl-tyrosine PET imaging on target definition for radiation therapy of high-grade glioma. *Neuro Oncol.* 2015;17:757–763.
69. Galldiks N, Dunkl V, Stoeffels G, et al. Diagnosis of pseudoprogression in patients with glioblastoma using O-(2-[¹⁸F]fluoroethyl)-L-tyrosine PET. *Eur J Nucl Med Mol Imaging.* 2015;42:685–695.
70. Ahluwalia MS, Wen PY. Antiangiogenic therapy for patients with glioblastoma: current challenges in imaging and future directions. *Expert Rev Anticancer Ther.* 2011;11:653–656.
71. Brendle C, Maier C, Bender B, et al. Impact of ¹⁸F-FET PET/MRI on clinical management of brain tumor patients. *J Nucl Med.* 2022;63:522–527.
72. Wen PY, Macdonald DR, Reardon DA, et al. Updated response assessment criteria for high-grade gliomas: Response Assessment in Neuro-Oncology Working Group. *J Clin Oncol.* 2010;28:1963–1972.
73. Reardon DA, Weller M. Pseudoprogression: fact or wishful thinking in neuro-oncology? *Lancet Oncol.* 2018;19:1561–1563.
74. Heinzel A, Dedic D, Galldiks N, et al. Two decades of brain tumour imaging with O-(2-[¹⁸F]fluoroethyl)-L-tyrosine PET: the Forschungszentrum Julich experience. *Cancers (Basel).* 2022;14:3336.
75. Mihovilovic MI, Kertels O, Hanscheid H, et al. O-(2-[¹⁸F]fluoroethyl)-L-tyrosine PET for the differentiation of tumour recurrence from late pseudoprogression in glioblastoma. *J Neurol Neurosurg Psychiatry.* 2019;90:238–239.
76. Jena A, Taneja S, Gambhir A, et al. Glioma recurrence versus radiation necrosis: single-session multiparametric approach using simultaneous O-(2-¹⁸F-fluoroethyl)-L-tyrosine PET/MRI. *Clin Nucl Med.* 2016;41:e228–e236.
77. Pyka T, Hiob D, Preibisch C, et al. Diagnosis of glioma recurrence using multiparametric dynamic ¹⁸F-fluoroethyl-tyrosine PET-MRI. *Eur J Radiol.* 2018;103:32–37.
78. Herrmann K, Czernin J, Cloughesy T, et al. Comparison of visual and semiquantitative analysis of ¹⁸F-FDOPA-PET/CT for recurrence detection in glioblastoma patients. *Neuro Oncol.* 2014;16:603–609.
79. Bashir A, Mathilde Jacobsen S, Molby Henriksen O, et al. Recurrent glioblastoma versus late posttreatment changes: diagnostic accuracy of O-(2-[¹⁸F]fluoroethyl)-L-tyrosine positron emission tomography (¹⁸F-FET PET). *Neuro Oncol.* 2019;21:1595–1606.
80. Werner JM, Stoeffels G, Lichtenstein T, et al. Differentiation of treatment-related changes from tumour progression: a direct comparison between dynamic FET PET and ADC values obtained from DWI MRI. *Eur J Nucl Med Mol Imaging.* 2019;46:1889–1901.
81. Steidl E, Langen KJ, Hmeidan SA, et al. Sequential implementation of DSC-MR perfusion and dynamic ¹⁸F-FET Pet allows efficient differentiation of glioma progression from treatment-related changes. *Eur J Nucl Med Mol Imaging.* 2021;48:1956–1965.
82. Werner JM, Weller J, Ceccan G, et al. Diagnosis of pseudoprogression following lomustine-temozolamide chemoradiation in newly diagnosed glioblastoma patients using FET-PET. *Clin Cancer Res.* 2021;27:3704–3713.
83. Minamimoto R, Saginoya T, Kondo C, et al. Differentiation of brain tumor recurrence from post-radiotherapy necrosis with ¹¹C-methionine PET: visual assessment versus quantitative assessment. *PLoS One.* 2015;10:e0132515.
84. Nihashi T, Dahabreh IJ, Terasawa T. Diagnostic accuracy of PET for recurrent glioma diagnosis: a meta-analysis. *AJNR.* 2013;34:944–950.
85. Salber D, Stoeffels G, Pauleit D, et al. Differential uptake of O-(2-¹⁸F-fluoroethyl)-L-tyrosine, ¹L-³H-methionine, and ³H-deoxyglucose in brain abscesses. *J Nucl Med.* 2007;48:2056–2062.
86. Nabavizadeh A, Bagley SJ, Doot RK, et al. Distinguishing progression from pseudoprogression in glioblastoma using ¹⁸F-fluciclovine PET. *J Nucl Med.* December 22, 2022 [Epub ahead of print].
87. Le Rhun E, Guckenberger M, Smits M, et al. EANO-ESMO clinical practice guidelines for diagnosis, treatment and follow-up of patients with brain metastasis from solid tumours. *Ann Oncol.* 2021;32:1332–1347.
88. Minniti G, Clarke E, Lanzetta G, et al. Stereotactic radiosurgery for brain metastases: analysis of outcome and risk of brain radionecrosis. *Radiat Oncol.* 2011;6:48.
89. Terakawa Y, Tsuyuguchi N, Iwai Y, et al. Diagnostic accuracy of ¹¹C-methionine PET for differentiation of recurrent brain tumors from radiation necrosis after radiotherapy. *J Nucl Med.* 2008;49:694–699.
90. Tsuyuguchi N, Sunada I, Iwai Y, et al. Methionine positron emission tomography of recurrent metastatic brain tumor and radiation necrosis after stereotactic radiosurgery: is a differential diagnosis possible? *J Neurosurg.* 2003;98:1056–1064.
91. Lizarraga KJ, Allen-Auerbach M, Czernin J, et al. ¹⁸F-FDOPA PET for differentiating recurrent or progressive brain metastatic tumors from late or delayed radiation injury after radiation treatment. *J Nucl Med.* 2014;55:30–36.
92. Ciccone F, Minniti G, Romano A, et al. Accuracy of F-DOPA PET and perfusion-MRI for differentiating radionecrosis from progressive brain metastases after radiosurgery. *Eur J Nucl Med Mol Imaging.* 2015;42:103–111.
93. Galldiks N, Stoeffels G, Filss CP, et al. Role of O-(2-¹⁸F-fluoroethyl)-L-tyrosine PET for differentiation of local recurrent brain metastasis from radiation necrosis. *J Nucl Med.* 2012;53:1367–1374.
94. Romagna A, Unterrainer M, Schmid-Tannwald C, et al. Suspected recurrence of brain metastases after focused high dose radiotherapy: can ¹⁸F-FET-PET overcome diagnostic uncertainties? *Radiat Oncol.* 2016;11:139.
95. Schlürmann T, Waschulzik B, Combs S, et al. Diagnostic utility of amino acid PET in the differential diagnosis of recurrent brain metastases and treatment-related changes: a meta-analysis. *J Nucl Med.* December 2, 2022 [Epub ahead of print].
96. Ciccone F, Carideo L, Scaringi C, et al. Long-term metabolic evolution of brain metastases with suspected radiation necrosis following stereotactic radiosurgery: longitudinal assessment by F-DOPA PET. *Neuro Oncol.* 2021;23:1024–1034.
97. Tawbi HA, Forsyth PA, Hodis FS, et al. Safety and efficacy of the combination of nivolumab plus ipilimumab in patients with melanoma and asymptomatic or symptomatic brain metastases (CheckMate 204). *Neuro Oncol.* 2021;23:1961–1973.
98. Tawbi HA, Forsyth PA, Algazi A, et al. Combined nivolumab and ipilimumab in melanoma metastatic to the brain. *N Engl J Med.* 2018;379:722–730.
99. Kebir S, Rauschenbach L, Galldiks N, et al. Dynamic O-(2-[¹⁸F]fluoroethyl)-L-tyrosine PET imaging for the detection of checkpoint inhibitor-related pseudoprogression in melanoma brain metastases. *Neuro Oncol.* 2016;18:1462–1464.
100. Galldiks N, Abdulla DSY, Scheffler M, et al. Treatment monitoring of immunotherapy and targeted therapy using ¹⁸F-FET PET in patients with melanoma and lung cancer brain metastases: initial experiences. *J Nucl Med.* 2021;62:464–470.
101. Macdonald DR, Cascino TL, Schold SC Jr, Cairncross JG. Response criteria for phase II studies of supratentorial malignant glioma. *J Clin Oncol.* 1990;8:1277–1280.
102. Galldiks N, Kracht LW, Burghaus L, et al. Use of ¹¹C-methionine PET to monitor the effects of temozolamide chemotherapy in malignant gliomas. *Eur J Nucl Med Mol Imaging.* 2006;33:516–524.
103. Galldiks N, Kracht LW, Burghaus L, et al. Patient-tailored, imaging-guided, long-term temozolamide chemotherapy in patients with glioblastoma. *Mol Imaging.* 2010;9:40–46.
104. Herholz K, Kracht LW, Heiss WD. Monitoring the effect of chemotherapy in a mixed glioma by C-11-methionine PET. *J Neuroimaging.* 2003;13:269–271.
105. Galldiks N, Langen KJ. Amino acid PET: an imaging option to identify treatment response, posttherapeutic effects, and tumor recurrence? *Front Neurol.* 2016;7:120.
106. Wyss M, Hofer S, Bruehlmeier M, et al. Early metabolic responses in temozolamide treated low-grade glioma patients. *J Neurooncol.* 2009;95:87–93.
107. Roelcke U, Wyss MT, Nowosielski M, et al. Amino acid positron emission tomography to monitor chemotherapy response and predict seizure control and progression-free survival in WHO grade II gliomas. *Neuro Oncol.* 2016;18:744–751.
108. Suchorska B, Unterrainer M, Biczok A, et al. ¹⁸F-FET-PET as a biomarker for therapy response in non-contrast enhancing glioma following chemotherapy. *J Neurooncol.* 2018;139:721–730.
109. Piroth MD, Pinkawa M, Holy R, et al. Prognostic value of early ¹⁸F-fluoroethyl-tyrosine positron emission tomography after radiochemotherapy in glioblastoma multiforme. *Int J Radiat Oncol Biol Phys.* 2011;80:176–184.
110. Galldiks N, Langen KJ, Holy R, et al. Assessment of treatment response in patients with glioblastoma using O-(2-¹⁸F-fluoroethyl)-L-tyrosine PET in comparison to MRI. *J Nucl Med.* 2012;53:1048–1057.
111. Ceccan G, Lohmann P, Werner JM, et al. Early treatment response assessment using ¹⁸F-FET PET compared with contrast-enhanced MRI in glioma patients after adjuvant temozolamide chemotherapy. *J Nucl Med.* 2021;62:918–925.
112. Weller M, van den Bent M, Preusser M, et al. EANO guidelines on the diagnosis and treatment of diffuse gliomas of adulthood. *Nat Rev Clin Oncol.* 2021;18:170–186.
113. Wollring MM, Werner JM, Bauer EK, et al. Prediction of response to lomustine-based chemotherapy in glioma patients at recurrence using MRI and FET PET. *Neuro Oncol.* October 10, 2022 [Epub ahead of print].
114. Reithmeier T, Lopez WO, Spehl TS, et al. Bevacizumab as salvage therapy for progressive brain stem gliomas. *Clin Neurol Neurosurg.* 2013;115:165–169.
115. Galldiks N, Rapp M, Stoeffels G, Dunkl V, Sabel M, Langen KJ. Earlier diagnosis of progressive disease during bevacizumab treatment using O-(2-¹⁸F-fluoroethyl)-L-tyrosine positron emission tomography in comparison with magnetic resonance imaging. *Mol Imaging.* 2013;12:273–276.
116. Galldiks N, Filss CP, Goldbrunner R, Langen KJ. Discrepant MR and ¹⁸F-fluoroethyl-L-tyrosine PET imaging findings in a patient with bevacizumab failure. *Case Rep Oncol.* 2012;5:490–494.
117. Morana G, Piccardo A, Garre ML, Nozza P, Consales A, Rossi A. Multimodal magnetic resonance imaging and ¹⁸F-L-dihydroxyphenylalanine positron emission tomography in early characterization of pseudoresponse and nonenhancing tumor progression in a pediatric patient with malignant transformation of ganglioglioma treated with bevacizumab. *J Clin Oncol.* 2013;31:e1–e5.

118. Hutterer M, Nowosielski M, Putzer D, et al. *O*-(2-¹⁸F-fluoroethyl)-L-tyrosine PET predicts failure of antiangiogenic treatment in patients with recurrent high-grade glioma. *J Nucl Med.* 2011;52:856–864.
119. Galldiks N, Rapp M, Stoffels G, et al. Response assessment of bevacizumab in patients with recurrent malignant glioma using [¹⁸F]fluoroethyl-L-tyrosine PET in comparison to MRI. *Eur J Nucl Med Mol Imaging.* 2013;40:22–33.
120. Schwarzenberg J, Czernin J, Cloughesy TF, et al. Treatment response evaluation using ¹⁸F-FDOPA PET in patients with recurrent malignant glioma on bevacizumab therapy. *Clin Cancer Res.* 2014;20:3550–3559.
121. Galldiks N, Dunkl V, Ceccon G, et al. Early treatment response evaluation using FET PET compared to MRI in glioblastoma patients at first progression treated with bevacizumab plus lomustine. *Eur J Nucl Med Mol Imaging.* 2018;45:2377–2386.
122. Lombardi G, De Salvo GL, Brandes AA, et al. Regorafenib compared with lomustine in patients with relapsed glioblastoma (REGOMA): a multicentre, open-label, randomised, controlled, phase 2 trial. *Lancet Oncol.* 2019;20:110–119.
123. Galldiks N, Werner JM, Tscherpel C, Fink GR, Langen KJ. Imaging findings following regorafenib in malignant gliomas: FET PET adds valuable information to anatomical MRI. *Neurooncol Adv.* 2019;1:vdz038.
124. Di Giorgio E, Cuocolo A, Mansi L, et al. Assessment of therapy response to regorafenib by ¹⁸F-DOPA-PET/CT in patients with recurrent high-grade gliomas: a case series. *Clin Transl Imaging.* 2021;9:265–274.
125. Lombardi G, Spimpolo A, Berti S, et al. PET/MR in recurrent glioblastoma patients treated with regorafenib: [¹⁸F]FET and DWI-ADC for response assessment and survival prediction. *Br J Radiol.* 2022;95:20211018.
126. Long GV, Trefzer U, Davies MA, et al. Dabrafenib in patients with Val600Glu or Val600Lys BRAF-mutant melanoma metastatic to the brain (BREAK-MB): a multicentre, open-label, phase 2 trial. *Lancet Oncol.* 2012;13:1087–1095.
127. Wu YL, Ahn MJ, Garassino MC, et al. CNS efficacy of osimertinib in patients with T790M-positive advanced non-small-cell lung cancer: data from a randomized phase III trial (AURA3). *J Clin Oncol.* 2018;36:2702–2709.
128. Bachelot T, Romieu G, Campone M, et al. Lapatinib plus capecitabine in patients with previously untreated brain metastases from HER2-positive metastatic breast cancer (LANDSCAPE): a single-group phase 2 study. *Lancet Oncol.* 2013;14:64–71.
129. Berghoff AS, Preusser M. New developments in brain metastases. *Ther Adv Neurol Disord.* 2018;11:1756286418785502.
130. Abdulla DSY, Scheffler M, Brandes V, et al. Monitoring treatment response to erlotinib in EGFR-mutated non-small-cell lung cancer brain metastases using serial *O*-(2-[¹⁸F]fluoroethyl)-L-tyrosine PET. *Clin Lung Cancer.* 2019;20:e148–e151.
131. Langen KJ, Watts C. Neuro-oncology: amino acid PET for brain tumours—ready for the clinic? *Nat Rev Neurol.* 2016;12:375–376.
132. Heinzel A, Müller D, Langen KJ, et al. The use of *O*-(2-¹⁸F-fluoroethyl)-L-tyrosine PET for treatment management of bevacizumab and irinotecan in patients with recurrent high-grade glioma: a cost-effectiveness analysis. *J Nucl Med.* 2013;54:1217–1222.
133. Heinzel A, Müller D, Yekta-Michael SS, et al. *O*-(2-¹⁸F-fluoroethyl)-L-tyrosine PET for evaluation of brain metastasis recurrence after radiotherapy: an effectiveness and cost-effectiveness analysis. *Neuro Oncol.* 2017;19:1271–1278.
134. Heinzel A, Stock S, Langen KJ, Müller D. Cost-effectiveness analysis of amino acid PET-guided surgery for supratentorial high-grade gliomas. *J Nucl Med.* 2012;53:552–558.
135. Heinzel A, Stock S, Langen KJ, Müller D. Cost-effectiveness analysis of FET PET-guided target selection for the diagnosis of gliomas. *Eur J Nucl Med Mol Imaging.* 2012;39:1089–1096.
136. Rosen J, Ceccon G, Bauer EK, et al. Cost effectiveness of ¹⁸F-FET PET for early treatment response assessment in glioma patients after adjuvant temozolamide chemotherapy. *J Nucl Med.* 2022;63:1677–1682.
137. Law I, Albert NL, Arbizu J, et al. Joint EANM/EANO/RANO practice guidelines/SNMMI procedure standards for imaging of gliomas using PET with radiolabelled amino acids and [¹⁸F]FDG: version 1.0. *Eur J Nucl Med Mol Imaging.* 2019;46:540–557.
138. Piccardo A, Albert NL, Borgwardt L, et al. Joint EANM/SIOPPE/RAPNO practice guidelines/SNMMI procedure standards for imaging of paediatric gliomas using PET with radiolabelled amino acids and [¹⁸F]FDG: version 1.0. *Eur J Nucl Med Mol Imaging.* 2022;49:3852–3869.
139. Lohmann P, Werner JM, Shah NJ, Fink GR, Langen KJ, Galldiks N. Combined amino acid positron emission tomography and advanced magnetic resonance imaging in glioma patients. *Cancers (Basel).* 2019;11:153.
140. Ziegenfeuter J, Delbridge C, Bernhardt D, et al. Sequential and hybrid PET/MRI acquisition in follow-up examination of glioblastoma show similar diagnostic performance. *Cancers (Basel).* 2022;15:83.

An Opinion on ChatGPT in Health Care—Written by Humans Only

Jens Kleesiek¹, Yonghui Wu², Gregor Stiglic³, Jan Egger¹, and Jiang Bian²

¹Institute for AI in Medicine, University Medicine Essen, Essen, Germany; ²Department of Health Outcomes and Biomedical Informatics, College of Medicine, University of Florida, Gainesville, Florida; and ³Faculty of Health Sciences, University of Maribor, Maribor, Slovenia

ChatGPT, created by OpenAI, has taken the world by storm, and its user base is growing even faster than the previous record held by TikTok, reaching 100 million users in just 2 mo after it launched. Textual context, presentations, and even source code are already being generated using ChatGPT. Many publications have been issued, and meanwhile, ChatGPT has been banned as an author by many publishing companies for several different reasons, such as plagiarism, incorrect information, or inaccurate information (1,2), whereas others argue its benefits, such as the ability to write more coherent sentences than nonnative speakers (3). But that does not stop people from all walks of health care from using it.

ChatGPT is powered by a generative pretrained transformer (GPT-3.5), which is a large language model (LLM) trained with 175 billion parameters (4). LLMs originate in natural language processing to formulate the probability distribution of a sequence of words or the next word in a sequence. Recent studies report that LLMs are foundation models in which a single model can be adapted to solve a wide range of different natural language-processing tasks because of few-shot learning, zero-shot learning, and transfer learning ability (5). The conversational artificial intelligence (AI) ability is achieved using LLM-based prompt learning (6). To alleviate the toxic responses and integrate human ethics, ChatGPT applied a strategy of reinforcement learning from human feedback to align LLMs to follow human instructions (7). These breakthroughs in natural language processing empower ChatGPT with conversational AI ability so good it has surprised the world. Even within OpenAI, ChatGPT has been a surprise. AI chatbots are not a new thing, but many previous attempts have not achieved the sensation that ChatGPT achieved. Meta's BlenderBot was a disappointment. What may be different for ChatGPT, beyond the unknown technologies, is OpenAI's goal of creating artificial general intelligence to match human-level intellect (8). ChatGPT certainly is not an artificial general intelligence, but it sure looks like one because of the breadth and depth of the knowledge it demonstrates through conversations.

Even though many are excited by its first use, disillusionment often sets in over time, for several reasons. On the one hand, ChatGPT gives wrong answers and is prone to confabulation ("a memory error defined as the production of fabricated, distorted, or misinterpreted

memories about oneself or the world" (9)). This is exacerbated by the fact that we set different standards for communication among humans and between humans and computers. The belief is that a computer will not make mistakes. Moreover, many users' expectations are wrong, especially for medical interactions. The program was trained and designed for conversation, not diagnostic support or treatment recommendations. Yet, questions arise as to whether ChatGPT is a medical product and who is liable, even though ChatGPT always generates a disclaimer that it is not a health-care professional licensed to give medical advice. This is a typical case of intended use versus actual use as described in the medical device regulation. We argue that there is a difference between general-purpose conversational AI—in which the focus is the conversational ability such as readability—and medical AI—in which the focus is the health facts about flesh-and-blood humans. Speaking a fake fact using elegant words is amusing (that is why many ChatGPT users are tricking this conversational AI), but providing a wrong fact in medical AI is dangerous—indeed, making ChatGPT a medical device if it should turn out that doctors are actually using it to diagnose and treat their patients. Nevertheless, philosophically, asking ChatGPT for health-related information (to inform health decision making) is not much different from asking Dr. Google, which has long been criticized for not just giving but spreading medical misinformation (10). Nevertheless, this is again not only the gap between intended use versus actual use but also the consistent push and pull between the expectations of the developers versus the end users.

As always with any potentially disruptive technologies, such use can be seen as either a threat or an opportunity. Many articles are optimistic, pointing to the potential symbiosis, the modern centaur, a combination of humans and computers leading to a beneficial augmentation of our capabilities. But pessimistic views also need to be discussed. Take the global positioning system, for example. Because of this technology, many young people are no longer able to navigate with a compass and map. Of course, one could argue that use of a map is not required as a basic skill anymore. But that is certainly not the case with language. If we as humans lose the ability to communicate, debate, and think critically, then we are taking a step backward, leading to devolution.

The question remains: what is the actual use of ChatGPT, despite all the hype during the last few months? Of course, it can be used to generate simple text and to produce code snippets (but often with errors). It can even quickly analyze a research topic and generate an academic paper—again, with frequent errors that may go unnoticed even by reviewers and editors of scientific journals (11).

Received Mar. 7, 2023; revision accepted Mar. 14, 2023.
For correspondence or reprints, contact Jens Kleesiek (jens.kleesiek@uk-essen.de).

Published online Apr. 13, 2023.

COPYRIGHT © 2023 by the Society of Nuclear Medicine and Molecular Imaging.
DOI: 10.2967/jnumed.123.265687

This application may be helpful for student assignments but will not be of much use for learning, in which an individual must come up with a solution through a step-by-step thought process. And when the teacher turns to an oral exam at the end of the semester, irresponsible students who have used the ChatGPT approach will most likely fail, as they might later in their actual work life.

In a health-care setting, one cannot afford to stay on the surface. ChatGPT produces false information that requires checking and correcting of every sentence. In addition to the significant time investment, which calls into question the efficiency of this approach, the real danger comes from false information that goes undetected by the human corrector.

We argue that this technology is worth building toward a clinical knowledge system that can provide health and clinical decision support and enable better self-care and patient care in an era of skill shortages. Hundreds of medical articles are published every day, and it is impossible for humans to cope with this flood of information. In particular, we must keep in mind that information is not the same as knowledge. Filtering information and extracting knowledge from it have enormous potential. Nevertheless, from a health behavior perspective, knowledge is only a small component of healthful behavior and decision making (12). Other aspects, such as beliefs, feelings, norms, and the importance of healthful behavior, are equally important. In our view, developing ChatGPT into a medical product such as a clinical decision support system needs to be considered in a broader context with a wider range of other aspects (e.g., reliability, ethics, and fairness) than just model performance, and like any other AI system, humans must be in the loop (13).

LLMs have much potential in health care. For example, text-to-text generation may help autocomplete the sentences and paragraphs of a clinical document (e.g., a progress report) based on

short phrases provided by a human clinician, thus reducing the documentation burden (14). When used for the generation of clinical documents, LLMs also have the potential to integrate the observations of clinicians and knowledge about clinical guidelines, thus reflecting real-world diagnosis and treatment patterns and subsequently being helpful for compiling a differential diagnosis and composing treatment plans. But much more research and development are needed to achieve this goal. We recently developed the first (to our knowledge) clinical LLM, GatorTron (8.9 billion parameters) using over 90 billion words of text (including 82 billion words of clinical text) and demonstrated its power in clinical natural language processing (15). We also examined the text generation ability of SynGatorTron (5 billion and 20 billion parameters), a generative clinical LLM based on the GPT-3 architecture (16). There is ongoing research on LLMs addressing fundamental issues, such as incorporating chains of reasoning through selection-inference and chain-of-thought prompting (17–19). Once current limitations have been addressed, many applications are conceivable using ChatGPT and the next generation of LLMs (Table 1).

More than a decade ago, self-driving cars were heralded as a disruptive technology. As with many technologies, the last 20% of development takes 80% of the total time. The same may be happening with ChatGPT, and additional development time will be needed for productive use in health care. Like the Human Genome Project, in which mapping out the base pairs in the human DNA is not the end but only the start of the genetic revolution, ChatGPT's eventual possibilities are certainly more exciting than the current hype. Whether this technology is a revolution or just an evolution remains to be seen. What is certain in any case is that there will be no more stepping back. As a society, we have the responsibility to shape its future development.

TABLE 1
Potential Applications and Areas of Health-Care Research for ChatGPT and Similar LLMs

Area no.	Description
1	Models and applications that can leverage multimodal data such as merging language and imaging, for example, highlighting anomalies in a natural way (with language) when reading PET images
2	Summary of complex medical histories and records
3	Summary of information from medical congresses/clinical trial results
4	Structuring/making information interoperable, for example, during medical documentation (20)
5	Facilitating clinical documentation such as writing discharge report; once we have structured information, is there really a need for free text? (facts should be communicated reliably and concisely)
6	Integration with hospital information systems to incorporate patient data, specifications, and requirements (institutional, payer) and resources (staff capacity, provider)
7	Interpretation and explanation of other AI algorithms (7)
8	Translation into other languages, with big potential for less frequently used languages for which use of natural language processing was limited in the past
9	Translation into patient-comprehensible language, making medical information communication more consumer-friendly
10	Anamnesis
11	Relief for nursing staff through automated ward communication
12	Medical writing (21)
13	Anonymization of clinical text
14	Fairness, bias in LLMs
15	Human-in-loop and human-centered design of LLM applications
16	Chain-of-thought and automated reasoning on LLMs

DISCLOSURE

No potential conflict of interest relevant to this article was reported.

REFERENCES

1. Shen Y, Heacock L, Elias J, et al. ChatGPT and other large language models are double-edged swords. *Radiology*. January 26, 2023 [Epub ahead of print].
2. Introducing ChatGPT. OpenAI website. <https://openai.com/blog/chatgpt>. Published November 30, 2022. Accessed March 20, 2023.
3. Ma Y, Liu J, Yi F, et al. AI vs. human: differentiation analysis of scientific content generation. arXiv website. <https://arxiv.org/abs/2301.10416>. Published January 24, 2023. Revised February 12, 2023. Accessed March 20, 2023.
4. Floridi L, Chiriaci M. GPT-3: its nature, scope, limits, and consequences. *Minds Machines*. 2020;30:681–694.
5. Brown T, Mann B, Ryder N, et al. Language models are few-shot learners. In: *Advances in Neural Information Processing Systems*. Vol 33. Curran Associates, Inc.; 2020:1877–1901.
6. Gao T, Fisch A, Chen D. Making pre-trained language models better few-shot learners. ACL Anthology website. <https://aclanthology.org/2021.acl-long.295/>. Published August 2021. Accessed March 20, 2023.
7. Aligning language models to follow instructions. OpenAI website. <https://openai.com/research/instruction-following>. Published January 27, 2022. Accessed March 20, 2023.
8. Roose K. How ChatGPT kicked off an A.I. arms race. *The New York Times* website. <https://www.nytimes.com/2023/02/03/technology/chatgpt-openai-artificial-intelligence.html>. Published February 3, 2023. Accessed March 6, 2023.
9. Confabulation. Wikipedia website. <https://en.wikipedia.org/wiki/Confabulation>. Updated March 16, 2023. Accessed April 4, 2023.
10. Granter SR, Papke DJ. Medical misinformation in the era of Google: computational approaches to a pervasive problem. *Proc Natl Acad Sci USA*. 2018;115:6318–6321.
11. Anderson N, Belavy DL, Perle SM, et al. AI did not write this manuscript, or did it? Can we trick the AI text detector into generated texts? The potential future of ChatGPT and AI in sports & exercise medicine manuscript generation. *BMJ Open Sport Exerc Med*. 2023;9:e001568.
12. Integrated behavior model. Perelman School of Medicine website. <https://www.med.upenn.edu/hbhe4/part2-ch4-integrated-behavior-model.shtml>. Accessed March 20, 2023.
13. Patel BN, Rosenberg L, Willcox G, et al. Human–machine partnership with artificial intelligence for chest radiograph diagnosis. *NPJ Digit Med*. 2019; 2:111.
14. Patel SB, Lam K. ChatGPT: the future of discharge summaries? *Lancet Dig Health*. 2023;5:E107–E108.
15. Yang X, Chen A, PourNejatian N, et al. A large language model for electronic health records. *NPJ Digit Med*. 2022;5:194.
16. SynGatorTron: a large clinical natural language generation model for synthetic data generation and zero-shot tasks. NVIDIA website. <https://www.nvidia.com/en-us/on-demand/session/gtcspring22-s41638/>. Published March 2022. Accessed March 20, 2023.
17. Creswell A, Shanahan M, Higgins I. Selection-inference: exploiting large language models for interpretable logical reasoning. arXiv website. <https://arxiv.org/abs/2205.09712>. Published May 19, 2022. Accessed March 20, 2023.
18. Tafjord O, Mishra BD, Clark P. Entailer: answering questions with faithful and truthful chains of reasoning. arXiv website. <https://arxiv.org/abs/2210.12217>. Published October 21, 2022. Accessed March 20, 2023.
19. Kazemi SM, Kim N, Bhatia D, Xu X, Ramachandran D. LAMBADA: backward chaining for automated reasoning in natural language. arXiv website. <https://arxiv.org/abs/2212.13894>. Published December 20, 2022. Accessed March 20, 2023.
20. Fink MA, Kades K, Bischoff A, et al. Deep learning–based assessment of oncologic outcomes from natural language processing of structured radiology reports. *Radiol Artif Intell*. 2022;4:e220055.
21. Biswas S. ChatGPT and the future of medical writing. *Radiology*. February 2, 2023 [Epub ahead of print].

⁶⁴Cu Treatment Planning and ⁶⁷Cu Therapy with Radiolabeled [⁶⁴Cu/⁶⁷Cu]MeCOSar-Octreotate in Subjects with Unresectable Multifocal Meningioma: Initial Results for Human Imaging, Safety, Biodistribution, and Radiation Dosimetry

Dale L. Bailey^{1–3}, Kathy P. Willowson^{1,4}, Matthew Harris⁵, Colin Biggin⁵, Alireza Aslani^{1,2}, Nigel A. Lengkeek⁶, Jon Stoner⁷, M. Enid Eslick¹, Harry Marquis^{3,4}, Michelle Parker⁵, Paul J. Roach^{1,2}, and Geoffrey P. Schembri^{1,2}

¹Department of Nuclear Medicine, Royal North Shore Hospital, Sydney, New South Wales, Australia; ²Faculty of Medicine and Health, University of Sydney, Sydney, New South Wales, Australia; ³Sydney Vital Translational Cancer Research Centre, Sydney, New South Wales, Australia; ⁴Institute of Medical Physics, University of Sydney, Sydney, New South Wales, Australia; ⁵Clarity Pharmaceuticals, Sydney, New South Wales, Australia; ⁶ANSTO Biosciences, Sydney, New South Wales, Australia; and ⁷Idaho Accelerator Center, Idaho State University, Pocatello, Idaho

Our aim was to report the use of ⁶⁴Cu and ⁶⁷Cu as a theranostic pair of radionuclides in human subjects. An additional aim was to measure whole-organ dosimetry of ⁶⁴Cu and ⁶⁷Cu attached to the somatostatin analog octreotide using the sarcophagine MeCOSar chelator (SARTATE) in subjects with somatostatin receptor-expressing lesions confined to the cranium, thereby permitting normal-organ dosimetry for the remainder of the body. **Methods:** Pretreatment PET imaging studies were performed up to 24 h after injection of [⁶⁴Cu]Cu-SARTATE, and normal-organ dosimetry was estimated using OLINDA/EXM. Subsequently, the trial subjects with multifocal meningiomas were given therapeutic doses of [⁶⁷Cu]Cu-SARTATE and imaged over several days using SPECT/CT. **Results:** Five subjects were initially recruited and imaged using PET/CT before treatment. Three of the subjects were subsequently administered 4 cycles each of [⁶⁷Cu]Cu-SARTATE followed by multiple SPECT/CT imaging time points. No serious adverse events were observed, and no adverse events led to withdrawal from the study or discontinuation from treatment. The estimated mean effective dose was 3.95×10^{-2} mSv/MBq for [⁶⁴Cu]Cu-SARTATE and 7.62×10^{-2} mSv/MBq for [⁶⁷Cu]Cu-SARTATE. The highest estimated organ dose was in spleen, followed by kidneys, liver, adrenals, and small intestine. The matched pairing was shown by PET and SPECT intrasubject imaging to have nearly identical targeting to tumors for guiding therapy, demonstrating a potentially accurate and precise theranostic product. **Conclusion:** ⁶⁴Cu and ⁶⁷Cu show great promise as a theranostic pair of radionuclides. Further clinical studies will be required to examine the therapeutic dose required for [⁶⁷Cu]Cu-SARTATE for various indications. In addition, the ability to use predictive ⁶⁴Cu-based dosimetry for treatment planning with ⁶⁷Cu should be further explored.

Key Words: radionuclide therapy; copper radionuclides; dosimetry; meningioma; safety; theranostics

J Nucl Med 2023; 64:704–710

DOI: 10.2967/jnmed.122.264586

A proposed pair of radionuclides potentially ideal for theranostics is ⁶⁴Cu and ⁶⁷Cu (1). ⁶⁴Cu has a 12.7-h physical half-life and emits positrons (β^+) with a maximum energy of 0.65 MeV at 17% abundance, making it suitable for imaging with PET. ⁶⁷Cu decays by β^- emissions in the range of 0.18–0.58 MeV at 100% abundance and emits readily imageable γ -photons at 0.092 MeV (23%) and 0.185 MeV (49%) with a physical half-life of 61.8 h. As both radionuclides are elemental copper, the chemistry for chelating the imaging agent and the therapeutic compound is essentially identical. ⁶⁴Cu is made in a cyclotron, and yields can be realized so that patient doses can be provided on a commercial scale. ⁶⁷Cu is produced by high-energy x-rays from an electron accelerator via the $^{68}\text{Zn}(\gamma,\text{p})^{67}\text{Cu}$ reaction (2). Moreover, the chelation chemistry of radiolabeled copper is well developed (1). Given these recent chelation and production developments, there is currently significant interest in the use of ⁶⁴Cu/⁶⁷Cu as a theranostic pair (recently termed targeted copper theranostic).

The ⁶⁴Cu/⁶⁷Cu pairing offers significant advantages over theranostic pairs such as ⁶⁸Ga/¹⁷⁷Lu, including the fact that the extended physical half-lives of both ⁶⁴Cu and ⁶⁷Cu permit centralized production and widespread transportation of ready-to-use theranostic agents for both diagnosis and therapy to remote sites, which is generally not possible with generator-produced ⁶⁸Ga. Another advantage is the scalable product supply for ⁶⁴Cu and ⁶⁷Cu due to favorable production methods using cyclotrons and accelerators, respectively. In addition, ⁶⁴Cu can be imaged on the day of administration (as with current PET radionuclides such as ⁶⁸Ga) but also offers the ability to collect images up to 48 h after administration for flexible patient scheduling and potentially improved lesion identification. ⁶⁷Cu emits abundant γ -photons, which are well suited for SPECT imaging, as well as a β^- particle for therapy with an energy and pathlength in tissue similar to those of ¹⁷⁷Lu. ⁶⁷Cu also has a shorter half-life (2.6 d) than ¹⁷⁷Lu (6.7 d), making it well matched to peptide pharmacokinetics presenting less of a radiation protection challenge and may allow more frequent administrations. A final advantage is that the longer physical half-life of ⁶⁴Cu than of

Received Jun. 28, 2022; revision accepted Nov. 28, 2022.
For correspondence or reprints, contact Dale L. Bailey (dale.bailey@sydney.edu.au).

Published online Dec. 2, 2022.

COPYRIGHT © 2023 by the Society of Nuclear Medicine and Molecular Imaging.

^{68}Ga improves the ability to obtain pretherapy dosimetry estimates using PET imaging at multiple time points, potentially leading to a personalized treatment approach.

In this paper, we report the first-in-humans use of ^{64}Cu and ^{67}Cu as a theranostic pair for treatment planning and therapy. The primary aims of the study were to assess the safety, biodistribution, and dosimetry of both copper radionuclides labeled to the somatostatin analog Tyr³-octreotate (H-d-Phe-Cys-Phe-d-Trp-Lys-Thr-Cys-Thr-OH) conjugated to the MeCOSar sarcophagine chelator (SARTATE) (3). The design was an open-label, nonrandomized phase I safety study on adults with meningiomas using fixed dosing of both the diagnostic and the therapeutic investigational medical products, [^{64}Cu]Cu-SARTATE and [^{67}Cu]Cu-SARTATE, respectively. [^{64}Cu]Cu-SARTATE binds to tumors expressing somatostatin receptor type 2 (4), which has been shown to be overexpressed in meningiomas (5). This population was selected for the study because of the high unmet clinical need and the expected normal uptake in organs outside the calvarium, thus permitting normal-organ dosimetry measures, which is not the case with typical somatostatin receptor type 2-expressing cancers in subjects with metastatic neuroendocrine tumors.

MATERIALS AND METHODS

Production of Radionuclides of Copper

[^{64}Cu]CuCl₂ was manufactured on a biomedical cyclotron (PET Trace; GE Healthcare) via the $^{64}\text{Ni}(\text{p},\text{n})^{64}\text{Cu}$ nuclear reaction and subsequently was purified on an automated synthesizer (Comecer) (6).

[^{67}Cu]CuCl₂ was obtained by irradiation of enriched ^{68}Zn targets at 40 MeV on a linear electron accelerator (Idaho Accelerator Center) via the reaction process $^{68}\text{Zn}(\gamma,\text{p})^{67}\text{Cu}$. After irradiation, zinc and copper are separated by low-pressure evaporation and subsequently purified using anion-exchange column chromatography. The final product pH was adjusted to 2.0 (nominal), and volume activity was more than 40 MBq/ μL ($\sim 1 \text{ mCi}/\mu\text{L}$). Typical specific activities were greater than 7 TBq/mg ($\sim 200 \text{ Ci}/\text{mg}$).

Subject Selection and Recruitment

The subjects had unresectable, multifocal meningiomas that were progressing despite chemotherapy and radiotherapy. The cranial localization of the disease enables assessment of the normal biodistribution in the visceral organs—with little prospect of the disease being present or affecting biodistribution—to derive normal-organ dosimetry. Previous studies using [^{64}Cu]Cu-SARTATE in humans (4) recruited neuroendocrine tumor subjects for whom metastatic disease was often present throughout the abdomen and in organs such as liver and pancreas and, thus, for whom estimation of normal-organ dosimetry was not always possible. Using subjects with cranial lesions avoids this issue. The study (ClinicalTrials.gov identifier NCT03936426) was approved by a nationally accredited Human Research Ethics Committee (St. Vincent's Hospital Melbourne HREC, reference number HREC/17/SVHM/238), and written informed consent was obtained from all subjects before recruitment.

Imaging Studies

Before the trial began, the quantitative accuracy of the PET scanner (Biograph mCT/64; Siemens Healthineers) was validated with a modified version of the protocol developed by our national imaging clinical trials group (the Australasian Radiopharmaceutical Trials Network) (7) adapted for ^{64}Cu PET imaging. The protocol used a National Electrical Manufacturers Association NU-2 image-quality phantom and demonstrated the SUV_{mean} in the main compartment of the phantom to be accurate to within $\pm 5\%$ of the true value of 1.0 (i.e., SUV = 0.95–1.05). ^{64}Cu used for the dose calibrator and camera validation was traceable to

the primary Australian ^{64}Cu standard established by the national nuclear science body, the Australian Nuclear Science and Technology Organization.

$^{64}\text{Cu}/\text{Cu-SARTATE Preparation, Administration, and Imaging}$. [^{64}Cu]Cu-SARTATE was prepared at a radiopharmaceutical manufacturing facility in Adelaide on day –1 and transported by plane overnight to our center in Sydney. No specific preparation was required of the subjects; in particular, no subjects were on any medication such as somatostatin analogs that could potentially interfere with uptake and biodistribution. The [^{64}Cu]Cu-SARTATE was administered on day 0 as an approximately 200-MBq slow-bolus intravenous injection. Imaging was acquired on the time-of-flight PET/CT system with a 21.6-cm axial field of view in fully 3-dimensional acquisition mode at multiple time points after administration: 1, 4, and 24 h. On day 0, scans were acquired for 3 min per bed position with coverage from the vertex of the skull to the mid thigh. To partially compensate for radionuclide decay, on day +1 the acquisition time was extended to 5 min per bed position. Image reconstruction used CT-based scatter and attenuation correction, time-of-flight localization, and a resolution recovery algorithm (TrueX; Siemens Healthineers) followed by a post-reconstruction gaussian 3-dimensional filter with a full width at half maximum of 5.0 mm.

$^{67}\text{Cu}/\text{Cu-SARTATE Preparation, Administration, and Imaging}$. [^{67}Cu]Cu-SARTATE was manufactured on-site in our local hospital radiopharmacy facility using the imported ^{67}Cu . The trial protocol was designed so that a reliable, repeatable administration of a minimum of 5 GBq of [^{67}Cu]Cu-SARTATE was achievable.

Briefly, the [^{67}Cu]Cu-SARTATE was prepared manually by the reaction of [^{67}Cu]CuCl₂ in 0.1 M HCl with SARTATE (60 μg , good-manufacturing-practice grade; Auspep Clinical Peptides) according to previously optimized methods for production and quality control. The purity and safety of the product for release were assessed with radio-thin-layer chromatography, radio-high-performance liquid chromatography, and testing of pH, pyrogenicity, sterile filter integrity, and post-release sterility.

The subjects in this trial received the [^{67}Cu]Cu-SARTATE as a ramped, slow infusion over 20 min. All subjects had coadministration of 1 L of amino acid solution (5.8 g of lysine and 11.5 g of arginine per liter) over 3–4 h for renal protection commencing 30 min before the [^{67}Cu]Cu-SARTATE administration. Regular clinical observations, including electrocardiography, were made from the time of administration. The subjects were asked to void their bladder before the injection and not to void again until after the first scan at +1 h, to allow a cross-check of the total radioactivity in the reconstructed images and comparison with the known amount of ^{67}Cu injected. All ^{67}Cu imaging was performed as whole-body SPECT/CT scans on a dual-detector γ -camera (Intevo.6; Siemens Healthineers), with a thicker scintillation detector (16 mm) than is standard, for increased sensitivity for medium- and higher-energy photons such as from ^{67}Cu . Scanning proceeded from the vertex of the skull to the mid thigh, and quantitative SPECT images subsequently were reconstructed using in-house protocols and software (8). A calibration source ($\sim 125 \text{ mL}$) containing about 40 MBq of ^{67}Cu was included in 1 bed position at each time point. The acquisition consisted of 3 contiguous bed positions, each being approximately 38 cm in axial extent. Imaging was acquired on days 0, +1, and +4 at the approximate time points of 1, 4, 24, and 96 h after administration. In addition, on day +1, a 2-dimensional planar anterior/posterior whole-body sweep was acquired. Images were acquired using a medium-energy collimator with the main pulse-height analyzer window over the 185 keV $\pm 10\%$ photopeak and a lower-energy scatter window (143–163 keV). All SPECT data were acquired using continuous detector rotation into 120 projections over 360° in a 128 \times 128 matrix. The time per projection varied; for both acquisitions on day 0 (1 and 4 h

after infusion), it was 8 s/projection; on day +1, it was 10 s/projection; and on day +4, it was 12 s/projection. Images were reconstructed using the ordered-subset expectation maximization algorithm (9) after scatter correction in projection space using an in-house implementation of the transmission-dependent scatter correction method (8,10). The reconstruction took place on a dedicated nuclear medicine workstation (Hermes Medical Solutions AB) and was followed by attenuation correction based on the CT scan using a modified version of the method of Chang (8,11). Finally, the images were converted to units of kBq/cc for further analysis.

The complete set of data acquired for the [⁶⁴Cu]Cu-SARTATE PET before treatment and the [⁶⁷Cu]Cu-SARTATE for each cycle provided 3 PET/CT scans and 16 (4 cycles × 4 time points per cycle) whole-body SPECT/CT scans per individual for analysis.

Biodistribution and Radiation Dosimetry

Both the PET data and the SPECT data were processed to determine organ biodistribution over time and whole-body radiation dosimetry. Organs of interest were defined on the CT and functional (PET or SPECT) multimodality images at the baseline time point in each image series and transferred to the subsequent time points. [⁶⁴Cu]Cu-SARTATE and [⁶⁷Cu]Cu-SARTATE studies were considered separately. The ⁶⁷Cu calibration source in the field of view was checked for total radioactivity remaining to assess the accuracy of the quantitative SPECT images. Whole-body retention was estimated on the basis of the imaging, with an adjustment for the missing lower limbs. Organs of interest were defined for liver, spleen, kidneys, lungs, blood pool, L4–L5 spine (for bone marrow estimates), adrenal and parotid glands, urinary bladder, and small bowel using a dedicated nuclear medicine workstation (MIM Encore; MIM Software). Brain estimates of radioactivity were not included because of the presence of disease within the skull. The total uptake in each organ was calculated and converted to percentage injected dose. The blood pool estimate was scaled by the blood volume based on the concentration of the radionuclide measured in the images and the total blood volume in the models (standard MIRD adult male and female models) used in the OLINDA/EXM program (12,13). A similar approach was used for thigh-based muscle volume of interest. The estimate of percentage injected dose in bone marrow was based on the L4–L5 vertebrae containing about 7% of the average total bone marrow in an adult (14,15). The corresponding time–activity curve data were imported into the OLINDA/EXM whole-organ dosimetry package after decay correction with the respective half-lives for each radionuclide.

Dosimetry for [⁶⁴Cu]Cu-SARTATE and [⁶⁷Cu]Cu-SARTATE

All subjects who were selected to proceed to therapy had dosimetry estimates calculated for the PET imaging component of the trial.

To allow direct comparison with the previously published dose estimates of a similar radiopharmaceutical, [⁶⁴Cu]DOTA-octreotide (16), we used a dynamic bladder model in the OLINDA analysis based on an estimated urinary excretion fraction of 10% with a presumed 2-h voiding interval and a biologic half-life of 1 h. The same assumptions and parameters used for the calculation of the absorbed radiation dose estimates for [⁶⁴Cu]Cu-SARTATE above were applied for the absorbed dose estimates from [⁶⁷Cu]Cu-SARTATE. All ⁶⁷Cu data were decay-corrected before entry into OLINDA.

RESULTS

Subject Selection and Recruitment

Five subjects (4 male, 1 female) were initially recruited to the trial, 3 of whom went on to receive the therapy. One subject did not proceed to therapy because the subject disclosed a previous malignancy (a skin lesion) after recruitment and hence did not meet the inclusion criteria. The other subject was diverted to [¹⁷⁷Lu]Lu-DOTA-octreotide treatment because of rapid disease progression and conflicts with the scheduling of the ⁶⁷Cu radionuclide. These 2 subjects were not included in the dosimetry calculations. All 3 remaining subjects (2 male, 1 female) had unresectable, multifocal meningiomas previously treated with radiotherapy and chemotherapy and no other malignancies. Table 1 shows the imaging data for the 3 therapy subjects at all imaging time points.

Imaging Studies

[⁶⁴Cu]Cu-SARTATE Preparation, Administration, and Imaging. The average amount of [⁶⁴Cu]Cu-SARTATE administered was 186 MBq (range, 176–207 MBq). No adverse events were recorded after the [⁶⁴Cu]Cu-SARTATE injection in any subject. An example set of images for 1 subject is shown in Figure 1.

[⁶⁷Cu]Cu-SARTATE Preparation, Administration, and Imaging. The amount of [⁶⁷Cu]Cu-SARTATE produced over the 12 cycles was 9,660 ± 828 MBq, and all batches were within specifications. The purity and safety of the product were measured by radio-thin-layer chromatography (average, 98.9% ± 0.6%), radio-high-performance liquid chromatography (average, 96.4% ± 2.8%), and testing of pH (7.0) and pyrogenicity (<5.0 EU/mL). Sterile filter integrity and post-release sterility were confirmed.

The 3 subjects received an average of 4,945 ± 100 MBq (range, 4,695–5,076 MBq) of [⁶⁷Cu]Cu-SARTATE over a combined total of 12 cycles of treatment. SPECT maximum-intensity projection images for the same subject as for Figure 1 are shown in Figure 2, with the additional time point (96 h) facilitated by the longer

TABLE 1
Imaging Data Acquired at Various Time Points in All Subjects

Postadministration time (h)	⁶⁴ Cu PET	⁶⁷ Cu SPECT			
		Cycle 1	Cycle 2	Cycle 3	Cycle 4
~1	Yes	Yes	Yes	Yes	Yes
~4	Yes	Yes	No (2/3)	Yes	Yes
~24	Yes	Yes	Yes	Yes	Yes
~96	NA	Yes	Yes	Yes	Yes

NA = not applicable; No = not all 3 subjects were imaged at this time point; Yes = all 3 subjects were imaged at this time point.

Only 1 time point in 1 subject was omitted (subject B, cycle 2, day 0, +4 h) because of very delayed start of infusion, precluding measurement late in evening.

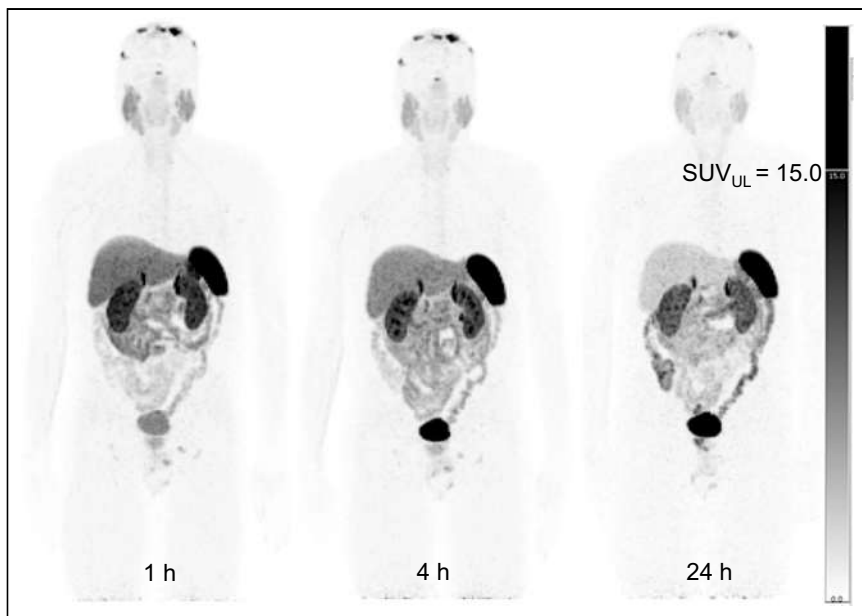


FIGURE 1. Example of multiple-time-point maximum-intensity projections with $[^{64}\text{Cu}]\text{Cu}$ -SARTATE PET at 1, 4, and 24 h after injection. Considerable washout of radiopharmaceutical is seen from liver, parotid glands, and intracranial lesions at 24 h. Gray scale is constant for all images, with SUV display range of 0–15. SUV_{UL} = upper limit of SUV.

half-life of ^{67}Cu . Figure 3 compares the uptake for both $[^{64}\text{Cu}]\text{Cu}$ -SARTATE and $[^{67}\text{Cu}]\text{Cu}$ -SARTATE through the largest tumor in the subject.

Safety, Biodistribution, and Radiation Dosimetry

Adverse Events. Both $[^{64}\text{Cu}]\text{Cu}$ -SARTATE and $[^{67}\text{Cu}]\text{Cu}$ -SARTATE were safe and well tolerated in all subjects. No serious adverse events, no potentially life-threatening (grade 4) treatment-emergent adverse events, and no deaths were recorded during the study period. Further, there were no treatment discontinuations or interruptions and no withdrawals from the study due to treatment-emergent adverse events. $[^{64}\text{Cu}]\text{Cu}$ -SARTATE had no treatment-emergent adverse events, and $[^{67}\text{Cu}]\text{Cu}$ -SARTATE had 16, which included 13 incidents of decreased lymphocyte count in the 3 therapy subjects. Further details of the adverse events are included in Supplemental Tables 1 and 2 (supplemental materials are available at <http://jnm.snmjournals.org>). There were no notable safety findings arising from review of the electrocardiographs, vital signs, or physical examination data.

Biodistribution Data. The decay-corrected radionuclide retention curves from the PET and SPECT imaging at all 4 cycles for each subject are shown in Figure 4. Whole-body retention was highly reproducible over all cycles of treatment. For the $[^{67}\text{Cu}]\text{Cu}$ -SARTATE biodistribution, the organ that exhibited the highest total uptake expressed as percentage injected dose was liver, followed by kidney, spleen, and lungs. The averaged biodistribution for all subjects and

all cycles of treatment is shown in Table 2 as the amount of the radiopharmaceutical in the organs at each time point. The individual-subject biodistribution data for each cycle and each time point are included in Supplemental Tables 3–5.

Dosimetry for $[^{64}\text{Cu}]\text{Cu}$ -SARTATE and $[^{67}\text{Cu}]\text{Cu}$ -SARTATE. The averaged radiation dosimetry estimates of $[^{64}\text{Cu}]\text{Cu}$ -SARTATE for the PET and SPECT imaging components of the trial from the 3 subjects who proceeded to therapy are shown in Table 3. The highest organ dose per megabecquerel was in spleen, followed by kidneys, liver, adrenals, and small intestine. This was consistent for both $[^{64}\text{Cu}]\text{Cu}$ -SARTATE and $[^{67}\text{Cu}]\text{Cu}$ -SARTATE. The difference in dosimetry between the 2 SARTATE radiopharmaceuticals averaged a factor of 2.6 (range, 1.3–4.0), with the ^{67}Cu product conferring the higher dose. However, this factor was not consistent among different organs, possibly because of altered biodistribution kinetics due to the use of the amino acid infusion when administering the therapeutic product, especially in the first 4 h.

DISCUSSION

The potential clinical use of the radionuclides of copper, predominantly ^{64}Cu and ^{67}Cu , was suggested over 40 y ago (17). Subsequently, in 1995, Schwarz et al. reported a preclinical study on rodents bearing lymphomas examining the radiation dosimetry from ^{64}Cu and ^{67}Cu radiolabeled $[\text{Cu}]$ benzyl-TETA-1A3 monoclonal antibody and reported a 5-fold increase in absorbed radiation dose per unit of radioactivity for the longer-lived ^{67}Cu compared with ^{64}Cu (18). Subsequently, DeNardo et al. reported the use of a ^{67}Cu -radiolabeled monoclonal antibody ($[^{67}\text{Cu}]$ 2IT-BAT-Lym-1)

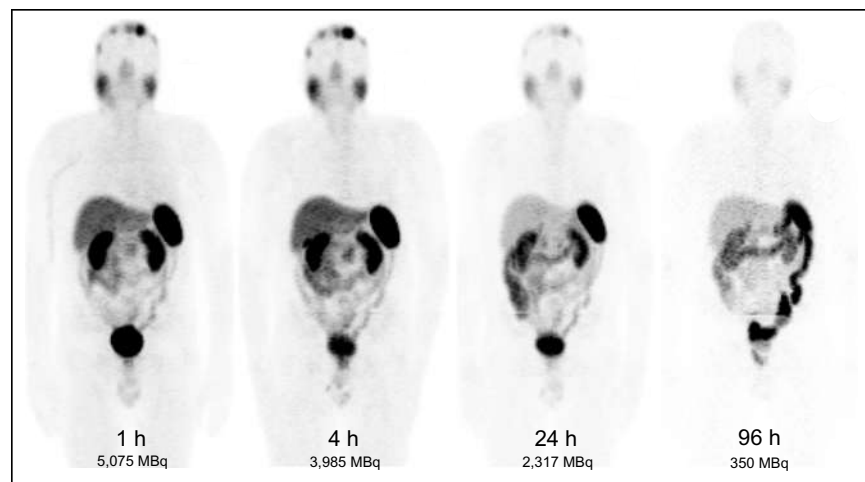


FIGURE 2. SPECT maximum-intensity projections for same subject as in Figure 1 are shown for each imaging time point in cycle 1 of treatment. Total radioactivity estimated in subject is shown at each time point. Gray scale is not constant in this example because of wide dynamic range and hence is not displayed. Good image quality with SPECT was obtained up to 96 h. Calibration standard was removed from images before display.

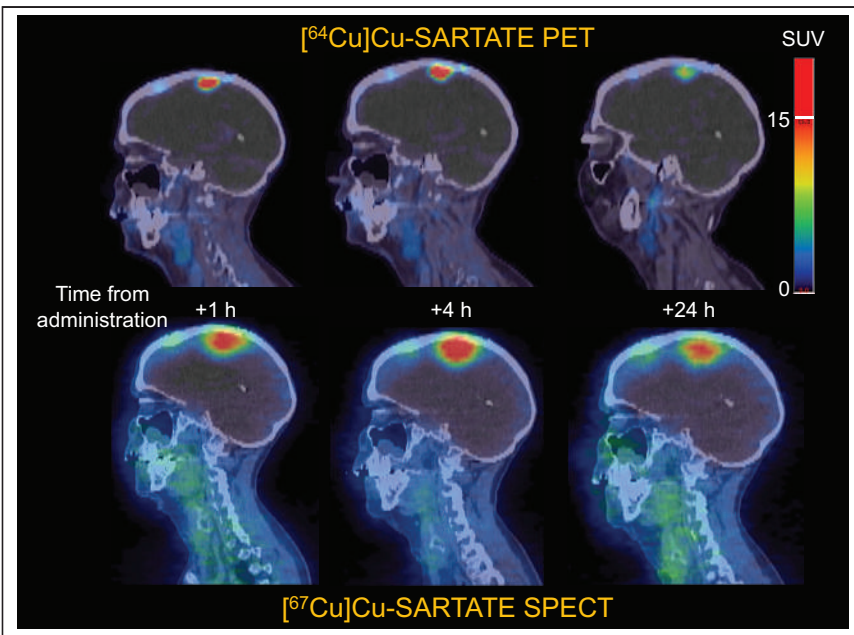


FIGURE 3. Reproducibility of copper theranostic PET and SPECT pairing is shown in this comparison of SARTATE showing targeting of 2 compounds using PET and SPECT at equivalent time points after administration. Change of radionuclide from ^{64}Cu to ^{67}Cu does not alter targeting to tumor in this subject. SPECT images are from cycle 1 of treatment. Volume of main lesion in SPECT images appears greater than in PET images because of poorer spatial resolution of SPECT. PET images are shown at fixed SUV upper threshold (maximum, 15), whereas SPECT images are shown with individual scaling. SPECT time point of 96 h has been omitted as there was no comparable PET image.

in subjects with stage 3 or 4 B-cell lymphoma to assess feasibility for subsequent treatment (19,20). Remarkably, although the investigators administered only what they believed would be an amount of $[^{67}\text{Cu}]2\text{IT-BAT-Lym-1}$ sufficient for their imaging and dosimetry studies, they achieved good clinical responses in 7 of the 11 subjects who displayed cutaneous lesions, achieving almost a 50% average reduction in lesion size. Further studies by this group compared the therapeutic potential of ^{64}Cu and ^{67}Cu in a hamster model bearing human colon cancers and found that the 2 radionuclides were equivalent in this cell line and animal model (21). Although ^{64}Cu is primarily thought of as a positron (β^+)-emitting radionuclide for PET imaging, the branching ratio for positrons is only 17% whereas ^{64}Cu also emits β^- particles with 39% abundance.

To the best of our knowledge, the data reported in this work represent the first documented use of combined ^{64}Cu and ^{67}Cu as a clinical theranostic pair in humans. The pairing of ^{64}Cu with ^{67}Cu has been used firstly to confirm and localize tumor targeting in the subjects (with ^{64}Cu) and subsequently to deliver the therapeutic product (with ^{67}Cu). Administration of almost identical diagnostic and therapeutic drug products using the different radioisotopes of copper for each role represents the ideal same-element theranostic pairing. The use of different-element theranostic pairs such as ^{68}Ga or ^{111}In for imaging paired with either ^{90}Y or ^{177}Lu for therapy has been shown to potentially alter the biodistribution of the product between

imaging and therapy (22). The imaging data in this paper provide a high level of confidence that the targeting seen in the PET study will truly reflect the therapeutic radiopharmaceutical delivery and retention, hence demonstrating a particularly attractive characteristic of the copper pairing (Fig. 3).

Compared with conventional radionuclides (e.g., ^{18}F , ^{68}Ga) for diagnostic imaging PET, which have physical half-lives of less than 2 h, the longer half-lives of the copper radionuclides used here have several advantages. One is that both SARTATE products can potentially be radiolabeled in a centralized, good-manufacturing-practice-licensed facility and transported to the clinical center for use. In our case, the $[^{64}\text{Cu}]$ Cu-SARTATE product is manufactured in Adelaide, South Australia, and flown overnight to Sydney, New South Wales, a distance of approximately 1,200 km. Centralized manufacture obviates investment in expensive radiopharmaceutical synthesis equipment by the local PET facility, along with the staff required to perform the radiolabeling, production, and quality assurance of the PET radiopharmaceutical. The $[^{67}\text{Cu}]$ -SARTATE can be made in the same production facility and transported in an identical manner.

However, for this early proof-of-principle

trial, we chose to perform the radiolabeling locally on-site because the ^{67}Cu was produced in Idaho and required several flights to be transported the 13,000 km to Sydney, with the half-life of just over 60 h being a consideration.

The effective dose of the most commonly used somatostatin receptor type 2-targeting PET radiopharmaceutical, $[^{68}\text{Ga}]$ -DOTA-octreotate, is 4.2 mSv for 200 MBq (23). The trial design used here was informed by previous preliminary dosimetry estimates using $[^{64}\text{Cu}]$ -Cu-SARTATE in subjects with neuroendocrine tumors (4); that previous work reported a whole-body effective dose of 4.5×10^{-2} mSv/MBq, or approximately 9 mSv per 200 MBq. Previously, dose estimates in major organs for a different

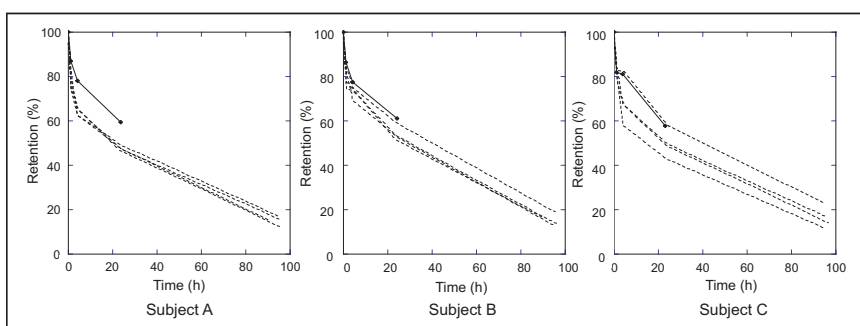


FIGURE 4. Whole-body retention determined from PET and SPECT imaging is shown for each subject. PET retention of $[^{64}\text{Cu}]$ -Cu-SARTATE is shown as solid line, whereas dashed lines are for each of 4 cycles of $[^{67}\text{Cu}]$ -Cu-SARTATE measured to approximately 96 h after treatment. Curves are corrected for radionuclide decay and normalized to amount of radiopharmaceutical administered (100%). $[^{64}\text{Cu}]$ -Cu-SARTATE retention remains on upper side of $[^{67}\text{Cu}]$ -Cu-SARTATE retention curves in all cases, possibly reflecting influence that coadministered amino acid infusion on treatment day has on retention of $[^{67}\text{Cu}]$ -Cu-SARTATE.

TABLE 2
Average [^{67}Cu]Cu-SARTATE Biodistribution Data

Parameter	Scan time point			
	1	2	3	4
Hours from infusion	1	4	24	96
Site				
Adrenals	0.05	0.05	0.04	0.02
Heart contents	0.39	0.26	0.19	0.02
Liver	8.7	8.6	4.4	1.9
Lungs	2.8	2.3	1.5	0.5
Kidneys	4.5	4.1	3.0	1.1
Lower large intestine	0.47	0.38	0.51	0.21
Pancreas	1.23	0.91	0.53	0.04
Red marrow	1.6	1.5	1.2	0.4
Small intestine	2.2	2.3	1.7	0.6
Spleen	2.8	3.1	2.4	0.7
Urinary bladder	5.6	1.3	1.5	0.6
Remainder of body	69.6	63.2	47.9	14.7
Total	100.0	88.0	64.9	20.7

Data are percentage injected dose (%ID) per organ for all 3 subjects over all 4 treatment cycles (values corrected for radioactive decay) at each time point.

^{64}Cu -labeled somatostatin receptor type 2-targeting agent, $[^{64}\text{Cu}]$ Cu-DOTA-octreotate, have been published (16). The effective dose of $[^{64}\text{Cu}]$ Cu-DOTA-octreotate was reported to be 6.3 mSv for 200 MBq (16). The average effective dose measured in the 3 subjects in this trial with $[^{64}\text{Cu}]$ Cu-SARTATE was 3.95×10^{-2} mSv/MBq, which equates to approximately 8 mSv for 200 MBq administered, similar to the value reported by Hicks et al. (4). The slight increase in the latter potentially reflects the fact that their subjects had metastatic disease, which may affect the estimates. In a PET/CT examination from vertex of skull to mid thigh, the CT contribution is an additional 8–15 mSv (24). Therefore, the estimated difference of about 4 mSv between $[^{68}\text{Ga}]$ Ga-DOTA-octreotate (4.2 mSv) and $[^{64}\text{Cu}]$ Cu-SARTATE (8 mSv) may be deemed acceptable when considering the total dose for the overall combined PET/CT examination.

This article does not include any estimates of the absorbed dose to the intracranial lesions that were the therapeutic targets in this trial, dose-response relationships, or efficacy. One reason is that the limited spatial resolution of SPECT with a medium-energy collimator and current technology is such that the radioactivity contained in any mass or lesion less than approximately 50 mm in cross-sectional dimension will be underestimated (25). New approaches to image reconstruction and postprocessing are attempting to address this limitation (26). Most organs measured in this study were larger than the intracranial lesions and hence not subject to the same magnitude of underestimation. With the limited number of enrolled subjects, it was felt that dose-response and efficacy, which were secondary endpoints of the trial, would not be reliable to report and that larger series would be required. Lesion dosimetry in the multifocal, metastatic setting currently remains time-consuming

TABLE 3
Organ-Absorbed Doses from $[^{64}\text{Cu}]$ Cu-SARTATE and $[^{67}\text{Cu}]$ Cu-SARTATE

Organ	Mean absorbed dose (mGy/MBq)		
	$[^{64}\text{Cu}]$ Cu-SARTATE	$[^{67}\text{Cu}]$ Cu-SARTATE	$^{67}\text{Cu}/^{64}\text{Cu}$ ratio (mGy)
Adrenals	8.30×10^{-2}	1.79×10^{-1}	2.2
Brain	1.29×10^{-2}	4.12×10^{-2}	3.2
Breasts	1.32×10^{-2}	3.85×10^{-2}	2.9
Gallbladder wall	2.42×10^{-2}	5.43×10^{-2}	2.2
LLI wall	3.68×10^{-2}	1.13×10^{-1}	3.1
Small intestine	5.00×10^{-2}	1.58×10^{-1}	3.2
Stomach wall	2.07×10^{-2}	4.88×10^{-2}	2.4
ULI wall	2.00×10^{-2}	5.14×10^{-2}	2.6
Heart wall	2.06×10^{-2}	5.42×10^{-2}	2.6
Kidneys	2.46×10^{-1}	5.45×10^{-2}	2.2
Liver	9.90×10^{-2}	1.73×10^{-1}	1.7
Lungs	3.85×10^{-2}	8.50×10^{-2}	2.2
Muscle	1.56×10^{-2}	2.54×10^{-2}	1.6
Ovaries	1.79×10^{-2}	4.85×10^{-2}	2.7
Pancreas	4.12×10^{-2}	7.98×10^{-2}	1.9
Red marrow	2.11×10^{-2}	6.19×10^{-2}	2.9
Osteogenic cells	3.22×10^{-2}	1.30×10^{-1}	4.0
Skin	1.20×10^{-2}	3.66×10^{-2}	3.0
Spleen	4.78×10^{-1}	6.42×10^{-1}	1.3
Testes	1.19×10^{-2}	4.08×10^{-2}	3.4
Thymus	1.46×10^{-2}	4.08×10^{-2}	2.8
Thyroid	1.35×10^{-2}	5.34×10^{-2}	3.9
Urinary bladder wall	3.81×10^{-2}	6.22×10^{-2}	1.6
Uterus	1.77×10^{-2}	5.23×10^{-2}	3.0
Total body	2.32×10^{-2}	5.19×10^{-2}	2.2

LLI = lower large intestine; ULI = upper large intestine.

Data are mean of 3 subjects. $[^{67}\text{Cu}]$ Cu-SARTATE estimates are based on all 4 cycles estimated independently in each subject and then averaged across all 3 subjects. Mean effective dose was 3.95×10^{-2} mSv/MBq for $[^{64}\text{Cu}]$ Cu-SARTATE and 7.62×10^{-2} mSv/MBq for $[^{67}\text{Cu}]$ Cu-SARTATE.

but might be improved with new machine-based learning approaches. We have not included $[^{64}\text{Cu}]$ Cu-SARTATE estimated dosimetry for the $[^{67}\text{Cu}]$ Cu-SARTATE treatment because of the differences in the physiologic conditions under which the respective radiopharmaceuticals were administered (with and without amino acid infusion). Also, there were differences in the imaging technologies due to the large difference in spatial resolution, leading to potential underestimation of the SPECT-based image radiopharmaceutical concentrations in organs and other tissues (27). An example can be seen by comparing the lesion sizes in PET and SPECT in Figure 3. This is the subject of further ongoing investigation.

CONCLUSION

To the best of our knowledge, this is the first reported use of [⁶⁴Cu]Cu-SARTATE and [⁶⁷Cu]Cu-SARTATE as a theranostic pair. Both compounds were shown to be safe, well-tolerated, and able to be studied over prolonged imaging time points. No life-threatening or serious adverse events were observed, nor were there any adverse events leading to withdrawal from the study or discontinuation of treatment. The matched pairing was shown by PET and SPECT imaging to have identical targeting to tumors for guiding therapy, demonstrating a nearly ideal theranostic product pair. The extended half-life and suitable PET imaging characteristics of ⁶⁴Cu should allow for personalized dosimetry before treatment—a capability not presently possible with conventional PET imaging radionuclides such as ¹⁸F and ⁶⁸Ga. Further studies will be required to examine the factors influencing the relationship between ⁶⁴Cu dosimetry and that observed after therapy with ⁶⁷Cu.

DISCLOSURE

Harry Marquis was funded by a doctoral scholarship from the Sydney Vital Translational Cancer Research Centre (Cancer Institute NSW) and has received travel grant support from Sydney Vital. Clarity Pharmaceuticals (Sydney, Australia) supplied the [⁶⁴Cu]Cu-SARTATE and [⁶⁷Cu]Cu-SARTATE used in this clinical trial. Matthew Harris, Colin Biggin, and Michelle Parker are employees and stockholders of Clarity Pharmaceuticals, the sponsor of this study. Dale Bailey has previously served as a member of the Clarity Pharmaceuticals Scientific Advisory Board. No other potential conflict of interest relevant to this article was reported.

KEY POINTS

QUESTION: How do the radiation dosimetry estimates compare between copper-labeled radiopharmaceuticals and conventional PET radiotracers?

PERTINENT FINDINGS: In the 3 individuals in this study, radiation dosimetry from copper-labeled radiopharmaceuticals was comparable to that from other widely used PET radiotracers such as ¹⁸F-FDG and ⁶⁸Ga-labeled peptides. ⁶⁴Cu and ⁶⁷Cu were found to be a suitable theranostic pair of radionuclides.

IMPLICATIONS FOR PATIENT CARE: Copper-labeled radiopharmaceuticals are safe to use in diagnostic imaging and for radionuclide therapy. In addition, the fact that the longer physical half-lives of these radiopharmaceuticals allow them to be manufactured in a central radiopharmacy and transported large distances to the PET scanner facility will provide greater access and convenience for patients.

REFERENCES

- Blower PJ, Lewis JS, Zweit J. Copper radionuclides and radiopharmaceuticals in nuclear medicine. *Nucl Med Biol*. 1996;23:957–980.
- Yagi M, Kondo K. Preparation of carrier-free ⁶⁷Cu by the ⁶⁸Zn(γ,p) reaction. *Int J Appl Radiat Isot*. 1978;29:757–759.
- Paterson BM, Roselt P, Denoyer D, et al. PET imaging of tumors with a ⁶⁴Cu labeled macrobicyclic cage amine ligand tethered to Tyr³-octreotate. *Dalton Trans*. 2014;43:1386–1396.
- Hicks RJ, Jackson P, Kong G, et al. ⁶⁴Cu-SARTATE PET imaging of patients with neuroendocrine tumors demonstrates high tumor uptake and retention, potentially allowing prospective dosimetry for peptide receptor radionuclide therapy. *J Nucl Med*. 2019;60:777–785.
- Dutour A, Kumar U, Panetta R, et al. Expression of somatostatin receptor subtypes in human brain tumors. *Int J Cancer*. 1998;76:620–627.
- Malinconico M, Boschi F, Asp J, et al. Automated production of Cu-64, Zr-89, Ga-68, Ti-45, I-123 and I-124 with a medical cyclotron, using a commercial solid target system. *Nucl Med Biol*. 2019;72:S6.
- Francis RJ, Bailey DL, Hofman MS, Scott AM. The Australasian Radiopharmaceutical Trials Network: clinical trials, evidence, and opportunity. *J Nucl Med*. 2021;62:755–756.
- Willowson K, Bailey DL, Baldock C. Quantitative SPECT reconstruction using CT-derived corrections. *Phys Med Biol*. 2008;53:3099–3112.
- Hudson HM, Larkin RS. Accelerated image reconstruction using ordered subsets of projection data. *IEEE Trans Med Imaging*. 1994;13:601–609.
- Meikle SR, Hutton BF, Bailey DL. A transmission dependent method for scatter correction in SPECT. *J Nucl Med*. 1994;35:360–367.
- Chang LT. A method for attenuation correction in radionuclide computed tomography. *IEEE Trans Nucl Sci*. 1978;NS-25:638–643.
- Stabin MG, Sparks RB, Crowe E. OLINDA/EXM: the second-generation personal computer software for internal dose assessment in nuclear medicine. *J Nucl Med*. 2005;46:1023–1027.
- Watson EE, Stabin MG, Siegel JA. MIRD formulation. *Med Phys*. 1993;20: 511–514.
- Cristy M. Active bone marrow distribution as a function of age in humans. *Phys Med Biol*. 1981;26:389–400.
- Stabin MG. *Fundamentals of Nuclear Medicine Dosimetry*. Springer; 2008:151.
- Pfeifer A, Knigge U, Mortensen J, et al. Clinical PET of neuroendocrine tumors using ⁶⁴Cu-DOTATATE: first-in-humans study. *J Nucl Med*. 2012;53:1207–1215.
- Apelgoj S, Coppey J, Gaudemer A, et al. Similar lethal effect in mammalian cells for two radioisotopes of copper with different decay schemes, ⁶⁴Cu and ⁶⁷Cu. *Int J Radiat Biol*. 1989;55:365–384.
- Schwarz SW, Cutler PD, Eichling JI. Tumor dosimetry for Cu-64 and Cu-67-labeled Mab 1A3 for radioimmunotherapy [abstract]. *J Nucl Med*. 1995;36(suppl 5):42.
- DeNardo SJ, DeNardo GL, Kukis DL, et al. ⁶⁷Cu-21T-BAT-Lym-1 pharmacokinetics, radiation dosimetry, toxicity and tumor regression in patients with lymphoma. *J Nucl Med*. 1999;40:302–310.
- DeNardo GL, Kukis DL, Shen S, DeNardo DA, Meares CF, DeNardo SJ. ⁶⁷Cu-versus ¹³¹I-labeled Lym-1 antibody: comparative pharmacokinetics and dosimetry in patients with non-Hodgkin's lymphoma. *Clin Cancer Res*. 1999;5:533–541.
- Connell JM, Anderson CJ, Guo LW, et al. Radioimmunotherapy with a ⁶⁴Cu-labeled monoclonal antibody: a comparison with ⁶⁷Cu. *Proc Natl Acad Sci USA*. 1996;93:6814–6818.
- Miller C, Rousseau J, Ramogida CF, Celler A, Rahmim A, Uribe CF. Implications of physics, chemistry and biology for dosimetry calculations using theranostic pairs. *Theranostics*. 2022;12:232–259.
- Walker RC, Smith GT, Liu E, Moore B, Clanton J, Stabin M. Measured human dosimetry of ⁶⁸Ga-DOTATATE. *J Nucl Med*. 2013;54:855–860.
- Willowson KP, Bailey EA, Bailey DL. A retrospective evaluation of radiation dose associated with low dose FDG protocols in whole-body PET/CT. *Australas Phys Eng Sci Med*. 2012;35:49–53.
- Ryu H, Meikle SR, Willowson KP, Eslick EM, Bailey DL. Performance evaluation of quantitative SPECT/CT using NEMA NU 2 PET methodology. *Phys Med Biol*. 2019;64:145017.
- Marquis H, Deidda D, Gillman A, et al. Theranostic SPECT reconstruction for improved resolution: application to radionuclide therapy dosimetry. *EJNMMI Physics*. 2021;8:16.
- Marquis H, Willowson KP, Bailey DL. Partial volume effect in SPECT & PET imaging and impact on radionuclide dosimetry estimates. *Asia Ocean J Nucl Med Biol*. 2023;11:44–54.

Fibroblast-Activation Protein PET and Histopathology in a Single-Center Database of 324 Patients and 21 Tumor Entities

Nader Hirmas¹, Rainer Hamacher², Miriam Sraieb¹, Marc Ingenwerth³, Lukas Kessler¹, Kim M. Pabst¹, Francesco Barbato¹, Katharina Lueckerath¹, Stefan Kasper², Michael Nader¹, Hans-Ulrich Schildhaus^{3,4}, Claudia Kesch⁵, Bastian von Tresckow⁶, Christine Hanoun⁶, Hubertus Hautzel¹, Clemens Aigner⁷, Martin Glas⁸, Martin Stuschke⁹, Sherko Kümmel¹⁰, Philipp Harter¹¹, Celine Lugnier¹², Waldemar Uhl¹³, Marco Niedergethmann¹⁴, Boris Hadaschik⁵, Viktor Grünwald⁵, Jens T. Siveke^{15,16}, Ken Herrmann¹, and Wolfgang P. Fendler¹

¹Department of Nuclear Medicine, University of Duisburg-Essen, and German Cancer Consortium (DKTK)-University Hospital Essen, Essen, Germany; ²Department of Medical Oncology, West German Cancer Center, University of Duisburg-Essen, and DKTK-University Hospital Essen, Essen, Germany; ³Institute of Pathology, University Hospital Essen, Essen, Germany; ⁴Targos Molecular Pathology Inc., Kassel, Germany; ⁵Department of Urology, University of Duisburg-Essen, and DKTK-University Hospital Essen, Essen, Germany; ⁶Department of Hematology and Stem Cell Transplantation, University of Duisburg-Essen, and DKTK-University Hospital Essen, Essen, Germany; ⁷Department of Thoracic Surgery and Thoracic Endoscopy, University of Duisburg-Essen, and DKTK-University Hospital Essen, Essen, Germany; ⁸Division of Clinical Neurooncology, Department of Neurology, University of Duisburg-Essen, and DKTK-University Hospital Essen, Essen, Germany; ⁹Department of Radiation Therapy, University of Duisburg-Essen, and DKTK-University Hospital Essen, Essen, Germany; ¹⁰Breast Unit, Kliniken Essen-Mitte, Essen, Germany, and Department of Gynecology with Breast Center, Charité-Universitätsmedizin Berlin, Berlin, Germany; ¹¹Department of Gynecology and Gynecologic Oncology, Evang. Kliniken Essen-Mitte, Essen, Germany; ¹²Department of Hematology and Oncology with Palliative Care, Ruhr University Bochum, Bochum, Germany; ¹³Department of General and Visceral Surgery, Ruhr University Bochum, Bochum, Germany; ¹⁴Clinic for General and Visceral Surgery, Alfried Krupp Hospital, Essen, Germany; ¹⁵Bridge Institute of Experimental Tumor Therapy, West German Cancer Center, University Hospital Essen, Essen, Germany; and ¹⁶Division of Solid Tumor Translational Oncology, DKTK (Partner Site Essen) and German Cancer Research Center, Heidelberg, Germany

We present an overview of our prospective fibroblast-activation protein inhibitor (FAP) registry study across a 3-y period, with head-to-head comparison of tumor uptake in ⁶⁸Ga-FAPi and ¹⁸F-FDG PET, as well as FAP immunohistochemistry. **Methods:** This is an interim analysis of the ongoing ⁶⁸Ga-FAPi PET prospective observational trial at our department. Patients who underwent clinical imaging with ⁶⁸Ga-FAPi PET between October 2018 and October 2021 were included. Tracer uptake was quantified by SUV_{max} for tumor lesions and by SUV_{mean} for normal organs. PET tumor volume (40% isocontour) and tumor-to-background ratios were calculated. Correlation between SUV_{max} and FAP staining in tissue samples was analyzed. **Results:** In total, 324 patients with 21 different tumor entities underwent ⁶⁸Ga-FAPi imaging; 237 patients additionally received ¹⁸F-FDG PET. The most common tumor entities were sarcoma (131/324, 40%), pancreatic cancer (67/324, 21%), and primary tumors of the brain (22/324, 7%). The mean primary tumor SUV_{max} was significantly higher for ⁶⁸Ga-FAPi than ¹⁸F-FDG among pancreatic cancer (13.2 vs. 6.1, $P < 0.001$) and sarcoma (14.3 vs. 9.4, $P < 0.001$), and the same was true for mean SUV_{max} in metastatic lesions of pancreatic cancer (9.4 vs. 5.5, $P < 0.001$). Mean primary tumor maximum tumor-to-background ratio was significantly higher for ⁶⁸Ga-FAPi than ¹⁸F-FDG across several tumor entities, most prominently pancreatic cancer (14.7 vs. 3.0, $P < 0.001$) and sarcoma (17.3 vs. 4.7, $P < 0.001$). Compared with ¹⁸F-FDG, ⁶⁸Ga-FAPi showed superior detection for locoregional disease in sarcoma (52 vs. 48 total regions detected) and for distant metastatic disease in both sarcoma (137 vs. 131) and pancreatic cancer

(65 vs. 57), respectively. Among 61 histopathology samples, there was a positive correlation between ⁶⁸Ga-FAPi SUV_{max} and overall FAP immunohistochemistry score ($r = 0.352$, $P = 0.005$). **Conclusion:** ⁶⁸Ga-FAPi demonstrates higher absolute uptake in pancreatic cancer and sarcoma, as well as higher tumor-to-background uptake along with improved tumor detection for pancreatic cancer, sarcoma, and other tumor entities when compared with ¹⁸F-FDG. ⁶⁸Ga-FAPi is a new tool for tumor staging with theranostic potential.

Key Words: FAPi; PET; oncology; staging; theranostic

J Nucl Med 2023; 64:711–716

DOI: 10.2967/jnumed.122.264689

Imaging is critically important in the diagnosis and staging of malignancies, with varying detection rates depending on the tumor entity and diagnostic modality. PET of cancer cells using ¹⁸F-FDG PET acquires additional molecular information useful for the management of disease and for improving treatment outcomes (1–3).

Tumor growth and spread are determined not only by cancer cells but also by the tumor microenvironment, which contains several nonmalignant components. Besides immune cells, important constituents are cancer-associated fibroblasts, which are known to be involved in tumor growth, migration, and progression (4). Although heterogeneous in their origin, cancer-associated fibroblasts have common properties that are distinct from normal fibroblasts, expressing proteins not found in their normal counterparts (5). A subpopulation of cancer-associated fibroblasts expresses, among other markers, fibroblast-activation protein (FAP) α (FAPα), which is associated with protumorigenic functions (6–10).

Received Jul. 18, 2022; revision accepted Nov. 8, 2022.

For correspondence or reprints, contact Wolfgang P. Fendler (wolfgang.fendler@uk-essen.de).

Published online Dec. 29, 2022.

COPYRIGHT © 2023 by the Society of Nuclear Medicine and Molecular Imaging.

Therefore, these cells represent attractive diagnostic and therapeutic targets. Since 2018, preclinical and clinical data have emerged on a variety of FAP-directed therapies, including radiolabeled, low-molecular-weight FAP inhibitors (FAPIs), further underlining their favorable properties in diagnosis and therapy (11–15).

Data for the superiority of ^{68}Ga -FAPI PET over conventional imaging have been reported previously in small cohorts (13,16). On the basis of the favorable imaging characteristics of ^{68}Ga -FAPI PET, patients were referred for clinical ^{68}Ga -FAPI PET staging both at initial diagnosis and after intervention and were offered enrollment in our prospective observational ^{68}Ga -FAPI registry. Clinical indications for ^{68}Ga -FAPI PET were staging of disease in high-risk patients, evaluation of the localization of tumor lesions before biopsy or surgery, further workup of equivocal imaging results, or evaluation of therapeutic options.

In this report, we present the largest cohort to date (to our knowledge), with an overview of the tumor entities diagnosed and staged with ^{68}Ga -FAPI across a 3-y period, including head-to-head comparison of tumor uptake in ^{68}Ga -FAPI and ^{18}F -FDG PET, as well as FAP immunohistochemistry.

MATERIALS AND METHODS

Study Design and Participants

Patients underwent imaging with ^{68}Ga -FAPI PET between October 2018 and October 2021 at the Department of Nuclear Medicine at the University Hospital Essen. This is an interim analysis of the ongoing ^{68}Ga -FAPI PET observational trial conducted at the University Hospital Essen (NCT04571086). Until October 2021, adult patients who underwent clinical ^{68}Ga -FAPI PET were offered the possibility to consent to a prospective observational trial for correlation and clinical follow-up of PET findings. Evaluation of data was approved by the ethics committee of the University Duisburg-Essen (approvals 20-9485-BO and 19-8991-BO). Patient subgroups have been reported in previous publications ($n = 47$ (17), $n = 69$ (18), and $n = 91$ (19)).

Details of data collection (20–22); imaging and administration of radioligands (18,23,24); imaging analysis, immunohistochemistry, and FAP scoring (17,25); and statistical analysis (26) are provided in the supplemental materials (available at <http://jnm.snmjournals.org>).

RESULTS

Patient Characteristics

Three hundred twenty-four patients were included; their characteristics are outlined in Table 1. The median age was 59 y (interquartile range, 16 y). The most common tumor entity was sarcoma (131/324, 40%), followed by primary tumors of the pancreas (67/324, 21%), brain (22/324, 7%), and lung (14/324, 4%) and pleural mesothelioma (12/324, 4%). Most patients (235/324, 73%) underwent ^{68}Ga -FAPI PET imaging for restaging purposes. A breakdown of histopathologic diagnoses, as well as the presence of primary and metastatic lesions for each category, is provided in Supplemental Table 1.

Tumor Diagnostics and ^{68}Ga -FAPI PET

The mean SUV_{\max} for primary lesions and metastatic lesions on ^{68}Ga -FAPI PET is shown in Figures 1A and 1B, respectively. Mean values of primary tumor SUV_{\max} ranged from 3.41 for brain tumors to 21.44 for ovarian tumors. The mean primary tumor SUV_{\max} was higher than 10 for 9 of 17 (53%) tumor entities with primary lesions, including prostate (10.4), bladder (10.5), pancreas (13.2), and sarcoma (14.1), among others. The mean SUV_{\max} for primary lesions and metastatic lesions using broader subgroups is provided in Supplemental Figure 1.

TABLE 1
Patient Characteristics ($n = 324$)

Variable	Data
Sex	
Male	168 (52%)
Female	156 (48%)
Median age at ^{68}Ga -FAPI scan (y)	59 (16)
Tumor entity	
Sarcoma	131 (40%)
Pancreas	67 (21%)
Brain	22 (7%)
Lung	14 (4%)
Pleura	12 (4%)
Cholangiocellular	11 (3%)
Colorectal	11 (3%)
Prostate	11 (3%)
Head and neck	9 (3%)
Bladder	8 (3%)
Lymphoma	7 (2%)
Myeloma	6 (2%)
Ovarian	4 (1%)
Breast	3 (1%)
Duodenum	2 (1%)
Other*	6 (2%)
Tumor staging with ^{68}Ga -FAPI scan [†]	
No evidence of disease	19 (8%)
Stage I	26 (10%)
Stage II	29 (12%)
Stage III	25 (10%)
Stage IV	149 (60%)
Scanning purposes	
Staging at initial diagnosis	88 (27%)
Restaging after therapy	235 (73%)
Prior therapy received	
None	88 (27%)
Surgery	176 (55%)
Chemotherapy	176 (55%)
Radiation therapy	83 (26%)
Immune therapy	27 (8%)
Hormone therapy	9 (3%)
Radionuclide therapy	3 (1%)
Median uptake time (min)	
^{68}Ga -FAPI	14 (24)
^{18}F -FDG	67 (23)
Median time between ^{68}Ga -FAPI and ^{18}F -FDG (d)	0 (2)

*Tumors of cervix ($n = 1$), liver ($n = 1$), skin ($n = 1$), thyroid ($n = 1$), and stomach ($n = 1$) and myoepithelial carcinoma of knee ($n = 1$).

[†]Among 7 most common tumor entities ($n = 248$), excluding brain tumors as well as 9 sarcoma patients (not stageable according to AJCC-8).

Qualitative data are number and percentage; continuous data are median and interquartile range.

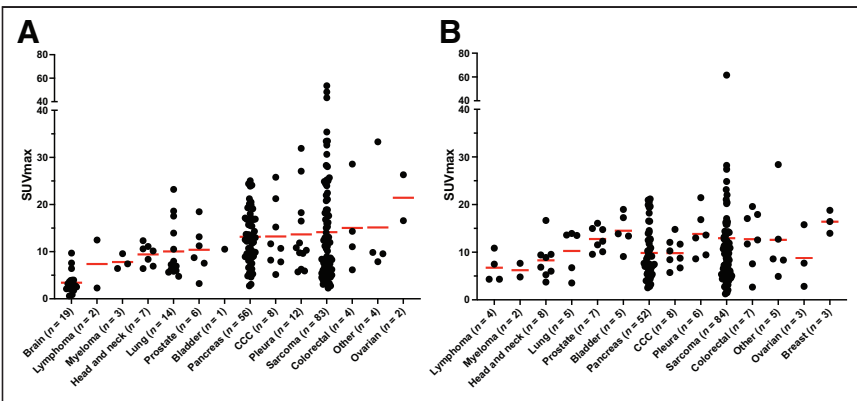


FIGURE 1. Mean SUV_{max} on ^{68}Ga -FAPI PET for primary lesions ($n = 221$) (A) and hottest metastatic lesions per patient ($n = 199$) (B). Data points represent hottest lesions for individual patients. Data in A and B were sorted by mean SUV_{max} in A. Numbers of patients included for every tumor entity are given on x-axis. Red lines represent mean values. y-axis is split to account for extreme values. Primary and metastatic lesions for every tumor entity are provided in Supplemental Table 1.

Staging by ^{68}Ga -FAPI PET is presented in Supplemental Figure 2 for the 7 most common tumor entities in our registry (with at least 10 patients, excluding brain tumors). In our prospective cohort, distant metastatic disease was detected in most patients with head and neck cancer (8/9, 89%), pancreatic cancer (44/67, 66%), sarcoma (79/122, 65%), colon or rectal cancer (7/11, 64%), prostate cancer (7/11, 64%), bladder cancer (5/8, 63%), and cholangiocellular carcinoma (CCC, 6/11, 55%). Locoregional-only disease was detected most often in lung carcinoma (11/14, 79%) and in pleural mesothelioma (9/12, 75%).

^{68}Ga -FAPI PET Versus ^{18}F -FDG PET Imaging

In our cohort, 237 of 324 patients (73%) had undergone additional ^{18}F -FDG PET, and a head-to-head analysis of both imaging modalities was performed. Mean SUV_{max} was significantly higher for ^{68}Ga -FAPI than for ^{18}F -FDG PET among primary tumors of the pancreas (13.2 vs. 6.1, $P < 0.001$) and sarcoma (14.3 vs. 9.4, $P < 0.001$), as shown in Figure 2A. Similarly, the mean SUV_{max} in metastatic lesions was significantly higher for ^{68}Ga -FAPI than for ^{18}F -FDG in pancreatic cancer (9.4 vs. 5.5, $P < 0.001$; Fig. 2B).

For primary tumors, mean tumor-to-background ratio (TBR_{max}) (with blood pool background) was significantly higher for ^{68}Ga -FAPI than for ^{18}F -FDG in pancreatic cancer (9.9 vs. 3.5, $P < 0.001$) and

sarcoma (10.4 vs. 5.8, $P < 0.001$), as shown in Figure 3A. Mean TBR_{max} (with liver background) was also significantly higher for ^{68}Ga -FAPI than for ^{18}F -FDG in pancreatic cancer (14.7 vs. 3.0, $P < 0.001$) and sarcoma (17.3 vs. 4.7, $P < 0.001$), in addition to prostate cancer (7.8 vs. 2.7, $P = 0.017$), pleural mesothelioma (12.9 vs. 5.0, $P = 0.003$), head and neck cancer (14.5 vs. 4.2, $P = 0.013$), and CCC (19.5 vs. 3.6, $P = 0.016$), as shown in Figure 3B. Conversely, mean TBR_{max} (with muscle background) was significantly lower for ^{68}Ga -FAPI than for ^{18}F -FDG in pleural mesothelioma (9.4 vs. 17.6, $P = 0.004$; Fig. 3C).

For metastatic lesions, the mean TBR_{max} (with blood pool background) was significantly higher for ^{68}Ga -FAPI than for ^{18}F -FDG in pancreatic cancer (7.0 vs. 3.4, $P < 0.001$) and sarcoma (9.8 vs. 5.8, $P = 0.028$), as shown in Figure 4A. Mean TBR_{max} (with liver background) was also significantly higher for ^{68}Ga -FAPI than for ^{18}F -FDG in pancreatic cancer (10.6 vs. 2.8, $P < 0.001$) and sarcoma (18.9 vs. 4.7, $P = 0.003$), in addition to prostate cancer (15.1 vs. 4.9, $P < 0.001$), pleural mesothelioma (13.5 vs. 4.8, $P = 0.017$), and CCC (14.5 vs. 3.9, $P = 0.012$), as shown in Figure 4B. Conversely, mean TBR_{max} (with muscle background) was significantly lower for ^{68}Ga -FAPI than for ^{18}F -FDG in pleural mesothelioma (9.4 vs. 17.8, $P = 0.027$), prostate cancer (8.0 vs. 15.6, $P = 0.009$), and CCC (10.0 vs. 15.4, $P = 0.024$), as shown in Figure 4C.

There were no significant differences between metabolic tumor volumes measured for primary lesions and metastatic lesions in ^{68}Ga -FAPI and ^{18}F -FDG PET scans across tumor entities, as shown in Supplemental Figure 3.

Examples of ^{68}Ga -FAPI and ^{18}F -FDG PET scans showing tumor uptake and FAP α staining in tumor samples are presented in Supplemental Figures 4–8.

A comparison of primary SUV_{max} and involved regions between ^{68}Ga -FAPI and ^{18}F -FDG PET among metastatic and nonmetastatic disease and across tumor entities is provided in Supplemental Table 2. When compared with ^{18}F -FDG, ^{68}Ga -FAPI showed superior detection for locoregional disease in sarcoma (52 vs. 48 total regions detected) and for distant metastatic disease in sarcoma (137 vs. 131), pancreatic cancer (65 vs. 57), head and neck cancer (15 vs. 13), CCC (12 vs. 11), lung cancer (9 vs. 8), and bladder cancer (8 vs. 7). However, ^{68}Ga -FAPI showed inferior detection of lymphoma compared with ^{18}F -FDG (7 vs. 10).

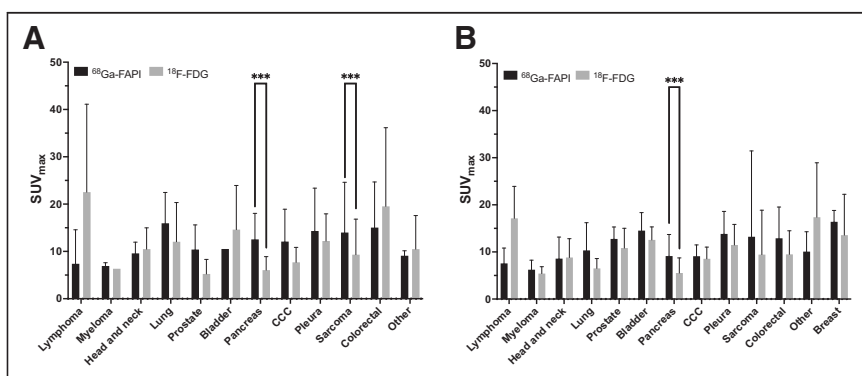


FIGURE 2. Comparison of mean SUV_{max} for primary lesions (A) and metastatic lesions (B) between ^{68}Ga -FAPI and ^{18}F -FDG PET across tumor entities. Entities are arranged as presented in Figure 1. Mean and SD are presented for every bar. Two-tailed paired t test was performed. * $P < 0.05$. ** $P < 0.01$. *** $P < 0.001$.

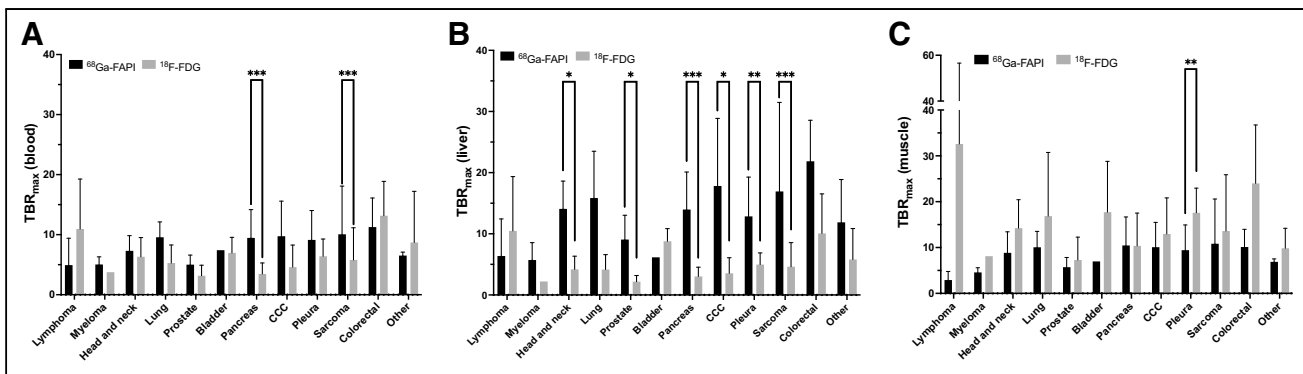


FIGURE 3. Comparison of mean TBR_{max} for primary lesions between ⁶⁸Ga-FAPI and ¹⁸F-FDG PET across tumor entities, with different reference backgrounds (blood [A], liver [B], and muscle [C]). Entities are arranged as presented in Figure 1. Mean and SD are presented for every bar. Two-tailed paired *t* test was performed. *P < 0.05. **P < 0.01. ***P < 0.001.

in the correlation analysis. Across the 61 samples, there was a significant positive correlation between the overall score for FAP α immunohistochemistry and ⁶⁸Ga-FAPI SUV_{max} ($r = 0.352$, $P = 0.005$, Fig. 5).

DISCUSSION

We report findings for 324 patients with 21 tumor entities diagnosed and staged by ⁶⁸Ga-FAPI PET as part of our registry study over a 3-y period, with a head-to-head analysis of ⁶⁸Ga-FAPI versus ¹⁸F-FDG PET uptake in tumor and metastatic lesions, as well as correlation between ⁶⁸Ga-FAPI uptake and FAP α expression in tissue samples. This represents the largest cohort, to our knowledge, of patients examined with this novel imaging modality. Our results demonstrate higher tumor-to-liver uptake ratios for ⁶⁸Ga-FAPI than for ¹⁸F-FDG in 6 of 14 (43%) of the evaluated tumor entities (most prominently sarcoma and pancreatic cancer, in addition to head and neck cancer, prostate cancer, CCC, and pleural mesothelioma) and comparable results in 8 of 14 (57%). Furthermore, we observed a positive correlation between radiotracer uptake and FAP α immunohistochemistry staining.

Relatively low ⁶⁸Ga-FAPI uptake in normal parenchyma improves tumor delineation, especially in regions with high physiologic glucose uptake. Thus, ⁶⁸Ga-FAPI demonstrates improved per-region tumor detection for pancreatic cancer, sarcoma, CCC, prostate

cancer, pleural mesothelioma, and head and neck cancer when compared with ¹⁸F-FDG. As such, ⁶⁸Ga-FAPI PET is a promising imaging modality for these entities, and it has the potential for more precise staging and management of patients, as well as therapeutic screening.

⁶⁸Ga-FAPI PET images the protein FAP α , which is located primarily on cancer-associated fibroblasts in the stroma, but this protein can also be found on tumor cells. High tumor uptake and low organ uptake support the potential use of FAPI ligands in a therapeutic context, particularly for sarcoma and pancreatic cancer. Use of FAP-directed radioligand therapy has been reported to be feasible for breast cancer (11), ovarian cancer (27), and sarcoma and pancreatic cancer (15,28), as well as multiple advanced and refractory tumors (14,29,30). All applications of FAP-directed radioligand therapy relied on baseline patient selection by high uptake on ⁶⁸Ga-FAPI PET. In addition, FAP-targeting drugs have been showing clinical promise across various tumor entities; 1 prominent example is talabostat, which has shown tumor control in 21% of patients with colorectal cancer (31). As such, future drug developments and their potential clinical applications may be enhanced through ⁶⁸Ga-FAPI imaging, which aids in selecting patients whose tumors exhibit high ⁶⁸Ga-FAPI uptake and low glycolytic phenotypes and who would potentially benefit from FAP-directed radioligand therapy.

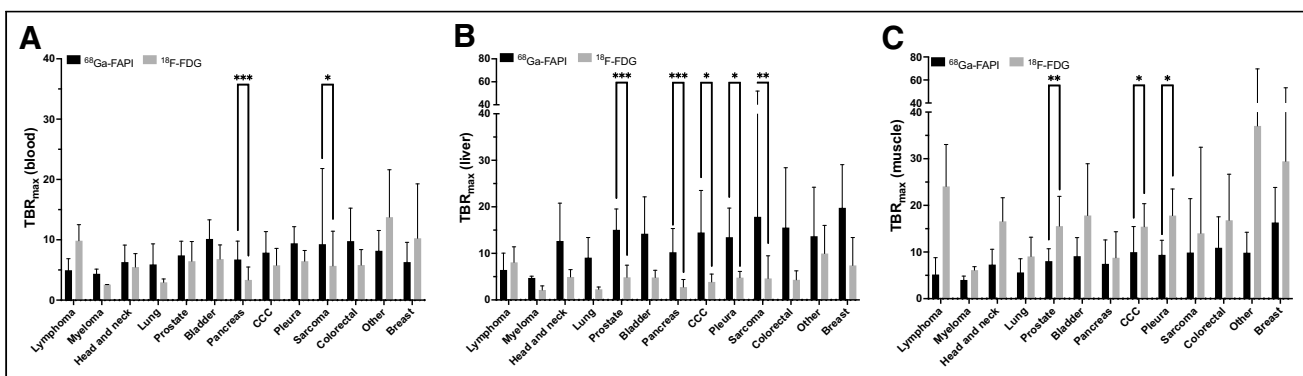


FIGURE 4. Comparison of mean TBR_{max} for metastatic lesions between ⁶⁸Ga-FAPI and ¹⁸F-FDG PET across tumor entities, with different reference backgrounds (blood [A], liver [B], and muscle [C]). Entities are arranged as presented in Figure 1. Mean and SD are presented for every bar. Two-tailed paired *t* test was performed. *P < 0.05. **P < 0.01. ***P < 0.001.

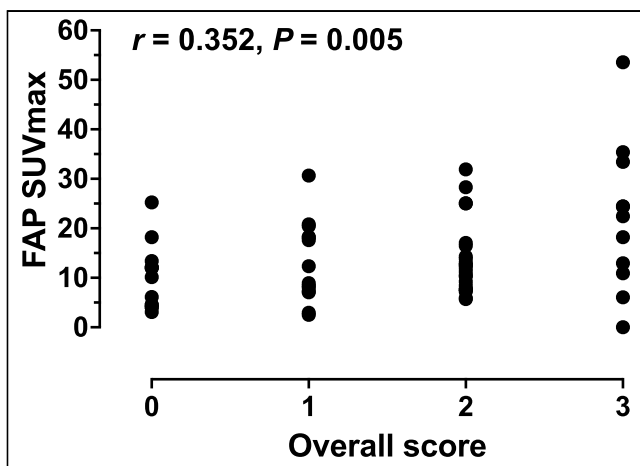


FIGURE 5. Correlation of ⁶⁸Ga-FAPI SUV_{max} with overall score for FAP-immunohistochemistry samples within 3 mo from ⁶⁸Ga-FAPI PET ($n = 61$). Overall FAP score refers to highest score assigned for tumor or stroma. r is Pearson correlation coefficient. Strength of correlation: negligible ($0.00 < r \leq \pm 0.29$), low ($\pm 0.30 \leq r \leq \pm 0.49$), moderate ($\pm 0.50 \leq r \leq \pm 0.69$), or high ($r \geq \pm 0.70$).

Another ongoing clinical trial at our department (NCT05160051) aims to explore the diagnostic accuracy of ⁶⁸Ga-FAPI-46 PET and its impact on management and interreader reproducibility for different FAP-expressing tumor entities. Here, tumor samples will be collected within 8 wk from the time of the ⁶⁸Ga-FAPI PET scan to better elucidate the correlation between ⁶⁸Ga-FAPI-46 uptake intensity and histopathologic FAP expression.

Our analysis has several limitations. SUV for ⁶⁸Ga-FAPI is reproducible at different time points (18) and is routinely measured but not yet a well-established metric. In addition, for some patient subgroups, there were low sample sizes and a referral bias. We report SUVs from different PET devices; despite cross calibration based on European Association of Nuclear Medicine Research Ltd. standards, SUV deviations may have occurred but were not statistically significantly (e.g., random samples with equal numbers of patients, $P = 0.949$). Moreover, the fact that quantitative immunohistochemistry assessment across all planes of whole-mount pathology specimens was not feasible may have led to deviations between ⁶⁸Ga-FAPI SUV_{max} and immunohistochemistry scores.

CONCLUSION

When compared with ¹⁸F-FDG, ⁶⁸Ga-FAPI demonstrates higher absolute uptake in pancreatic cancer and sarcoma, as well as higher tumor-to-background uptake along with improved tumor detection for pancreatic cancer, sarcoma, CCC, prostate cancer, pleural mesothelioma, and head and neck cancer. A prospective clinical trial at our department (NCT05160051) is currently under way.

DISCLOSURE

Rainer Hamacher is supported by the Clinician Scientist Program of the University Medicine Essen Clinician Scientist Academy (UMEA) sponsored by the faculty of medicine and Deutsche Forschungsgemeinschaft (DFG) and has received travel grants from Lilly, Novartis, and Pharma Mar, as well as fees from Lilly

and Pharma Mar. Lukas Kessler is a consultant for AAA and BTG and received fees from Sanofi. Kim Pabst has received a Junior Clinician Scientist Stipend of UMEA sponsored by the Faculty of Medicine at the University of Duisburg-Essen and DFG, and he has received research funding from Bayer outside the submitted work. Katharina Lueckerath is a consultant for Sofie Biosciences and receives research funding from Curie Therapeutics. Stefan Kasper reports personal fees and grants from AstraZeneca, Merck Serone, Merck Sharpe & Dohme, Amgen, Bristol Myers Squibb, Roche, Lilly, Servier, Incyte, and SanofiAventis outside the submitted work. Claudia Kesch has received consultant fees from Apogeha, research funding from AAA/Novartis and Curie Therapeutics, and compensation for travel from Janssen R&D. Bastian von Tresckow is an advisor or consultant for Allogene, BMS/Celgene, Cerus, Incyte, Miltenyi, Novartis, Pentixafarm, Roche, Amgen, Pfizer, Takeda, Merck Sharp & Dohme, and Gilead Kite; has received honoraria from AstraZeneca, Novartis, Roche Pharma AG, Takeda, and Merck Sharp & Dohme; reports research funding from Novartis, Merck Sharp & Dohme, and Takeda; and reports travel support from AbbVie, AstraZeneca, Kite-Gilead, Merck Sharp & Dohme, Takeda, and Novartis. Christine Hanoun received honoraria from BMS, Takeda, and AstraZeneca; travel grants from AbbVie; and research funding from Novartis. Hubertus Hautzel reports research funding and travel support from PARI GmbH outside the submitted work. Ken Herrmann reports personal fees from Bayer, SIRTEX, Adacap, Curium, Endocyte, IPSEN, Siemens Healthineers, GE Healthcare, Amgen, Novartis, ymabs, Aktis, Oncology, and Pharma15, as well as personal and other fees from Sofie Biosciences, nonfinancial support from ABX, and grants and personal fees from BTG, all of which are outside the submitted work. Boris Hadaschik has had advisory roles for ABX, AAA/Novartis, Astellas, AstraZeneca, Bayer, Bristol Myers Squibb, Janssen R&D, Lightpoint Medical, Inc., and Pfizer; has received research funding from Astellas, Bristol Myers Squibb, AAA/Novartis, the German Research Foundation, Janssen R&D, and Pfizer; and has received compensation for travel from Astellas, AstraZeneca, Bayer, and Janssen R&D. Philipp Harter reports grants, personal fees, and nonfinancial support from AstraZeneca and GSK; grants and personal fees from Roche, MSD, Clovis, and Immunogen; personal fees from Mersana, Sotio, Stryker, and Zai Lab; and grants from Boehringer Ingelheim, Medac, Genmab, Deutsche Krebsforschung, Deutsche Forschungs gemeinschaft, and the European Union, all of which are outside the submitted work. Jens T. Siveke received honoraria as a consultant or for continuing medical education presentations from AstraZeneca, Bayer, Bristol-Myers Squibb, Eisbach Bio, Immunocore, Novartis, Roche/Genentech, and Servier; his institution receives research funding from Bristol-Myers Squibb, Celgene, Eisbach Bio, and Roche/Genentech, and he holds ownership and serves on the Board of Directors of Pharma15, all outside the submitted work. Wolfgang Fendler reports fees from SOFIE Bioscience (research funding), Janssen (consultant, speakers' bureau), Calyx (consultant), Bayer (consultant, speakers' bureau, research funding), and Parexel (image review), as well as financial support from Mercator Research Center Ruhr (MERCUR, An-2019-0001), IFORES (D/107=81260, D/107=30240), and Wiedenfeld-Stiftung/Stiftung Krebsforschung Duisburg, all outside the submitted work. No other potential conflict of interest relevant to this article was reported.

KEY POINTS

QUESTION: What is the ^{68}Ga -FAPI PET uptake for different tumor entities?

PERTINENT FINDINGS: Mean SUV_{max} was significantly higher for ^{68}Ga -FAPI than for ^{18}F -FDG in primary and metastatic pancreatic cancer lesions and in sarcoma. Mean TBR_{max} in primary lesions was better for ^{68}Ga -FAPI than for ^{18}F -FDG in sarcoma, CCC, and cancers of the head and neck, prostate, pancreas, and pleura and was comparable for the remaining entities. Radiotracer uptake correlated positively with FAP expression levels in tissue samples. ^{68}Ga -FAPI was superior to ^{18}F -FDG in detecting locoregional disease in sarcoma and distant metastatic disease in sarcoma, CCC, and cancers of the pancreas, head and neck, lung, and bladder.

IMPLICATIONS FOR PATIENT CARE: ^{68}Ga -FAPI PET offers theranostic screening and has the potential for more precise staging and management of patients with these entities.

REFERENCES

1. van Tinteren H, Hoekstra OS, Smit EF, et al. Effectiveness of positron emission tomography in the preoperative assessment of patients with suspected non-small-cell lung cancer: the PLUS multicentre randomised trial. *Lancet*. 2002;359:1388–1393.
2. Ell PJ. The contribution of PET/CT to improved patient management. *Br J Radiol*. 2006;79:32–36.
3. Choi JY, Lee KH, Shim YM, et al. Improved detection of individual nodal involvement in squamous cell carcinoma of the esophagus by FDG PET. *J Nucl Med*. 2000;41:808–815.
4. Erdogan B, Ao M, White LM, et al. Cancer-associated fibroblasts promote directional cancer cell migration by aligning fibronectin. *J Cell Biol*. 2017;216:3799–3816.
5. Gascard P, Tilsky TD. Carcinoma-associated fibroblasts: orchestrating the composition of malignancy. *Genes Dev*. 2016;30:1002–1019.
6. Chen WT, Kelly T. Separase complexes in cellular invasiveness. *Cancer Metastasis Rev*. 2003;22:259–269.
7. Keane FM, Nadvi NA, Yao TW, Gorrell MD. Neuropeptide Y, B-type natriuretic peptide, substance P and peptide YY are novel substrates of fibroblast activation protein- α . *FEBS J*. 2011;278:1316–1332.
8. Huang Y, Wang S, Kelly T. Separase promotes rapid tumor growth and increased microvessel density in a mouse model of human breast cancer. *Cancer Res*. 2004;64:2712–2716.
9. Kelly T. Fibroblast activation protein- α and dipeptidyl peptidase IV (CD26): cell-surface proteases that activate cell signaling and are potential targets for cancer therapy. *Drug Resist Updat*. 2005;8:51–58.
10. Mueller SC, Ghersi G, Akiyama SK, et al. A novel protease-docking function of integrin at invadopodia. *J Biol Chem*. 1999;274:24947–24952.
11. Lindner T, Loktev A, Altmann A, et al. Development of quinoline-based theranostic ligands for the targeting of fibroblast activation protein. *J Nucl Med*. 2018;59:1415–1422.
12. Loktev A, Lindner T, Mier W, et al. A tumor-imaging method targeting cancer-associated fibroblasts. *J Nucl Med*. 2018;59:1423–1429.
13. Giesel FL, Kratochwil C, Lindner T, et al. ^{68}Ga -FAPI PET/CT: biodistribution and preliminary dosimetry estimate of 2 DOTA-containing FAP-targeting agents in patients with various cancers. *J Nucl Med*. 2019;60:386–392.
14. Baum RP, Schuchardt C, Singh A, et al. Feasibility, biodistribution, and preliminary dosimetry in peptide-targeted radionuclide therapy of diverse adenocarcinomas using ^{177}Lu -FAP-2286: first-in-humans results. *J Nucl Med*. 2022;63:415–423.
15. Ferdinandus J, Fragoso Costa P, Kessler L, et al. Initial clinical experience with ^{90}Y -FAPI-46 radioligand therapy for advanced stage solid tumors: a case series of nine patients. *J Nucl Med*. 2022;63:727–734.
16. Kratochwil C, Flechsig P, Lindner T, et al. ^{68}Ga -FAPI PET/CT: tracer uptake in 28 different kinds of cancer. *J Nucl Med*. 2019;60:801–805.
17. Kessler L, Ferdinandus J, Hirmas N, et al. ^{68}Ga -FAPI as a diagnostic tool in sarcoma: data from the ^{68}Ga -FAPI PET prospective observational trial. *J Nucl Med*. 2022;63:89–95.
18. Ferdinandus J, Kessler L, Hirmas N, et al. Equivalent tumor detection for early and late FAPI-46 PET acquisition. *Eur J Nucl Med Mol Imaging*. 2021;48:3221–3227.
19. Kessler L, Ferdinandus J, Hirmas N, et al. Pitfalls and common findings in ^{68}Ga -FAPI-PET: a pictorial analysis. *J Nucl Med*. 2022;63:890–896.
20. Harris PA, Taylor R, Minor BL, et al. The REDCap consortium. Building an international community of software platform partners. *J Biomed Inform*. 2019;95:103208.
21. Harris PA, Taylor R, Thielke R, Payne J, Gonzalez N, Conde JG. Research electronic data capture (REDCap): a metadata-driven methodology and workflow process for providing translational research informatics support. *J Biomed Inform*. 2009;42:377–381.
22. Amin MB, Edge S, Greene F, et al. *AJCC Cancer Staging Manual*. 8th ed. Springer International Publishing; 2017:55–986.
23. Lindner T, Loktev A, Giesel F, Kratochwil C, Altmann A, Haberkorn U. Targeting of activated fibroblasts for imaging and therapy. *EJNMMI Radiopharm Chem*. 2019;4:16.
24. Loktev A, Lindner T, Burger EM, et al. Development of fibroblast activation protein-targeted radiotracers with improved tumor retention. *J Nucl Med*. 2019;60:1421–1429.
25. Henry LR, Lee HO, Lee JS, et al. Clinical implications of fibroblast activation protein in patients with colon cancer. *Clin Cancer Res*. 2007;13:1736–1741.
26. Hinkle DE, Wiersma W, Jurs SG. *Applied Statistics for the Behavioral Sciences*. 2nd ed. Houghton Mifflin; 2003:118.
27. Lindner T, Altmann A, Kramer S, et al. Design and development of $^{99\text{m}}\text{Tc}$ -labeled FAPI tracers for SPECT imaging and ^{188}Re therapy. *J Nucl Med*. 2020;61:1507–1513.
28. Kratochwil C, Giesel FL, Rathke H, et al. $[^{153}\text{Sm}]$ samarium-labeled FAPI-46 radioligand therapy in a patient with lung metastases of a sarcoma. *Eur J Nucl Med Mol Imaging*. 2021;48:3011–3013.
29. Kuyumcu S, Kovanci B, Sanli Y, et al. Safety of fibroblast activation protein-targeted radionuclide therapy by a low-dose dosimetric approach using ^{177}Lu -FAPI04. *Clin Nucl Med*. 2021;46:641–646.
30. Assadi M, Rekabpour SJ, Jafari E, et al. Feasibility and therapeutic potential of ^{177}Lu -fibroblast activation protein inhibitor-46 for patients with relapsed or refractory cancers: a preliminary study. *Clin Nucl Med*. 2021;46:e523–e530.
31. Narra K, Mullins SR, Lee HO, et al. Phase II trial of single agent Val-boroPro (Talabostat) inhibiting fibroblast activation protein in patients with metastatic colorectal cancer. *Cancer Biol Ther*. 2007;6:1691–1699.

Initial Results of ^{68}Ga -FAPI-46 PET/MRI to Assess Response to Neoadjuvant Chemotherapy in Breast Cancer

Philipp Backhaus*^{1,3}, Matthias C. Burg*⁴, Inga Asmus¹, Michaela Pixberg¹, Florian Büther^{1,2}, Hans-Jörg Breyholz¹, Randy Yeh³, Stefanie B. Weigel⁴, Patricia Stichling⁴, Walter Heindel⁴, Stefanie Bobe^{2,5}, Peter Barth⁵, Joke Tio⁶, and Michael Schäfers^{1,2}

¹Department of Nuclear Medicine, University Hospital Münster, Münster, Germany; ²European Institute for Molecular Imaging, University of Münster, Münster, Germany; ³Molecular Imaging and Therapy Service, Department of Radiology, Memorial Sloan Kettering Cancer Center, New York City, New York; ⁴Clinic for Radiology, University Hospital Münster, Münster, Germany;

⁵Gerhard-Domagk Institute for Pathology, University of Münster, Münster, Germany; and ⁶Department of Gynecology and Obstetrics, University Hospital Münster, Münster, Germany

Improving imaging-based response after neoadjuvant chemotherapy (NAC) in breast cancer assessment could obviate histologic confirmation of pathologic complete response (pCR) and facilitate deescalation of chemotherapy or surgery. Fibroblast activation protein inhibitor (FAPI) PET/MRI is a promising novel molecular imaging agent for the tumor microenvironment with intense uptake in breast cancer. We assessed the diagnostic performance of follow-up breast ^{68}Ga -FAPI-46 (^{68}Ga -FAPI) PET/MRI in classifying the response status of local breast cancer and lymph node metastases after completion of NAC and validated this approach immunohistochemically. **Methods:** In women who completed NAC for invasive breast cancer, follow-up ^{68}Ga -FAPI PET/MRI and corresponding fibroblast activation protein (FAP) immunostainings were retrospectively analyzed. Metrics of ^{68}Ga -FAPI uptake and FAP immunoreactivity in women with or without pCR were compared using the Mann–Whitney *U* test. Diagnostic performance to detect remnant invasive cancer was calculated for tracer uptake metrics using receiver-operating-characteristic curves and for masked readers' visual assessment categories of PET/MRI and MRI alone. **Results:** Thirteen women (mean age \pm SD, 47 \pm 9 y) were evaluated. Seven of the 13 achieved pCR in the breast and 6 in the axilla. FAP immunoreactivity was significantly associated with response status. The ^{68}Ga -FAPI PET/MRI mean breast tumor-to-background ratio was 0.9 (range, 0.6–1.2) for pCR and 2.1 (range, 1.4–3.1) for no pCR ($P = 0.001$). Integrated PET/MRI could classify breast response correctly in all 13 women based on readers' visual assessment or tumor-to-background ratio. Evaluation of MRI alone resulted in at least 2 false-positives. For lymph nodes, PET/MRI readers had at least 2 false-negative classifications, whereas MRI alone resulted in 2 false-negatives and 1 false-positive. **Conclusion:** To our knowledge, this was the first analysis of ^{68}Ga -FAPI PET/MRI for response assessment after NAC for breast cancer. The diagnostic performance of PET/MRI in a small study sample trended toward a gain over MRI alone, clearly supporting future prospective studies.

Key Words: FAPI; PET/MRI; breast cancer; neoadjuvant chemotherapy; deescalation

J Nucl Med 2023; 64:717–723

DOI: 10.2967/jnmed.122.264871

Received Sep. 2, 2022; revision accepted Nov. 1, 2022.
For correspondence or reprints, contact Philipp Backhaus (philipp.backhaus@ukmuenster.de).

*Contributed equally to this work.

Published online Nov. 17, 2022.

COPYRIGHT © 2023 by the Society of Nuclear Medicine and Molecular Imaging.

In breast cancer, application of systemic neoadjuvant chemotherapy (NAC) before curative surgery may achieve resectability, increase the frequency of breast-conserving treatment, and reduce the extent of axillary surgery. Moreover, the remission status at the primary cancer site gives valuable implications on prognosis and subsequent therapy decisions (1). In German breast centers, neoadjuvant application of chemotherapy rose from 20% to 58% from 2008 to 2017, and the pathologic complete response (pCR) rate rose from 15% to 34% (2). Importantly, pCR implies local cure from invasive cancer by NAC alone. Knowledge of pCR status would thus allow for deescalation of therapy—either abbreviation of chemotherapy (3) or even omission of breast and axillary surgery (4). However, pCR can currently be reliably determined only by histopathologic confirmation, and all patients therefore undergo complete NAC followed by surgery.

Breast MRI has been shown to provide the most accurate preoperative guidance for resection volumes and is sensitive in detecting remnant cancer (5). Combinations with breast MRI can increase diagnostic accuracy, such as combination with ultrasound (6), biopsies (7), machine learning (8), or ^{18}F -FDG PET/MRI (9). However, no method has yet proven sufficiently accurate and feasible to allow for deescalation of chemotherapy or surgery.

In a recent study, we introduced ^{68}Ga -labeled fibroblast activation protein inhibitor (FAPI) PET as a novel molecular readout for invasive breast cancer in integrated breast PET/MRI (10). This technique takes advantage of expression of the fibroblast activation protein (FAP) by cancer-associated fibroblasts in the tumor microenvironment. Further studies have substantiated superior detection of breast cancer lesions of ^{68}Ga -FAPI PET/CT over ^{18}F -FDG (11,12). In this study, we aimed to assess the diagnostic performance of follow-up breast ^{68}Ga -FAPI-46 (^{68}Ga -FAPI) PET/MRI in classifying the response status in local breast cancer and lymph node (LN) metastases after completion of NAC and to validate this approach immunohistochemically.

MATERIALS AND METHODS

Patients

We retrospectively analyzed ^{68}Ga -FAPI PET/MRI scans and corresponding FAP immunostainings of women with breast cancer. Patients were referred by their treating oncologist on an individual, clinical basis to support response assessment after NAC. All patients gave

written informed consent for ^{68}Ga -FAPI PET/MRI and retrospective scientific analysis. Analysis was approved by the Ethics Committee of the Medical Association of Westphalia–Lippe and the Medical Faculty of the University of Münster (reference number: 2021-408-f-S). This study included all breast cancer patients who underwent ^{68}Ga -FAPI PET/MRI after NAC at the University Hospital Münster from May 2020 to May 2021. No exclusion criteria were applied. The baseline scans of 12 of the 13 patients were previously reported (10).

Radiochemistry

Application and production of ^{68}Ga -FAPI were performed according to the German Pharmaceuticals Act §13(2b). Precursor was kindly provided under a material transfer agreement by Uwe Haberkorn (Heidelberg, Germany), and radiolabeling was performed as previously described (10).

Imaging

Women were injected intravenously with $99 \pm 33 \text{ MBq}$ (mean \pm SD) of ^{68}Ga -FAPI and examined in a hybrid PET/MRI 3-T scanner with a 4-channel dedicated PET/MRI breast coil (mMR; Siemens Healthineers). Breast list-mode PET (25 min) with the patient prone was started an average of 35 min after injection (range, 23–70 min), combined with a standard breast MRI protocol consisting of the following sequences: transversal T2-weighted turbo spin-echo spectral attenuated inversion recovery, diffusion-weighted imaging, T1-weighted fast low-angle shot contrast-enhanced dynamic imaging (gadobutrol, 0.1 mmol/kg of body weight [Gadovist; Bayer]), and contrast-enhanced high-spatial-resolution fat-saturated T1-weighted fast low-angle shot imaging, as described previously (10). In 11 of 13 patients, no whole-body scans were performed and lower radiotracer doses corresponding to 1–1.25 MBq/kg of body weight were injected, compared with baseline doses of $156 \pm 51 \text{ MBq}$ (10). An interim analysis had established unbiased assessment of breast PET/MRI at these reduced doses (Supplemental Figs. 1–3; supplemental materials are available at <http://jnm.snmjournals.org>).

Image Analysis

Prone single-bed-position follow-up breast PET/MR images after NAC were analyzed. Visual categorization of MRI alone and integrated PET/MRI was performed separately by 3 readers for each modality, with masking of the pathology results. The initial clinical report, finalized before pathology was available, was analyzed in consensus by an MRI reader and a PET/MRI reader: 1 board-certified specialist in radiology (7 y experience in breast imaging) and nuclear medicine (7 y of experience in nuclear oncology). In addition, anonymized imaging studies were separately read as MRI alone and integrated PET/MRI by 2 independent readers: 1 senior trainee and 1 board-certified specialist in radiology (1 and >20 y of experience in breast imaging) and nuclear medicine (3 and >15 y of experience in nuclear oncology), respectively. These individuals were previously not involved in reading the cases. The readers were masked to the clinical report of the follow-up PET/MRI and all data collected afterward but had access to previous examinations, including baseline prone breast PET/MRI and supine whole-body PET/MRI or PET/CT. The MRI readers did not have access to the PET component of follow-up PET/MR images and were given the reports of previous studies when deemed necessary. Integrated PET/MRI readers evaluated the radiotracer uptake and had additional access to the MR images, including interpretation when relevant for tumor bed delineation.

Measurements were performed with spheric and ellipsoid volumes of interest as described previously (10). Tumor-to-background ratios ($\text{TBR}_{\text{max/max}}$) represent the ratio of the lesion and entire contralateral breast SUV_{max} or a healthy part of the ipsilateral breast when patients had prior contralateral mastectomy. Follow-up PET measurements are

the means for all readers. Only the main breast lesion and most suggestive LN were considered for analysis.

Breast lesions and LNs were visually assigned to 1 of 3 categories. For MRI of the breast, the categories were no residual tumor or contrast enhancement greater than the background level (category A), possible residual tumor (i.e., faint contrast enhancement) (category B), and probable (>75%) residual tumor (i.e., mass lesion with contrast enhancement) (category C). For MRI of the axilla, the categories were normal LNs (category A), possible metastasis (discrete change or enhancement) (category B), and probable (>75%) metastasis (category C). For PET/MRI of the breast and axilla, the categories were no focal uptake (category A), possible focal uptake and possible background noise (category B), and certain focal uptake (category C). Majority reads were the most prevalent category, or category B if all categories were synchronously selected.

Histology

Pathologic response and immunostaining were assessed as part of the clinical routine according to common standards on resected breast and axillary tissue as reported previously (10). pCR in the breast was defined as absence of invasive cancer. One patient had remnant tumor cells in lymphatic vessels only and was classified as no pCR. FAP immunohistochemistry was conducted as described previously (10) and categorized as FAP-negative (category A), mildly positive (category B), or intensely positive (category C).

Statistical Analysis

Statistical analysis was performed using Matlab (version R2020a; MathWorks). Mann–Whitney U tests were used to compare tracer uptake metrics and FAP immunoreactivity for women with or without pCR and uptake metrics between baseline and follow-up. A P value of less than 0.05 was considered statistically significant. For the optimal threshold in receiver-operating characteristics (ROCs), the costs for false negatives (FN) and false positives (FP) were weighed as 80% and 20%, respectively. The calculation of sensitivity and specificity considered no pCR as positive. Cited diagnostic performance values were adapted when based on an inverse definition.

RESULTS

Patient Characteristics

We analyzed overall 13 follow-up ^{68}Ga -FAPI PET/MRI scans of the breast after completion of NAC for breast cancer in 13 women (nonexcluded) (mean age, 47 ± 9 y). Twelve women received prior baseline ^{68}Ga -FAPI PET/MRI scans, published previously (10). PET/MRI was conducted 12 ± 8 d after completion of NAC. Surgery that established the reference standard was conducted 13 ± 5 d after PET/MRI. Seven of 13 women achieved pCR in the breast, 6 of 10 women with LN metastases at baseline achieved axillary pCR, and 7 of 13 achieved overall pCR. More patient characteristics are available in Table 1.

Breast Assessment

Tracer uptake by primary breast lesions in follow-up was markedly decreased to a mean SUV_{max} of 1.8 (range, 0.9–3.5) from the baseline mean SUV_{max} of 14.2 (range, 8.6–29.9) ($P < 0.001$; mean reduction to 12% [range, 4–22]). Breast background uptake was also decreased to a mean SUV_{max} of 1.3 (range, 0.8–2.7) from the baseline mean SUV_{max} of 2.6 (range, 1.1–6.9) ($P = 0.006$; mean reduction to 62% [range, 24–104]). This resulted in a reduced mean $\text{TBR}_{\text{max/max}}$ of 1.4 (range, 0.6–3.1), compared with a baseline mean $\text{TBR}_{\text{max/max}}$ of 7.0 (range, 1.9–16.0) ($P < 0.001$) (Fig. 1; Supplemental Table 1; Supplemental Figs. 4 and 5).

TABLE 1
Patient Characteristics

Patient no.	Age (y)	Type	Grade	Receptor status	Systemic therapy	Interval from last cycle to PET (d)
1	56	Ductal	2	HR+, HER2+	AC T H*	15
2	51	Ductal	2	HR+, HER2+	EC T H	15
3	51	Ductal	1	HR+, HER2+	EC T H	6
4	35	Ductal	3	TNBC	EC T Cb	10
5	46	Ductal	3	HR+, HER2-	EC T	6
6	58	Ductal	3	HR-, HER2+	EC T H	0
7	56	Lobular	2	HR+, HER2+	EC T H	29
8	43	Ductal	2	TNBC	T Cb	15
9	38	Ductal	2	HR-, HER2+	EC T H	1
10	36	Lobular	2	HR+, HER2-	EC T	20
11	59	Ductal	2	HR+, HER2-	EC T	14
12	48	Ductal	3	HR-, HER2+	EC T H	15
13	34	Ductal	2	HR+, HER2-	EC T	8

*Additional investigational drug.

HR = hormone receptor; HER2 = human epidermal growth factor receptor 2; TNBC = triple-negative breast cancer; AC = doxorubicin; T = taxane; H = HER2-antibodies; EC = epirubicin; Cb = carboplatin.

For integrated PET/MRI, the primary breast lesion visual categories were consistent in 9 of 13 women among the 3 readers. The readers' majority visual classification resulted in an FN rate of 0, FP rate of 0, sensitivity of 100%, and specificity of 100%, when only category C (certain focal uptake) was defined as positive. Considering categories B (possible focal uptake) and C as positive resulted in an FN rate of 0, FP rate of 2, sensitivity of 100%, and specificity of 71% (Figs. 1, 2C, and 2D; Table 2). Among readers, the SD was 0.1 for lesion and background SUV_{max} and TBR_{max/max}. TBR_{max/max} demonstrated perfect classification of remission status (breast pCR: mean TBR_{max/max}, 0.9 [range, 0.6–1.2]; no pCR: mean TBR_{max/max}, 2.1 [range, 1.4–3.1] [$P = 0.001$]) (ROC optimal threshold TBR_{max/max}, 1.4; sensitivity, 100%; specificity, 100%) (Figs. 1, 2A, and 2D). In contrast, SUV_{max}

measurements showed relevant overlap between response categories (pCR: mean SUV_{max}, 1.1 [range, 0.9–1.8]; no pCR: mean SUV_{max}, 2.5 [range, 1.3–3.5] [$P = 0.002$]) (ROC optimal threshold SUV_{max}, 1.3; sensitivity, 100%; specificity, 86%) (Figs. 2B and 2D). The relative SUV_{max} reduction from baseline was significantly different, but with a high overlap between response groups in 12 eligible women (pCR: mean reduction to 10% [range, 4%–20%]; no pCR: mean reduction to 16% [range, 10%–22%] [$P = 0.03$]). Baseline SUV_{max} was not significantly different ($P = 0.20$).

In patient 5, the primary breast lesion was not evaluable on MRI because of a marker clip susceptibility artifact. MRI-alone breast lesion categories were consistent in 6 of 12 evaluable women among readers. Majority categorization for MRI resulted

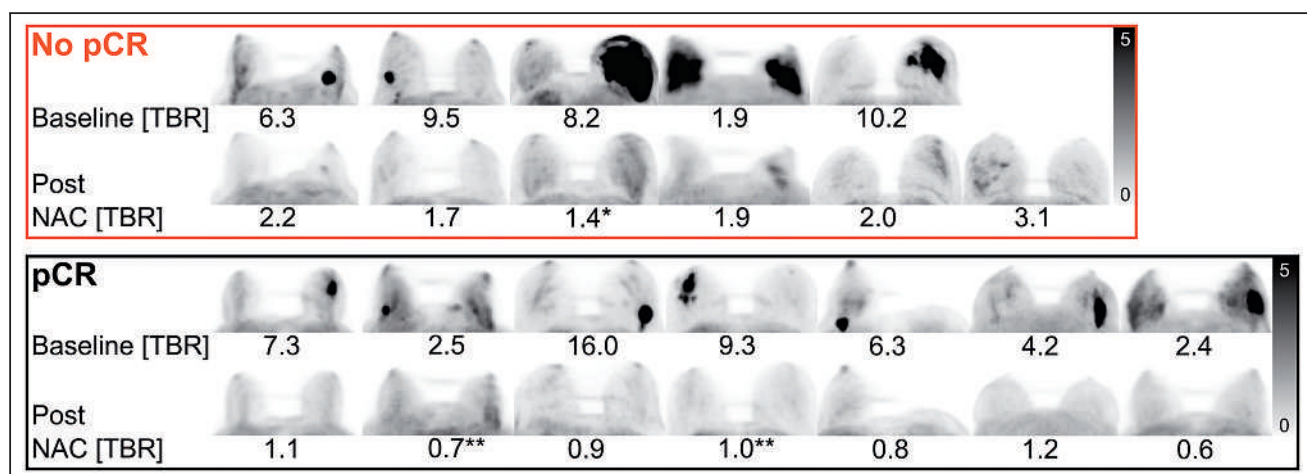


FIGURE 1. Craniocaudal maximum-intensity projections of whole-breast ⁶⁸Ga-FAPI before and after NAC of patients not achieving or achieving pCR in breast. Patients with no pCR are, from left to right, patients 2, 3, 4, 10, 11, and 13. Patients with pCR are, from left to right, patients 1, 5, 6, 7, 8, 9, and 12. Baseline and post-NAC TBR_{max/max} is given for each patient. All images are tuned to an SUV range of 0–5 (Supplemental Figs. 4 and 5). *No pCR with remnant tumor cells only in lymphatic vessels. **pCR with residual carcinoma in situ.

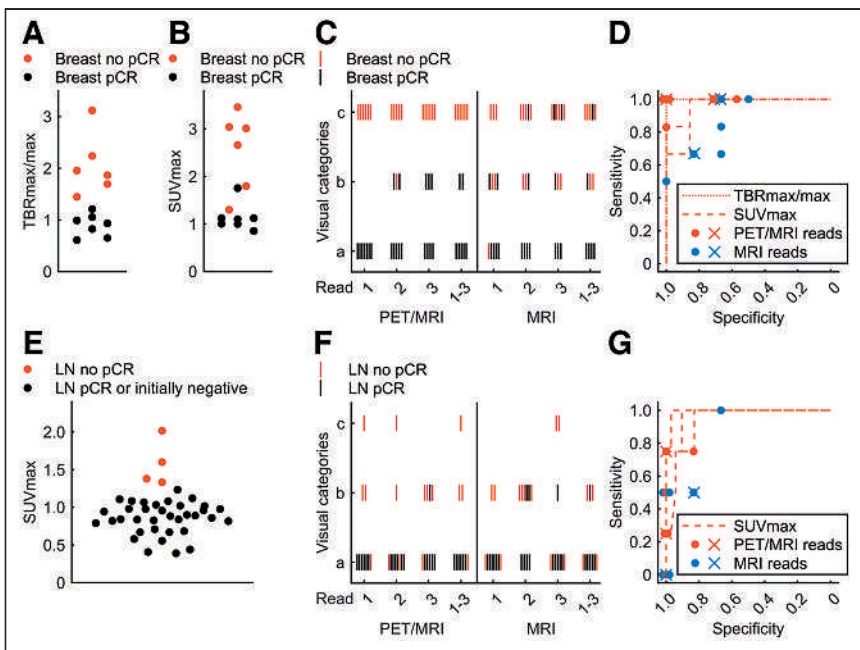


FIGURE 2. (A) Breast lesion TBR_{max/max} bee swarm plots of no pCR and pCR. (B) Corresponding plots by SUV_{max}. (C) Category for breast lesions for individual and majority PET/MRI and MRI reads. (D) ROC curves by TBR_{max/max} or SUV_{max} corresponding to individual measurements of 3 readers. Sensitivity and specificity for individual (dots) and majority (crosses) reads are plotted for PET/MRI and MRI alone either considering categories B and C positive or considering only category C positive. Overlying dots were slightly shifted to allow visualization. (E) Axillary node SUV_{max} for axillary level 1 LNs. (F) Visual assessment category for LNs. (G) ROC curves for LNs with additionally plotted results from individual and majority reads.

in an FN rate of 2, FP rate of 1, sensitivity of 67%, and specificity of 83% when only category C (probable tumor) was defined as positive. Considering categories B (possible tumor) and C as positive led to an FN rate of 0, FP rate of 2, sensitivity of 100%, and specificity of 67% (Figs. 2C and 2D). Figure 3 shows 2 examples of superior visualization of remnant breast cancer by the ⁶⁸Ga-FAPI PET component compared with MRI alone and of crucial guidance of the MRI component toward correct integrated PET/MRI assessment, respectively.

In 13 patients with available immunohistochemistry, FAP staining categories were associated with remission status (breast pCR: category A [FAP negative], 1/7; category B [mildly positive], 6/7; category C [intensely positive], 0/7) (no pCR: category A, 0/6; category B, 2/6; category C, 4/6) ($P = 0.033$) (Figs. 4A and 4B).

Axillary Assessment

Uptake by LN metastases was reduced after NAC to a mean SUV_{max} of 1.2, (range, 0.8–2.0), compared with a baseline mean SUV_{max} of 10.0 (range, 3.4–18.7) ($P < 0.001$; reduction to 14% [range, 5–40]) (Supplemental Table 2).

TABLE 2
Visual Assessment Categories A–C for Individual Readers

Patient no.	Response	Breast		Response	LN		
		Follow-up category			PET/MRI	MRI	
		PET/MRI	MRI				
1	pCR	AAA	AAA	pCR	AAA	AAA	
2	No pCR	CCC	CCC	pCR	AAB	ABB	
3	No pCR	CBC	BCC	NA	NA	NA	
4	No pCR*	CCC	BBB	No pCR	BAB	BBC	
5	pCR†	AAA	NA‡	pCR	AAA	AAA	
6	pCR	ABB	BAC	pCR	AAA	AAA	
7	pCR†	AAB	AAA	pCR	AAA	AAA	
8	pCR	ABB	BCC	NA	NA	NA	
9	pCR	AAA	AAB	pCR	AAA	ABA	
10	No pCR	CCC	CCB	No pCR	AAA	ABA	
11	No pCR	CCC	ABB	No pCR	BBB	BBC	
12	pCR	AAA	ABA	NA	NA	NA	
13	No pCR	CCC	CCC	No pCR	CCB	ABA	

*No pCR, with remnant tumor cells only in lymphatic vessels.

†pCR, with residual carcinoma in situ.

‡Clip artifact prevented breast assessment.

NA = not applicable.

Majority assessment is highlighted in bold.

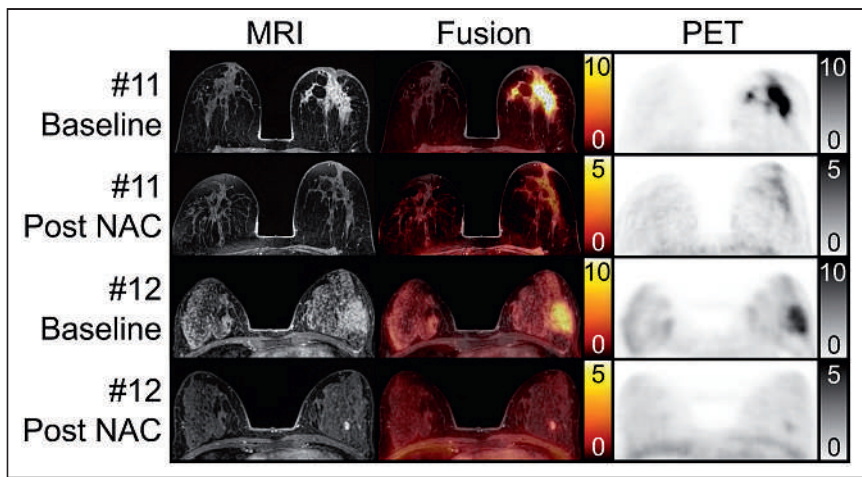


FIGURE 3. Examples of breast lesion patients with prone transverse contrast-enhanced fat-saturated T1-weighted MRI scan, fusion image, and ^{68}Ga -FAPI PET scan at baseline and at follow-up after NAC. In patient 11, follow-up showed extensive remnant ^{68}Ga -FAPI uptake ($\text{TBR}_{\text{max/max}}$, 2.0) in breast, whereas MRI was negative or slightly positive in circumscribed area near nipple, depending on reader. Pathology revealed remnant 10-cm invasive cancer matching PET assessment. In patient 12, follow-up showed focal mild ^{68}Ga -FAPI and intense MRI contrast enhancement adjacent to tumor bed. MRI characteristics established fibroadenoma, allowing classification of tumor bed as negative on MRI and PET/MRI, later confirmed by pathology.

In integrated PET/MRI, visual assessment of LNs was consistent among readers in 7 of 10 women. Majority classification resulted in an FN rate of 3, FP rate of 0, sensitivity of 25%, and specificity of 100% when only category C was defined as positive. Considering categories B and C as positive resulted in an FN rate

of 1, FP of 0, sensitivity of 75%, and specificity of 100% (Figs. 2F and 2G). Among readers, the SD of SUV_{max} measurements of the most intense ipsilateral node was 0.2. Despite imperfect visual assessment, all readers' mean SUV_{max} measurements of LNs could perfectly classify pCR and no pCR in the group of 10 affected women (LN pCR: mean SUV_{max} , 0.9 [range, 0.8–1.1]; no pCR: mean SUV_{max} , 1.6 [range, 1.3–2.0] [$P = 0.001$]) (ROC optimal threshold SUV_{max} , 1.3; sensitivity, 100%; specificity, 100%). Adding up to 29 contralateral and ipsilateral initially nonmetastatic LNs to pCR LNs still resulted in perfect SUV_{max} -based classification (pCR and nonmetastatic LNs: mean SUV_{max} , 0.9 [range, 0.4–1.2]; ROC optimal threshold: SUV_{max} , 1.3; sensitivity, 100%; specificity, 100%) (Fig. 2E). However, when analyzing readers' individual measurements, classification was imperfect (ranges of 3 readers: ROC optimal threshold SUV_{max} , 1.1–1.5; sensitivity, 75%–100%; specificity, 90%–97%) (Fig. 2G). The relative SUV_{max} reduction from baseline was

significantly different between response groups in 9 eligible women (pCR: mean reduction to 9% [range, 5%–13%]; no pCR: mean reduction to 23% [range, 14%–40%]; $P = 0.02$). Baseline SUV_{max} was not significantly different ($P = 0.38$).

MRI-alone readers were consistent in 4 of 10 women. Majority MRI categorization resulted in an FN of 4, FP of 0, sensitivity of 0%, and specificity of 100% when only category C was defined as positive. Considering categories B and C as positive resulted in an FN of 2, FP of 1, sensitivity of 50%, and specificity of 83% (Figs. 2F and 2G). Figure 5 gives 2 examples of better visualization of LN metastases by the MRI and ^{68}Ga -FAPI PET components.

In 8 patients with available immunohistochemistry, LN FAP staining categories were associated with remission status (LN pCR: category A, 4/4; category B, 0/4; category C, 0/4) (no pCR: category A, 0/4; category B, 2/4; category C, 2/4) ($P = 0.029$) (Figs. 4C and 4D).

Combined Assessment

For combined assessment of axillary and breast response status, majority classification resulted in an FN of 0, FP of 0, sensitivity of 100%, and specificity of 100% for PET/MRI and an FN of 2, FP of 1, sensitivity of 67%, and specificity of 86% for MRI alone when only category C was defined as positive. Considering categories B and C as positive resulted in an FN of 0, FP of 2, sensitivity of 100%, and specificity of 71% for both PET/MRI and MRI alone.

DISCUSSION

Currently, no imaging test can identify breast cancer patients with pCR after NAC with sufficient accuracy to allow for deescalation of therapy by abbreviating chemotherapy or even omitting surgery.

In this study, we were the first—to our knowledge—to analyze the diagnostic performance of ^{68}Ga -FAPI PET/MRI in assessing response to NAC in breast cancer. Combined and breast pathologic response could be correctly classified in all 13 patients based on ^{68}Ga -FAPI uptake on PET/MRI, whereas MRI alone assigned at least 2 patients falsely. PET/MRI could also classify LN status

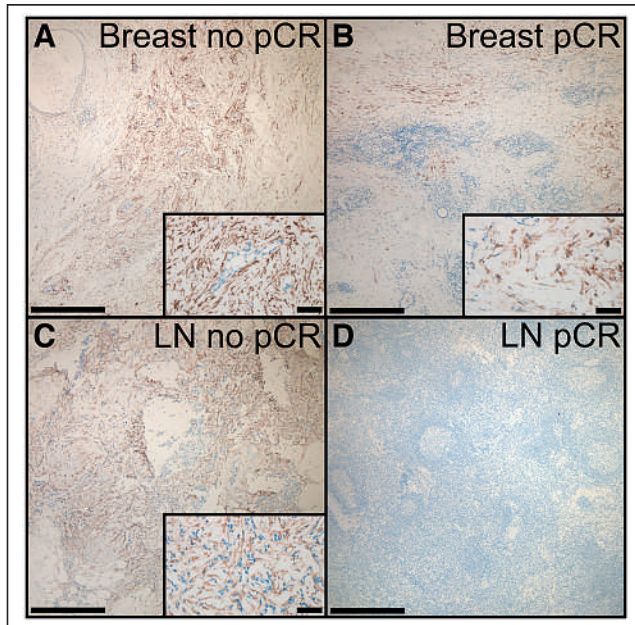


FIGURE 4. Example immunostainings of FAP in breast and LN tissue. (A) Breast no pCR classified as intensely positive (category C), showing clustering of FAP-positive fibroblasts, with area and amount exceeding small areas of remnant cancer cells. (B) Breast pCR with regressive changes and scattered FAP-positive fibroblasts (category B). (C) LN no pCR with remnant cancer cells and intermingled FAP-positive fibroblasts (category C). (D) LN pCR with absence of FAP immunoreactivity (category A). Bars indicate 500 μm for $\times 4$ magnification and 50 μm for $\times 40$ magnification in insets.

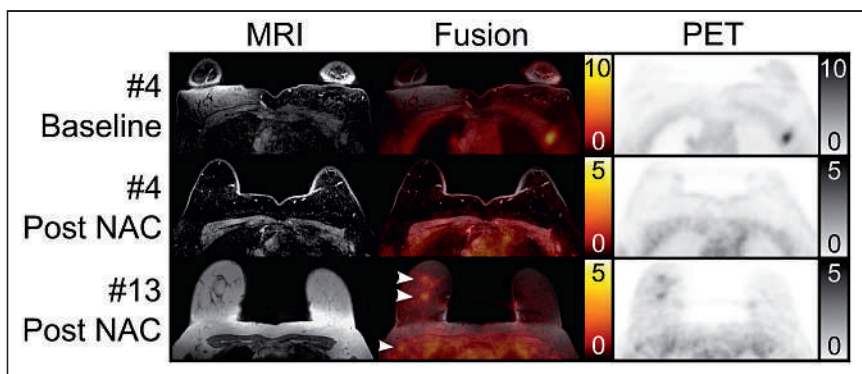


FIGURE 5. Examples of LN metastasis patients with prone transverse contrast-enhanced fat-saturated T1-weighted MRI scan (top and middle MRI rows), native T1-weighted MRI scan (bottom MRI row), fusion image, and ^{68}Ga -FAPI PET scan at baseline and at follow-up after NAC. In patient 4, follow-up showed that nodal remnant tracer uptake was not readily distinguishable from adjacent muscle. This was found to be remnant LN metastasis at pathology, classified as possible focal uptake on PET/MRI and as probable remnant metastasis on MRI. In patient 13, follow-up showed clear breast remnants on PET/MRI and MRI (top 2 arrowheads). PET/MRI, but not MRI, demonstrated clear abnormalities in right axillary nodes (bottom arrowhead), which were found to be remnant metastases at pathology.

correctly in at least 2 more patients than MRI alone. Metaanalyses showed that in the detection of breast cancer remnants after NAC, MRI had a sensitivity of 88%–92% and a specificity at 60%–69% (13–16). This makes MRI the most sensitive widely clinically available noninvasive imaging modality. ^{18}F -FDG/PET complements breast MRI not in terms of sensitivity (66%–77%) but in terms of specificity (78%–86%) (15–17). In the context of deescalation, FNs are far more important than FPs. The observed trend of FAPI-based assessment to improve sensitivity and specificity is thus particularly remarkable. This trend from our small study sample is substantiated by the observed higher interobserver agreement and correlation with semiquantitative measures of FAP uptake and immunohistochemistry. Furthermore, the observation of a higher number and area of FAP-positive fibroblasts than of vital remnant cancer cells in some specimens provides a strong rationale for our chosen molecular target. In comparison to the breast, for the LNs the conclusions on assessment of remission status are not as clear, considering the nonideal prone breast MRI protocol for axillary nodes with variable image quality and overall less intriguing diagnostic PET/MRI performance. However, it is important to consider that the combination of breast pCR without axillary pCR is rare and appeared in only 3.3% of initially node-positive patients in a review of approximately 20,000 U.S. patients (18).

In accordance with the most recent American Society of Clinical Oncology guidelines (1), we adopted a pCR definition of absence of invasive cancer, thus allowing remnant *in situ* cancer in pCR. This owes to the fact that the response rate of, for example, ductal carcinoma *in situ* (DCIS) (19,20) is much lower and that the predictive-ness of survival of residual DCIS is not given (21) after NAC in contrast to residual invasive cancer. Therefore, *in situ* cancer can be considered a confounder in NAC and associated deescalation concepts. Although our definition of pCR is probably most appropriate for chemotherapy deescalation, residual DCIS should not be missed in surgical deescalation. It is important to know that an immunohistochemistry study did not find FAP expression in DCIS, in contrast to invasive cancer (22). Consistently in our cohort, 2 PET- and MRI-negative women with known carcinoma *in situ* at baseline had noninvasive remnants despite pCR. Even patients with no DCIS at baseline can have isolated remnant DCIS after NAC, as was found,

for example, in approximately 12% of patients (19,20) in 2 studies. Thus, when considering FAPI PET/MRI for surgical deescalation in future trials, reliable exclusion of DCIS by breast imaging modalities, such as mammography, would probably be required.

Our study had limitations, the most important one being the low number of patients and its retrospective nature. The obtained diagnostic performance values thus must be considered as trends rather than a true approximation of diagnostic performance. Considering the overlap with our previous publication, our study features the same potential selection bias as discussed previously (10). We used ^{68}Ga -FAPI scanning only before and after completion of NAC, whereas the best accuracies in, for example, ^{18}F -FDG PET are achieved in interim response assessments during chemotherapy (17). Thus, more appropriate imaging time

points may exist for ^{68}Ga -FAPI scanning, particularly if considering its use for chemotherapy deescalation.

CONCLUSION

Integrated ^{68}Ga -FAPI PET/MRI shows highly promising trends toward gains in diagnostic performance over MRI alone to correctly classify response status in the breast and axilla in a small study sample. Future larger prospective studies are warranted to more closely approximate the true diagnostic performance and evaluate whether ^{68}Ga -FAPI PET/MRI ultimately possesses the potential to guide deescalation of chemotherapy or even surgery.

DISCLOSURE

This study was partly funded by the ninth Deutsche Forschungsgemeinschaft (DFG) NAMT, DFG-CRC1450-431460824, Münster, Germany (project B06), and a rotational clinician scientist position of the DFG-CRC1009, Münster, Germany, to Philipp Backhaus. No other potential conflict of interest relevant to this article was reported.

KEY POINTS

QUESTION: Can ^{68}Ga -FAPI PET/MRI classify response status after NAC in breast cancer?

PERTINENT FINDINGS: In a retrospective study of 13 women who completed NAC for breast cancer, follow-up ^{68}Ga -FAPI PET/MRI perfectly assessed the pathologic response status of the breast. MRI alone classified at least 2 women falsely.

IMPLICATIONS FOR PATIENT CARE: The diagnostic performance of ^{68}Ga -FAPI PET/MRI trended toward a gain over MRI alone, clearly supporting future prospective studies.

REFERENCES

- Korde LA, Somerfield MR, Carey LA, et al. Neoadjuvant chemotherapy, endocrine therapy, and targeted therapy for breast cancer: ASCO guideline. *J Clin Oncol*. 2021;39:1485–1505.

2. Riedel F, Hoffmann AS, Moderow M, et al. Time trends of neoadjuvant chemotherapy for early breast cancer. *Int J Cancer*. 2020;147:3049–3058.
3. Sacchini V, Norton L. Escalating de-escalation in breast cancer treatment. *Breast Cancer Res Treat*. 2022;195:85–90.
4. Heil J, Kuerer HM, Pfob A, et al. Eliminating the breast cancer surgery paradigm after neoadjuvant systemic therapy: current evidence and future challenges. *Ann Oncol*. 2020;31:61–71.
5. Slanetz PJ, Moy L, Baron P, et al. ACR Appropriateness Criteria® monitoring response to neoadjuvant systemic therapy for breast cancer. *J Am Coll Radiol*. 2017;14:S462–S475.
6. Nakashima K, Uematsu T, Harada TL, et al. Can breast MRI and adjunctive Doppler ultrasound improve the accuracy of predicting pathological complete response after neoadjuvant chemotherapy? *Breast Cancer*. 2021;28:1120–1130.
7. Sutton EJ, Braunstein LZ, El-Tamer MB, et al. Accuracy of magnetic resonance imaging-guided biopsy to verify breast cancer pathologic complete response after neoadjuvant chemotherapy. *JAMA Netw Open*. 2021;4:e2034045.
8. Choi JH, Kim H-A, Kim W, et al. Early prediction of neoadjuvant chemotherapy response for advanced breast cancer using PET/MRI image deep learning. *Sci Rep*. 2020;10:21149.
9. Cho N, Im S-A, Cheon GJ, et al. Integrated ¹⁸F-FDG PET/MRI in breast cancer: early prediction of response to neoadjuvant chemotherapy. *Eur J Nucl Med Mol Imaging*. 2018;45:328–339.
10. Backhaus P, Burg MC, Roll W, et al. Simultaneous FAPI PET/MRI targeting the fibroblast-activation protein for breast cancer. *Radiology*. 2022;302:39–47.
11. Elboga U, Sahin E, Kus T, et al. Superiority of ⁶⁸Ga-FAPI PET/CT scan in detecting additional lesions compared to ¹⁸F-FDG PET/CT scan in breast cancer. *Ann Nucl Med*. 2021;35:1321–1331.
12. Kömek H, Can C, Güzel Y, et al. ⁶⁸Ga-FAPI-04 PET/CT, a new step in breast cancer imaging: a comparative pilot study with the ¹⁸F-FDG PET/CT. *Ann Nucl Med*. 2021;35:744–752.
13. Marinovich ML, Houssami N, Macaskill P, et al. Meta-analysis of magnetic resonance imaging in detecting residual breast cancer after neoadjuvant therapy. *J Natl Cancer Inst*. 2013;105:321–333.
14. Yuan Y, Chen X-S, Liu S-Y, Shen K-W. Accuracy of MRI in prediction of pathologic complete remission in breast cancer after preoperative therapy: a meta-analysis. *AJR*. 2010;195:260–268.
15. Liu Q, Wang C, Li P, Liu J, Huang G, Song S. The role of ¹⁸F-FDG PET/CT and MRI in assessing pathological complete response to neoadjuvant chemotherapy in patients with breast cancer: a systematic review and meta-analysis. *BioMed Res Int*. 2016;2016:1–10.
16. Li H, Yao L, Jin P, et al. MRI and PET/CT for evaluation of the pathological response to neoadjuvant chemotherapy in breast cancer: a systematic review and meta-analysis. *Breast*. 2018;40:106–115.
17. Wang Y, Zhang C, Liu J, Huang G. Is ¹⁸F-FDG PET accurate to predict neoadjuvant therapy response in breast cancer? A meta-analysis. *Breast Cancer Res Treat*. 2012;131:357–369.
18. Fayajju OM, Ren Y, Thomas SM, et al. The clinical significance of breast-only and node-only pathologic complete response (pCR) after neoadjuvant chemotherapy (NACT). *Ann Surg*. 2018;268:591–601.
19. Groen EJ, van der Noordaa MEM, Schaapveld M, et al. Pathologic response of ductal carcinoma in situ to neoadjuvant systemic treatment in HER2-positive breast cancer. *Breast Cancer Res Treat*. 2021;189:213–224.
20. von Minckwitz G, Darb-Esfahani S, Loibl S, et al. Responsiveness of adjacent ductal carcinoma in situ and changes in HER2 status after neoadjuvant chemotherapy/trastuzumab treatment in early breast cancer: results from the Gepar-Quattro study (GBG 40). *Breast Cancer Res Treat*. 2012;132:863–870.
21. Mazouni C, Peintinger F, Wan-Kau S, et al. Residual ductal carcinoma in situ in patients with complete eradication of invasive breast cancer after neoadjuvant chemotherapy does not adversely affect patient outcome. *J Clin Oncol*. 2007;25:2650–2655.
22. Huo X, Yu L, Huang X, Liao Z, Xian Q. Expression and role of fibroblast activation protein-alpha in microinvasive breast carcinoma. *Diagn Pathol*. 2011;6:111.

Noninvasive Assessment of Human Epidermal Growth Factor Receptor 2 (HER2) in Esophagogastric Cancer Using ⁸⁹Zr-Trastuzumab PET: A Pilot Study

Melissa A. Lumish^{1,2}, Steven B. Maron^{1,2}, Viktoriya Paroder³, Joanne F. Chou⁴, Marinela Capanu⁴, Steven Philemond³, Joseph A. O'Donoghue⁵, Heiko Schöder⁶, Jason S. Lewis^{3,7,8}, Serge K. Lyashchenko^{7,8}, Neeta Pandit-Taskar^{*3,6,9}, and Yelena Y. Janjigian^{*1,2}

¹Department of Medicine, Memorial Sloan Kettering Cancer Center, New York, New York; ²Department of Medicine, Weill Cornell Medical College, New York, New York; ³Department of Radiology, Memorial Sloan Kettering Cancer Center, New York, New York;

⁴Department of Epidemiology and Biostatistics, Memorial Sloan Kettering Cancer Center, New York, New York; ⁵Department of Medical Physics, Memorial Sloan Kettering Cancer Center, New York, New York; ⁶Molecular Imaging and Therapy Service, Memorial Sloan Kettering Cancer Center, New York, New York; ⁷Molecular Pharmacology Program, Memorial Sloan Kettering Cancer Center, New York, New York; ⁸Radiochemistry and Molecular Imaging Probes Core, Memorial Sloan Kettering Cancer Center, New York, New York and ⁹Department of Radiology, Weill Cornell Medical College, New York, New York

Variations in human epidermal growth factor receptor 2 (HER2) expression between the primary tumor and metastases may contribute to drug resistance in HER2-positive (HER2+) metastatic esophagogastric cancer (mEGC). ⁸⁹Zr-trastuzumab PET (HER2 PET) holds promise for noninvasive assessment of variations in HER2 expression and target engagement. The aim of this study was to describe HER2 PET findings in patients with mEGC. **Methods:** Patients with HER2+ mEGC were imaged with HER2 PET, ¹⁸F-FDG PET, and CT. Lesions were annotated using measurements (on CT) and maximum SUVs (on HER2 PET). Correlation of visualized disease burden among imaging modalities with clinical and pathologic characteristics was performed. **Results:** Thirty-three patients with HER2+ mEGC were imaged with HER2 PET and CT (12% esophageal, 64% gastroesophageal junction, and 24% gastric adenocarcinoma), 26 of whom were also imaged with ¹⁸F-FDG PET. More lesions were identified on ¹⁸F-FDG PET (median, 7 [range, 1–14]) than HER2 PET (median, 4 [range, 0–11]). Of the 8 lesions identified on HER2 but not on ¹⁸F-FDG PET, 3 (38%) were in bone and 1 was in the brain. Of the 68 lesions identified on ¹⁸F-FDG but not on HER2 PET, 4 (6%) were in bone and the remainder were in the lymph nodes (35, 51%) and liver (16, 24%). Of the 33 total patients, 23 (70%) were HER2 imaging-positive ($\geq 50\%$ of tumor load positive). Only 10 patients had 100% of the tumor load positive; 2 had 0% positive. When only patients receiving HER2-directed therapy as first-line treatment were considered ($n = 13$), median progression-free survival (PFS) therapy was not significantly different between HER2 imaging-positive and -negative patients. Median PFS for patients with at least 1 intense or very intense lesion ($SUV \geq 10$) was 16 (95% CI: 11–not reached) mo ($n = 7$), compared with 12 (95% CI: 6.3–not reached) mo for patients without an intense or very intense lesion ($n = 6$) ($P = 0.35$). **Conclusion:** HER2 PET may identify heterogeneity of HER2 expression and allow assessment of lesions throughout the entire body. A potential application of HER2 PET is noninvasive evaluation of HER2 status including assessment of intrapatient disease heterogeneity not captured by standard imaging or single-site biopsies.

Key Words: HER2 heterogeneity; esophageal adenocarcinoma; gastric adenocarcinoma; trastuzumab; HER2 PET

J Nucl Med 2023; 64:724–730

DOI: 10.2967/jnumed.122.264470

Esophagogastric cancer (EGC) is the third most common cause of cancer-related death worldwide, and 20%–30% of patients with metastatic EGC (mEGC) have human epidermal growth factor receptor 2 (HER2)-positive disease (1–4). On the basis of data from 2 trials—the phase III randomized controlled ToGA (5), which demonstrated improved response rate and survival when trastuzumab was added to chemotherapy, and the phase III Keynote-811 (6,7), which demonstrated a better response rate and survival when trastuzumab was added to chemotherapy in combination with PD-1 blockade—HER2 is a validated treatment target in mEGC. Although HER2 immunohistochemistry, HER2-to-CEP17 ratio, and ERBB2 gene copy number can be used to predict response to trastuzumab-based chemotherapy (8), many patients with HER2-positive (HER2+) EGC develop resistance to HER2-directed therapies (3). Heterogeneity of HER2 expression between the primary tumor and metastases and loss of HER2 expression during trastuzumab therapy contribute to therapeutic resistance in HER2+ mEGC (9). Whole-body imaging with ⁸⁹Zr-trastuzumab PET (HER2 PET) has a potential advantage over single-site biopsy as it can noninvasively assess variations in HER2 expression and target engagement.

We previously published the pharmacokinetics, biodistribution, and dosimetry of ⁸⁹Zr-trastuzumab in HER2+ mEGC (10). HER2 PET images showed optimal tumor visualization 5–8 d after injection, and no clinically significant toxicities were observed. Here, we expand the cohort from 10 to 33 patients to further evaluate the baseline biodistribution of ⁸⁹Zr-trastuzumab and the association between imaging results and response to treatment. The distribution of ⁸⁹Zr-trastuzumab uptake, compared with standard imaging with ¹⁸F-FDG PET and CT, in HER2+ mEGC and the ability of this metric to predict response to HER2-directed therapy have not been described.

Received Jun. 16, 2022; revision accepted Nov. 8, 2022.

For correspondence or reprints, contact Melissa A. Lumish (lumishm@mskcc.org) and Neeta Pandit-Taskar (pandit-n@mskcc.org).

*Contributed equally to this work.

Published online Nov. 23, 2022.

COPYRIGHT © 2023 by the Society of Nuclear Medicine and Molecular Imaging.

We sought to investigate HER2 PET as a noninvasive tool to evaluate disease heterogeneity and predict response to treatment. We hypothesized that the intensity of ^{89}Zr -trastuzumab uptake, as measured by maximum SUV, and HER2 imaging positivity ($\geq 50\%$ of active lesions with ^{89}Zr -trastuzumab uptake) would be associated with response to HER2-directed therapy.

MATERIALS AND METHODS

Patients and Study Design

Eligible patients had HER2+ (immunohistochemistry 3+, immunohistochemistry 2+ and fluorescence in situ hybridization [FISH] > 2.0) mEGC, measurable or evaluable disease, Karnofsky performance $\geq 60\%$, and adequate organ function. This was a single-site, prospective open-label pilot imaging protocol approved by the institutional review board and ethics committee at Memorial Sloan Kettering Cancer Center (ClinicalTrials.gov identifier NCT02023996). The study included 2 groups of patients who were imaged with HER2 PET, ^{18}F -FDG PET, and CT. The purpose of imaging in the first group of patients (group 1) was to find the optimal time for imaging after injection of the radiotracer and define its pharmacokinetics. Patients in group 2 underwent imaging to increase the study sample size and accomplish the secondary objectives of the study including correlation with tumor molecular analysis and response to treatment, reported here. All patients gave informed consent for participation in the study. All visualized lesions (maximum 5/organ) were annotated in detail using individual-lesion measurements on CT and SUV on HER2 and ^{18}F -FDG PET by Memorial Sloan Kettering radiologists. Clinical characteristics, including baseline demographic data and previous treatments, were manually extracted from the medical record and managed using REDCap electronic data capture tools (11,12). Visualized disease burden on each imaging modality and pathologic tumor characteristics were annotated for each patient.

^{89}Zr -Trastuzumab Drug Product

The details of the drug product, imaging protocol, and biodistribution have been published previously (10). The ^{89}Zr -trastuzumab was manufactured by the Memorial Sloan Kettering Radiochemistry and Molecular Imaging Probes Core Facility in compliance with a Food and Drug Administration investigational new drug application. Clinical-grade trastuzumab (Herceptin; Genentech) was conjugated with p-SCN-Bn-deferoxamine (Macrocyclics) chelator, followed by radiolabeling with ^{89}Zr , a positron emitter with a 78.4-h half-life. Patient unit doses of 185 MBq/3 mg of ^{89}Zr -trastuzumab were mixed with nonradiolabeled trastuzumab to achieve a total mass of 50 mg.

Imaging

Each patient underwent whole-body PET/CT from mid skull to proximal thigh in 3-dimensional mode with attenuation, scatter, and other standard corrections applied and using iterative reconstruction. PET images were acquired 5 d after injection, based on the optimal imaging time of 5–8 d defined previously (10). Patients receiving therapies directed at HER2 were offered repeat imaging 2- to 6-wk after treatment, at the discretion of the treating physician and the study primary investigator, to evaluate changes in tumor uptake.

Patients underwent CT imaging of the chest, abdomen, and pelvis at a median of 7 d from the date of HER2 PET (range, 1–43 d). Localization in the tumor was defined as focal accumulation greater than adjacent background in areas in which physiologic activity was not expected. SUVs normalized to lean body mass were determined. We subclassified each lesion as negative (SUV < 3), low positive (SUV 3–5), moderate (SUV 5–10), intense (SUV 10–15), or very intense (SUV > 15).

Definition of HER2 Imaging Positivity

Any lesion that was identified by one of the above imaging methods and was clinically determined to represent a tumor was categorized as an active lesion. A patient with a HER2+ tumor was considered to be HER2 imaging-positive if $\geq 50\%$ of the active lesions were detectable by HER2 PET. The total number of active lesions identified on CT, ^{18}F -FDG PET, or HER2 PET was used as the denominator for the tumor load. To determine HER2 imaging positivity, we divided the total number of lesions identified on HER2 PET by the tumor load.

Definition of HER2 Heterogeneity

Heterogeneity of HER2 status on biopsy was defined on the basis of variation in HER2 overexpression in multiple disease sites biopsied (median 3 samples per patient; range, 1–8). For example, a case with 1 lesion that was HER2 immunohistochemistry 3+ or 2+ and amplified by FISH and a second lesion that was either negative (immunohistochemistry 1+ or 0+) or equivocal by FISH would be classified as having heterogeneous disease. Genomic assessment of ERBB2 amplification was not used to establish heterogeneity, as not all patients underwent somatic mutation analysis. Heterogeneity of HER2 expression by HER2 PET was defined in the protocol, on the basis of previously published data (13), by the percentage of tumor load that showed tracer uptake. Group stratification was as follows: group A, the entire tumor load showed tracer uptake (100%); group B, the dominant part of the tumor load showed tracer uptake ($\geq 50\%$); group C, only a minor part of the tumor load showed tracer uptake ($< 50\%$); and group D, the entire tumor load lacked tracer uptake (0%). Groups B and C were considered to have heterogeneous uptake ($> 0\%$ and $< 100\%$ of tumor load positive).

Statistical Analysis

The primary objectives of the protocol were to evaluate the feasibility of detecting tumors using HER2 PET in the first 10 patients with HER2+ EGC and to evaluate the safety, biodistribution, and pharmacokinetics of ^{89}Zr -trastuzumab, all of which were reported previously (10). HER2 PET imaging was considered feasible on the basis of antibody imaging positivity in 7 or more of the 10 patients in the first cohort. Secondary objectives, reported here, were to describe tumor molecular analysis with imaging results and to evaluate imaging results in the context of response to treatment. HER2 imaging positivity was estimated on the basis of the 33 patients with the 1-sided 90% confidence limit. Patients with $\geq 50\%$ of the total tumor load with ^{89}Zr -trastuzumab uptake were considered HER2 imaging-positive, and patients with $< 50\%$ were considered HER2 imaging-negative.

Overall survival (OS) and progression-free survival (PFS) were calculated from the date of treatment until time of death (for OS) or until the date of progression or death, whichever came first (for PFS). Patients who did not experience the event of interest by the end of the study were censored at the time of last available follow-up (for OS) or last available CT (for PFS). Because the study population was heterogeneous and included both patients receiving first-line treatment for metastatic disease and those receiving treatment for refractory disease, we restricted the OS and PFS analyses to the homogenous group of patients who were receiving first-line therapy at the time of the HER2 PET ($n = 13$). OS and PFS were estimated using Kaplan–Meier methods and compared between subgroups (A/B vs. C/D; SUV intensity) using the permuted log-rank test. All P values were based on 2-tailed statistical analysis, and a P value of less than 0.05 was considered to indicate statistical significance. All analyses were conducted in R version 4.0.4 (R Development Core Team, 2022) (14).

RESULTS

Summary of Patients

Thirty-three patients with metastatic HER2+ gastric (24%), gastroesophageal junction (GEJ) (64%), or esophageal (12%)

TABLE 1
Patient and Treatment Characteristics

Characteristic	Prior trastuzumab (n = 19)	No prior trastuzumab (n = 14)	Total (n = 33)
Median age at diagnosis (y)	59 (range, 40–76)	59 (range, 34–79)	59 (range, 34–79)
Patients with metastasis at diagnosis (n)	17 (89)	10 (71)	27 (82)
Primary tumor site (n)			
Esophageal	2 (11)	2 (14)	4 (12)
GEJ (Siewert I-II)	14 (74)	7 (50)	21 (64)
Gastric	3 (16)	5 (36)	8 (24)
Method used to confirm sample is HER2+ (n)			
FISH	3 (16)	3 (21)	6 (18)
IHC	15 (79)	11 (79)	26 (79)
NGS	1 (5)	0 (0)	1 (3)
Patients with HER2 heterogeneity across samples (n)	3 (16)	6 (43)	9 (27)
Patients receiving HER2-directed therapy at the time of scan (n)	16 (84)	14 (100)	30 (91)
Median no. of lines of treatment at the time of HER2 PET	3 (range, 2–6)	1 (range, 1–2)	2 (range, 1–6)
Median total lines of treatment received	3 (range, 2–7)	3 (range, 1–9)	3 (range, 1–9)
Median time on treatment at the time of HER2 PET (d)	93 (range, 0–212)	394 (range, 7–1,410)	126 (range, 0–1,410)
Total lesions detected on imaging (all patients)			
Median, CT	5 (range, 1–11)	5.5 (range, 1–15)	5 (range, 1–15)
Median, HER2	4 (range, 1–7)	3.5 (range, 0–11)	4 (range, 0–11)
Median, ¹⁸ F-FDG PET	6.5 (range, 1–13)	7 (range, 1–14)	7 (range, 1–14)
Patients with ≥ 1 lesion intense or very intense on HER2 PET (n)	8 (42)	7 (50)	15 (45)
Median SUV _{max} per patient on HER2 PET	7.8 (range, 3.20–23.8)	9.8 (range, 0–22.2)	9.2 (range, 0–23.8)
Median SUV _{mean} per lesion on HER2 PET	6.5 (range, 2.8–14.2)	7.8 (range, 0–15.9)	7.0 (range, 0–15.9)

Data are number, with percentages in parentheses, or median, with the minimum to maximum in parentheses.

IHC = immunohistochemistry; NGS = next-generation sequencing.

adenocarcinoma were imaged with HER2 PET and CT, and 26 of these patients were also imaged with ¹⁸F-FDG PET (Table 1). HER2 status was assessed using biopsy or resection specimens of the primary tumor (21/33, 64%) or metastasis (12/33, 36%) and was confirmed by immunohistochemistry 3+ (26/33, 79%), immunohistochemistry 2+ and amplification by FISH (6/33, 18%), or ERBB2 amplification by next-generation sequencing with MSK-IMPACT (Memorial Sloan Kettering-Integrated Mutation Profiling of Actionable Cancer Targets) (1/33, 3%) (15). All patients had metastatic disease at the time of enrollment; most patients had metastases to the lymph nodes (23/33, 70%) or liver (19/33, 58%), followed by lung (11/33, 33%), peritoneum (8/33, 24%), bone (3/33, 9%), or other tissues. Most patients underwent prior treatment with HER2-directed therapy (20/33, 61%, had received at least 1 line of HER2-directed therapy); the median time from diagnosis to HER2 PET was 13 mo. The median number of lines of therapy received at the time of HER2 PET was 2 (range, 1–6), and the median number of total lines of therapy received throughout the course of illness was 3 (range, 1–9). Thirty patients (91%) were receiving HER2-directed therapy, and 13 (39%) were receiving

first-line HER2-directed therapy at the time of HER2 PET (Supplemental Table 1; supplemental materials are available at <http://jnm.snmjournals.org>). Among patients receiving HER2-directed therapy at the time of HER2 PET, the median time on treatment was 4 mo (range, 0–47 mo) for all patients and 14 mo (range, 4–47 mo) for those receiving first-line therapy (Supplemental Table 2).

The total number of lesions identified on each imaging modality is summarized in Table 1. The median number of lesions identified by each modality is as follows: baseline CT, 5 (range, 1–15); HER2 PET, 4 (range, 0–11); and ¹⁸F-FDG PET, 7 (range, 1–14) (Supplemental Table 3).

⁸⁹Zr-Trastuzumab PET Captures Nonstandard Disease Sites

The potential clinical applications of HER2 PET imaging include identification of disease sites not captured by standard imaging, establishment of sites of HER2 heterogeneity not captured by biopsy, and early assessment of response to HER2-directed therapy. We included specific case examples to illustrate these points. The first is a case of metastatic HER2+ GEJ poorly differentiated carcinoma in which HER2 PET identified a right cerebellar metastasis (SUV 2.6) that had not been detected on ¹⁸F-FDG PET (Fig. 1A).

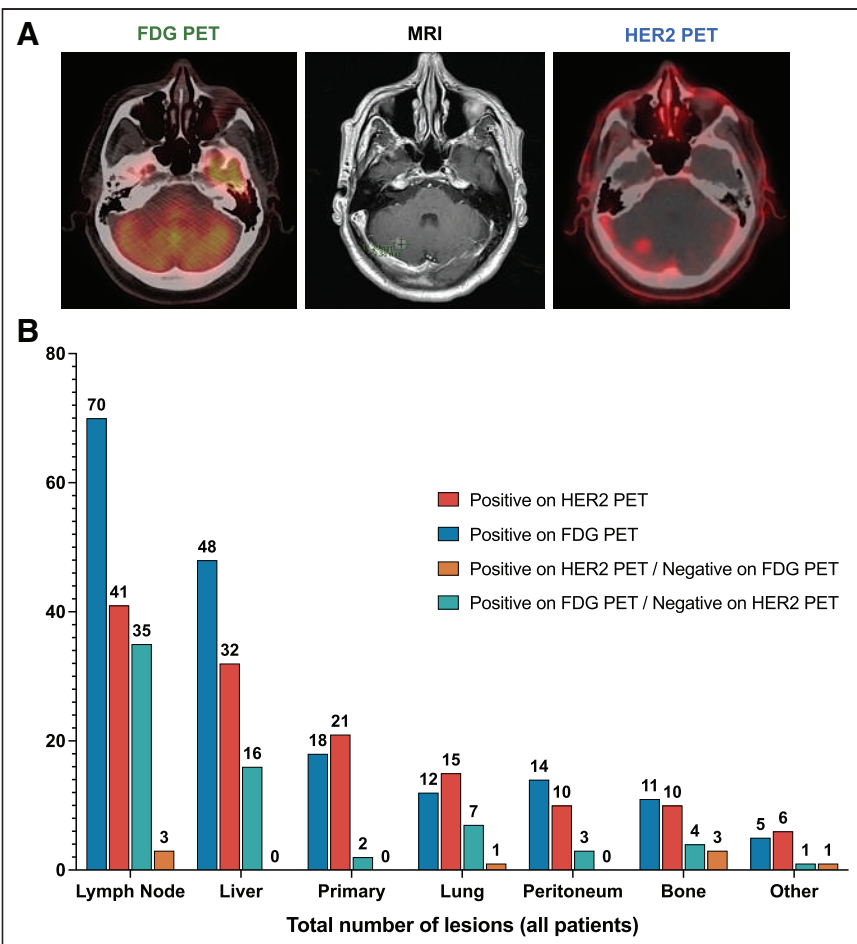


FIGURE 1. Disease sites captured by HER2 and ^{18}F -FDG PET. (A) ^{18}F -FDG PET, MRI, and HER2 PET images from a patient with cerebellar metastasis. The images shown are from a patient with de novo metastatic HER2+ GEJ poorly differentiated carcinoma with mixed adeno and squamous differentiation. HER2 PET (right) demonstrated a right cerebellar metastasis (SUV 2.6) without corresponding uptake on ^{18}F -FDG PET (left) and confirmed on brain MRI (middle). (B) Number of lesions identified by HER2 PET and ^{18}F -FDG PET among all patients. Total number of lesions avid on HER2 PET (red) and ^{18}F -FDG PET (blue) is shown. Total numbers of lesions better identified only on HER2 (orange) or ^{18}F -FDG PET (green) are also shown.

The finding was confirmed on brain MRI, and the patient underwent stereotactic radiosurgery to treat this lesion.

Among all patients, more total lesions were visualized on ^{18}F -FDG PET ($n = 178$) than on HER2 PET ($n = 135$) (Fig. 1B). Of the total lesions positive on HER2 PET, most were in lymph nodes (41/135 [30%]) or the liver (32/135 [24%]). For ^{18}F -FDG PET, most were also in lymph nodes (70/178 [39%]) or the liver (48/178 [27%]). However, primary tumor and bone lesions were detected at a higher frequency on HER2 PET (primary tumor: 21/135 [16%]; bone: 10/135 [7%]) than on ^{18}F -FDG PET (primary tumor: 18/178 [10%]; bone: 11/178 [6%]).

Five patients had at least 1 lesion positive on HER2 PET and negative on ^{18}F -FDG PET (range, 0–4); 18 patients had at least 1 lesion positive on ^{18}F -FDG PET and negative on HER2 PET (range, 0–8). Of the 8 lesions that were positive on HER2 PET and negative on ^{18}F -FDG PET, 3 were in the bone (38%) and 3 were in lymph nodes (38%) (Fig. 1B). In contrast, most lesions that were positive on ^{18}F -FDG PET and negative on HER2 PET were in the lymph nodes (35/68 [51%]) and the liver (16/68 [24%]); only 4 of 68 (6%) were in the bone.

HER2 PET Illustrates HER2 Heterogeneity

The next case example illustrates heterogeneous liver uptake of the radiotracer on HER2 PET, suggesting that HER2 overexpression is heterogeneous (Fig. 2A). However, liver biopsy for this patient, obtained from a single site of ^{89}Zr -trastuzumab avidity, showed HER2 immunohistochemistry 3+ and, as expected, did not capture the intrapatient heterogeneity seen on imaging.

As defined in our prespecified analysis, patients with $\geq 50\%$ of the total tumor load with ^{89}Zr -trastuzumab uptake were considered HER2 imaging-positive, and patients with $< 50\%$ were considered HER2 imaging-negative. As described in the “Materials and Methods” section, we stratified patients into 4 groups by percentage of tumor load that showed tracer uptake (13). Of the 33 patients, 23 (70%) were HER2 imaging-positive (group A or B) (1-sided 90% confidence limit, 57% for feasibility) (Fig. 2B). Only 10 patients had 100% of the tumor load positive; 2 had 0% positive. Of the 30 patients who were receiving HER2-directed therapy at the time of the scan, 20 (66%) had $\geq 50\%$ active lesions (group A or B). Of the 13 patients who were receiving first-line HER2-directed therapy at the time of the scan, 8 (62% of the group, 24% of the total cohort) had $\geq 50\%$ active lesions (group A or B). Although all the patients without any tracer uptake (6% of the cohort) were receiving second-line or later treatment, most patients receiving advanced lines of therapy were HER2 imaging-positive, supporting the notion that HER2 remains a relevant biomarker beyond the first-line setting.

We next describe the proportion of patients in group A or B and group C or D

with at least 1 intense or very intense lesion on HER2 PET. Among those with $\geq 50\%$ of tumor load positive (group A or B), 57% of patients had at least 1 intense or very intense lesion, whereas only 20% in those with $< 50\%$ of tumor load positive (group C or D) had at least 1 intense or very intense lesion. Biopsy-proven HER2 heterogeneity was present in 30% of patients in group A or B and in 20% of patients in group C or D. A slightly higher proportion of patients in group A or B (61%) had received trastuzumab therapy at the time of the scan, relative to those in group C or D (50%).

In addition to looking at individual-lesion positivity by HER2 PET, we subclassified each lesion as negative (SUV < 3), low positive (SUV 3–5), moderate (SUV 5–10), intense (SUV 10–15), or very intense (SUV > 15). In the case example shown in Figure 2A in which all biopsies were HER2 immunohistochemistry 3+, the tumor load positivity for ^{89}Zr -trastuzumab uptake was $< 50\%$ (group C). Although the patient had at least 1 intense or very intense lesion, the patient’s PFS on second-line HER2-directed therapy (3 mo) was less than the median among all patients with at least 1 intense or very intense lesion (5 mo).

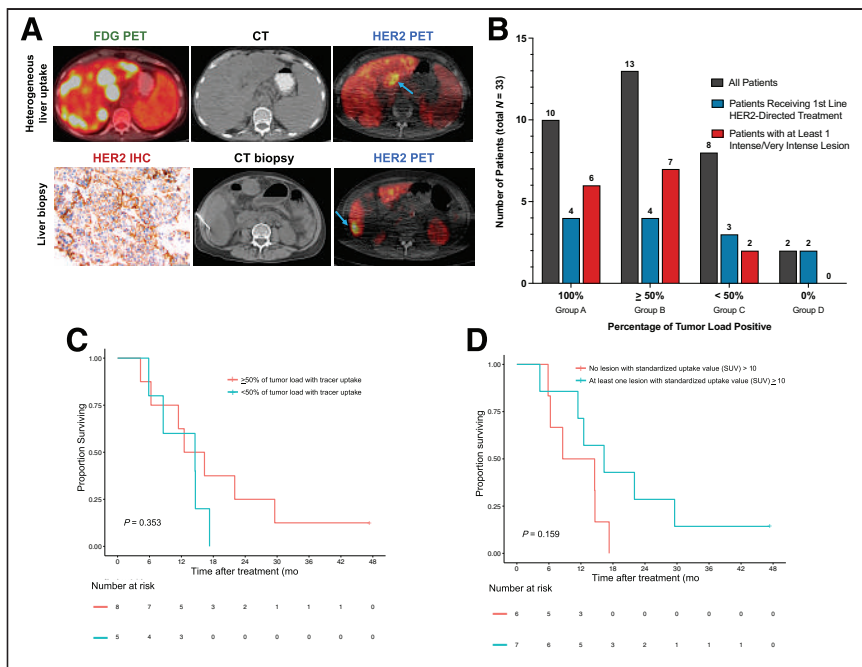


FIGURE 2. HER2 disease heterogeneity illustrated by ^{89}Zr -trastuzumab PET (HER2 PET). (A) ^{18}F -FDG PET and HER2 PET images from a patient with metastatic HER2+ gastric adenocarcinoma with heterogeneous HER2 expression in the liver. Heterogeneous ^{89}Zr -trastuzumab uptake on imaging is shown (blue arrows demonstrate positive lesions, upper figure). Liver biopsy at a site of ^{89}Zr -trastuzumab uptake demonstrates HER2 positivity with immunohistochemistry 3+ in 60% of cells (lower). (B) The percentage of tumor load with ^{89}Zr -trastuzumab uptake. Patients were stratified into 4 groups by percentage of tumor load showing tracer uptake. Total patients in groups A–D are shown in gray. Number of patients receiving first-line HER2-directed therapy in each group is represented in blue. Patients with at least 1 intense or very intense lesion on HER2 PET ($\text{SUV} \geq 10$) are represented in red. Of the 15 patients with at least 1 intense or very intense lesion (15/33 [45%]), 6 were in group A (6/33 [18%]) and 7 were in group B (7/33 [21%]). (C) PFS stratified by percentage of tumor load positive in patients receiving first-line HER2-directed therapy ($P = 0.353$, using permuted log-rank test comparing the 2 groups). (D) PFS stratified by presence of at least 1 lesion with intense or very intense ^{89}Zr -trastuzumab uptake ($\text{SUV} \geq 10$) in patients receiving first-line HER2-directed therapy ($P = 0.159$, using permuted log-rank test comparing the 2 groups). IHC = immunohistochemistry.

Survival of Patients Receiving First-Line Treatment at the Time of the Scan

Survival was evaluated only among patients receiving first-line HER2-directed therapy at the time of the HER2 PET ($n = 13$). The baseline characteristics of this group are summarized in Supplemental Table 4. Among surviving patients ($n = 2$), the median follow-up time was 50.0 mo (range, 45.8–54.3 mo). At the time of the data lock in July 2021, 11 total deaths and 12 progression events had been observed. When only patients receiving HER2-directed therapy in the first-line setting were considered, the median PFS was 15 mo (95% CI: 8.6–not reached).

The median PFS among patients in group A or B ($n = 8$) was 14 mo (95% CI: 11.0–not reached), compared with 15 mo (95% CI: 8.6–not reached) among patients in group C or D ($n = 5$) (Fig. 2C). Among patients receiving HER2-directed therapy in the second-line setting, most patients in both groups (A/B $n = 7$, C/D $n = 2$) progressed or died before 3 mo. Given the small number of patients in this subgroup, PFS should be interpreted with caution.

HER2 PET and Response to HER2-Directed Therapy

We next stratified patients by the presence or absence of at least 1 intense or very intense lesion on baseline HER2 PET and

compared PFS among patients receiving first-line HER2-directed therapy at the time of the scan ($n = 13$). The median PFS was 16 mo (95% CI: 11–not reached) and 12 mo (95% CI: 6.3–not reached), respectively (Fig. 2D). Given the small number of patients in this subgroup, PFS should be interpreted with caution.

The final 2 case examples (Fig. 3) illustrate the potential role of HER2 PET in predicting response to HER2-directed therapy. In Figure 3A, a patient with HER2+ mEGC had $\geq 50\%$ tumor load uptake of ^{89}Zr -trastuzumab on baseline imaging (group B) and at least 1 intense or very intense lesion. Both HER2 and ^{18}F -FDG PET showed primary tumor avidity; less than 3 wk after initiation of trastuzumab-based treatment, the primary tumor remained ^{18}F -FDG PET–avid but was no longer avid on HER2 PET, indicating HER2 receptor saturation by trastuzumab. This patient had a PFS of 13 mo on first-line HER2-directed therapy, and the disease remained HER2+ on postprogression biopsy, with subsequent response to second-line HER2-directed therapy. In contrast, the patient in Figure 3B, who had $\geq 50\%$ tumor load uptake of ^{89}Zr -trastuzumab on baseline imaging (group B) but no intense or very intense lesions, had no change in primary tumor ^{89}Zr -trastuzumab uptake after initiation of first-line HER2-directed treatment and had a relatively short PFS of 6 mo on treatment.

Patients Not Receiving HER2-Directed Therapy

Of the 3 patients who were not receiving HER2-directed therapy at the time of the scan, 1 underwent repeat liver biopsy that demonstrated equivocal HER2 status by both immunohistochemistry and FISH (the initial specimen, obtained at an outside institution, was HER2 immunohistochemistry 3+). The second patient recently had disease progression on HER2-directed therapy, and biopsy of a splenic lesion demonstrated HER2 immunohistochemistry 1–2+ and nonamplification on FISH. The third patient underwent repeat biopsy of the primary GEJ mass, which showed HER2 immunohistochemistry 1+ (negative); therefore, this patient did not receive additional HER2-directed therapy.

DISCUSSION

Our data suggest that antibody imaging with HER2 PET is feasible and allows noninvasive assessment of global variations in HER2 expression and target enhancement. HER2 PET identified bone lesions more so than soft-tissue lesions. Compared with HER2 PET, ^{18}F -FDG PET identified more lymph node lesions and it is unclear whether these findings represent true disease or inflammation.

HER2 PET may help visualize heterogeneity of HER2 expression and allow assessment of lesions throughout the entire body. The percentage of tumor load positive for ^{89}Zr -trastuzumab varied

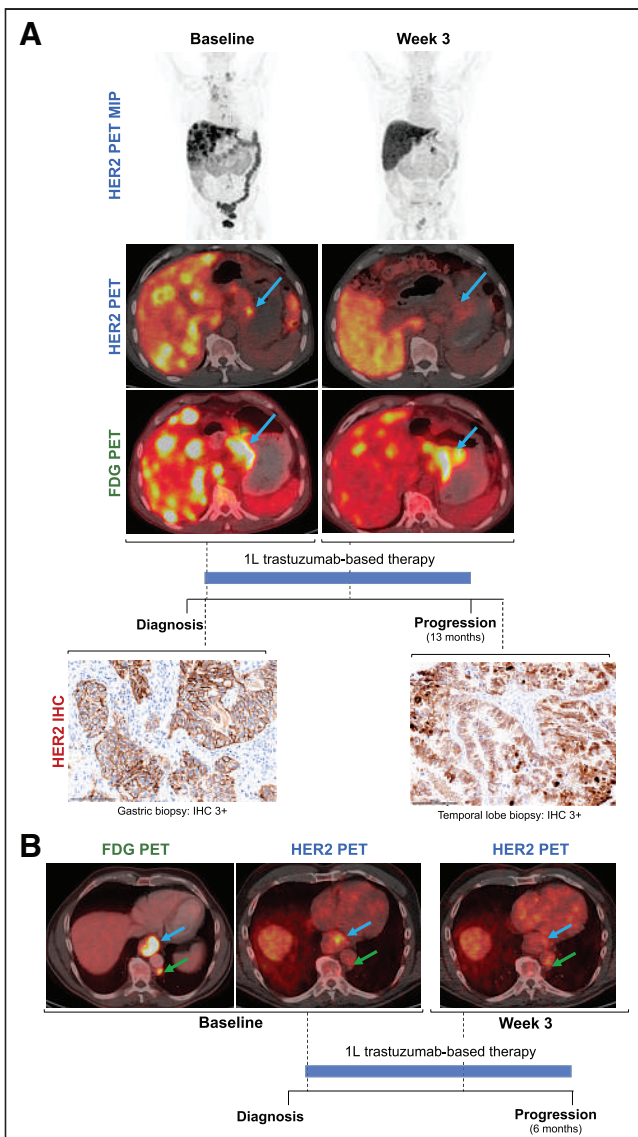


FIGURE 3. ^{89}Zr -trastuzumab PET (HER2 PET) and early assessment of response to HER2-directed therapy. (A) ^{18}F -FDG PET, HER2 PET, and HER2 immunohistochemistry (IHC) in a patient with metastatic HER2+ esophagogastric cancer with a long response to first-line HER2-directed therapy. Patient had > 50% of tumor load with ^{89}Zr -trastuzumab uptake on baseline imaging (group B) and at least 1 lesion with SUV ≥ 10 . Although primary tumor was avid on baseline HER2 and ^{18}F -FDG PET, less than 3 wk after initiation of trastuzumab-based treatment, primary tumor remained ^{18}F -FDG PET avid but was no longer avid on HER2 PET, likely indicating HER2 saturation by trastuzumab. This patient had a PFS of 13 mo on first-line HER2-directed therapy. (B) ^{18}F -FDG PET and HER2 PET in a patient metastatic HER2+ esophageal adenocarcinoma with a short response to first-line HER2-directed therapy. Patient had > 50% of the tumor load with ^{89}Zr -trastuzumab uptake on baseline imaging (group B) but no lesions with SUV ≥ 10 ; patient had no change in primary tumor ^{89}Zr -trastuzumab uptake (SUV 8.1 from 6.6, blue arrows) or in posterior left paraaortic node ^{89}Zr -trastuzumab uptake (green arrows) after initiation of first-line HER2-directed treatment. Patient had a relatively short PFS of 6 mo on treatment. 1 L = first-line.

among patients: approximately two thirds of the patients in our study had $\geq 50\%$ tumor load positivity and one third had $< 50\%$ positivity. The percentage of tumor load with tracer uptake was not

significantly associated with PFS in the small subgroup analysis of patients receiving first-line HER2-directed therapy. The case example shown in Figure 1 highlights the potential for HER2 PET to identify lesions in the brain before symptomatic presentation, without a biopsy. This has not been previously demonstrated in the literature. In addition, the case example shown in Figure 2 illustrates the potential for biomarker-directed imaging to identify sites of disease heterogeneity that are not captured by standard imaging and biopsy. There was a trend toward improved PFS among patients with at least 1 lesion on HER2 PET with SUV greater than or equal to 10 who were receiving first-line HER2-directed therapy, though this difference was not significant. A larger study would be needed to associate HER2 PET findings with PFS.

Although the clinical application of evaluating disease heterogeneity by HER2 PET has not been clearly established for EGC, HER2 PET has been used to help guide clinical decision making for other HER2+ tumor types. In a study of 20 patients with breast cancer, including 7 patients with metastases that were inaccessible for biopsy, HER2 PET was used to support clinical decision making and changed management in 8 of 20 patients (40%) (16). Similarly, in a cohort of 12 patients with HER2-mutant lung cancer, pretreatment HER2 PET identified ^{89}Zr -trastuzumab-avid lesions in 4 patients, all of whom responded to HER2-directed therapy with ado-trastuzumab emtansine (T-DM1); in contrast, among the 8 patients without uptake of ^{89}Zr -trastuzumab, only 3 (37%) responded to T-DM1 treatment (17).

Our study demonstrates that intensity of ^{89}Zr -trastuzumab uptake varies between and within patients and can be used to stratify patients, although the clinical application of this has not yet been determined. At least 1 lesion with an SUV ≥ 10 on HER2 PET may be associated with response to HER2-directed therapy, though this remains to be validated in future studies. Although the percentage of tumor load positive was used to establish feasibility in this study, it remains unclear whether this is a marker of likelihood to respond to HER2-directed therapy.

HER2 PET is limited by the high background tracer uptake in several key organs, including the liver, making it challenging to identify discrete tumors using this technique. The current study is limited by its descriptive design. In addition, the study is limited by patient exposure to trastuzumab before HER2 PET due to partial target saturation. Further investigation specifically including previously untreated patients is required to determine whether HER2 PET can be used as a clinical predictive tool in patients with HER2+ mEGC.

CONCLUSION

HER2 PET may identify heterogeneity of HER2 expression and allows assessment of lesions throughout the entire body. HER2 PET has a potential advantage over single-site biopsy in assessment of HER2 heterogeneity. Bone lesions were better identified than soft-tissue lesions on HER2 PET. Until further studies validate the preliminary clinical findings presented, we anticipate that HER2 PET will remain a valuable research tool.

DISCLOSURE

Financial support for this study was received from Department of Defense Congressionally Directed Medical Research Program (CA 150646, Yelena Y. Janjigian and Jason S. Lewis), NIH/NCI Cancer Center Support Grant P30 CA008748, 2013 Conquer Cancer Foundation ASCO Career Development Award (Yelena Y. Janjigian),

2014 and 2016 Mr. William H. Goodwin and Mrs. Alice Goodwin and the Commonwealth Foundation for Cancer Research and The Center for Experimental Therapeutics at Memorial Sloan Kettering Cancer Center (Yelena Y. Janjigian and Jason S. Lewis), and 2015 Cycle for Survival Award (Yelena Y. Janjigian). Yelena Y. Janjigian has received research funding from Bayer, Bristol Myers Squibb, Cycle for Survival, Department of Defense, Eli Lilly, Fred's Team, Genentech/Roche, Merck, the National Cancer Institute, and RGENIX and has served on advisory boards or in a consulting role for Amerisource Bergen, Arcus Biosciences, Astra Zeneca, Basilea Pharmaceutica, Bayer, Bristol Myers Squibb, Daiichi Sankyo, Eli Lilly, Geneos Therapeutics, GlaxoSmithKline, Imedex, Imugene, Lynx Health, Merck, Merck Serono, Michael J. Hennessy Associates, Paradigm Medical Communications, PeerView Institute, Pfizer, Research to Practice, RGENIX, Seagen, Silverback Therapeutics, and Zymeworks Inc. Neeta Pandit-Taskar has received research funding from Bayer Health, Bristol Myers Squibb, Clarity Pharmaceuticals, Imaginab, Janssen, and Regeneron; has served in consulting or advisory roles for Illumina and Progenics; and has received honoraria from Actinium Pharmaceuticals and AstraZeneca/MedImmune. Steven B. Maron has received research funding from Guardant Health (Inst) and Roche/Genentech (Inst); has served on advisory boards or in consulting roles for Basilea, Health Advances and Natera; and has stock in Calithera Biosciences. Joseph A. O'Donoghue has served in a consulting or advisory role for Janssen Research & Development. No other potential conflict of interest relevant to this article was reported.

KEY POINTS

QUESTION: Is HER2 PET an effective tool for noninvasive assessment of variations in HER2 expression and target engagement in patients with HER2+ mEGC?

PERTINENT FINDINGS: In a pilot study of HER2 PET in 33 patients with HER2+ mEGC, 70% of patients were HER2 imaging-positive ($\geq 50\%$ of tumor load positive) and most patients had variable HER2 uptake across disease sites. Among patients receiving HER2-directed therapy as first-line treatment, median PFS was longer for those with at least 1 intense or very intense lesion on HER2 PET.

IMPLICATIONS FOR PATIENT CARE: A potential application of HER2 PET is noninvasive evaluation of intrapatient heterogeneity of HER2 status not captured by single-site biopsies in patients with HER2+ mEGC.

REFERENCES

- Bray F, Ferlay J, Soerjomataram I, Siegel RL, Torre LA, Jemal A. Global cancer statistics 2018: GLOBOCAN estimates of incidence and mortality worldwide for 36 cancers in 185 countries. *CA Cancer J Clin.* 2018;68:394–424.
- Reichelt U, Duesedau P, Tsourlakis MC, et al. Frequent homogeneous HER-2 amplification in primary and metastatic adenocarcinoma of the esophagus. *Mod Pathol.* 2007;20:120–129.
- Janjigian YY, Werner D, Pauligk C, et al. Prognosis of metastatic gastric and gastroesophageal junction cancer by HER2 status: a European and USA International collaborative analysis. *Ann Oncol.* 2012;23:2656–2662.
- Schoppmann SF, Jesch B, Friedrich J, et al. Expression of Her-2 in carcinomas of the esophagus. *Am J Surg Pathol.* 2010;34:1868–1873.
- Bang YJ, Van Cutsem E, Feyereislava A, et al. Trastuzumab in combination with chemotherapy versus chemotherapy alone for treatment of HER2-positive advanced gastric or gastro-oesophageal junction cancer (ToGA): A phase 3, open-label, randomised controlled trial. *Lancet.* 2010;376:687–697.
- Janjigian YY, Maron SB, Chatila WK, et al. First-line pembrolizumab and trastuzumab in HER2-positive oesophageal, gastric, or gastro-oesophageal junction cancer: an open-label, single-arm, phase 2 trial. *Lancet Oncol.* 2020;21:821–831.
- Janjigian YY, Kawazoe A, Yáñez P, et al. The KEYNOTE-811 trial of dual PD-1 and HER2 blockade in HER2-positive gastric cancer. *Nature.* 2021;600:727–730.
- Ock CY, Lee KW, Kim JW, et al. Optimal patient selection for trastuzumab treatment in HER2-Positive advanced gastric cancer. *Clin Cancer Res.* 2015;21:2520–2529.
- Gajria D, Chandrarlapaty S. HER2-amplified breast cancer: mechanisms of trastuzumab resistance and novel targeted therapies. *Expert Rev Anticancer Ther.* 2011; 11:263–275.
- O'Donoghue JA, Lewis JS, Pandit-Taskar N, et al. Pharmacokinetics, biodistribution, and radiation dosimetry for ^{89}Zr -trastuzumab in patients with esophagogastric cancer. *J Nucl Med.* 2018;59:161–166.
- Harris PA, Taylor R, Thielke R, Payne J, Gonzalez N, Conde JG. Research electronic data capture (REDCap): a metadata-driven methodology and workflow process for providing translational research informatics support. *J Biomed Inform.* 2009;42:377–381.
- Harris PA, Taylor R, Minor BL, et al. The REDCap consortium: building an international community of software platform partners. *J Biomed Inform.* 2019;95:103208.
- Gebhart G, Lamberts LE, Wimana Z, et al. Molecular imaging as a tool to investigate heterogeneity of advanced HER2-positive breast cancer and to predict patient outcome under trastuzumab emtansine (T-DM1): The ZEPHIR trial. *Ann Oncol.* 2016;27:619–624.
- R Core Team (2022). R: A language and environment for statistical computing. R Foundation for Statistical Computing, Vienna, Austria. R Project website. <https://www.R-project.org/>. Accessed March 24, 2023.
- Cheng DT, Mitchell TN, Zehir A, et al. Memorial Sloan Kettering-Integrated Mutation Profiling of Actionable Cancer Targets (MSK-IMPACT): A hybridization capture-based next-generation sequencing clinical assay for solid tumor molecular oncology. *J Mol Diagn.* 2015;17:251–264.
- Bensch F, Brouwers AH, Hooge MNL, et al. ^{89}Zr -trastuzumab PET supports clinical decision making in breast cancer patients, when HER2 status cannot be determined by standard work up. *Eur J Nucl Med Mol Imaging.* 2018;45:2300–2306.
- Ulaner GA, Hyman DM, Lyashchenko SK, Lewis JS, Carrasquillo JA. ^{89}Zr -trastuzumab PET/CT for detection of human epidermal growth factor receptor 2-positive metastases in patients with human epidermal growth factor receptor 2-negative primary breast cancer. *Clin Nucl Med.* 2017;42:912–917.

Is ¹⁸F-FDG PET Needed to Assess ¹⁷⁷Lu-PSMA Therapy Eligibility? A VISION-like, Single-Center Analysis

Robert Seifert^{1–4}, Tugce Telli^{1,3,4}, Boris Hadaschik^{3–5}, Wolfgang P. Fendler^{1,3,4}, Phillip H. Kuo⁶, and Ken Herrmann^{1,3,4}

¹Department of Nuclear Medicine, University Hospital Essen, Essen, Germany; ²Department of Nuclear Medicine, University Hospital Münster, Münster, Germany; ³German Cancer Consortium (DKTK), University Hospital Essen, Essen, Germany; ⁴West German Cancer Center, University Hospital Essen, Essen, Germany; ⁵Department of Urology, University Hospital Essen, Essen, Germany; and ⁶Departments of Medical Imaging, Medicine, and Biomedical Engineering, University of Arizona, Tucson, Arizona

¹⁸F-FDG and prostate-specific membrane antigen (PSMA) PET have been used to assess eligibility for PSMA-targeted therapy by some centers. However, it remains unclear whether both examinations are needed as a part of workup in the clinical practice or whether PSMA PET alone, as was done in the positive phase 3 VISION trial, is sufficient to identify suitable candidates. The aim was to reanalyze all patients who underwent both ¹⁸F-FDG and PSMA PET for PSMA-targeted therapy eligibility assessment using the VISION trial criteria. **Methods:** Eighty-nine men with metastatic castration-resistant prostate cancer referred to ¹⁷⁷Lu-PSMA therapy from June 2019 to October 2021 who underwent both ¹⁸F-FDG and PSMA PET (using either ⁶⁸Ga-PSMA-11 or ¹⁸F-PSMA-1007) examinations within 2 wk were included in this analysis. Eligibility status was determined in accordance with either knowledge of both ¹⁸F-FDG and PSMA PET (clinical routine) or VISION criteria with PSMA PET-only (study reassessment, done twice with liver only for PSMA-11 and liver/spleen as reference for PSMA-1007). A metastasis seen on ¹⁸F-FDG PET or CT but not on PSMA PET was denoted as a mismatch finding and led to exclusion from ¹⁷⁷Lu-PSMA therapy. On the basis of clinical assessment, 52 patients received ¹⁷⁷Lu-PSMA therapy, and 37 did not; all patients were reassessed. **Results:** Patients treated with ¹⁷⁷Lu-PSMA therapy had significantly longer overall survival than those not treated (12.4 vs. 6.8 mo, $P < 0.01$). PSMA-only analysis (spleen/liver reference) and ¹⁸F-FDG/PSMA mismatch reads had substantial agreement (Cohen $\kappa = 0.73$). Eighteen percent ($n = 16/89$) of patients had a mismatch finding based on ¹⁸F-FDG/PSMA PET. With the liver/spleen reference, a minor fraction of patients who had no mismatch finding (and were therefore treated) would have been withheld from therapy by PSMA-only analysis (3%). Three percent ($n = 3$) of all patients had an ¹⁸F-FDG/PSMA mismatch finding not detected by PSMA PET-only (VISION-like) analysis. For patients not receiving PSMA therapy, the overall survival was not statistically significantly different comparing ¹⁸F-FDG/PSMA mismatch versus nonmismatch ($P = 0.61$) patients. **Conclusion:** ¹⁸F-FDG and PSMA PET provide complementary information, yet less than 5% of patients had mismatch findings not detected using PSMA PET-only. Based on our data, ¹⁸F-FDG/PSMA mismatch examination and PSMA-only analysis have a substantial level of agreement.

Key Words: prostate cancer; PET; PSMA-11; PSMA-1007; PSMA therapy

J Nucl Med 2023; 64:731–737

DOI: 10.2967/jnunmed.122.264741

Received Aug. 1, 2022; revision accepted Dec. 6, 2022.
For correspondence or reprints, contact Robert Seifert (robert.seifert@uk-essen.de).

Published online Dec. 15, 2022.

COPYRIGHT © 2023 by the Society of Nuclear Medicine and Molecular Imaging.

Radioligand therapy targeting the prostate-specific membrane antigen (PSMA) with ¹⁷⁷Lu (¹⁷⁷Lu-PSMA) is an efficacious therapy option in patients with end-stage metastatic castration-resistant prostate cancer (1). Recently, the VISION trial, an open-label international phase 3 trial comparing PSMA therapy against standard of care, demonstrated superiority of the additional ¹⁷⁷Lu-PSMA therapy compared with standard of care only; overall survival was significantly longer when receiving ¹⁷⁷Lu-PSMA therapy with standard of care (2). This led to U.S. Food and Drug Administration approval in March 2022. This approval is a hallmark for nuclear medicine, as it is the first novel theragnostic treatment option available for an entity with high prevalence (in contrast to relatively rare neuroendocrine tumors).

Men with metastatic castration-resistant prostate cancer have multiple treatment options available, and ¹⁷⁷Lu-PSMA is now being tested in earlier treatment lines (3,4). Identification of patients who are most suited for PSMA therapy is critical for outcome, given the rate of nonresponders of approximately 50% (RECIST response in the VISION trial) (2). This is relevant, because pretherapeutic PSMA PET should allow for an improved prognostication of overall survival time and prediction of response, as it directly assesses the expression of the PSMA target (5,6). To assess eligibility, the VISION trial relied on PSMA PET in combination with diagnostic CT to exclude patients with low PSMA expression in metastases that meet specific size criteria (7). Patients not fulfilling the criteria had worse overall survival, which was shown by a subsequent analysis (8). The use of PSMA PET-only to assess ¹⁷⁷Lu-PSMA therapy eligibility was adopted by many departments of nuclear medicine and is considered the clinical standard (9).

In contrast, the initial prospective ¹⁷⁷Lu-PSMA therapy trials used both PSMA and ¹⁸F-FDG PET examinations to assess therapy eligibility; this procedure was adopted by many departments of nuclear medicine, including ours (10,11). Dual tracer screening was implemented assuming that a PSMA-negative metastasis that is missed by PSMA PET might heavily influence the response to ¹⁷⁷Lu-PSMA therapy. An ¹⁸F-FDG-positive and PSMA-negative metastasis is denoted as a mismatch finding.

However, it remains unclear whether the combination of PSMA and ¹⁸F-FDG is clinically needed. Therefore, the aim of this study was to compare ¹⁸F-FDG/PSMA mismatch evaluation head-to-head with an analysis relying only on PSMA PET. To this end, we performed a retrospective reread of the pretherapeutic PSMA PET images according to the VISION trial protocol.

MATERIALS AND METHODS

Patient Cohort

Among 119 patients who were referred to PSMA and ¹⁸F-FDG PET to assess ¹⁷⁷Lu-PSMA therapy eligibility at the University Hospital Essen between June 2019 and October 2021, the patients whose image data were available and whose ¹⁸F-FDG and PSMA PET images were obtained within 2 wk of each other ($n = 89$) were included. Patient characteristics are shown in Table 1. A total number of 52 patients were treated with ¹⁷⁷Lu-PSMA therapy, whereas 37 patients were not treated with ¹⁷⁷Lu-PSMA therapy. Median prostate-specific antigen (PSA) level was 176 ng/mL (interquartile range, 32.5–526.3) in the cohort receiving ¹⁷⁷Lu-PSMA therapy and 65.7 ng/mL (interquartile range, 16.8–290.7) in the remaining patients. In total, 53 (59.6%) patients underwent PSMA-11 PET, whereas 36 (40.4%) patients underwent PSMA-1007 PET examination. Ethical approval for this retrospective study was present (local ethics committee approval no. 19-8570-BO).

Clinical ¹⁸F-FDG/PSMA Mismatch Analysis to Assess Therapy Eligibility

Patients with PSMA and ¹⁸F-FDG PET for PSMA therapy assessment with a maximum interval of 2 wk between the PET examinations were analyzed. In our clinical routine, ¹⁷⁷Lu-PSMA therapy eligibility was assessed based on visual analysis of PSMA PET and ¹⁸F-FDG PET to rule out clinically relevant mismatch. Inspired by the target lesion definition of the RECIST 1.1 criteria, visceral metastases/soft-tissue lesions with longest diameter of at least 10 mm and lymph nodes with short-axis diameter exceeding 15 mm that have ¹⁸F-FDG uptake higher than liver and PSMA uptake lower than spleen/liver were considered as clinically relevant mismatches. In addition, for the bone lesions, more than 3 bone metastases without osteolytic correlates, which are regarded as unmeasurable in RECIST 1.1 criteria, with ¹⁸F-FDG uptake higher than liver and PSMA uptake lower than liver was regarded as a clinically relevant mismatch (12). Visual uptake generally higher than liver or spleen for all lesions on PSMA PET was necessary for therapy eligibility. All men were discussed in a multidisciplinary tumor board. A metastasis in organs or bone delineated on ¹⁸F-FDG PET with no corresponding PSMA uptake was rated as a mismatch finding, and the patient was excluded from ¹⁷⁷Lu-PSMA therapy. The mean activities administered for ⁶⁸Ga-PSMA-11 and ¹⁸F-PSMA-1007 PET were 117.5 ± 56.5 and 328.3 ± 76.3 MBq, respectively. Supplemental Table 1 (supplemental materials are available at <http://jnm.snmjournals.org>) provides details on the criteria used to assess ¹⁷⁷Lu-PSMA therapy eligibility. Clinical reads of PET images have been reassessed by 2 nuclear medicine physicians to ensure consistency.

Retrospective Application of the VISION PSMA PET-Only Eligibility Criteria

All PSMA PET examinations were analyzed by the same nuclear radiologist who helped design the criteria, trained the readers, and supervised the centralized eligibility analysis for the VISION trial. The reader was unaware of the clinical assessment and ¹⁸F-FDG PET acquisition. If available, diagnostic contrast-enhanced CT was used as was done for the VISION trial, and if not available, the in-line CT from the PET/CT was used. Images were viewed using MIM Software 7.1.7. Analysis was completed twice and in accordance with VISION criteria, which only used PSMA-11; first, the liver was regarded as a reference organ for positivity threshold. In a second approach, for patients who were imaged with PSMA-1007 and excluded because of low PSMA expression, the spleen was used as a reference organ. In summary, to be VISION eligible, PSMA-positive lesions above the organ threshold (liver or spleen) and no PSMA-negative lesion had to be present; to ensure the latter, the CT component was used. PSMA negativity of the following CT findings meeting these size criteria led to exclusion: lymph node of at least 2.5 cm; solid organ metastases of

TABLE 1
Patient Characteristics

Parameter	Total
Median age (y)	71 (IQR, 65–78)
Gleason sum score (<i>n</i>)	67
≤7	11 (16.4)
≥8	56 (83.6)
Median previous therapy lines	4 (IQR, 2–4)
Previous therapies (<i>n</i>)	86
Abiraterone	74 (86.0)
Enzalutamide	61 (70.9)
Docetaxel	77 (89.5)
Cabazitaxel	25 (29.1)
Other	23 (26.7)
ECOG PS	53
0	20 (37.7)
1	25 (47.2)
2	8 (15.1)
Treated with ¹⁷⁷ Lu-PSMA (<i>n</i>)	52 (58.4)
Median cycles	4 (IQR, 2–4)
Median cumulative dose (GBq)	24.4 (IQR, 12.3–29.8)
Median PSA (ng/mL)	113 (IQR, 25.4–461.5)
Median ALP (U/L)	158.5 (IQR, 91.5–330.2)
Median LDH (U/L)	269.5 (IQR, 223.7–438)
Median Hb (g/dL)	11.4 (IQR, 9.6–12.7)
Mismatch, <i>n</i> (%)	16 (18.5)
Low PSMA uptake according to PSMA-only VISION evaluation (with spleen) (<i>n</i>)	18 (20.2)

IQR = interquartile range; ECOG PS = Eastern Cooperative Oncology Group Performance Status; ALP = alkaline phosphatase; LDH: lactate dehydrogenase; Hb = hemoglobin.

Data in parentheses are percentages, unless otherwise indicated.

at least 1-cm short axis; bone metastases with soft-tissue component of at least 1 cm.

PSMA Therapy

Besides the previously described image-based criteria for therapy eligibility, the EANM procedure guidelines were followed (9). ¹⁷⁷Lu-PSMA therapy was performed as previously published (13). Briefly, the PSMA-617 ligand (ABX GmbH) was conjugated with ¹⁷⁷Lu (ITG Isotope Technology). A median cumulative dose of 24.4 (interquartile range, 12.3–29.8) GBq was administered per patient; cycles were repeated every 6–8 wk.

Statistical Analysis

R and SPSS (Version 29; IBM) were used for statistical analysis, testing, and plotting. Kaplan-Meier estimates were used. Cox regression analysis was used for analysis of censored data, and the log rank test was used to compare groups regarding survival time. Agreement between PSMA-only analysis (using spleen/liver as a reference organ) and ¹⁸F-FDG/PSMA mismatch read was evaluated with Cohen κ analysis.

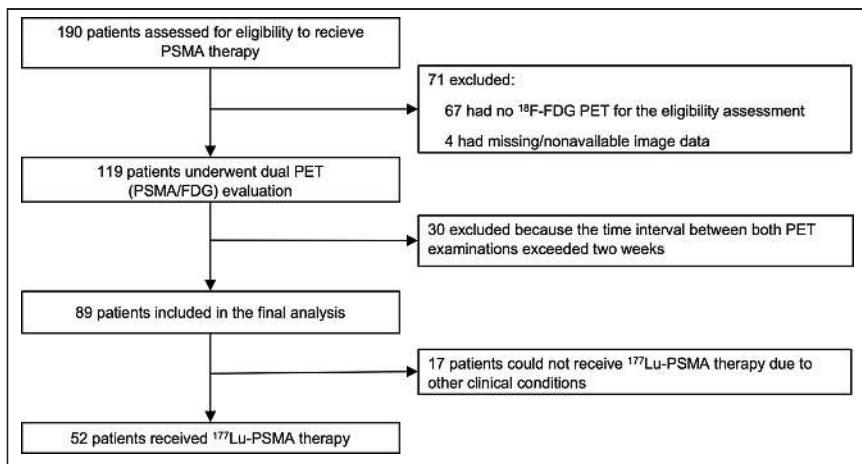


FIGURE 1. Flow chart of included patients.

Difference in PSA response rate of at least 50% for the patients treated with ^{177}Lu -PSMA was analyzed with a χ^2 test. $P < 0.05$ was regarded as statistically significant.

RESULTS

Detection of ^{18}F -FDG/PSMA Mismatch Using PSMA PET Alone

Eighty-nine of 119 patients referred to PSMA therapy underwent ^{18}F -FDG and PSMA PET within 2 wk of each other (Fig. 1). The rate of ^{18}F -FDG/PSMA mismatch findings was 18% ($n = 16/89$). Substantial agreement between PSMA-only analysis (in accordance to modified VISION criteria using liver/spleen as a reference organ) and ^{18}F -FDG/PSMA mismatch read was observed ($n = 81/89$, 91%, Cohen κ : 0.73; Fig. 2). Three percent ($n = 3/89$, denominator: total cohort) had an ^{18}F -FDG/PSMA mismatch finding, although they were deemed eligible for PSMA therapy by the PSMA-only analysis (Fig. 3; Table 2). Twelve percent ($n = 11/89$, denominator: total cohort) had no mismatch finding and were not eligible for ^{177}Lu -PSMA therapy according to the VISION-like analysis (of this group, not all patients were treated with PSMA therapy because of insufficient clinical parameters).

Of the 89 analyzed patients referred to PSMA therapy, 52 patients (58%) received PSMA therapy. Table 2 provides details of the reasons for exclusion from ^{177}Lu -PSMA therapy. Of those patients treated,

7 patients (13%, $n = 7/52$, denominator: treated patients) were treated because of the clinical assessment but would not have been eligible for ^{177}Lu -PSMA therapy according to the PSMA-only (VISION-like) analysis. Of patients treated with ^{177}Lu -PSMA therapy, 23 patients (44%, $n = 23/52$, denominator: treated patients) had undergone PSMA-1007 PET for eligibility assessment.

VISION-like Analysis of Patients (Separated According to the PSMA Ligand Used)

This first assessment used the VISION-prescribed threshold of activity greater than liver for PSMA positivity and likewise activity equal to or less than liver for PSMA negativity. In the cohort imaged with PSMA-11, 3 patients (6%, $n = 3/53$, denominator: patients imaged with PSMA-11) deemed eligible by the PSMA-only analysis would have been ineligible because of ^{18}F -FDG/PSMA mismatch findings. In the PSMA-1007 cohort, no patient with a mismatch finding was rated as therapy eligible by the PSMA-only analysis.

Only 1 treated patient (2%, $n = 1/53$, denominator: patients imaged with PSMA-11) without an ^{18}F -FDG/PSMA mismatch finding was excluded in the PSMA-11 cohort though the VISION read. However, 6 treated patients imaged with PSMA-1007 (17%, $n = 6/36$, denominator: patients imaged with PSMA-1007) were excluded from PSMA therapy based on the PSMA-only read without a mismatch finding.

VISION-like Analysis of Patients with Adjusted Reference Organ

To adjust for the higher hepatic PSMA uptake, the eligibility of patients imaged with PSMA-1007 was reassessed using the spleen as additional reference organ (Fig. 4). After this adjustment, only 3 patients (3%, $n = 3/89$, denominator: total cohort) of the total cohort including patients imaged with either PSMA tracer were not eligible because of the PSMA-only VISION analysis but showed no mismatch finding and were treated. For PSMA-1007, only 2 patients (6%, $n = 2/36$, denominator: patients imaged with PSMA-1007) were excluded without a mismatch finding and were treated.

However, only 3 patients (3%, $n = 3/89$, denominator: total cohort) of the total cohort had a mismatch finding, which was not detected by the PSMA-only analysis (Table 2). See supplemental Table 2 for details on mismatch and PSMA-only VISION evaluation deviations. For comparison, supplemental Figure 1 provides the cross tables for the clinical reads (mismatch finding or low PSMA expression) and the VISION analysis (original and spleen adjusted) separately for the used ligand.

Overall Survival of Total Cohort and Untreated Patients

The overall survival of patients treated with ^{177}Lu -PSMA therapy was significantly longer than that of those not treated (12.4 [95% CI, 8.6–25.5] vs. 6.8 [95% CI, 4.2–9.5] mo, $P < 0.01$; hazard ratio, 0.454, $P < 0.01$).

The overall survival of patients not treated with ^{177}Lu -PSMA therapy was not

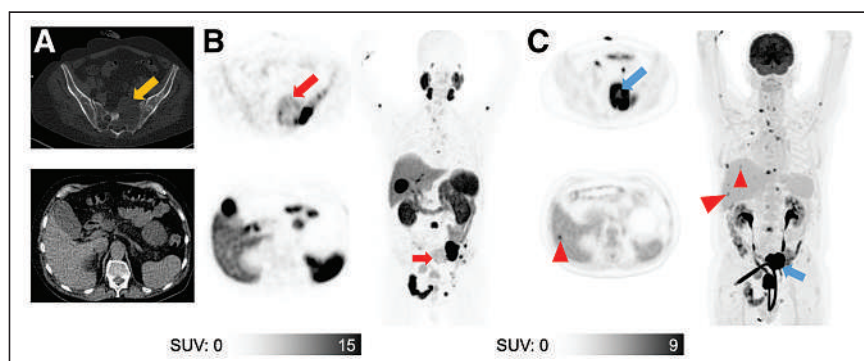


FIGURE 2. Exemplary patient who was ineligible for ^{177}Lu -PSMA therapy (PSMA-only evaluation and ^{18}F -FDG/PSMA assessment). Large osteolytic lesion in the sacrum with soft-tissue component (A, yellow arrow) with low PSMA uptake (B, red arrows) and intensive ^{18}F -FDG uptake (C, blue arrows). ^{18}F -FDG has also shown additional liver metastases that were not detected by non-contrast-enhanced CT or PSMA PET (C, arrowheads).

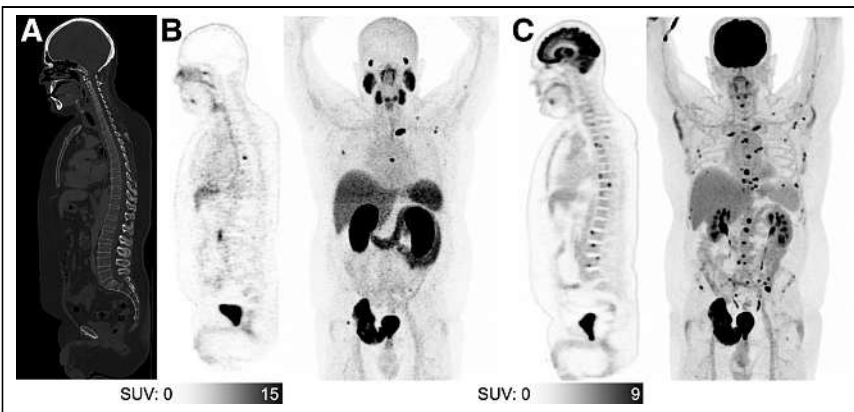


FIGURE 3. Exemplary patient who showed ¹⁸F-FDG/PSMA mismatch that was not detected by PSMA-only analysis. PSMA-11 PET/CT showed no significant CT correlate of bone lesions (A), which have high PSMA uptake (B). However, ¹⁸F-FDG PET/CT showed more than 20 additional bone lesions (C).

statistically significantly different between those with ($n = 15$) or without an ¹⁸F-FDG/PSMA mismatch ($n = 22$) finding (4.7 [95% CI, 2.4–6.8] vs. 9.2 [95% CI, 3.3–14.3] mo, $P = 0.61$; hazard ratio, 1.224, $P = 0.6$), but this analysis was limited because of the low number of patients ($n = 37$). Patients not treated with ¹⁷⁷Lu-PSMA therapy did not have a statistically significantly different survival time if they were VISION (spleen adjusted) eligible or not (4.7 [95% CI, 2.4–16.1] vs. 9.2 [95% CI, 3.3–14.3] mo, $P = 0.42$; hazard ratio, 0.73, $P = 0.4$; Fig. 5).

Outcome of the Patients Receiving ¹⁷⁷Lu-PSMA

Of the 89 analyzed patients referred to our department, 52 patients (58%) received ¹⁷⁷Lu-PSMA therapy. PSA50RR of all patients treated with ¹⁷⁷Lu-PSMA was 51%. Of those patients treated, 7 patients would not have been eligible for ¹⁷⁷Lu-PSMA therapy according to the PSMA-only (VISION-like, only liver used as reference) analysis but were still treated because of the clinical assessment. PSA50RR of those patients was not statistically significantly different from patients who were eligible (40% vs. 52.4%, $P = 0.66$). The overall survival time of patients who were clinically treated with ¹⁷⁷Lu-PSMA, although they should have been excluded according to VISION reevaluation, was 7.46 mo

($n = 7$; 95% CI, 5.2–18.3) in contrast to 12.4 mo (95% CI, 4.7–20.1) of the patients who were eligible and treated with ¹⁷⁷Lu-PSMA; the difference was not statistically significant ($P = 0.7$).

DISCUSSION

In the present study, we investigated different imaging approaches to assess eligibility for ¹⁷⁷Lu-PSMA therapy and found high agreement of PSMA-only and ¹⁸F-FDG/PSMA mismatch assessment. Specifically, we explored the need for ¹⁸F-FDG PET in addition to PSMA PET. Only 3% of patients were deemed ineligible for therapy in excess of a PSMA-only analysis because of ¹⁸F-FDG/PSMA mismatch findings on ¹⁸F-FDG and PSMA PET. Seven patients ($n = 7/89$; 8%, denominator: total cohort) were excluded because of the PSMA-only VISION-like analysis but clinically treated with PSMA therapy, and this was only 3 patients (3%) if the reader used the PSMA-only modified VISION criteria with liver as the reference organ for PSMA-11 and spleen for PSMA-1007.

¹⁷⁷Lu-PSMA therapy is an emerging treatment option in prostate cancer, which builds on the theragnostics principle, meaning that the diagnostic target can be used for whole-body imaging and therapeutic approaches (14). The assessment of PSMA expression is therefore a prerequisite to assess therapeutic eligibility (15). However, the rate of nonresponders is considerably high, motivating the search for additional selective examinations before ¹⁷⁷Lu-PSMA therapy. The reason for this lies in the tumor biology of advanced prostate cancer. Prostate cancer has a remarkable early tendency to spread to distant organs; at the time of prostatectomy, up to 70% of patients have prostate cancer cells in the bone marrow (16). This may lead to a parallel progression of distinct cancer phenotypes and dedifferentiation throughout the course of the disease, leading to tumor heterogeneity (17). In fact, neuroendocrine transdifferentiation may lead to loss of PSMA expression and often occurs in liver metastases (18). Therefore, liver metastases are associated with worse overall survival rate and require dedicated treatment,

TABLE 2

Differences Between ¹⁷⁷Lu-PSMA Eligibility Decisions Made by Our Department (Using ¹⁸F-FDG and PSMA PET) and PSMA-Only (VISION-like) Reevaluation

Visual criteria used for PET analysis	Eligibility decision	Clinical ¹⁷⁷ Lu-PSMA eligibility decisions			
		Ineligible: mismatch despite of sufficient PSMA uptake	Ineligible: low PSMA uptake and mismatch	Ineligible: low PSMA uptake	Eligible and received therapy
PSMA-only criteria (using liver)	Ineligible	0	13	4	7
	Eligible	2	1	0	45
PSMA-only criteria (using spleen/liver for PSMA-1007)	Ineligible	0	13	2	3
	Eligible	2	1	2	49

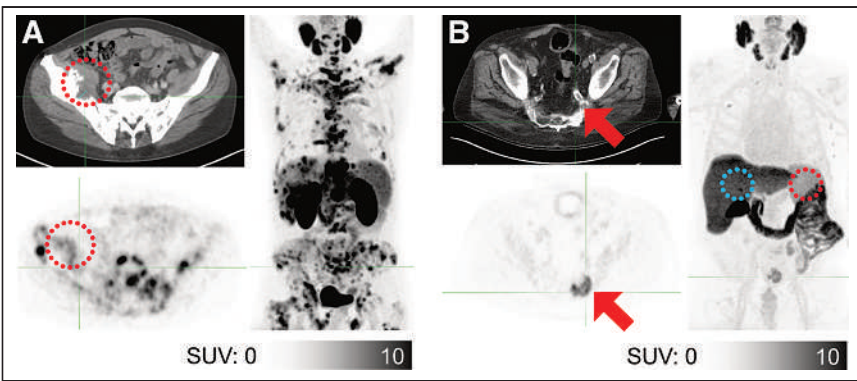


FIGURE 4. Exemplary cases of patients referred to ^{177}Lu -PSMA therapy. PSMA-11 PET imaging showed destructive osseous metastasis with large PSMA-negative soft-tissue component (A, dashed red circle). Therefore, patient was rated as not eligible for ^{177}Lu -PSMA therapy by PSMA PET-only VISION analysis. PSMA-1007 PET imaging demonstrates bone metastasis (B, arrow) with uptake lower than liver (B, blue dashed circle), and thus VISION analysis excluded the patient from ^{177}Lu -PSMA therapy. In the modified VISION analysis using spleen instead of liver as threshold organ, the patient was included as bone metastasis had higher uptake than spleen (B, red dashed circle).

especially when ^{177}Lu -PSMA therapy is used; otherwise, transdifferentiated metastases without PSMA expression would not be adequately targeted (19,20).

The assessment of tumor heterogeneity of advanced prostate cancer is challenging (21). Using PSMA PET alone, distinct uptake patterns can be observed that are associated with distinct rates of overall survival (22). Especially, low PSMA expression is associated with short overall survival time (6,22,23). The PSMA expression is also relevant to assess the PSMA tumor volume response to systemic therapy; otherwise, decreasing PSMA tumor volume can be erroneously assessed as response to therapy, which could also represent a reduction of differentiated tumor volume with an increase of dedifferentiated proportions (24). To this end, PSMA/ ^{18}F -FDG mismatch examination may be used; multitracer approaches may reveal

considerable tumor heterogeneity in prostate cancer, especially in end-stage prostate cancer under PSMA therapy (25,26).

We have found a rate of patients with mismatch findings of 18%, which is in line with previous reports (27). Interestingly, the overall survival rate of patients who were not treated with PSMA therapy was not different comparing patients with and without mismatch finding (4.7 vs. 9.2 mo, $P = 0.61$). However, a tendency to shorter overall survival in case of mismatch is recognizable in the cohort of patients who did not receive ^{177}Lu -PSMA therapy. This could indicate that the tumor phenotype may not be adequately characterized by manual mismatch analysis (i.e., searching for metastases with a flip-flop phenomenon). We have presented the characteristics of patients who have not received PSMA therapy in Supplemental Table 3 for those with and without a

mismatch finding. There was no difference regarding the levels of PSA, lactate dehydrogenase, alkaline phosphatase, or hemoglobin. However, a confounding effect could still be present, causing the mismatch and nonmismatch groups to have a similar overall survival by disguising a potential difference. Also, the finding might partially be explained by the definition of mismatch; patients rated as mismatch could potentially also show less PSMA uptake and would therefore have been excluded from therapy in a PSMA-only VISION analysis. In contrast, Michalski et al. (28) showed that patients receiving ^{177}Lu -PSMA therapy have a significantly shorter overall survival in case of a mismatch finding. This could be in line with our finding because we compared the implications of mismatch in a cohort not treated with PSMA therapy; therefore, the lower PSMA expression of patients with mismatch was not linked to treatment

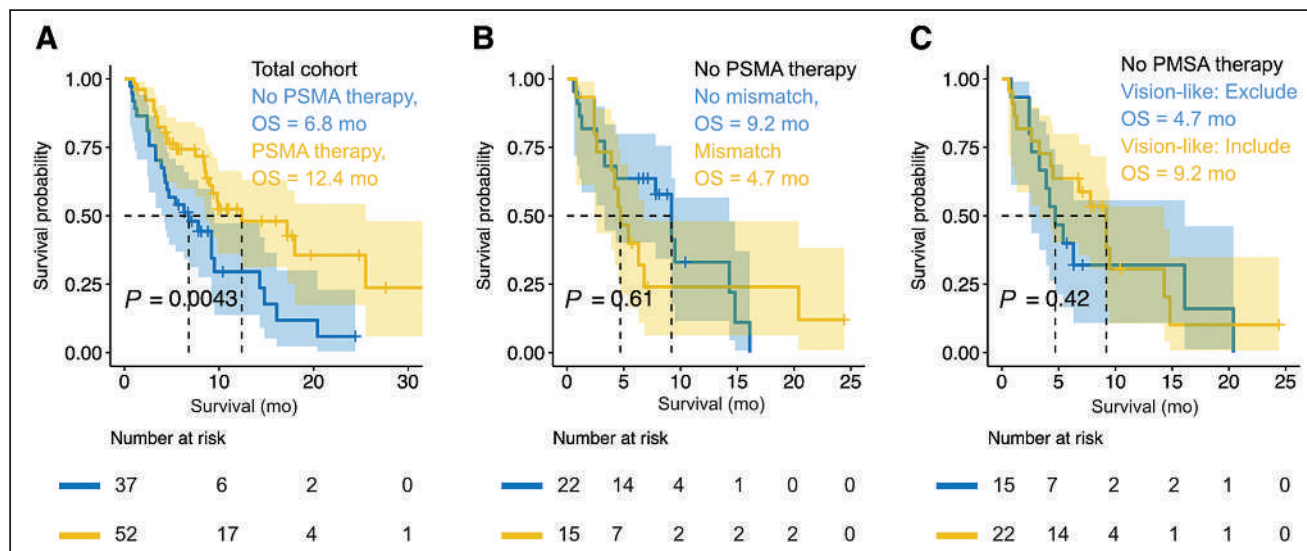


FIGURE 5. Overall survival of entire cohort and patients not treated with ^{177}Lu -PSMA therapy. Overall survival for total cohort of patients with appropriate PET examinations is shown (A); patients treated with ^{177}Lu -PSMA therapy have significantly longer overall survival time. Looking at patients who were not treated with ^{177}Lu -PSMA therapy, there was no statistically significant difference in patients with a mismatch finding compared with those without (B). Likewise, patients excluded from ^{177}Lu -PSMA therapy according to the PSMA-only VISION evaluation (spleen-adjusted threshold for PSMA-1007 group) did not have shorter survival compared with excluded patients (C).

efficacy. However, the potential value of ¹⁸F-FDG PET before PSMA therapy start might be in assessing the prognosis of the patient. Recently, it was shown that PSMA PET was predicting response to PSMA therapy, whereas ¹⁸F-FDG PET was prognosticating the outcome (29). Therefore, ¹⁸F-FDG PET might have a valuable role in addition to the mismatch assessment.

In contrast to previous phase 2 trials, we did not require a specific SUV threshold for therapy eligibility but used visual uptake higher than liver (10,11). The TheraP study and earlier LuPSMA trial required higher PSMA positivity for eligibility (SUV_{max} of 20 in 1 lesion and of 10 in remaining lesions or SUV_{max} higher than 1.5 times liver activity) (10,21). This higher threshold may select for patients who respond better to ¹⁷⁷Lu-PSMA but also withhold therapy from many patients who would have benefited. We found that the liver as the reference organ for PSMA-1007 may lead to the exclusion of patients who were clinically treated with ¹⁷⁷Lu-PSMA therapy. Therefore, we proposed the spleen as an alternative reference organ for patients imaged with PSMA-1007 before ¹⁷⁷Lu-PSMA therapy, which is in line with previous publications. For example, the spleen was recently recommended as a reference organ for the PROMISE framework (miTNM criteria) instead of the liver for PSMA ligands with liver dominant excretion (30). Also, the spleen was used as reference in a study comparing PSMA-11 and PSMA-1007 (31).

CONCLUSION

The combination of ¹⁸F-FDG and PSMA PET may help in the assessment of tumor heterogeneity and dedifferentiation in end-stage prostate cancer, yet only a small fraction of patients was withheld from therapy because of ¹⁸F-FDG/PSMA mismatch findings not detected by PSMA-only VISION analysis. Further studies investigating the potential of ¹⁸F-FDG/PSMA imaging for predicting treatment response to ¹⁷⁷Lu-PSMA therapy are warranted.

DISCLOSURE

Phillip Kuo is a consultant or speaker for Amgen, Bayer, Chimerix, Eisai, Fusion Pharma, General Electric Health Care, Invicro (also prior employee), Novartis, and UroToday. He is a recipient of research grants from Blue Earth Diagnostics and General Electric Health Care. Robert Seifert has received research funding from the Else Kröner-Fresenius-Stiftung and from Boehringer Ingelheim Fonds. Wolfgang Fendler reports fees from SOFIE Bio-science (research funding), Janssen (consultant, speakers bureau), Calyx (consultant), Bayer (consultant, speakers bureau, research funding), Parexel (image review), and AAA (speakers bureau) outside of the submitted work. Ken Herrmann received personal fees from BTG, Bayer, Sofie Biosciences, SIRTEX, Adacap, Curium, Endocyte, IPSEN, Siemens Healthineers, GE Healthcare, Amgen, Novartis, ymabs, Aktis, Oncology, and Pharma15, as well as non-financial support from ABX and grants from BTG. Boris Hadachik has had advisory roles for ABX, AAA/Novartis, Astellas, AstraZeneca, Bayer, Bristol Myers Squibb, Janssen R&D, Lightpoint Medical, Inc., and Pfizer; has received research funding from Astellas, Bristol Myers Squibb, AAA/Novartis, German Research Foundation, Janssen R&D, and Pfizer and has received compensation for travel from Astellas, AstraZeneca, Bayer, and Janssen R&D. Tugce Telli received support from the German Academic Exchange Service. No other potential conflict of interest relevant to this article was reported.

KEY POINTS

QUESTION: Is ¹⁸F-FDG PET needed to assess ¹⁷⁷Lu-PSMA therapy eligibility?

PERTINENT FINDINGS: The VISION-like analysis, which only regarded PSMA PET and CT to assess eligibility for ¹⁷⁷Lu-PSMA therapy, resulted in a minor rate of patients who showed an ¹⁸F-FDG/PSMA mismatch finding that has been not detected; therefore, the mismatch evaluation before the start of PSMA therapy might be omitted. A spleen-adjusted threshold should be used for PSMA-1007 imaging studies to assess therapy eligibility.

IMPLICATION FOR PATIENT CARE: With careful evaluation, PSMA PET/CT alone might be sufficient for ¹⁷⁷Lu-PSMA therapy eligibility assessment. However, further studies investigating the potential of ¹⁸F-FDG/PSMA for outcome prognosticating of patients treated with ¹⁷⁷Lu-PSMA therapy are warranted.

REFERENCES

- Seifert R, Alberts IL, Afshar-Oromieh A, Rahbar K. Prostate cancer theranostics: PSMA targeted therapy. *PET Clin.* 2021;16:391–396.
- Sartor O, de Bono J, Chi KN, et al. Lutetium-177-PSMA-617 for metastatic castration-resistant prostate cancer. *N Engl J Med.* 2021;385:1091–1103.
- EAU. EAU guideline prostate cancer. <https://uroweb.org/guidelines/prostate-cancer>. Accessed March 10, 2022.
- NCCN. NCCN guideline prostate cancer. <https://www.nccn.org/guidelines/guidelines-detail?category=1&id=1459>. Accessed January 10, 2022.
- Violet J, Jackson P, Ferdinandus J, et al. Dosimetry of ¹⁷⁷Lu-PSMA-617 in metastatic castration-resistant prostate cancer: correlations between pretherapeutic imaging and whole-body tumor dosimetry with treatment outcomes. *J Nucl Med.* 2019;60:517–523.
- Kuo P, Hesterman J, Rahbar K, et al. ^{[68]Ga}Ga-PSMA-11 PET baseline imaging as a prognostic tool for clinical outcomes to ^{[177]Lu}Lu-PSMA-617 in patients with mCRPC: a VISION substudy. *J Clin Oncol.* 2022;40(16_suppl):5002.
- Kuo PH, Benson T, Messmann R, Groening M. Why we did what we did: PSMA PET/CT selection criteria for the VISION trial. *J Nucl Med.* 2022;63: 816–818.
- Hotta M, Gafita A, Czernin J, Calais J. Outcome of patients with PSMA-PET/CT screen failure by VISION criteria and treated with ¹⁷⁷Lu-PSMA therapy: a multi-center retrospective analysis. *J Nucl Med.* 2022;63:1484–1488.
- Kratochwil C, Fendler WP, Eiber M, et al. EANM procedure guidelines for radio-nuclide therapy with ¹⁷⁷Lu-labelled PSMA-ligands (¹⁷⁷Lu-PSMA-RLT). *Eur J Nucl Med Mol Imaging.* 2019;46:2536–2544.
- Hofman MS, Violet J, Hicks RJ, et al. ^{[177]Lu}-PSMA-617 radionuclide treatment in patients with metastatic castration-resistant prostate cancer (LuPSMA trial): a single-centre, single-arm, phase 2 study. *Lancet Oncol.* 2018;19:825–833.
- Hofman MS, Emmett L, Sandhu S, et al. ^{[177]Lu}Lu-PSMA-617 versus cabazitaxel in patients with metastatic castration-resistant prostate cancer (TheraP): a randomised, open-label, phase 2 trial. *Lancet.* 2021;397:797–804.
- Eisenhauer EA, Therasse P, Bogaerts J, et al. New response evaluation criteria in solid tumours: revised RECIST guideline (version 1.1). *Eur J Cancer.* 2009;45: 228–247.
- Seifert R, Kessel K, Schlack K, et al. PSMA PET total tumor volume predicts outcome of patients with advanced prostate cancer receiving ^{[177]Lu}Lu-PSMA-617 radioligand therapy in a bicentric analysis. *Eur J Nucl Med Mol Imaging.* 2021;48: 1200–1210.
- Herrmann K, Schwaiger M, Lewis JS, et al. Radiotheranostics: a roadmap for future development. *Lancet Oncol.* 2020;21:e146–e156.
- Srinivas S, lagaru A. To scan or not to scan: an unnecessary dilemma for PSMA radioligand therapy. *J Nucl Med.* 2021;62:1487–1488.
- Morgan TM, Lange PH, Porter MP, et al. Disseminated tumor cells in prostate cancer patients after radical prostatectomy and without evidence of disease predicts biochemical recurrence. *Clin Cancer Res.* 2009;15:677–683.
- Weckermann D, Polzer B, Ragg T, et al. Perioperative activation of disseminated tumor cells in bone marrow of patients with prostate cancer. *J Clin Oncol.* 2009; 27:1549–1556.

18. Wang HT, Yao YH, Li BG, Tang Y, Chang JW, Zhang J. Neuroendocrine prostate cancer (NEPC) progressing from conventional prostatic adenocarcinoma: factors associated with time to development of NEPC and survival from NEPC— a systematic review and pooled analysis. *J Clin Oncol*. 2014;32:3383–3390.
19. Seifert R, Kessel K, Boegemann M, et al. Additional local therapy for liver metastases in patients with metastatic castration-resistant prostate cancer receiving systemic PSMA-targeted therapy. *J Nucl Med*. 2020;61:723–728.
20. Halabi S, Kelly WK, Ma H, et al. Meta-analysis evaluating the impact of site of metastasis on overall survival in men with castration-resistant prostate cancer. *J Clin Oncol*. 2016;34:1652–1659.
21. Jadvar H. The VISION forward: recognition and implication of PSMA-/FDG+ mCRPC. *J Nucl Med*. 2022;63:812–815.
22. Seifert R, Seitzer K, Herrmann K, et al. Analysis of PSMA expression and outcome in patients with advanced prostate cancer receiving ¹⁷⁷Lu-PSMA-617 radioligand therapy. *Theranostics*. 2020;10:7812–7820.
23. Thang SP, Violet J, Sandhu S, et al. Poor outcomes for patients with metastatic castration-resistant prostate cancer with low prostate-specific membrane antigen (PSMA) expression deemed ineligible for ¹⁷⁷Lu-labelled PSMA radioligand therapy. *Eur Urol Oncol*. 2019;2:670–676.
24. Seifert R, Kessel K, Schlack K, et al. Total tumor volume reduction and low PSMA expression in patients receiving Lu-PSMA therapy. *Theranostics*. 2021;11: 8143–8151.
25. Khreish F, Ribbat K, Bartholomä M, et al. Value of combined PET imaging with [¹⁸F]FDG and [⁶⁸Ga]Ga-PSMA-11 in mCRPC patients with worsening disease during [¹⁷⁷Lu]Lu-PSMA-617 RLT. *Cancers (Basel)*. 2021;13:4134.
26. Fourquet A, Rosenberg A, Mena E, et al. A comparison of ¹⁸F-DCFPyL, ¹⁸F-NaF and ¹⁸F-FDG PET/CT in prospective cohort of men with metastatic prostate cancer. *J Nucl Med*. 2022;63:735–741.
27. Chen R, Wang Y, Zhu Y, et al. The added value of ¹⁸F-FDG PET/CT compared to ⁶⁸Ga-PSMA PET/CT in patients with castration-resistant prostate cancer. *J Nucl Med*. 2022;63:69–75.
28. Michalski K, Ruf J, Goetz C, et al. Prognostic implications of dual tracer PET/CT: PSMA ligand and [¹⁸F]FDG PET/CT in patients undergoing [¹⁷⁷Lu]PSMA radioligand therapy. *Eur J Nucl Med Mol Imaging*. 2021;48:2024–2030.
29. Buteau JP, Martin AJ, Emmett L, et al. PSMA and FDG-PET as predictive and prognostic biomarkers in patients given [¹⁷⁷Lu]Lu-PSMA-617 versus cabazitaxel for metastatic castration-resistant prostate cancer (TheraP): a biomarker analysis from a randomised, open-label, phase 2 trial. *Lancet Oncol*. 2022;23:1389–1397.
30. Eiber M, Herrmann K, Calais J, et al. Prostate cancer molecular imaging standardized evaluation (PROMISE): proposed miTNM classification for the interpretation of PSMA-ligand PET/CT. *J Nucl Med*. 2018;59:469–478.
31. Hoberück S, Löck S, Borkowetz A, et al. Intraindividual comparison of [⁶⁸Ga]-Ga-PSMA-11 and [¹⁸F]-F-PSMA-1007 in prostate cancer patients: a retrospective single-center analysis. *EJNMMI Res*. 2021;11:109.

Unspecific ¹⁸F-PSMA-1007 Bone Uptake Evaluated Through PSMA-11 PET, Bone Scanning, and MRI Triple Validation in Patients with Biochemical Recurrence of Prostate Cancer

Robert Seifert^{1–4}, Tugce Telli^{1,3,4}, Marcel Opitz^{3,4,5}, Francesco Barbato^{1,3,4}, Christoph Berliner^{1,3,4}, Michael Nader¹, Lale Umutlu^{3–5}, Martin Stuschke^{3,4,6}, Boris Hadaschik^{3,4,7}, Ken Herrmann^{1,3,4}, and Wolfgang P. Fendler^{1,3,4}

¹Department of Nuclear Medicine, University Hospital Essen, Essen, Germany; ²Department of Nuclear Medicine, University Hospital Münster, Münster, Germany; ³German Cancer Consortium (DKTK), University Hospital Essen, Essen, Germany; ⁴West German Cancer Center, University Hospital Essen, Essen, Germany; ⁵Department of Diagnostic and Interventional Radiology and Neuroradiology, University Hospital Essen, Essen, Germany; ⁶Department of Radiation Oncology, University Hospital Essen, Essen, Germany; and ⁷Department of Urology, University Hospital Essen, Essen, Germany

¹⁸F-PSMA-1007 PET is used in the management of patients with prostate cancer. However, recent reports indicate a high rate of unspecific bone uptake (UBU) with ¹⁸F-PSMA-1007, which may lead to a false-positive diagnosis. UBU has not been evaluated thoroughly. Here, we evaluate the frequency of UBU and bone metastases separately for ¹⁸F-PSMA-1007 and ⁶⁸Ga-PSMA-11 in biochemical recurrence (interindividual comparison). Additionally, we investigate UBU seen in ¹⁸F-PSMA-1007 through follow-up examinations (intraindividual comparison) using ⁶⁸Ga-PSMA-11 PET, bone scintigraphy, and MRI. **Methods:** First, all patients ($n = 383$) who underwent ⁶⁸Ga-PSMA-11 PET between January 2020 and December 2020 and all patients ($n = 409$) who underwent ¹⁸F-PSMA-1007 PET between January 2020 and November 2021 due to biochemical recurrence were included for an interindividual comparison of bone metastases and UBU rate. In a second approach, we regarded all patients with UBU in ¹⁸F-PSMA-1007, characterized by focal bone uptake with an SUV_{max} > 4 and prostate-specific antigen (PSA) ≤ 5 ng/mL, who underwent additional ⁶⁸Ga-PSMA-11 PET ($n = 17$) (interindividual comparison). Of these, 12 patients also had bone scintigraphy and whole-body MRI within a 1- to 5-wk interval. Bone uptake seen on ¹⁸F-PSMA-1007 but not on any of the other 4 modalities (CT, MRI [$n = 1$], bone scanning, and ⁶⁸Ga-PSMA-11 PET) was recorded as false-positive. **Results:** Patients scanned with ¹⁸F-PSMA-1007 PET had a significantly higher rate of UBU than those scanned with ⁶⁸Ga-PSMA-11 (140 vs. 64; $P < 0.001$); however, the rate of bone metastases was not significantly different (72 vs. 64; $P = 0.7$). In the intraindividual comparison group, workup by CT, MRI, bone scanning, and ⁶⁸Ga-PSMA-11 PET resulted in a positive predictive value for ¹⁸F-PSMA-1007 focal bone uptake (mean SUV_{max}: 6.1 ± 2.9) per patient and per lesion of 8.3% and 3.6%, respectively. **Conclusion:** In patients with PSA ≤ 5 ng/mL and SUV > 4 at biochemical recurrence, most ¹⁸F-PSMA-1007 focal bone uptake is likely to be false-positive and therefore due to UBU. In the case of low clinical likelihood of metastatic disease, ¹⁸F-PSMA-1007 bone uptake without morphologic surrogate should be assessed carefully with regard to localization and clinical context. However, the rate of bone metastases was not higher with ¹⁸F-PSMA-1007 in the clinical routine, indicating that experienced reporting physicians adjust for UBU findings.

Key Words: prostate cancer; PET; PSMA-11; PSMA-1007

Received Aug. 13, 2022; revision accepted Nov. 17, 2022.
For correspondence or reprints, contact Robert Seifert (robert.seifert@uk-essen.de).

Published online Dec. 2, 2022.

COPYRIGHT © 2023 by the Society of Nuclear Medicine and Molecular Imaging.

J Nucl Med 2023; 64:738–743

DOI: 10.2967/jnumed.118.215434

Up to 60% of prostate cancer patients develop biochemical recurrence (BCR) after initial radiotherapy or radical prostatectomy in 10 y of follow-up (1). Local salvage therapy and complete metastatic ablation of oligometastatic prostate cancer may provide a curative pathway and an alternative to initiation of palliative androgen deprivation therapy (2). Therefore, to determine location and extent of recurrent PC is of the utmost importance for directing salvage therapy.

The recent European Association of Urology Prostate Cancer guideline recommended that prostate-specific membrane antigen (PSMA) PET should be offered to BCR patients with a persistent prostate-specific antigen (PSA) level greater than 0.2 ng/mL if the results will influence subsequent treatment decisions (3). PSMA PET readers need proper training, as each PSMA ligand features distinct characteristics (4,5).

More recently, ⁶⁸Ga-labeled PSMA ligands are increasingly replaced by ¹⁸F-labeled compounds offering mostly technical and logistic advantages including lower positron energy; improved spatial resolution; longer half-life; high-yield production in cyclotrons; and large batch production, thereby enabling long-distance distribution and potential cost savings (4). Moreover, ¹⁸F-PSMA-1007 exhibits blood clearance through the liver that leads to only minimal urinary excretion, yielding potential advantages for pelvic tumor assessment (6,7). However, unspecific bone uptake (UBU) on ¹⁸F-PSMA-1007 PET, reported in a considerable fraction of patients, may lead to false-positive findings as metastasis; this in turn may result in overstaging, leading to inadequate therapy (4,8,9). However, despite large observational data, UBU have not been correlated systematically by other imaging, including ⁶⁸Ga-PSMA-11 PET/CT, MRI, and bone scanning.

Therefore, the aim of this study was 2-fold. First, we evaluated the rate of UBU and bone metastases reported in clinical reads separately for ¹⁸F-PSMA-1007 and ⁶⁸Ga-PSMA-11 PET to estimate the relevance of UBUs (interindividual group). Second, we present a single-center experience with ¹⁸F-PSMA-1007 UBU in 17 patients, who underwent follow-up examinations to clarify the nature of the bone uptake. In those patients, we evaluated ¹⁸F-PSMA-1007 UBUs intraindividually with bone scanning, ⁶⁸Ga-PSMA-11 PET, and MRI.

MATERIALS AND METHODS

Patient Characteristics

Patient characteristics are shown in Table 1 and Supplemental Table 1 (supplemental materials are available at <http://jnm.snmjournals.org>). All patients were recruited at the Department of Nuclear Medicine of the University Hospital Essen. The analysis was performed retrospectively, and the need for study-specific written consent was waived (Ethics approval no. 22-10694-BO and 21-9865-BO). Briefly, 2 patient cohorts were investigated: First, the rate of UBU and bone metastases in all patients scanned with ⁶⁸Ga-PSMA-11 in the last year before the introduction of ¹⁸F-PSMA-1007 was compared with the respective rates in all patients scanned with ¹⁸F-PSMA-1007 in the first year of its use in our Department (interindividual comparison group). Additionally, patients who received ¹⁸F-PSMA-1007 and underwent ⁶⁸Ga-PSMA-11 due to ¹⁸F-PSMA-1007 UBU clinical workup were included (intraindividual group).

Inclusion Criteria of the Interindividual Comparison Group

All patients who received ⁶⁸Ga-PSMA-11 PET between January 2020 and December 2020 and all patients who received ¹⁸F-PSMA-1007 PET between January 2020 and November 2021 were regarded for the interindividual comparison group. Of these, 383 and 409 patients were referred to PET due to BCR or persistence and further analyzed with regard to the rate of UBU and bone metastases. For this group of patients, bone-related imaging findings were retrospectively extracted from our archives regardless of the finding's SUV_{max} and regardless of preimaging prostate-specific antigen (PSA) values in the case of histologically proven prostate

TABLE 1
Patient Characteristics (*n* = 17)

Characteristic	Data
Median age (y)	71 (69.5–74)
Initial T (<i>n</i>)	
T1	0
T2	5 (29.5%)
T3	8 (47%)
T4	0
Unknown	4 (23.5%)
Gleason score (<i>n</i>)	
3 + 3	1 (5.9%)
3 + 4	2 (11.8%)
4 + 3	5 (29.4%)
4 + 4	2 (11.8%)
5 + 5	1 (5.9%)
Unknown	6 (35.3%)
Previous therapy to prostate (<i>n</i>)	
Radical prostatectomy	17 (100%)
Additional adjuvant/salvage radiotherapy	8 (47.1%)
Blood levels	
Median PSA (ng/mL)	0.5 (0.2–1)
Median ALP (IU/L)	70 (55–83)
Median bone-specific ALP	12.7 (11.5–17.8)

IQR = interquartile range; ALP = alkaline phosphatase.

Data in parentheses are IQRs, unless otherwise specified.

cancer and biochemical recurrence (BCR) or PSA persistence without any known metastases.

The incidence of UBU and bone metastases on ¹⁸F-PSMA-1007 and ⁶⁸Ga-PSMA were compared in different preimage PSA-level groups (PSA < 1 ng/mL vs. 1–5 ng/mL vs. > 5 ng/mL).

Inclusion Criteria of the Intraindividual Comparison Group

The SUV_{max} of UBU was reported among different studies with similar image acquisition, and the measurements ranged between 3.6 and 21.1 (4,10). Therefore, in this study, UBU was defined as focally increased ¹⁸F-PSMA-1007 uptake in the bone with an SUV_{max} higher than 4 and clear visualization in the maximum-intensity-projection images without CT correlate (no lytic or osteoplastic reaction). Patients with ¹⁸F-PSMA-1007 PET UBU were offered additional workup in the case of histologically proven prostate cancer, BCR of prostate cancer, PSA levels at the time of imaging ≤ 5 ng/mL, and no known distant metastases.

Patients underwent additional clinical whole-body ⁶⁸Ga-PSMA-11 PET/MRI and bone scanning (together with SPECT/CT). Patient datasets were analyzed retrospectively.

Imaging and Image Interpretation of the Intraindividual Comparison Group

Tracer precursors (PSMA-11 and PSMA-1007) were obtained from ABX advanced biochemical compounds (ABX GmbH). ¹⁸F-PSMA-1007 and ⁶⁸Ga-PSMA-11 were synthesized on site using a kit-based approach on automated platforms with comprehensive pH, radiochemical, chemical, and radionuclide purity control tests.

After intravenous injection (111 ± 20 min) of ¹⁸F-PSMA-1007 (350.6 ± 61.8 MBq), PET/CT was obtained between the base of the skull and mid-thighs with the patient supine. A Biograph Vision and Biograph mCT were used for image acquisition (all: Siemens Healthineers). Full-dose CT was acquired for attenuation correction (210 mAs, 120 keV, 512 × 512 matrix, 128 × 0.6 mm slice thickness). PET emission data were attenuation corrected by help of the CT data and iteratively reconstructed (Vision—4 iterations; 5 subsets; voxel size, 3.3 × 3.3 × 3 mm³; Gauss filtering, 4 mm, and mCT—3 iterations; 21 subsets; voxel size; 4.07 × 4.07 × 3 mm³; Gauss filtering; 4 mm) with time-of-flight information and point-spread function correction (HD PET).

⁶⁸Ga-PSMA-11 PET/MR (*n* = 14) or PET/CT (*n* = 3) was used to acquire coregistered images. The mean injected dose and mean imaging delay were 133.3 ± 81.2 MBq and 67 ± 14 min, respectively. PET/MRI examination was performed with an integrated 3.0-T Biograph mMR scanner (Siemens Healthineers), and simultaneous PET and 3D Dixon-volumetric interpolated breath-hold examination (VIBE) sequences for MRI-based scatter correction were performed, followed by a standardized whole-body MRI protocol. The following MR sequences of choice were acquired: high-resolution T2-weighted fast spin-echo sequences (axial, coronal, and sagittal planes), diffusion-weighted sequences (*b* values, *b* = 0, 500, 1,000 s/mm²), and dynamic contrast-enhanced imaging sequences (namely, T1-weighted VIBE sequence obtained every 7 s during 5–10 min). PET emission data were iteratively reconstructed (3 iterations; 21 subsets; voxel size, 2.09 × 2.09 × 2.03 mm³, Gauss filtering, 4 mm).

Whole-body planar bone scintigraphy was performed after 2.5–4 h of the administration of the median dose of 628.5 MBq (range, 584–652 MBq) ^{99m}Tc-3,3-diphosphono-1,2-propanodicarboxylic acid radiopharmaceutical in a continuous mode at a rate of 15 cm/min on a 256 × 1,024 acquisition matrix of anterior and posterior planes with a dual-head γ-camera equipped with a low-energy, high-resolution collimator (Symbia T2 or Intevo; Siemens Healthineers). In all cases of uncertain radionuclide accumulations on bone scan, SPECT/CT images were acquired (15 s/view step and shoot with 128 × 128 matrix).

The time interval between the PET image acquisitions was between 1 and 5 wk. Images were interpreted using a dedicated workstation and software (SyngoVia; Siemens). All available imaging modalities were present

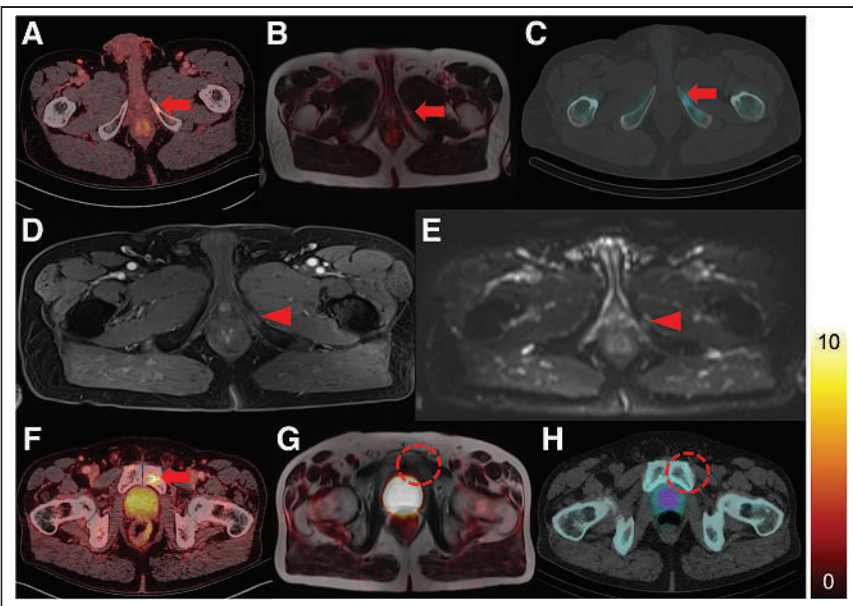


FIGURE 1. Exemplary cases of UBU regarded as true-positive and false-positive. Axial slices of a patient with suspected UBU on ^{18}F -PSMA-1007 PET (A, arrow). Suggestive uptake was seen on ^{68}Ga -PSMA-11 PET/MRI (B, arrow) and on bone scan SPECT/CT (C, arrow). Corroborating these findings, the MRI showed contrast enhancement (D, arrowhead) and diffusion restriction (E, arrowhead). Therefore, the bone uptake was rated as true-positive. A second patient is shown in F–H. Axial slices of a patient with unspecific ^{18}F -PSMA-1007 uptake rated as false-positive in left inferior pubic ramus (SUV_{\max} , 5.6) without any CT correlate (F, arrow) are shown. There was no suspicious finding either in ^{68}Ga -PSMA-11 PET/MRI (G, dashed circle) or bone SPECT/CT (H, dashed circle). Therefore, this bone uptake was considered as false-positive.

for retrospective image reading. All PET and bone scintigraphy images were interpreted by 2 nuclear medicine physicians, and MR images were interpreted by 2 radiologists. Two nuclear medicine physicians performed semiquantitative analyses of the PET data retrospectively in consensus. For example, a focal bone uptake of ^{18}F -PSMA-1007 (Fig. 1A) showing contrast enhancement (Fig. 1D), diffusion restriction (Fig. 1E), and radiotracer uptake in ^{68}Ga -PSMA PET (Fig. 1B) and bone scintigraphy (Fig. 1C) was rated as bone metastasis. Conversely, a focal ^{18}F -PSMA-1007 uptake of the bone without any suspicious finding on bone scan, ^{68}Ga -PSMA-11, and MRI was rated as false-positive (Figs. 1F–1H).

Statistical Analysis

SPSS Statistics (version 22; IBM Inc.) was used for statistical analyses. The compliance of variables to normal distribution was determined using the Kolmogorov–Smirnov test. Patient characteristics were presented as median (interquartile range [IQR] or range) or mean \pm SD in accordance with the data distribution. The χ^2 or Pearson goodness-of-fit tests were used to compare the differences of bone metastases and UBU in between 2 PSMA PET agents. A P value of less than 0.05 was considered statistically significant. A Sankey diagram was designed with the online Diagram Generator (Acquire Procurement Services, <http://sankey-diagram-generator.acquireprocure.com>).

RESULTS

Rate of Reported Bone Metastases and UBU in the Interindividual Group (Comparing ^{68}Ga -PSMA-11 and ^{18}F -PSMA-1007 Cohorts, $n = 792$)

A total of 792 PSMA PET scans of patients with BCR were included ($n = 409$ for ^{18}F -PSMA-1007 and $n = 383$ for ^{68}Ga -PSMA-11) to evaluate the frequency of UBU and bone metastases. Among the patients who were imaged with ^{18}F -PSMA-1007, 332 (81.2%), 33 (8%), 13 (3.2%), 3 (0.1%), and 115 (28.1%) patients underwent

radical prostatectomy, definitive radiotherapy, transurethral prostate resection, local ablative treatments, and adjuvant/salvage radiotherapy as previous local therapy, respectively. Among the patients who were imaged with ^{68}Ga -PSMA-11, 324 (84.6%), 28 (7.3%), 7 (1.8%), 1 (0.2%), and 99 (25.8%) patients underwent radical prostatectomy, definitive radiotherapy, transurethral prostate resection, local ablative treatments, and adjuvant/salvage radiotherapy as previous local therapy, respectively. Overall, there was no statistically significant difference for the bone metastases rate when the final reports of ^{18}F -PSMA-1007 and ^{68}Ga -PSMA-11 were compared (72 vs. 64; $P = 0.7$). Stratifying by PSA value, 229 of 397 (57.7%) patients undergoing ^{18}F -PSMA-1007 and 201 of 360 (55.8%) patients undergoing ^{68}Ga -PSMA-11 PET had PSA levels lower than 1 ng/mL. A fraction of the 138 of 397 (34.8%) patients undergoing ^{18}F -PSMA-1007 and the 147 of 360 (40.8%) patients undergoing ^{68}Ga -PSMA-11 PET had PSA levels between 1 and 5 ng/mL. Thirty of 397 (7.6%) patients undergoing ^{18}F -PSMA-1007 and 12 of 360 (3.3%) patients undergoing ^{68}Ga -PSMA-11 PET had >5 ng/mL of PSA. There was no statistically significant difference of bone metastasis detection between ^{18}F -PSMA-1007 and ^{68}Ga -PSMA-11 among different PSA groups ($P = 0.2$, 0.2, and 0.6 for PSA levels groups < 1 ng/mL, 1–5 ng/mL, and > 5 ng/mL, respectively) (Fig. 2).

and ^{68}Ga -PSMA-11 among different PSA groups ($P = 0.2$, 0.2, and 0.6 for PSA levels groups < 1 ng/mL, 1–5 ng/mL, and > 5 ng/mL, respectively) (Fig. 2).

UBU was reported at a significantly higher rate with ^{18}F -PSMA-1007 than it was in the ^{68}Ga -PSMA-11 group (140 [34.2%] vs. 64 [16.7%]; $P < 0.001$). Moreover, there was at least 1 identifiable benign bone lesion with focal PSMA uptake in 22 (5.4%) and 11 (2.9%) of the ^{18}F -PSMA-1007 and ^{68}Ga -PSMA-11 PET reports, respectively. There was no significant difference between the PSA-level groups and UBU rate for both agents ($P = 0.4$ and 0.6, respectively, for ^{18}F -PSMA-1007 and ^{68}Ga -PSMA-11).

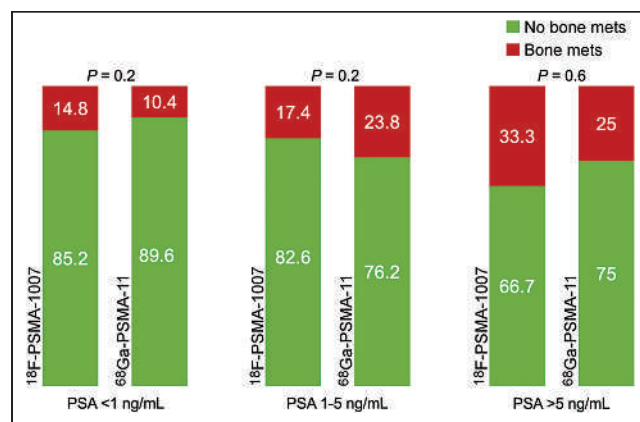


FIGURE 2. Frequency of bone metastases is presented separately for PSA groups and PET tracers (^{18}F -PSMA-1007 or ^{68}Ga -PSMA-11). There was no statistically significant difference of bone metastasis detection between ^{18}F -PSMA-1007 and ^{68}Ga -PSMA-11 among 3 different PSA level groups. mets = metastasis.

Patient Characteristics of the ^{18}F -PSMA-1007 and ^{68}Ga -PSMA-11 PET Intraindividual Comparison Cohort ($n = 17$)

Seventeen prostate cancer patients (mean age, 70.9 y; median duration of disease, 43.7 mo [IQR, 18.6–122.9]) underwent both ^{68}Ga -PSMA-11 and ^{18}F -PSMA-1007 PET due to clinical indication. The median time interval between PET scans was 22 d (IQR 8.0–29.5) days. Most patients were also evaluated with bone scanning and SPECT/CT ($n = 14$) and whole-body MRI ($n = 15$), and 12 patients were evaluated with all 4 modalities. All the patients had PSA recurrence after radical prostatectomy, and 8 of 17 patients also had undergone adjuvant or salvage radiation therapy. Twelve of 17 patients had a PSA level lower than 1, and 5 of 17 had PSA levels between 1 and 5 ng/mL. Further characteristics of the patients are outlined in Table 1.

Local recurrence was detected on ^{18}F -PSMA-1007 in 7 (41.1%) of the patients with a median SUV_{max} of 8.1 (range, 3.48–24.6); 41.1% (7/17) of the patients were rated as pelvic lymph node–positive on ^{18}F -PSMA-1007 PET. The median SUV_{max} and size of the most prominent pelvic lymph node was 10.9 (range, 3.2–37.6) and 0.5 cm (range, 0.4–1.2), respectively. Moreover, 4 patients were staged as extrapelvic lymph node–positive ($n = 2$ inguinal and 2 retroperitoneal; median SUV_{max} = 5.1 [range: 3.4–10.2]) by ^{18}F -PSMA-1007.

Intraindividual Analysis of ^{18}F -PSMA-1007 Bone Uptake by Bone Scanning and ^{68}Ga -PSMA-11 PET/MRI

In ^{18}F -PSMA-1007 PET, 34 suggestive bone uptake findings (in 17 patients) were seen (Supplemental Figs. 1–17 for details on patients). Evaluation of the UBUs and final decisions are summarized in Figure 3. Eleven patients (64.7%) showed unifocal, 4 patients (23.5%) showed oligofocal, and 2 patients (11.8%)

showed multifocal ^{18}F -PSMA-1007 bone uptake without any correlative lesion on CT ($n = 13$ ribs, $n = 10$ pelvis, $n = 4$ vertebrae, $n = 3$ scapula, $n = 2$ sternum, $n = 1$ clavicle, $n = 1$ humerus head). Distribution of the false-positive bone uptake on ^{18}F -PSMA-1007 is presented in Figure 4.

The per-patient true-positive rate was 8.3%, the per-lesion ($n = 28$) true-positive rate was 3.6%; the positive predictive value of bone uptake seen in ^{18}F -PSMA-1007 PET was 8.3% (95% CI, –7%–23.8%) per patient ($n = 12$) and 3.6% (95% CI, –3.3%–10.5%) per lesion ($n = 28$) (only $n = 12$ patients with all modalities, that is, MRI, bone scanning, and ^{68}Ga -PSMA-11 PET, were included).

One lesion with PSMA expression (SUV_{max} 6.7 and 3 on ^{18}F -PSMA-1007 and ^{68}Ga -PSMA-11 PET, respectively) in the left ischiopubical junction without any correlative CT lesion was regarded as true-positive because it was also positive on the bone scan and showed contrast enhancement on T1-weighted images with diffusion restriction on MRI (Fig. 1). The patient with true-positive pelvic bone metastasis had a PSA level of 0.91 ng/mL, PSA doubling time of 1 mo, 83 IU/L of alkaline phosphatase, and 21.5 ug/L of bone-specific alkaline phosphatase.

One lesion with PSMA expression (SUV_{max} 6.1 and 2.3 on ^{18}F -PSMA-1007 and ^{68}Ga -PSMA-11 PET, respectively) without any significant CT correlation was evaluated as enchondroma on MRI (Supplemental Fig. 17). Follow-up examinations of the bone findings are summarized in Figure 3.

All other sites of ^{18}F -PSMA-1007 focal bone uptake were rated as false-positive and likely UBU.

DISCUSSION

In this article, we investigated ^{18}F -PSMA-1007 PET UBU in patients with BCR by ^{68}Ga -PSMA-11 PET, MRI, and bone scanning correlation. In patients with correlative imaging, the positive predictive value of ^{18}F -PSMA-1007 PET for bone metastases was very low. We present a systematic confirmation of ^{18}F -PSMA-1007 PET UBU. However, the higher rate for ^{18}F -PSMA-1007 than for ^{68}Ga -PSMA-11 PET did not translate into more frequent diagnosis of bone metastases if images were read by experienced readers.

PSMA PET has become the reference standard examination of the staging and re-staging of patients with prostate cancer (11,12). It was shown previously that PSMA PET is superior to CT and bone scanning in primary staging of patients with high-risk prostate cancer (12). PSMA-11 was assessed in most prospective trials on PSMA-directed imaging, which led to recent Food and Drug Administration approval. Several other PSMA ligands have been studied. For example, ^{18}F -DCF-Pyl showed high diagnostic accuracy and was also approved by the Food and Drug Administration (13). Head-to-head comparison of ^{18}F -DCF-Pyl and ^{18}F -PSMA-1007 revealed near equal tumor detection in a small group of patients with newly diagnosed prostate cancer (14). In France, the ligand ^{18}F -PSMA-1007 is available through expanded access.

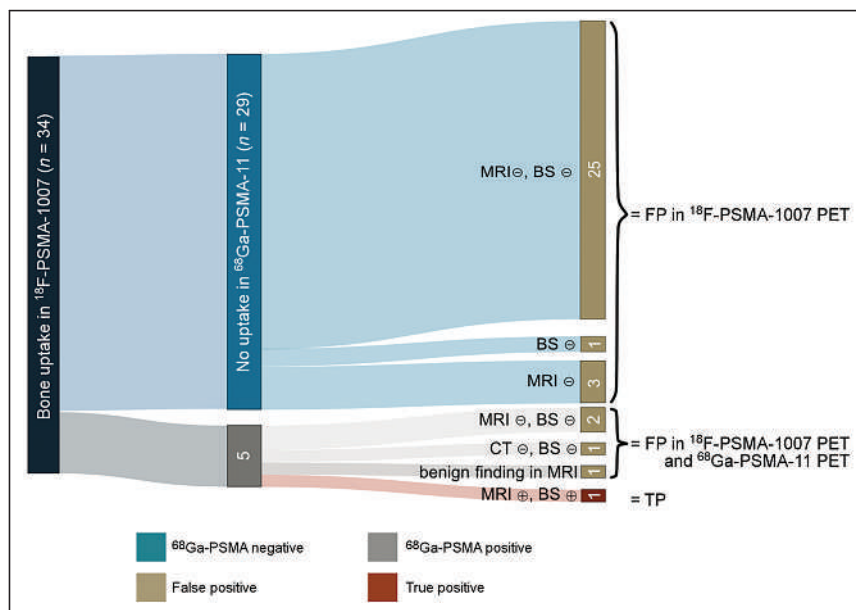


FIGURE 3. Sankey Diagram summarizing the evaluation of UBUs seen on ^{18}F -PSMA-1007 PET. BS = bone scan; FP = false-positive; TP = true-positive; PSMA = prostate-specific membrane antigen; \ominus = no suspicious finding; \oplus = suspicious finding. A total number of 34 UBUs were detected on ^{18}F -PSMA-1007 PET. One lesion was regarded as true-positive (bone metastasis) and 1 lesion was rated as benign because of characteristic MRI findings. Thirty-three UBU were rated as false-positive on ^{18}F -PSMA-1007 PET and 4 instances of false-positive bone uptake were seen on ^{68}Ga -PSMA-11 PET (triple validation was only available in a subcohort).

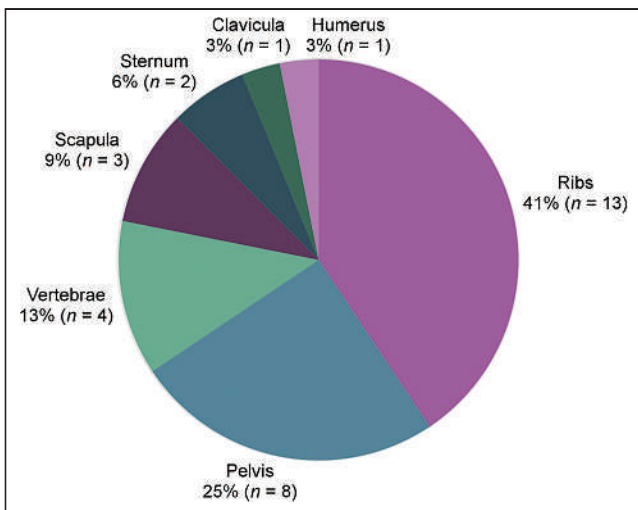


FIGURE 4. Anatomic distribution of UBU seen on ^{18}F -PSMA-1007 PET. Thirty-two instances of bone uptake were seen on ^{18}F -PSMA-1007 PET (in multiple regions) and 4 instances of bone uptake were seen on ^{68}Ga -PSMA-11 (all located in ribs). Most common UBU localizations for ^{18}F -PSMA-1007 were ribs and pelvis.

PSMA ligands show comparable tumor uptake and distribution, but also have distinctive biodistribution features (5). ^{18}F -PSMA-1007 has a liver-dominant excretion, which offers advantages for the assessment of local prostate cancer infiltration (6). Because of lesser ligand accumulation in the bladder, the differentiation between true tracer uptake and urinary background activity is often easier, which facilitates the detection of local recurrence.

The rise of ^{18}F -PSMA-1007 is mainly caused by the ease of cyclotron-based ^{18}F -fluorine production, which enables the syntheses of larger quantities of PSMA ligands compared with ^{68}Ga generators (4). Additionally, ^{18}F -fluorine offers a longer half-life than ^{68}Ga , enabling an optimized patient management (4). Moreover, the lower positron energy of ^{18}F enables a higher spatial resolution and higher signal-to-background ratio than ^{68}Ga (4).

Despite these benefits of ^{18}F -PSMA-1007, it has been reported that the rate of UBU is notably higher than that of ^{68}Ga -PSMA-11 (8,15). In our study, 33 UBUs have been reported for ^{18}F -PSMA-1007 PET and 4 for ^{68}Ga -PSMA-11 (triple validation was available only in a subcohort). This makes the clear delineation of bone metastases challenging in patient cohorts in which bone metastases have a low prevalence, such as in men with biochemically recurrent prostate cancer at low PSA level. The false-positive assessment of bone uptake may potentially lead to inadequate treatment when anticipating that ^{18}F -PSMA-1007 has the same high specificity of other PSMA ligands.

UBU has also been reported in other PSMA-targeting tracers. For example, preliminary reports indicate that rhPSMA-7 also shows UBU (16). The cause of UBU is not yet known. Unconjugated fluorine, activated bone marrow granulocytes (15), and PSMA expression in nonprostate cancer tissue have been discussed previously (17,18).

Interestingly, UBUs of ^{18}F -PSMA-1007 show a distinct distribution pattern. Especially, uptake in the ribs and pelvis can be observed, yet the explanation for this is unknown. Despite a higher UBU rate for ^{18}F -PSMA-1007, the rate of bone metastases was not different in the cohorts of patients imaged with ^{18}F -PSMA-1007

versus ^{68}Ga -PSMA-11 in patients with BCR. For this, all patients scanned in the year before transition to ^{18}F -PSMA-1007 were compared with all patients scanned in the year after the tracer switch. This observation indicates that experienced nuclear medicine physicians can detect the UBU pattern and identify the lesions as unspecific. The distinctive pattern of UBU at the above-described locations may contribute to this observation. Current knowledge on UBU for ^{18}F -PSMA-1007 and radioligands with similar bone pattern should be summarized in a comprehensive reader training before local implementation of these tracers.

This study comes with limitations. First, the comparisons of patient cohorts before and after the change of PSMA tracers (from ^{68}Ga -PSMA-11 to ^{18}F -PSMA-1007) were analyzed retrospectively. Therefore, the analysis might be prone to selection bias and missing information. In the subgroup of patients undergoing MRI, bone scanning, and ^{68}Ga -PSMA-11 as well as ^{18}F -PSMA-1007 PET, the additional PSMA PET and bone scintigraphy were performed only when clinically indicated and after patient approval and the data collection was done retrospectively. Therefore, our cohort with 4 imaging assessments was relatively small, and the results may not be transferable to larger cohorts. Finally, histopathologic confirmation and follow-up imaging were not acquired for this study.

CONSLUSION

In patients with BCR of prostate cancer and PSA $\leq 5\text{ ng/mL}$, focal bone uptake on ^{18}F -PSMA-1007 PET ($\text{SUV} > 4$) was most often false-positive/UBU when compared with ^{68}Ga -PSMA-11 PET, MRI, and bone scanning. ^{18}F -PSMA-1007 false-positive/UBU findings were most commonly located in the ribs and pelvis. Bone uptake in ^{18}F -PSMA-1007 and ^{18}F radioligands with similar bone pattern should therefore be evaluated carefully with regards to the location and clinical context. Most likely due to reader experience, the rate of bone metastases was not higher when clinical cohorts of patients with BCR imaged with ^{68}Ga -PSMA-11 and ^{18}F -PSMA-1007 were compared. To prevent false bone upstaging and consequently incorrect therapy management of the patients, ^{18}F -PSMA-1007 PET should be performed by experienced physicians with knowledge of UBU distribution pattern and characteristics.

DISCLOSURE

Wolfgang P. Fendler reports fees from SOFIE Bioscience (research funding), Janssen (consultant, speakers bureau), Calyx (consultant), Bayer (consultant, speakers bureau, research funding), Parexel (image review), and AAA (speakers bureau) outside of the submitted work. Boris Hadischik has had advisory roles for ABX, AAA/Novartis, Astellas, AstraZeneca, Bayer, Bristol Myers Squibb, Janssen R&D, Lightpoint Medical, Inc., and Pfizer; has received research funding from Astellas, Bristol Myers Squibb, AAA/Novartis, German Research Foundation, Janssen R&D, and Pfizer; and has received compensation for travel from Astellas, AstraZeneca, Bayer and Janssen R&D. Robert Seifert has received research funding from the Else Kröner Fresenius-Stiftung and Boehringer Ingelheim Fonds. No other potential conflict of interest relevant to this article was reported.

ACKNOWLEDGMENT

We thank Andrei Iagaru for his support in revising the article.

KEY POINTS

QUESTION: How clinically relevant is the previously reported occurrence of UBU on ^{18}F -PSMA-1007 PET in prostate cancer?

PERTINENT FINDINGS: Bone uptake seen on ^{18}F -PSMA-1007 PET in patients with BCR, PSA $\leq 5 \text{ ng/mL}$, and SUV > 4 is likely false-positive. Common locations for false positive findings were ribs and pelvis. However, in the clinical routine, the rate of reported bone metastases of patients imaged with ^{18}F -PSMA-1007 or ^{68}Ga -PSMA-11 is comparable, indicating that reporting physicians adapt to the tracer characteristics.

IMPLICATIONS FOR PATIENT CARE: When metastatic disease is suspected in biochemical recurrent prostate cancer, osseous ^{18}F -PSMA-1007 uptake without morphologic correlate has to be carefully assessed.

REFERENCES

- Mullins JK, Feng Z, Trock BJ, Epstein JI, Walsh PC, Loeb S. The impact of anatomical radical retropubic prostatectomy on cancer control: the 30-year anniversary. *J Urol.* 2012;188:2219–2224.
- Phillips R, Shi WY, Deek M, et al. Outcomes of observation vs stereotactic ablative radiation for oligometastatic prostate cancer: The ORIOLE phase 2 randomized clinical trial. *JAMA Oncol.* 2020;6:650–659.
- Cornford P, van den Berg RCN, Briere E, et al. EAU-EANM-ESTRO-ESUR-SIOG guidelines on prostate cancer: part ii—2020 update: treatment of relapsing and metastatic prostate cancer. *Eur Urol.* 2021;79:263–282.
- Rauscher I, Krönke M, König M, et al. Matched-pair comparison of ^{68}Ga -PSMA-11 PET/CT and ^{18}F -PSMA-1007 PET/CT: frequency of pitfalls and detection efficacy in biochemical recurrence after radical prostatectomy. *J Nucl Med.* 2020;61:51–57.
- Eiber M, Herrmann K, Calais J, et al. Prostate cancer molecular imaging standardized evaluation (PROMISE): proposed miTNM classification for the interpretation of PSMA-ligand PET/CT. *J Nucl Med.* 2018;59:469–478.
- Dietlein F, Kobe C, Hohberg M, et al. Intraindividual comparison of ^{18}F -PSMA-1007 with renally excreted PSMA ligands for PSMA PET imaging in patients with relapsed prostate cancer. *J Nucl Med.* 2020;61:729–734.
- Seifert R, Schafiq D, Bogemann M, Weckesser M, Rahbar K. Detection of local relapse of prostate cancer with ^{18}F -PSMA-1007. *Clin Nucl Med.* 2019;44:e394–e395.
- Arnfield EG, Thomas PA, Roberts MJ, et al. Clinical insignificance of [^{18}F]PSMA-1007 avid non-specific bone lesions: a retrospective evaluation. *Eur J Nucl Med Mol Imaging.* 2021;48:4495–4507.
- Pattison DA, Debowski M, Gulhane B, et al. Prospective intra-individual blinded comparison of [^{18}F]PSMA-1007 and [^{68}Ga]Ga-PSMA-11 PET/CT imaging in patients with confirmed prostate cancer. *Eur J Nucl Med Mol Imaging.* 2022;49:763–776.
- Vollnberg B, Alberts I, Genitsch V, Rominger A, Afshar-Oromieh A. Assessment of malignancy and PSMA expression of uncertain bone foci in [^{18}F]PSMA-1007 PET/CT for prostate cancer—a single-centre experience of PET-guided biopsies. *Eur J Nucl Med Mol Imaging.* 2022;49:3910–3916.
- Fendler WP, Calais J, Eiber M, et al. Assessment of ^{68}Ga -PSMA-11 PET accuracy in localizing recurrent prostate cancer: a prospective single-arm clinical trial. *JAMA Oncol.* 2019;5:856–863.
- Hofman MS, Lawrentschuk N, Francis RJ, et al. Prostate-specific membrane antigen PET-CT in patients with high-risk prostate cancer before curative-intent surgery or radiotherapy (proPSMA): a prospective, randomised, multicentre study. *Lancet.* 2020;395:1208–1216.
- Morris MJ, Rowe SP, Gorin MA, et al. Diagnostic performance of ^{18}F -DCFPyL-PET/CT in men with biochemically recurrent prostate cancer: results from the CONDOR phase III, multicenter study. *Clin Cancer Res.* 2021;27:3674–3682.
- Giesel FL, Will L, Lawal I, et al. Intraindividual comparison of ^{18}F -PSMA-1007 and ^{18}F -DCFPyL PET/CT in the prospective evaluation of patients with newly diagnosed prostate carcinoma: a pilot study. *J Nucl Med.* 2018;59:1076–1080.
- Grüning H, Maurer A, Thali Y, et al. Focal unspecific bone uptake on [^{18}F]PSMA-1007 PET: a multicenter retrospective evaluation of the distribution, frequency, and quantitative parameters of a potential pitfall in prostate cancer imaging. *Eur J Nucl Med Mol Imaging.* 2021;48:4483–4494.
- Eiber M, Kroenke M, Wurzer A, et al. ^{18}F -rhPSMA-7 PET for the detection of biochemical recurrence of prostate cancer after radical prostatectomy. *J Nucl Med.* 2020;61:696–701.
- Silver DA, Pellicer I, Fair WR, Heston WD, Cordon-Cardo C. Prostate-specific membrane antigen expression in normal and malignant human tissues. *Clin Cancer Res.* 1997;3:81–85.
- Backhaus P, Noto B, Avramovic N, et al. Targeting PSMA by radioligands in non-prostate disease—current status and future perspectives. *Eur J Nucl Med Mol Imaging.* 2018;45:860–877.

A Pilot Study of ^{68}Ga -PSMA11 and ^{68}Ga -RM2 PET/MRI for Biopsy Guidance in Patients with Suspected Prostate Cancer

Heying Duan¹, Pejman Ghanouni², Bruce Daniel², Jarrett Rosenberg¹, Alan Thong³, Christian Kunder⁴, Carina Mari Aparici¹, Guido A. Davidzon¹, Farshad Moradi¹, Geoffrey A. Sonn³, and Andrei Iagaru¹

¹Division of Nuclear Medicine and Molecular Imaging, Department of Radiology, Stanford University, Stanford, California;

²Division of Body MRI, Department of Radiology, Stanford University, Stanford, California; ³Department of Urology, Stanford University, Stanford, California; and ⁴Department of Pathology, Stanford University, Stanford, California

Targeting of lesions seen on multiparametric MRI (mpMRI) improves prostate cancer (PC) detection at biopsy. However, 20%–65% of highly suspicious lesions on mpMRI (PI-RADS [Prostate Imaging-Reporting and Data System] 4 or 5) are false-positives (FPs), while 5%–10% of clinically significant PC (csPC) are missed. Prostate-specific membrane antigen (PSMA) and gastrin-releasing peptide receptors (GRPRs) are both overexpressed in PC. We therefore aimed to evaluate the potential of ^{68}Ga -PSMA11 and ^{68}Ga -RM2 PET/MRI for biopsy guidance in patients with suspected PC. **Methods:** A highly selective cohort of 13 men, aged 58.0 ± 7.1 y, with suspected PC (persistently high prostate-specific antigen [PSA] and PSA density) but negative or equivocal mpMRI results or negative biopsy were prospectively enrolled to undergo ^{68}Ga -PSMA11 and ^{68}Ga -RM2 PET/MRI. PET/MRI included whole-body and dedicated pelvic imaging after a delay of 20 min. All patients had targeted biopsy of any lesions seen on PET followed by standard 12-core biopsy. The SUV_{max} of suspected PC lesions was collected and compared with gold standard biopsy. **Results:** PSA and PSA density at enrollment were 9.8 ± 6.0 (range, 1.5–25.5) ng/mL and 0.20 ± 0.18 (range, 0.06–0.68) ng/mL², respectively. Standardized systematic biopsy revealed a total of 14 PCs in 8 participants: 7 were csPC and 7 were nonclinically significant PC (ncsPC). ^{68}Ga -PSMA11 identified 25 lesions, of which 11 (44%) were true-positive (TP) (5 csPC). ^{68}Ga -RM2 showed 27 lesions, of which 14 (52%) were TP, identifying all 7 csPC and also 7 ncsPC. There were 17 concordant lesions in 11 patients versus 14 discordant lesions in 7 patients between ^{68}Ga -PSMA11 and ^{68}Ga -RM2 PET. Incongruent lesions had the highest rate of FP (12 FP vs. 2 TP). SUV_{max} was significantly higher for TP than FP lesions in delayed pelvic imaging for ^{68}Ga -PSMA11 (6.49 ± 4.14 vs. 4.05 ± 1.55 , $P = 0.023$) but not for whole-body images, nor for ^{68}Ga -RM2. **Conclusion:** Our results show that ^{68}Ga -PSMA11 and ^{68}Ga -RM2 PET/MRI are feasible for biopsy guidance in suspected PC. Both radiopharmaceuticals detected additional clinically significant cancers not seen on mpMRI in this selective cohort. ^{68}Ga -RM2 PET/MRI identified all csPC confirmed at biopsy.

Key Words: ^{68}Ga -RM2; ^{68}Ga -PSMA11; biopsy guidance; PET/MRI; prostate cancer

J Nucl Med 2023; 64:744–750

DOI: 10.2967/jnumed.122.264448

T

he most common pathway to diagnose prostate cancer (PC) is through prostate needle biopsy driven by high serum prostate-specific antigen (PSA). PSA is a highly sensitive but not very specific marker for PC. Therefore, relying solely on elevated PSA for prostate biopsy leads to unnecessary biopsies with negative results or overdiagnosing of nonclinically significant PC (ncsPC) (1). Transrectal ultrasound (TRUS) is widely available and used to guide prostate biopsies. It consists of systematic sampling of the entire prostate using 12 passes through the rectum or perineum. This standardized procedure can miss cancers located in the prostate anteriorly (2). Multiple trials showed that multiparametric MRI (mpMRI)-guided prostate biopsy had higher accuracy in detecting clinically significant PC (csPC), that is, Gleason score $\geq 3 + 4$, than TRUS (3–5). However, 20%–65% of suspicious lesions on mpMRI (PI-RADS [Prostate Imaging-Reporting and Data System] 4 or 5) are false-positives (FPs), while 5%–10% of csPC may be missed by mpMRI (6–10). Like TRUS, mpMRI also has blind spots in the transition and central zone of the prostate where PC lesions may be overlooked (11).

PET combined with MRI and prostate-specific membrane antigen (PSMA) targeting radiopharmaceuticals improved PC imaging significantly. However, PSMA-targeted compounds have certain limitations related to expression in other normal tissues and pathologies, while up to 10% of PC are PSMA-negative (12,13). ^{68}Ga -RM2 is a PET radiopharmaceutical that targets gastrin-releasing peptide receptors (GRPRs), which are highly overexpressed in PC, while benign prostate tissues show lower expression (14). GRPR expression is particularly high at earlier stages of prostatic carcinogenesis, making it an interesting target for initial staging (15,16). PSMA- and GRPR-targeting radiotracers have been reported as being complementary (17,18). ^{68}Ga -PSMA11 PET/CT-targeted prostate biopsy showed a high accuracy of 80.6% (19) whereas ^{68}Ga -PSMA11 PET/MRI, with its high soft-tissue contrast and various functional sequences, performed better, with an accuracy of 90% (20).

In this prospective pilot study, we aimed to evaluate the potential of combined ^{68}Ga -PSMA11 and ^{68}Ga -RM2 PET/MRI for biopsy guidance in a highly selective patient cohort who had prior negative or equivocal mpMRI (PI-RADS 1–3) results or prior negative prostate biopsy but persistent elevated PSA and PSA density, therefore considered highly suspicious of having PC. We also assessed the potential for detection of csPC.

MATERIALS AND METHODS

Participants

Participants with negative or equivocal mpMRI (PI-RADS 1–3) results or prior negative prostate biopsy with clinical suspicion for PC,

Received May 24, 2022; revision accepted Nov. 1, 2022.

For correspondence or reprints, contact Andrei Iagaru (aiagaru@stanford.edu).

Published online Nov. 17, 2022.

COPYRIGHT © 2023 by the Society of Nuclear Medicine and Molecular Imaging.

defined as persistently elevated and rising PSA and PSA density, were prospectively enrolled and underwent either ^{68}Ga -PSMA11 PET/MRI first followed by ^{68}Ga -RM2 PET/MRI within 2 wk or vice versa. This prospective, open-label, Health Insurance Portability and Accountability Act-compliant study was approved by the local institutional review board and was registered on ClinicalTrials.gov (NCT03809078). All patients provided written informed consent. The intended total number of participants was 20; however, the Food and Drug Administration approval for ^{68}Ga -PSMA11 during the timeline of the protocol made funding and completion of planned enrollment unfeasible.

Scanning Protocols

PET/MRI. Imaging was performed using a 3T time-of-flight-enabled PET/MRI scanner (SIGNA PET/MRI; GE Healthcare), as previously described (17,21). Image acquisition started at 46 ± 3 (range, 40–51) min after injection of 176 ± 39 (range, 81–208) MBq of ^{68}Ga -PSMA11 and at 45 ± 3 (range, 40–49) min after injection of 139 ± 9 (range, 116–155) MBq of ^{68}Ga -RM2. Simultaneous PET/MRI was acquired from vertex to midthigh with an acquisition time of 4 min per bed position. Additional dedicated 20-min pelvic images were acquired after a delay of 26 ± 6 (range, 19–41) min for ^{68}Ga -PSMA11 and 25 ± 6 (range, 13–38) min for ^{68}Ga -RM2. The PET/MRI scans were acquired 7 ± 3 (range, 2–12) d apart. Synthesis of ^{68}Ga -PSMA11 and ^{68}Ga -RM2 was previously described (17).

mpMRI. mpMRI was performed as routine clinical scanning before prostate biopsy using a 3T scanner (MR750; GE Healthcare) with an external 32-channel body array coil. The imaging protocol consisted of T2-weighted imaging, diffusion-weighted imaging, and dynamic contrast-enhanced imaging sequences. Diffusion-weighted imaging was obtained using a combination of b-values ($b50/800/1,400/\text{calculated } 2,000 \text{ s/mm}^2$). Detailed acquisition parameters were previously described (22).

Image Analysis

Two nuclear medicine physicians reviewed and analyzed PET images independently and in random order. Any focal uptake of ^{68}Ga -RM2 or ^{68}Ga -PSMA11 with an SUV_{max} above adjacent prostate background and not associated with physiologic accumulation was recorded as suspicious for PC. A region of interest was drawn over suspected lesions to measure SUV_{max} and SUV_{peak} and served as an identification marker. SUV_{peak} is defined as the average SUV within a small, fixed-size region of interest (1 cm^3) (23). The MR portion was used for anatomic and lesion (if any were seen) correlation. For segment-based sensitivity and specificity calculation, the prostate was divided into the same 12 segments as for systematic prostate biopsy on MR images.

mpMRI was analyzed using the PI-RADS criteria, version 2 (24). Lesions with a PI-RADS score ≥ 3 were recorded. A PI-RADS score of 3 was considered equivocal, PI-RADS of 4 likely, and PI-RADS 5 highly likely for PC.

Prostate Biopsy. Prostate biopsies were performed transrectally under peripheral nerve block anesthesia by a single urologist. ^{68}Ga -RM2 and ^{68}Ga -PSMA PET/MRI and mpMRI were reviewed by the urologist, radiologist, and nuclear medicine physician. Any PET-positive lesions were annotated on the correlating mpMRI. The transrectal ultrasound probe (Noblus; Hitachi Aloka) was attached to the robotic arm of a prostate fusion biopsy system (Eigen/Artemis), which enabled registration and fusion of mpMRI with real-time ultrasound to create a 3-dimensional model of the prostate with delineated annotations. PET-guided biopsy included a maximum of 3 cores per target lesion. Next, systematic 12-core biopsy was obtained consisting of 1 core through the apex, mid, and base regions, both medially and laterally, from left and right prostate lobes (25,26).

Statistical Analysis

Statistical analysis was performed using Stata 16.1 (StataCorp LP) and R version 4.1.1 (r-project.org). Continuous data are presented as

median \pm SD, minimum (min)–maximum (max) values. Sensitivity and specificity are given in percentage with 95% CI. A Student *t* test was used to assess significance between SUV of whole-body and delayed pelvic imaging. Comparison between biopsy-positive and biopsy-negative prostate segments for PI-RADS and SUV_{max} was done by Wilcoxon rank-sum testing adjusted for clustering.

RESULTS

Thirteen men, aged 58.0 ± 7.1 y (range, 41.0–69.0 y), with suspected PC were prospectively enrolled. PSA and PSA density at the time of PET/MRI were 9.8 ± 6.0 (range, 1.5–25.5) ng/mL and 0.20 ± 0.18 (range, 0.06–0.68) ng/mL², respectively. Prostate biopsy before imaging was available in 12 of 13 patients of whom 9 were negative and 3 showed Gleason 3 + 4 cancer (negative mpMRI). All patients' characteristics are summarized in Table 1.

mpMRI

All participants underwent routine prebiopsy mpMRI: 5 participants had a negative scan result and 10 lesions were seen in 8 participants. There were 3 PI-RADS 3 (equivocal), 6 PI-RADS 4, and 1 PI-RADS 5 lesions. At study enrollment, 4 of the PI-RADS 4 lesions had a negative prostate biopsy result and 2 PI-RADS 4 and the 1 PI-RADS 5 lesion were equivocal on prior mpMRI from outside institutions (Table 1). Biopsy confirmed 3 true-negative (TN) participants and 6 true-positive (TP) lesions, of which all were csPC, and 4 FP lesions. The highest number of false-negatives (FNs) was seen in mpMRI with 9; however, only 2 FNs were csPC. Sensitivity and specificity were 30% (95% CI, 5, 77%) and 95% (95% CI, 85, 98%), respectively.

Prostate Biopsy

Prostate biopsies were performed 19 ± 12 (range, 2–38) d after PET/MRI. A median of 8 ± 3 (range, 2–13) additional PET-guided biopsies were performed in addition to systematic 12-core template. One patient refused to undergo systematic biopsy and had PET-guided biopsy only. Histopathology showed PC in 8 of 13 (61.5%) patients, with a total of 14 PC lesions (multifocal disease in 6 patients), of which 7 (50%) were csPC. Standard template prostate biopsy found 6 of 14 (42.9%) PC, of which 2 were csPC. PET-guided biopsy identified 8 of 14 (57.1%) PC lesions, of which 5 were csPC. Standard template biopsy was negative in 1 patient, for whom both ^{68}Ga -RM2 and ^{68}Ga -PSMA PET-guided biopsy showed Gleason 3 + 4 cancer.

^{68}Ga -PSMA11 PET/MRI

^{68}Ga -PSMA11 PET/MRI found 25 intraprostatic lesions in the 13 participants (Fig. 1). SUV_{max} decreased significantly from the whole-body to the dedicated pelvic images, but all lesions were identified at both time points. Biopsy confirmed 11 PC lesions, of which 5 were csPC, 14 FP, and 2 FN (both csPC). The SUV_{max} of TP lesions was significantly higher than FP on the delayed pelvic but not on the whole-body images. No other statistically significant differences were observed between SUV_{max} and SUV_{peak} for ^{68}Ga -PSMA11 PET/MRI, including comparison of csPC and ncsPC. SUV measurements are summarized in Table 2. Sensitivity and specificity were 63% (95% CI, 19, 92%) and 83% (95% CI, 73, 94%), respectively.

^{68}Ga -RM2 PET/MRI

^{68}Ga -RM2 PET/MRI showed 27 intraprostatic lesions in 12 of 13 participants. The participant with a negative ^{68}Ga -RM2 PET result had negative prostate biopsies and was considered TN as

TABLE 1
Patients' Characteristics

Characteristic	Data (n = 13)
Age (y)	58.0 ± 7.1 (41.0–69.0)
PSA (ng/mL)	9.8 ± 6.0 (1.5–25.5)
PSA density (ng/mL ²)	0.20 ± 0.18 (0.06–0.68)
Prior biopsy (n)	12/13
	Negative: 9/13
	Gleason score 3 + 4: 3/13
Prior mpMRI (n)	13/13
	Negative: 6/13
	PI-RADS 3: 3/13
	PI-RADS 4: 4/13
	PI-RADS 5: 0/13
⁶⁸ Ga-PSMA11	
Injected activity (MBq)	176 ± 39 (81–208)
Uptake time (min)	46 ± 3 (40–51)
Delay time to pelvic PET/MRI (min)	26 ± 6 (19–41)
Time between scans (d)	7 ± 3 (2–12)
⁶⁸ Ga-RM2	
Injected activity (MBq)	139 ± 9 (116–155)
Uptake time (min)	45 ± 3 (40–49)
Delay time to pelvic PET/MRI (min)	25 ± 6 (13–38)
Time between scans (d)	7 ± 3 (2–12)

Numeric factors are expressed as median ± SD, with range in parentheses.

cancer of unknown primary was found (FP in ⁶⁸Ga-PSMA11 PET). No statistically significant changes were found between SUV_{max} and SUV_{peak} from whole-body and delayed pelvic images. ⁶⁸Ga-RM2 PET detected all lesions identified on standard and PET-guided biopsy (14 TP, of which 7 were csPC and 7 ncsPC). There were 13 FP on ⁶⁸Ga-RM2, of which 12 were the same lesions as on ⁶⁸Ga-PSMA11. When the SUV_{max} and SUV_{peak} of TP and FP lesions were compared, no statistically significant changes were

found on whole-body or delayed pelvic images (Table 2). Sensitivity was 83% (95% CI, 40, 97%), whereas specificity was 67% (95% CI, 40, 86%).

Comparison Between ⁶⁸Ga-PSMA11 and ⁶⁸Ga-RM2

Concordance between both radiopharmaceuticals was seen in 17 lesions in 11 participants. Of these, 11 lesions were PC, with 6 being csPC (Supplemental Fig. 1; supplemental materials are available at <http://jnm.snmjournals.org>). Noncongruent uptake was observed in 14 lesions in 7 patients. Among these, 3 were PC with 1 csPC seen on ⁶⁸Ga-RM2 (Supplemental Fig. 2), whereas 10 were FP (⁶⁸Ga-PSMA11 and ⁶⁸Ga-RM2 each had 5 FP). In 3 patients, a difference in intensity of tracer uptake was observed (Fig. 2). Table 3 gives a semiquantitative measurement (target tumor-to-normal prostate ratio) of lesions for ⁶⁸Ga-PSMA11 and ⁶⁸Ga-RM2 PET.

No lymph node or other distant metastases were identified on ⁶⁸Ga-PSMA11 or ⁶⁸Ga-RM2 PET/MRI.

DISCUSSION

In this pilot study, we evaluated the utility of ⁶⁸Ga-PSMA11 and ⁶⁸Ga-RM2 PET/MRI for prostate biopsy guidance in men with suspected PC but negative or equivocal mpMRI results or negative prostate biopsy. In this small cohort, PET-guided biopsy detected more PC lesions than systematic 12-core biopsy, which was not surprising given the plethora of work showing the superiority of mpMRI-guided over standard biopsy (3,4,8). When compared with

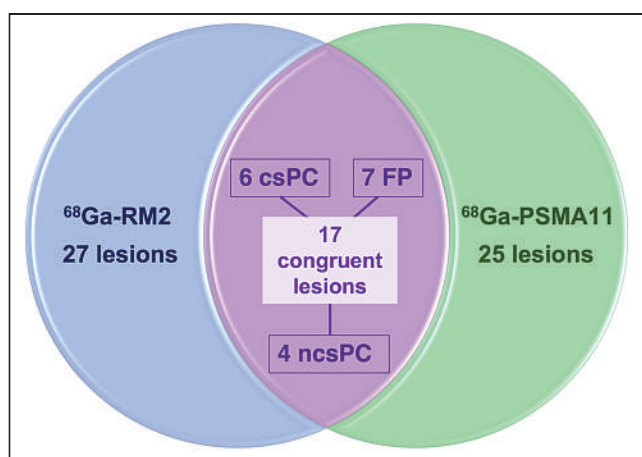


FIGURE 1. Venn diagram of ⁶⁸Ga-PSMA11 and ⁶⁸Ga-RM2 positivity with their congruent lesional uptake compared with biopsy results.

TABLE 2
 SUV_{max} and SUV_{peak} of All PET-positive, True-Positive, and False-Positive Lesions, Stratified to Gleason Score at Whole-Body and Delayed Pelvic Imaging for
⁶⁸Ga-PSMA11 and ⁶⁸Ga-RM2

Lesion	⁶⁸ Ga-PSMA11			⁶⁸ Ga-RM2		
	Whole-body PET/MRI	Pelvic PET/MRI	Whole-body PET/MRI	Pelvic PET/MRI	Whole-body PET/MRI	Pelvic PET/MRI
All						
SUV _{max}	4.56 ± 4.03 (3.20–22.46)	4.42 ± 3.27 (2.87–17.94)	9.10 ± 7.95 (4.31–40.15)	7.93 ± 9.49 (3.57–44.08)		
P value	0.007	0.007	0.244	0.244		
SUV _{peak}	3.83 ± 2.03 (2.54–10.88)	3.60 ± 2.12 (2.27–10.80)	6.42 ± 5.68 (3.94–29.01)	6.06 ± 6.36 (3.00–31.95)		
P value	0.072	0.072	0.163	0.163		
True-positive SUV _{max}	6.57 ± 5.36 (3.98–22.46)	6.49 ± 4.14 (3.34–17.94)	8.64 ± 10.36 (4.31–40.15)	6.80 ± 12.34 (3.57–44.08)		
P value	0.067	0.023	0.452	0.532		
False-positive SUV _{max}	4.54 ± 1.54 (3.20–7.99)	4.05 ± 1.55 (2.87–9.11)	9.69 ± 3.54 (5.18–16.99)	8.92 ± 4.50 (4.49–19.26)		
True-positive SUV _{peak}	4.35 ± 2.57 (2.84–10.88)	4.82 ± 2.65 (2.50–10.80)	6.11 ± 7.10 (3.94–29.01)	5.80 ± 8.14 (3.00–31.95)		
P value	0.086	0.085	0.647	0.651		
False-positive SUV _{peak}	3.52 ± 1.15 (2.54–5.80)	3.43 ± 1.74 (2.27–9.56)	7.34 ± 3.48 (4.22–16.99)	6.92 ± 3.46 (3.94–15.71)		
ncsPC SUV _{max}	5.42 ± 1.22 (4.06–7.66)	5.24 ± 1.87 (3.34–8.68)	8.16 ± 8.87 (5.96–34.18)	5.63 ± 12.67 (4.83–44.08)		
P value	0.120	0.116	0.540	0.740		
cSPC SUV _{max}	6.96 ± 6.77 (3.98–22.46)	6.81 ± 4.90 (4.70–17.94)	10.56 ± 11.73 (4.31–40.15)	8.86 ± 11.74 (3.57–38.72)		
ncsPC SUV _{peak}	3.99 ± 1.37 (2.84–6.05)	3.78 ± 1.86 (2.50–6.78)	5.79 ± 7.67 (4.75–29.01)	4.74 ± 8.96 (4.03–31.95)		
P value	0.167	0.167	0.908	0.954		
cSPC SUV _{peak}	4.35 ± 3.06 (3.95–10.88)	4.82 ± 2.87 (4.18–10.80)	7.63 ± 6.26 (3.94–22.87)	6.10 ± 6.89 (3.00–23.83)		

Numeric factors are expressed as median ± SD, with range in parentheses.

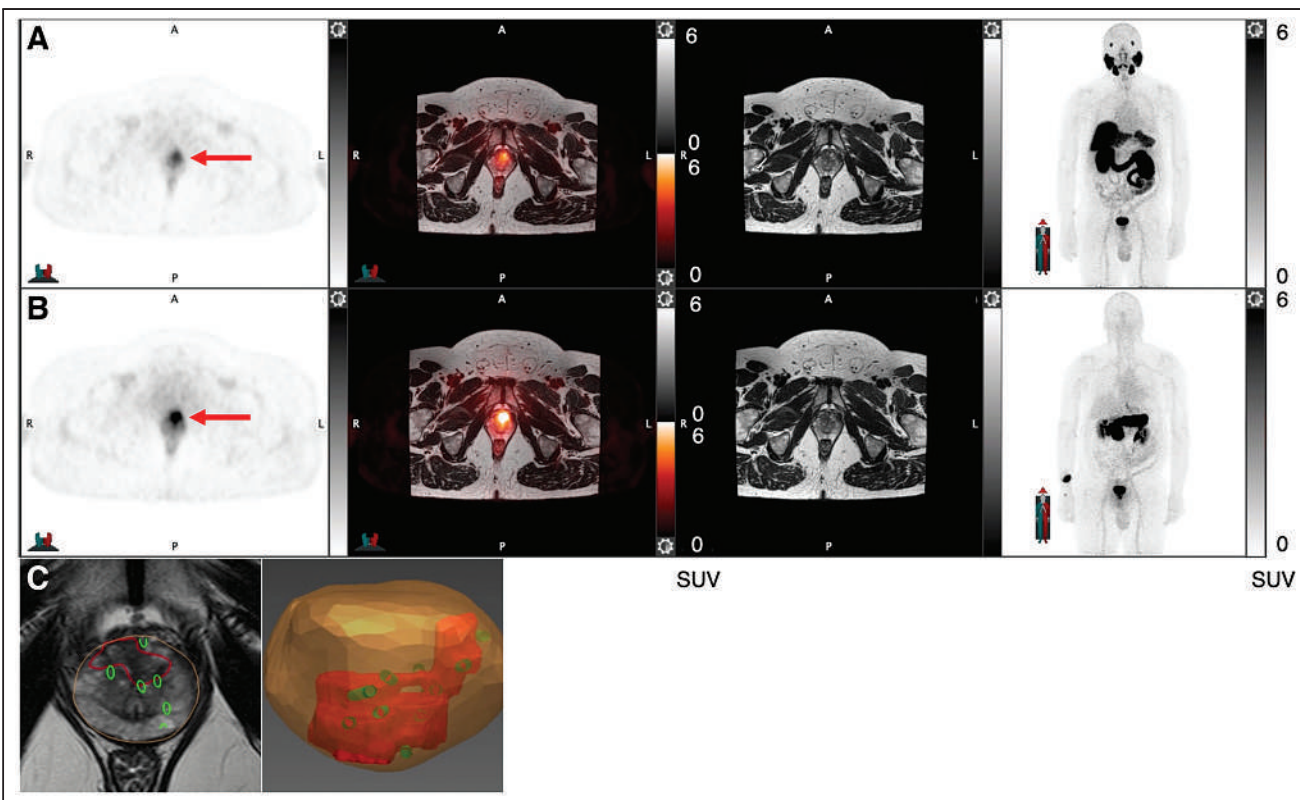


FIGURE 2. A 58-y-old man presenting with PSA of 12.8 ng/mL and PSA density of 0.41 ng/mL². (A and B) ⁶⁸Ga-RM2 (B, axial PET [left-most image], fused PET/MRI [second image], MRI [third image], and maximum-intensity-projection images [right-most image]) shows intense uptake in anterior prostate (red arrows), which is less pronounced on ⁶⁸Ga-PSMA11 PET/MRI (A). PET-guided biopsy demonstrated Gleason 3 + 4 prostate cancer. (C) Coregistration of biopsy needle tracks are shown in green; index tumor is outlined in red on mpMRI as well as on 3-dimensional-rendered image. A = anterior; P = posterior.

mpMRI, PET-guided biopsy not only found more TP lesions, but also more importantly, more csPC.

A recently published study explored ⁶⁸Ga-PSMA617 and ⁶⁸Ga-RM26 PET/CT for biopsy guidance in 112 men with suspected PC (27). Of these participants, 35% had csPC and 4% ncsPC. Dual-tracer PET/CT-guided biopsy showed the highest detection rate without misdiagnosis of csPC (77%), followed by ⁶⁸Ga-PSMA617 (70%), ⁶⁸Ga-RM26 (56%), and mpMRI (36%). Despite the small number of participants and selective cohort, we identified a higher percentage of csPC (7/14 lesions, 50%) and ncsPC (7/14 lesions, 50%). The overall high sensitivity for PET-guided biopsy seen in Qiu et al. (27) was comparable with our study; however, we observed a higher sensitivity for ⁶⁸Ga-RM2 (83%), leading to the detection of all biopsy-verified csPC and ncsPC with an FP rate similar to that of ⁶⁸Ga-PSMA11. This might suggest that this specific subgroup of men with negative anatomic imaging despite persistent elevated PSA may have a different tumor biology. PSMA and GRPR expression have been reported as complementary (17,18), with GRPR showing particular overexpression in earlier stages of PC (15). Therefore, GRPR-targeting radiopharmaceuticals may be a suitable alternative for biopsy guidance in men with suspected PC.

⁶⁸Ga-PSMA11 PET/MRI (sensitivity, 96%; specificity, 81%) showed a better performance than PET/CT (sensitivity, 100%; specificity, 68%) for guiding prostate biopsy (19,20). In this study, sensitivity for ⁶⁸Ga-PSMA11 was slightly less at 63%, which might be related to the specific subgroup of patients; however, specificity was higher at 83%. These overall high rates for PET/MRI are certainly attributable to the high soft-tissue contrast of MRI but also related to

the vast experience in MRI-fusion biopsy. The opportunity of switching from MRI to PET fusion for targeted prostate biopsy enables improved detection rates of csPC, especially in cases for which mpMRI is inconclusive, as seen in this present study. As PET/MRI scanners are not ubiquitously available, software fusion of MRI and PET has been shown to be feasible and demonstrated increased sensitivity of index lesion identification (28).

The PRIMARY trial investigated the added value of combining ⁶⁸Ga-PSMA11 PET/CT with mpMRI for detecting csPC in men undergoing initial biopsy for suspected PC (29,30). Interestingly, all men with an SUV_{max} of ≥ 12 on ⁶⁸Ga-PSMA11 PET had csPC at biopsy, independent of mpMRI results. In cases of PI-RADS ≥ 4 , an SUV_{max} of ≥ 9 showed 100% specificity and positive predictive value in csPC detection. In our study, the median SUV_{max} for csPC on ⁶⁸Ga-PSMA11 PET was 7. This again could indicate a different tumor biology and expression pattern of PSMA in this specific subgroup of patients or differences in imaging technique.

The SUV_{max} from ⁶⁸Ga-RM2 PET was higher than that from ⁶⁸Ga-PSMA11, but so was the SD for csPC and ncsPC, resulting in no significant differences. Despite earlier reports that GRPR expression is low to none in benign prostatic hyperplasia (BPH) (14,15), we observed uptake in BPH nodules.

We chose to additionally measure SUV_{peak} because SUV_{max} is a single pixel value that might be affected by noise (31,32). SUV_{peak} may be a more robust quantitative measure because of its larger volume (23,33). We did not find any significant differences in SUV_{peak} between TP and FP lesions or csPC and ncsPC for ⁶⁸Ga-PSMA11 or ⁶⁸Ga-RM2. SUV_{peak} might be a more suitable measure

TABLE 3

SUV_{max} and SUV_{peak} of All PET-Positive Lesions, Normal Prostate Tissue, and TNR for Whole-Body and Delayed Pelvic Imaging for ⁶⁸Ga-PSMA11 and ⁶⁸Ga-RM2

PET/MRI	Prostate tumor	SUV _{max}	Normal prostate	TNR	Prostate tumor	SUV _{peak}	Normal prostate	TNR
⁶⁸Ga-PSMA11								
Whole-body PET/MRI	4.56 ± 4.03 (3.20–22.46)	2.46 ± 0.45 (1.91–3.57)	2.23 ± 2.81 (1.51–11.76)	3.83 ± 2.03 (2.54–10.88)	2.61 ± 0.47 (2.01–3.63)	1.48 ± 1.21 (0.99–5.41)		
Pelvic PET/MRI	4.42 ± 3.27 (2.87–17.94)	2.21 ± 0.29 (1.88–2.91)	2.39 ± 1.96 (1.36–8.50)	3.60 ± 2.12 (2.27–10.80)	2.37 ± 0.43 (1.62–3.27)	1.82 ± 1.52 (1.12–6.67)		
⁶⁸Ga-RM2								
Whole-body PET/MRI	9.10 ± 7.95 (4.31–40.15)	3.25 ± 0.86 (2.10–5.66)	2.77 ± 4.87 (1.32–19.12)	6.42 ± 5.68 (3.94–29.01)	3.26 ± 0.73 (2.54–5.29)	2.36 ± 2.49 (1.21–8.87)		
Pelvic PET/MRI	7.93 ± 9.49 (3.57–44.08)	3.00 ± 0.78 (2.24–5.16)	2.52 ± 4.96 (1.59–17.49)	6.06 ± 6.36 (3.00–31.95)	3.34 ± 0.60 (2.47–4.46)	2.19 ± 3.33 (1.20–12.43)		

Numeric factors are expressed as median ± SD, with range in parentheses.

TNR = tumor-to-normal-tissue ratio.

for assessment of treatment response than single-time-point measurements (34).

Prostate biopsy bears an array of risks such as hematuria, rectal bleeding, infection, and pain (35,36). It is critical to identify the patients who will benefit from biopsy and distinguish csPC from indolent cancers. An area of unmet need are men whose mpMRI results are negative or equivocal but who have a high suspicion for PC. These patients usually undergo serial imaging procedures, even multiple biopsies to find the source of their elevated PSA. Our results indicate that a combined approach of ⁶⁸Ga-RM2 and ⁶⁸Ga-PSMA11 PET/MRI has high sensitivity and specificity in localizing csPC and may help the urologist making subsequent treatment decisions. The higher upfront cost of such an approach may be cost-effective when compared with subsequent costs in its absence. This needs to be validated in larger studies.

The limitations of this study include the small number of participants, although this is common for pilot studies, and the highly selective patient cohort. However, the latter may be a positive differentiator for the use of PET/MRI in this clinical scenario. The sequence of biopsies performed—PET-guided prostate biopsy first, followed by standard template biopsy—might have affected the results of standard template biopsy due to swelling, bleeding, and tissue distortion.

CONCLUSION

⁶⁸Ga-PSMA11 and ⁶⁸Ga-RM2 PET/MRI are feasible for biopsy guidance in men with suspected PC despite negative or equivocal mpMRI results. Both radiopharmaceuticals detected additional csPC not seen on mpMRI. ⁶⁸Ga-RM2 identified all csPC and ncsPC confirmed at biopsy. The incongruent uptake pattern for ⁶⁸Ga-PSMA11 and ⁶⁸Ga-RM2 reflect their different biologic targets and expression. Larger studies are needed to shed light on their respective expression pattern at various stages of PC as well as to guide future clinical use.

DISCLOSURE

The study was partially supported by GE Healthcare. No other potential conflict of interest relevant to this article was reported.

KEY POINTS

QUESTION: Are ⁶⁸Ga-PSMA11 and ⁶⁸Ga-RM2 PET/MRI useful tools for guiding prostate biopsies in patients with suspected PC despite negative or equivocal mpMRI results?

PERTINENT FINDINGS: ⁶⁸Ga-PSMA11– and ⁶⁸Ga-RM2–guided prostate biopsy led to the detection of additional csPC not seen on mpMRI in this selective cohort of patients with prior negative or equivocal mpMRI results or negative prostate biopsy but persistently elevated PSA and PSA density. ⁶⁸Ga-RM2 PET/MRI accurately identified all csPC and ncsPC confirmed at biopsy.

IMPLICATIONS FOR PATIENT CARE: ⁶⁸Ga-PSMA11– and ⁶⁸Ga-RM2–guided prostate biopsy help detecting csPC and might therefore avoid unnecessary biopsies and associated risks.

REFERENCES

- Brooks JD. Managing localized prostate cancer in the era of prostate-specific antigen screening. *Cancer*. 2013;119:3906–3909.

2. Mottet N, Bellmunt J, Bolla M, et al. EAU-ESTRO-SIOG guidelines on prostate cancer. part 1: screening, diagnosis, and local treatment with curative intent. *Eur Urol*. 2017;71:618–629.
3. Ahmed HU, El-Shater Bosaily A, Brown LC, et al. Diagnostic accuracy of multiparametric MRI and TRUS biopsy in prostate cancer (PROMIS): a paired validation confirmatory study. *Lancet*. 2017;389:815–822.
4. Kasivisvanathan V, Rannikko AS, Borghi M, et al. MRI-targeted or standard biopsy for prostate-cancer diagnosis. *N Engl J Med*. 2018;378:1767–1777.
5. Ahdoot M, Wilbur AR, Reese SE, et al. MRI-targeted, systematic, and combined biopsy for prostate cancer diagnosis. *N Engl J Med*. 2020;382:917–928.
6. Le JD, Tan N, Shkolyar E, et al. Multifocality and prostate cancer detection by multiparametric magnetic resonance imaging: correlation with whole-mount histopathology. *Eur Urol*. 2015;67:569–576.
7. Rouvière O, Puech P, Renard-Penna R, et al. Use of prostate systematic and targeted biopsy on the basis of multiparametric MRI in biopsy-naïve patients (MRI-FIRST): a prospective, multicentre, paired diagnostic study. *Lancet Oncol*. 2019; 20:100–109.
8. van der Leest M, Cornel E, Israel B, et al. Head-to-head comparison of transrectal ultrasound-guided prostate biopsy versus multiparametric prostate resonance imaging with subsequent magnetic resonance-guided biopsy in biopsy-naïve men with elevated prostate-specific antigen: a large prospective multicenter clinical study. *Eur Urol*. 2019;75:570–578.
9. Truong M, Hollenberg G, Weinberg E, Messing EM, Miyamoto H, Frye TP. Impact of Gleason subtype on prostate cancer detection using multiparametric magnetic resonance imaging: correlation with final histopathology. *J Urol*. 2017; 198:316–321.
10. Johnson DC, Raman SS, Mirak SA, et al. Detection of individual prostate cancer foci via multiparametric magnetic resonance imaging. *Eur Urol*. 2019;75:712–720.
11. Helfrich O, Puech P, Betrouni N, et al. Quantified analysis of histological components and architectural patterns of Gleason grades in apparent diffusion coefficient restricted areas upon diffusion weighted MRI for peripheral or transition zone cancer locations. *J Magn Reson Imaging*. 2017;46:1786–1796.
12. Minner S, Wittmer C, Graefen M, et al. High level PSMA expression is associated with early PSA recurrence in surgically treated prostate cancer. *Prostate*. 2011;71: 281–288.
13. Maurer T, Gschwend JE, Rauscher I, et al. Diagnostic efficacy of ^{68}Ga -PSMA positron emission tomography compared to conventional imaging for lymph node staging of 130 consecutive patients with intermediate to high risk prostate cancer. *J Urol*. 2016;195:1436–1443.
14. Accardo A, Galli F, Mansi R, et al. Pre-clinical evaluation of eight DOTA coupled gastrin-releasing peptide receptor (GRP-R) ligands for in vivo targeting of receptor-expressing tumors. *EJNMMI Res*. 2016;6:17.
15. Körner M, Waser B, Rehmann R, Reubi JC. Early over-expression of GRP receptors in prostatic carcinogenesis. *Prostate*. 2014;74:217–224.
16. Duan H, Baratto L, Fan RE, et al. Correlation of ^{68}Ga -RM2 PET with post-surgery histopathology findings in patients with newly diagnosed intermediate- or high-risk prostate cancer. *J Nucl Med*. 2022;63:1829–1835.
17. Minamimoto R, Sonni I, Hancock S, et al. Prospective evaluation of ^{68}Ga -RM2 PET/MRI in patients with biochemical recurrence of prostate cancer and negative findings on conventional imaging. *J Nucl Med*. 2018;59:803–808.
18. Touijer KA, Michaud L, Alvarez HAV, et al. Prospective study of the radiolabeled GRPR antagonist BAY86-7548 for positron emission tomography/computed tomography imaging of newly diagnosed prostate cancer. *Eur Urol Oncol*. 2019;2: 166–173.
19. Liu C, Liu T, Zhang Z, et al. ^{68}Ga -PSMA PET/CT combined with PET/ultrasound-guided prostate biopsy can diagnose clinically significant prostate cancer in men with previous negative biopsy results. *J Nucl Med*. 2020;61:1314–1319.
20. Ferraro DA, Becker AS, Kranzbuhler B, et al. Diagnostic performance of ^{68}Ga -PSMA-11 PET/MRI-guided biopsy in patients with suspected prostate cancer: a prospective single-center study. *Eur J Nucl Med Mol Imaging*. 2021;48:3315–3324.
21. Minamimoto R, Hancock S, Schneider B, et al. Pilot comparison of ^{68}Ga -RM2 PET and ^{68}Ga -PSMA-11 PET in patients with biochemically recurrent prostate cancer. *J Nucl Med*. 2016;57:557–562.
22. Sonn GA, Fan RE, Ghanouni P, et al. Prostate magnetic resonance imaging interpretation varies substantially across radiologists. *Eur Urol Focus*. 2019;5:592–599.
23. Wahl RL, Jacene H, Kasamon Y, Lodge MA. From RECIST to PERCIST: evolving considerations for PET response criteria in solid tumors. *J Nucl Med*. 2009; 50(suppl 1):122S–150S.
24. Weinreb JC, Barentsz JO, Choyke PL, et al. PI-RADS prostate imaging: reporting and data system—2015, version 2. *Eur Urol*. 2016;69:16–40.
25. Heidenreich A, Bastian PJ, Bellmunt J, et al. EAU guidelines on prostate cancer. part 1: screening, diagnosis, and local treatment with curative intent-update 2013. *Eur Urol*. 2014;65:124–137.
26. Wolf AM, Wender RC, Etzioni RB, et al. American Cancer Society guideline for the early detection of prostate cancer: update 2010. *CA Cancer J Clin*. 2010;60:70–98.
27. Qiu DX, Li J, Zhang JW, et al. Dual-tracer PET/CT-targeted, mpMRI-targeted, systematic biopsy, and combined biopsy for the diagnosis of prostate cancer: a pilot study. *Eur J Nucl Med Mol Imaging*. 2022;49:2821–2832.
28. Arslan A, Karaarslan E, Guner AL, et al. Comparison of MRI, PSMA PET/CT, and fusion PSMA PET/MRI for detection of clinically significant prostate cancer. *J Comput Assist Tomogr*. 2021;45:210–217.
29. Amin A, Blazevski A, Thompson J, et al. Protocol for the PRIMARY clinical trial, a prospective, multicentre, cross-sectional study of the additive diagnostic value of gallium-68 prostate-specific membrane antigen positron-emission tomography/computed tomography to multiparametric magnetic resonance imaging in the diagnostic setting for men being investigated for prostate cancer. *BJU Int*. 2020;125: 515–524.
30. Emmett L, Buteau J, Papa N, et al. The additive diagnostic value of Prostate-specific Membrane Antigen Positron Emission Tomography Computed Tomography to Multiparametric Magnetic Resonance Imaging Triage in the Diagnosis of Prostate Cancer (PRIMARY): a prospective multicentre study. *Eur Urol*. 2021;80:682–689.
31. Boellaard R, Krak NC, Hoekstra OS, Lammertsma AA. Effects of noise, image resolution, and ROI definition on the accuracy of standard uptake values: a simulation study. *J Nucl Med*. 2004;45:1519–1527.
32. Laffon E, Lamare F, de Clermont H, Burger IA, Marthan R. Variability of average SUV from several hottest voxels is lower than that of SUVmax and SUVpeak. *Eur Radiol*. 2014;24:1964–1970.
33. Akamatsu G, Ikari Y, Nishida H, et al. Influence of statistical fluctuation on reproducibility and accuracy of SUVmax and SUVpeak: a phantom study. *J Nucl Med Technol*. 2015;43:222–226.
34. Vanderhoek M, Perlman SB, Jeraj R. Impact of the definition of peak standardized uptake value on quantification of treatment response. *J Nucl Med*. 2012;53:4–11.
35. Loeb S, Vellekoop A, Ahmed HU, et al. Systematic review of complications of prostate biopsy. *Eur Urol*. 2013;64:876–892.
36. Wagenlehner FM, van Oostrum E, Tenke P, et al. Infective complications after prostate biopsy: outcome of the Global Prevalence Study of Infections in Urology (GPIU) 2010 and 2011, a prospective multinational multicentre prostate biopsy study. *Eur Urol*. 2013;63:521–527.

Targeted α -Therapy Using ^{225}Ac Radiolabeled Single-Domain Antibodies Induces Antigen-Specific Immune Responses and Instills Immunomodulation Both Systemically and at the Tumor Microenvironment

Thomas Ertveldt¹, Ahmet Krasniqi², Hannelore Ceuppens¹, Janik Puttemans², Yana Dekempeneer², Kevin De Jonghe², Wout de Mey¹, Quentin Lecocq¹, Yannick De Vlaeminck¹, Robin Maximilian Awad¹, Cleo Goyvaerts¹, Kim De Veirman³, Alfred Morgenstern⁴, Frank Bruchertseifer⁴, Marleen Keyaerts^{2,5}, Nick Devoogdt², Matthias D'Huyvetter^{*2}, and Karine Breckpot^{*1}

¹Department of Biomedical Sciences, Laboratory for Molecular and Cellular Therapy, Vrije Universiteit Brussel, Brussels, Belgium;

²Department of Medical Imaging, In Vivo Cellular and Molecular Imaging Laboratory, Vrije Universiteit Brussel, Brussels, Belgium;

³Department of Hematology and Immunology, Myeloma Center Brussels, Vrije Universiteit Brussel, Brussels, Belgium; ⁴European Commission, Joint Research Centre, Directorate for Nuclear Safety and Security, Karlsruhe Institut, Germany; and ⁵Department of Nuclear Medicine, UZ Brussel, Brussels, Belgium

Targeted radionuclide therapy (TRT) using targeting moieties labeled with α -particle-emitting radionuclides (α -TRT) is an intensely investigated treatment approach as the short range of α -particles allows effective treatment of local lesions and micrometastases. However, profound assessment of the immunomodulatory effect of α -TRT is lacking in literature. **Methods:** Using flow cytometry of tumors, splenocyte restimulation, and multiplex analysis of blood serum, we studied immunologic responses ensuing from TRT with an antihuman CD20 single-domain antibody radiolabeled with ^{225}Ac in a human CD20 and ovalbumin expressing B16-melanoma model. **Results:** Tumor growth was delayed with α -TRT and increased blood levels of various cytokines such as interferon- γ , C-C motif chemokine ligand 5, granulocyte-macrophage colony-stimulating factor, and monocyte chemoattractant protein-1. Peripheral antitumoral T-cell responses were detected on α -TRT. At the tumor site, α -TRT modulated the cold tumor microenvironment (TME) to a more hospitable and hot habitat for antitumoral immune cells, characterized by a decrease in protumoral alternatively activated macrophages and an increase in antitumoral macrophages and dendritic cells. We also showed that α -TRT increased the percentage of programmed death-ligand 1 (PD-L1)-positive (PD-L1^{pos}) immune cells in the TME. To circumvent this immunosuppressive countermeasure we applied immune checkpoint blockade of the programmed cell death protein 1-PD-L1 axis. Combination of α -TRT with PD-L1 blockade potentiated the therapeutic effect, however, the combination aggravated adverse events. A long-term toxicity study revealed severe kidney damage ensuing from α -TRT. **Conclusion:** These data suggest that α -TRT alters the TME and induces systemic antitumoral immune responses, which explains why immune checkpoint blockade enhances the therapeutic effect of α -TRT. However, further optimization is warranted to avoid adverse events.

Key Words: actinium-225; immunology; oncology; single-domain antibody; radionuclide therapy

J Nucl Med 2023; 64:751–758

DOI: 10.2967/jnmed.122.264752

In patients with disseminated malignancies, targeted radionuclide therapy (TRT) holds promise for treatment of both primary lesions and micrometastases for which local radiotherapy is no longer applicable (1). In TRT, radiolabeled compounds are systemically administered to deliver radiation proximal to cancer cells. Therefore, tumor-targeting agents are coupled to α -, β^- -, or Auger electron-emitting radionuclides (2). Various targeting modalities were developed and engineered to serve as TRT agents, with most prominent examples being radiolabeled monoclonal antibodies (mAbs), variants thereof and peptides (3). However, mAb-based TRT has been hampered by poor tissue penetration and myelosuppression as a result of bone marrow accumulation (4,5). So, the use of mAb fragments has been reassessed, leading to the development of single-domain antibodies (sdAbs), the antigen-binding fragments of heavy chain-only mAbs (6). SdAbs retain high affinity to their cognate epitope, with the additional benefit of binding to epitopes often inaccessible to mAbs. Hence, sdAbs have been extensively studied for many applications in the field of oncology, including imaging (7). Imaging studies have shown accumulation of sdAbs in local and disseminated cancer deposits with low background, a much-desired trait for TRT agents (8).

TRT with α -emitting radionuclides (α -TRT) is an intensely investigated treatment modality, as the short range of α -particles ($<100\ \mu\text{m}$) allows effective treatment of local lesions and micrometastases with little to no crossfire (1). Because of the short range of α -particles, these were initially assumed to be of limited use in larger tumors and primarily intended for treatment of micrometastases. However, Kratochwil et al. described a reduction of tumor burden in patients with sizeable tumors (9). Whether this feature can be ascribed solely to the radiation aspect of α -TRT is up for debate as it has been shown that bystander immune activation contributes to the therapy outcome (10). Despite ongoing clinical

Received Aug. 10, 2022; revision accepted Dec. 6, 2022.

For correspondence or reprints, contact Karine Breckpot (Karine.Breckpot@vub.be).

*Contributed equally to this work.

Published online Apr. 13, 2023.

COPYRIGHT © 2023 by the Society of Nuclear Medicine and Molecular Imaging.

translation, immunologic changes as a result of α -TRT have not been studied in detail. To investigate immune involvement on α -TRT, we treated melanoma-bearing mice with sdAb-mediated α -TRT.

We used an immunocompetent mouse B16-melanoma model expressing the transgenes human complex of differentiation 20 (huCD20) and ovalbumin to assess the outcome and immune-modifying properties of α -TRT performed with well-characterized antihuCD20 sdAb 9079 labeled with ^{225}Ac (11). We analyzed tumor cell targeting in vivo and the ability of the therapy to delay tumor growth. Systemic effects on ^{225}Ac -9079 were studied through analysis of serum cytokine levels and tumor specificity of CD8^{pos} splenocytes. The tumor microenvironment (TME) was analyzed by flow cytometry to assess tumor-infiltrating immune cells and their expression of inhibitory immune checkpoint ligands and receptors. Furthermore, we ventured into immuno- α -TRT, where we supplemented the ^{225}Ac -9079 treatment regimen with immune checkpoint blockade (ICB) of the programmed cell death protein 1 (PD-1)-programmed death-ligand 1 (PD-L1) axis. Finally, we assessed the radiation burden in the long term in healthy mice 4 mo after administration of ^{225}Ac -9079.

MATERIALS AND METHODS

Cell Line

Mycoplasma-free huCD20 transgenic B16-melanoma cells (B16-huCD20) were provided by Jan Tavernier (VIB-UGent). These were cultured and tested for antigen expression and cell surface expression of huCD20 as previously described (11).

sdAb and ^{225}Ac Radiolabeling

SdAb 9079 binds huCD20 and serves as a targeting moiety for TRT in the B16-huCD20 model (11). SdAb R3B23 binds the M protein of 5T2MM cells and was used as a nontargeting control sdAb throughout this study (12). Carrier-free ^{225}Ac (DG Joint Research Centre) was conjugated to sdAbs using 2-(4-isothiocyanatobenzyl)-1,4,7,10-tetraazacyclododecane-1,4,7,10-tetraacetic acid (DOTA; Macrocylics). Radiochemical purity was evaluated using instant thin-layer chromatography. [^{225}Ac]Ac-DOTA-sdAbs with a radiochemical purity of more than 95% and molar activity of 78.8 and 158.9 kBq/nmol were used for therapy and biodistribution purposes, respectively. Henceforth, [^{225}Ac]Ac-DOTA-9079 will be referred to as ^{225}Ac -9079, [^{225}Ac]Ac-DOTA-R3B23 as ^{225}Ac -R3B23, and [^{225}Ac]Ac-DOTA-sdAbs as ^{225}Ac -sdAbs.

Animal Model

C57BL/6 mice (Charles River) were transplanted subcutaneously in the right thigh with 10E^5 B16-huCD20 cells. Experiments were performed in accordance with the European guidelines for animal experimentation and approved by the ethical committee for use of laboratory animals of the Vrije Universiteit Brussel.

Ex Vivo Biodistribution of ^{225}Ac -sdAbs and Dosimetry

Mice bearing subcutaneous tumors of $250 \pm 100 \text{ mm}^3$ were injected intravenously with a single injection of 25 kBq ($\pm 5.0 \text{ } \mu\text{g}$) of ^{225}Ac -9079 or ^{225}Ac -R3B23 coinjected with Gelofusine (150 mg/kg) (13). Various organs, tissues, and tumors were isolated and weighed, and their level of radioactivity was analyzed using a γ -counter (Wizard²; Perkin Elmer). Results were expressed as percentage injected activity per gram of tissue. Next, the absorbed doses were calculated by multiplying the obtained residence time with the corresponding S value.

Therapy

For the therapy experiments studying α -TRT as a stand-alone therapy, mice received 3 repeated intravenous injections of $52.8 \pm 1.7 \text{ kBq}$ or $98.1 \pm 4.7 \text{ kBq}$ of ^{225}Ac -9079 ($\pm 3.3 \text{ } \mu\text{g}$) on days 3, 9, and 14 of subcutaneous B16-huCD20 tumor growth, with a cumulative radioactive dose of 180 kBq or 300 kBq, respectively. Control mice received 3 repeated intravenous injections of $95.8 \pm 4.6 \text{ kBq}$ of ^{225}Ac -R3B23 ($\pm 3.3 \text{ } \mu\text{g}$), with a cumulative radioactive dose of 300 kBq. All mice had palpable subcutaneous tumors when therapy started.

A similar set-up was used for immuno- α -TRT therapy in which α -TRT was combined with ICB. Mice received repeated intravenous injections of $98.1 \pm 4.7 \text{ kBq}$ of ^{225}Ac -9079 ($\pm 3.3 \text{ } \mu\text{g}$) on days 3, 6, and 15 of subcutaneous B16-huCD20 tumor growth, with a cumulative radioactive dose of 300 kBq. ICB was performed by intraperitoneal administration of 100 μg /injection of antibody on days 7, 10, 14, and 17. Antimurine PD-L1 blocking antibody (RRID:AB_2800597), rat IgG2b, κ isotype control (IC) antibody (RRID:AB_11149687), antimurine PD-1 blocking antibody (RRID:AB_2800576), and rat IgG2a, κ IC antibody (RRID:AB_11149687) were used.

Acute Serum Cytokine Analysis

To analyze the immediate inflammatory response to α -TRT on serum cytokine levels, blood was collected 6 h after the last treatment. Cytokine content was determined using the Bio-Plex Pro Mouse Cytokine 23-plex Assay (RRID:AB_2857368).

Single Cell Suspensions

Tumors were mechanically dissected and enzymatically digested by an enzyme mix of DNase I (Sigma-Aldrich), Dispase II (Roche), and Collagenase I (Sigma-Aldrich) to obtain a single cell suspension. Red blood cell lysis was performed using NH₄Cl-Tris solution.

Flow Cytometry

Surface antigen staining was performed on single-cell suspensions preincubated with anti-CD16/32 antibodies (RRID:AB_312801) and a live/dead marker (LIVE/DEAD Fixable Green Dead Cell Stain Kit; Thermo Fisher Scientific). Cells were washed and stained with 2 antibody panels binding CD45.2 (RRID:AB_1727492), CD3e (RRID:AB_2737945), CD4 (RRID:AB_396956), CD8 α (RRID:AB_394081), CD11b (RRID:AB_396960), CD11c (RRID:AB_2725779), CD206 (RRID:AB_10895754), PD-L1 (RRID:AB_2738911), PD-L2 (RRID:AB_2739947), PD-1 (RRID:AB_394284), F4/80 (RRID:AB_2743450), Ly6G (RRID:AB_1727560), and MHC-II (RRID:AB_2565979). Cells were acquired on the Celesta flow cytometer (BD Biosciences) and analyzed using the FlowJo X software (RRID:SCR_008520; BD Biosciences). t-SNE plots arising from this process were generated using the FlowJo X software.

Restimulation of Splenocytes

Spleens were mashed through a 40- μm cell strainer (Falcon) and transferred to a tube containing RPMI1640 medium, after which cells were stimulated for 48 h with 100 pmol of peptides (Anaspec). As a control, splenocytes were cultured in RPMI1640 medium. ELISA (enzyme-linked immunosorbent assay) was performed on culture supernatant to measure interferon (IFN)- γ in supernatant (mouse IFN- γ ELISA; Invitrogen).

Statistical Analysis

Kaplan-Meier curves showing the time to reach humane endpoints were statistically analyzed using log-rank (Mantel-Cox) and Gehan-Breslow-Wilcoxon tests. One-way ANOVA was performed for all other results and corrected for multiple comparisons via Tukey's multiple-comparisons correction. All statistical analyses were conducted in GraphPad Prism 9.3.1 (GraphPad Software). Sample sizes (n) and the number of times experiments were repeated (N) are indicated in the figure legends. The asterisks in the figures indicate the

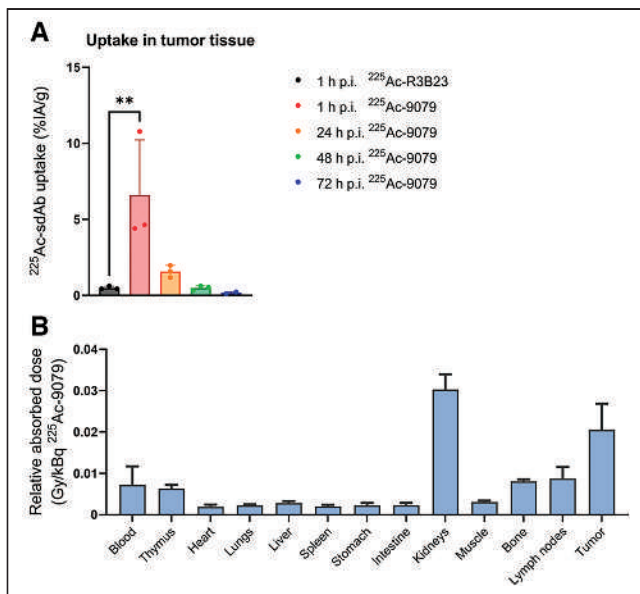


FIGURE 1. Ex vivo biodistribution data show accumulation of ^{225}Ac -9079 in B16-huCD20 tumors. (A) Tumor uptake of ^{225}Ac -9079 and ^{225}Ac -R3B23 was quantified at 1, 24, 48, and 72 h after injection and 1 h after injection, respectively ($N = 1$, $n = 2$ –3 per time point). Bar graph shows individual values with grouped mean \pm SD. (B) Tissue dosimetry on administration of ^{225}Ac -9079 was performed using trapezoid exponential fitting with grouped mean \pm SD ($N = 1$, $n = 3$). %IA/g = percentage injected activity per gram of tissue; p.i. = after injection.

level of statistical significance (* $P < 0.05$; ** $P < 0.01$; *** $P < 0.001$; **** $P < 0.0001$). Nonsignificant changes are not indicated.

Data Availability Statement

The data generated in this study are available within the article and the supplemental files (supplemental materials are available at <http://jnm.snmjournals.org>). Biodistribution files, multiplex data, and flow cytometry files are available on request from the corresponding author.

RESULTS

^{225}Ac -9079 Specifically Accumulates in B16-huCD20 Tumors

We evaluated accumulation of ^{225}Ac -9079 in B16-huCD20 tumor and tissues that do not express huCD20 at 1, 24, 48, and 72 h after intravenous injection. Mice injected with ^{225}Ac -R3B23 were euthanized at 1 h after injection for comparison. B16-huCD20 tumors showed a significant accumulation of ^{225}Ac -9079, yet not ^{225}Ac -R3B23, at 1 h after injection ($P < 0.0061$) (Fig. 1A). We observed little uptake and retention over time of ^{225}Ac -9079 in nontumor tissues, with the exception of the kidneys via which sdAbs are excreted from the body. Dosimetry calculations showed an absorbed dose delivered to B16-huCD20 tumors than that to the spleen, bone marrow and other tissues (excluding kidneys) (Fig. 1B).

^{225}Ac -9079 Delays B16-huCD20 Tumor Growth

Mice injected subcutaneously in the thigh with B16-huCD20 cells were randomized 3 d after injection to receive a cumulative dose of 180 or 300 kBq of ^{225}Ac -9079. Fractionated treatment was given on days 3, 9, and 14 after tumor cell inoculation, resulting in delivery of a cumulative absorbed dose of 4 or 6 Gy to B16-huCD20 tumors, respectively (Supplemental Fig. 1A). For comparison, mice received a cumulative dose of 300 kBq of ^{225}Ac -R3B23. Tumor growth was delayed when mice were treated with 300 kBq of ^{225}Ac -9079 ($P = 0.0148$; Fig. 2A). This therapeutic effect translated into an increased time to reach humane endpoints in mice treated with 180 or 300 kBq of ^{225}Ac -9079 ($P = 0.0236$ and $P = 0.0014$, respectively; Fig. 2B). No evidence of acute, systemic treatment-related toxicity was observed, as indicated by the animals' body weight (Fig. 2C).

Peripheral Immune Responses Suggest Antigen-Specific Immune Activation on Treatment with ^{225}Ac -9079

We analyzed 23 cytokines in serum collected at 6 h after the last treatment to address the immune activating potential of α -TRT. All cytokines, except for interleukin (IL)-3, were detected in blood samples (Fig. 3A; Supplemental Fig. 2). Statistical tests compared ^{225}Ac -9079 conditions with ^{225}Ac -R3B23, with P values displayed separately in Supplemental Table 1. Cytokine serum levels of IL-1 β , IL-10, tumor necrosis factor (TNF)- α , keratinocyte chemoattractant (KC), IFN- γ , C-C motif chemokine Ligand 5 (CCL5), monocyte chemoattractant protein-1 (MCP-1), and granulocyte-macrophage colony-stimulating factor (GM-CSF) were significantly upregulated in both ^{225}Ac -9079 conditions (Fig. 3A; Supplemental Fig. 2). The serum levels of IL-4, IL-12(p40), and granulocyte colony-stimulating factor (G-CSF) were significantly increased only in mice administered 300 kBq of ^{225}Ac -9079 (Fig. 3A; Supplemental Fig. 2). The serum levels of IL-9 and macrophage inflammatory protein (MIP)-1 α were significantly increased only in mice administered 180 kBq of ^{225}Ac -9079 condition (Fig. 3A; Supplemental Fig. 2). No significant changes were observed for the cytokines IL-1 α , IL-2, IL-5, IL-6, IL-12p70, IL-13, IL-17, eotaxin, MIP-1 β (Fig. 3A; Supplemental Fig. 2).

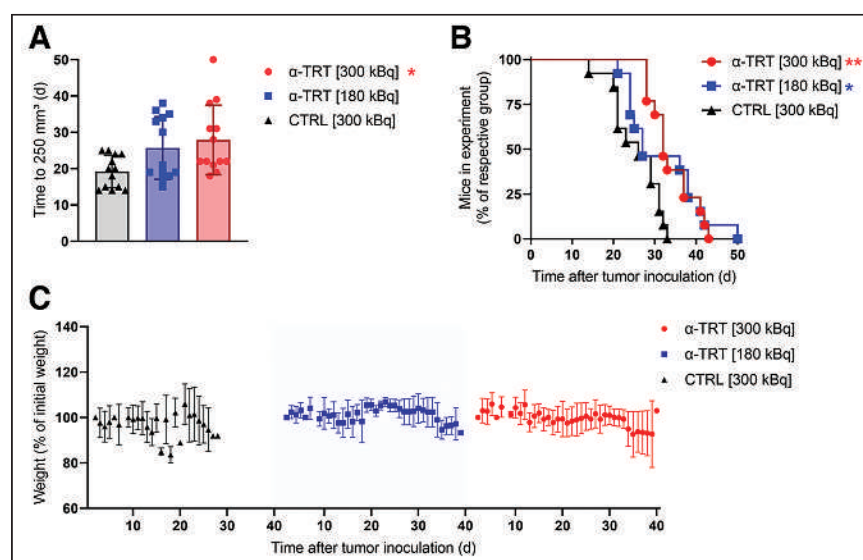


FIGURE 2. Therapy with ^{225}Ac -9079 impedes tumor growth. (A) Pooled times to reach tumor volume of 250 mm 3 are shown by group. Bar graph shows individual values with grouped mean \pm SD. (B) Pooled Kaplan-Meier curve showing time at which mice reached humane endpoints. (C) Pooled weight of treated mice over course of time. Graph shows grouped mean \pm SD ($N = 2$, $n = 6$). CTRL = ^{225}Ac -labeled nontargeting sdAb.

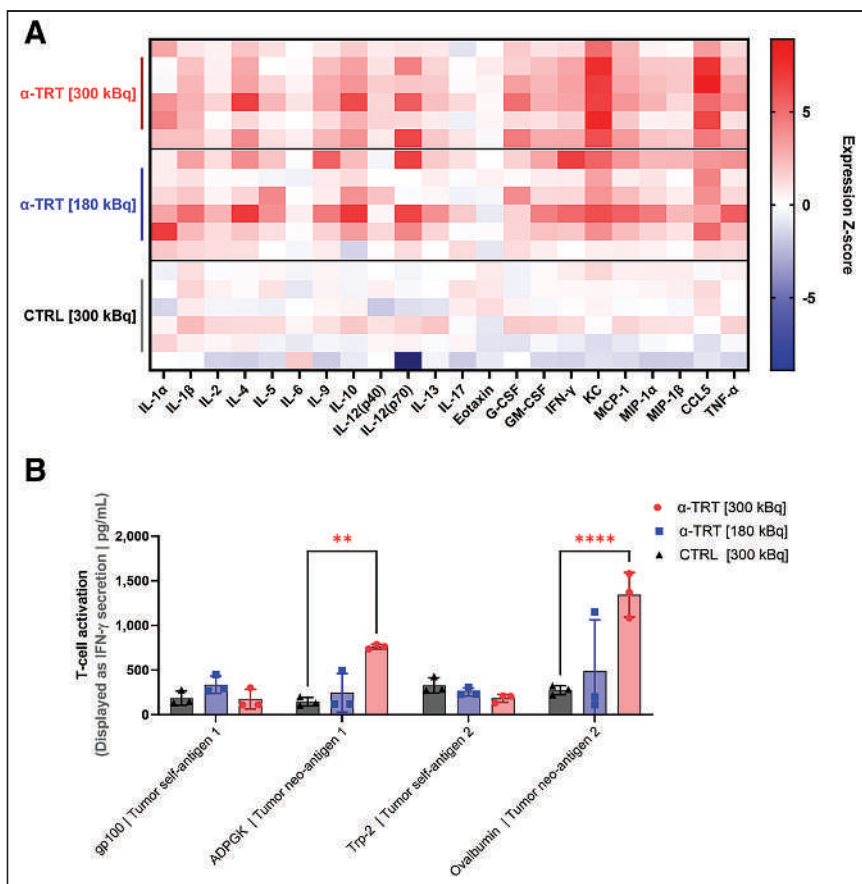


FIGURE 3. Peripheral immune responses suggest immune activation on treatment with ^{225}Ac -9079. (A) Multiplex analysis of cytokine levels 6 h after last administration of ^{225}Ac -sdAbs. Heatmap is generated using z-transformed cytokine levels ($N = 1, n = 6$). (B) Analysis of IFN- γ production by splenocytes stimulated with cancer antigen-derived peptides. Graph shows individual values with grouped mean \pm SD ($N = 1, n = 3$). CTRL = ^{225}Ac -labeled nontargeting sdAb; G-CSF = granulocyte colony-stimulating factor; GM-CSF = granulocyte-macrophage colony-stimulating factor; KC = keratinocyte chemoattractant; TNF- α = tumor necrosis factor- α .

CD8 $^{\text{pos}}$ splenocytes were stimulated with peptides, derived from antigens expressed by B16-huCD20 tumor cells, including the 2 melanoma differentiation antigens glycoprotein 100 (gp100) $_{25-33}$ and tyrosinase-related protein 2 (Trp2) $_{181-188}$ next to 2 model neoantigens: ADP dependent glucokinase (ADPGK) $_{299-307}$ and ovalbumin $_{257-264}$. Production of IFN- γ , a measure of T-cell activation, was demonstrated only in mice treated with 300 kBq of ^{225}Ac -9079 in response to ADPGK and ovalbumin ($P = 0.0019$ and $P < 0.0001$, respectively) (Fig. 3B). In contrast, we were unable to show IFN- γ induction on stimulation with gp100 or Trp2 peptides.

^{225}Ac -9079 Modulated the TME to Favor Antitumoral Cells

B16-huCD20 tumors were isolated when they reached $250 \pm 100 \text{ mm}^3$. Single-cell suspensions of these tumors were subjected to flow cytometry analysis to study the tumor immune signature (Supplemental Figs. 3 and 4). Statistical tests compared ^{225}Ac -9079 conditions with ^{225}Ac -R3B23, and P values are displayed separately in Supplemental Table 2. Multicolor flow cytometry analyses of TME showed a similar T-cell count and no major differences among T-cell subpopulations (Fig. 4A). PD-1-expression on CD4 $^{\text{pos}}$ T-cells was significantly upregulated in tumors of mice treated with ^{225}Ac -9079 (Fig. 4B; Supplemental Fig. 5B).

Among tumor-infiltrating myeloid cells, the significant decrease in total myeloid numbers coincided with a significant decrease in protumoral alternatively activated macrophages (M2) in tumors treated with ^{225}Ac -9079 (Fig. 5A; Supplemental Fig. 5E). Furthermore, a significant increase in antitumoral classically activated macrophages (M1) and dendritic cells (DCs) was also observed in tumors treated with ^{225}Ac -9079 (Fig. 5A; Supplemental Figs. 5F and 5G). Within the immune cells, we observed that PD-L1 was significantly increased on cDC2s and M1 macrophages residing in tumors treated with ^{225}Ac -9079 (Fig. 5B; Supplemental Fig. 5H). No difference in expression level was observed for inhibitory immune checkpoint ligand PD-L2 (Fig. 5B).

PD-L1 Checkpoint Blockade Further Reduces Tumor Growth After ^{225}Ac -9079 Therapy Yet Coincides with Severe Weight Loss

Mice injected subcutaneously in the thigh with B16-huCD20 cells were randomized 3 d after injection to receive a cumulative dose of 300 kBq of ^{225}Ac -9079 on days 3, 6, and 15 intravenously or 100 μg of mAbs on days 7, 10, 14, and 17 intraperitoneally after tumor cell inoculation (Supplemental Fig. 1B). Tumor growth was delayed when mice were treated with 300 kBq of ^{225}Ac -9079 combined with PD-L1 but not with PD-1 ICB (Fig. 6A). However, administration of both ^{225}Ac -9079 and PD-L1 ICB resulted in extensive weight loss, which was not observed with the combination of ^{225}Ac -9079 and PD-1 ICB (Fig. 6B).

Long-Term Toxicity Study Reveals Organ Damage After α -TRT with ^{225}Ac -9079

Healthy mice received a single injection of 300 kBq of ^{225}Ac -9079 or phosphate-buffered saline and were monitored until month 4 after treatment, at which time mice treated with ^{225}Ac -9079 showed a weight loss of 20% or more (Supplemental Fig. 1C). All mice were euthanized, and organs of interest were isolated and weighed. Liver, heart, and lungs displayed a minor reduction in weight, whereas the mass of the spleen and kidneys was significantly reduced by $29.5\% \pm 4.3\%$ ($P = 0.0011$) and $65.5\% \pm 1.8\%$ ($P < 0.0001$) in mice treated with ^{225}Ac -9079 (Fig. 7).

DISCUSSION

In this study, we showed that α -TRT with ^{225}Ac -9079 in the B16-huCD20 melanoma mouse model has therapeutic potential as it delays tumor growth. We further showed stimulation of cytokine release, tumor-specific CD8 $^{\text{pos}}$ T-cell responses, and a shift from a tumor-promoting TME to a TME characterized by an immune contexture that enables tumor cell rejection, including activated (PD-1 $^{\text{pos}}$) T-cells, classically activated macrophages, and DCs. Finally, we showed that ICB with anti-PD-L1 mAbs combined with α -TRT improves tumor control compared with either therapy alone, albeit coinciding with adverse events (i.e., weight loss).

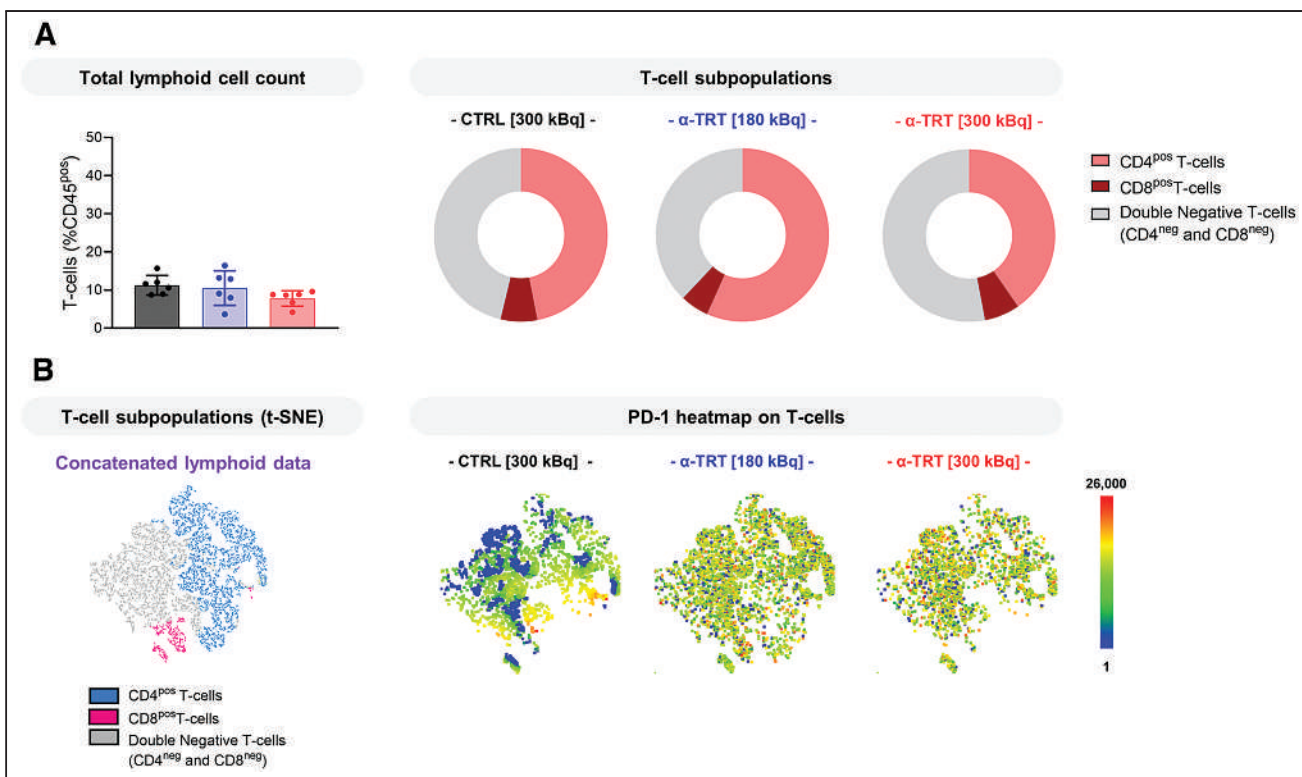


FIGURE 4. α-TRT increased PD-1 expression on tumoral CD4^{pos} T-cells. (A) Composition of T-cell subpopulations, among T-cells. (B) Concatenated t-distributed stochastic neighbor embedding (t-SNE) plot of the T-cell lineage, overlaid with T-cell subpopulations. Concatenated t-SNE heatmaps show expression of PD-1 on T-cell subpopulations per treatment group. Heatmap range represents marker mean fluorescence intensity (MFI). Graph shows individual values with grouped mean ± SD ($N = 1, n = 6$). CTRL = ^{225}Ac -labeled nontargeting sdAb.

We evaluated the potential of ^{225}Ac -9079 as an α-TRT agent and showed specific accumulation in B16-huCD20 tumors of immunocompetent mice, sparing muCD20^{pos} cells. This observation is in line with previous work performed with the same sdAb, albeit conjugated to another linker and radionuclide (11). For therapeutic efficacy, a dose approximating 5 Gy was desired as literature described little therapeutic effect given solid tumors' resilience to radiation (14). Hence 180 and 300 kBq of ^{225}Ac -9079 were administered, corresponding to respective delivery of 4 and 6 Gy in tumor. The observed delay in tumor growth with ^{225}Ac -9079 is in line with published studies that highlight the potential of ^{225}Ac as a therapeutic radionuclide (9).

Serum cytokine levels were quantified as markers for systemic immune activation, and various cytokines were enhanced. Increased levels of MCP-1 and GM-CSF suggest monocytes or macrophage migration or infiltration and DC maturation, respectively (15,16). Furthermore, elevation of antitumoral cytokines such as IFN-γ and CCL5 advocates activation of CD8^{pos} T-cells and serves as predictor of response to ICB (17). A recent study investigating adoptive cell transfer and α-TRT described the secretion CCL5 and IFN-γ from tumor on treatment (18). These results prompted us to resuscitate isolated spleens with cancer-associated epitopes. Intriguingly, IFN-γ secretion revealed that splenocytes recognized and reacted to ADPGK and ovalbumin but not toward melanoma differentiation antigens. Evidence of high-avidity antitumoral CD8^{pos} T-cells responses on α-TRT has not yet been published.

After analyzing systemic responses, we evaluated α-TRT-mediated alteration of the TME, which is emphasized by an increase

in professional antigen presenting cells at the expense of immunosuppressive subsets of myeloid cells. More specifically, alternatively activated macrophages (M2) are significantly decreased in numbers. These cells are involved in wound healing under physiologic conditions and attenuating immune responses to prevent collateral tissue damage (19). In malignancy, M2 macrophages are enthralled by tumor cells to overexert immunosuppressive functions, quench uprising antitumoral responses, and facilitate tumor progression and metastasis (19). Unlike, M2 macrophages, we documented an increase in M1 macrophages and DCs, professional antigen presenting cells involved in the education of T-cell responses (20). This observation is consistent with the cytokine profile of MCP-1 and GM-CSF, hinting at macrophage infiltration and DC maturation. DCs can acquire antigens, migrate, and present these to T-cells within lymph structures to elicit a clonal T-cell response, which ties in with the identification of antitumoral T-cells in the spleen (21). Regarding the expression pattern of immune checkpoint receptors in the TME, we noted that α-TRT upregulated expression of PD-1 on CD4^{pos} T-cells as well as its ligand, PD-L1, on various cell types in the TME. In recent studies involving α-TRT, a similar observation was made (18). Ligation of PD-1 to PD-L1 impairs T-cell receptor signaling, in turn interfering with the effector function of antitumoral T-cells (20). In short, we observed that ^{225}Ac -9079 altered the tumor immune compartment, favoring myeloid cells that likely facilitate antigen processing, presentation, and education of T-cell responses, were it not for the presence of inhibitory markers such as PD-1 and PD-L1. To overcome this hurdle we performed ICB of the PD-1–PD-L1 axis to enhance the therapeutic effect of sdAb-mediated α-TRT.

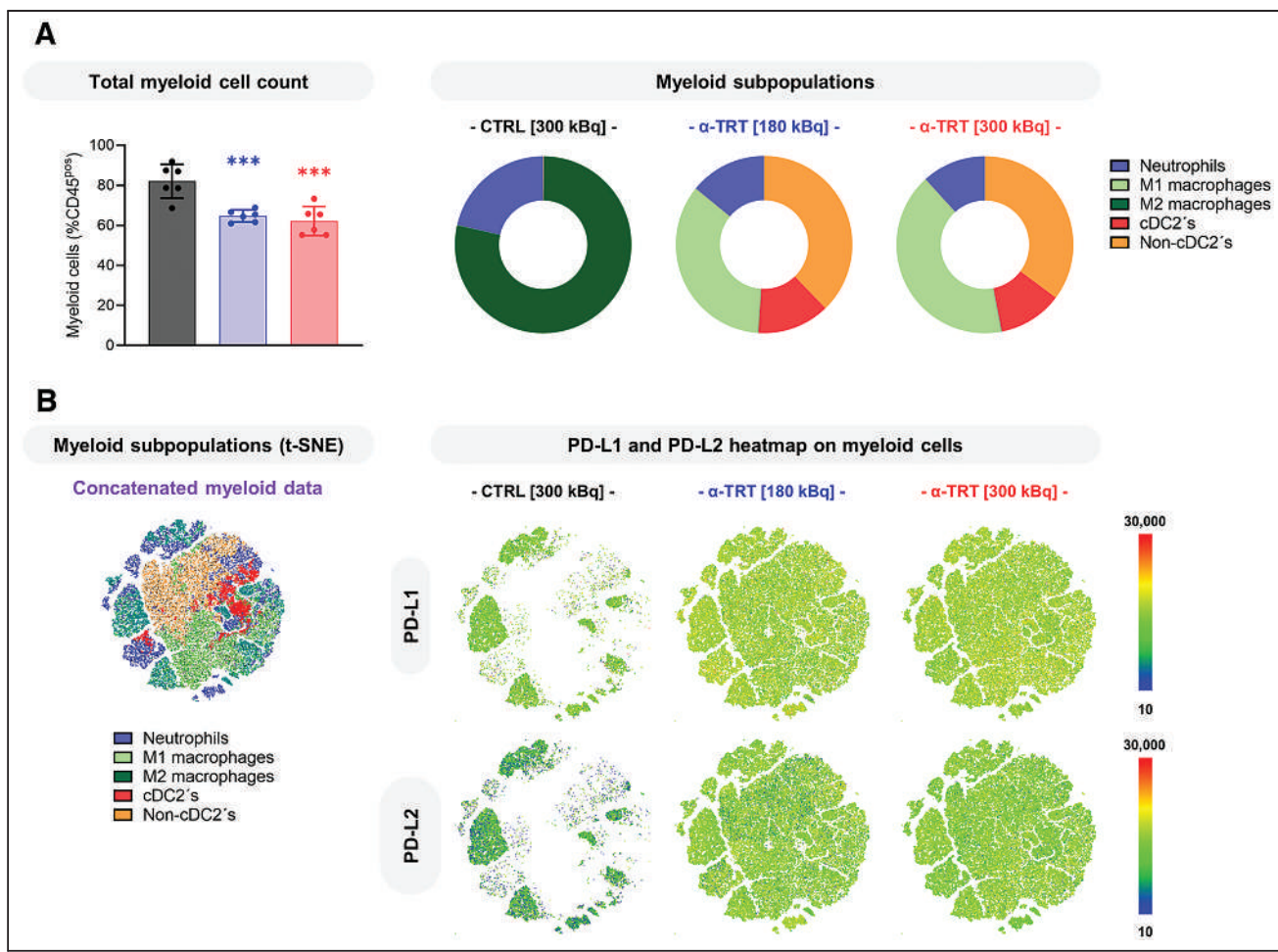


FIGURE 5. α-TRT reduced M2 macrophage and increased M1 macrophage and DC count in tumor tissue. (A) Composition of myeloid subpopulations among myeloid cells. (B) Concatenated t-SNE plot of myeloid lineage, overlaid with myeloid subpopulations. Concatenated t-SNE heatmaps showing expression of PD-L1 and PD-L2 on myeloid subpopulations per treatment group. Heatmap ranges represent marker mean fluorescence intensity (MFI). Graph shows individual values with grouped mean ± SD ($N = 1, n = 6$). CTRL = ^{225}Ac -labeled nontargeting sdAb.

Synergy between α-TRT and ICB occurred only in combination with PD-L1 blockade in these experiments, despite literature stating PD-1 synergizes with α-TRT as well (22). Intriguingly, PD-L1 ICB on its own did not amount to a therapeutic effect, compared with the IC, whereas PD-1 had therapeutic benefit on its own. We surmise that PD-L1 ICB after α-TRT is this effective because of the immune alterations induced on α-TRT, setting the stage to unleash all this immunologic potential. Besides the effect of anti-PD-L1 mAbs as a blocking agent, antibody-dependent cellular cytotoxicity (ADCC) also comes into play. Unlike the PD-1 mAb, the PD-L1 mAb used in this study is able to induce ADCC (23). Hence, we surmised that PD-L1^{pos} tumor and stromal cells in the TME are clad with mAbs on PD-L1 ICB, flagging them for ADCC by Fc γ R^{pos} effector cells, such as B cells, NK cells, and M1 macrophages, which highly infiltrate tumors subjected to α-TRT (24). Unfortunately, mice that received a combination of α-TRT and PD-L1 ICB experienced extensive weight loss, resulting in premature attainment of a humane endpoint. We presume that this phenomenon is the result of the combination therapy's ensuing cytokine storm as mice receiving a similar amount of radioactivity or ICB, as monotherapy, did not lose weight during the course of

the experiment. Curiously, α-TRT with PD-1 ICB did not result in weight loss, suggesting the onset of ADCC by the PD-L1 mAb may have played a crucial role in this process.

To investigate late-stage systemic radiation burden, we administered similar therapeutic doses to healthy mice, which allowed long-term follow up. We noted that 4 mo after administration of ^{225}Ac -9079, mice started losing weight. The spleen and kidneys of these mice were severely reduced in size compared with unirradiated mice, suggesting that α-TRT inflicted severe damage to these organs. Damage to tubular epithelial cells and loss of renal function on α-TRT was described by Scheinberg et al. (25). Unlike the kidneys, spleen biodistribution data does not advocate for a substantial accumulation of ^{225}Ac -9079. Hence, we surmise that the loss of spleen weight is not directly related to the radiation aspect and is more likely a systemic effect due to the extensive weight loss. Cheal et al. demonstrated that injection of 296 kBq of ^{225}Ac is tolerated by mice; however, the study relied on a pretargeted approach using haptens, resulting in minimal kidney retention (26). With about 10 times the size of a hapten, a 15 kDa sdAb is excreted via the kidneys' glomerulus with moderate retention, resulting in kidneys being the dose-limiting organ of sdAb-mediated TRT.

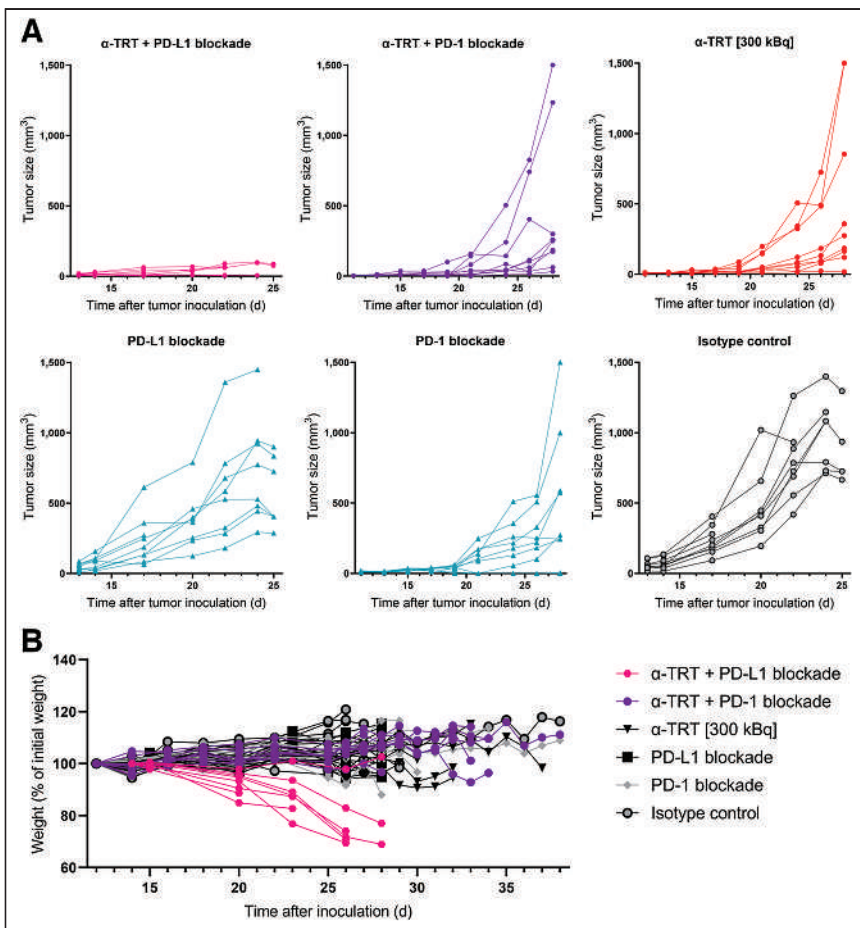


FIGURE 6. Therapy with ^{225}Ac -9079 acts in synergy with immune checkpoint blockade but potentiates adverse effects. (A) Grouped tumor kinetics are shown during course of experiment by individual mouse. (B) Weight of treated mice during course of experiment, displayed as individual values ($N = 1$, $n = 9$).

Hence, the pretargeting approach is worthwhile investigating to circumvent the limitations imposed by the kidneys for sdAb-mediated TRT (27). Other possible avenues are modulation of sdAb protein sequence, cleavable linkers, and novel coupling methods to avoid a high radiation burden on the kidneys (28). In this regard, a limitation of this study is the lack of histologic evaluation of kidneys, which would have yielded more insight into the extent of renal

damage inflicted upon $\alpha\text{-TRT}$. Furthermore, immune analyses were performed at a single time point. Though this provided valuable insights, it might not reflect the dynamic nature of the immune system and its contribution to immune-related adverse events. Finally, the antihuCD20 sdAb used in this study does not bind mouse CD20, thus introducing a bias in the healthy organ dosimetry. However, antihuCD20 TRT using mAbs was previously performed in patients and displayed an acceptable safety profile (5).

Future perspectives for ameliorating the therapeutic index of $\alpha\text{-TRT}$ consists of combination strategies to reduce the radiation burden on dose-limiting organs such as kidneys as well as titration of ICB. Further tweaking of the therapy regimen should circumvent kidney damage as well as immune-related adverse events.

CONCLUSION

To our knowledge, this is the first study addressing immune activation in a melanoma model on $\alpha\text{-TRT}$ with ^{225}Ac -sdAbs. Our findings suggest that $\alpha\text{-TRT}$ alters the TME and induces systemic antitumoral immune responses, which in turn were unhinged via ICB to enhance therapeutic effect but warrants further optimization because of synergistic adverse effects.

DISCLOSURE

This research was supported by the Belgian Foundation against Cancer (2016-076/FAF-F/2016/798); Kom op tegen Kanker (Stand-up to Cancer); the Flemish Cancer Society and the Research Council of the Vrije Universiteit Brussel (Strategic Research Program 48 and 62). Furthermore, Thomas Ertveldt and Robin Maximilian Awad are PhD fellows funded via the Research Foundation-Flanders (FWO-V, grants 1S06622N and 1S05020N, respectively). Yannick De Vlaeminck, Quentin Lecocq, and Janik Puttemans were supported by FWO-V during the execution of this work (1S24817N, 1S24220N and I001618N, respectively). Marleen Keyaerts and both Matthias D'Huyvetter and Kim De Veirman are, respectively, senior clinical investigator (1801619N) and postdoctoral fellows (12H3619N and 12I0921N) of FWO-V. The BD Celesta flow cytometer was funded via an FWO-Hercules grant (I001618N). Karine Breckpot, Nick Devoogdt, Matthias D'Huyvetter, Marleen Keyaerts, Ahmet Krasniqi, and Quentin Lecocq have patents on the use of single-domain antibodies. Nick Devoogdt and Marleen Keyaerts have ownership in AbScint, which leverages sdAb imaging tracers into clinical application. Marleen Keyaerts received research funding from Precirix, a biotech company that develops novel radiopharmaceuticals. Nick Devoogdt and Matthias D'Huyvetter are, respectively, consultant and employee for and hold ownership in Precirix. No other potential conflict of interest relevant to this article was reported.

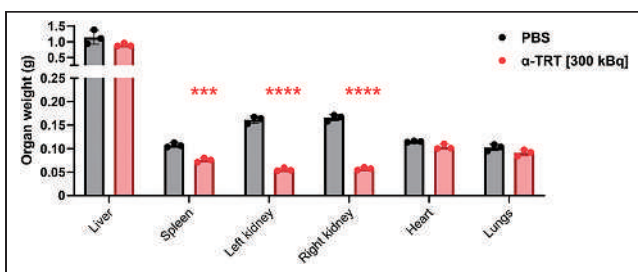


FIGURE 7. Long-term toxicity study reveals major organ damage 4 mo after administration of ^{225}Ac -sdAbs. Weight of whole isolated organs, 4 mo after administration of ^{225}Ac -9079 or phosphate-buffered saline (PBS). Bar graph shows individual datapoints and grouped mean \pm SD ($N = 1$, $n = 3$).

KEY POINTS

QUESTION: Does α -TRT result in a sufficient release of immunologic cues to induce systemic antigen-specific T-cell responses?

PERTINENT FINDINGS: Upon restimulation of spleens with cancer-associated peptides, we observed a significant T-cell activation, suggesting that α -TRT can induce tumor-specific immunity toward immunogenic neoantigens.

IMPLICATIONS FOR PATIENT CARE: Induction of T-cell responses with α -TRT implies that synergistic immunologic applications enhance the therapeutic effect by potentiating antitumoral T-cells. Hence, combination trials gain in interest, especially at the advent of pembrolizumab (PD-1 blocking mAb) being approved for treatment of non-Hodgkin lymphoma and various other malignancies.

REFERENCES

1. Pouget JP, Constanzo J. Revisiting the radiobiology of targeted alpha therapy. *Front Med (Lausanne)*. 2021;8:692436.
2. Turner JH. An introduction to the clinical practice of theranostics in oncology. *Br J Radiol*. 2018;91:20180440.
3. Gill MR, Falzone N, Du Y, Vallis KA. Targeted radionuclide therapy in combined-modality regimens. *Lancet Oncol*. 2017;18:e414–e423.
4. Scott AM, Wolchok JD, Old LJ. Antibody therapy of cancer. *Nat Rev Cancer*. 2012;12:278–287.
5. Witzig TE, White CA, Gordon LI, et al. Safety of yttrium-90 ibritumomab tiuxetan radioimmunotherapy for relapsed low-grade, follicular, or transformed non-Hodgkin's lymphoma. *J Clin Oncol*. 2003;21:1263–1270.
6. Muyldermans S. Nanobodies: natural single-domain antibodies. *Annu Rev Biochem*. 2013;82:775–797.
7. Awad RM, Meeus F, Ceuppens H, et al. Emerging applications of nanobodies in cancer therapy. *Int Rev Cell Mol Biol*. 2022;369:143–199.
8. Keyaerts M, Xavier C, Heemskerk J, et al. Phase I study of ^{68}Ga -HER2-nanobody for PET/CT assessment of HER2 expression in breast carcinoma. *J Nucl Med*. 2016;57:27–33.
9. Kratochwil C, Bruchertseifer F, Giesel FL, et al. ^{225}Ac -PSMA-617 for PSMA-targeted α -radiation therapy of metastatic castration-resistant prostate cancer. *J Nucl Med*. 2016;57:1941–1944.
10. Brady D, O'Sullivan JM, Prise KM. What is the role of the bystander response in radionuclide therapies? *Front Oncol*. 2013;3:215.
11. Ertweldt T, de Beck L, de Ridder K, et al. Targeted radionuclide therapy with low and high-dose Lutetium-177 labeled single domain antibodies induces distinct immune signatures in a mouse melanoma model. *Mol Cancer Ther*. 2022;21:1136–1148.
12. Lemaire M, D'Huyvetter M, Lahoutte T, et al. Imaging and radioimmunotherapy of multiple myeloma with anti-idiotypic Nanobodies. *Leukemia*. 2014;28:444–447.
13. D'Huyvetter M, Vincke C, Xavier C, et al. Targeted radionuclide therapy with a 177 Lu-labeled anti-HER2 nanobody. *Theranostics*. 2014;4:708–720.
14. Patel RB, Hernandez R, Carlson P, et al. Low-dose targeted radionuclide therapy renders immunologically cold tumors responsive to immune checkpoint blockade. *Sci Transl Med*. 2021;13:eabb3631.
15. Inaba K, Inaba M, Romani N, et al. Generation of large numbers of dendritic cells from mouse bone marrow cultures supplemented with granulocyte/macrophage colony-stimulating factor. *J Exp Med*. 1992;176:1693–1702.
16. Deshmane SL, Kremlev S, Amini S, Sawaya BE. Monocyte chemoattractant protein-1 (MCP-1): an overview. *J Interferon Cytokine Res*. 2009;29:313–326.
17. Karachaliou N, Gonzalez-Cao M, Crespo G, et al. Interferon gamma, an important marker of response to immune checkpoint blockade in non-small cell lung cancer and melanoma patients. *Ther Adv Med Oncol*. 2018;10.
18. Perrin J, Capitao M, Allard M, et al. Targeted alpha particle therapy remodels the tumor microenvironment and improves efficacy of immunotherapy. *Int J Radiat Oncol Biol Phys*. 2022;112:790–801.
19. Awad RM, de Vlaeminck Y, Maebe J, Goyaerts C, Breckpot K. Turn back the TIME: targeting tumor infiltrating myeloid cells to revert cancer progression. *Front Immunol*. 2018;9:1977.
20. Peng Q, Qiu X, Zhang Z, et al. PD-L1 on dendritic cells attenuates T cell activation and regulates response to immune checkpoint blockade. *Nat Commun*. 2020;11:4835.
21. Chiang MC, Tullett KM, Lee YS, et al. Differential uptake and cross-presentation of soluble and necrotic cell antigen by human DC subsets. *Eur J Immunol*. 2016;46:329–339.
22. Czernin J, Current K, Mona CE, et al. Immune-Checkpoint Blockade Enhances ^{225}Ac -PSMA-617 efficacy in a mouse model of prostate cancer. *J Nucl Med*. 2021;62:228–231.
23. Dahan R, Segal E, Engelhardt J, Selby M, Korman AJ, Ravetch J v. Fc γ Rs modulate the anti-tumor activity of antibodies targeting the PD-1/PD-L1 axis. *Cancer Cell*. 2015;28:285–295.
24. Nimmerjahn F, Ravetch J v. Translating basic mechanisms of IgG effector activity into next generation cancer therapies. *Cancer Immun*. 2012;12:13.
25. Scheinberg DA, McDevitt MR. Actinium-225 in targeted alpha-particle therapeutic applications. *Curr Radiopharm*. 2011;4:306–320.
26. Cheal SM, McDevitt MR, Santich BH, et al. Alpha radioimmunotherapy using ^{225}Ac -proteus-DOTA for solid tumors: safety at curative doses. *Theranostics*. 2020;10:11359–11375.
27. Cheal SM, Chung SK, Vaughn BA, Cheung NK v., Larson SM. Pretargeting: a path forward for radioimmunotherapy. *J Nucl Med*. 2022;63:1302–1315.
28. Chigoh DM, Bridoux J, Hernot S. Reducing the renal retention of low- to moderate-molecular-weight radiopharmaceuticals. *Curr Opin Chem Biol*. 2021;63:219–228.

Fibroblast Activation Protein–Targeted Radioligand Therapy for Treatment of Solid Tumors

Spencer D. Lindeman¹, Ramesh Mukkamala¹, Autumn Horner¹, Pooja Tudi¹, Owen C. Booth¹, Roxanne Huff¹, Joshua Hinsey¹, Anders Hovstadius¹, Peter Martone¹, Fenghua Zhang¹, Madduri Srinivasarao¹, Abigail Cox², and Philip S. Low¹

¹Department of Chemistry and Institute for Drug Discovery, Purdue University, West Lafayette, Indiana; and ²Department of Comparative Pathobiology, Purdue College of Veterinary Medicine, West Lafayette, Indiana

Fibroblast activation protein (FAP) has received increasing attention as an oncologic target because of its prominent expression in solid tumors but virtual absence from healthy tissues. Most radioligand therapies (RLTs) targeting FAP, however, suffer from inadequate tumor retention or clearance from healthy tissues. Herein we report a FAP-targeted RLT comprising an FAP6 ligand conjugated to DOTA and an albumin binder (4-*p*-iodophenylbutyric acid, or IP) for enhanced pharmacokinetics. We evaluated the performance of the resulting FAP6-IP-DOTA conjugate in 4 tumor models, 3 of which express FAP only on cancer-associated fibroblasts, that is, analogously to human tumors. **Methods:** Single-cell RNA-sequencing data were analyzed from 34 human breast, ovarian, colorectal, and lung cancers to quantify FAP-overexpressing cells. FAP6-DOTA conjugates were synthesized with or without an albumin binder (IP) and investigated for binding to human FAP-expressing cells. Accumulation of ¹¹¹In- or ¹⁷⁷Lu-labeled conjugates in KB, HT29, U87MG, and 4T1 murine tumors was also assessed by radioimaging or biodistribution analyses. Radiotherapeutic potency was quantitated by measuring tumor volumes versus time. **Results:** Approximately 5% of all cells in human tumors overexpressed FAP (cancer-associated fibroblasts comprised ~77% of this FAP-positive subpopulation, whereas ~2% were cancer cells). FAP6 conjugates bound to FAP-expressing cells with high affinity (dissociation constant, ~1 nM). ¹⁷⁷Lu-FAP6-IP-DOTA achieved an 88-fold higher tumor dose than ¹⁷⁷Lu-FAP6-DOTA and improved all tumor-to-healthy-organ ratios. Single doses of ¹⁷⁷Lu-FAP6-IP-DOTA suppressed tumor growth by about 45% in all tested tumor models without causing reproducible toxicities. **Conclusion:** We conclude that ¹⁷⁷Lu-FAP6-IP-DOTA constitutes a promising candidate for FAP-targeted RLT of solid tumors.

Key Words: radioligand therapy; FAP; albumin binder; scRNA-seq; cancer-associated fibroblasts

J Nucl Med 2023; 64:759–766

DOI: 10.2967/jnumed.122.264494

A subset of cancer-associated fibroblasts (CAFs) is characterized by expression of a cell-surface serine protease termed fibroblast activation protein (FAP) that participates in remodeling of the extracellular matrix during tumor growth and metastasis (1). Approximately 90% of epithelial cancers upregulate FAP (2), and FAP-targeted PET tracers have been shown to image at least 28

different cancer types in humans (3). Because of FAP's broad expression on CAFs and its nearly complete absence from healthy tissues, FAP has recently been explored as a receptor for targeted radioligand therapy (RLT) in a diversity of solid tumors (4,5).

Optimal FAP-targeted radiotherapy might be expected to satisfy several criteria. First, it will contain a therapeutic radionuclide that effectively irradiates multiple cancer cells near each CAF. Second, the targeting ligand will possess high affinity and specificity for FAP to minimize uptake by its homologs in healthy organs. Third, the pharmacokinetic properties of the resulting conjugate will be optimized to ensure prolonged tumor accumulation and rapid clearance from normal tissues.

To achieve these objectives, we first derivatized a new FAP-targeting ligand (FAP6) with DOTA via a polyethylene glycol spacer. We then incorporated the established albumin binder 4-*p*-iodophenylbutyric acid (IP) (6) into our FAP-targeting radioligand (Fig. 1), since such appendages have been observed to prolong the pharmacokinetics and improve tumor uptake of RLTs (7–10). We demonstrate here that the resulting conjugate, FAP6-IP-DOTA, exhibits high FAP affinity, prolonged circulation, increased tumor uptake, and minimal retention in healthy tissues. Moreover, the final ¹⁷⁷Lu-labeled RLT causes no obvious toxicity to healthy tissues while achieving significant anticancer efficacy in 4 different murine tumor models.

MATERIALS AND METHODS

Reagents, vendors, syntheses, and full experimental procedures are detailed in the supplemental materials (available at <http://jnm.snmjournals.org>).

Single-Cell RNA-Sequencing (scRNA-Seq) Analysis

We analyzed scRNA-seq data collected on fresh human tumor samples; the results of this analysis were reported elsewhere previously (11). FAP gene expression was extracted, quantitated, and plotted on a log(2) scale for comparison among different cell types in each cancer tissue, according to online tutorials (12).

Cell Culture and Transduction

4T1, KB, HT29, and U87MG cells were purchased from American Type Culture Collection and cultured as reported previously (13,14). HEK-293T cells with high levels of FAP expression (HEK-hFAP) were generated as formerly described (13).

Radiolabeling

FAP6 conjugates were diluted in ammonium acetate (0.5 M, pH 8.0). ¹¹¹In[InCl₃] (Cardinal Health) was added to obtain a specific activity of

Received Jun. 6, 2022; revision accepted Nov. 28, 2022.

For correspondence or reprints, contact Philip S. Low (plow@purdue.edu).

Published online Dec. 8, 2022.

COPYRIGHT © 2023 by the Society of Nuclear Medicine and Molecular Imaging.

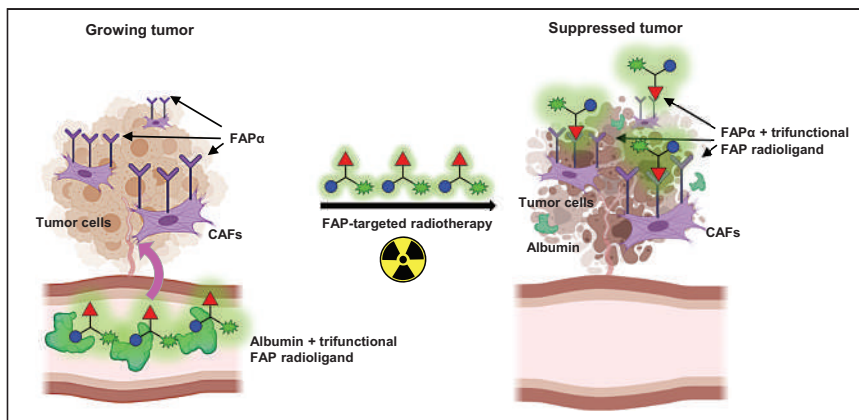


FIGURE 1. Circulation of radiolabeled FAP6-IP-DOTA is prolonged because of affinity of iodophenyl-butyrin acid (blue circles) for serum albumin. This enables conjugate to perfuse poorly vascularized solid tumors so that ligand (red triangles) may bind to FAP receptors on CAFs. Chelated radionuclide (green symbols) emits radiation that induces DNA-strand breaks inside tumor cells, thereby suppressing tumor growth.

no more than 4.0 MBq/nmol, or $^{177}\text{Lu}[\text{LuCl}_3]$ (RadioMedix) was added to obtain a specific activity of no more than 11.0 MBq/nmol. The resulting solutions were heated to 90°C for 10–20 min, and the radiopurities of the products were analyzed by radio-high-performance liquid chromatography. Radiopurity exceeded 95% in all studies.

Cell Binding Studies

Flow Cytometry. Antihuman FAP antibody conjugated to allophycocyanin dye was used for staining all cell lines except 4T1 cells, which were stained with antimouse FAP antibody and then a secondary allophycocyanin-conjugated antibody.

Displacement Assay. HEK-hFAP cells grown to confluence in 24-well plates were coincubated with FAP6-rhodamine and increasing concentrations of FAP6-DOTA or FAP6-IP-DOTA. The cells were then washed, dissolved, and analyzed by a fluorescent plate reader.

Binding Assay. Hs894 CAFs grown to confluence in 24-well plates were incubated with increasing concentrations of ^{111}In -FAP6-DOTA or ^{111}In -FAP6-IP-DOTA in the absence or presence of an excess of FAP6 ligand. The cells were then washed, dissolved, and analyzed by a γ -counter.

Animal Husbandry

The mice were provided normal rodent chow and water ad libitum and maintained on a standard 12-h light–dark cycle. All animal procedures were approved by the Purdue Animal Care and Use Committee.

Tumor Models

BALB/c mice were inoculated on their shoulder with 1×10^5 4T1 cells. Nu/nu mice were inoculated on their shoulder with 5×10^6 HT29, KB, or U87MG cells.

SPECT/CT Scans

Tumor-bearing mice were intravenously injected with FAP6 conjugate radiolabeled with about 13 MBq of ^{111}In . At indicated times, the mice were anesthetized and then scanned using an MILabs VECToR/CT instrument. CT scans were reconstructed using NRecon software (Micro Photonics Inc.). The datasets were fused, filtered, and processed using PMOD software (version 3.2).

Radioactive Biodistribution

Tumor-bearing mice ($n = 3$ –5) were intravenously injected with ^{177}Lu -FAP6-DOTA or ^{177}Lu -FAP6-IP-DOTA. At indicated times, the

mice were euthanized, and organs of interest were harvested, weighed, and analyzed by a γ -counter.

Radiotherapy

Mice bearing 4T1, HT29, KB, or U87MG tumors were randomly divided into control and treatment groups to ensure equal starting tumor volumes. Each cohort received a single intravenous injection of either vehicle alone or vehicle with ^{177}Lu -radiolabeled FAP6 conjugate on day 0. Tumors were measured with a caliper in 2 perpendicular directions every other day. The mice were euthanized on reaching one of the predefined endpoint criteria according to the regulations of the Institutional Animal Care and Use Committee.

Toxicology

The mice were weighed every other day during radiotherapy as a gross evaluation of health. Tissue sections from organs of interest ($n = 1$ –8 per organ per mouse) were preserved and examined for lesions in a masked manner by a board-certified veterinary pathologist.

Statistical Analysis

Data were analyzed using GraphPad Prism, version 8, unless otherwise stated. All results are presented as mean \pm SE.

RESULTS

scRNA-Seq Analysis of FAP Gene Expression in Multiple Human Tumor Types

To better understand how FAP might serve as a target for RLT, we first sought to quantify cells in human tumors that upregulate FAP expression. For this purpose, FAP gene expression data (Fig. 2) were extracted from a curated database containing scRNA-seq analyses of tumors from 14 breast, 5 ovarian, 7 colorectal, and 8 lung cancer patients (11). Quantification of the scRNA-seq data (Supplemental Fig. 1) revealed that about 30% of all CAFs overexpress FAP RNA. Although about 10% of endothelial cells also overexpressed FAP RNA, only about 2% of cancer cells and less than 1% of all other cell types upregulated FAP gene expression. Moreover, about 77% of all FAP-overexpressing cells in the average tumor were fibroblasts, suggesting that animal models used for evaluation of FAP-targeted RLTs should derive their FAP-positive cell population primarily from CAFs. And because FAP-overexpressing cells constituted no more than 10% of all cells in the average cancer mass (mean, 5%), a radionuclide with a large killing radius (e.g., ^{177}Lu) was deemed prudent for effective FAP-targeted radiotherapy. The variability of FAP expression among different human tumor types further suggested that adjusted doses of radioactivity might be necessary to achieve effective therapeutic responses in different patients.

Binding of FAP6 Conjugates to Different Cell Lines

Because FAP was not overexpressed on most human cancer cells, we mimicked FAP expression in human tumors more accurately by selecting cancer cell lines that did not directly express FAP. As documented in Figure 3A, flow cytometry analyses of 4T1, KB, and HT29 cells using species-specific anti-FAP antibodies demonstrated no FAP expression, even though the same cancers are shown to be FAP-positive in murine tumor models

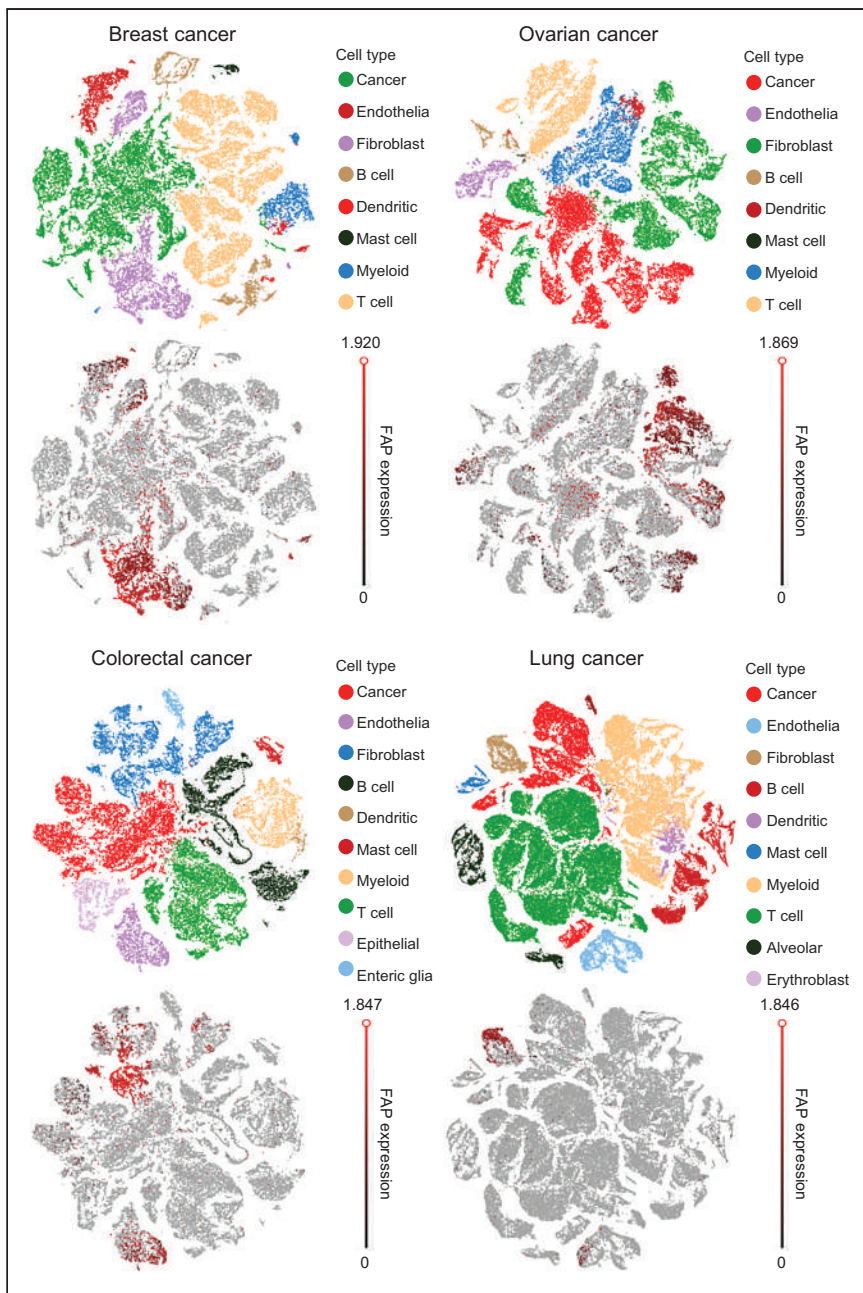


FIGURE 2. t-distributed stochastic-neighbor-embedding plots of scRNA-seq data from human breast, ovarian, colorectal, and lung cancers.

(Supplemental Fig. 2) because of infiltration of CAFs (13–17). In contrast, fibroblast cell lines Hs894 and WI38, as well as the glioblastoma cell line U87MG, displayed similarly low levels of endogenous FAP expression. HEK293 cells that do not naturally express FAP were transduced to express artificially high levels of human FAP for use as a positive control.

To develop a FAP ligand that can mediate protracted retention of FAP-targeted RLTs in solid tumors, we identified a FAP inhibitor comprising a scaffold different from that of the quinoline-based ligands most used to date (17–23). The FAP6 ligand contains a pyroglutamic-isoindoline-based moiety (13,24), which is reported to possess higher selectivity for FAP than PREP (a ubiquitously

expressed homolog) (24) and longer retention in tumors when conjugated to a near-infrared dye (13,25). We then linked FAP6 with DOTA via a polyethylene glycol spacer to yield the FAP6-DOTA conjugate (Supplemental Scheme 1). To evaluate the merit of attaching an albumin binder to FAP6-DOTA, an iodophenyl butyric acid (IP) moiety was inserted to generate FAP6-IP-DOTA (Supplemental Scheme 2). The final structures of FAP6-DOTA (Fig. 3B) and FAP6-IP-DOTA (Fig. 3C) were characterized by liquid chromatography–mass spectrometry (Supplemental Fig. 3). Radiolabeling with ^{111}In and ^{177}Lu was evaluated by radio–high-performance liquid chromatography (Supplemental Fig. 4).

To obtain an initial estimate of the affinity of the FAP6 ligand for FAP, competitive displacement and direct binding curves were generated with both conjugates (Figs. 3B and 3C) in HEK-hFAP and Hs894 CAFs, respectively. FAP6-DOTA and FAP6-IP-DOTA exhibited affinities of about 1 nM for FAP in both cell lines, suggesting that appending the albumin binder did not significantly affect conjugate affinity. Binding was competitively suppressed by coincubation with a 100-times excess of FAP6 ligand, confirming that targeting of FAP6 conjugates to FAP-positive cells was receptor-mediated. Both FAP6 conjugates were also found to internalize into FAP-positive cells (Supplemental Fig. 5), mirroring FAP6-dye conjugates (13).

Tumor Accumulation and Biodistribution of FAP6 Radioligands

To determine whether insertion of the albumin binder improves accumulation of FAP6 conjugates in solid tumors, we next compared the biodistributions of both radioligands in tumor-bearing mice wherein the primary FAP-positive cells were CAFs. BALB/c mice inoculated with FAP-negative 4T1 cancer cells were intravenously injected with either ^{111}In -FAP6-DOTA or ^{111}In -FAP6-IP-DOTA for radioimaging (Supplemental Figs. 6–7 show studies to optimize

mass doses). The SPECT/CT scans demonstrated high uptake of ^{111}In -FAP6-DOTA in the liver but negligible accumulation in the tumors at 2 and 4 h after injection (Fig. 4A), presumably because of rapid excretion of ^{111}In -FAP6-DOTA before its perfusion into poorly vascularized 4T1 tumors. In contrast, radioimages of mice injected with the same dose of ^{111}In -FAP6-IP-DOTA showed prominent tumor uptake that persisted for at least 120 h after injection (Fig. 4B). Additional SPECT/CT scans of HT29, KB, and U87MG tumors demonstrated the versatility of ^{111}In -FAP6-IP-DOTA tumor targeting and retention (Supplemental Figs. 7 and 8). Competition and untargeted radioimages confirmed that *in vivo* tumor uptake was FAP-mediated (Supplemental Fig. 9). Although

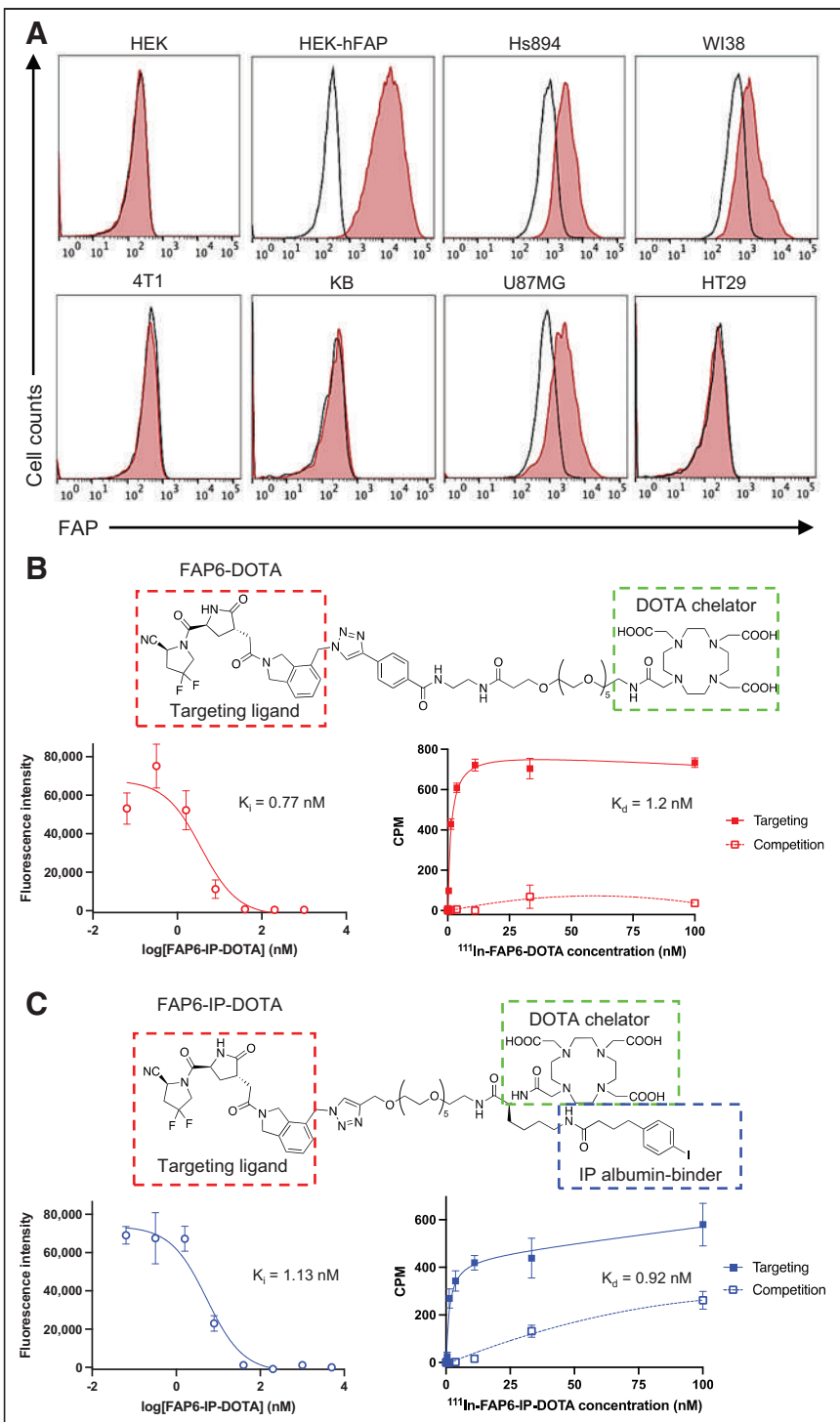


FIGURE 3. (A) Histograms of FAP expression by indicated cell lines (unstained controls = black; anti-FAP stained cells = red). (B and C) Structures, HEK-hFAP competition assays, and Hs894 CAF binding assays of FAP6-DOTA (B) and FAP6-IP-DOTA (C). K_i = inhibition constant; K_d = dissociation constant.

transient retention was also observed in the kidneys, the absence of significant accumulation in the liver suggested that FAP6-IP-DOTA might constitute an RLT worthy of further scrutiny.

To confirm these results, we next quantitated the biodistributions of each FAP6 conjugate in separate cohorts of 4T1 tumor-bearing mice over time. ^{177}Lu -FAP6-DOTA demonstrated prolonged

accumulation in the spleen and liver yet rapid excretion from the bloodstream and tumors (Fig. 4A), whereas ^{177}Lu -FAP6-IP-DOTA readily cleared from healthy organs despite its protracted retention in blood and tumors (Fig. 4B). The data thus confirm that insertion of an iodophenyl albumin binder facilitates FAP6 circulation in the bloodstream, thereby avoiding premature capture by excretory organs, enabling increased FAP6 uptake by the CAFs and, ultimately, saturation of the tumor. Dosimetry estimates (Supplemental Fig. 10), ^{177}Lu -FAP6-IP-DOTA SPECT/CT scans, and ^{111}In -FAP6-IP-DOTA biodistribution studies were also performed (Supplemental Fig. 11; Supplemental Table 1).

Effect of Albumin Binder on Radiotherapeutic Potencies of FAP6 RLTs

Encouraged by the improved tumor accumulation conferred by insertion of an albumin binder, we next compared the radiotherapeutic potencies of the 2 FAP-targeted RLTs. Moreover, to expand the diversity of tumor types in which the FAP-targeted RLTs would be compared, we used a human cancer xenograft model (KB cells) reported to respond to radiotherapy (7) and in which the only cells overexpressing FAP were again CAFs (13,14). Mice bearing tumors generated from FAP-negative KB cells were injected intravenously with a single dose of vehicle alone or with ^{177}Lu -FAP6-DOTA or ^{177}Lu -FAP6-IP-DOTA on day 0. Tumor sizes and body weights were then measured every other day for 10 wk.

Consistent with the above SPECT/CT and biodistribution results, ^{177}Lu -FAP6-DOTA provided no therapeutic benefit, suppressing tumor growth by only 3% and conferring no prolongation of overall survival (Fig. 5A). In contrast, ^{177}Lu -FAP6-IP-DOTA radiotherapy suppressed tumor growth by about 36% and improved overall survival by an average of about 3 wk (Fig. 5B, P = not statistically significant). Although mice treated with ^{177}Lu -FAP6-IP-DOTA experienced minor weight loss immediately after injection, the same mice quickly recovered and displayed no persisting toxicities, as also is consistent with the clearance of ^{177}Lu -FAP6-IP-DOTA from healthy tissues.

Evaluation of ^{177}Lu -FAP6-IP-DOTA Treatment in Multiple Tumor Types

Satisfied that ^{177}Lu -FAP6-IP-DOTA constituted the better FAP-targeted RLT, we next investigated whether ^{177}Lu -FAP6-IP-DOTA might effectively treat a diversity of solid tumors, as frequently envisioned by others (3,18). Mice bearing HT29, U87MG, or 4T1

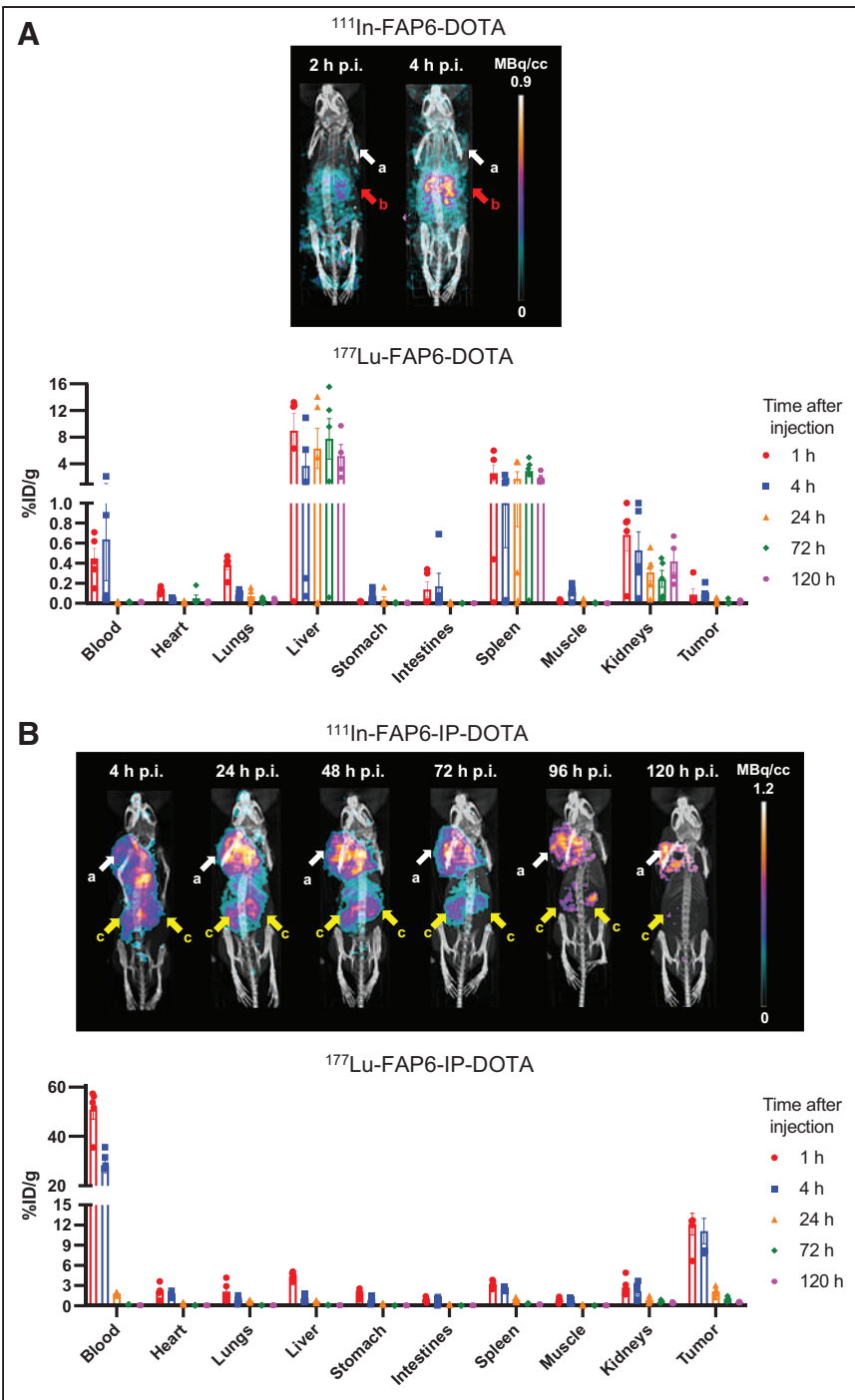


FIGURE 4. SPECT/CT and biodistribution analyses of FAP6-DOTA (A) vs. FAP6-IP-DOTA (B) in 4T1 tumors. %ID = percentage injected dose; a = tumors; b = liver; c = kidneys; p.i. = after injection.

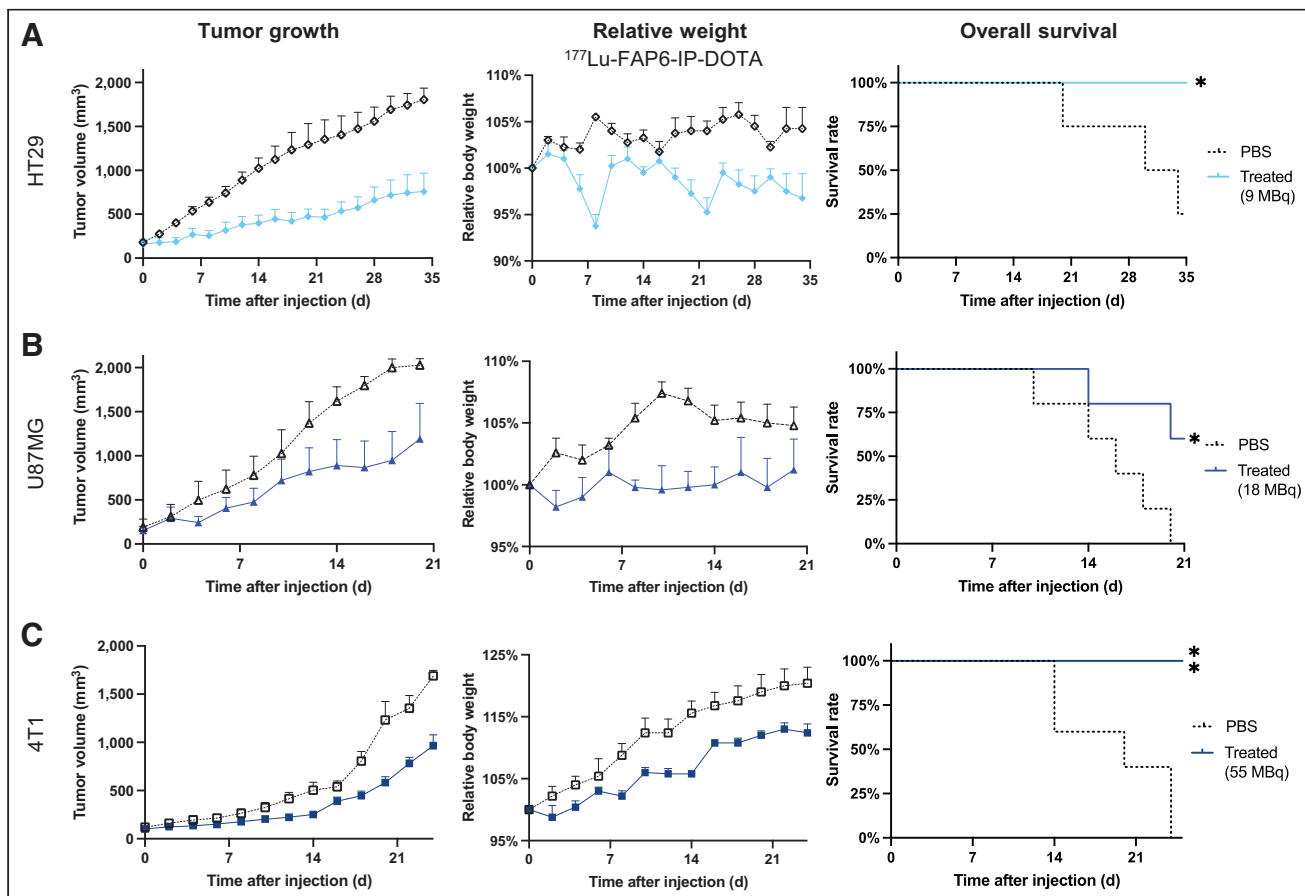
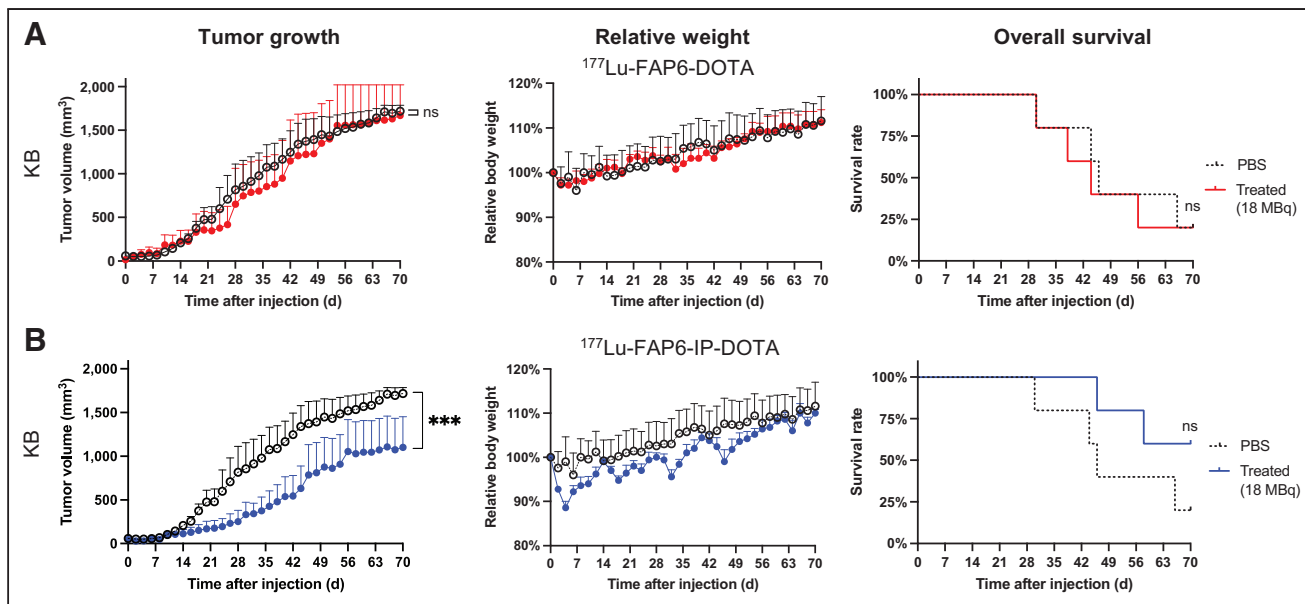
tumors were injected intravenously with a single dose of either vehicle alone or vehicle with ¹⁷⁷Lu-FAP6-IP-DOTA on day 0, after which tumor sizes and body weights were measured every other day. Growth of HT29 tumors was suppressed by about 58% by 9 MBq of ¹⁷⁷Lu-FAP6-IP-DOTA (Fig. 6A), but surprisingly, this dose did not affect U87MG or 4T1 tumors (Supplemental Figs. 12A and 12B). To determine whether U87MG or 4T1 tumors might respond to a higher dose of ¹⁷⁷Lu-FAP6-IP-DOTA, additional

cohorts of 5 mice per group were injected with 18 MBq of ¹⁷⁷Lu-FAP6-IP-DOTA and monitored. Growth of U87MG tumors was reduced by about 41% (Fig. 6B), but 4T1 tumors again continued to grow unabated (Supplemental Fig. 12B). Finally, 4T1 tumors treated with 55 MBq of ¹⁷⁷Lu-FAP6-IP-DOTA responded with an approximately 43% decrease in growth (Fig. 6C). Overall survival was significantly prolonged by at least 12 d at the respective doses without inducing persistent weight loss.

To further explore the potential toxicity of a single dose of ¹⁷⁷Lu-FAP6-IP-DOTA, tissues from mice treated with 18 or 55 MBq were prepared for histologic examination. No diagnostic lesions or other significant morphologic differences between treated and control mice were identified (Supplemental Table 2). Hepatic extramedullary hematopoiesis and increases in circulating neutrophils were observed in several of the mice treated with 18 MBq, but this finding is expected in mice regardless of the treatment received (26). Surprisingly, mice treated with 55 MBq showed fewer histopathologic changes in the heart and liver than did untreated controls. Although mild lesions were observed in several kidneys, the lesions were deemed nonspecific (representative photomicrographs of tissue sections after both doses are shown in Supplemental Fig. 13). One lesion observed in the myocardium of a mouse 21 d after treatment with a 55-MBq dose revealed mineralization and epicarditis. Although this inflammation may be drug-related, carditis can be simply spontaneous (27). The minimal radioactivity in the heart and the mouse's healthy weight gain both raise a question regarding any causal relationship between the treatment and the lesion. Taken together, these data demonstrate that the radiation doses used here were able to suppress tumor growth without causing acute tissue changes.

DISCUSSION

Most preclinical studies of FAP-targeted imaging and therapeutic agents to date have used murine tumor models in which the cancer cells themselves directly express FAP (19,20,28–34). As shown in Figure 2, FAP is either absent or weakly expressed on malignant cells from breast, lung, colorectal, and ovarian human cancer patients. Although tumor models derived from cancer cells that were transduced to overexpress FAP can be useful for proof-of-concept studies, their high FAP expression may also obscure a need to modify the molecular design of an RLT to increase tumor accumulation in humans, such as by the addition of an albumin



binder. Tumor models with physiologically relevant levels of FAP expression should therefore be encouraged in RLT studies intended for clinical development.

It was noteworthy that our 4 tumor models displayed different sensitivities to ^{177}Lu -FAP6-IP-DOTA, according to the ranking HT29 > U87MG \approx KB > 4T1 tumors. Although variations in FAP expression will directly influence initial uptake of our RLT and may account for some of these different radiotherapy responses, no clear correlation was observed with *in vivo* FAP staining intensity (Supplemental Fig. 2). Discrepancies in intrinsic resistance mechanisms such as DNA damage repair pathways may help clarify the observed radiosensitivities *in vivo*, but analysis of the growth of the 4 cancer cell lines *in vitro* after radiation exposure also did not reveal a direct correlation (Supplemental Fig. 14). Considering that additional characteristics such as growth rates, vascularization, extracellular matrix densities, drug efflux pumps, and CAF distributions can all influence radiobiology (35), we suspect that no single variable will account for the disparities observed in these 4 tumor models. One limitation of this work is that preclinical radiotherapy studies typically translate poorly into humans because of alterations of such characteristics in murine tumor models (36). For future RLT studies on mice to predict response rates more reliably in humans, it will be important to identify tumor models that more accurately mimic the radiation resistance mechanisms and general biology of human cancers.

Motivated by previous successes in using a FAP6 near-infrared dye conjugate to image 7 different murine tumor models (13), we attempted to adapt the same FAP6 ligand as a radiopharmaceutical. Although the inability of FAP6-DOTA to concentrate in tumors generated by FAP-negative 4T1 cells may seem initially surprising, it should be noted that Watabe (18) and Slania (25) also observed minimal uptake with FAPI conjugates when imaging pancreatic and prostate tumor models, respectively, in which the cancer cells did not directly express FAP. Because FAP6 exhibits higher affinity for FAP than FAPI (19,20,32), is readily internalized by an endocytic mechanism (32), and did not show tumor accumulation even when high mass doses of compound were administered (Supplemental Fig. 6), we hypothesized that the lack of tumor uptake of FAP6-DOTA was due to its rapid excretion before sufficient perfusion into the tumors. Therefore, to prolong the circulation, we inserted the iodophenyl butyryl moiety to generate FAP6-IP-DOTA, which accumulated prominently in 4T1 tumors. The net effect was an approximately 88-times increase in tumor dose, more than a 1,500-times improvement in tumor-to-total-body dosimetry ratio (Supplemental Fig. 10), and effective radiotherapy of 4 tumor models.

Whether greater improvements can still be achieved with better FAP ligands (14,37), albumin binders (34,38), or linker modifications (20,23,32) is a question worthy of further scrutiny. The dosimetry estimates of FAP6-IP-DOTA revealed most tumor-to-healthy-organ ratios to be favorable (Supplemental Fig. 10), but the 2:1 tumor-to-kidney ratio may require additional improvement (39). This can be achieved by altering the albumin binder as described by others (38,40), but one limitation of drug development is that translating optimal pharmacokinetics in mice to humans is complicated by differences in metabolism and excretion (10). Another aspect of drug development is evaluating the performance of the FAP6-IP-DOTA candidate with respect to other FAP-targeted RLTs. FAP6-IP-DOTA demonstrates tumor retention seemingly superior to that of FAPI-46, as well as clearance from healthy organs faster than that of other FAP-targeted

albumin-binding radioligands (19,20,30,32). However, direct comparisons should be limited because most other studies used different tumor models in which the cancer cells directly overexpressed FAP and necessitated immunocompromised mouse strains. What structural elements result in optimal properties for FAP-targeted RLT in humans remains an important question for research.

Finally, it should be noted that tumors characterized by lower numbers of FAP-positive cells may still be less responsive to an optimized FAP-targeted RLT. Thus, successful treatment of some solid tumors may require combination with conventional therapies, combination with an orthogonal RLT targeted to other cells in the same tumor, or use of a FAP-targeted radioimaging companion diagnostic to select only patients with high FAP expression for radiotherapy (5,41). With these improvements, it remains conceivable that a FAP-targeted RLT may prove useful for treatment of many solid tumors.

CONCLUSION

To design a more clinically relevant study, 4 different tumor models with ostensibly physiologic (i.e., lower) levels of FAP expression were selected after analysis of scRNA-seq data from human cancers. The FAP6-IP-DOTA molecule demonstrated high affinity for FAP and prolonged circulation, resulting in strong accumulation in all 4 tumors and significant suppression of tumor growth when radiolabeled with ^{177}Lu . The data suggest that ^{177}Lu -FAP6-IP-DOTA may potentially be optimized for human use.

DISCLOSURE

Spencer Lindeman, Ramesh Mukkamala, Madduri Srinivasarao, and Philip Low hold a patent on FAP-targeted radioligand therapy. Financial support was received through a Purdue professorship. No other potential conflict of interest relevant to this article was reported.

ACKNOWLEDGMENTS

We acknowledge Dr. James A. Schaber and the Purdue Imaging Facility for assistance with SPECT/CT, Kristina Grayson and the Bindley Science Center for cell sorting, MacKenzie McIntosh and the Purdue Histology Research Laboratory for preparation of mouse tissue samples and histology work, and Dr. Isabelle F. Vanhaezebrouck and the Purdue University College of Veterinary Medicine for irradiation of cell samples. Spencer Lindeman thanks Jackson N. Moss, Taylor C. Schleinkofer, and Kate A. Kragness for help with the studies.

KEY POINTS

QUESTION: Can a FAP-targeted radioligand therapy demonstrate sufficient safety and efficacy for preclinical development in murine tumor models in which FAP expression is limited to CAFs?

PERTINENT FINDINGS: scRNA-seq data on 34 human breast, lung, ovarian, and colon cancers demonstrated that about 5% of all cells in human tumors overexpress FAP. ^{177}Lu -FAP6-IP-DOTA successfully treated multiple murine tumor models generated from FAP-negative cancer cells.

IMPLICATIONS FOR PATIENT CARE: These data suggest that ^{177}Lu -FAP6-IP-DOTA constitutes a promising candidate for development of FAP-targeted radiotherapy for solid tumors.

REFERENCES

1. Liu R, Li H, Liu L, et al. Fibroblast activation protein: a potential therapeutic target in cancer. *Cancer Biol Ther.* 2012;13:123–129.
2. Garin-Chesa P, Old LJ, Rettig WJ. Cell surface glycoprotein of reactive stromal fibroblasts as a potential antibody target in human epithelial cancers. *Proc Natl Acad Sci USA.* 1990;87:7235–7239.
3. Kratochwil C, Flechsig P, Lindner T, et al. ^{68}Ga -FAPI PET/CT: tracer uptake in 28 different kinds of cancer. *J Nucl Med.* 2019;60:801–805.
4. Ferdinandus J, Costa PF, Kessler L, et al. Initial clinical experience with ^{90}Y -FAPI-46 radioligand therapy for advanced-stage solid tumors: a case series of 9 patients. *J Nucl Med.* 2022;63:727–734.
5. Baum RP, Schuchardt C, Singh A, et al. Feasibility, biodistribution, and preliminary dosimetry in peptide-targeted radionuclide therapy of diverse adenocarcinomas using ^{177}Lu -FAP-2286: first-in-humans results. *J Nucl Med.* 2022;63:415–423.
6. Dumelin CE, Trüssel S, Buller F, et al. A portable albumin binder from a DNA-encoded chemical library. *Angew Chem Int Ed Engl.* 2008;47:3196–3201.
7. Müller C, Struthers H, Winiger C, et al. DOTA conjugate with an albumin-binding entity enables the first folic acid-targeted ^{177}Lu -radionuclide tumor therapy in mice. *J Nucl Med.* 2013;54:124–131.
8. Kuo H-T, Merkens H, Zhang Z, et al. Enhancing treatment efficacy of ^{177}Lu -PSMA-617 with the conjugation of an albumin-binding motif: preclinical dosimetry and endoradiotherapy studies. *Mol Pharm.* 2018;15:5183–5191.
9. Tian R, Jacobson O, Niu G, et al. Evans blue attachment enhances somatostatin receptor subtype-2 imaging and radiotherapy. *Theranostics.* 2018;8:735–745.
10. Kramer V, Fernández R, Lehnert W, et al. Biodistribution and dosimetry of a single dose of albumin-binding ligand [^{177}Lu]Lu-PSMA-ALB-56 in patients with mCRPC. *Eur J Nucl Med Mol Imaging.* 2021;48:893–903.
11. Qian J, Olbrecht S, Boeckx B, et al. A pan-cancer blueprint of the heterogeneous tumor microenvironment revealed by single-cell profiling. *Cell Res.* 2020;30:745–762.
12. SCope tutorial. Pan-Cancer TME Blueprint Website. <http://scope.lambrechtslab.org/#/a0f9b96f-e2d9-4156-9899-993e37a62c03/Breast.loom/tutorial>. Accessed January 4, 2023.
13. Mukkamala R, Lindeman SD, Kragness KA, et al. Design and characterization of fibroblast activation protein targeted pan-cancer imaging agent for fluorescence-guided surgery of solid tumors. *J Mater Chem B.* 2022;10:2038–2046.
14. Roy J, Hettiarachchi SU, Kaake M, et al. Design and validation of fibroblast activation protein alpha targeted imaging and therapeutic agents. *Theranostics.* 2020;10:5778–5789.
15. Cheng JD, Dunbrack RL Jr, Valianou M, et al. Promotion of tumor growth by murine fibroblast activation protein, a serine protease, in an animal model. *Cancer Res.* 2002;62:4767–4772.
16. Venning FA, Zornhagen KW, Wulkopf L, et al. Deciphering the temporal heterogeneity of cancer-associated fibroblast subpopulations in breast cancer. *J Exp Clin Cancer Res.* 2021;40:175.
17. Moon ES, Elvas F, Vliegen G, et al. Targeting fibroblast activation protein (FAP): next generation PET radiotracers using squaramide coupled bifunctional DOTA and DOTA^{5m} chelators. *EJNMMI Radiopharm Chem.* 2020;5:19.
18. Watabe T, Liu Y, Kaneda-Nakashima K, et al. Theranostics targeting fibroblast activation protein in the tumor stroma: ^{64}Cu - and ^{225}Ac -labeled FAPI-04 in pancreatic cancer xenograft mouse models. *J Nucl Med.* 2020;61:563–569.
19. Xu M, Zhang P, Ding J, et al. Albumin binder-conjugated fibroblast activation protein inhibitor radiopharmaceuticals for cancer therapy. *J Nucl Med.* 2022;63:952–958.
20. Wen X, Xu P, Shi M, et al. Evans blue-modified radiolabeled fibroblast activation protein inhibitor as long-acting cancer therapeutics. *Theranostics.* 2022;12:422–433.
21. Liu Y, Watabe T, Kaneda-Nakashima K, et al. Fibroblast activation protein targeted therapy using [^{177}Lu]FAPI-46 compared with [^{225}Ac]FAPI-46 in a pancreatic cancer model. *Eur J Nucl Med Mol Imaging.* 2022;49:871–880.
22. Kelly JM, Jeitner TM, Ponnala S, et al. A trifunctional theranostic ligand targeting fibroblast activation protein- α (FAP α). *Mol Imaging Biol.* 2021;23:686–696.
23. Meng L, Fang J, Zhao L, et al. Rational design and pharmacocomodulation of protein-binding theranostic radioligands for targeting the fibroblast activation protein. *J Med Chem.* 2022;65:8245–8257.
24. Tsai T-Y, Yeh T-K, Chen X, et al. Substituted 4-carboxymethylpyroglutamic acid diamides as potent and selective inhibitors of fibroblast activation protein. *J Med Chem.* 2010;53:6572–6583.
25. Slania SL, Das D, Lisok A, et al. Imaging of fibroblast activation protein in cancer xenografts using novel (4-quinolinoyl)-glycyl-2-cyanopyrrolidine-based small molecules. *J Med Chem.* 2021;64:4059–4070.
26. Mende N, Laurent E. Hematopoietic stem and progenitor cells outside the bone marrow: where, when, and why. *Exp Hematol.* 2021;104:9–16.
27. Glass AM, Coombs W, Taffet SM. Spontaneous cardiac calcinosis in BALB/cByJ mice. *Comp Med.* 2013;63:29–37.
28. Fischer E, Chaitanya K, Wüest T, et al. Radioimmunotherapy of fibroblast activation protein positive tumors by rapidly internalizing antibodies. *Clin Cancer Res.* 2012;18:6208–6218.
29. Zboralski D, Osterkamp F, Simmons A, et al. Preclinical evaluation of FAP-2286, a peptide-targeted radionuclide therapy (PTRT) to fibroblast activation protein alpha (FAP) [abstract]. *Ann Oncol.* 2020;31(suppl 4):S488.
30. Zhang P, Xu M, Ding J, et al. Fatty acid-conjugated radiopharmaceuticals for fibroblast activation protein-targeted radiotherapy. *Eur J Nucl Med Mol Imaging.* 2022;49:1985–1996.
31. Lindner T, Loktev A, Altmann A, et al. Development of quinoline-based theranostic ligands for the targeting of fibroblast activation protein. *J Nucl Med.* 2018;59:1415–1422.
32. Loktev A, Lindner T, Burger E-M, et al. Development of fibroblast activation protein-targeted radiotracers with improved tumor retention. *J Nucl Med.* 2019;60:1421–1429.
33. Galbiati A, Zana A, Bocci M, et al. A dimeric FAP-targeting small-molecule radioconjugate with high and prolonged tumor uptake. *J Nucl Med.* 2022;63:1852–1858.
34. Lin J-J, Chuang C-P, Lin J-Y, et al. Rational design, pharmacocomodulation, and synthesis of [^{68}Ga]Ga-Alb-FAPtp-01, a selective tumor-associated fibroblast activation protein tracer for PET imaging of glioma. *ACS Sens.* 2021;6:3424–3435.
35. Henke E, Nandigama R, Ergün S. Extracellular matrix in the tumor microenvironment and its impact on cancer therapy. *Front Mol Biosci.* 2020;6:160.
36. Koontz BF, Verhaegen F, De Ryuysscher D. Tumour and normal tissue radiobiology in mouse models: how close are mice to mini-humans? *Br J Radiol.* 2017;90:20160441.
37. Hettiarachchi SU, Li Y-H, Roy J, et al. Targeted inhibition of PI3 kinase/mTOR specifically in fibrotic lung fibroblasts suppresses pulmonary fibrosis in experimental models. *Sci Transl Med.* 2020;12:eaay3724.
38. Kuo HT, Lin KS, Zhang Z, et al. ^{177}Lu -labeled albumin-binder-conjugated PSMA-targeting agents with extremely high tumor uptake and enhanced tumor-to-kidney absorbed dose ratio. *J Nucl Med.* 2021;62:521–527.
39. Emami B, Lyman J, Brown A, et al. Tolerance of normal tissue to therapeutic irradiation. *Int J Radiat Oncol Biol Phys.* 1991;21:109–122.
40. Umbricht CA, Benešová M, Schibl R, et al. Preclinical development of novel PSMA-targeting radioligands: modulation of albumin-binding properties to improve prostate cancer therapy. *Mol Pharm.* 2018;15:2297–2306.
41. Fendler WP, Pabst KM, Kessler L, et al. Safety and efficacy of ^{90}Y -FAPI-46 radioligand therapy in patients with advanced sarcoma and other cancer entities. *Clin Cancer Res.* 2022;28:4346–4353.

Toward Single-Time-Point Image-Based Dosimetry of ^{177}Lu -PSMA-617 Therapy

Julia Brosch-Lenz^{1,2}, Astrid Delker¹, Friederike Völter¹, Lena M. Unterrainer¹, Lena Kaiser¹, Peter Bartenstein¹, Sibylle Ziegler¹, Arman Rahmim^{2–4}, Carlos Uribe^{3,5}, and Guido Böning¹

¹Department of Nuclear Medicine, University Hospital, LMU Munich, Munich, Germany; ²Department of Integrative Oncology, BC Cancer Research Institute, Vancouver, British Columbia, Canada; ³Department of Radiology, University of British Columbia, Vancouver, British Columbia, Canada; ⁴Department of Physics, University of British Columbia, Vancouver, British Columbia, Canada; and ⁵Department of Functional Imaging, BC Cancer, Vancouver, British Columbia, Canada

Radiopharmaceutical therapies (RPTs) with ^{177}Lu -prostate-specific membrane antigen (PSMA) ligands have demonstrated promising results for the treatment of metastatic castration-resistant prostate cancer. The lack of absorbed-dose–effect relationships currently prevents patient-specific activity personalization. To ease the implementation of dosimetry in the routine clinical workflow for RPT, simplified methods such as single-time-point (STP) instead of multiple-time-point (MTP) imaging protocols are required. This work aimed at assessing differences in the time-integrated activity (TIA) of STP versus MTP image-based dosimetry for ^{177}Lu -PSMA-617 therapy. **Methods:** Twenty metastatic castration-resistant prostate cancer patients with MTP quantitative ^{177}Lu -SPECT imaging data (~24, 48, and 72 h post injection (p.i.)) available on first and second ^{177}Lu -PSMA-617 therapy cycles were included in this study. Time–activity curves were fitted for kidneys and lesions to derive effective half-lives and yield a reference TIA. STP approaches involved the formula by Hänscheid (STP_H) and a prior-information method (STP_{prior}) that uses the effective half-lives from the first therapy cycle. All time points were considered for the STP approaches. Percentage differences (PDs) in TIA between STP and MTP were compared for the second therapy cycle. **Results:** Using STP_H at 48 h p.i. for kidneys showed a $-1.3\% \pm 5.6\%$ PD from MTP, whereas STP_{prior} showed a PD of $4.6\% \pm 6.2\%$. The smallest average PDs for the 56 investigated individual lesions were found using STP_{prior} at 48 h p.i., at only $0.4\% \pm 14.9\%$, whereas STP_H at 72 h p.i. had a smallest PD of $-1.9\% \pm 14.8\%$. **Conclusion:** STP dosimetry for ^{177}Lu -PSMA-617 therapy using a single SPECT/CT scan at 48 or 72 h p.i. is feasible, with a PD of less than $\pm 20\%$ compared with MTP. The validity of both STP_H and STP_{prior} has been demonstrated. We believe this finding can increase the adoption of dosimetry and facilitate implementation in routine clinical RPT workflows. Doing so will ultimately enable the finding of dose–effect relationships based on fixed therapy activities that may, in future, allow for absorbed-dose–based RPT activity personalization.

Key Words: single-time-point dosimetry; ^{177}Lu ; PSMA therapy

J Nucl Med 2023; 64:767–774

DOI: 10.2967/jnumed.122.264594

Received Jun. 29, 2022; revision accepted Nov. 14, 2022.
For correspondence or reprints, contact Julia Brosch-Lenz (jbrosch@bccrc.ca).

Published online Jan. 19, 2023.

Immediate Open Access: Creative Commons Attribution 4.0 International License (CC BY) allows users to share and adapt with attribution, excluding materials credited to previous publications. License: <https://creativecommons.org/licenses/by/4.0/>. Details: <http://jnm.snmjournals.org/site/misc/permission.xhtml>.

COPYRIGHT © 2023 by the Society of Nuclear Medicine and Molecular Imaging.

Radiopharmaceutical therapy (RPT) targeting the prostate-specific membrane antigen (PSMA) has shown significant promise in the treatment of metastatic castration-resistant prostate cancer (mCRPC) (1–3). PSMA radioligand therapy with ^{177}Lu was first conducted in 2013 (4), and shortly afterward, dosimetry results were reported for ^{177}Lu -PSMA-617 (5). Considerable improvements in overall survival and radiographic progression-free survival for mCRPC patients receiving ^{177}Lu -PSMA-617 therapy plus the standard of care, against the standard of care alone in the VISION trial (NCT03511664) (1), led to approval by the U.S. Food and Drug Administration in 2022. Although some evidence of the advantage of dosimetry-based treatment personalization has been shown recently for ^{90}Y liver radioembolization (6), current practice for most RPTs relies on fixed injected activities. The therapeutic scheme for ^{177}Lu -PSMA therapy involves 4–6 therapy cycles with fixed activities (7), whereas optimal patient treatment would consider individual factors during RPT planning, such as weight, height, tumor burden, pretreatments, dosimetry, and patients' preferences (8). The lack of broadly available absorbed doses (ADs) for RPT prevents reliable dose–effect relationships for lesions and healthy organs from being obtained, impeding treatment personalization in terms of activity and number of cycles (9). The possibility of correlating pretherapy information with dosimetry and patient outcome was recently shown (10) and should motivate the community to implement routine dosimetry within RPTs and actively plan and adapt an RPT to personalize treatment and maximize patient therapeutic benefit.

The evidence of patient benefit from personalized RPTs is limited by the fact that image-based dosimetry is still not routinely implemented along with RPTs. One limitation preventing clinical adoption of individualized dosimetry is that pharmacokinetic measurements typically require image acquisitions at multiple time points (MTPs) post injection (p.i.) of the radiopharmaceutical. Other factors, such as limited clinical resources (e.g., scanner availability and personnel), as well as the additional costs of MTP imaging and the unclear reimbursement (11), limit the application of personalized dose assessments. This lack of clinical adoption, however, goes against European council directive 2013/79/Euratom, which requests individual planning and verification of exposed target volumes and minimization of dose to nontarget regions, according to the ALARA principle (12).

In this work, we aimed to assess single-time-point (STP) image-based dosimetry for ^{177}Lu -PSMA-617 therapy for the second therapy cycle. Specifically, we considered the formula by Hänscheid et al.

(STP_H) (13) and a prior-information approach ($\text{STP}_{\text{prior}}$) that uses MTP imaging during the first therapy cycle and STP imaging for subsequent cycles. We believe that validation of a simple dosimetry approach that requires a single SPECT/CT scan can increase the adoption of dosimetry and facilitate implementation in routine clinical RPT workflows. Doing so can enable the finding of dose-response relationships based on fixed therapy activities that will ultimately allow for AD-based RPT activity personalization.

MATERIALS AND METHODS

Patients

This study was conducted on a cohort of patients with mCRPC who received two 6-GBq cycles of ^{177}Lu -PSMA-617. Twenty patients with MTP imaging data available for both therapy cycles were included. Therapeutic injections and subsequent imaging were performed at the department of nuclear medicine of the university hospital of Ludwig Maximilian University of Munich. Data were irreversibly anonymized. The institutional ethics committee approved this retrospective study (approval 21-0618), and the requirement to obtain informed consent was waived.

Imaging Protocol

The details of the MTP imaging protocol (Fig. 1) are in the supplemental materials (available at <http://jnm.snmjournals.org>) (5,14–17).

Determination of Time–Activity Curves

Images were processed using PMOD (version 4.005; PMOD Technologies LLC). The 24 h p.i. SPECT scan of each therapy cycle was chosen as a reference image to which the 48 h p.i. and 72 h p.i. SPECT scans were rigidly registered. Segmentation was performed on the 24 h p.i. SPECT scans of each cycle. The kidneys were segmented by applying a 20% fixed threshold, which produced good alignment when overlying the kidney volumes of interest (VOIs) on the CT scan, excluding the kidney pelvis. Manual adjustments were made when necessary. The qPSMA approach of Gafita et al. (18) was adopted for segmentation of individual lesions on the 24 h p.i. SPECT scan per cycle, which was converted into standardized uptake values (SUVs) based on body weight. The determined patient- and cycle-specific threshold was applied to the 24 h p.i. SPECT scan with an automatic multiregion approach. Physiologic uptake regions that were mistakenly selected as VOIs by the automatic multiregion threshold approach, such as in the gastrointestinal tract or bladder, were removed. Lastly, a whole-field-of-view (FOV) tumor burden (TB_{FOV}) VOI containing all individual lesions was created. The lesion segmentation

was verified and, if necessary, manually adjusted on the SPECT and CT scans by 2 experienced readers in a consensus reading.

All VOIs were copied to the coregistered 48 h p.i. and 72 h p.i. SPECT scans, and the activity values of each VOI were extracted to generate time–activity curves. These were fit to a monoexponential function using MATLAB (version R2019b; The MathWorks, Inc.) to determine the effective half-lives ($T_{1/2}^{\text{eff}}$) (17) for kidneys, TB_{FOV} , and individual lesions. The procedure was performed for both therapy cycles.

Time-Integrated Activity (TIA) with MTP and STP Approaches

The TIA for each VOI in the second therapy cycle was calculated using 3 different methods: the first used the monoexponential fit with all points available from the MTP scans in the second cycle (considered the reference TIA (TIA_{ref}), determined from activity at time $t = 0$ for the second therapy cycle, A_0^{2nd} , and $T_{1/2}^{\text{eff}}$ for the second therapy cycle, $T_{1/2}^{\text{2nd eff}}$ [Eq. 1]); the second used $T_{1/2}^{\text{eff}}$ determined from the curve fitting of the first cycle ($T_{1/2}^{\text{1st eff}}$; prior information) and the STP activity value of the second cycle; and the third used the approach suggested by Hänscheid (13).

$$\text{TIA}_{\text{ref}} = \frac{A_0^{\text{2nd}}}{\ln 2 / T_{1/2}^{\text{2nd eff}}} \quad \text{Eq. 1}$$

Three different STP TIAs were calculated for the second method, $\text{STP}_{\text{prior}}$, with Equation 2 by combining $T_{1/2}^{\text{1st eff}}$ with the single activities $A(t)$ measured at time $t = 24, 48$, or 72 h p.i.

$$\text{STP}_{\text{prior}} \text{ TIA} = \frac{A(t) \cdot 2^{\frac{t}{T_{1/2}^{\text{1st eff}}}}}{\ln 2} \quad \text{Eq. 2}$$

The third method, STP_H , estimated the STP TIA using the method of Hänscheid (13). This approach assumes that if the imaging time point t is within the interval from 0.75 to 2.5 times the $T_{1/2}^{\text{eff}}$ of the respective VOI, one can replace Equation 2 by a simplified formula (Eq. 3) with less than 10% error in TIA compared with MTP. Three different STP TIAs were calculated using the activities $A(t)$ measured at time $t = 24, 48$, or 72 h p.i.

$$\text{STP}_H \text{ TIA} \approx \frac{A(t) \cdot 2 \cdot t}{\ln 2} \quad \text{Eq. 3}$$

Comparisons

The STP approaches for the second therapy cycles were compared with the MTP reference. The percentage difference (PD) in STP TIA versus TIA_{ref} was calculated for each kidney, for TB_{FOV} , and for up to 6 lesions

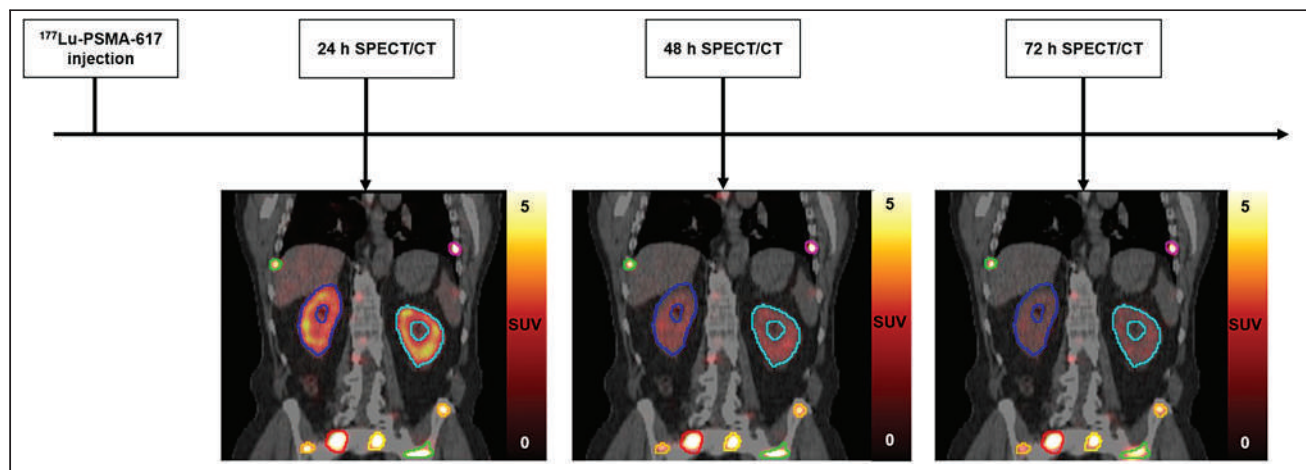


FIGURE 1. Overview of MTP imaging protocol.

per patient if they were visible in the FOV of both cycles. Bland–Altman plots were used to compare the STP approaches with MTP (19,20).

Statistical Analyses

Statistical analysis used the Wilcoxon signed-rank test for comparisons between MTP and each STP approach and between the $T_{1/2}$ eff of the first and second cycles.

RESULTS

Unless otherwise stated, all reported values are given as average \pm SD (minimum; maximum).

Patients

Twenty patients with mCRPC were included in this analysis. The average administered activity of ^{177}Lu -PSMA-617 for all patients and therapy cycles was 6.09 ± 0.13 GBq (5.74; 6.70 GBq). Left and right

kidneys were analyzed separately. The patients' TB_{FOV} volume averaged 462 ± 361 ml (8; 1,229 ml). One patient had no lesions within the SPECT FOV. In total, 56 lesions that were seen within the FOV for the first and second therapy cycles were analyzed.

Distribution of Effective Half-Lives

Figure 2 shows the $T_{1/2}$ eff distributions obtained with the MTP approach. The average $T_{1/2}$ eff for the first and second therapy cycles was 32.5 ± 7.0 h (17.8; 51.9 h) and 31.7 ± 6.4 h (21.6; 45.7 h), respectively, for kidneys; 75.3 ± 41.8 h (45.5; 240.0 h) and 64.8 ± 35.0 h (14.5; 192.8 h), respectively, for TB_{FOV} ; and 69.0 ± 40.0 h (20.1; 249.7 h) and 66.6 ± 34.2 h (19.7; 216.2 h), respectively, for individual lesions. Twenty-six of the 56 investigated lesions had a $T_{1/2}$ eff PD of more than $\pm 20\%$.

When $T_{1/2}$ eff obtained with the MTP approach was compared between the first and second therapy cycles using the Wilcoxon

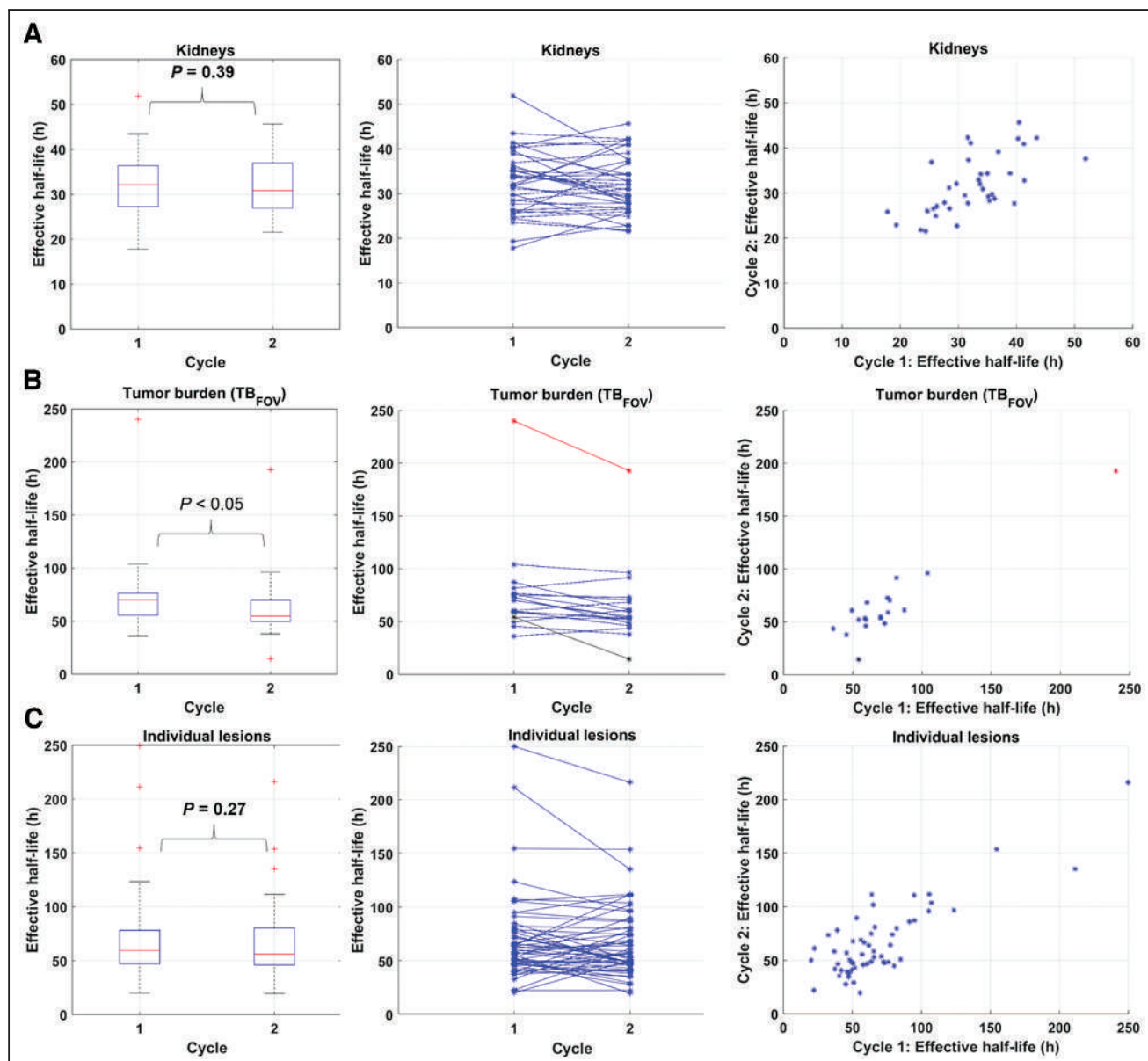


FIGURE 2. Distribution of $T_{1/2}$ eff calculated using MTP method for kidneys (A), TB_{FOV} (B), and individual lesions (C) for both therapy cycles. Plots further include results of statistical analysis using Wilcoxon signed-rank test for $T_{1/2}$ eff between cycles 1 and 2.

signed-rank test, significant differences (i.e., $P < 0.05$) were found for TB_{FOV} ($P = 0.02$) ($n = 19$; 1 patient had no lesions) but not for kidneys ($P = 0.39$) ($n = 37$; 3 patients had only 1 active kidney) or individual lesions ($P = 0.27$) ($n = 56$).

Comparison of TIA with Respect to STP Approaches

Figure 3 shows the PDs in TIA between the MTP and STP approaches. Supplemental Table 1 displays the values.

The Bland–Altman plots of STP_{prior} and STP_H compared with MTP are given in Figures 4 and 5. The mean relative difference between MTP and STP_{prior} was closest to zero for kidneys at 24 h p.i., for TB_{FOV} at 72 h p.i., and for individual lesions at 48 h p.i. (Fig. 4). However, the limits of agreement were smallest for kidneys at 48 h p.i., for TB_{FOV} at 72 h p.i., and for individual lesions at 48 h p.i. For STP_H, the difference from MTP was closest to zero, with the smallest limits of agreement at 48 h p.i. for kidneys and at 72 h p.i. for individual lesions (Fig. 5). For TB_{FOV}, the difference was smallest at 72 h p.i., whereas the limits of agreements were slightly smaller at 48 h p.i.

Statistical Analyses

The results of the statistical analysis for the STP approaches compared with the MTP reference are shown in Figure 3. In general, no significant difference in TIA for kidneys was found for an STP_{prior} at 24 h p.i. or an STP_H at 48 h p.i. For TB_{FOV}, no significant difference in TIA was found for an STP_{prior} at 48 h p.i. or STP_H at 72 h p.i. Lastly, for individual lesions, no significant difference in TIA was

found for an STP_{prior} at 24 h p.i., STP_{prior} at 48 h p.i., or STP_H at 72 h p.i.

Table 1 summarizes the number and percentage of VOIs for which the imaging time points per therapy cycle were within the interval from 0.75 to 2.5 times the $T_{1/2, \text{eff}}$ of that region as calculated with the MTP approach. The imaging time point at 48 h p.i. lay within that range for 97% and 100% of kidneys for both cycles 1 and 2, whereas for TB_{FOV} and individual lesions, the largest number of VOIs within that range was at 72 h p.i. However, for 25% of individual lesions and 21% of the TB_{FOV} VOIs, 72 h p.i. was outside the interval for cycle 2.

Figure 6 shows the percentage of VOIs for which the STP TIA was within $\pm 10\%$ and $\pm 20\%$ of TIA_{ref} for both the STP_{prior} and STP_H approaches. For STP_H, 95% of kidneys were within $\pm 10\%$ of TIA_{ref} at 48 h p.i., compared with 86% for STP_{prior}. For TB_{FOV}, 95% of VOIs were within $\pm 20\%$ of TIA_{ref} at 48 h p.i. and 72 h p.i. for STP_{prior}, compared with 68% and 89% for STP_H, respectively. For STP_{prior}, 86% and 91% of the individual lesions were within $\pm 20\%$ of TIA_{ref} at 48 h p.i. and 72 h p.i., compared with 63% and 86% for STP_H, respectively.

DISCUSSION

In this work, we aimed at comparing STP with MTP image-based dosimetry methods, which could increase clinical adoption. STP dosimetry methods have been studied predominantly for

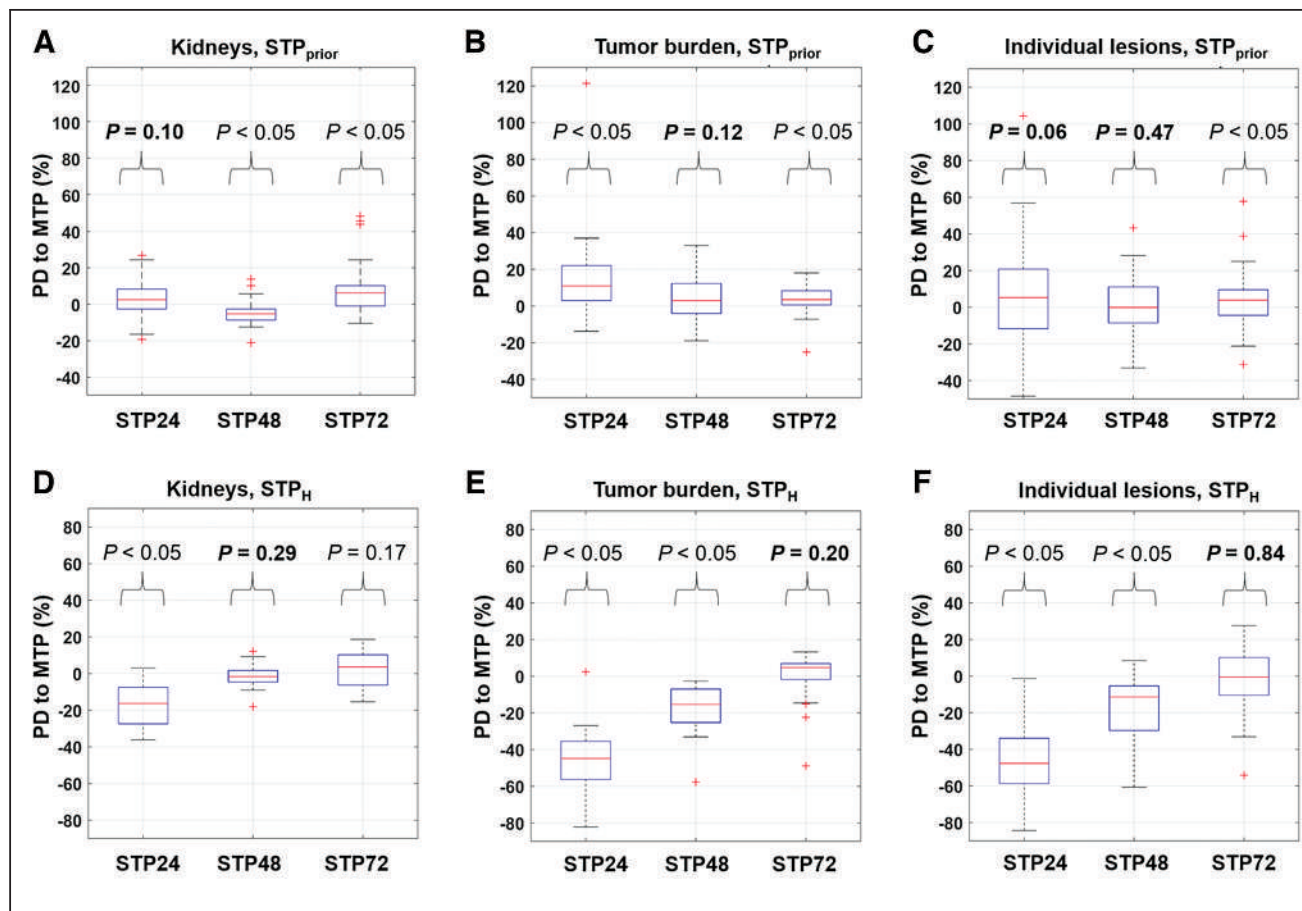


FIGURE 3. Distribution of PD of TIA in STP_{prior} (A–C) and STP_H (D–F) vs. MTP reference for kidneys (A and D), TB_{FOV} (B and E), and individual lesions (C and F). Plots further include results of statistical analysis using Wilcoxon signed-rank test between MTP and each respective STP approach.

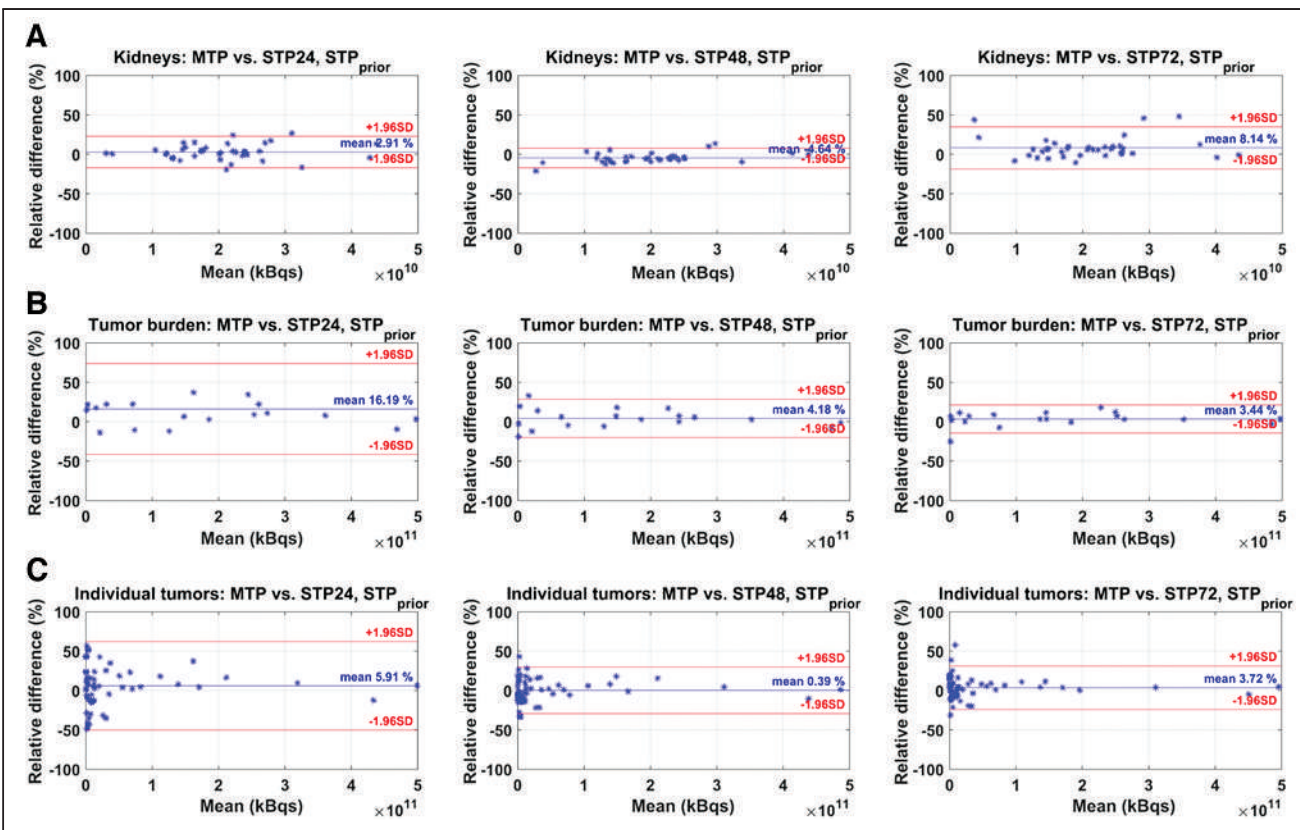


FIGURE 4. Bland-Altman plots of STP_{prior} vs. MTP reference for kidneys (A), TB_{FOV} (B), and individual lesions (C). STP24 = STP at 24 h p.i.; STP48 = STP at 48 h p.i.; STP72 = STP at 72 h p.i.

¹⁷⁷Lu-DOTATATE therapy (13,21–23) but also for ¹⁷⁷Lu-PSMA therapy (24–26). Three different approaches for STP dosimetry have been proposed: population-based mean $T_{1/2}$ eff (27), using prior information from the first therapy cycle for subsequent cycles (26), and using the formula by Hänscheid et al. (13). The first approach has been suggested to be valid for calculation of kidney ADs in ¹⁷⁷Lu-DOTATATE and ⁹⁰Y-DOTATOC therapies (22,27). Given the mean $T_{1/2}$ eff of 32.5 ± 7.0 h p.i. and 31.7 ± 6.4 h p.i. for the first and second ¹⁷⁷Lu-PSMA-617 therapy cycles determined from MTP imaging in this work, this approach may be a valid assumption. However, given the high variation and large spread of $T_{1/2}$ eff for TB_{FOV} and individual lesions (Figs. 2B and 2C), the population-based approach may not be suitable for lesion AD calculations in ¹⁷⁷Lu-PSMA therapies. Therefore, we compared clinically feasible dosimetry approaches for kidneys and lesions with a reduced number of imaging time points based on STP_{prior} and STP_H.

STP-based approaches showed smaller differences between TIA and TIA_{ref} for kidneys than for lesions. These differences can be associated with the smaller variations in $T_{1/2}$ eff (Fig. 2). For the STP_{prior} approach, our analysis indicated that an STP at 24 h p.i. results in TIA differences from MTP that are on average closer to zero (Fig. 3A). However, 48 h p.i. is more favorable if a smaller range of variations in PD versus TIA_{ref} is preferred (Figs. 3A and 4A). Our results agree with those reported by Kurth et al. (26), who applied the STP_{prior} approach for cycles 2–6 and found differences in AD of $\pm 6\%$ for kidneys and $\pm 10\%$ for parotid glands when using a single SPECT scan at 48 h p.i. of ¹⁷⁷Lu-PSMA-617, compared with MTP. Our analysis also suggests that when using

the STP_H approach, an STP at either 48 h p.i. or 72 h p.i. is favorable. However, an STP_H at 48 h p.i. may be optimal for kidney AD calculations given the smaller range of variations in STP TIA versus TIA_{ref} (Figs. 3B and Fig. 5A). For kidneys, STP_H outperformed STP_{prior} at 48 h p.i. in terms of PD in TIA with respect to MTP (Fig. 6). With STP_H, most (95%) kidney TIAs are expected to be within 10% of those calculated with MTP, with few (5%) falling within 10%–20%. For all kidneys except one, the 48 h p.i. imaging time point was within the interval from 0.75 to 2.5 times the $T_{1/2}$ eff. STP_H therefore yielded TIA estimates very close to TIA_{ref}. STP_{prior}, on the other hand, relies on a comparable $T_{1/2}$ eff for cycles 1 and 2. We observed up to a 45% difference in $T_{1/2}$ eff for some investigated kidneys. However, this translated to a PD in TIA_{ref} of between only -6% and 14% , which could be tolerated as long as the overall kidney function of the patient was good before therapy and the cumulative kidney AD was far below the considered toxicity threshold of 23 Gy.

For TB_{FOV} and individual lesions, an imaging time point of 72 h p.i. seems optimal, as the ranges of PD when compared with MTP are the smallest (Figs. 3A, 4B, and 4C) for the STP_{prior} approach. Similarly for STP_H, the PD when compared with MTP was closer to zero at 72 h p.i. (Figs. 3B, 5B, and 5C). However, to obtain TIA estimates for both kidneys and lesions in a single scan, an STP at 48 h p.i. might be a valid compromise. But this compromise comes at a higher variation in PD with respect to MTP for lesions.

STP_{prior} performed better overall for TB_{FOV} and individual lesions than did STP_H (Fig. 6). The performance of STP_H improved with later imaging time points. This finding agrees with findings reported by Hänscheid et al. for ¹⁷⁷Lu-DOTATATE (13) and Jackson et al.

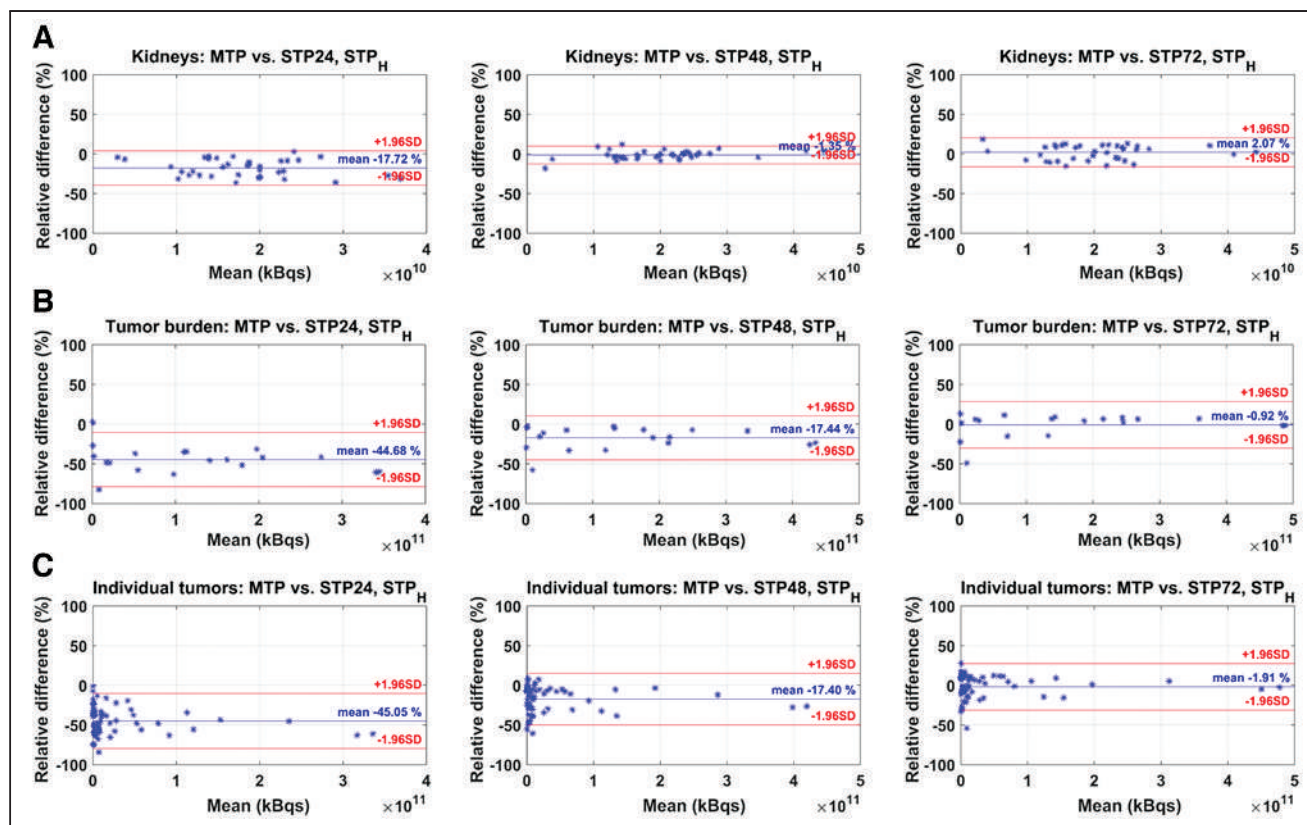


FIGURE 5. Bland-Altman plots of STP_H vs. MTP reference for kidneys (A), TB_{FOV} (B), and individual lesions (C). STP24 = STP at 24 h p.i.; STP48 = STP at 48 h p.i.; STP72 = STP at 72 h p.i.

for ¹⁷⁷Lu-PSMA-617 (25), both of whom found better agreement between STP and MTP for lesions at imaging time points even beyond 72 h p.i. STP_H showed an overall underestimation of TIA for TB_{FOV} and individual lesions (Fig. 3B). A similar negative skew for STP_H was previously observed by Gustafsson and Taprogge (28), underlining that STP approaches are limited in accuracy and that the distribution of $T_{1/2 \text{ eff}}$ in a population must be carefully determined. Our results, however, suggest that STP_{prior} is more suitable for tumor dosimetry, especially if the time point is 48 h p.i., matching our recommendation for kidneys. For STP_{prior}, it is expected that most TIAs will fall within 20% of those calculated with MTP. Our suggestion of performing SPECT at 48 h p.i. agrees with the analysis of Hou et al. (24). Generally, this recommendation is limited for STP_H, since, as shown in Table 1, the imaging time point of 48 h p.i. was outside the interval

from 0.75 to 2.5 times the $T_{1/2 \text{ eff}}$ for about 50% of the individual lesions for cycles 1 and 2 and for 50%–60% of TB_{FOV}.

The hybrid MTP/STP (STP_{prior}) approach presented here allows for collection of all required SPECT images during the routine 3-d hospital stay for patients receiving ¹⁷⁷Lu-PSMA-617 therapy at our institution. This data collection should, however, still be feasible for other institutions with in-patient therapies and for centers that discharge patients on day 0 if they agree to return during the following 2 days. We understand that the latter situation is not optimal, but open communication with the patient highlighting the benefit of MTP imaging during first therapy cycle may increase the patient's willingness to cooperate and participate in multiple scans. When a patient can tolerate only STP imaging (e.g., because of pain) or when only a single scan is feasible due to scanner

TABLE 1
Number of VOIs for Which Imaging Time Point was Within Interval from 0.75 to 2.5 Times $T_{1/2 \text{ eff}}$ of Cycle 1 or 2

Parameter	Cycle	VOIs (n)		
		24 h p.i.	48 h p.i.	72 h p.i.
Kidneys (N = 37)	1	7 (19%)	36 (97%)	28 (76%)
	2	12 (32%)	37 (100%)	27 (73%)
TB _{FOV} (N = 19)	1	0 (0%)	6 (32%)	17 (89%)
	2	1 (5%)	9 (47%)	15 (79%)
Individual lesions (N = 56)	1	3 (5%)	26 (46%)	43 (77%)
	2	2 (4%)	30 (54%)	42 (75%)

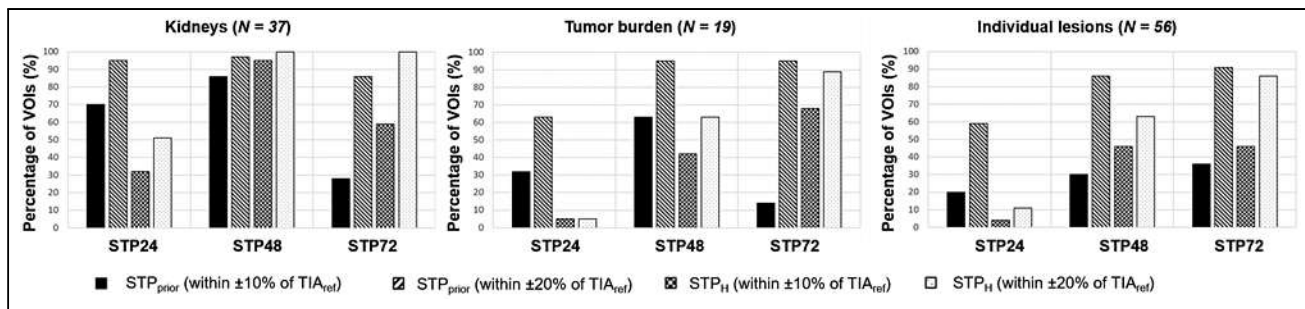


FIGURE 6. Percentage of VOIs for which difference in TIA for STP vs. MTP fell within $\pm 10\%$ or $\pm 20\%$.

availability or there are reimbursement issues, the STP_H approach can still be valid. However, imaging should be performed at 72 h p.i. or later (Fig. 6), when differences in TIA were within $\pm 20\%$ for all kidneys and for over 85% of the investigated TB_{FOV} and individual lesions. In our investigation, this imaging time point was within the interval from 0.75 to 2.5 times the $T_{1/2 \text{ eff}}$ for over 70% of kidneys, TB_{FOV}, and individual lesions, as shown in Table 1.

Specific patient situations should be considered when STP methods are applied. The STP_{prior} approach may be more prone to deviations from TIA_{ref} for lesions in cases of progressive disease or fast response (Supplemental Fig. 1). Protection of healthy organs from radiation-induced toxicities trumps achieving the highest possible lesion doses. When considering the minimum and maximum PDs of -21% and 14% for kidney TIA achieved with an STP_{prior} at 48 h p.i., and of -18.1% to 12.1% with STP_H, these PDs bear the risk of under- or overestimation of the actual kidney dose. Dose underestimation in the individual patient may lead to application of subsequent therapy cycles even if the kidney dose threshold has already been exceeded. ADs obtained from STP methods should therefore be interpreted with caution, in view of the approximately 20% underestimation in a few patients. The condition and kidney function of the individual patient before and during treatment must be closely monitored to prevent radiation-induced toxicity. Our analysis revealed large minimum and maximum PDs of -19% to 33% for TB_{FOV} and -33% to 43% for individual lesions for an STP_{prior} at 48 h p.i., and of -58% to -3% for TB_{FOV} and -61% to 8% for individual lesions when using STP_H. Since current clinical practice focuses on protection of healthy organs, these large ranges will likely not influence the patient's course of treatment. However, this variation in lesion AD, with possible over- or underestimation of the actual lesion AD, can potentially impact the derivation of dose-response relationships for prostate cancer lesions. The research community should therefore focus on MTP-derived lesion ADs to determine the response of lesions to ^{177}Lu -PSMA-617 therapy of prostate cancer. In case the therapeutic scheme for PSMA therapy includes PET/CT staging after every second therapy cycle, this information can be used to guide whether MTP imaging might become necessary for the subsequent therapy cycle because of large changes in tumor burden.

We recognize the limitation that our imaging protocol did not include time points after 72 h p.i. This study was based on the available imaging data at our institution—data that were acquired during the routine 3-d hospital stay for patients receiving ^{177}Lu -PSMA-617 therapy. However, our ranges of collected imaging time points are comparable to those of other institutions (26,29–31). Further research is needed to assess the validity of our results, including time points of 96 h p.i. or later, and may lead to a different favorable time point for the STP approach for lesions due to their longer retention time

(32) than was shown in our study. Our suggested imaging time point of 48 h p.i. ensured that the TIA determined with STP_{prior} was within $\pm 20\%$ of the TIA_{ref} for 97% of kidneys, 95% of TB_{FOV}, and 86% of individual lesions (Fig. 6). However, this 48 h p.i. time point is outside the interval from 0.75 to 2.5 times the $T_{1/2 \text{ eff}}$ for about 50% of the individual lesions for cycles 1 and 2 and for 50%–60% of TB_{FOV} (Table 1). An imaging time point of 72 h p.i. may be more applicable for STP_H for lesions but with larger differences from TIA_{ref} for kidneys.

Patients with mCRPC may present with extensive metastases which can challenge the tracking of lesions across cycles and the calculation of ADs on an individual-lesion basis. Our analysis for individual lesions was therefore limited to 6 representative lesions per patient. Organ and lesion $T_{1/2 \text{ eff}}$ not only may depend on the individual patient but may vary widely between radiopharmaceuticals (Table 2 of Hou et al. (24) and Fig. 3 of Schuchardt et al. (33)). The applicability of different STP dosimetry approaches should therefore be carefully investigated for different organs, tumors, and radiopharmaceuticals. Future work should include organs that were outside or not entirely within the FOV of our 1-bed SPECT, as well as including all lesions per patient and expanding the analysis to other PSMA compounds. Further studies should investigate how parameters that can be acquired prior to therapy may impact $T_{1/2 \text{ eff}}$. MTP imaging may be advisable when certain parameters, such as the estimated glomerular filtration rate, are outside the reference range to precisely capture the patient-individual $T_{1/2 \text{ eff}}$. On the other hand, it can be assessed whether STP approaches are still valid but at different favorable imaging time points. Nevertheless, our results suggest that STP dosimetry is feasible for ^{177}Lu -PSMA-617 therapies. We hope that these findings simplify dosimetry clinical workflows and ease the implementation of routine dosimetry in RPTs.

CONCLUSION

The present study assessed STP image-based dosimetry for ^{177}Lu -PSMA-617 therapy of prostate cancer. Use of a single SPECT/CT scan at 48 or 72 h p.i. after injection of the radiopharmaceutical led to differences from the MTP-based dosimetry that were, overall, within $\pm 20\%$. Both STP_H and STP_{prior} were valid for ^{177}Lu -PSMA-617. Since STP-based dosimetry reduces the burden for patients and the overall costs and complexity of dosimetry, it facilitates the implementation of RPT dosimetry into routine clinical practice.

DISCLOSURE

This work was partly funded by the German Research Foundation (DFG) within the Research Training Group GRK2274 (Julia

Brosch-Lenz). No other potential conflict of interest relevant to this article was reported.

KEY POINTS

QUESTION: Can the number of imaging time points required for dosimetry be reduced?

PERTINENT FINDINGS: STP dosimetry is feasible using either the simplified formula by Hänscheid or a prior information approach that uses MTP imaging for the first therapy cycle with STP imaging for subsequent therapy cycles. Both methods allowed for patient-individual dosimetry for kidneys and lesions, with less than $\pm 20\%$ PD from MTP-based approaches.

IMPLICATIONS FOR PATIENT CARE: Patients will benefit from personalized dosimetry and prediction of related risks and outcome.

REFERENCES

1. Sartor O, de Bono J, Chi KN, et al. Lutetium-177-PSMA-617 for metastatic castration-resistant prostate cancer. *N Engl J Med*. 2021;385:1091–1103.
2. Hofman MS, Violet J, Hicks RJ, et al. [^{177}Lu]-PSMA-617 radionuclide treatment in patients with metastatic castration-resistant prostate cancer (LuPSMA trial): a single-centre, single-arm, phase 2 study. *Lancet Oncol*. 2018;19:825–833.
3. Baum RP, Kulkarni HR, Schuchardt C, et al. ^{177}Lu -labeled prostate-specific membrane antigen radioligand therapy of metastatic castration-resistant prostate cancer: safety and efficacy. *J Nucl Med*. 2016;57:1006–1013.
4. Ahmadzadehfari H, Rabbar K, Kürpig S, et al. Early side effects and first results of radioligand therapy with ^{177}Lu -DKFZ-617 PSMA of castrate-resistant metastatic prostate cancer: a two-centre study. *EJNMMI Res*. 2015;5:114.
5. Delker A, Fendler WP, Kratochwil C, et al. Dosimetry for ^{177}Lu -DKFZ-PSMA-617: a new radiopharmaceutical for the treatment of metastatic prostate cancer. *Eur J Nucl Med Mol Imaging*. 2016;43:42–51.
6. Garin E, Tselikas L, Guiu B, et al. Personalised versus standard dosimetry approach of selective internal radiation therapy in patients with locally advanced hepatocellular carcinoma (DOSISPHERE-01): a randomised, multicentre, open-label phase 2 trial. *Lancet Gastroenterol Hepatol*. 2021;6:17–29.
7. Kratochwil C, Fendler WP, Eiber M, et al. EANM procedure guidelines for radionuclide therapy with ^{177}Lu -labelled PSMA-ligands (^{177}Lu -PSMA-RLT). *Eur J Nucl Med Mol Imaging*. 2019;46:2536–2544.
8. Brosch-Lenz J, Yousefirizi F, Zukotynski K, et al. Role of artificial intelligence in theranostics: toward routine personalized radiopharmaceutical therapies. *PET Clin*. 2021;16:627–641.
9. Strigari L, Konijnenberg M, Chiesa C, et al. The evidence base for the use of internal dosimetry in the clinical practice of molecular radiotherapy. *Eur J Nucl Med Mol Imaging*. 2014;41:1976–1988.
10. Violet J, Jackson P, Ferdinandus J, et al. Dosimetry of ^{177}Lu -PSMA-617 in metastatic castration-resistant prostate cancer: correlations between pretherapeutic imaging and whole-body tumor dosimetry with treatment outcomes. *J Nucl Med*. 2019;60:517–523.
11. Graves SA, Bageac A, Crowley JR, Merlino DAM. Reimbursement approaches for radiopharmaceutical dosimetry: current status and future opportunities. *J Nucl Med*. 2021;62(suppl 3):48S–59S.
12. Council directive 2013/59/Euratom of 5 December 2013 laying down basic safety standards for protection against the dangers arising from exposure to ionising radiation, and repealing directives 89/618/Euratom, 90/641/Euratom, 96/29/Euratom, 97/43/Euratom and 2003/122/Euratom. Eur-lex website. <https://eur-lex.europa.eu/eli/dir/2013/59/oj>. Published December 5, 2013. Updated January 17, 2014. Accessed February 1, 2023.
13. Hänscheid H, Lapa C, Buck AK, Lassmann M, Werner RA. Dose mapping after endoradiotherapy with ^{177}Lu -DOTATATE/DOTATOC by a single measurement after 4 days. *J Nucl Med*. 2018;59:75–81.
14. Ljungberg M, Celler A, Konijnenberg MW, et al. MIRD pamphlet no. 26: joint EANM/MIRD guidelines for quantitative ^{177}Lu SPECT applied for dosimetry of radiopharmaceutical therapy. *J Nucl Med*. 2016;57:151–162.
15. Uribe CF, Esquinas PL, Tanguay J, et al. Accuracy of ^{177}Lu activity quantification in SPECT imaging: a phantom study. *EJNMMI Phys*. 2017;4:2.
16. Gosewisch A, Delker A, Tattenberg S, et al. Patient-specific image-based bone marrow dosimetry in Lu-177-[DOTA⁰,Tyr³]-octreotate and Lu-177-DKFZ-PSMA-617 therapy: investigation of a new hybrid image approach. *EJNMMI Res*. 2018;8:76.
17. Brosch-Lenz J, Uribe C, Gosewisch A, et al. Influence of dosimetry method on bone lesion absorbed dose estimates in PSMA therapy: application to mCRPC patients receiving Lu-177-PSMA-I&T. *EJNMMI Phys*. 2021;8:26.
18. Gafita A, Bieth M, Krönke M, et al. qPSMA: semiautomatic software for whole-body tumor burden assessment in prostate cancer using ^{68}Ga -PSMA11 PET/CT. *J Nucl Med*. 2019;60:1277–1283.
19. Bland JM, Altman DG. Statistical methods for assessing agreement between two methods of clinical measurement. *Lancet*. 1986;1:307–310.
20. Bland JM, Altman DG. Measuring agreement in method comparison studies. *Stat Methods Med Res*. 1999;8:135–160.
21. Del Prete M, Arsenault F, Saighi N, et al. Accuracy and reproducibility of simplified QSPECT dosimetry for personalized ^{177}Lu -octreotide PRRT. *EJNMMI Phys*. 2018;5:25.
22. Zhao W, Esquinas PL, Frezza A, Hou X, Beauregard JM, Celler A. Accuracy of kidney dosimetry performed using simplified time activity curve modelling methods: a ^{177}Lu -DOTATATE patient study. *Phys Med Biol*. 2019;64:175006.
23. Willowson KP, Eslick E, Ryu H, Poon A, Bernard EJ, Bailey DL. Feasibility and accuracy of single time point imaging for renal dosimetry following ^{177}Lu -DOTA-Tate ('Lutate') therapy. *EJNMMI Phys*. 2018;5:33.
24. Hou X, Brosch J, Uribe C, et al. Feasibility of single-time-point dosimetry for radiopharmaceutical therapies. *J Nucl Med*. 2021;62:1006–1011.
25. Jackson PA, Hofman MS, Hicks RJ, Scalzo M, Violet J. Radiation dosimetry in ^{177}Lu -PSMA-617 therapy using a single posttreatment SPECT/CT scan: a novel methodology to generate time- and tissue-specific dose factors. *J Nucl Med*. 2020;61:1030–1036.
26. Kurth J, Heuschkel M, Tonn A, et al. Streamlined schemes for dosimetry of ^{177}Lu -labeled PSMA targeting radioligands in therapy of prostate cancer. *Cancers (Basel)*. 2021;13:3884.
27. Madsen MT, Menda Y, O'Dorisio TM, O'Dorisio MS. Technical note: single time point dose estimate for exponential clearance. *Med Phys*. 2018;45:2318–2324.
28. Gustafsson J, Taprogge J. Theoretical aspects on the use of single-time-point dosimetry for radionuclide therapy. *Phys Med Biol*. 2022;67.
29. Hohberg M, Eschner W, Schmidt M, et al. Lacrimal glands may represent organs at risk for radionuclide therapy of prostate cancer with ^{177}Lu -DKFZ-PSMA-617. *Mol Imaging Biol*. 2016;18:437–445.
30. Peters SMB, Privé BM, de Bakker M, et al. Intra-therapeutic dosimetry of ^{177}Lu -Lu-PSMA-617 in low-volume hormone-sensitive metastatic prostate cancer patients and correlation with treatment outcome. *Eur J Nucl Med Mol Imaging*. 2022;49:460–469.
31. Privé BM, Peters SMB, Muselaers CHJ, et al. Lutetium-177-PSMA-617 in low-volume hormone-sensitive metastatic prostate cancer: a prospective pilot study. *Clin Cancer Res*. 2021;27:3595–3601.
32. Rinscheid A, Klettling P, Eiber M, Beer AJ, Glattling G. Influence of sampling schedules on ^{177}Lu -Lu-PSMA dosimetry. *EJNMMI Phys*. 2020;7:41.
33. Schuchardt C, Zhang J, Kulkarni HR, Chen X, Müller D, Baum RP. Prostate-specific membrane antigen radioligand therapy using ^{177}Lu -PSMA I&T and ^{177}Lu -PSMA-617 in patients with metastatic castration-resistant prostate cancer: comparison of safety, biodistribution, and dosimetry. *J Nucl Med*. 2022;63:1199–1207.

Biodistribution, Dosimetry, and Pharmacokinetics of ^{68}Ga -CBP8: A Type I Collagen–Targeted PET Probe

David Izquierdo-Garcia^{1–4}, Pauline Désogère^{1,5}, Mariane Le Fur^{1,2,5}, Sergey Shuvayev^{1,2,5}, Iris Y. Zhou^{1,2,5}, Ian Ramsay¹, Michael Lanuti^{2,6}, Onofrio A. Catalano^{1,2}, Ciprian Catana^{1,2,5}, Peter Caravan^{1,2,5}, and Sydney B. Montesi^{2,5,7}

¹Athinoula A. Martinos Center for Biomedical Imaging, Department of Radiology, Massachusetts General Hospital, Boston, Massachusetts; ²Harvard Medical School, Boston, Massachusetts; ³Harvard–MIT Division of Health Sciences and Technology, Cambridge, Massachusetts; ⁴Bioengineering Department, Universidad Carlos III de Madrid, Spain; ⁵Institute for Innovation in Imaging, Massachusetts General Hospital, Boston, Massachusetts; ⁶Division of Thoracic Surgery, Massachusetts General Hospital, Boston, Massachusetts; and ⁷Division of Pulmonary and Critical Care Medicine, Massachusetts General Hospital, Boston, Massachusetts

The ^{68}Ga -Collagen Binding Probe #8, ^{68}Ga -CBP8, is a peptide-based, type I collagen–targeted probe developed for imaging of tissue fibrosis. The aim of this study was to determine the biodistribution, dosimetry, and pharmacokinetics of ^{68}Ga -CBP8 in healthy human subjects. **Methods:** Nine healthy volunteers (5 male and 4 female) underwent whole-body ^{68}Ga -CBP8 PET/MRI using a Biograph mMR scanner. The subjects were imaged continuously for up to 2 h after injection of ^{68}Ga -CBP8. A subset of subjects underwent an additional imaging session 2–3 h after probe injection. OLINDA/EXM software was used to calculate absorbed organ and effective dose estimates based on up to 17 regions of interest (16 for men) defined on T2-weighted MR images and copied to the PET images, assuming a uniform distribution of probe concentration in each region. Serial blood sampling up to 90 min after probe injection was performed to assess blood clearance and metabolic stability. **Results:** The mean injected activity ($\pm \text{SD}$) of ^{68}Ga -CBP8 was 220 ± 100 MBq (range, 113–434 MBq). No adverse effects related to probe administration were detected. ^{68}Ga -CBP8 demonstrated an extracellular distribution with predominantly rapid renal clearance. Doses on the urinary bladder were 0.15 versus 0.19 mGy/MBq for men versus women. The highest absorbed doses for the rest of the organs were measured in the kidneys (0.078 vs. 0.088 mGy/MBq) and the liver (0.032 vs. 0.041 mGy/MBq). The mean effective dose was 0.018 ± 0.0026 mSv/MBq using a 1-h voiding model. The ^{68}Ga -CBP8 signal in the blood demonstrated biexponential pharmacokinetics with an initial distribution half-life of 4.9 min (95% CI, 2.4–9.4 min) and a 72-min elimination half-life (95% CI, 47–130 min). The only metabolite observed had a long blood plasma half-life, suggesting protein-bound ^{68}Ga . **Conclusion:** ^{68}Ga -CBP8 displays favorable in-human characteristics and dosimetry similar to that of other gallium-based probes. ^{68}Ga -CBP8 could therefore be used for noninvasive collagen imaging across a range of human fibrotic diseases.

Key Words: ^{68}Ga -CBP8; PET; fibrosis; collagen; dosimetry

J Nucl Med 2023; 64:775–781

DOI: 10.2967/jnmed.122.264530

Organ fibrosis is a major cause of morbidity and mortality. Fibrotic diseases, such as cirrhosis, pulmonary fibrosis, and systemic sclerosis, or diseases with a fibroproliferative component, such as

atherosclerosis, account for nearly half of all human deaths in the United States (1). Despite the high burden of fibrotic diseases, limitations exist regarding diagnosis and prognostication (2). For many types of fibrosis, diagnosis hinges on histopathology. However, biopsy carries risks and may be impractical for certain fibrotic diseases. Prognostication can be particularly challenging. Disease progression can be heterogeneous, and current imaging modalities such as CT or ultrasound are limited in their ability to determine fibrotic disease activity unless performed serially. In addition, the development of effective antifibrotic therapies has been hampered by difficulties in determining response to therapy and lack of validated noninvasive surrogate markers of early treatment response (3).

Several probes have been developed to assess processes driving or associated with tissue fibrosis (4,5). Because the mechanistic pathways causing fibrogenesis are similar across organ systems, a molecular probe developed for a specific indication, such as pulmonary fibrosis, may be broadly applicable to other diseases. Noninvasive molecular characterization of fibrosis may offer many advantages over traditional imaging approaches in terms of assessing disease activity, performing molecular phenotyping, and determining treatment response (6). Such technology may also be used for drug development to assist with confirming target engagement and assessing drug effect.

Fibrosis is characterized by the excessive deposition of collagen (7). We recently developed a type I collagen-targeted PET probe, ^{68}Ga -Collagen Binding Probe #8 (^{68}Ga -CBP8), and performed the first noninvasive collagen visualization in patients with idiopathic pulmonary fibrosis (8,9). ^{68}Ga -CBP8 is a peptide-based PET probe that was found to bind to type I collagen with high specificity (8). The ^{68}Ga -CBP8 lung signal strongly correlated with the amount of hydroxyproline, as a measure of collagen content, in 2 animal models of lung fibrosis. In addition, this probe was sensitive to detecting treatment response to an antifibrotic therapy. In humans, this probe detected increased collagen in the lungs of those with idiopathic pulmonary fibrosis compared with healthy volunteers (9).

The promising results enabled by ^{68}Ga -CBP8 require a more in-depth characterization of the probe properties, including biodistribution, clearance, and dosimetry, for further clinical translation. Here, we present the whole-body distribution, dosimetry estimates, pharmacokinetics, and metabolism of ^{68}Ga -CBP8 in healthy subjects.

MATERIALS AND METHODS

Subject Recruitment and Safety Monitoring

This study was approved by the Mass General Brigham (formerly Partners) Institutional Review Board (protocol 2017P002718) and

Received Jun. 15, 2022; revision accepted Nov. 29, 2022.

For correspondence or reprints, contact David Izquierdo-Garcia (dizquierdogarcia@mgh.harvard.edu) and Sydney Montesi (sbmontesi@partners.org).

Published online Dec. 8, 2022.

COPYRIGHT © 2023 by the Society of Nuclear Medicine and Molecular Imaging.

registered at clinicaltrials.gov (NCT03535545). All subjects provided written informed consent. Nine healthy subjects (5 men and 4 women) with a median age of 59 y (range, 23–76 y) were included. The subject characteristics are further summarized in Supplemental Table 1 (supplemental materials are available at <http://jnm.snmjournals.org>). The subjects were closely monitored for safety. Assessment for adverse effects of ^{68}Ga -CBP8 administration included monitoring of vital signs throughout the imaging session and a phone call the day after by a study physician. In addition, the first 6 subjects had electrocardiograms performed before probe injection and after completion of the imaging session.

Synthesis of ^{68}Ga -CBP8

^{68}Ga -CBP8 was manufactured under current good manufacturing practices at the Athinoula A. Martinos Center for Biomedical Imaging radiopharmacy. Two commercially available clinical-grade $^{68}\text{Ge}/^{68}\text{Ga}$ generators were used to produce ^{68}Ga -CBP8: the Isotope Technologies Garching generator and the Galli Eo (IRE Elit) generator. Further details about the synthesis of ^{68}Ga -CBP8 can be found in the supplemental materials.

PET/MRI Data Acquisition

Simultaneous PET and MRI (3-tesla) data were acquired using a Biograph mMR scanner (Siemens Healthineers). PET emission data were acquired for approximately 2 h from the start of the injection of ^{68}Ga -CBP8 using 5 bed positions of 240 s each. This allowed the acquisition of 5 time points (frames) per bed position starting around 0, 20, 40, 60, and 85 min after injection (supplemental materials).

PET images were reconstructed in 3-dimensional mode using the standard reconstruction parameters provided by the manufacturer, that is, ordinary Poisson ordered-subset expectation maximization with 3 iterations and 21 subsets with a postreconstruction isotropic gaussian filter of 4 mm with a maximum extended axial coverage (head to mid thigh) of up to 1 m. Simultaneously with the PET data acquisition, the MRI data were acquired with several sequences, including T2-weighted short-tau inversion recovery half-Fourier acquisition single-shot turbo spin-echo images acquired coronally during 2 concatenated breath holds and a dual-echo Dixon for attenuation correction purposes. The supplemental materials provide further details about the PET/MRI data acquisition.

Dosimetry Analysis

Human dosimetry estimates were calculated using OLINDA software, version 2.2 (OLINDA/EXM), using the International Commission on Radiological Protection 103 standard male and female models (10).

A uniform distribution of radiotracer concentration throughout the organs was assumed. Regions of interest were drawn at each individual multibed acquisition, as described by Pfeifer et al. (11) and Laforest et al. (12), on the coronal T2-weighted (half-Fourier single-shot turbo spin-echo) images using OsiriX MD, version 12 (Pixmeo SARL), covering all organs with visible uptake above the background (supplemental materials). Regions of interest were then resliced and propagated into the corresponding PET frames. Mean radiotracer concentrations were obtained per slice, and a weighted average was used to obtain 1 mean concentration value per organ. The average region-of-interest values were then converted into the percentage injected dose (%ID) per organ by normalizing to the total injected activity and using the phantom organ mass scaled by the ratio of the phantom's weight over the patient's actual weight, as shown by Laforest et al. (12,13) (supplemental materials). The time-dependent curves of the %ID per organ were then fit using an in-house script (Python, version 3.1) to provide the corresponding estimates of the organ time-integrated activity coefficients by analytic integration of a function using a combination of mono- and biexponentials (Supplemental Table 2) (12). The lumbar vertebrae dose was assigned to the red marrow using the weight provided in OLINDA, version 2.2, which follows the European Association of Nuclear Medicine guidelines (14). The time-integrated activity coefficient for the urinary bladder was calculated using the voiding model on the OLINDA software in a similar manner, as explained by Sprague et al. (15).

Finally, the value assigned for the remainder of the body was calculated as the difference from the total activity at a time point minus the accounted activity in all organs (11). Total organ-absorbed doses were calculated for each subject and then averaged together to create both the male and the female phantom estimated doses.

Blood Analyses

Serial venous blood sampling for measurement of ^{68}Ga -CBP8 blood clearance and metabolism was performed on 8 of the 9 subjects using an intravenous catheter placed in the arm opposite the one used for probe injection. Up to 6 samples per subject were collected at around 3, 10, 20, 30, 60, and 90 min after injection. The exact time points were used in data analysis. A 300- μL aliquot of each whole-blood sample was weighed, its radioactivity was measured with a γ -counter (Wizard 2480; PerkinElmer), and the %ID per gram was calculated (the supplemental materials describe γ -counter calibration). Another 2 mL of each blood sample was centrifuged at 4,000g for 5 min at 4°C to separate plasma. A 300- μL aliquot of plasma was weighed, and its activity was counted. Whole blood as the %ID per gram and

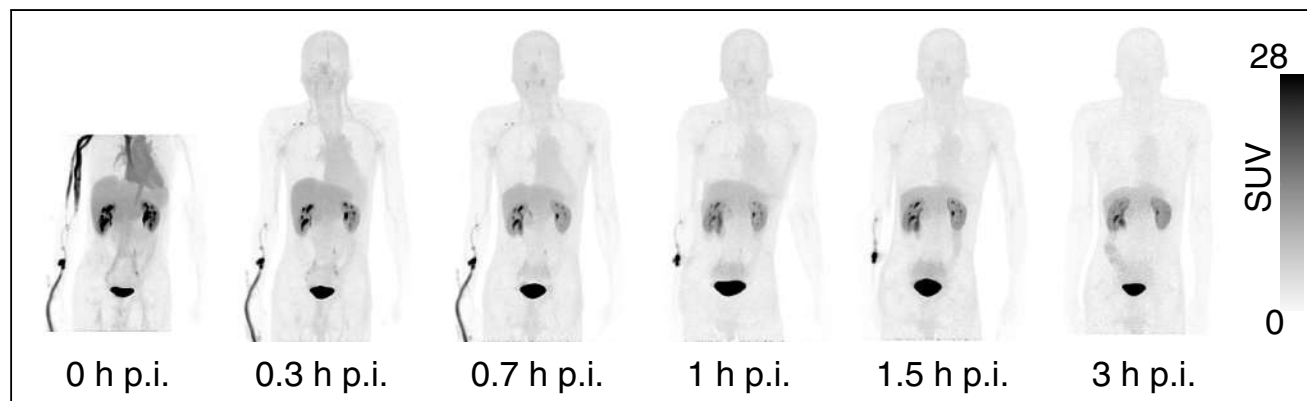


FIGURE 1. Maximum-intensity-projection coronal images of representative subject (subject 4) showing probe uptake pattern of ^{68}Ga -CBP8 from time of injection up to 3 h after injection across all organs. Note fast clearance of tracer from main organs, mostly through renal excretion, and smaller portion through hepatobiliary system, providing desired low, nonspecific background activity across all organs. p.i. = after injection.

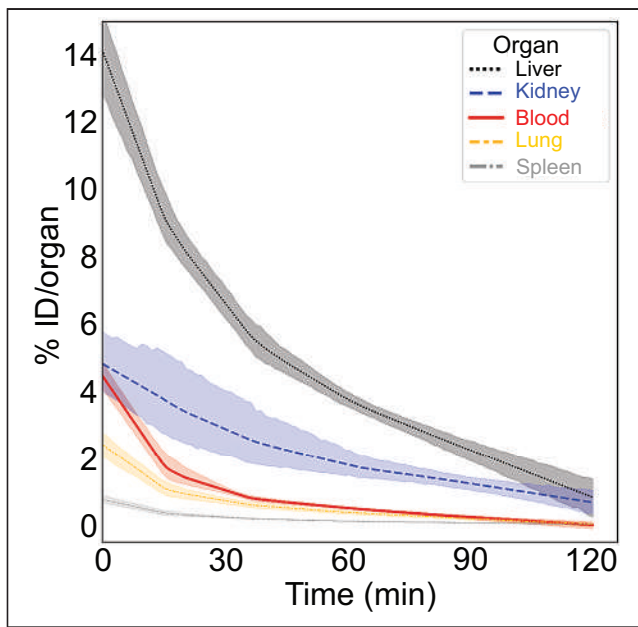


FIGURE 2. Time-activity curves for selected organs representing %ID per organ across time from injection up to 120 min. Each postinjection curve represents average across subjects, with shaded area representing 95% CI of mean.

plasma %ID per gram were plotted as a function of time and fit to a biexponential model:

$$\%ID/g(t) = Ae^{-\alpha t} + Be^{-\beta t},$$

where t is time, A and B are the fraction of injected activity for each individual exponential and α and β are the exponential rate constants for each individual exponential function.

Distribution half-life is given as $\ln(2)/\alpha$, and elimination half-life is given as $\ln(2)/\beta$. The supplemental materials show metabolite analysis using analytic high-performance liquid chromatography.

RESULTS

Synthesis

^{68}Ga -CBP8 was initially produced using ^{68}Ga from an Isotope Technologies Garching generator. The formulation of the precursor and the labeling protocol were optimized for this generator (Supplemental Table 3). The precursor was formulated in 3 M sodium acetate buffer (pH 4.5). Such a high buffer concentration was required to reach an optimal labeling pH of 4.0 after adding the $^{68}\text{Ga}^{3+}$ radioisotope eluted in 6 mL of 0.05 M HCl. Purification of the labeled product was required to remove radiometal impurities, including any ^{68}Ge , and excess buffer was required to meet quality control specifications. During the study, the U.S. Nuclear Regulatory Commission and the Massachusetts Department of Health issued a requirement that ^{68}Ga generators for human use have a specification of less than 0.001% ^{68}Ge breakthrough. The specification for the Isotope Technologies Garching generator was less than 0.005%, and although the ^{68}Ga -CBP8 process had a purification step to remove any ^{68}Ge , we were required to change to a different generator. When we moved to the Galli Eo generator, radiolabeling with the initial precursor formulation was unsuccessful, with radiochemical purity in the 90%–95% range. The formulation of the precursor was reoptimized and the labeling protocol was adapted for $^{68}\text{GaCl}_3$ eluted from the Galli Eo generator in 1.1 mL of 0.1 M HCl. Optimal labeling conditions were found using the CBP8 precursor formulated in 1.5 M sodium acetate at pH 4.0 (Supplemental Table 3). After the labeling reaction, the pH was adjusted to pH 6–8 using a 0.5 M solution of sodium phosphate dibasic, and the solution was diluted to 20 mL with an 80 mM sucrose solution to reach an osmolality suitable for intravenous injection (320–380 mOsm). No further purification was required since the

TABLE 1
SUV_{mean} at 90 min Postinjection for Several Organs Across All Subjects

Region of interest	All*	SUV _{mean} at 90 min			P , female vs. male†
		Female	Male		
Left ventricle	0.96 (0.73–1.28)	1.05 (0.73–1.28)	0.91 (0.73–1.12)		0.65
Myocardium	0.62 (0.27–1.36)	0.65 (0.27–0.86)	0.58 (0.37–1.36)		0.99
Lung	0.31 (0.19–0.47)	0.33 (0.22–0.47)	0.29 (0.19–0.38)		0.79
Skeletal muscle	0.32 (0.29–0.47)	0.31 (0.29–0.47)	0.32 (0.29–0.42)		0.99
Pancreas	1.13 (0.73–1.49)	1.42 (1.23–1.49)	0.89 (0.73–1.44)		0.14
Small intestine	0.85 (0.58–1.54)	0.79 (0.66–0.86)	0.94 (0.58–1.54)		0.39
Large intestine	0.71 (0.34–1.15)	0.58 (0.34–1.15)	0.79 (0.52–0.93)		0.79
Liver	2.44 (1.88–2.97)	2.56 (2.46–2.97)	2.31 (1.88–2.82)		0.14
Kidney	6.98 (5.18–9.32)	8.25 (7.33–9.20)	6.55 (5.18–9.32)		0.25
Uterus	NA	2.01 (1.81–3.47)	NA		NA
Prostate	NA	NA	1.55 (0.04–4.09)		NA
Brain	0.08 (0.03–0.09)	0.06 (0.03–0.09)	0.08 (0.05–0.09)		0.64

*Except subject 7 because of unavailable data around 90 min.

†Wilcoxon rank sum test.

NA = not applicable.

Data are median and range.

TABLE 2

Organ-Absorbed Doses and Effective Doses for Standard Male and Female Phantoms Using International Commission on Radiological Protection 103 Models

Target organ	Organ dose (mGy/MBq)		
	Male	Female	P*
Adrenals	0.018 (0.0032)	0.019 (0.0025)	0.016
Brain	0.0021 (0.0003)	0.0025 (0.0003)	<0.0001
Breasts	NA	0.011 (0.0022)	N/A
Esophagus	0.0093 (0.0010)	0.011 (0.0012)	<0.0001
Eyes	0.0076 (0.0009)	0.0092 (0.0011)	<0.0001
Gallbladder wall	0.019 (0.0067)	0.021 (0.0078)	<0.0001
Left colon	0.020 (0.0050)	0.022 (0.0047)	<0.0001
Small intestine	0.020 (0.0020)	0.024 (0.0024)	<0.0001
Stomach wall	0.013 (0.0018)	0.015 (0.0020)	<0.0001
Right colon	0.011 (0.0011)	0.013 (0.0014)	<0.0001
Rectum	0.012 (0.0005)	0.018 (0.0006)	<0.0001
Heart wall	0.016 (0.0013)	0.021 (0.0017)	<0.0001
Kidneys	0.078 (0.030)	0.088 (0.034)	<0.0001
Liver	0.032 (0.0036)	0.041 (0.0045)	<0.0001
Lungs	0.0067 (0.0008)	0.0085 (0.0010)	<0.0001
Ovaries	NA	0.014 (0.0007)	N/A
Pancreas	0.017 (0.0023)	0.021 (0.0027)	<0.0001
Prostate	0.021 (0.013)	NA	N/A
Salivary glands	0.0082 (0.0010)	0.010 (0.0012)	<0.0001
Red marrow	0.010 (0.0006)	0.012 (0.0008)	<0.0001
Osteogenic cells	0.0085 (0.0006)	0.0089 (0.0007)	<0.0001
Spleen	0.013 (0.0020)	0.016 (0.0023)	<0.0001
Testes	0.013 (0.0058)	NA	N/A
Thymus	0.0089 (0.0010)	0.011 (0.0012)	<0.0001
Thyroid	0.0085 (0.0010)	0.010 (0.0012)	<0.0001
Urinary bladder wall	0.15 (0.034)	0.19 (0.043)	<0.0001
Uterus	NA	0.029 (0.015)	N/A
Total body	0.011 (0.0009)	0.014 (0.0010)	<0.0001
Effective dose (mSv/MBq)	0.016 (0.0008)	0.021 (0.0012)	<0.0001

*Paired *t* test.

NA = not applicable.

Data are mean followed by SD in parentheses.

generator met specifications for ^{68}Ge breakthrough. Using this formulation and labeling protocol, ^{68}Ga -CBP8 was obtained with high radiochemical purity (>95%) and radiochemical yield greater than 80% after sterile filtration.

Safety, Biodistribution, and Dosimetry Estimates

The mean administered activity was 220 ± 100 MBq (range, 113–434 MBq). There were no adverse or clinically detectable pharmacologic effects related to ^{68}Ga -CBP8 in any of the 9 subjects. No significant changes in vital signs or electrocardiograms were observed.

Figure 1 demonstrates a typical biodistribution of ^{68}Ga -CBP8 over time. ^{68}Ga -CBP8 demonstrated rapid renal clearance, with some

uptake in the liver and biliary tract and low background uptake in other organs, such as the lungs. Figure 2 shows the time–activity curves for selected organs, including the lungs, liver, kidneys, spleen, and blood pool, demonstrating fast probe clearance and low background activity in healthy regions. Table 1 lists SUV_{mean} at 90 min after injection for various tissues. No differences were observed in SUV_{mean} between men and women. The ^{68}Ga -CBP8 signal in the blood, measured in the left ventricular region of interest, demonstrated biexponential pharmacokinetics with an initial distribution half-life of 4.4 min (95% CI, 3.1–5.8 min) and a 70.4-min elimination half-life (95% CI, 70.2–70.5 min). These values align with estimates of distribution and elimination half-life determined from venous blood sampling. Median fractions and half-lives for the bladder

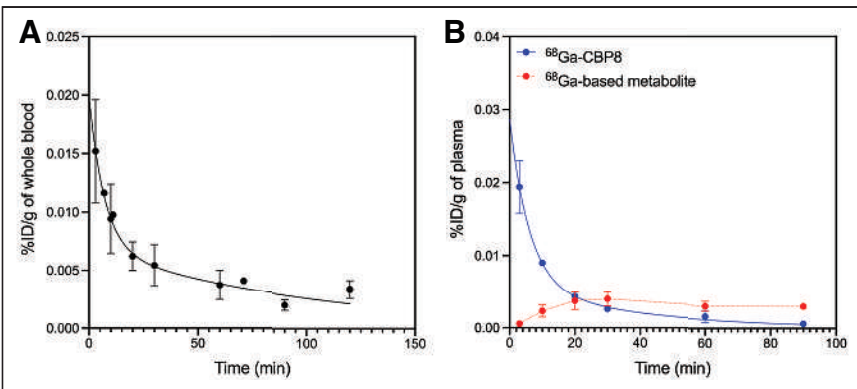


FIGURE 3. (A) Whole-blood clearance of ⁶⁸Ga-CBP8 in 8 subjects. (B) Blood plasma clearance of intact ⁶⁸Ga-CBP8 probe and ⁶⁸Ga-based metabolite observed by high-performance liquid chromatography.

model were 34% (range, 17%–38%) and 29 min (range, 15–47 min), respectively.

The organ-absorbed doses and the estimated effective doses for a 1-h voiding cycle are shown in Table 2. The urinary bladder was the organ with the highest absorbed dose for men and women (0.15 vs. 0.19 mGy/MBq, respectively), followed by the kidneys (0.078 vs. 0.088 mGy/MBq, respectively) and the liver (0.032 vs. 0.041 mGy/MBq, respectively). The mean effective dose was 0.018 ± 0.0026 mSv/MBq (0.016 ± 0.0008 mSv/MBq for men and 0.021 ± 0.0012 mSv/MBq for women). All organs showed higher absorbed doses for women to a significance level of $P < 0.0001$, except for the adrenals ($P = 0.016$). Overall, time-integrated activity coefficients did not show significant differences between men and women (Supplemental Table 4). An example of the data fitting and the square of the Pearson correlation coefficient (r^2) per organ are shown in Supplemental Figure 1 and Supplemental Table 4, respectively.

Pharmacokinetics and Metabolism

Analysis of radioactivity in serial venous blood samples showed a biexponential elimination (Fig. 3A). Fitting the blood radioactivity versus time curves to a biexponential function gave a distribution

half-life of 4.9 min (95% CI, 2.4–9.4 min) and an elimination half-life of 72 min (95% CI, 47–130 min), consistent with a probe that has low protein binding, predominantly renal elimination, and an extracellular distribution.

Radio-high-performance liquid chromatography analysis of plasma samples showed that ⁶⁸Ga-CBP8 is fairly stable with respect to metabolism (Supplemental Fig. 2). A single, small metabolite was observed, and this metabolite had a much longer blood half-life than ⁶⁸Ga-CBP8 (Fig. 3B). Because ⁶⁸Ga-CBP8 is rapidly eliminated from the plasma but the metabolite is not, the fraction of intact ⁶⁸Ga-CBP8 circulating changed as a function of time, with 97.1%, 79.9%, 54.1%, 39.8%, 22.9%, and 17.3% of the circulating dose corresponding to the intact probe at 3, 10, 20,

30, 60, and 90 min, respectively, after injection of the probe (Fig. 3B). On the basis of the long plasma half-life of the metabolite, we speculate that this may be due to the transmetalation of ⁶⁸Ga to a plasma protein.

DISCUSSION

Here we present the first-in-humans dosimetry and pharmacokinetic results of ⁶⁸Ga-CBP8. Our study has several notable findings. In a small group of healthy volunteers, there were no adverse events deemed related to ⁶⁸Ga-CBP8. ⁶⁸Ga-CBP8 had an extracellular distribution, displayed good metabolic stability, and was rapidly cleared from the circulation, with a distribution half-life of about 5 min and an elimination half-life of about 70 min. Doses were higher in women than men, similar to other dosimetry studies (13,16–19). However, neither the probe uptake (SUV_{mean} at 90 min; Table 1) nor the time-integrated activity coefficients (Supplemental Table 4) showed significant sex differences, suggesting that the higher S values per organ on the female phantom, as a result of the smaller female organ and body sizes (19), are responsible for the observed doses differences. ⁶⁸Ga-CBP8 displays dosimetry values

TABLE 3
Comparison of ⁶⁸Ga-CBP8 with Mean Effective Doses of Other ⁶⁸Ga-Based PET Probes and ¹⁸F-FDG

Compound	Effective dose (mSv/MBq)	Voiding model	Reference
⁶⁸ Ga-NODAGA-RGBYK	0.016–0.024	30 min and 1 h	(16)
⁶⁸ Ga-NODAGA-MJ9	0.018–0.023	30 min and 1 h	(17)
⁶⁸ Ga-P16–093	0.022–0.027	55 min (single)	(18)
⁶⁸ Ga-DOTA-E-[c(RGDfK)]2	0.017–0.024	1 h	(19)
⁶⁸ Ga-DOTATATE	0.021	Urine collection	(20)
⁶⁸ Ga-DOTATOC	0.021	Urine collection	(20)
⁶⁸ Ga-FAPI-2	0.018	Unspecified	(21)
⁶⁸ Ga-FAPI-4	0.016	Unspecified	(21)
⁶⁸ Ga-FAPI-74	0.016	Unspecified	(22)
¹⁸ F-FDG	0.020 (0.013–0.029)	Unspecified	(23)
⁶⁸ Ga-CBP8	0.018	1 h	This study

Effective doses are mean and/or range.

similar to those of other state-of-the-art ^{68}Ga -based tracers, including other NODAGA-based probes (Table 3) (16–22). In addition, the mean effective dose of 0.018 mSv/MBq with ^{68}Ga -CBP8 is in line with the standard and widely used ^{18}F -FDG, with mean effective doses of about 0.02 mSv/MBq (range, 0.013–0.029 mSv/MBq) (23). The mean effective dose was higher in women than men (0.021 vs. 0.016 mSv/MBq) because of the higher absorbed dose in the uterus and ovaries than in the testes and prostate.

There is increasing development and application of molecular probes for detection of fibrosis (24,25). Collagen is a particularly attractive target because it is the most abundant of proteins in the fibrotic extracellular matrix (26). ^{68}Ga -CBP8 is the first collagen-specific PET probe that has been translated into humans for fibrosis imaging. ^{68}Ga -CBP8 is a peptide-based probe that binds type I collagen with high specificity and a dissociation constant of $2.1 \pm 0.1 \mu\text{M}$ for human collagen (8). Ex vivo correlation of the %ID and lung collagen was strong in both bleomycin-injured mice and explanted lungs from patients with pulmonary fibrosis. In humans, ^{68}Ga -CBP8 uptake was increased in the whole lungs of subjects with idiopathic pulmonary fibrosis compared with healthy volunteers (0.65 vs. 0.48 SUV_{mean} at 60 min) (9). However, the PET signal in the lungs of subjects with pulmonary fibrosis is notably heterogeneous, with SUV_{mean} greater than 2 in areas of high ^{68}Ga -CBP8 uptake, presumably indicative of active fibrosis. In the healthy volunteers in this study, there was a reduced background signal (<1 SUV_{mean} at 90 min) for most organs, suggesting that this probe is likely to be useful for the detection of active fibrosis across multiple organ systems. ^{68}Ga -CBP8 has several advantages over other clinically used approaches to fibrosis detection. ^{68}Ga -CBP8 enables noninvasive collagen detection, thus obviating the risks associated with biopsy for histopathologic characterization. Imaging modalities such as CT or ultrasound can detect structural changes resulting from tissue fibrosis but have a limited ability to assess fibrotic disease activity at any one time point.

Our results expand on prior experience with ^{68}Ga -CBP8 by demonstrating favorable pharmacokinetic parameters and dosimetry estimates in humans. In healthy volunteers, ^{68}Ga -CBP8 had an extracellular distribution, fast clearance, and metabolic stability. Murine studies with ^{64}Cu -CBP7, a probe similar to ^{68}Ga -CBP8, also demonstrated fast clearance (blood half-life of 20 min in mice) and metabolic stability, with more than 80% of the probe still intact at 120 min (27).

Our results have several implications for broader clinical translation of ^{68}Ga -CBP8. First, we found that the synthesis of ^{68}Ga -CBP8 needed to be adapted to the type of generator used because of generator-dependent changes in yield and purity. Next, because of the rapid clearance, image acquisition can occur within a short time from probe injection. In healthy individuals, ^{68}Ga -CBP8 displayed low background uptake in all organs other than the urinary tract, liver, and biliary tree. Thus, ^{68}Ga -CBP8 may be applied to detect excess collagen in multiple organ systems. The favorable dosimetry estimates lessen the risks of repeated ^{68}Ga -CBP8 PET for detection of fibrosis progression and response to treatment.

Our study has several limitations. First, the increased bladder uptake induced large partial-volume effects on neighboring tissues. These partial-volume effects largely affected measurements of the ovaries. To avoid biasing the dosimetry estimates, we did not include the ovaries' measured uptake in the dosimetry calculations in OLINDA; instead, they were considered part of the remainder of the body region. However, increased uptake in the ovaries is not anticipated for younger healthy volunteers (our female cohort's average

age was <40 y); thus, its inclusion as part of the remainder of the body remains valid. Lastly, we used a simultaneous PET/MRI scanner to obtain our PET images. Although the use of PET/MRI compared with PET/CT eliminates the extra ionizing radiation from the CT component, the use of MRI-based techniques for attenuation correction on the whole-body level is still not ideal (28). Despite these limitations, our results are highly encouraging, demonstrating low organ doses and low mean effective doses and further supporting the clinical application of this probe to fibrotic diseases.

CONCLUSION

^{68}Ga -CBP8 demonstrates an extracellular distribution, rapid renal clearance, and metabolic stability in the blood. Dosimetry estimates are similar to those of other gallium-based probes. Thus, ^{68}Ga -CBP8 is a promising probe for imaging of collagen and tissue fibrosis.

DISCLOSURE

This work was supported by grants from the National Heart Lung and Blood Institute (R01HL116315, R01HL131907, R01HL153606, K23HL150331, and K25HL148837) and the National Institutes of Health (NIH) Office of the Director (S10OD028499). Peter Caravan and Pauline Désogère are inventors on U.S. patent US10,471,162, which covers ^{68}Ga -CBP8. David Izquierdo-Garcia has received consulting fees from Collagen Medical LLC. Michael Lanuti receives consulting fees from BMS, AstraZeneca, and Iovance. Peter Caravan holds equity in and receives consulting income from Collagen Medical LLC, holds equity in Reveal Pharmaceuticals, and has research funding from Takeda, Pliant Therapeutics, and Janssen. Sydney Montesi was supported by the NIH (K23HL15033), the Francis Family Foundation, and the National Scleroderma Foundation during the conduct of this study. She has received funding through her institution from Merck, United Therapeutics, Boehringer Ingelheim, and Pliant Therapeutics. She has also received funding from the American Thoracic Society and Three Lakes Foundation. She has received consulting fees from DevPro Biopharma, Gilead Sciences, and Roche; advisory board fees from APIE Therapeutics; and royalties from Wolters Kluwer. No other potential conflict of interest relevant to this article was reported.

ACKNOWLEDGMENTS

We thank the Athinoula A. Martinos Center for Biomedical Imaging PET/MRI core, Grae Arabasz, Shirley Hsu, Regan Butterfield, Oliver Ramsay, Matthew Drummond, Samantha Zygmont, Dr. Leo Ginns, Layla Rahimi, Staci Mangini, and Demi Ajao for their assistance.

KEY POINTS

QUESTION: What are the dosimetry and kinetic characteristics of the collagen-targeted probe ^{68}Ga -CBP8 in healthy volunteers?

PERTINENT FINDINGS: ^{68}Ga -CBP8 displays favorable kinetics with an extracellular distribution, fast renal clearance, and metabolic stability. Effective doses are similar to those reported for other gallium tracers.

IMPLICATIONS FOR PATIENT CARE: ^{68}Ga -CBP8 is a promising probe for noninvasive imaging of collagen that might be applied to a range of fibrotic diseases.

REFERENCES

1. Wynn TA. Fibrotic disease and the TH1/TH2 paradigm. *Nat Rev Immunol*. 2004;4:583–594.
2. Spagnolo P, Ryerson CJ, Putman R, et al. Early diagnosis of fibrotic interstitial lung disease: challenges and opportunities. *Lancet Respir Med*. 2021;9:1065–1076.
3. White ES, Thomas M, Stowasser S, Tetzlaff K. Challenges for clinical drug development in pulmonary fibrosis. *Front Pharmacol*. 2022;13:823085.
4. Klinkhammer BM, Lammers T, Mottaghy FM, Kiessling F, Floege J, Boor P. Non-invasive molecular imaging of kidney diseases. *Nat Rev Nephrol*. 2021;17:688–703.
5. Désogère P, Montesi SB, Caravan P. Molecular probes for imaging fibrosis and fibrogenesis. *Chemistry*. 2019;25:1128–1141.
6. Montesi SB, Désogère P, Fuchs BC, Caravan P. Molecular imaging of fibrosis: recent advances and future directions. *J Clin Invest*. 2019;129:24–33.
7. Wynn TA. Cellular and molecular mechanisms of fibrosis. *J Pathol*. 2008;214:199–210.
8. Désogère P, Tapia LF, Hariri LP, et al. Type I collagen–targeted PET probe for pulmonary fibrosis detection and staging in preclinical models. *Sci Transl Med*. 2017;9:eaaf4696.
9. Montesi SB, Izquierdo-García D, Désogère P, et al. Type I collagen–targeted positron emission tomography imaging in idiopathic pulmonary fibrosis: first-in-human studies. *Am J Respir Crit Care Med*. 2019;200:258–261.
10. Stabin MG, Siegel JA. RADAR dose estimate report: a compendium of radiopharmaceutical dose estimates based on OLINDA/EXM version 2.0. *J Nucl Med*. 2018;59:154–160.
11. Pfeifer A, Knigge U, Mortensen J, et al. Clinical PET of neuroendocrine tumors using ^{64}Cu -DOTATATE: first-in-humans study. *J Nucl Med*. 2012;53:1207–1215.
12. Laforest R, Dehdashti F, Lewis JS, Schwarz SW. Dosimetry of $^{60/61/62/64}\text{Cu}$ -ATSM: a hypoxia imaging agent for PET. *Eur J Nucl Med Mol Imaging*. 2005;32:764–770.
13. Laforest R, Ghai A, Fraum TJ, et al. First-in-human evaluation of safety and dosimetry of ^{64}Cu -LLP2A for PET imaging. *J Nucl Med*. 2022;64:320–328.
14. Hindorf C, Glatting G, Chiesa C, Lindén O, Flux G. EANM dosimetry committee guidelines for bone marrow and whole-body dosimetry. *Eur J Nucl Med Mol Imaging*. 2010;37:1238–1250.
15. Sprague DR, Chin FT, Liow JS, et al. Human biodistribution and radiation dosimetry of the tachykinin NK1 antagonist radioligand [^{18}F]SPA-RQ: comparison of thin-slice, bisected, and 2-dimensional planar image analysis. *J Nucl Med*. 2007;48:100–107.
16. Gnesin S, Mitsakis P, Ciccone F, et al. First in-human radiation dosimetry of ^{68}Ga -NODAGA-RGDyK. *EJNMMI Res*. 2017;7:43.
17. Gnesin S, Ciccone F, Mitsakis P, et al. First in-human radiation dosimetry of the gastrin-releasing peptide (GRP) receptor antagonist ^{68}Ga -NODAGA-MJ9. *EJNMMI Res*. 2018;8:108.
18. Green MA, Hutchins GD, Bahler CD, et al. [^{68}Ga]Ga-P16-093 as a PSMA-targeted PET radiopharmaceutical for detection of cancer: initial evaluation and comparison with [^{68}Ga]Ga-PSMA-11 in prostate cancer patients presenting with biochemical recurrence. *Mol Imaging Biol*. 2020;22:752–763.
19. López-Rodríguez V, Galindo-Sarco C, García-Pérez FO, Ferro-Flores G, Arrieta O, Avila-Rodríguez MA. PET-based human dosimetry of the dimeric $\alpha_1\beta_3$ integrin ligand ^{68}Ga -DOTA-E-[c(RGDFK)] 2, a potential tracer for imaging tumor angiogenesis. *J Nucl Med*. 2016;57:404–409.
20. Sandström M, Velikyan I, Garske-Román U, et al. Comparative biodistribution and radiation dosimetry of ^{68}Ga -DOTATOC and ^{68}Ga -DOTATATE in patients with neuroendocrine tumors. *J Nucl Med*. 2013;54:1755–1759.
21. Giesel FL, Kratochwil C, Lindner T, et al. ^{68}Ga -FAP1 PET/CT: biodistribution and preliminary dosimetry estimate of 2 DOTA-containing FAP-targeting agents in patients with various cancers. *J Nucl Med*. 2019;60:386–392.
22. Giesel FL, Adeberg S, Syed M, et al. FAPI-74 PET/CT using either ^{18}F -AIF or cold-kit ^{68}Ga labeling: biodistribution, radiation dosimetry, and tumor delineation in lung cancer patients. *J Nucl Med*. 2021;62:201–207.
23. Quinn B, Dauer Z, Pandit-Taskar N, Schoder H, Dauer LT. Radiation dosimetry of ^{18}F -FDG PET/CT: incorporating exam-specific parameters in dose estimates. *BMC Med Imaging*. 2016;16:41.
24. Brody SL, Gunsten SP, Luehmann HP, et al. Chemokine receptor 2–targeted molecular imaging in pulmonary fibrosis: a clinical trial. *Am J Respir Crit Care Med*. 2021;203:78–89.
25. Lukey PT, Coello C, Gunn R, et al. Clinical quantification of the integrin $\alpha v\beta 6$ by [^{18}F]FB-A20FMDV2 positron emission tomography in healthy and fibrotic human lung (PETAL study). *Eur J Nucl Med Mol Imaging*. 2020;47:967–979.
26. Frantz C, Stewart KM, Weaver VM. The extracellular matrix at a glance. *J Cell Sci*. 2010;123:4195–4200.
27. Désogère P, Tapia LF, Rietz TA, et al. Optimization of a collagen-targeted PET probe for molecular imaging of pulmonary fibrosis. *J Nucl Med*. 2017;58:1991–1996.
28. Keller SH, Holm S, Hansen AE, et al. Image artifacts from MR-based attenuation correction in clinical, whole-body PET/MRI. *MAGMA*. 2013;26:173–181.

Dosimetric Variability Across a Library of Computational Tumor Phantoms

Lukas M. Carter¹, Simone Krebs², Harry Marquis¹, Juan C. Ocampo Ramos¹, Edmond A. Olgun³, Emilia O. Mason⁴, Wesley E. Bolch⁵, Pat B. Zanzonico¹, and Adam L. Kesner¹

¹Department of Medical Physics, Memorial Sloan Kettering Cancer Center, New York, New York; ²Department of Radiology, Memorial Sloan Kettering Cancer Center, New York, New York; ³Department of Radiology, Beth Israel Deaconess Medical Center, Harvard University, Boston, Massachusetts; ⁴Department of Medicine, Sylvester Comprehensive Cancer Center, University of Miami, Miami, Florida; and ⁵J. Crayton Pruitt Department of Biomedical Engineering, University of Florida, Gainesville, Florida

In radiopharmaceutical therapy, dosimetry-based treatment planning and response evaluation require accurate estimates of tumor-absorbed dose. Tumor dose estimates are routinely derived using simplistic spherical models, despite the well-established influence of tumor geometry on the dosimetry. Moreover, the degree of disease invasiveness correlates with departure from ideal geometry; malignant lesions often possess lobular, spiculated, or otherwise irregular margins in contrast to the commonly regular or smooth contours characteristic of benign lesions. To assess the effects of tumor shape, size, and margin contour on absorbed dose, an array of tumor geometries was modeled using computer-aided design software, and the models were used to calculate absorbed dose per unit of time-integrated activity (i.e., S values) for several clinically applied therapeutic radionuclides (⁹⁰Y, ¹³¹I, ¹⁷⁷Lu, ²¹¹At, ²²⁵Ac, ²¹³Bi, and ²²³Ra). **Methods:** Three-dimensional tumor models of several different shape classifications were generated using Blender software. Ovoid shapes were generated using axial scaling. Lobulated, spiculated, and irregular contours were generated using noise-based mesh deformation. The meshes were rigidly scaled to different volumes, and S values were then computed using PARaDIM software. Radiomic features were extracted for each shape, and the impact on S values was examined. Finally, the systematic error present in dose calculations that model complex tumor shapes versus equivalent-mass spheres was estimated. **Results:** The dependence of tumor S values on shape was largest for extreme departures from spherical geometry and for long-range emissions (e.g., ⁹⁰Y β-emissions). S values for spheres agreed reasonably well with lobulated, spiculated, or irregular contours if the surface perturbation was small. For marked deviations from spherical shape and small volumes, the systematic error of the equivalent-sphere approximation increased to 30%–75% depending on radionuclide. The errors were largest for shapes with many long spicules and for spherical shells with a thickness less than or comparable to the particle range in tissue. **Conclusion:** Variability in tumor S values as a function of tumor shape and margin contour was observed, suggesting use of contour-matched phantoms to improve the accuracy of tumor dosimetry in organ-level dosimetry paradigms. Implementing a library of tumor phantoms in organ-level dosimetry software may facilitate optimization strategies for personalized radionuclide therapies.

Key Words: tumor dosimetry; phantoms; MIRD; Monte Carlo

J Nucl Med 2023; 64:782–790

DOI: 10.2967/jnmed.122.264916

T

umors are inherently variable, and tumor geometric characteristics including volume, shape (e.g., ovoid or irregular), margin morphology (e.g., circumscribed, lobulated, or spiculated), and composition (e.g., calcifications) are routinely assessed as anatomic imaging biomarkers or radiomic features (1,2). For tumors and normal organs, geometric features and composition influence the absorbed doses received from therapeutic radiopharmaceuticals. Over the last 50 y, human computational phantoms have evolved with tools for simulating radiation transport. Software programs implementing phantoms with anatomically realistic 3-dimensional organ shapes are now in widespread use for organ-level internal dosimetry (3–6). In contrast to organs, tumors are generally modeled as soft-tissue spheres of equivalent mass in organ-level dosimetry workflows—that is, tumor shape, margin morphology, and composition are rarely, if ever, incorporated into tumor dosimetry analyses.

A principal barrier to incorporation of these factors has been the lack of computational phantoms representative of shapes and compositions other than soft-tissue spheres and ellipsoids (7,8). In a recent study, Olgun et al. comprehensively investigated the dependence of tumor self-dose on tissue composition using a series of spheroid phantoms comprising various combinations of soft-tissue and mineral bone content (8). This study illustrated that assuming soft-tissue composition for highly mineralized tumors may translate to relative errors exceeding 80% in tumor dose estimates. Absorbed doses per unit of time-integrated activity (i.e., S values) derived from this study were built into the new MIRDcalc dosimetry software to enable routine consideration of tumor composition in tumor dosimetry calculations (5). The present study expands on previous work (8) to more comprehensively investigate the effect of tumor shape and margin contour on tumor self-dose.

In the present work, a procedural noise-based method for generating mesh-type representative tumor computational phantoms is described. Using this method, a library of tumor phantoms of differing volume, shape, and margin contour was generated. Using the library, S values for several therapeutic radionuclides were computed to provide insights into the influence of shape and contour on tumor-absorbed dose. Finally, practical application of such a library in routine clinical organ-level dosimetry workflows is discussed.

Received Sep. 13, 2022; revision accepted Nov. 29, 2022.
For correspondence or reprints, contact Lukas M. Carter (carterl1@mskcc.org).

Published online Dec. 8, 2022.
COPYRIGHT © 2023 by the Society of Nuclear Medicine and Molecular Imaging.

MATERIALS AND METHODS

Tumor Modeling

The 3-dimensional modeling software Blender (version 3.0.0; Blender Foundation) was used to generate the tumor phantom library (Fig. 1). Blender's icosphere geometric primitive (a triangulated

spherical surface) was used as the base mesh from which all other library members were generated. Specific procedures for generating additional shapes and contours are described below.

Spheroids. Spheroid shapes were generated by scaling the unit icosphere along the z-axis. Two oblate spheroids were generated using z-axis scale factors of 0.25 and 0.5. Two prolate spheroids were generated using z-axis scale factors of 2.0 and 4.0. Isotropic scaling was then used to generate similar spheroids of a range of volumes.

Spherical Shells. Spherical shells were modeled to approximate lesions with target-expressing malignant cells concentrated at the periphery (e.g., lesions with central necrosis). These were generated using a unit icosphere and a smaller icosphere. The latter icosphere partitions the phantom into an inner spherical core and an outer spherical shell or annulus. The relative shell thicknesses T were defined in relation to the outer (i.e., overall tumor) radius R : $T = 0.2, 0.4, 0.6$, or $0.8 R$. Isotropic scaling was then used to generate similar spherical shells of a range of volumes.

Lobulated, Spiculated, and Irregular Contours. Tumor surface contours were generated by radially displacing the vertices of the icosphere. Let \mathbf{r} be a vertex on the unit icosphere centered on the origin. Let $f : \mathbf{r} \rightarrow \mathbb{R}$ be a function for the relative radial displacement of each vertex; the range of f is 0–1. A point on the surface of the deformed shape is defined as...

$$\mathbf{P}(\mathbf{r}) = (1 + L \cdot f(\mathbf{r})) \cdot \mathbf{r},$$

where L is a scaling factor for controlling the magnitude of the displacement.

There are numerous basis functions that might be used to determine suitable values of f to approximate tumor contours. Here, Worley noise (9), a procedural noise function implemented in Blender's Voronoi texture node, was used. Worley noise is often used in 3-dimensional design to simulate structures with discernable boundaries, such as pebbles, cell clusters, soap bubbles, or other self-organizing structures. In the present case, the Worley noise field was generated by seeding random points in 3-dimensional space and evaluating the Euclidean distance to the closest random point as a function of position. The range of distances in the noise field are then normalized to range between 0 and 1 (i.e., a relative noise field). Optionally, thresholding, smoothing, or other manipulations can be applied to the field before normalization. The values of f are obtained by sampling the relative noise field at each vertex. The positions of the vertices in the deformed shape then follow from Equation 1. Finally, the shape can be scaled to an arbitrary volume by isotropic scaling.

Our method for generating tumor surface contours is based on 3 central inputs that parameterize the Worley noise field and a fourth isotropic scaling factor. The first parameter, L , is discussed above. Second, a density parameter, D , is varied to control the number of bump or spike projections from the sphere surface. Third, a coverage threshold parameter, C , influences the fraction of the sphere surface that can be perturbed. Finally, an isotropic scaling factor, I , is used to scale the tumor to an arbitrary volume:

$$I = \sqrt[3]{\frac{V}{V_0}} = \frac{F}{F_0},$$

where V is the desired volume and V_0 is the initial volume. Alternatively, the tumor may be scaled to an arbitrary Feret diameter (10,11), F , which represents the greatest dimension of a tumor (formally, the maximal pairwise Euclidean distance between the surface mesh vertices). F_0 is the Feret diameter of the initial (i.e., nonscaled) shape.

Notably, by adjustment of the parameters, the morphologic characteristics of the output shape can be made to mimic tumor margin pathology including lobulations, microlobulations, spiculations, or irregularity (Fig. 2). A range of representative margin contours has been generated using parameter combinations guided by clinical experience and the

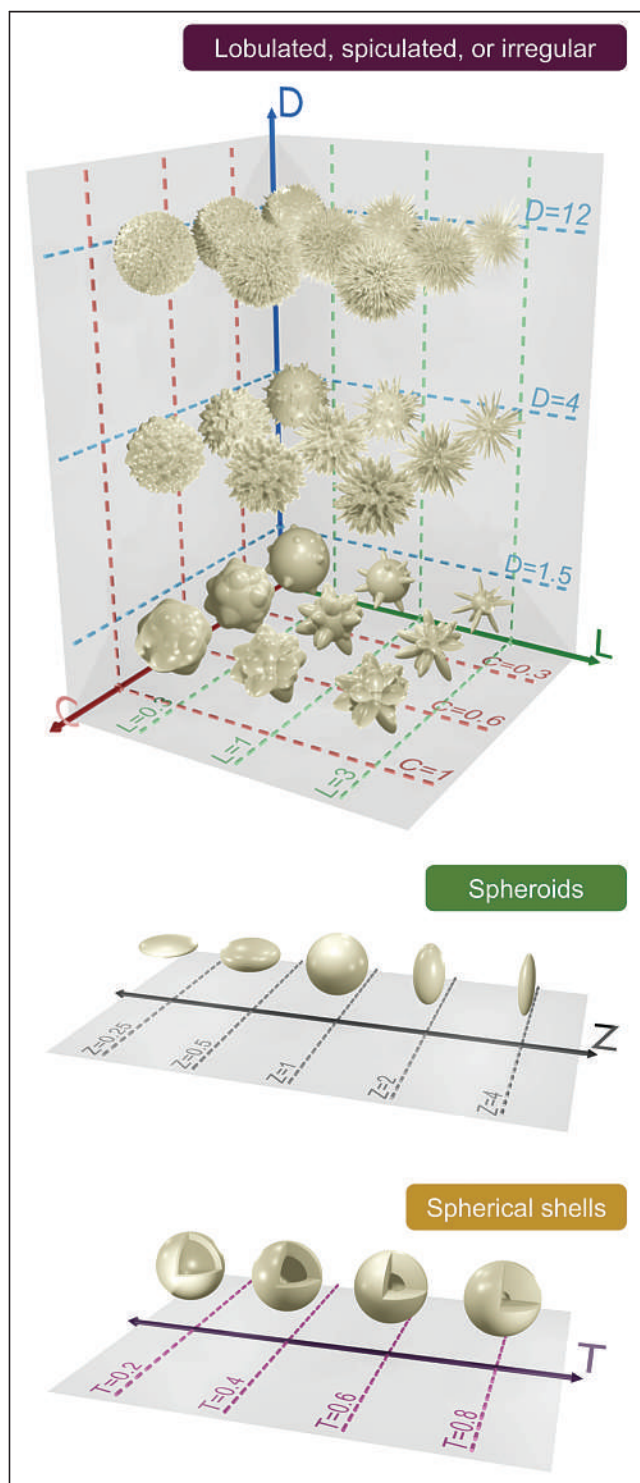


FIGURE 1. Tumor phantom library scaled to constant Feret diameter. Relevant parameters defining each shape or contour are provided on axis gridlines. C = coverage parameter; D = density parameter; L = length parameter; T = relative shell thickness; Z = z-axis scale factor.

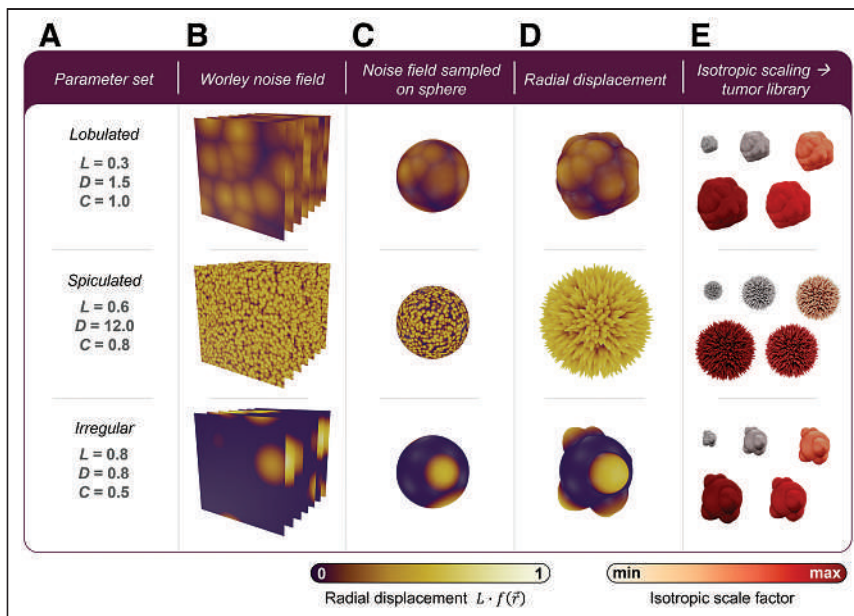


FIGURE 2. Method for generating representative lobulated, spiculated, or irregular tumor phantoms. (A and B) Contours are parameterized by length parameter L , density parameter D , and threshold parameter C (A), which together determine 3-dimensional Worley noise field (B). (C) Noise field is sampled at vertices of unit icosphere. (D) Vertices are radially displaced on basis of value sampled from noise field. (E) Shape is then isotropically scaled to desired volume.

literature. Readers themselves may generate tumor phantoms by adjusting the node input parameters in the Blender file as described in the supplemental material (available at <http://jnm.snmjournals.org>).

The tumor surface meshes were exported from Blender in stereolithography (*.stl) format and converted to tetrahedral meshes with Tetgen (12) (using the *-pAY* command line arguments) in preparation for S-value computations. The volumes of the n tetrahedral elements comprising the volumetric tumor mesh were summed to yield V_0 , namely ...

$$V_0 = \sum_{i=1}^n \frac{|\mathbf{(a}_i - \mathbf{d}_i) \cdot ((\mathbf{b}_i - \mathbf{d}_i) \times (\mathbf{c}_i - \mathbf{d}_i))|}{6},$$

where $\mathbf{a}_i = (a_1, a_2, a_3)$, $\mathbf{b}_i = (b_1, b_2, b_3)$, $\mathbf{c}_i = (c_1, c_2, c_3)$, and $\mathbf{d}_i = (d_1, d_2, d_3)$. These are position vectors defining the vertices of the i^{th} tetrahedral element.

The surface area of each phantom was computed by summing the n triangular elements comprising the surface of the phantoms:

$$A_0 = \sum_{i=1}^n \frac{\|(\mathbf{b}_i - \mathbf{a}_i) \times (\mathbf{c}_i - \mathbf{a}_i)\|}{2},$$

where \mathbf{a}_i , \mathbf{b}_i , and \mathbf{c}_i are position vectors defining the vertices of the i^{th} triangle.

S-Value Computation

In the MIRD dosimetry formalism, the S value $S(r_T \leftarrow r_S, {}_Z^AX)$ (Gy/Bq·s) (13) quantifies the absorbed dose $D(r_T)$ (Gy) to a radiosensitive target r_T per unit of time-integrated activity $A(r_S)$ (Bq·s) of radionuclide ${}_Z^AX$ in source r_S :

$$D(r_T) = \tilde{A}(r_S, {}_Z^AX) \cdot S(r_T \leftarrow r_S, {}_Z^AX).$$

In the present case, tumor self-dose (i.e., $r_S = r_T$) was considered and the distribution of activity in the tumor was assumed to be spatially uniform.

For each tumor phantom, self-S values for 3 β-particle emitters (${}^{90}\text{Y}$, ${}^{131}\text{I}$, and ${}^{177}\text{Lu}$) and 4 α-emitters or α-generating decay chains (${}^{225}\text{Ac}$, ${}^{213}\text{Bi}$, ${}^{223}\text{Ra}$, and ${}^{211}\text{At}$) were computed using PARaDIM software (3). S values for the radionuclides with radioactive progeny were computed separately. Relevant decay information for each radionuclide are provided in Table 1.

PARaDIM used PHITS, version 3.24 (14), for Monte Carlo simulations. Each calculation used the PARaDIM default parameters for physical models in PHITS, which used the International Commission on Radiological Protection publication 107 library for decay spectra (15), the PHITS-EGS5 method for treatment of multiple scattering, explicit treatment of fluorescent x-rays, consideration of Rayleigh and incoherent scattering, and consideration of electron-impact ionization. Sampling was used to determine bremsstrahlung polar angles, electron-positron pair polar angles, and distribution of photoelectrons. A cutoff energy of 1.0 keV were used for electrons and photons. Soft-tissue elemental composition and density, as defined in International Commission on Radiation Units and Measurements report 46 (16), were the attributes assigned to the tetrahedral mesh tumor region and surrounding

material. A sufficient number of particle histories was run such that the relative statistical uncertainties in the S values were less than 1%. For the β-particle emitters, the full β-spectrum was used. For all radionuclides, the contributions of monoenergetic electrons (e.g., conversion and Auger or Coster-Kronig electrons) were included.

The S-value calculations were repeated for different tumor volumes using the phantom scaling function in PARaDIM. Specific volumes were selected by sampling values for the equivalent-sphere diameter at semiregular intervals. For an arbitrary tumor shape of the same composition, the radius of the equivalent-mass sphere is $R_{\text{eq}} = \sqrt[3]{3V/4\pi}$, where V is the volume of the shape. The equivalent-sphere diameter is $2R_{\text{eq}}$. The range of sampled values for the equivalent-sphere diameter was deemed clinically relevant based on concordance with the eighth edition TNM staging system (Table 2) (17,18).

Comparative Evaluation

Of interest here are the systematic errors that arise when tumors with various morphologic characteristics are modeled as equivalent-mass spheres in self-absorbed dose calculations. The percentage error in the S value is defined as follows:

$$\% \text{ error} = \frac{S_{\text{equivalent sphere}}({}_Z^AX) - S_{\text{tumor}}({}_Z^AX)}{S_{\text{tumor}}({}_Z^AX)} \times 100\%,$$

where S_{tumor} is the S value for the actual tumor shape and $S_{\text{equivalent sphere}}$ is the self-S value for the icosphere (representing a sphere) of equivalent mass.

Validation of S-Value Calculations

S values computed for the icosphere were compared with those for spheres obtained from the new MIRDcalc dosimetry software tool (5,8) as a validation measure.

Radiomic Shape Features

The imaging subfield of radiomics involves the identification of quantitative features in digital images that may be predictive of tumor

TABLE 1
Radionuclides Considered in Present Study

Radionuclide	Physical half-life	Principal therapeutic radiations	R_{CSDA}	Clinical use examples
^{225}Ac	10.0 d	α (5.8 MeV)	47 μm	^{225}Ac -lintuzumab (25), ^{225}Ac -PSMA-617 (26)
^{221}Fr	4.9 mo	α (6.3 MeV)	53 μm	Progeny of ^{225}Ac
^{217}At	32 μs	α (7.1 MeV)	64 μm	Progeny of ^{225}Ac
^{213}Bi	46 mo	α (5.8 MeV)	47 μm	^{213}Bi -Hum195 (27), ^{213}Bi -DOTATOC, ^{213}Bi -PSMA-617, progeny of ^{225}Ac
		β^- ($E_{\text{max}} = 1.42$ MeV) ($E_{\text{avg}} = 434$ keV)	6.5 mm 1.4 mm	
^{213}Po	4.2 μs	α (8.4 MeV)	84 μm	Progeny of $^{225}\text{Ac}/^{213}\text{Bi}$
^{209}TI	2.2 mo	β^- ($E_{\text{max}} = 1.9$ MeV) ($E_{\text{avg}} = 655$ keV)	9.1 mm 2.5 mm	Progeny of $^{225}\text{Ac}/^{213}\text{Bi}$
^{209}Pb	3.3 h	β^- ($E_{\text{max}} = 644$ keV) ($E_{\text{avg}} = 197$ keV)	2.4 mm 0.4 mm	Progeny of $^{225}\text{Ac}/^{213}\text{Bi}$
^{211}At	7.2 h	α (5.9 MeV)	48 μm	^{211}At -chimeric antitensin monoclonal antibody 81C6 (28)
^{211}Po	0.52 s	α (7.4 MeV)	68 μm	Progeny of ^{211}At
^{223}Ra	11.4 d	α (5.7 MeV)	45 μm	^{223}Ra -dichloride (Xofigo; Bayer)
^{219}Rn	4.0 s	α (6.8 MeV)	60 μm	Progeny of ^{223}Ra
^{215}Po	1.8 μs	α (7.4 MeV)	68 μm	Progeny of ^{223}Ra
^{211}Pb	36 mo	β^- ($E_{\text{max}} = 1.37$ MeV) ($E_{\text{avg}} = 450$ keV)	6.3 mm 1.5 mm	Progeny of ^{223}Ra
^{211}Bi	2.1 mo	α (6.6 MeV); β^- ($E_{\text{max}} = 575$ keV) ($E_{\text{avg}} = 173$ keV)	57 μm 2.1 mm 0.3 mm	Progeny of ^{223}Ra
^{211}Po	0.52 s	α (7.4 MeV)	68 μm	Progeny of ^{223}Ra
^{207}TI	4.8 mo	β^- ($E_{\text{max}} = 1.43$ MeV) ($E_{\text{avg}} = 495$ keV)	6.6 mm 1.7 mm	Progeny of ^{223}Ra
^{177}Lu	6.6 d	β^- ($E_{\text{max}} = 498$ keV) ($E_{\text{avg}} = 133$ keV)	1.7 mm 0.2 mm	^{177}Lu -DOTATOC (Lutathera; Advanced Accelerator Applications), ^{177}Lu -PSMA-617 (Pluvicto; Advanced Accelerator Applications)
^{131}I	8.0 d	β^- ($E_{\text{max}} = 807$ keV) ($E_{\text{avg}} = 182$ keV)	3.3 mm 0.4 mm	^{131}I -NaI, ^{131}I -tositumomab (Bexxar; GlaxoSmithKline)
^{90}Y	2.7 d	β^- ($E_{\text{max}} = 2.28$ MeV) ($E_{\text{avg}} = 933$ keV)	11 mm 3.9 mm	^{90}Y -ibritumomab tiuxetan (Zevalin; Acrotech Biopharma), ^{90}Y -microspheres (TheraSphere; Boston Scientific Corp.; SIR-Spheres; Sirtex)

R_{CSDA} = particle ranges in continuous-slowing-down approximation, obtained from National Institutes of Standards and Technology ASTAR database for α -particles in muscle tissue (<https://physics.nist.gov/PhysRefData/Star/Text/ASTAR.html>) and ESTAR database for β -particles in soft tissue (<https://physics.nist.gov/PhysRefData/Star/Text/ESTAR.html>); E_{max} = maximum energy; E_{avg} = mean energy.

TABLE 2
Tumor Volumes Used to Compute S Values in This Study

Volume (cm ³)	Equivalent-sphere radius (cm)	Equivalent-sphere diameter (cm)	Equivalent-sphere TNM classification*
0.00418	0.10	0.20	T _{1a}
0.0141	0.15	0.30	T _{1a}
0.0335	0.20	0.40	T _{1a}
0.113	0.30	0.60	T _{1a}
0.268	0.40	0.80	T _{1a}
0.524	0.50	1.0	T _{1a}
0.905	0.60	1.2	T _{1b}
2.14	0.80	1.6	T _{1b}
4.19	1.0	2.0	T _{1b}
14.1	1.5	3.0	T _{1c}
33.5	2.0	4.0	T _{2a}
113	3.0	6.0	T ₃
268	4.0	8.0	T ₄
524	5.0	10	T ₄
905	6.0	12	T ₄

*TNM system is based on greatest dimension of tumor. Realistic tumor shapes will have larger greatest dimension than their equivalent spheres, and thus TNM classifications listed will not necessarily apply for nonspherical tumors.

pathophysiology; one large class of radiomic features includes shape- and size-based features (2,10,11,19–21). We hypothesized that these features may inform dosimetric relationships—namely, the influences of tumor shape on the S values and the systematic errors in S values associated with the equivalent-sphere approximation. Eight shape features, in addition to the parameters defining our tumor shape library, were extracted. Potential correlations among the shape features and S values were then considered. Definitions and descriptions of each feature are provided in Table 3.

RESULTS

S values for ⁹⁰Y, ¹³¹I, ¹⁷⁷Lu, ²²⁵Ac, ²¹³Bi, ²²³Ra, ²¹¹At, and decay chain members, when applicable, are provided in Supplemental Tables 1–19 for each phantom in the tumor library. The contributions of radioactive progeny are tabulated separately from the parent.

Figures 3 and 4 demonstrate that the standard practice of defining lesions as equivalent-mass spheres systematically overestimates

TABLE 3
Radiomic Features Derived Across Tumor Phantom Library

Feature	Formula	Description
Volume	= V	Shape volume; volumes were selected in range of 0.004–905 cm ³
Surface area	= A ₀ · I ² = A ₀ · (V/V ₀) ^{2/3}	Surface area of scaled shape
Surface area-to-volume ratio	= A/V	Ratio of surface area to volume for scaled shape
Sphericity (11,20,21)	= ∛36πV ² /A	Roundness of shape relative to sphere; range of sphericities is 0–1, with 1 indicating perfect sphere
Spherical disproportion (11,20,21)	= A/4πR _{eq} ²	Ratio of surface area of shape to surface area of its volume-equivalent sphere (defined by R _{eq})
Compactness 1	= V/√πA ³	Measure of how compact the shape is relative to sphere; compactness 1 ranges from 0 to 1/6π, with 1/6π indicating perfect sphere
Compactness 2	= 36πV ² /A	Compactness 2 ranges from 0 to 1, with 1 indicating perfect sphere
Feret diameter (11,20)	= F ₀ · I	Maximal pairwise Euclidean distance between surface mesh vertices; F ₀ is Feret diameter of initial (i.e., nonscaled) shape

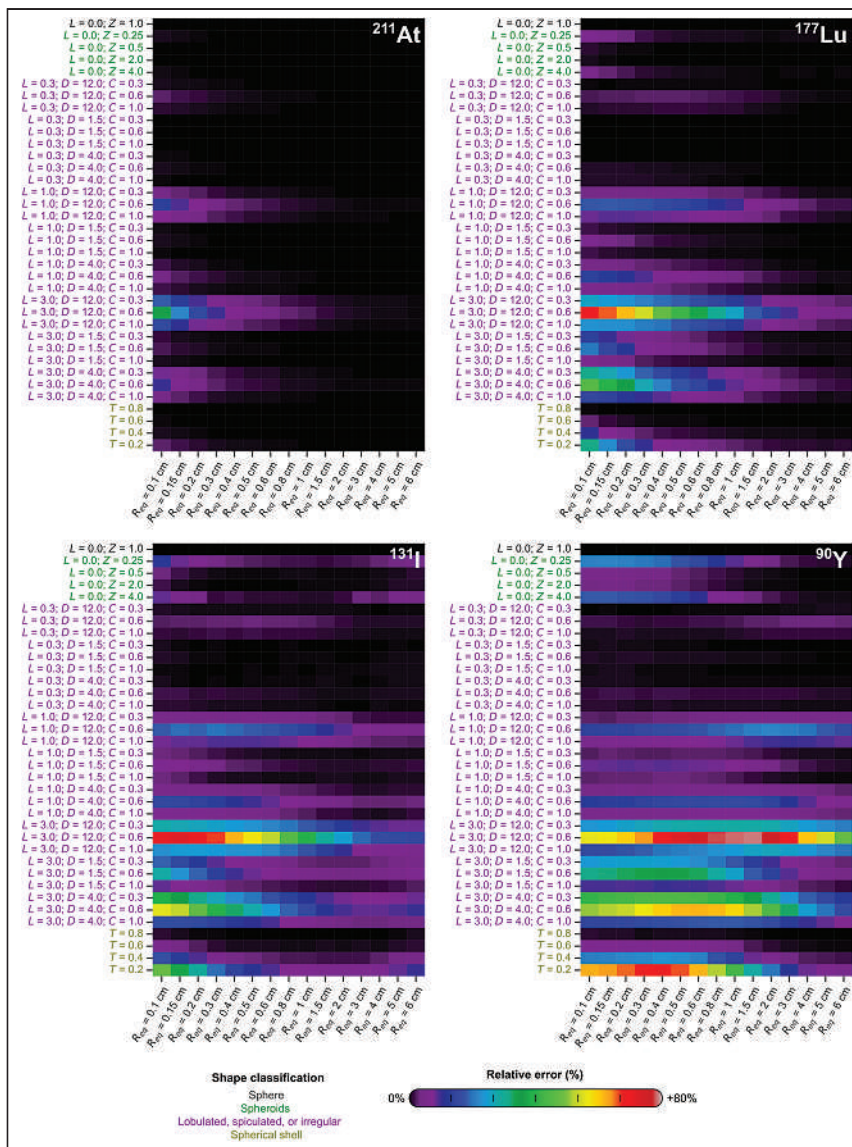


FIGURE 3. Relative error in absorbed dose if equivalent mass spheres are used to approximate various representative nonspherical tumors. R_{eq} values on abscissa are centimeters; corresponding volumes can be obtained from Table 2. C = coverage parameter; D = density parameter; L = length parameter; T = relative shell thickness; Z = z-axis scale factor.

the absorbed dose and, further, that the magnitude of the error is influenced by the radionuclide, shape, volume, and margin contour. In the case of high-energy β -emitters (e.g., ^{90}Y), relative errors of up to 75% were observed for spiculated contours with high values of L and up to 68% for thin spherical shells (Fig. 3). Relative errors for all isotopes are provided in Supplemental Tables 20–38. Radiomic features associated with each shape are provided in Supplemental Tables 39–49. Figure 4 provides insight on how the relative errors in the equivalent-sphere S values trend with different radiomic features and provides an indication of the potential magnitude of dosimetric error when the equivalent-sphere approximation is applied for specific radionuclides. For example, for the α -emitter ^{211}At , relative errors were less than 10% across the entire shape library for volumes of more than 0.2 cm^3 , sphericity values of more than 0.2, and area-to-volume ratios of less than 150. Over the present shape library, the relative errors tended to increase with

surface area-to-volume ratio and tended to decrease with increasing sphericity, volume, and Feret diameter. None of the examined radiomic features yielded quantitatively predictive relationships with S values or with their relative errors.

Validation

S values obtained from MIRDcalc for soft-tissue spheres agreed within 2.5% of the S values derived in this work for the icosphere geometry (Supplemental Fig. 1). The differences may be attributed to subtle differences in geometry definition or simulation settings.

DISCUSSION

A library of tumor computational phantoms of various shapes and contours, created using 3-dimensional design software, has been assembled to improve accuracy in tumor dosimetry.

Envisioned Practical Use

Radionuclide S values were generated across the library for tumor self-absorbed dose calculations via a shape lookup table. In general, the dose calculations will involve 3 steps: shape matching, time-integrated activity estimation, and absorbed dose calculation. The latter 2 steps are commonly performed using organ-level dosimetry software (4–6), but these software applications currently support only spherical phantoms; the S-value database generated in this work might be integrated into these existing software tools to enhance their versatility for tumor dosimetry.

Shape-Matching Considerations

The library phantom that is the closest match should be identified, guided by quantitative or semiquantitative analysis of anatomic images and the visual interpretation and clinical judgment of the users.

Some characteristics for appearance-based semiquantitative matching might include lobule or spicule count, apparent spicule length, or apparent Feret diameter. Quantitative features might be extracted via image segmentation and compared with feature values extracted from the library phantoms to determine the optimal match. The uncertainty associated with each feature might be estimated to determine which features to prioritize. For example, the lesion volume can be difficult to estimate accurately if features such as spiculations are not well resolved or if only planar images are available; in that case, the Feret diameter may be a better indicator of the true tumor S value. Finally, if several phantoms provide a reasonable match to the tumor, their corresponding S values might be averaged, or alternatively, an interpolation scheme might be applied.

Importantly, the techniques for visualizing the library phantoms and the tumor should be congruent. For example, CT slices should be

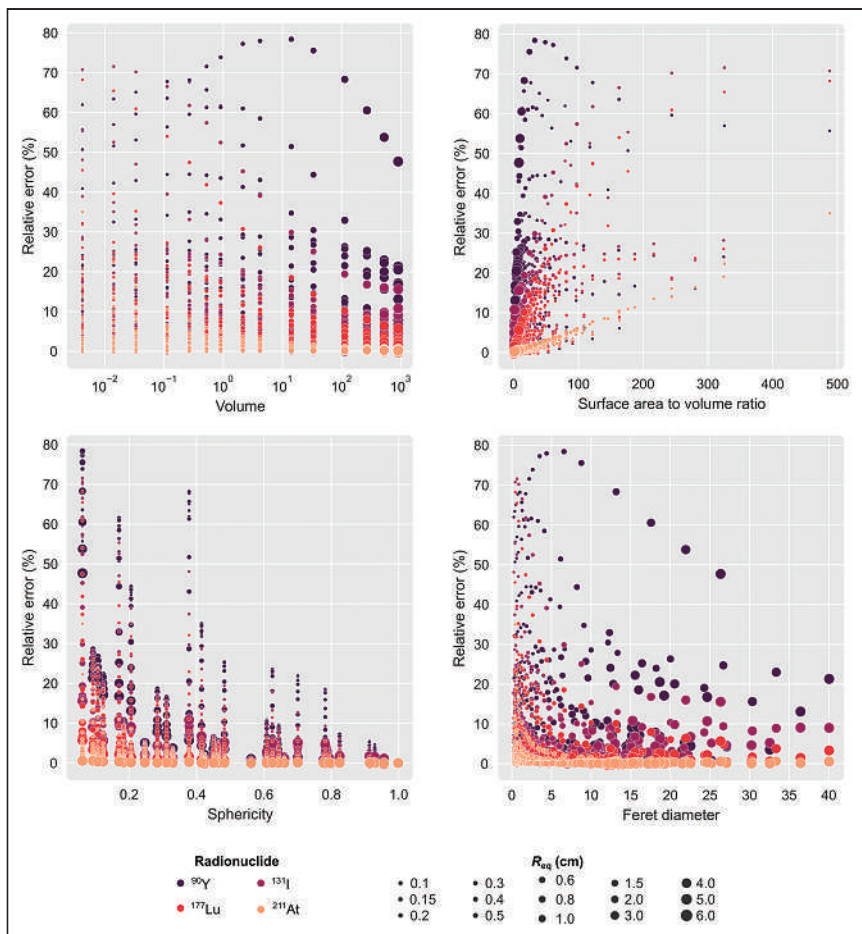


FIGURE 4. Correlation of relative errors with radiomic shape features for various shapes and radionuclides. Progeny are not included for ^{211}At .

compared with corresponding slices of the phantoms, whereas projections of the phantoms would be more appropriate comparators for CT maximum-intensity projections, radiographic projections such as mammography, or digitally reconstructed radiographs (Fig. 5).

The method for generating the tumor phantom library was designed to be versatile but with minimal parameter inputs, such that the library can be systematically expanded if it proves useful. Through variation of up to 4 parameters, representative tumor phantoms can be generated with characteristic features—size, shape, and margin contour—observable in planar or tomographic anatomic images or expected on the basis of knowledge of the pathology. The Blender file used to generate the library phantoms has been provided in the supplemental materials. This enables one to optimize each parameter to more closely replicate observed tumor features. In that case, several Monte Carlo particle transport codes can compute the S value with the output shape, including GEANT4, PHITS, and MCNP.

Advantages and Limitations

There cannot realistically be a 1:1 correspondence between a representative phantom and a real tumor, and the approach is somewhat subjective. However, by accounting for the salient features that influence the mean absorbed dose, a more accurate result should be achievable than is possible with the first-order equivalent-mass-sphere approximation that has typically been used.

Ideally, one would account for the unique characteristics of each lesion in dosimetry calculations, including lesion size, lesion shape, lesion contour, intratumoral heterogeneity, the dynamics of radiopharmaceutical distribution, and their collective impact on the dose distribution. Recent progress toward this goal includes advancements in nuclear imaging instrumentation, image segmentation, image registration, and software developments that enable voxel-level dosimetry calculations. One inherent limitation of traditional voxel-level dosimetry is that the accuracy ultimately depends on the resolution of the nuclear imaging modality, which at best approaches 5 mm (clinical PET); this can be insufficient to capture activity concentration gradients or absorbed dose gradients that are dosimetrically relevant (22). The resolution of anatomic imaging modalities is far superior, with submillimeter resolution achievable with modern CT and MR scanners that accompany modern PET and SPECT systems; especially for high-contrast scenarios (e.g., lung nodules), these anatomic imaging modalities might provide lesion contour information to inform selection of a representative tumor phantom from our library. Moreover, for metastatic or multifocal disease, the concept of the index tumor is commonly used, wherein a representative lesion (usually, the largest lesion) is presumed to determine the overall clinical behavior of the disease. An analogous strategy might be applied for dosimetric evaluation, wherein the morphology of the index tumor is pre-

sumed to dictate the shape and contour of other foci. This strategy might have merit when the margin morphology of an index tumor is resolvable by the anatomic imaging modality or can be plausibly inferred from other available anatomic information such as biopsy specimens, a surgically resected lesion, or correlations with other biomarkers. However, the accuracy of such inferences would need to be rigorously evaluated before use in practice.

CONCLUSION

A tumor phantom library was generated to enable integration of tumor shape and contour into routine tumor dosimetry calculations. Using the library, we have shown that mean absorbed doses are systematically overestimated for tumors when the equivalent-sphere approximation is applied to tumors with distinctly different shapes. Integrating the phantom library within internal dosimetry software would enable greater versatility and might increase the accuracy of tumor-absorbed dose estimates.

DISCLOSURE

Funding support was received from NIH P30 CA008748 and NIH U01 EB028234. Simone Krebs is supported in part by NIH R37 CA262557 and P50 CA192937. No other potential conflict of interest relevant to this article was reported.

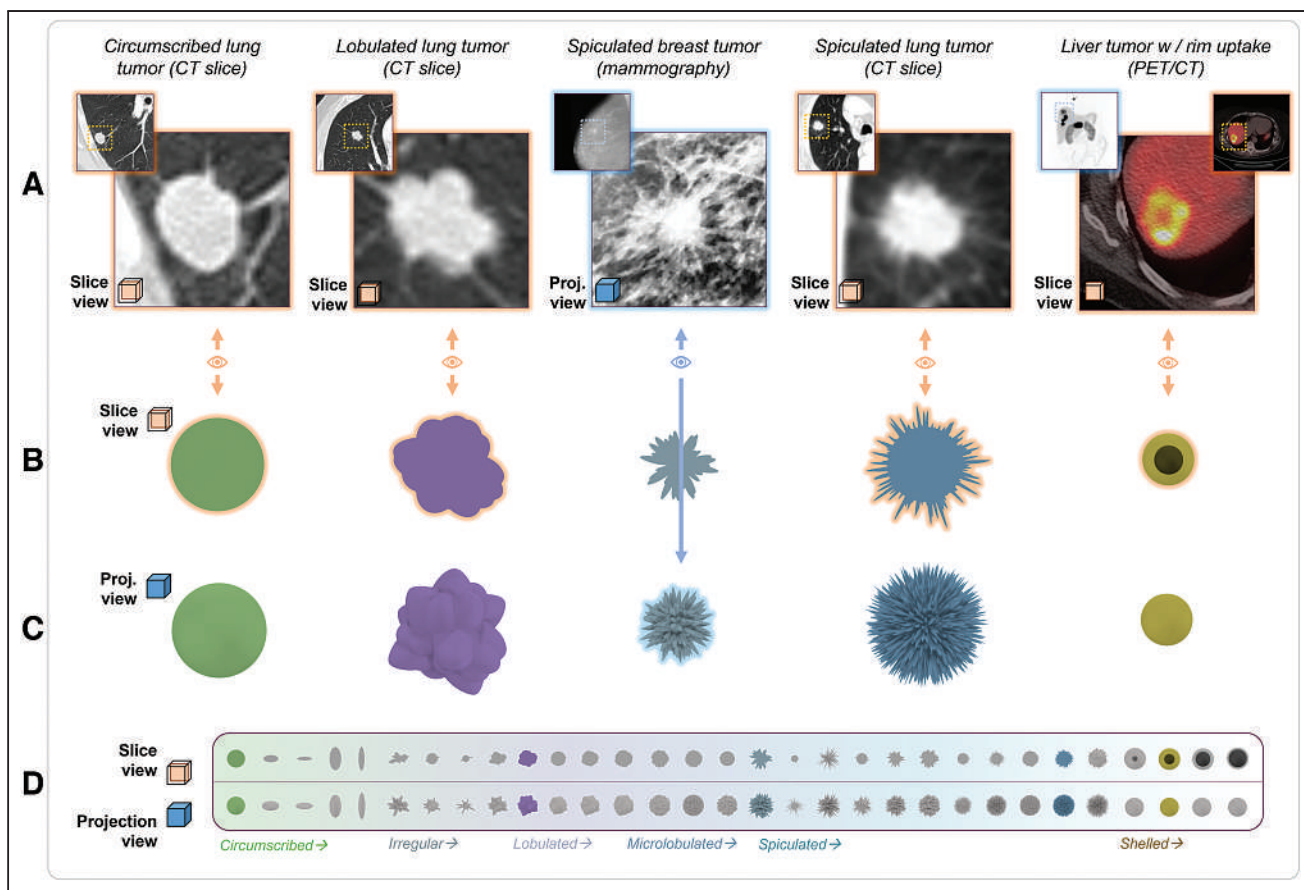


FIGURE 5. When matching phantom to image data, shape visualization technique should be appropriate for imaging modality. (A) Tumors imaged with different imaging modalities. (B and C) Slice (B) and rendered projection (C) views of most closely matching phantoms from library, assessed by authors. (D) Entire phantom library displayed for reference. (Lung tumor CT images adapted from (23); breast tumor mammography image adapted from (24).)

KEY POINTS

QUESTION: How accurate are the spherical tumor models implemented in common organ-level internal dosimetry software, and can these models be improved?

PERTINENT FINDINGS: Using a library of computational tumor phantoms that recapitulate dosimetrically relevant tumor morphology, we found that spherical tumor models may systematically overestimate the absorbed dose by over 75% for certain therapeutic radionuclides.

IMPLICATIONS FOR PATIENT CARE: Tumor phantom libraries might improve software programs for organ-level dosimetry by allowing the morphology of the real tumor to be accounted for in dosimetry calculations, thereby translating to dosimetry estimates that are more tumor-specific.

REFERENCES

- Byrd BK, Krishnaswamy V, Gui J, et al. The shape of breast cancer. *Breast Cancer Res Treat*. 2020;183:403–410.
- Gu H, Zhang X, di Russo P, Zhao X, Xu T. The current state of radiomics for meningiomas: promises and challenges. *Front Oncol*. 2020;10:567736.
- Carter LM, Crawford TM, Sato T, et al. PARaDIM: a PHITS-based Monte Carlo tool for internal dosimetry with tetrahedral mesh computational phantoms. *J Nucl Med*. 2019;60:1802–1811.
- Stabin MG, Sparks RB, Crowe E. OLINDA/EXM: the second-generation personal computer software for internal dose assessment in nuclear medicine. *J Nucl Med*. 2005;46:1023–1027.
- Kesner A, Olgun E, Zanzonico P, Bolch W. MIRDcalc V 1.0: a community spreadsheet tool for organ-level radiopharmaceutical absorbed dose calculations [abstract]. *J Nucl Med*. 2018;59(suppl 1):473.
- Andersson M, Johansson L, Eckerman K, Mattsson S. IDAC-Dose 2.1, an internal dosimetry program for diagnostic nuclear medicine based on the ICRP adult reference voxel phantoms. *EJNMMI Res*. 2017;7:88.
- Amato E, Lizio D, Baldari S. Absorbed fractions for electrons in ellipsoidal volumes. *Phys Med Biol*. 2011;56:357–365.
- Olgun E, President B, Ghaly M, Frey E, Sgouros G, Bolch WE. Specific absorbed fractions and radionuclide S-values for tumors of varying size and composition. *Phys Med Biol*. 2020;65:235015.
- Worley S. A cellular texture basis function. In: *SIGGRAPH '96: Proceedings of the 23rd Annual Conference on Computer Graphics and Interactive Techniques*. Association for Computing Machinery; 1996:291–294.
- Lambin P, Leijenaar RTH, Deist TM, et al. Radiomics: the bridge between medical imaging and personalized medicine. *Nat Rev Clin Oncol*. 2017;14:749–762.
- van Griethuysen JJM, Fedorov A, Parmar C, et al. Computational radiomics system to decode the radiographic phenotype. *Cancer Res*. 2017;77:e104–e107.
- Si H. TetGen, a Delaunay-based quality tetrahedral mesh generator. *ACM Trans Math Softw*. 2015;41:1.
- Bolch WE, Eckerman KF, Sgouros G, Thomas SR. MIRD pamphlet no. 21: a generalized schema for radiopharmaceutical dosimetry—standardization of nomenclature. *J Nucl Med*. 2009;50:477–484.
- Sato T, Iwamoto Y, Hashimoto S, et al. Features of Particle and Heavy Ion Transport code System (PHITS) version 3.02. *J Nucl Sci Technol*. 2018;55:684–690.
- Eckerman K, Endo A. ICRP publication 107: nuclear decay data for dosimetric calculations. *Ann ICRP*. 2008;38:7–96.

16. *Photon, Electron, Proton and Neutron Interaction Data for Body Tissues*. International Commission on Radiation Units and Measurements; 1992:11. ICRU report 46.
17. Detterbeck FC, Boffa DJ, Kim AW, Tanoue LT. The eighth edition lung cancer stage classification. *Chest*. 2017;151:193–203.
18. Lababde O, Meziane MA. The eighth edition of TNM staging of lung cancer: reference chart and diagrams. *Oncologist*. 2018;23:844–848.
19. Visvikis D, Lambin P, Beuschau Mauridsen K, et al. Application of artificial intelligence in nuclear medicine and molecular imaging: a review of current status and future perspectives for clinical translation. *Eur J Nucl Med Mol Imaging*. 2022;49:4452–4463.
20. Coroller TP, Grossmann P, Hou Y, et al. CT-based radiomic signature predicts distant metastasis in lung adenocarcinoma. *Radiother Oncol*. 2015;114:345–350.
21. Limkin EJ, Reuzé S, Carré A, et al. The complexity of tumor shape, spiculatedness, correlates with tumor radiomic shape features. *Sci Rep*. 2019;9:4329.
22. Chiesa C, Bardiès M, Zaidi H. Voxel-based dosimetry is superior to mean absorbed dose approach for establishing dose-effect relationship in targeted radionuclide therapy. *Med Phys*. 2019;46:5403–5406.
23. Choromańska A, Macura KJ. Evaluation of solitary pulmonary nodule detected during computed tomography examination. *Pol J Radiol*. 2012;77:22–34.
24. Mahmood T, Li J, Pei Y, Akhtar F, Rehman MU, Wasti SH. Breast lesions classifications of mammographic images using a deep convolutional neural network-based approach. *PLoS One*. 2022;17:e0263126.
25. Rosenblat TL, McDevitt MR, Carrasquillo JA, et al. Treatment of patients with acute myeloid leukemia with the targeted alpha-particle nanogenerator actinium-225-lintuzumab. *Clin Cancer Res*. 2022;28:2030–2037.
26. Kratochwil C, Bruchertseifer F, Giesel FL, et al. ^{225}Ac -PSMA-617 for PSMA-targeted α -radiation therapy of metastatic castration-resistant prostate cancer. *J Nucl Med*. 2016;57:1941–1944.
27. Sgouros G, Ballangrud AM, Jurcic JG, et al. Pharmacokinetics and dosimetry of an α -particle emitter labeled antibody: ^{213}Bi -HuM195 (anti-CD33) in patients with leukemia. *J Nucl Med*. 1999;40:1935–1946.
28. Zalutsky MR, Reardon DA, Akabani G, et al. Clinical experience with α -particle-emitting ^{211}At : treatment of recurrent brain tumor patients with ^{211}At -labeled chimeric antitenascin monoclonal antibody 81C6. *J Nucl Med*. 2008;49:30–38.

Long-Term Prognostic Value of ^{82}Rb PET/CT–Determined Myocardial Perfusion and Flow Reserve in Cancer Patients

Josef J. Fox¹, Audrey Mauguen², Kimiteru Ito¹, Dipti Gupta³, Alice Yu¹, Thomas H. Schindler⁴, H. William Strauss¹, and Heiko Schöder¹

¹Department of Radiology, Memorial Sloan Kettering Cancer Center, New York, New York; ²Department of Epidemiology and Biostatistics, Memorial Sloan Kettering Cancer Center, New York, New York; ³Department of Medicine, Memorial Sloan Kettering Cancer Center, New York, New York; and ⁴Division of Nuclear Medicine, Mallinckrodt Institute of Radiology, Washington University, St. Louis, Missouri

Myocardial flow reserve (MFR), derived from quantitative measurements of myocardial blood flow during PET imaging, provides prognostic information on patients with coronary artery disease (CAD), but it is not known if this also applies to cancer patients with a competing risk for mortality. **Methods:** To determine the prognostic value of MFR in patients with cancer, we designed a retrospective cohort study comprising 221 patients with known or suspected CAD (median age, 71 y; range, 41–92 y) enrolled between June 2009 and January 2011. Most patients were referred for perioperative risk assessment. Patients underwent measurement of myocardial blood flow at rest and during pharmacologic stress, using quantitative ^{82}Rb PET imaging. They were divided into early-stage versus advanced-stage cancer groups based on cancer histopathology and clinical state and were further stratified by myocardial perfusion summed stress score, summed difference score, and calculated MFR. Overall survival (OS) was assessed using the Kaplan–Meier estimator, and Cox proportional-hazards regression helped identify independent predictors for OS. **Results:** During a follow-up of 85.6 mo, 120 deaths occurred. MFR, summed difference score, and cancer stage were significantly associated with OS. In the age-adjusted Cox hazard multivariable analysis, MFR and cancer stage remained independent prognostic factors. MFR combined with cancer stage enhanced OS discrimination. The groups had significantly different outcomes ($P < 0.001$), with 5-y OS of 88% (MFR ≥ 1.97 and early-stage), 53% (MFR < 1.97 and early-stage), 33% (MFR ≥ 1.97 and advanced-stage), and 13% (MFR < 1.97 and advanced-stage). **Conclusion:** Independent of cancer stage, MFR derived from quantitative PET was prognostic of OS in our cohort of cancer patients with known or suspected CAD. Combining these 2 parameters enhanced discrimination of OS, suggesting that MFR improves risk stratification and may serve as a treatment target to increase survival in cancer patients.

Key Words: rubidium PET; quantitative myocardial perfusion imaging; myocardial flow reserve; cancer; survival

J Nucl Med 2023; 64:791–796

DOI: 10.2967/jnmed.122.264795

An increasing number of adults with cancer also have coronary artery disease (CAD) (1). Therefore, it is important to monitor the

cardiovascular health of cancer patients with risk factors for CAD or documented cardiovascular events. Cancer itself creates an immunocompromised and hypercoagulable milieu, which, in combination with potentially cardiotoxic cancer therapies, renders patients increasingly vulnerable to cardiac morbidity and mortality (2,3). Cardiotoxic culprits include mediastinal irradiation, fluoropyrimidines, alkylating agents, androgen deprivation therapy, and targeted therapies such as tyrosine kinase inhibitors.

Whereas SPECT and SPECT/CT myocardial perfusion imaging (MPI) is widely available and well established for evaluating cardiac risk in the general population (4), PET/CT MPI offers 2 major advantages (5–7): superior diagnostic accuracy and the ability to quantify myocardial blood flow at rest and during vasodilator stress and hence derive myocardial flow reserve (MFR). Although PET/CT MPI has prognostic value beyond routine clinical predictors for all-cause mortality and major adverse cardiovascular events (8,9), its prognostic value in patients with cancer (a major competing risk for death) is unclear. Therefore, we set out to evaluate the prognostic value of myocardial blood flow and MFR in patients with cancer and a suspected or known CAD comorbidity.

MATERIALS AND METHODS

Study Population

This was a retrospective investigation of consecutive patients with cancer who underwent rest–stress ^{82}Rb -chloride PET/CT MPI over a 20-mo period between June 2009 and January 2011. During this time, 1,233 patients were referred for MPI, including 236 who underwent ^{82}Rb -chloride PET MPI (19%) and 997 (81%) who underwent SPECT/CT MPI. MPI modality (PET vs. SPECT) was generally determined by logistic factors (e.g., availability of ^{82}Rb -chloride generator) rather than clinical criteria. Exclusion criteria for pharmacologic cardiac stress testing included acute myocardial infarction, unstable angina, overt heart failure, a history of severe asthma, or contraindications to vasodilation with adenosine, dipyridamole, or regadenoson (10). Fifteen patients were excluded because dynamic PET/CT datasets were not available for analysis. The final study population comprised 221 patients, most of whom were referred for perioperative risk assessment (Fig. 1). A detailed history was obtained from the patient, the referring clinician, and the center's electronic medical record before MPI PET/CT to define the cardiac risk factor profile. Lipid profiles were not available for all patients, as these are not a part of routine diagnostic evaluation. Clinical risk factors were scored and summed according to the risk assessment of Morise et al. for predicting cardiac events (11). The electronic medical record was reviewed to identify the incidence of cardiac catheterization, percutaneous revascularization, coronary artery bypass grafting, or cardiac death

Received Aug. 15, 2022; revision accepted Dec. 6, 2022.

For correspondence or reprints, contact Heiko Schöder (schoderh@mskcc.org).

Published online Jan. 5, 2023.

COPYRIGHT © 2023 by the Society of Nuclear Medicine and Molecular Imaging.

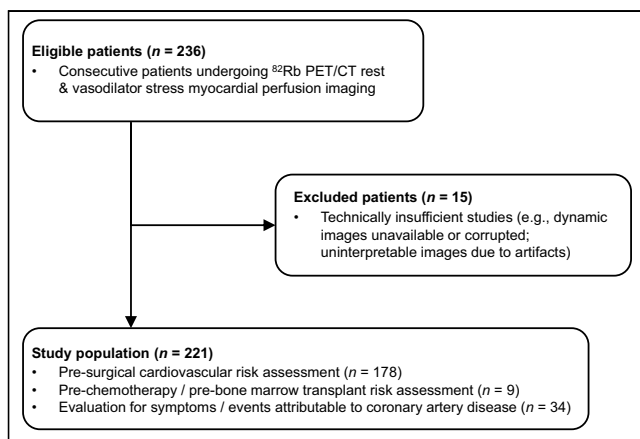


FIGURE 1. Flowchart of study patients.

within 90 d after ^{82}Rb -chloride PET/CT. Patient survival was accurately determined by scrupulous review of the electronic medical record. The institutional review board approved this retrospective, Health Insurance Portability and Accountability Act-compliant, single-institution study (institutional review board approval 11-150) and waived the requirement for informed consent. Data collection was finalized in December 2021. Details of the ^{82}Rb -chloride PET/CT rest-stress protocol, as well as details on image analysis, are shown in the supplemental materials (available at <http://jnm.snmjournals.org>) (12–17).

Cancer Status

The patients had a variety of primary cancers and disease stages (Supplemental Table 1). We divided the population into 2 groups, advanced-stage versus early-stage cancer, using an estimated cancer life expectancy based on historical 5-y survival rates at the time of ^{82}Rb PET/CT imaging. The advanced-stage cancer group was defined as patients with an expected 5-y survival rate of less than 50%, unknown primary cancer, or confirmed local recurrence or distant metastases within 3 mo after the ^{82}Rb PET/CT scan. The remaining patients were assigned to the early-stage cancer group. If patients had multiple primary cancers, staging was determined by the cancer with the lowest expected 5-y survival rate. Expected 5-y survival rates were based on the seventh edition of the AJCC Cancer Staging Manual (18). Lymphomas were staged according to the Ann Arbor classification.

Statistical Analysis

Data are expressed as mean \pm SD, median and range, or frequency and percentage. The Welch 2-sample *t* test was used for comparison of normally distributed continuous variables between groups, whereas the Wilcoxon rank sum test was used for nonnormal variables. The Pearson χ^2 or Fisher exact test were used to compare categoric variables.

The Kaplan-Meier estimator was used to determine whether there was an association between clinical parameters or PET MPI and overall survival (OS), which was defined as the time from ^{82}Rb PET/CT until death from any cause. Patients who remained alive were censored at the last follow-up. The median follow-up time was calculated using the reverse Kaplan-Meier method (19). The dates of death and last follow-up were obtained from the electronic medical record. A log-rank test was performed to test for differences between survival curves. Hazard ratios and 95% CIs were calculated using univariable and multivariable Cox proportional-hazards regression models. To assess potential confounding effects on survival due to the retrospective nature of the study, multivariable analyses were performed as stepwise backward regression, with an entry probability for each variable set at 0.05. The final model was defined as the model after

variable selection, that is, after exclusion of variables that were not significant after adjustment. A sensitivity analysis was conducted by repeating the analysis on patients with both a normal summed stress score (SSS) (<4) and a normal summed difference score (SDS) (<3) only. Only a few missing values were observed, and a complete case analysis was conducted. Reported *P* values were 2-tailed; a *P* value of 0.05 or less was considered to indicate statistical significance. Statistical analysis was performed using SPSS (version 25) and R (version 6.3.0).

RESULTS

Patient Characteristics and Qualitative Assessment of Regional Perfusion

A flowchart summarizing patient selection is shown in Figure 1. Patient characteristics are detailed in Table 1. In total, 221 patients were included in the study. Most had at least an intermediate pretest probability for CAD (96.4%); 178 patients were referred for risk assessment before cancer surgery, 9 patients for risk assessment before undergoing chemotherapy or bone marrow transplantation, and 34 patients for evaluation of symptoms or signs attributable to coronary disease.

Myocardial Perfusion and Function

Abnormal stress perfusion (SSS ≥ 4) was observed in 52 of 221 patients (23.5%). Regional ischemia (SDS ≥ 3) was found in 46 patients (20.8%). In patients referred for symptoms, 14 of 34 (41.2%) showed evidence of ischemia, with an SDS of at least 3. Within 90 d after ^{82}Rb PET/CT, 7 patients underwent percutaneous coronary intervention, 1 patient underwent coronary artery bypass grafting, and 1 patient experienced cardiac death after myocardial infarction; all 9 patients had ischemia (SDS ≥ 3) on PET MPI.

A left ventricular ejection fraction of less than 50% was observed at rest in 26 patients (11.8%) and at stress in 22 patients (10.0%). An abnormal left ventricular ejection fraction reserve was observed in 24 patients.

Myocardial Blood Flow and MFR

Mean rest MBF was 1.01 mL/min/g (SD, 0.42), mean rest MBF after adjusting for RPP was 0.88 mL/min/g (SD, 0.32), and mean stress MBF was 1.93 mL/min/g (SD, 0.74). Mean MFR was 2.04 (SD, 0.74), and mean-adjusted MFR was 2.31 (SD, 0.85). Factors correlating with a low MFR (defined as an MFR lower than the median of 1.97) were a lower stress MBF (*P* < 0.001), a higher rest MBF or adjusted rest MBF (*P* < 0.001), a higher rest heart rate (*P* = 0.006), a lower stress ejection fraction (*P* = 0.002), and a higher SSS (*P* = 0.003) and SDS (*P* = 0.021, Table 2). In addition, a lower hemoglobin level (*P* < 0.001), a history of CAD (*P* < 0.001), an Agatston score classified as severe (score > 400 , *P* < 0.001), and older age (*P* < 0.001) were all associated with a lower MFR (Table 2). However, stress heart rate, rest ejection fraction, body mass index, and type of vasodilator were not significantly associated with a low MFR.

Survival Outcome

The median follow-up time was 7.1 y (95% CI, 6.6–7.5 y). Median OS was 5.1 y (range, 14 d–8.8 y). During follow-up, 120 patients died. OS was significantly worse in patients with advanced-stage cancer than in those with early-stage cancer (adjusted hazard ratio, 4.06; *P* < 0.001; Supplemental Table 2). A higher stress MBF and lower rest MBF were both significantly associated with better OS in univariable analysis (*P* = 0.007 and 0.012, respectively). However, they were not entered in the multivariable model because of

TABLE 1
Demographics and Characteristics of Study Cohort ($n = 221$)

Characteristic	Data	Characteristic	Data
Age (y)	71 (41–92)	Vasodilator	
Age, binary		Dipyridamole	93 (42.1%)
<65 y	73 (33.0%)	Regadenoson	128 (57.9%)
≥65 y	148 (67.0%)	Heart rate (rest)	70.05 ± 13.15
Sex		Heart rate (stress)	87.44 ± 16.56 (2*)
Female	97 (43.9%)	Rest systolic blood pressure	140.60 ± 20.55
Male	124 (56.1%)	Stress systolic blood pressure	131.53 ± 22.53 (3*)
Height (cm)	168 (132–193)	Transient ischemic dilatation ratio	1.06 ± 0.15 (1*)
Weight (kg)	79 (36–161)	Stress MBF (mg/mL/min)	1.93 ± 0.74
Body mass index	27.82 (16.00–68.78)	Rest MBF (mg/mL/min)	1.01 ± 0.42
Body mass index, binary		Adjusted rest MBF (mg/mL/min)	0.88 ± 0.32
<30	136 (61.5%)	MFR	2.04 ± 0.74
≥30	85 (38.5%)	Adjusted MFR	2.31 ± 0.85
Stress LVEF (%)	71 (18–90) (1*)	Morise risk assessment	
Stress LVEF (%), binary	1*	Low (0–8)	8 (3.6%)
≥50	198 (90.0%)	Intermediate (9–15)	93 (42.1%)
<50	22 (10.0%)	High (>15)	120 (54.3%)
Rest LVEF (%)	66 (21–90) (1*)	SSS	
Rest LVEF (%), binary	1*	Normal (0–3)	169 (76.5%)
≥50	194 (88.2%)	Mild (4–7)	26 (11.8%)
<50	26 (11.8%)	Moderate (8–11)	8 (3.6%)
LVEF reserve	5 (-22–21) (1*)	Severe (>12)	18 (8.1%)
Abnormal LVEF reserve	1*	Ischemia (SDS ≥ 3)	
Normal	196 (89.1%)	Abnormal	46 (20.8%)
Abnormal	24 (10.9%)	Normal	175 (79.2%)
Hemoglobin (g/dL)	12.40 (7.60–16.70) (4*)	Coronary calcium (Agatston score)	5*
Hemoglobin, binary	4*	None/minimal (0–10)	47 (21.8%)
≥10 g/dL	189 (87.1%)	Mild (11–100)	37 (17.1%)
<10 g/dL	28 (12.9%)	Moderate (101–400)	46 (21.3%)
Diabetes		Severe (>400)	68 (31.5%)
No	143 (64.7%)	Stent	9 (4.2%)
Yes	78 (35.3%)	Coronary artery bypass graft	9 (4.2%)
Dyslipidemia	157 (71.0%)	eGFR (mL/min/1.73 m ²)	64 (22–109)
Hypertension	172 (77.8%)	eGFR, binary	
Smoker/former smoker	159 (71.9%)	≤60	96 (43.4%)
History of CAD	82 (37.1%)	>60	125 (56.6%)

*Unknown.

LVEF = left ventricular ejection fraction; MBF = myocardial blood flow; eGFR = estimated glomerular filtration rate.

Qualitative data are number and percentage; continuous data are median and range or mean ± SD.

collinearity with adjusted MFR. A lower adjusted MFR was significantly associated with a higher risk of death (increased by 3% for every 0.1-unit decrease in MFR); this translates to an increase in the risk of death of 17% when MFR decreases by 0.5 ($P = 0.026$). When stratifying MFR by quartiles, the 5-y survival rate for patients with an MFR of less than 1.45 was 22%, whereas for those with an MFR of more than 2.45 it was 73% (Supplemental Fig. 1). Other independent predictors of OS were age, history of

CAD, hemoglobin, and obesity (Supplemental Table 2). Therefore, MFR provided additional prognostic value to known clinical risk factors. Four risk categories were defined by stratifying the patients on MFR and cancer stage: patients with early-stage cancer and MFR ≥ 1.97 ; those with early-stage cancer and MFR < 1.97; those with advanced-stage cancer and MFR ≥ 1.97 ; and those with advanced-stage cancer and MFR < 1.97. These groups had significantly different outcomes, with 5-y OS of 88%, 53%, 33%, and

TABLE 2
Factors Contributing to Low MFR (All Patients)

Characteristic	MFR ≥ 1.97 , n = 111	MFR < 1.97, n = 110	P [†]
Stress MBF (mg/mL/min)	2.14 (0.85–4.64)	1.57 (0.39–3.64)	<0.001
Rest MBF (mg/mL/min)	0.81 (0.40–2.25)	1.01 (0.48–2.61)	<0.001
Adjusted rest MBF (mg/mL/min)	0.77 (0.31–1.40)	0.88 (0.39–2.60)	<0.001
Heart rate (stress)	87 (52–126) (2*)	84 (51–141)	0.33
Heart rate (rest)	66 (44–102)	71 (42–112)	0.006
Ejection fraction (stress, %)	73 (40–90)	67 (18–90) (1*)	0.002
Ejection fraction (rest, %)	67 (27–90)	64 (21–86) (1*)	0.084
SSS	0.0 (0.0–21.0)	1.0 (0.0–40.0)	0.003
SDS	0.0 (0.0–9.0)	0.0 (0.0–26.0)	0.021
Hemoglobin (g/dL)	12.85 (7.60–16.70) (1*)	11.80 (7.60–15.60) (3*)	<0.001
Body mass index	28 (19–51)	27 (16–69)	0.26
Vasodilator			0.64
Dipyridamole	45 (41%)	48 (44%)	
Regadenoson	66 (59%)	62 (56%)	
History of CAD	29 (26%)	53 (48%)	<0.001
Coronary calcium (Agatston score)	(2*)	(3*)	<0.001
None/minimal (0–10)	32 (29%)	15 (14%)	
Mild (11–100)	25 (23%)	12 (11%)	
Moderate (101–400)	25 (23%)	21 (20%)	
Severe (>400)	25 (23%)	43 (40%)	
Stent	1 (1%)	8 (7%)	
Coronary artery bypass graft	1 (1%)	8 (7%)	
Age (y)	67 (44–92)	75 (41–90)	<0.001

*Unknown.

[†]Welch 2-sample t test, Wilcoxon rank sum test, Pearson χ^2 test; Fisher exact test.

MBF = myocardial blood flow.

Qualitative data are number and percentage; continuous data are median and range.

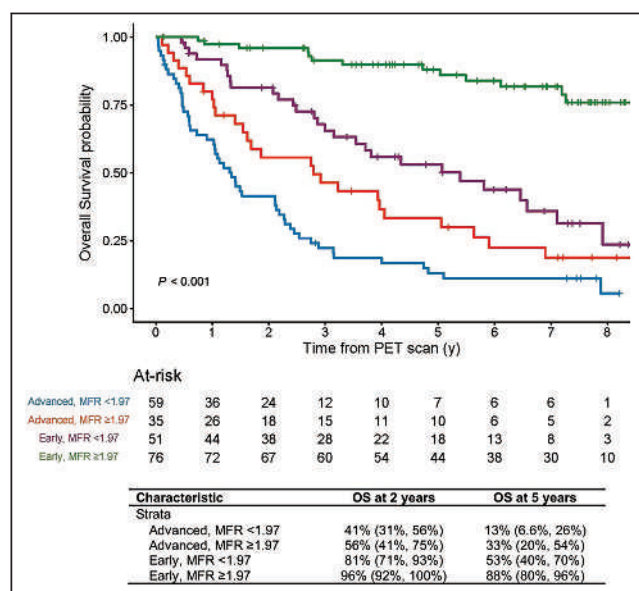


FIGURE 2. Kaplan-Meier overall survival analysis stratified by MFR (<1.97 versus ≥ 1.97) and cancer stage (early versus advanced) in the overall cohort (n = 221).

13%, respectively (Fig. 2). Additional analyses classified by cancer staging and MFR are shown in Supplemental Table 3. When analysis was restricted to the 163 patients without regional perfusion abnormalities (SSS < 4 and SDS < 3), MFR still provided additional prognostic value for OS (Supplemental Fig. 2), with 5-y OS of 88%, 55%, 36%, and 15%, for patients with early-stage cancer and MFR ≥ 1.97 ; those with early-stage cancer and MFR < 1.97; those with advanced-stage cancer and MFR ≥ 1.97 ; and those with advanced-stage cancer and MFR < 1.97, respectively. Factors associated with OS in this restricted analysis of patients without regional perfusion abnormalities are listed in Supplemental Table 4.

DISCUSSION

This study demonstrated that MFR is an independent predictor of OS in a population of patients with active cancer, even after stratifying for cancer stage and regardless of the presence or absence of visual perfusion defects, suggesting that cardiovascular risk assessment and appropriate care remain paramount even in a population with significant competing morbidity.

PET-derived MFR is an established prognostic biomarker for the risk of major adverse cardiovascular events in the general population (5). In our cohort, we chose to focus on overall outcome

rather than limiting our investigation to these adverse events and cardiac-specific death. Given the complex nature of cancer care and follow-up, cardiac symptoms and events may be underestimated and erroneously ascribed to the underlying oncologic disease or therapy. On the other hand, OS is a robust and reliable outcome measure (20) and may indicate a holistic significance of impaired MFR beyond its association with cardiac health.

In a large study of over 4,000 patients (21), an MFR of less than 2.0 was an independent prognostic factor of all-cause mortality (hazard ratio, 1.72), with an average mortality of 4.4% per year during a median follow-up of 5.6 y (total mortality, 24.9%). In comparison, our patients had a higher all-cause mortality of 7.6% per year during a median follow-up of 7.1 y (total mortality, 54.3%). Although patient populations differ, MFR as an independent prognostic factor and the median values for MFR (1.97 vs. 2.0, respectively) were quite similar. In a study of 87 patients with breast cancer, those with an MFR in the lowest tertile had a higher cumulative incidence of MACE than those with an MFR in the highest tertile (22). In another study (23), an abnormal MFR remained predictive of cardiovascular death in patients with chronic kidney disease. Similarly, in a retrospective study of 198 patients with systemic inflammatory disorders, those in the lowest tertile of MFRs (defined as <1.65) experienced higher all-cause mortality than those in the highest tertile (hazard ratio, 2.4), regardless of other variables (24). In aggregate, these data suggest that a reduced MFR is a useful prognostic indicator even in the presence of significant noncardiac comorbidities. Accordingly, cardiac risk stratification should be performed in cancer patients with known or suspected CAD, and primary and secondary prevention strategies should be implemented to improve outcomes, similar to current practice in nonselected populations (25–28).

Previous epidemiologic studies have demonstrated that cardiovascular disease has a major impact on the long-term survival of cancer patients (29). Our study suggested that an impaired MFR during periods of stress may be a significant contributing factor. There are several potential ways in which cancer, by itself or by virtue of cancer therapy, may affect the cardiovascular system and control of vasomotion.

First, a recognized hallmark of cancer is the systemic inflammatory state (30,31), which may contribute to coronary microvascular dysfunction (32,33), akin to traditional cardiac risk factors (34). Inflammation-induced microvascular dysfunction is proposed to result from a reduction in microvascular nitric oxide bioavailability. The principal mechanism for the effect of nitric oxide on vasomotion is its binding to and activation of guanylate cyclase, increasing the production of cyclic guanosine monophosphate, which through second messengers promotes arterial smooth-muscle relaxation. Interestingly, phosphodiesterase 5 inhibition, preventing the breakdown of cyclic guanosine monophosphate, has recently gained interest as a potential anticancer therapy (35) beyond its established role as a systemic arterial vasodilator.

Another prevalent finding in cancer is autonomic dysfunction (36–39), a recognized contributor to abnormal MFR (40,41). The sympathetic nervous system can regulate the tumor microenvironment in multiple ways (42,43), and chronic activation of the sympathetic nervous system can promote cancer progression. β -adrenergic signaling, for instance, stimulates the transcription of proinflammatory cytokines and inhibits the transcription of interferons, thereby contributing to tumor progression and metastasis (42). Conversely, experimental inhibition of the sympathetic nervous system (44–46) has been shown to decrease tumor growth and improve outcomes.

Thus, impaired MFR, as seen in our study, may signify cancer-related coronary endothelial dysfunction or autonomic dysfunction. In contrast, cancer and CAD may simply coexist. Regardless of a causal link, our data suggest that cardiovascular risk assessment and appropriate care are important targets in the management of cancer patients.

This study had some limitations. It was retrospective, with potential deficiencies in the documentation of cardiovascular risk factors. It included only patients who were referred for MPI PET by their oncologist or cardiologist, which may introduce a selection bias. Its population was heterogeneous regarding age, cancer type, and treatment applied. Also, 11.8% had a resting left ventricular ejection fraction of less than 50%, and 31.5% had a coronary calcium score above 400. Nevertheless, none of these factors proved significant in the statistical analysis.

CONCLUSION

PET MFR is a strong, independent prognostic marker of OS, irrespective of cancer stage. Therefore, MFR assessment may contribute to better risk stratification and may serve as a treatment target to optimize cardiovascular care and improve survival in cancer patients. Prospective studies are warranted to validate this concept.

DISCLOSURE

This research was funded in part through National Institutes of Health/National Cancer Institute Cancer Center support grant P30 CA008748. Thomas Schindler receives support from NIH through grant R01 HL142297-01A1. No other potential conflict of interest relevant to this article was reported.

KEY POINTS

QUESTION: Are cancer patients with abnormal myocardial blood flow and MFR, as derived from quantitative PET imaging, at higher risk for mortality, independent of their underlying disease?

PERTINENT FINDINGS: In a retrospective cohort study of 221 patients, we found that an abnormal MFR provides independent prognostic information; patients with an abnormal MFR had shorter survival, regardless of cancer type and stage.

IMPLICATIONS FOR PATIENT CARE: MFR improves risk stratification in cancer patients and may serve as a treatment target to increase their survival, suggesting a need for dedicated cardiac care in cancer patients, regardless of competing risk from their underlying disease.

REFERENCES

- Schoormans D, Husson O, Oerlemans S, Ezendam N, Mols F. Having co-morbid cardiovascular disease at time of cancer diagnosis: already one step behind when it comes to HRQoL? *Acta Oncol.* 2019;58:1684–1691.
- Abe J, Martin JF, Yeh ET. The future of onco-cardiology: we are not just “side effect hunters.” *Circ Res.* 2016;119:896–899.
- Gupta D, Pun SC, Verma S, Steingart RM. Radiation-induced coronary artery disease: a second survivorship challenge? *Future Oncol.* 2015;11:2017–2020.
- Chang K, Sarkiss M, Won KS, Swafford J, Broemeling L, Gayed I. Preoperative risk stratification using gated myocardial perfusion studies in patients with cancer. *J Nucl Med.* 2007;48:344–348.
- Murthy VL, Bateman TM, Beanlands RS, et al. Clinical quantification of myocardial blood flow using PET: joint position paper of the SNMMI Cardiovascular Council and the ASNC. *J Nucl Med.* 2018;59:273–293.

6. Weinstein H, Steingart R. Myocardial perfusion imaging for preoperative risk stratification. *J Nucl Med*. 2011;52:750–760.
7. Juárez-Orozco LE, Tio RA, Alexanderson E, et al. Quantitative myocardial perfusion evaluation with positron emission tomography and the risk of cardiovascular events in patients with coronary artery disease: a systematic review of prognostic studies. *Eur Heart J Cardiovasc Imaging*. 2018;19:1179–1187.
8. Murthy VL, Naya M, Foster CR, et al. Improved cardiac risk assessment with non-invasive measures of coronary flow reserve. *Circulation*. 2011;124:2215–2224.
9. Fukushima K, Javadi MS, Higuchi T, et al. Prediction of short-term cardiovascular events using quantification of global myocardial flow reserve in patients referred for clinical ^{82}Rb PET perfusion imaging. *J Nucl Med*. 2011;52:726–732.
10. Henzlova MJ, Duvall WL, Einstein AJ, Travin MI, Verberne HJ. ASNC imaging guidelines for SPECT nuclear cardiology procedures: stress, protocols, and tracers. *J Nucl Cardiol*. 2016;23:606–639.
11. Morise A, Evans M, Jalisi F, Shetty R, Stauffer M. A pretest prognostic score to assess patients undergoing exercise or pharmacological stress testing. *Heart*. 2007;93:200–204.
12. Chow BJ, Dorbala S, Di Carli MF, et al. Prognostic value of PET myocardial perfusion imaging in obese patients. *JACC Cardiovasc Imaging*. 2014;7:278–287.
13. Pen A, Yam Y, Chen L, et al. Prognostic value of Rb-82 positron emission tomography myocardial perfusion imaging in coronary artery bypass patients. *Eur Heart J Cardiovasc Imaging*. 2014;15:787–792.
14. Arasaratnam P, Sadreddini M, Yam Y, et al. Prognostic value of vasodilator response using rubidium-82 positron emission tomography myocardial perfusion imaging in patients with coronary artery disease. *Eur J Nucl Med Mol Imaging*. 2018;45:538–548.
15. Rischpler C, Higuchi T, Fukushima K, et al. Transient ischemic dilation ratio in ^{82}Rb PET myocardial perfusion imaging: normal values and significance as a diagnostic and prognostic marker. *J Nucl Med*. 2012;53:723–730.
16. Lortie M, Beanlands RS, Yoshinaga K, Klein R, Dasilva JN, DeKemp RA. Quantification of myocardial blood flow with ^{82}Rb dynamic PET imaging. *Eur J Nucl Med Mol Imaging*. 2007;34:1765–1774.
17. Agatston AS, Janowitz WR, Hildner FJ, Zusmer NR, Viamonte M, Jr., Detrano R. Quantification of coronary artery calcium using ultrafast computed tomography. *J Am Coll Cardiol*. 1990;15:827–832.
18. Edge SBB, Compton CC, Fritz AG, Greene FL, Trotti A, eds. *AJCC Cancer Staging Manual*. 7th ed. Springer; 2010.
19. Schemper M, Smith TL. A note on quantifying follow-up in studies of failure time. *Control Clin Trials*. 1996;17:343–346.
20. Lauer MS, Blackstone EH, Young JB, Topol EJ. Cause of death in clinical research: time for a reassessment? *J Am Coll Cardiol*. 1999;34:618–620.
21. Gupta A, Taqueti VR, van de Hoef TP, et al. Integrated noninvasive physiological assessment of coronary circulatory function and impact on cardiovascular mortality in patients with stable coronary artery disease. *Circulation*. 2017;136:2325–2336.
22. Divakaran S, Caron JP, Zhou W, et al. Coronary vasomotor dysfunction portends worse outcomes in patients with breast cancer. *J Nucl Cardiol*. 2022;29:3072–3081.
23. Charytan DM, Skali H, Shah NR, et al. Coronary flow reserve is predictive of the risk of cardiovascular death regardless of chronic kidney disease stage. *Kidney Int*. 2018;93:501–509.
24. Weber BN, Stevens E, Perez-Chada LM, et al. Impaired coronary vasodilator reserve and adverse prognosis in patients with systemic inflammatory disorders. *JACC Cardiovasc Imaging*. 2021;14:2212–2220.
25. Mancini GBJ, Maron DJ, Hartigan PM, et al. Lifestyle, glycosylated hemoglobin A1c, and survival among patients with stable ischemic heart disease and diabetes. *J Am Coll Cardiol*. 2019;73:2049–2058.
26. Maron DJ, Mancini GBJ, Hartigan PM, et al. Healthy behavior, risk factor control, and survival in the COURAGE trial. *J Am Coll Cardiol*. 2018;72:2297–2305.
27. Solomon MD, Leong TK, Levin E, et al. Cumulative adherence to secondary prevention guidelines and mortality after acute myocardial infarction. *J Am Heart Assoc*. 2020;9:e014415.
28. Camici PG, Crea F. Coronary microvascular dysfunction. *N Engl J Med*. 2007;356:830–840.
29. Sturgeon KM, Deng L, Bluethmann SM, et al. A population-based study of cardiovascular disease mortality risk in US cancer patients. *Eur Heart J*. 2019;40:3889–3897.
30. Diakos CI, Charles KA, McMillan DC, Clarke SJ. Cancer-related inflammation and treatment effectiveness. *Lancet Oncol*. 2014;15:e493–e503.
31. Hanahan D, Weinberg RA. Hallmarks of cancer: the next generation. *Cell*. 2011;144:646–674.
32. Schindler TH, Nitzsche EU, Olschewski M, et al. Chronic inflammation and impaired coronary vasoactivity in patients with coronary risk factors. *Circulation*. 2004;110:1069–1075.
33. Recio-Mayoral A, Rimoldi OE, Camici PG, Kaski JC. Inflammation and microvascular dysfunction in cardiac syndrome X patients without conventional risk factors for coronary artery disease. *JACC Cardiovasc Imaging*. 2013;6:660–667.
34. Paulus WJ, Tschope C. A novel paradigm for heart failure with preserved ejection fraction: comorbidities drive myocardial dysfunction and remodeling through coronary microvascular endothelial inflammation. *J Am Coll Cardiol*. 2013;62:263–271.
35. Cruz-Burgos M, Losada-Garcia A, Cruz-Hernández CD, et al. New approaches in oncology for repositioning drugs: the case of PDE5 inhibitor sildenafil. *Front Oncol*. 2021;11:627229.
36. Adams SC, Schondorf R, Benoit J, Kilgour RD. Impact of cancer and chemotherapy on autonomic nervous system function and cardiovascular reactivity in young adults with cancer: a case-controlled feasibility study. *BMC Cancer*. 2015;15:414.
37. Arab C, Vanderlei LCM, da Silva Paiva L, et al. Cardiac autonomic modulation impairments in advanced breast cancer patients. *Clin Res Cardiol*. 2018;107:924–936.
38. Lakoski SG, Jones LW, Krone RJ, Stein PK, Scott JM. Autonomic dysfunction in early breast cancer: incidence, clinical importance, and underlying mechanisms. *Am Heart J*. 2015;170:231–241.
39. Teng AE, Noor B, Ajijola OA, Yang EH. Chemotherapy and radiation-associated cardiac autonomic dysfunction. *Curr Oncol Rep*. 2021;23:14.
40. Di Carli MF, Bianco-Battles D, Landa ME, et al. Effects of autonomic neuropathy on coronary blood flow in patients with diabetes mellitus. *Circulation*. 1999;100:813–819.
41. Zobel EH, Hasbak P, Winther SA, et al. Cardiac autonomic function is associated with myocardial flow reserve in type 1 diabetes. *Diabetes*. 2019;68:1277–1286.
42. Cole SW, Nagaraja AS, Lutgendorf SK, Green PA, Sood AK. Sympathetic nervous system regulation of the tumour microenvironment. *Nat Rev Cancer*. 2015;15:563–572.
43. Zahalka AH, Arnal-Estabé A, Maryanovich M, et al. Adrenergic nerves activate an angio-metabolic switch in prostate cancer. *Science*. 2017;358:321–326.
44. Ben-Shaanan TL, Schiller M, Azulay-Dubby H, et al. Modulation of anti-tumor immunity by the brain's reward system. *Nat Commun*. 2018;9:2723.
45. Melhem-Bertrandt A, Chavez-Macgregor M, Lei X, et al. Beta-blocker use is associated with improved relapse-free survival in patients with triple-negative breast cancer. *J Clin Oncol*. 2011;29:2645–2652.
46. Grytki HH, Fagerland MW, Fosså SD, Taskén KA. Association between use of β -blockers and prostate cancer-specific survival: a cohort study of 3561 prostate cancer patients with high-risk or metastatic disease. *Eur Urol*. 2014;65:635–641.

Molecular Imaging of Pulmonary Inflammation in Users of Electronic and Combustible Cigarettes: A Pilot Study

Reagan R. Wetherill¹, Robert K. Doot², Anthony J. Young², Hsiaoju Lee², Erin K. Schubert², Corinde E. Wiers^{1,2}, Frank T. Leone³, Robert H. Mach², Henry R. Kranzler^{1,4}, and Jacob G. Dubroff²

¹Department of Psychiatry, Perelman School of Medicine, University of Pennsylvania, Philadelphia, Pennsylvania; ²Department of Radiology, Perelman School of Medicine, University of Pennsylvania, Philadelphia, Pennsylvania; ³Comprehensive Smoking Treatment Program, Penn Lung Center, Philadelphia, Pennsylvania; and ⁴Crescenz VAMC, Philadelphia, Pennsylvania

Electronic cigarette (EC) use has increased dramatically, particularly among adolescents and young adults, and, like cigarette use, can cause pulmonary inflammation and increase the risk of lung disease. **Methods:** This preliminary study used PET with ¹⁸F-6-(1/2)(2-fluoropropyl)-4-methylpyridin-2-amine (¹⁸F-NOS) to quantify inducible nitric oxide synthase expression to characterize oxidative stress and inflammation in the lungs *in vivo* in 3 age- and sex-matched groups: 5 EC users, 5 cigarette smokers, and 5 controls who had never smoked or vaped. **Results:** EC users showed greater ¹⁸F-NOS nondisplaceable binding potential (BP_{ND}) than cigarette smokers ($P = 0.03$) and controls ($P = 0.01$), whereas BP_{ND} in cigarette smokers did not differ from that in controls ($P > 0.1$). ¹⁸F-NOS lung tissue delivery and inducible nitric oxide synthase distribution volume did not significantly differ among groups. Although there were no group differences in peripheral inflammatory biomarker concentrations, ¹⁸F-NOS BP_{ND} correlated with the proinflammatory cytokine tumor necrosis factor- α concentrations ($r_s = 0.87$, $P = 0.05$) in EC users. Additionally, when EC users and cigarette smokers were pooled together, number of vaping episodes or cigarettes per day correlated with interleukin-6 levels ($r_s = 0.86$, $P = 0.006$). **Conclusion:** This is the first PET imaging study to compare lung inflammation between EC and cigarette users *in vivo*. We found preliminary evidence that EC users have greater pulmonary inflammation than cigarette smokers and controls, with a positive association between pulmonary and peripheral measures of inflammation.

Key Words: electronic cigarettes; cigarettes; PET; ¹⁸F-NOS; inflammation

J Nucl Med 2023; 64:797–802

DOI: 10.2967/jnmed.122.264529

Tobacco use is the world's leading preventable cause of morbidity and mortality, accounting for more than 8 million deaths annually (1). Although public awareness of smoking-related risks has increased and tobacco smoking has declined, electronic cigarette (EC) use has increased dramatically, particularly among adolescents and young adults (1–3). The increase in EC use is driven

partially by the assumption that ECs are safer than conventional cigarettes. Although ECs are often advertised as an alternative smoking cessation tool (4,5), their long-term effectiveness and safety have not been rigorously evaluated (6,7). Given the emergence of an epidemic of injuries associated with ECs or vaping products (8), EC use has become a major public health concern, and the adverse pulmonary effects of EC use remain unclear.

ECs deliver nicotine by heating e-liquids (i.e., the liquid used in ECs) containing nicotine in a vegetable glycerin or propylene glycol vehicle with flavorings that are vaporized and inhaled, thus delivering nicotine without combusting tobacco. Although the propylene glycol and vegetable glycerin found in e-liquids are regarded as safe by the U.S. Food and Drug Administration, aerosols from ECs contain tobacco-specific nitrosamines, metals, polycyclic aromatic hydrocarbons, and volatile organic compounds that are known toxicants and carcinogens (9). As with smoking, several EC-related compounds are associated with inflammation, altered innate immune response, oxidative stress, and cytotoxicity (9–11). However, the existing human literature on the pulmonary effects of EC use is limited and comprises mainly studies that use invasive approaches (e.g., induced sputum and bronchoalveolar lavage) that do not adequately assess the impact of EC use on the lungs.

PET imaging has been used to quantify and track inflammatory responses associated with smoking and EC use *in vivo* without the need for invasive diagnostic studies (12,13). PET with ¹⁸F-FDG has been used extensively to detect enhanced glucose metabolic activity of activated immune cells in inflammatory diseases, including pneumonia (14), cystic fibrosis (14), and chronic obstructive pulmonary disease (15). Although associations between ¹⁸F-FDG quantification and inflammation have been observed, biologic processes, including fibrosis and neoplasia, use glucose and limit the specificity of ¹⁸F-FDG (16). PET radiotracers targeting the 18-kDa translocator protein, also known as the peripheral benzodiazepine receptor, have also been used to measure pulmonary inflammation (17,18). These radiotracers were initially considered putative markers of neuroinflammation; however, their specificity for inflammation is limited (19). Thus, recent efforts have focused on imaging specific aspects of immune regulation and response, such as nitric oxide synthase enzymes, with promising results (16,20).

Nitric oxide plays an important role in immune regulation and is produced by 3 nitric oxide synthase enzymes: neuronal nitric oxide synthase, endothelial nitric oxide synthase, and inducible nitric oxide synthase (iNOS) (21). iNOS is associated with acute and chronic inflammatory diseases, including asthma and chronic obstructive pulmonary disease (22,23), and is expressed in normal lung epithelium (24). Convergent evidence indicates that iNOS

Received Jun. 14, 2022; revision accepted Nov. 28, 2022.

For correspondence or reprints, contact Reagan R. Wetherill (rweth@pennmedicine.upenn.edu).

Published online Jan. 19, 2023.

Immediate Open Access: Creative Commons Attribution 4.0 International License (CC BY) allows users to share and adapt with attribution, excluding materials credited to previous publications. License: <https://creativecommons.org/licenses/by/4.0/>. Details: <http://jnmd.snmjournals.org/site/misc/permission.xhtml>.

COPYRIGHT © 2023 by the Society of Nuclear Medicine and Molecular Imaging.

plays a central role in mediating inflammation in smokers of combustible cigarettes, thereby contributing to smoking-related lung diseases. Preclinical models show that chronic exposure to cigarette smoke increases iNOS expression (25), whereas pharmacologic inhibition of iNOS reverses tobacco-induced lung disease (26). Additionally, pre-clinical research has provided a mechanistic link between iNOS expression in the lung and inflammatory lung diseases (26,27). These findings strongly support iNOS as a mechanistically relevant target for molecular imaging of lung inflammation and inflammatory lung diseases.

The PET radiotracer ^{18}F -6-(1/2)(2-fluoro-propyl)-4-methylpyridin-2-amine (^{18}F -NOS) permits the visualization and measurement of in vivo iNOS expression (16,28). ^{18}F -NOS is a radiolabeled version of a reversible iNOS inhibitor with better selectivity than other nitric oxide synthase enzymes (28). ^{18}F -NOS has been validated in an animal model of lipopolysaccharide-induced lung injury (29) and was used successfully to image iNOS expression in humans to characterize oxidative stress and inflammation in the heart and lungs (16,28). This study uses ^{18}F -NOS PET lung imaging to quantify differences in iNOS expression among EC users, cigarette smokers, and control subjects who have never smoked or vaped. On the basis of preclinical research showing that exposure to e-liquid vapor and cigarette smoke increases iNOS expression (25,30), we hypothesized that EC users and cigarette smokers would show greater pulmonary iNOS uptake than would controls. We also assessed blood and plasma inflammatory biomarker concentrations (tumor necrosis factor- α [TNF- α], interleukin-6 [IL-6], and C-reactive protein) and examined their association with ^{18}F -NOS PET lung imaging parameters.

MATERIALS AND METHODS

Participants

The study protocol was approved by the University of Pennsylvania Institutional Review Board and conducted in compliance with the Health Insurance Portability and Accountability Act under exploratory investigational new-drug number 140,976 for ^{18}F -NOS. Participants were recruited via local print media, social media, and previous research studies. Interested individuals completed a brief telephone screen and, if eligible, an in-person intake session during which they provided written informed consent and were screened for eligibility. Twenty-four participants underwent screening, including a physical examination, medical history, routine clinical laboratory tests, and toxicologic urine analysis. Briefly, exclusion criteria included a history or evidence of significant medical disorders, a lifetime *Diagnostic and Statistical Manual of Mental Disorders, Fifth Edition* diagnosis of a psychiatric or substance use disorder (except tobacco use disorder for EC users and cigarette smokers), a positive urine drug screen of drugs of abuse, use of inhaled or oral corticosteroids or antiinflammatory medications, and a past-month history of lung trauma or active lung infection that could impact the uptake of ^{18}F -NOS. All female participants had a negative pregnancy test on the scanning day before receiving the radiotracer. Daily for the past 6 mo, EC users had vaped nicotine and cigarette smokers had smoked. The current smoking status was confirmed by carbon monoxide levels greater than 10 parts per million and urine cotinine levels greater than 150 ng/mL. Fifteen age- and sex-matched participants (5 exclusive EC users [mean age, 27 ± 7 y], 5 cigarette smokers [mean age, 35 ± 9 y], and 5 controls [mean age, 28 ± 7 y]), comprising 2 women and 3 men in each group, met the eligibility criteria and completed the study (Supplemental Fig. 1; supplemental materials are available at <http://jnm.snmjournals.org>).

Before scanning, participants completed the Hospital Depression and Anxiety Scale (31) to assess symptoms of depression and anxiety. EC users completed measures of vaping behavior, including the Penn

State Electronic Cigarette Dependence Index (32), and cigarette smokers completed measures of tobacco smoking behavior, including the Fagerström Test for Cigarette Dependence (33). A blood sample was obtained to measure blood or plasma cytokine concentrations (TNF- α , IL-6, and C-reactive protein). Participants underwent dynamic thoracic ^{18}F -NOS PET/CT with venous blood sampling.

Data Acquisition

The PET radiotracer ^{18}F -NOS was synthesized as previously described (28). Participants were scanned with an Ingenuity PET/CT scanner (Philips Healthcare), which has a PET spatial resolution of 5 mm in full width at half maximum and an 18-cm axial field of view (34). For each scan, a nuclear medicine physician determined the thoracic field of view that best included the heart and lungs. After a low-dose attenuation-correction CT scan, a 1-h PET dynamic acquisition was started at the time of an intravenous bolus injection of ^{18}F -NOS (199 ± 27 MBq) with the following framing schedule: 24×5 s, 6×10 s, 3×20 s, 2×30 s, 5×60 s, and 10×5 min. On the basis of published effective dose estimates of $15.9 \mu\text{Sv}/\text{MBq}$ for ^{18}F -NOS, 199 MBq delivers an effective dose of 3.16 mSv, with a maximum critical dose to the urinary bladder wall of 19.0 mSv (28). The attenuation-correction CT images were reconstructed into PET images using a previously described list-mode, blob-based ordered-subsets maximum-likelihood expectation-maximization algorithm, including flight-time and physical-data corrections (34). The radiologist who reviewed the images was masked to participant group status, as was the data analyst.

Metabolite Analysis

Venous blood was sampled at approximately 2, 5, 10, 15, 30, 45, and 60 min after injection to measure radiometabolites. The whole-blood and plasma activity concentrations were counted using a WIZARD² 2480 γ -counter (Perkin Elmer). Acetonitrile-treated plasma supernatant was analyzed in a 1260 Infinity Series (Agilent Technologies) high-performance liquid chromatography system using an Agilent ZORBAX StableBond C18 column via a mobile phase of 73% 0.1 M ammonium formate buffer and 27% methanol. The resulting plasma-to-whole-blood ratio as a function of time was used to convert the image-derived whole-blood input function into a plasma input function. The resulting parent PET radiotracer fraction as a function of time and the plasma input function were inputted for subsequent kinetic analysis.

Volumes of Interest

Time-activity curves for the whole blood pool were measured using 1 cm³ peak volumes of interest within 2-cm-diameter spherical volumes of interest within the pulmonary artery, as this blood pool is sufficiently large to minimize partial-volume effects and is located immediately before blood enters the lungs (Fig. 1). Lung uptake time-activity curves were extracted from all lung tissue in the PET field of view (Fig. 1).

Kinetic Analysis

Three models of kinetic analysis were compared for estimating the total volume of distribution (V_T) from the observed reversible tracer binding: graphical Logan plot (35), 1 tissue compartment, and 2 tissue compartments (2TCs). The 2TC model, with an average whole-lung Akaike information criterion (36,37) of 184 ± 31 , was selected over the 1-tissue-compartment model, with a corresponding Akaike information criterion of 295 ± 24 , because the 2TC had the lower, and therefore better, Akaike information criterion score. V_T values estimated via the Logan and 2TC models were similar ($R^2 = 0.99$). As expected, V_T values from Logan plots were less biased than when using the 2TC model, with the magnitude of the Logan plot V_T bias decreasing with increases in the duration of the PET acquisition. Thus, we used the 2TC model to quantify tracer uptake to avoid having metrics dependent on the PET scan duration.

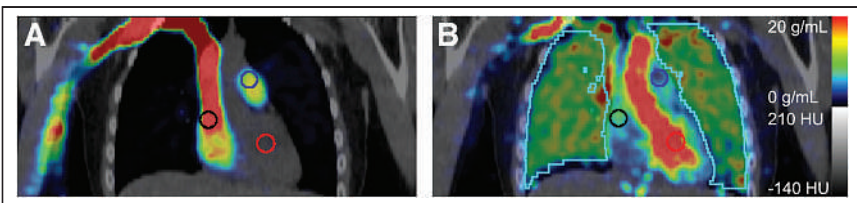


FIGURE 1. Representative coronal PET/CT images after injecting 207 MBq of ^{18}F -NOS, with lung volume of interest (cyan) and 2-cm-diameter spheric blood pool volumes of interest in right atrium (black), pulmonary artery (blue), and left ventricle (red). PET summed uptake is shown from 0 to 15 s after injection (A) and from 37 to 42 s after injection (B). HU = Hounsfield units.

Two approaches for blood volume fraction (v_B) were examined for each model: fixed at 0.15 and floating between 0.05 and 0.3. The floating v_B resulted in the least model variability. Kinetic analyses using a 2TC model with a floating lung v_B were performed to estimate V_T , transport into the first tissue compartment (K_1), the distribution volume of the first tissue compartment (K_1/k_2), and nondisplaceable binding potential (BP_{ND}) via Pmod image analysis software (version 3.7; PMOD Technologies Ltd.) using the combined lung time–activity curve and PET image-derived plasma input function from the pulmonary artery blood pool (Fig. 1) (38). Kinetic analyses were based on the first 40 min of the PET acquisition to allow a consistent analysis of all participants' data after 1 participant's excessive motion resulted in unevaluable PET images after 40 min.

Statistical Analysis

All statistical tests were 2-sided. Nonparametric Mann–Whitney and Kruskal–Wallis tests were used to assess group differences. Spearman rank-order correlations measured the strength and direction of associations between inflammatory biomarkers, nicotine use behaviors (cigarettes per day for cigarette smokers; vaping episodes per day for EC users), and imaging parameters.

RESULTS

On average, EC users reported 7 ± 4 vaping episodes/d, with Penn State Electronic Cigarette Dependence Index scores of 6 ± 4 , indicating moderate-to-high levels of EC dependence. Cigarette smokers reported smoking 8 ± 4 cigarettes/d, with Fagerström Test for Cigarette Dependence scores of 5 ± 2 , indicating moderate levels of cigarette dependence. There were no significant group

differences in age, depression and anxiety scores, injected mass radioactivity dose, or plasma-free fraction.

Selection of the pulmonary artery to measure the blood input function is supported by the example PET/CT images in Figure 1, where the distribution of ^{18}F -NOS before entry into the lungs and then the left ventricle indicates that ^{18}F -NOS enters the right atrium, followed by the pulmonary artery. Figure 2 shows average lung ^{18}F -NOS uptake for all participants as a function of time. Table 1 presents kinetic analysis results,

where the average estimate of 0.15 ± 0.02 for lung v_B is consistent with the reported normal lung v_B range of 0.14–0.19 from ^{18}F -FDG PET/CT scans (39).

^{18}F -NOS BP_{ND} values differed significantly among groups ($H(2) = 7.50$, $P = 0.02$; Fig. 3). Post hoc comparisons revealed that EC users had higher BP_{ND} values than cigarette smokers ($P = 0.03$) and controls ($P = 0.01$). ^{18}F -NOS V_T and K_1 values did not differ among groups ($P > 0.09$).

Peripheral inflammatory biomarker concentrations did not differ among groups ($P > 0.16$). Spearman rank-order correlations examined the associations between daily smoking or vaping behavior, inflammatory biomarker concentrations, and imaging parameters. There was a positive correlation among EC users between ^{18}F -NOS BP_{ND} and TNF- α concentration ($r_s = 0.87$, $P = 0.05$; Supplemental Fig. 2). Among EC users and cigarette smokers, cigarettes per day and vaping episodes per day correlated with IL-6 levels ($r_s = 0.89$, $P = 0.001$; Supplemental Fig. 3). No other correlations were statistically significant.

DISCUSSION

EC use has increased dramatically, particularly among adolescents and young adults. Consequently, well-controlled studies are urgently needed to examine and compare the effects of EC use and cigarette smoking. The existing literature comprises mainly cell culture studies or in vivo animal studies. A few studies examine the effects of EC use on the human lung based on invasive approaches that do not assess the global burden of EC use on the lungs. This preliminary study addressed these gaps using noninvasive, ^{18}F -NOS PET lung imaging to quantify and compare lung inflammation in exclusive EC users, exclusive cigarette smokers, and controls. Our preliminary ^{18}F -NOS PET findings show that EC users, cigarette smokers, and controls have similar delivery of ^{18}F -NOS to the lung tissue and similar iNOS availability. However, ^{18}F -NOS BP_{ND} was significantly higher in the EC group than in cigarette smokers and controls. Moreover, ^{18}F -NOS BP_{ND} in EC users was associated with the proinflammatory cytokine TNF- α . Number of cigarettes and vaping episodes per day correlated with IL-6 levels. To our knowledge, this was the first PET lung imaging study demonstrating that EC users show a unique PET lung phenotype associated with known inflammatory biomarkers.

Although we did not see the expected increase in ^{18}F -NOS uptake in cigarette smokers, our findings are consistent with recent work that used bronchoscopy to isolate alveolar macrophages from bronchoalveolar lavage samples in smokers, EC users, and never-smokers and found that EC users showed greater iNOS expression in alveolar macrophages than did smokers or never-smokers (40). Animal and human studies have shown that iNOS

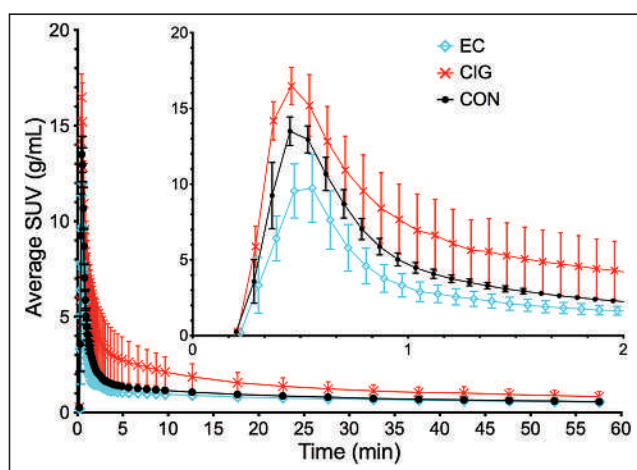


FIGURE 2. Average lung ^{18}F -NOS uptake for each group as function of time, with SD error bars. CIG = cigarette smokers; CON = controls.

TABLE 1
Kinetic Analysis Results

Patient no.	Sex	V _T	K ₁	K ₁ /k ₂	BP _{ND}	vB
EC-07	F	1.17	1.62	0.51	1.31	0.15
EC-10	M	0.63	1.42	0.28	1.23	0.16
EC-13	F	0.99	1.58	0.42	1.34	0.18
EC-20	M	1.20	2.67	0.39	2.12	0.18
EC-23	M	0.83	1.26	0.31	1.66	0.13
CIG-12	M	1.10	2.71	0.57	0.93	0.14
CIG-14	M	4.74	2.29	3.42	0.39	0.14
CIG-17	M	1.14	3.24	0.52	1.21	0.16
CIG-22	F	1.45	2.70	0.66	1.29	0.11
CIG-24	F	1.06	1.62	0.51	1.09	0.15
CON-01	F	1.15	1.95	0.58	0.98	0.18
CON-03	M	1.04	1.85	0.48	1.17	0.15
CON-05	M	0.91	1.37	0.40	1.27	0.15
CON-06	F	1.53	3.19	0.74	1.07	0.17
CON-09	M	1.18	1.62	0.56	1.13	0.13
ECs		0.97 ± 0.24	1.71 ± 0.56	0.38 ± 0.09*	1.53 ± 0.37*	0.16 ± 0.02
CIGs		1.90 ± 1.60	2.51 ± 0.60	1.13 ± 1.28	0.98 ± 0.36	0.14 ± 0.02
CONs		1.16 ± 0.23	1.99 ± 0.70	0.55 ± 0.13	1.12 ± 0.11	0.16 ± 0.02
All		1.34 ± 0.97	2.07 ± 0.67	0.69 ± 0.77	1.21 ± 0.37	0.15 ± 0.02
P		0.36	0.09	0.03	0.02	0.31

*P < 0.05 on comparison between ECs and NUs.

EC = EC user; CIG = combustible cigarette user; CON = control.

Data are mean values and mean ± SD. P values are from Kruskal-Wallis test comparing 3 groups.

expression is induced in most cell types on exposure to inflammatory stimuli (41) and is associated with increased pulmonary nitric oxide (42). Nitric oxide mediates neutrophil and macrophage actions that are thought to contribute to pulmonary oxidant stress and acute lung injury (43). Thus, our findings suggest that EC use may alter

pulmonary oxidative stress responses and predispose them to acute lung injury.

Although groups showed similar levels of inflammatory biomarkers, EC users showed positive associations between ¹⁸F-NOS PET imaging parameters and TNF- α concentration. TNF- α is a proinflammatory cytokine produced by macrophages and secreted by neutrophil granulocytes at sites of injury (44) and is involved in the inflammatory cascade of acute lung injury (45). Indeed, studies have shown that proinflammatory cytokines induce iNOS expression in human alveolar cells in response to exposure to fine particulate matter (46). As such, our findings provide additional evidence of the altered immune responses in the lungs of EC users.

Several limitations of this study should be considered. First, we did not account for vaping topography (i.e., how an EC is used, including puff duration, puff volume, and EC device and power settings). These factors are important in differential exposure to nicotine and toxicants among EC users (47). Although we used individually measured PET radiotracer parent fractions as a function of time to correct for the presence of radiolabeled metabolites in the blood, we could not separate lung ¹⁸F-NOS uptake due to binding of parent ¹⁸F-NOS from any binding of radiolabeled metabolites. Huang et al. asserted that “because of [the metabolite’s] polarity, this metabolite is most likely excluded by the lung endothelium from entering the lung parenchyma” (16). Impacts of any lung binding of radiolabeled metabolites on estimates of ¹⁸F-NOS BP_{ND} will likely be inversely related to the validity of the assumption that polar ¹⁸F-NOS metabolites cannot penetrate lung endothelium.

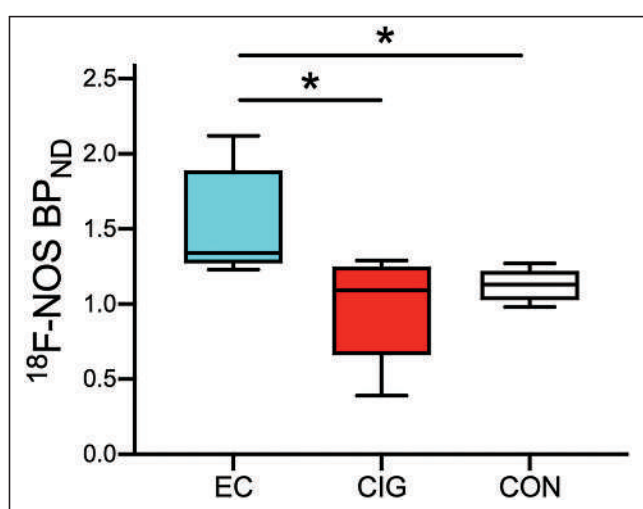


FIGURE 3. Box plot of ¹⁸F-NOS BP_{ND} by group. EC users show higher ¹⁸F-NOS BP_{ND} than controls (P = 0.01) and cigarette smokers (P = 0.03). *P < 0.05. CIG = cigarette smokers; CON = controls.

To date, no studies have provided information on the reproducibility of the ^{18}F -NOS PET assay; however, previous research showed consistent findings in left- and right-lung ^{18}F -NOS parameters (16). In addition, because the sample sizes were small, additional larger studies are needed to replicate these findings and provide greater statistical power for secondary analyses.

CONCLUSION

Using rigorous quantitative methods and a global technique to examine pulmonary oxidative stress, we found evidence that EC use causes a unique inflammatory response in the lungs, reflected by PET measures of iNOS expression and correlations with inflammatory biomarker concentrations. Future work is needed to elucidate the effect of EC use on respiratory health, especially the effects of chronic EC use.

DISCLOSURE

The study was supported by the National Heart, Lung, and Brain Institute (R21HL144673), the National Institute on Drug Abuse (P30DA046345), the National Center for Advancing Translational Sciences of the National Institutes of Health (UL1TR001878), and in part by the Institute for Translational Medicine and Therapeutics' (ITMAT) Transdisciplinary Program in Translational Medicine and Therapeutics. Henry Kranzler is a member of advisory boards for Dicerna Pharmaceuticals, Sophrosyne Pharmaceuticals, and Enthion Pharmaceuticals; a consultant to Sobraa Pharmaceuticals; recipient of grant funds and medication supplies from Alkermes for an investigator-initiated study; a member of the American Society of Clinical Psychopharmacology's Alcohol Clinical Trials Initiative, which was supported by Alkermes, Dicerna, Ethypharm, Lundbeck, Mitsubishi, and Otsuka; and a holder of U.S. patent 10,900,082, titled: "Genotype-Guided Dosing of Opioid Agonists," issued January 26, 2021. Jacob Dubroff, Robert Doot, and Robert Mach have received support from the Michael J. Fox Foundation. No other potential conflict of interest relevant to this article was reported.

KEY POINTS

QUESTION: What are the effects of EC use on pulmonary inflammation compared with combustible cigarette use and no use of cigarettes or vaping, as measured with ^{18}F -NOS PET imaging?

PERTINENT FINDINGS: In this preliminary PET imaging study, EC users showed greater ^{18}F -NOS BP_{ND} than cigarette smokers and controls. ^{18}F -NOS BP_{ND} significantly correlated with the proinflammatory cytokine TNF- α in EC users. Additionally, when EC users and cigarette smokers were pooled together, vaping episodes and cigarettes per day correlated with IL-6 levels.

IMPLICATIONS FOR PATIENT CARE: Preliminary data indicate that EC users show a unique PET lung imaging phenotype associated with known proinflammatory cytokines, suggesting that EC use may increase pulmonary inflammation.

REFERENCES

- WHO Report on the Global Tobacco Epidemic 2021: Addressing New and Emerging Products. World Health Organization; 2021.
- Wang TW, Gentzke AS, Neff LJ, et al. Disposable e-cigarette use among U.S. youth: an emerging public health challenge. *N Engl J Med*. 2021;384:1573–1576.
- Miech R, Johnston L, O'Malley PM, Bachman JG, Patrick ME. Trends in adolescent vaping, 2017–2019. *N Engl J Med*. 2019;381:1490–1491.
- Ioakeimidis N, Vlachopoulos C, Tousoulis D. Efficacy and safety of electronic cigarettes for smoking cessation: a critical approach. *Hellenic J Cardiol*. 2016;57:1–6.
- Kalkhoran S, Glantz SA. E-cigarettes and smoking cessation in real-world and clinical settings: a systematic review and meta-analysis. *Lancet Respir Med*. 2016;4:116–128.
- Pisinger C, Dössing M. A systematic review of health effects of electronic cigarettes. *Prev Med*. 2014;69:248–260.
- Lundbäck B, Katsaounou P, Lötvall J. The up-rise in e-cigarette use: friend or foe? *Respir Rev*. 2016;17:52.
- Cherian SV, Kumar A, Estrada-Y-Martin RM. E-Cigarette or vaping product-associated lung injury: a review. *Am J Med*. 2020;133:657–663.
- Goniewicz ML, Smith DM, Edwards KC, et al. Comparison of nicotine and toxicant exposure in users of electronic cigarettes and combustible cigarettes. *JAMA Netw Open*. 2018;1:e185937.
- Shields PG, Berman M, Brasky TM, et al. A review of pulmonary toxicity of electronic cigarettes in the context of smoking: a focus on inflammation. *Cancer Epidemiol Biomarkers Prev*. 2017;26:1175–1191.
- Reidel B, Radicioni G, Clapp PW, et al. E-cigarette use causes a unique innate immune response in the lung, involving increased neutrophilic activation and altered mucin secretion. *Am J Respir Crit Care Med*. 2018;197:492–501.
- Tong LQ, Sui Y, Jiang S, Yin Y. The association between lung fluorodeoxyglucose metabolism and smoking history in 347 healthy adults. *J Asthma Allergy*. 2021;14:301–308.
- Sahota A, Naidu S, Jacobi A, et al. Atherosclerosis inflammation and burden in young adult smokers and vapers measured by PET/MR. *Atherosclerosis*. 2021;325:110–116.
- Tateishi U, Hasegawa T, Seki K, Terauchi T, Moriyama N, Arai Y. Disease activity and ^{18}F -FDG uptake in organising pneumonia: semi-quantitative evaluation using computed tomography and positron emission tomography. *Eur J Nucl Med Mol Imaging*. 2006;33:906–912.
- Jones HA, Marino PS, Shakur BH, Morrell NW. In vivo assessment of lung inflammatory cell activity in patients with COPD and asthma. *Eur Respir J*. 2003;21:567–573.
- Huang HJ, Isakow W, Byers DE, et al. Imaging pulmonary inducible nitric oxide synthase expression with PET. *J Nucl Med*. 2015;56:76–81.
- Hatori A, Yui J, Yamasaki T, et al. PET imaging of lung inflammation with [^{18}F]FJFEDAC, a radioligand for translocator protein (18 kDa). *PLoS One*. 2012;7:e45065.
- Branley HM, du Bois RM, Wells AU, Jones HA. Peripheral-type benzodiazepine receptors in bronchoalveolar lavage cells of patients with interstitial lung disease. *Nucl Med Biol*. 2007;34:553–558.
- Notter T, Coughlin JM, Sawa A, Meyer U. Reconceptualization of translocator protein as a biomarker of neuroinflammation in psychiatry. *Mol Psychiatry*. 2018;23:36–47.
- Koch A, Burgschweiger A, Herpel E, et al. Inducible NO synthase expression in endomyocardial biopsies after heart transplantation in relation to the postoperative course. *Eur J Cardiothorac Surg*. 2007;32:639–643.
- Alderton WK, Cooper CE, Knowles RG. Nitric oxide synthases: structure, function and inhibition. *Biochem J*. 2001;357:593–615.
- Islam T, Breton C, Salam MT, et al. Role of inducible nitric oxide synthase in asthma risk and lung function growth during adolescence. *Thorax*. 2010;65:139–145.
- Csoma B, Bikov A, Nagy L, et al. Dysregulation of the endothelial nitric oxide pathway is associated with airway inflammation in COPD. *Respir Res*. 2019;20:156.
- Guo FH, De Raeve HR, Rice TW, Stuehr DJ, Thunissen FB, Erzurum SC. Continuous nitric oxide synthesis by inducible nitric oxide synthase in normal human airway epithelium in vivo. *Proc Natl Acad Sci U S A*. 1995;92:7809–7813.
- Khanna A, Guo M, Mehra M, Royal W. Inflammation and oxidative stress induced by cigarette smoke in Lewis rat brains. *J Neuroimmunol*. 2013;254:69–75.
- Seimetz M, Parajuli N, Pichl A, et al. Inducible NOS inhibition reverses tobacco-smoke-induced emphysema and pulmonary hypertension in mice. *Cell*. 2011;147:293–305.
- Bhandari V, Choo-Wing R, Chapoval SP, et al. Essential role of nitric oxide in VEGF-induced, asthma-like angiogenic, inflammatory, mucus, and physiologic responses in the lung. *Proc Natl Acad Sci U S A*. 2006;103:11021–11026.
- Herrero P, Laforest R, Shoghi K, et al. Feasibility and dosimetry studies for ^{18}F -NOS as a potential PET radiopharmaceutical for inducible nitric oxide synthase in humans. *J Nucl Med*. 2012;53:994–1001.
- Zhou D, Lee H, Rothfuss JM, et al. Design and synthesis of 2-amino-4-methylpyridine analogues as inhibitors for inducible nitric oxide synthase and

- in vivo evaluation of [¹⁸F]6-(2-fluoropropyl)-4-methyl-pyridin-2-amine as a potential PET tracer for inducible nitric oxide synthase. *J Med Chem.* 2009;52:2443–2453.
30. Kuntic M, Oelze M, Steven S, et al. Short-term e-cigarette vapour exposure causes vascular oxidative stress and dysfunction: evidence for a close connection to brain damage and a key role of the phagocytic NADPH oxidase (NOX-2). *Eur Heart J.* 2020;41:2472–2483.
 31. Zigmond AS, Snaith RP. The Hospital Anxiety and Depression Scale. *Acta Psychiatr Scand.* 1983;67:361–370.
 32. Foulds J, Veldheer S, Yingst J, et al. Development of a questionnaire for assessing dependence on electronic cigarettes among a large sample of ex-smoking E-cigarette users. *Nicotine Tob Res.* 2015;17:186–192.
 33. Fagerström K. Determinants of tobacco use and renaming the FTND to the Fagerström Test for Cigarette Dependence. *Nicotine Tob Res.* 2012;14:75–78.
 34. Kolthammer JA, Su K-H, Grover A, Narayanan M, Jordan DW, Muzic RF. Performance evaluation of the Ingenuity TF PET/CT scanner with a focus on high count-rate conditions. *Phys Med Biol.* 2014;59:3843–3859.
 35. Logan J, Fowler JS, Volkow ND, et al. Graphical analysis of reversible radioligand binding from time-activity measurements applied to [¹¹C-methyl](-)-cocaine PET studies in human subjects. *J Cereb Blood Flow Metab.* 1990;10:740–747.
 36. Akaike H. Likelihood of a model and information criteria. *J Econom.* 1981;16:3–14.
 37. Golla SSV, Adriaanse SM, Yaqub M, et al. Model selection criteria for dynamic brain PET studies. *EJNMMI Phys.* 2017;4:30.
 38. Doot R, Young A, Dominguez T, et al. Blood pool selection for quantifying lung inflammation via [¹⁸F]NOS uptake in nicotine users and healthy humans [abstract]. *J Nucl Med.* 2020;61(suppl 1):205.
 39. Holman BF, Cuplov V, Millner L, et al. Improved correction for the tissue fraction effect in lung PET/CT imaging. *Phys Med Biol.* 2015;60:7387–7402.
 40. Davis ES, Ghosh A, Coakley RD, et al. Chronic e-cigarette exposure alters human alveolar macrophage morphology and gene expression. *Nicotine Tob Res.* 2022;24:395–399.
 41. Zamora R, Vodovotz Y, Billiar TR. Inducible nitric oxide synthase and inflammatory diseases. *Mol Med.* 2000;6:347–373.
 42. Mehta AJ, Guidot D. Alcohol and the lung. *Alcohol Res.* 2017;38:243–254.
 43. Chow C-W, Herrera Abren MT, Suzuki T, Downey GP. Oxidative stress and acute lung injury. *Am J Respir Cell Mol Biol.* 2003;29:427–431.
 44. Tonstad S, Cowan JL. C-reactive protein as a predictor of disease in smokers and former smokers: a review. *Int J Clin Pract.* 2009;63:1634–1641.
 45. Cross LJM, Matthay MA. Biomarkers in acute lung injury: insights into the pathogenesis of acute lung injury. *Crit Care Clin.* 2011;27:355–377.
 46. Niu X, Ho KF, Hu T, et al. Characterization of chemical components and cytotoxicity effects of indoor and outdoor fine particulate matter (PM2.5) in Xi'an, China. *Environ Sci Pollut Res Int.* 2019;26:31913–31923.
 47. Lee YO, Nonnemaker JM, Bradfield B, Hensel EC, Robinson RJ. Examining daily electronic cigarette puff topography among established and nonestablished cigarette smokers in their natural environment. *Nicotine Tob Res.* 2018;20:1283–1288.

Detection of Early Esophageal Neoplastic Barrett Lesions with Quantified Fluorescence Molecular Endoscopy Using Cetuximab-800CW

Ruben Y. Gabriëls^{*1}, Lisanne E. van Heijst^{*1}, Wouter T.R. Hooghiemstra¹, Anne M. van der Waaij¹, Gursah Kats-Ugurlu², Arend Karrenbeld², Dominic J. Robinson³, Anna Tenditnaya^{4,5}, Vasilis Ntziachristos^{4,5}, Dimitris Gorpas^{4,5}, and Wouter B. Nagengast¹

¹Department of Gastroenterology and Hepatology, University Medical Center Groningen, University of Groningen, Groningen, The Netherlands; ²Department of Pathology and Medical Biology, University Medical Center Groningen, University of Groningen, Groningen, The Netherlands; ³Otolaryngology, Center for Optic Diagnostics and Therapy, Erasmus University Medical Center, Rotterdam, The Netherlands; ⁴Chair of Biological Imaging at the Central Institute for Translational Cancer Research (TranslaTUM), School of Medicine, Technical University of Munich, Munich, Germany; and ⁵Institute of Biological and Medical Imaging, Helmholtz Zentrum München, Neuherberg, Germany

Esophageal adenocarcinoma causes 6% of cancer-related deaths worldwide. Near-infrared fluorescence molecular endoscopy (NIR-FME) uses a tracer that targets overexpressed proteins. In this study, we aimed to investigate the feasibility of an epidermal growth factor receptor (EGFR)-targeted tracer, cetuximab-800CW, to improve detection of early-stage esophageal adenocarcinoma. **Methods:** We validated EGFR expression in 73 esophageal tissue sections. Subsequently, we topically administered cetuximab-800CW and performed high-definition white-light endoscopy (HD-WLE), narrow-band imaging, and NIR-FME in 15 patients with Barrett esophagus (BE). Intrinsic fluorescence values were quantified using multidiameter single-fiber reflectance and single-fiber fluorescence spectroscopy. Back-table imaging, histopathologic examination, and EGFR immunohistochemistry on biopsy samples collected during NIR-FME procedures were performed and compared with *in vivo* imaging results. **Results:** Immunohistochemical preanalysis showed high EGFR expression in 67% of dysplastic tissue sections. NIR-FME visualized all 12 HD-WLE-visible lesions and 5 HD-WLE-invisible dysplastic lesions, with increased fluorescence signal in visible dysplastic BE lesions compared with nondysplastic BE as shown by multidiameter single-fiber reflectance/single-fiber fluorescence, reflecting a target-to-background ratio of 1.5. Invisible dysplastic lesions also showed increased fluorescence, with a target-to-background ratio of 1.67. Immunohistochemistry analysis showed EGFR overexpression in 16 of 17 (94%) dysplastic BE lesions, which all showed fluorescence signal. **Conclusion:** This study has shown that NIR-FME using cetuximab-800CW can improve detection of dysplastic lesions missed by HD-WLE and narrow-band imaging.

Key Words: Barrett esophagus; cetuximab; epidermal growth factor receptor; esophageal adenocarcinoma; fluorescence molecular imaging

J Nucl Med 2023; 64:803–808

DOI: 10.2967/jnumed.122.264656

Received Jul. 13, 2022; revision accepted Dec. 6, 2022.
For correspondence or reprints, contact Wouter B. Nagengast (w.b.nagengast@umcg.nl).

*Contributed equally to this work.

Published online Jan. 5, 2023.

COPYRIGHT © 2023 by the Society of Nuclear Medicine and Molecular Imaging.

Esophageal cancer is responsible for approximately 6% of cancer-related deaths worldwide, with studies predicting a rise in the incidence of esophageal adenocarcinoma (EAC) (1). Late-stage detection leads to a 5-y survival rate of 15%–20% (2).

Surveillance of Barrett esophagus (BE) is performed by high-definition white-light endoscopy (HD-WLE) and narrow-band imaging (NBI) combined with random biopsies following the Seattle protocol to detect early EAC lesions (3). A study performing a follow-up endoscopy procedure 1 y after the primary endoscopy detected 24% more EAC lesions (4). This finding indicates a high miss-rate by HD-WLE and NBI in combination with random biopsies during endoscopic surveillance (4,5).

In the quest to improve detection of early-stage EAC, near-infrared fluorescence molecular endoscopy (NIR-FME) has recently shown potential to perform better than the current endoscopic standard (6). A phase I trial conducted here at the University Medical Center Groningen used the tracer bevacizumab-800CW, targeting vascular endothelial growth factor A, and showed an approximately 33% improvement in early lesion detection compared with conventional HD-WLE and NBI (7).

NIR-FME can provide additional guidance in histopathologic assessment and has been shown to reduce sampling error (8,9). This technique in combination with the tracer cetuximab-800CW, targeting epidermal growth factor receptor (EGFR), has been described to provide additional real-time information assisting intraoperative decision making aiding tumor delineation (10). Recently, multiplexed imaging was successfully introduced in which 2 fluorescently labeled tracers targeting EGFR and human EGFR 2 were evaluated for detection of EAC (11).

We validated EGFR expression in BE lesions and aimed to investigate the feasibility of NIR-FME with cetuximab-800CW, an EGFR-targeted tracer, compared with HD-WLE and NBI, to improve detection of early-stage EAC in BE patients.

MATERIALS AND METHODS

This phase I feasibility study with cetuximab-800CW is embedded in an ongoing intervention study performed at the University Medical Center Groningen (NCT03877601). All included patients are priorly diagnosed with low-grade dysplasia (LGD), high-grade dysplasia (HGD),

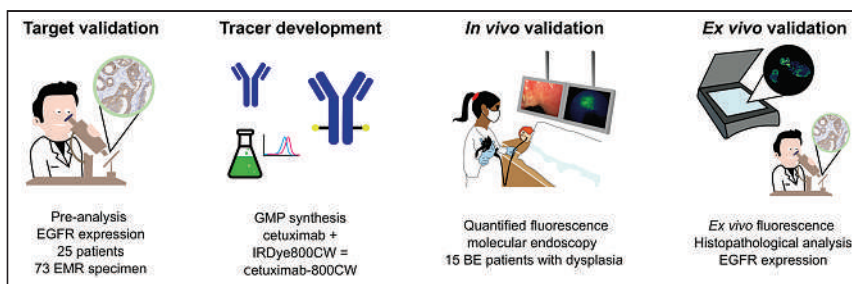


FIGURE 1. Overview of study design. EMR = endoscopic mucosal resection; GMP = good manufacturing practice.

or early-stage EAC at a regional hospital and referred to the University Medical Center Groningen, which is the BE expert center for the northern Netherlands. Included patients underwent HD-WLE combined with an NIR-FME procedure using topical administration of cetuximab-800CW (12).

Inclusion and Exclusion Criteria

For the immunohistochemistry preanalysis, we have included esophageal endoscopic mucosal resection specimens of 25 patients. Following all preanalysis study procedures, we selected and included 15 patients eligible for cetuximab-800CW administration. These patients were prior diagnosed with LGD, HGD, or early-stage EAC and scheduled for an endoscopic procedure. Patients received both oral and written information on study procedures and the tracer. Patients less than 18 y old, allergic to immunoglobulins, pregnant, or breastfeeding were excluded. Additionally, patients who received prior cetuximab treatment, radiation therapy, chemotherapy, immunotherapy, or surgery for esophageal cancer were excluded. All patients interested in participating in either the ex vivo preanalysis or the in vivo procedure with administration of cetuximab-800CW before endoscopy had to give written informed consent within 2 wk but not earlier than 48 h after receiving information. The design of the current study is shown in Figure 1.

Ex Vivo Preanalysis EGFR Expression

Ex vivo preanalysis was performed by 2 independent researchers to investigate EGFR expression. Endoscopic mucosal resection specimens were formalin-fixed for 24 h, and specimens were histologically sectioned into 4- μ m tissue slices ($n = 73$), which were then stained for hematoxylin and eosin, P53, and EGFR. The slices were scanned by a Hamamatsu NanoZoomer (Hamamatsu Photonics) and viewed with NDP.view2 (Hamamatsu Photonics). H-scores were independently calculated in a masked manner by the 2 researchers to quantify EGFR staining intensity.

Synthesis of Cetuximab-800CW

Production of cetuximab-800CW (peak excitation/emission at 778/795 nm) was performed in the cleanroom facility of the Clinical Pharmacy and Pharmacology Department of the University Medical Center Groningen (12).

Fluorescence Molecular Endoscopy Combined with Spectroscopy

Real-time in vivo NIR-FME with cetuximab-800CW was achieved by coupling a fiberscope (Schölly Fiberoptic GmbH) to the SurgVision Explorer Endoscope (SurgVision BV), which is based on a system previously developed by our group (13).

Multidiameter single-fiber reflectance and single-fiber fluorescence spectroscopy, developed by the University Medical Center Rotterdam, Erasmus MC, was used as a reference for the NIR-FME measurements (14,15). The process leading to quantification of tracer's intrinsic

fluorescence was previously described (14,15). Both NIR-FME and multidiameter single-fiber reflectance/single-fiber fluorescence were performed through the working channel of a standard endoscope.

Procedure

HD-WLE and NBI were performed for general evaluation of the BE segment and suspected lesions. Acetyl cysteine, 0.1%, was used to reduce mucus during the procedure. After a 5-min incubation of the topically administered cetuximab-800CW, the esophagus was rinsed with water to remove

abundant, unbound tracer. We administered 1 mL of a 0.1 mg/mL concentration of cetuximab-800CW per 1 cm of BE segment. NIR-FME was performed to examine the esophagus and investigate whether all HD-WLE suspected lesions could be detected and whether additional lesions, missed by HD-WLE/NBI, could be identified. We calculated the target-to-background ratio (TBR): the ratio between the mean NIR-FME image pixel intensities from the region of interest (ROI) (e.g., lesion of fluorescence foci) and the nondysplastic BE (NDBE), determined as the background. The mean value of each ROI was calculated for those pixels within the upper 70% of the corresponding histogram.

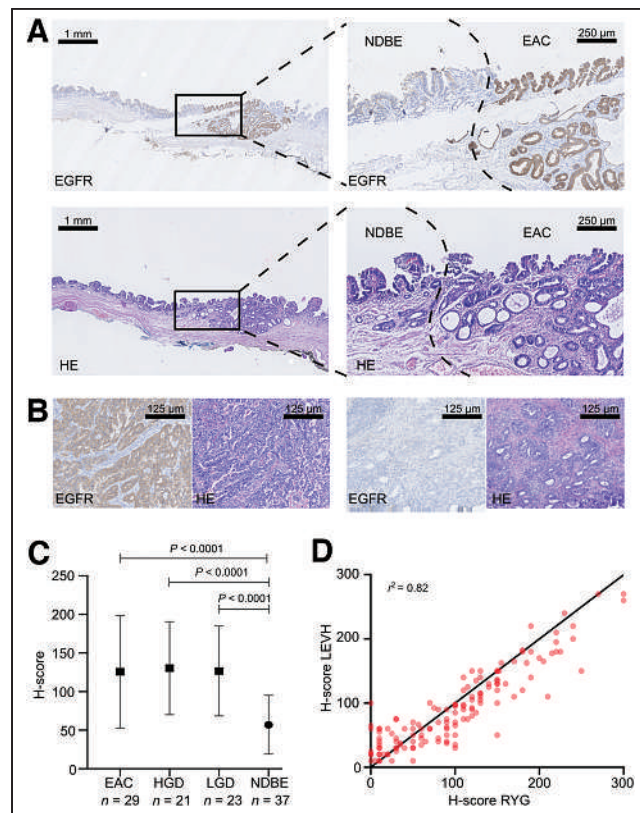


FIGURE 2. (A) Immunohistochemistry results of EGFR staining (brown, top) and hematoxylin and eosin staining (purple, bottom), with pathologic delineation of EAC and NDBE. Left images are at low magnification ($\times 5$), and right images are at high magnification ($\times 20$). (B) Histopathologic tissue slices at high magnification ($\times 40$), with high staining of EAC on left and no staining of EAC on right, showing variable EGFR expression. (C) Mean and SD for H-scoring by 2 independent researchers. (D) Scoring consistency between 2 independent researchers as determined with Pearson correlation coefficient. HE = hematoxylin and eosin.

TABLE 1
Patient Characteristics ($n = 15$)

Characteristic	Histology				Data
	NDBE	LGD	HGD	EAC	
Male (n)	1 (100%)	2 (100%)	5 (100%)	5 (71.4%)	13 (86.7%)
Mean age (y)	74.5	67.0	64.0	64.2	66
Mean body mass index	28.00	27.10	27.05	27.46	27.43
Lesions identified by referring endoscopist	0	0	1	8	9 (7 patients)
Lesions identified with HD-WLE at BE expert center	0	0	3	9	12 (9 patients)
Additional NIR-FME lesions	0	2	3	0	5 (5 patients)

Five invisible HD-WLE dysplastic lesions were detected using FME.

To assess the quality of the data acquired with the NIR-FME system, we calculated the signal-to-background-noise ratio in decibel scale and the contrast-to-noise ratio for every frame containing visible or invisible lesions (16). The reliability of the data was then assessed through the Rose criterion for contrast-to-noise ratio and the 95% confidence level of a measurement for the signal-to-background-noise ratio, which requires a contrast-to-noise ratio of more than 3 and a signal-to-background-noise ratio of more than 6 dB for a lesion to be distinguishable from the background (17).

Subsequently, HD-WLE-guided spectroscopy was performed to measure the intrinsic fluorescence of cetuximab-800CW from the NIR-FME-identified suspected or invisible lesions. All measurements were done in triplicate, and mean values were used to quantify cetuximab-800CW fluorescence, serving as control measurements for validation of NIR-FME findings (18).

Ex Vivo Analysis

Tissue biopsy samples were collected from unsuspected BE tissue, lesions, and invisible lesions during *in vivo* NIR-FME procedures. They were then formalin-fixed and paraffin-embedded. From these specimens, 10- μ m tissue sections were deparaffinized and imaged with an Odyssey CLx flatbed scanner (LI-COR Biosciences), whereas 4- μ m-thick sections were stained with hematoxylin and eosin and P53 and subsequently histopathologically analyzed by 2 pathologists. Immunohistochemistry on EGFR staining was performed on additional 4- μ m tissue sections, after which they were scanned by a NanoZoomer (Hamamatsu Photonics) and digitally analyzed using NDP.view2. H-scores were calculated to quantify the staining intensity of EGFR by 2 researchers. A total of 32 formalin-fixed tissue sections stained with EGFR were analyzed.

Statistical Analysis

Analyses and graph layouts were implemented using Prism (version 8.4.2, GraphPad Software Inc.). Normality tests were performed on all data. Descriptive statistics were performed to calculate the mean and SD of the H-scores, and Pearson correlation was used to assess the interobserver agreement of manual H-scoring by the 2 independent

researchers. H-scores, TBRs, and *in vivo* and *ex vivo* spectroscopy data were analyzed by 1-way ANOVA. P values of less than 0.05 were considered statistically significant. All data are displayed as mean \pm SD.

Ethical Considerations

This study was approved by the Medical Ethics Committee at the University Medical Center Groningen (METc number 2018/701).

RESULTS

Ex Vivo EGFR Expression Analysis

In total, 73 formalin-fixed and paraffin-embedded tissue slices were analyzed for EGFR expression levels and histopathology. Two pathologists selected areas containing NDBE, LGD, HGD, and EAC. H-score quantification showed that membranous staining for most of

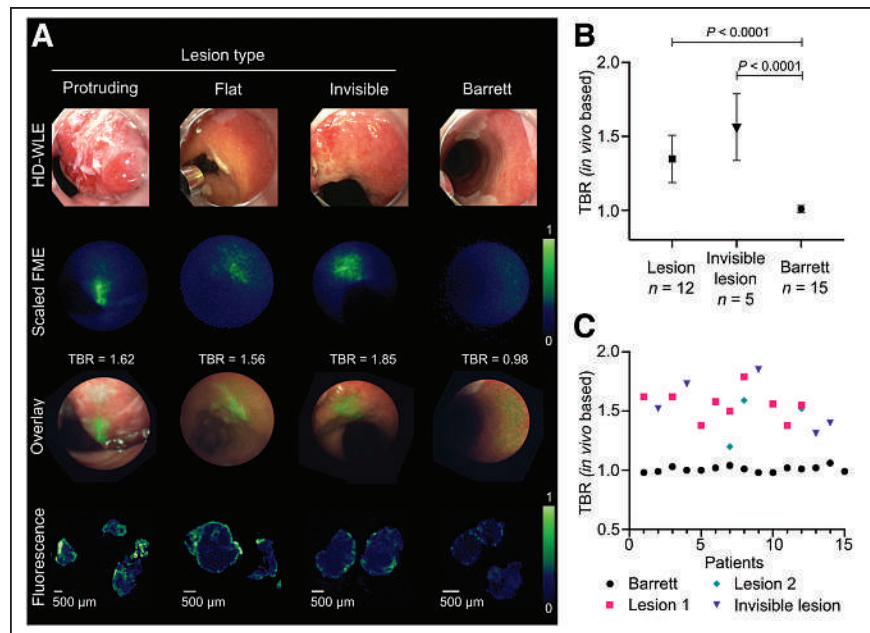


FIGURE 3. (A) Different lesion and tissue types visualized with different imaging techniques. From top to bottom are shown HD-WLE images, corresponding frames acquired with NIR-FME system in fluorescence channel, overlay of color and fluorescence data acquired with NIR-FME, and *ex vivo* fluorescence images acquired with Odyssey CLx flatbed scanner. Fluorescence images were linearly normalized to common global maximum (1) and minimum (0) values to enable visual comparison of signal strength between different lesion types. (B and C) Calculated TBRs combined and in every single patient separately, respectively.

TABLE 2

Metrics with Corresponding Formulas and Reference Values for Image Quality Assessment

Metric	Formula	Reference value
SNR	$20 \cdot \log_{10} \frac{S}{\text{RMSN}}$	6 dB
CNR	$\frac{ S-N }{\text{RMSN}}$	1

SNR = signal-to-background noise ratio; S = mean intensity signal; RMSN = root mean square noise calculated as SD from background area; CNR = contrast-to-noise ratio; N = noise calculated as mean background signal.

the dysplastic BE tissue (LGD, HGD, and EAC) were scored intermediate or high ($n = 49$, 67%) (Fig. 2). However, 24 dysplastic BE tissue areas were scored negatively or low (33%). Subsequently, the H-score for EGFR of NDBE tissue was negative or low in 33 tissue areas (89%). The calculated mean H-score for NDBE was 57 ± 38 and significantly lower than LGD (127 ± 58 , $P < 0.0001$), HGD (130 ± 60 , $P < 0.0001$), and EAC (126 ± 73 , $P < 0.0001$). The fraction of variance between the 2 researchers was calculated with the Pearson correlation coefficient ($r = 0.9056$) (Fig. 2).

Patient Characteristics

Fifteen patients, 2 of whom were female and 13 male, were included in the trial. All included patients received cetuximab-800CW during the procedure, and none of the patients experienced any serious adverse events. The patient characteristics are shown in Table 1.

NIR-FME

All 9 lesions detected by the referring endoscopist at the regional hospitals were detected by our BE expert endoscopist. Furthermore, our BE expert endoscopist additionally detected 3 flat lesions by HD-WLE that were not described by the referring endoscopist. All 12 HD-WLE-visible lesions were visualized by the NIR-FME camera, showing increased fluorescence intensity. Histopathologic assessment by a BE expert pathologist showed dysplasia in all visible and invisible lesions. We observed a clear ex vivo fluorescence signal on the epithelial side of all biopsy samples in dysplastic lesions.

The TBRs of the complete delineated visible lesions were a mean of 1.3 ± 0.2 ($P < 0.0001$), whereas the invisible lesions presented a higher mean TBR of 1.6 ± 0.2 ($P < 0.0001$). We could not detect a lesion using either HD-WLE or the NIR-FME system in 1 patient referred with LGD, and additional random biopsies according to the Seattle protocol did not detect dysplasia either. The distribution of mean TBRs per tissue and per patient is shown in Figure 3. Data quality assessment showed an average signal-to-background-noise ratio of 21.79 ± 1.65 dB and an average contrast-to-noise ratio of 4.54 ± 1.57 , both being above the corresponding critical values for discrimination between lesion and background, as defined in Table 2.

In 5 patients, NIR-FME detected areas that did not show morphologic changes suggestive of dysplasia by HD-WLE or NBI. These areas showed dysplasia on histology and thus counted as invisible lesions by standard imaging technology (Fig. 4).

In Vivo Multidiameter Single-Fiber Reflectance/Single-Fiber Fluorescence Spectroscopy

Multidiameter single-fiber reflectance/single-fiber fluorescence spectroscopy measurements were performed to quantify the intrinsic fluorescence values of the tracer in vivo by correcting for optical properties of the tissue. Measurements of NDBE were completed for all patients, with the tracer showing a mean intrinsic fluorescence of $0.012 \pm 0.003 \text{ } Q \cdot \mu_{a,x}^f$. The mean value for visible lesions ($n = 10$) was calculated from 30 measurements and was higher, at $0.018 \pm 0.004 \text{ } Q \cdot \mu_{a,x}^f$, than for NDBE ($P = 0.0014$), with a spectroscopy TBR of 1.5. These findings are comparable to the in vivo analysis of the raw fluorescence images. In vivo spectroscopy measurements were not feasible for 2 lesions. In one, it was impossible to perform reliable measurements because the spectroscopy fiber was angled toward the lesion. In the other, the spectroscopy measurements failed because we had unstable contact between the lesion and the fiber. Invisible lesions ($n = 5$) showed a higher mean of $0.020 \pm 0.005 \text{ } Q \cdot \mu_{a,x}^f$ than did NDBE ($P = 0.0003$). This results in a calculated spectroscopy TBR of 1.67, confirming the data from the in vivo raw fluorescence image analysis of HD-WLE-invisible lesions. In vivo spectroscopy results are shown in Figure 5.

Ex Vivo EGFR Expression

All 17 dysplastic esophageal lesions showed a moderate to strong ex vivo fluorescence signal. LGD was found in 2 tissue slices, HGD in 6 tissue slices, and EAC in 9 tissue slices. NDBE was found in 15 tissue slices collected from endoscopically unsuspected BE tissue. Examples of EGFR expression levels in the samples are shown in Figure 6. H-score quantification showed that in 94% of dysplastic BE tissue (LGD, HGD, and EAC) collected from visible and invisible lesions, epithelial EGFR staining was scored intermediate or high. NDBE tissue showed an ex vivo negative

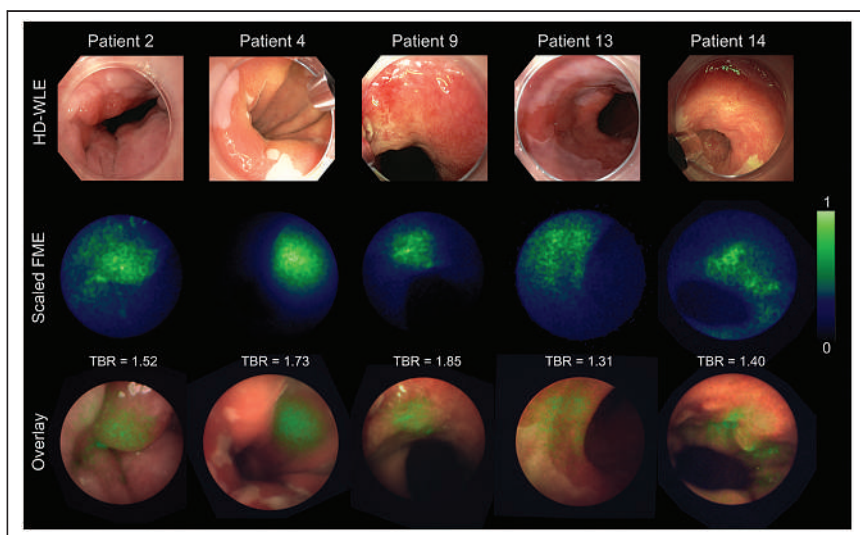


FIGURE 4. HD-WLE-invisible dysplastic lesions detected by NIR-FME. From top to bottom are shown HD-WLE images, corresponding NIR-FME fluorescence images of HD-WLE-invisible lesions, and overlay of NIR-FME color and fluorescence data from 5 different patients. All fluorescence images were normalized with regard to their individual maximum (1) and minimum (0) values to enable visual assessment of fluorescence localization.

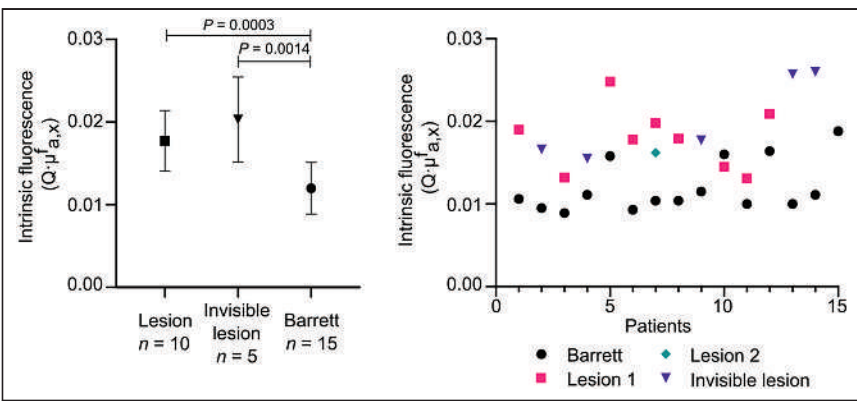


FIGURE 5. In vivo spectroscopy results. (Left) In vivo spectroscopy differences between HD-WLE-visible lesions, HD-WLE-invisible lesions, and NDBE. (Right) In vivo spectroscopy fluorescence values for NDBE, HD-WLE-visible lesions, and HD-WLE-invisible lesions within each patient.

fluorescence signal and lower EGFR expression H-score results than HGD and EAC tissue.

DISCUSSION

Early detection of dysplastic BE and early-stage EAC can prevent progression toward locally advanced EAC and thereby improve morbidity and mortality rates significantly. In the current study, we investigated EGFR expression in dysplastic BE and early-stage EAC tissue. Furthermore, we tested the safety and feasibility of cetuximab-800CW in vivo to improve malignant and premalignant esophageal lesion detection with NIR-FME in BE. Our immunohistochemistry preanalysis showed intermediate to high EGFR expression within 67% of the dysplastic areas. NIR-FME with cetuximab-800CW detected all visible dysplastic lesions and additionally revealed 5 dysplastic lesions missed using HD-WLE/NBI. The specificity of the results was confirmed by 2 independent BE expert pathologists, and 16 of the 17 dysplastic lesions (94%) showed intermediate or high EGFR expression levels. This finding signifies the ability of cetuximab-800CW to visualize dysplastic areas in BE even if morphologic abnormalities cannot be detected by HD-WLE/NBI.

Results from our previous in vivo feasibility study with the tracer bevacizumab-800CW showed that NIR-FME could improve early lesion detection significantly (7). Another published phase I proof-of-concept study demonstrated the feasibility of using an EGFR-targeted tracer in combination with a tracer targeting human EGFR 2 for the

detection of early EAC lesions using dual-channel spectral endoscopic imaging (11). However, EGFR or human EGFR 2 expression analysis was not performed, and in vivo imaging results were not quantified (11). The follow-up clinical trial showed an in vivo TBR of 1.5 using an EGFR-targeted tracer in 31 patients, although additional lesions were not detected (19). In our phase I clinical trial, we found that the EGFR-targeted tracer cetuximab-800CW detected all known dysplastic lesions and, more importantly, detected 5 invisible dysplastic lesions confirmed by histopathology, which were also shown to be EGFR-positive. Quantified NIR-FME improves early lesion detection by 29% over the current clinical standard using HD-WLE/NBI endoscopy. We quantified EGFR expression

in an extensive preanalysis in esophageal endoscopic mucosal resection specimens and subsequently in all esophageal biopsy samples taken during the NIR-FME procedure. Moreover, we confirmed our in vivo NIR-FME findings with unbiased spectroscopy measurements.

Our ex vivo analysis regarding the biopsies showed relatively high EGFR expression within dysplastic esophageal tissue. One reason for these higher EGFR expression levels than reported in the literature might be our relatively small patient sample size from the phase 1 trial in which we analyzed EGFR expression. All 17 NIR-FME-identified lesions, HD-WLE-visible and HD-WLE-invisible, showed in vivo fluorescence after incubation with cetuximab-800CW, suggesting that when lesions are EGFR-positive, they can be detected by cetuximab-800CW. However, 1 lesion did not show clear EGFR expression in the ex vivo analysis, possibly because of sampling error during biopsy.

Fluorescence molecular imaging can be further developed and improved by addressing several study limitations. We included solely referred BE patients with a suspected lesion. Consequently, our cohort consisted mainly of patients with EAC, resulting in a distorted representation of the overall BE population. Research has shown that endoscopists at regional, non-BE expert, centers detect significantly fewer EAC lesions than endoscopists at a BE expert center (20). Therefore, we most likely detected more suspected lesions using HD-WLE than did referring centers, potentially indicating that this novel red flag imaging technique is of even greater value for regional, non-BE expert, centers. It would be of great interest to include non-BE experts in a follow-up study to evaluate the impact of this technique. We manually calculated the TBRs from in vivo images by comparing the fluorescence signal of the region for the area of interest with the unspecific fluorescence signal of a region for NDBE. A reason for these relatively low TBRs could be the heterogeneous distribution of the topically administered tracer. Another limitation is that we could not visualize the tracer on a microscopic level. The obtained biopsy samples were directly formalin-fixed after the endoscopic procedure. Our previous study with bevacizumab-800CW demonstrated that the tracer is almost entirely washed away during paraffin embedding, resulting in a loss of fluorescence signal (13). However, in the best

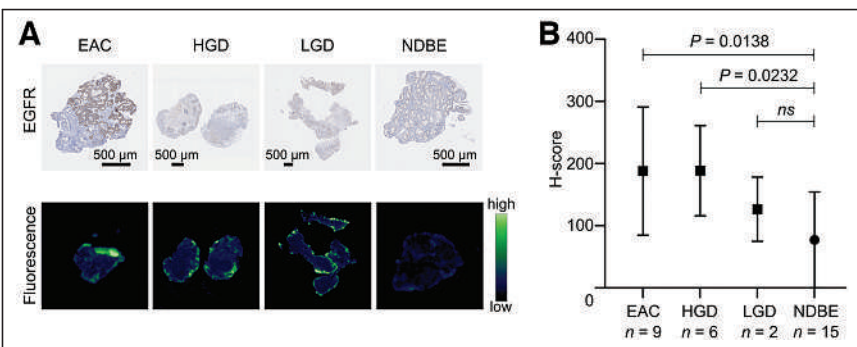


FIGURE 6. EGFR expression and ex vivo fluorescence in different tissue types. (A) Tissue slices with EGFR staining (top) and corresponding deparaffinized tissue slices scanned with Odyssey CLx flatbed scanner, showing fluorescence at luminal side of tissue where tracer was sprayed (bottom). (B) Calculated H-score of EGFR staining.

possible manner, ex vivo images made with the Odyssey CLx fluorescence flatbed scanner showed a clear signal only on the luminal side of the tissue. Finally, we could not take real-time spectroscopy measurements. All measurements were calculated and analyzed after completion of all study procedures. Since we needed the endoscopic working channel for both the fluorescence molecular endoscope and the spectroscopy fibers, we could not measure the intrinsic fluorescence and search for the most intensely fluorescent spot simultaneously. This limitation might explain why the measured fluorescence signal was not higher in the lesion than in the background in one of the included patients.

Over the last few years, several new imaging techniques have been developed to improve early EAC lesion detection in BE patients. Among them are computer-aided diagnosis algorithms (21), which might be used as a second assessor. Computer-aided diagnosis already performs better at EAC detection than general endoscopists with HD-WLE images alone, showing a sensitivity of 93% versus 72% and a specificity of 83% versus 74% (22). We envision that HD-WLE and FME assisted by computer-aided diagnosis can further improve detection of early EAC lesions, with the aim of making the Seattle protocol redundant and improving patient outcome.

CONCLUSION

We validated that EGFR is overexpressed in malignant and premalignant esophageal tissue. We demonstrated *in vivo* that this novel red flag imaging technique in combination with cetuximab-800CW has potential to improve early lesion detection in BE patients. We expect that a dual-channel spectral imaging study using an EGFR-targeted tracer in combination with a vascular endothelial growth factor A-targeted tracer can further improve detection of early malignant and premalignant lesions in these patients.

DISCLOSURE

This project has received funding from the European Union's Horizon 2020 research and innovation programme under grant agreement no. 643638 (TRANSCAN-2; project ESCEND) as well as the Dutch Cancer Society, Amsterdam, the Netherlands and the Bundesministerium für Bildung und Forschung (BMBF), Bonn, Germany (FKZ 01KT1809).

KEY POINTS

QUESTION: Does NIR-FME in combination with cetuximab-800CW, an EGFR-targeted tracer, improve detection of early-stage EAC.

PERTINENT FINDINGS: This study adds an extensive ex vivo validation of EGFR expression in dysplastic and nondysplastic esophageal tissue to gain insight into the variability of this expression. In vivo, we additionally detected 5 HD-WLE-invisible lesions, further quantified *in vivo* fluorescence results with spectroscopy, and validated these results ex vivo with EGFR expression levels.

IMPLICATIONS FOR PATIENT CARE: Dual-channel spectral NIR-FME including an EGFR-targeted tracer will further improve detection of malignant and premalignant lesions in the esophagus.

REFERENCES

- Sung H, Ferlay J, Siegel RL, et al. Global Cancer Statistics 2020: GLOBOCAN estimates of incidence and mortality worldwide for 36 cancers in 185 countries. *CA Cancer J Clin.* 2021;71:209–249.
- Alsop BR, Sharma P. Esophageal cancer. *Gastroenterol Clin North Am.* 2016;45:399–412.
- Sharma P, Hawes RH, Bansal A, et al. Standard endoscopy with random biopsies versus narrow band imaging targeted biopsies in Barrett's oesophagus: a prospective, international, randomised controlled trial. *Gut.* 2013;62:15–21.
- Visrodi K, Singh S, Krishnamoorthi R, et al. Magnitude of missed esophageal adenocarcinoma after Barrett's oesophagus diagnosis: a systematic review and meta-analysis. *Gastroenterology.* 2016;150:599–607.e7.
- van Putten M, Johnston BT, Murray LJ, et al. 'Missed' oesophageal adenocarcinoma and high-grade dysplasia in Barrett's oesophagus patients: a large population-based study. *United European Gastroenterol J.* 2018;6:519–528.
- de Boer E, Harlaar NJ, Taruttis A, et al. Optical innovations in surgery. *Br J Surg.* 2015;102:56–72.
- Nagengast WB, Hartmans E, Garcia-Allende PB, et al. Near-infrared fluorescence molecular endoscopy detects dysplastic oesophageal lesions using topical and systemic tracer of vascular endothelial growth factor A. *Gut.* 2019;68:7–10.
- Lee YJ, Krishnan G, Nishio N, et al. Intraoperative fluorescence-guided surgery in head and neck squamous cell carcinoma. *Laryngoscope.* 2021;131:529–534.
- Warram JM, de Boer E, van Dam G, et al. Fluorescence imaging to localize head and neck squamous cell carcinoma for enhanced pathological assessment. *J Pathol Clin Res.* 2016;2:104–112.
- Morland AB, Moore LS, Johnson AO, et al. Fluorescently labeled cetuximab-IRDye800 for guided surgical excision of ameloblastoma: a proof of principle study. *J Oral Maxillofac Surg.* 2020;78:1736–1747.
- Chen J, Jiang Y, Chang TS, et al. Multiplexed endoscopic imaging of Barrett's neoplasia using targeted fluorescent heptapeptides in a phase 1 proof-of-concept study. *Gut.* 2021;70:1010–1013.
- Linssen MD, Ter Weele EJ, Allersma DP, et al. Roadmap for the development and clinical translation of optical tracers cetuximab-800CW and trastuzumab-800CW. *J Nucl Med.* 2019;60:418–423.
- Glatz J, Varga J, Garcia-Allende PB, Koch M, Greten FR, Ntziachristos V. Concurrent video-rate color and near-infrared fluorescence laparoscopy. *J Biomed Opt.* 2013;18:101302.
- Koller M, Qiu SQ, Linssen MD, et al. Implementation and benchmarking of a novel analytical framework to clinically evaluate tumor-specific fluorescent tracers. *Nat Commun.* 2018;9:3739.
- Hoy CL, Gamm UA, Sterenborg HJCM, Robinson DJ, Amelink A. Method for rapid multidiameter single-fiber reflectance and fluorescence spectroscopy through a fiber bundle. *J Biomed Opt.* 2013;18:107005.
- Bao Q, Chatzioannou AF. Estimation of the minimum detectable activity of pre-clinical PET imaging systems with an analytical method. *Med Phys.* 2010;37:6070–6083.
- Cherry SR, Sorenson JA, Phelps ME. *Physics in Nuclear Medicine.* Elsevier; 2012:244.
- van Leeuwen-van Zaanen F, Gamm UA, van Driel PB, et al. *In vivo* quantification of the scattering properties of tissue using multi-diameter single fiber reflectance spectroscopy. *Biomed Opt Express.* 2013;4:696–708.
- Chen J, Yang J, Chang TS, et al. Detection of Barrett's neoplasia with near-infrared fluorescent heterodimeric peptide. *Endoscopy.* 2022;54:1198–1204.
- Schölvink DW, van der Meulen K, Bergman JJGHM, Weusten BLAM. Detection of lesions in dysplastic Barrett's esophagus by community and expert endoscopists. *Endoscopy.* 2017;49:113–120.
- van Heijst LE, Zhao X, Gabriëls RY, Nagengast WB. Today's mistakes and tomorrow's wisdom in endoscopic imaging of Barrett's esophagus. *Visc Med.* 2022;38:182–188.
- de Groot AJ, Struyvenberg MR, van der Putten J, et al. Deep-learning system detects neoplasia in patients with Barrett's esophagus with higher accuracy than endoscopists in a multistep training and validation study with benchmarking. *Gastroenterology.* 2020;158:915–929.e4.

Imaging Diverse Pathogenic Bacteria In Vivo with ^{18}F -Fluoromannitol PET

Spenser R. Simpson^{1,2}, Alexandria E. Kesterson³, Justin H. Wilde², Zoraiz Qureshi^{2,4}, Bijoy Kundu^{2,5}, Mark P. Simons³, and Kiel D. Neumann^{1,2,6}

¹Department of Diagnostic Imaging, St. Jude Children's Research Hospital, Memphis, Tennessee; ²Department of Radiology and Medical Imaging, University of Virginia, Charlottesville, Virginia; ³Combat Wounds Division, Naval Medical Research Center, U.S. Navy, Silver Spring, Maryland; ⁴Department of Computer Science, University of Virginia, Charlottesville, Virginia;

⁵Department of Biomedical Engineering, University of Virginia, Charlottesville, Virginia; and ⁶Department of Chemistry, University of Virginia, Charlottesville, Virginia

Infectious disease remains the main cause of morbidity and mortality throughout the world. Of growing concern is the rising incidence of multidrug-resistant bacteria, derived from various selection pressures. Many of these bacterial infections are hospital-acquired and have prompted the Centers for Disease Control and Prevention in 2019 to reclassify several pathogens as urgent threats, its most perilous assignment. Consequently, there is an urgent need to improve the clinical management of bacterial infection via new methods to specifically identify bacteria and monitor antibiotic efficacy *in vivo*. In this work, we developed a novel radiopharmaceutical, 2- ^{18}F -fluoro-2-deoxy-mannitol (^{18}F -fluoromannitol), which we found to specifically accumulate in both gram-positive and gram-negative bacteria but not in mammalian cells *in vitro* or *in vivo*. **Methods:** Clinical isolates of bacteria were serially obtained from wounds of combat service members for all *in vitro* and *in vivo* studies. Bacterial infection was quantified *in vivo* using PET/CT, and infected tissue was excised to confirm radioactivity counts *ex vivo*. We used these same tissues to confirm the presence of bacteria by extracting and correlating radioactive counts with colony-forming units of bacteria. **Results:** ^{18}F -fluoromannitol was able to differentiate sterile inflammation from *Staphylococcus aureus* and *Escherichia coli* infections *in vivo* in a murine myositis model using PET imaging. Our study was extended to a laceration wound model infected with *Acinetobacter baumannii*, an important pathogen in the nosocomial and battlefield setting. ^{18}F -fluoromannitol PET rapidly and specifically detected infections caused by *A. baumannii* and several other important pathogens (*Enterococcus faecium*, *S. aureus*, *Klebsiella pneumoniae*, *A. baumannii*, *Pseudomonas aeruginosa*, and *Enterobacter* spp.). Importantly, ^{18}F -fluoromannitol PET was able to monitor the therapeutic efficacy of vancomycin against *S. aureus* *in vivo*. **Conclusion:** The ease of production of ^{18}F -fluoromannitol is anticipated to facilitate wide radiopharmaceutical dissemination. Furthermore, the broad sensitivity of ^{18}F -fluoromannitol for bacterial infection *in vivo* suggests that it is an ideal imaging agent for clinical translation to detect and monitor infections and warrants further studies in the clinical setting.

Key Words: ^{18}F ; PET imaging; infection; bacteria

Received Aug. 29, 2022; revision accepted Nov. 28, 2022.

For correspondence or reprints, contact Kiel Neumann (kiel.neumann@stjude.org).

Published online Dec. 15, 2022.

Immediate Open Access: Creative Commons Attribution 4.0 International License (CC BY) allows users to share and adapt with attribution, excluding materials credited to previous publications. License: <https://creativecommons.org/licenses/by/4.0/>. Details: <http://jnm.snmjournals.org/site/misc/permission.xhtml>.

COPYRIGHT © 2023 by the Society of Nuclear Medicine and Molecular Imaging.

J Nucl Med 2023; 64:809–815
DOI: 10.2967/jnumed.122.264854

Infection is responsible for the highest morbidity and the third most deaths among all human diseases worldwide (1). Most health-care-associated infections in the United States arise from several common pathogens, including *Staphylococcus aureus*, *Acinetobacter baumannii*, *Pseudomonas aeruginosa*, and those of the Enterobacteriaceae family (*Escherichia coli* and *Salmonella* spp., among others). The rising trend of antimicrobial resistance, compounded by a growing population of immunocompromised individuals (HIV/AIDS, chemotherapy, organ transplantation, diabetes) creates an enormous economic strain on the U.S. health-care system, with estimates ranging from \$28 billion to \$45 billion annually (2). Current estimates project that drug-resistant infections will become the leading cause of global death, surpassing cancer-associated mortality by 2050 (3). The Centers for Disease Control and Prevention has recently listed carbapenem-resistant *Acinetobacter* and Enterobacteriaceae, extended-spectrum β -lactamase-producing Enterobacteriaceae, multidrug-resistant *P. aeruginosa*, methicillin-resistant *S. aureus*, and others as urgent or serious threats to human health (4). Carbapenem-resistant *A. baumannii* alone was responsible for 8,500 hospitalizations, 700 deaths, and \$281 million in U.S. health-care costs in 2017 (4). Carbapenem-resistant *A. baumannii* infections are particularly problematic for patients who have comorbidities or are immunocompromised (5); however, *A. baumannii*-associated infections are also well-described complications of severe combat-related injuries in military service members (6). Accordingly, there is an urgent need to improve the diagnosis and treatment of bacterial infection.

Traditional approaches to diagnosing infection include obtaining a biopsy sample from tissue or blood and subsequently culturing pathogens in media to identify an organism. Bacterial cultures from tissue biopsy specimens remain the gold standard for confirming the presence, identity, and drug sensitivity of a microorganism; however, deep-seated infections that are difficult to access or identify often rely on noninvasive imaging techniques based on changes in anatomy or tissue morphology. The most common anatomic imaging modalities used, such as CT and MRI, are frequently nonspecific for delineating active infection from sterile inflammatory disease. Nuclear medicine uses labeled leukocytes

(^{99m}Tc - or ^{111}In -oxine) (7) and ^{67}Ga -citrate scintigraphy (8), which rely on indirect measurements of leukocyte recruitment to an area of interest. PET imaging with ^{18}F -FDG is increasingly used; however, none of these imaging techniques can distinguish active infection from cancer or inflammation. Consequently, current clinically available imaging techniques are not adequately specific to diagnose deep-seated infection.

To address this challenge, many recently developed radiopharmaceuticals seek to exploit various bacteria-specific signatures such as metabolism (9–11), cofactor biosynthesis (12,13), and labeled antibiotics (14,15). Despite these scientific advances, a dire need persists for imaging agents that meet the challenges of clinical infectious disease practice; the ideal agent should possess broad bacterial strain sensitivity, have optimal pharmacokinetics (rapid target engagement, clearance of nonspecific signals to promote contrast), and be widely deployable and available for clinical use.

The phosphoenolpyruvate-dependent sugar phosphotransferase system catalyzes phosphorylation of incoming sugar substrates, with concomitant translocation across the cell membrane, and is widely found in bacteria (16–18). Because of this metabolic signature, ^3H - and ^{14}C -D-mannitol analogs were recently evaluated in a panel of pathogens (19). We hypothesized that a positron-emitting analog of mannitol, $2\text{-}^{18}\text{F}$ -fluoro-2-deoxy-mannitol (^{18}F -fluoromannitol), would be a specific precursor for bacterial metabolism and, subsequently, a suitable imaging agent for *in vivo* use with PET. Here, we report a simple, widely deployable radiosynthesis of ^{18}F -fluoromannitol and demonstrate that this imaging agent possesses broad-spectrum bacterial sensitivity both *in vitro* and *in vivo* using clinical isolates of bacteria from combat wounds in military service members. Moreover, we demonstrate that ^{18}F -fluoromannitol can quantify antimicrobial efficacy *in vivo*.

MATERIALS AND METHODS

Manual Radiosynthesis of ^{18}F -Fluoromannitol

^{18}F -fluoromannitol was synthesized from commercially available cyclotron-derived ^{18}F -fluoride ions and isolated in a radiochemical yield of $23\% \pm 2\%$ (end of synthesis) with an estimated molar activity of $5.5 \pm 0.37 \text{ GBq}/\mu\text{mol}$ ($n = 14$). Detailed radiosynthetic procedures are described in the supplemental methods (supplemental materials are available at <http://jnm.snmjournals.org>).

Murine Myositis Model

CBA/J mice (male, 5–6 wk old) were inoculated with $50 \mu\text{L}$ (typical inoculations were 10^6 colony forming units [CFUs]) of bacteria into the triceps brachii muscle as previously described (10,12,20).

Wound Infection Model

C57BL/6 mice (male, 5–6 wk old) were used for all experiments. A 3-mm laceration in the dorsal fascia was injected with $50 \mu\text{L}$ (typical inoculations were 10^6 CFUs) of *A. baumannii* into the open wound, and the infection was allowed to develop for 6 h (11) before imaging.

PET/CT Imaging

For all studies, $5.5 \pm 1.8 \text{ MBq}$ were injected via a lateral tail-vein catheter. After injection, mice were imaged by dynamic (60 min) or

static (45–60 min) PET acquisition. All scans were immediately followed by a 10-min CT scan for attenuation correction and anatomic coregistration. Afterward, the mice were euthanized for biodistribution studies and CFU analysis when applicable. γ -counting of harvested tissue was performed using an automatic γ -counter (Hidex). Detailed protocols are described in the supplemental methods.

Computation, Registration, and Quantification of Parametric PET Maps

Parametric PET maps of the total rodent body were generated and computed as previously described (21). Net influx rate maps were computed and coregistered with CT images using PMOD (version 3.9, PMOD Technologies). The regional average net influx rate was quantified and correlated with CFUs. Detailed protocols are described in the supplemental methods.

Statistical Methods

Quantitative data are expressed as mean \pm SEM unless otherwise noted. Means were compared using 1-way ANOVA or, for multiple comparisons, 2-way ANOVA. The Mann–Whitney *U* test was used to test significant differences in SUV comparisons over time (dynamic imaging). *P* values smaller than 0.05 were considered statistically significant.

RESULTS

^{18}F -Fluoromannitol Radiosynthesis

The radiosynthesis of ^{18}F -fluoromannitol commences through a 2-step, 1-pot production of $2\text{-}^{18}\text{F}$ -fluoro-2-deoxy-mannose (**1**) (Fig. 1). We synthesized the fully protected ^{19}F -isotopic precursor of $2\text{-}^{18}\text{F}$ -fluoro-2-deoxy-mannose (**9**) (Supplemental Schemes 1–3) to identify the ^{18}F -labeled intermediate (Supplemental Figs. 1 and 2) and calculate the molar activity (Supplemental Figs. 3–5) by high-performance liquid chromatography. The production of ^{18}F -fluoromannitol generates a $7.31 \pm 0.25 \text{ } \mu\text{g}/\text{mL}$ concentration of ^{19}F -fluoromannitol, which meets the Food and Drug Administration microdose definition (22) and is suitable for clinical studies. $2\text{-}^{18}\text{F}$ -fluoro-2-deoxy-mannose is converted to ^{18}F -fluoromannitol (**2**) (Fig. 1) by sodium borohydride-mediated reduction and isolated in more than 99% radiochemical purity in a $23\% \pm 2\%$ radiochemical yield ($n = 14$) (end of synthesis) and an estimated molar activity of $5.5 \pm 0.4 \text{ GBq}/\mu\text{mol}$.

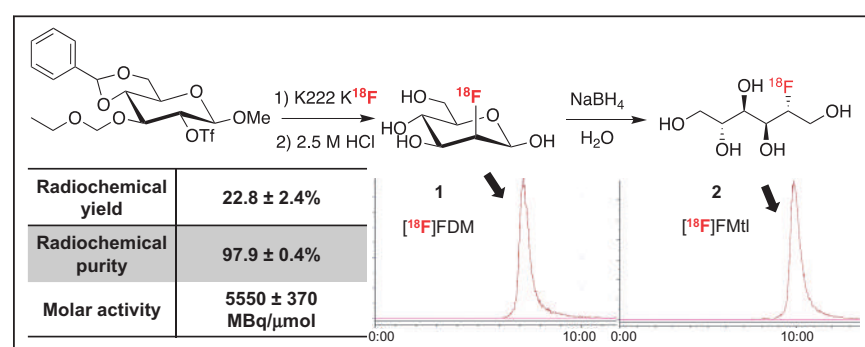


FIGURE 1. Radiochemical synthesis of ^{18}F -fluoromannitol is a straightforward 3-step, 2-pot process using commercially available precursor. Radiosynthesis produces ^{18}F -fluoromannitol in high radiochemical yield and purity, which are easily determined by radio-HPLC. Molar activity was measured of 3 radiosyntheses. Intermediates were verified using fully characterized ^{19}F isotopic standard and matched to HPLC retention times. FDM = $2\text{-}^{18}\text{F}$ -fluoro-2-deoxy-mannose; FMtl = fluoromannitol.

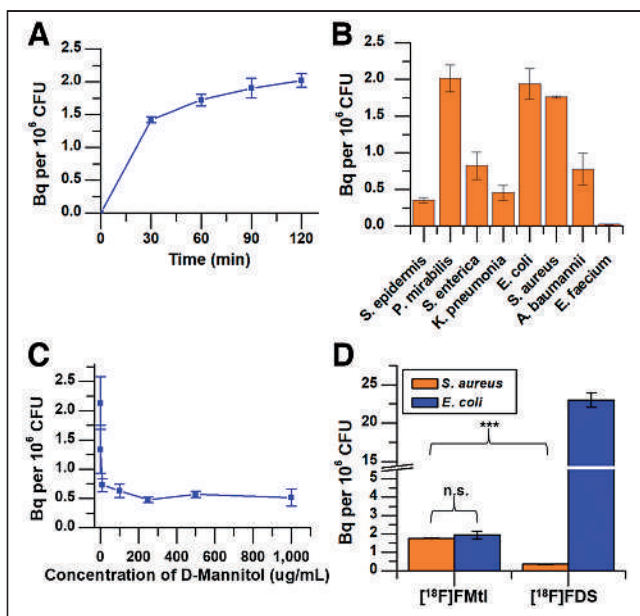


FIGURE 2. Accumulation of ^{18}F -fluoromannitol in bacteria in vitro. (A) Rapid accumulation of ^{18}F -fluoromannitol in *S. aureus* cultures, commensurate with ideal imaging times. (B) Uptake of ^{18}F -fluoromannitol in pathogens of clinical interest determined at 60 min of incubation. (C) Competitive uptake assay of ^{18}F -fluoromannitol in presence of unlabeled d-mannitol in *S. aureus*. (D) *S. aureus* and *E. coli* cultures incubated with ^{18}F -fluoromannitol or ^{18}F -FDS. Data are mean \pm SEM ($n = 6$). *** $P < 0.001$. FMTI = fluoromannitol; n.s. = not statistically significant.

Characterization of ^{18}F -Fluoromannitol In Vitro

Over time, both *S. aureus* and *E. coli* readily incorporated ^{18}F -fluoromannitol (Fig. 2A) but not heat-killed bacteria, demonstrating metabolic specificity of bacteria for ^{18}F -fluoromannitol. We next evaluated accumulation of ^{18}F -fluoromannitol in a broad panel of bacterial strains (Supplemental Table 1). All strains tested, except for *P. aeruginosa* and *Enterococcus faecium*, showed rapid and significant accumulation (Fig. 2B). Coincubation of ^{18}F -fluoromannitol with d-mannitol in *S. aureus* cultures demonstrated target specificity and that accumulation of ^{18}F -fluoromannitol is not concentration-dependent (Fig. 2C); concentrations of at least 10 $\mu\text{g}/\text{mL}$ of d-mannitol blocked ^{18}F -fluoromannitol accumulation in bacteria. We also compared the accumulation of ^{18}F -fluoromannitol in *S. aureus* (gram-positive) and *E. coli* (gram-negative) cultures against ^{18}F -FDG, the current workhorse of nuclear medicine, and 2-deoxy-2- ^{18}F -fluorosorbitol (^{18}F -FDS), which has demonstrated high specificity for Enterobacteriaceae organisms (10). As anticipated, ^{18}F -fluoromannitol accumulated in both *E. coli* and *S. aureus*, and in *S. aureus* this accumulation was significantly higher than that of ^{18}F -FDS ($P < 0.001$) (Fig. 2D; Supplemental Fig. 6). The accumulation of ^{18}F -fluoromannitol in *S. aureus* and *E. coli* did not significantly differ ($P = 0.64$), and the accumulation of ^{18}F -FDS in *S. aureus* did not significantly differ from that in negative control (10-times heat-killed bacteria, $P = 0.35$; Supplemental Fig. 7). Taken together, these data show that ^{18}F -fluoromannitol accumulates rapidly in a wide panel of bacteria and thus may serve as a broad-spectrum imaging agent of infection in vivo.

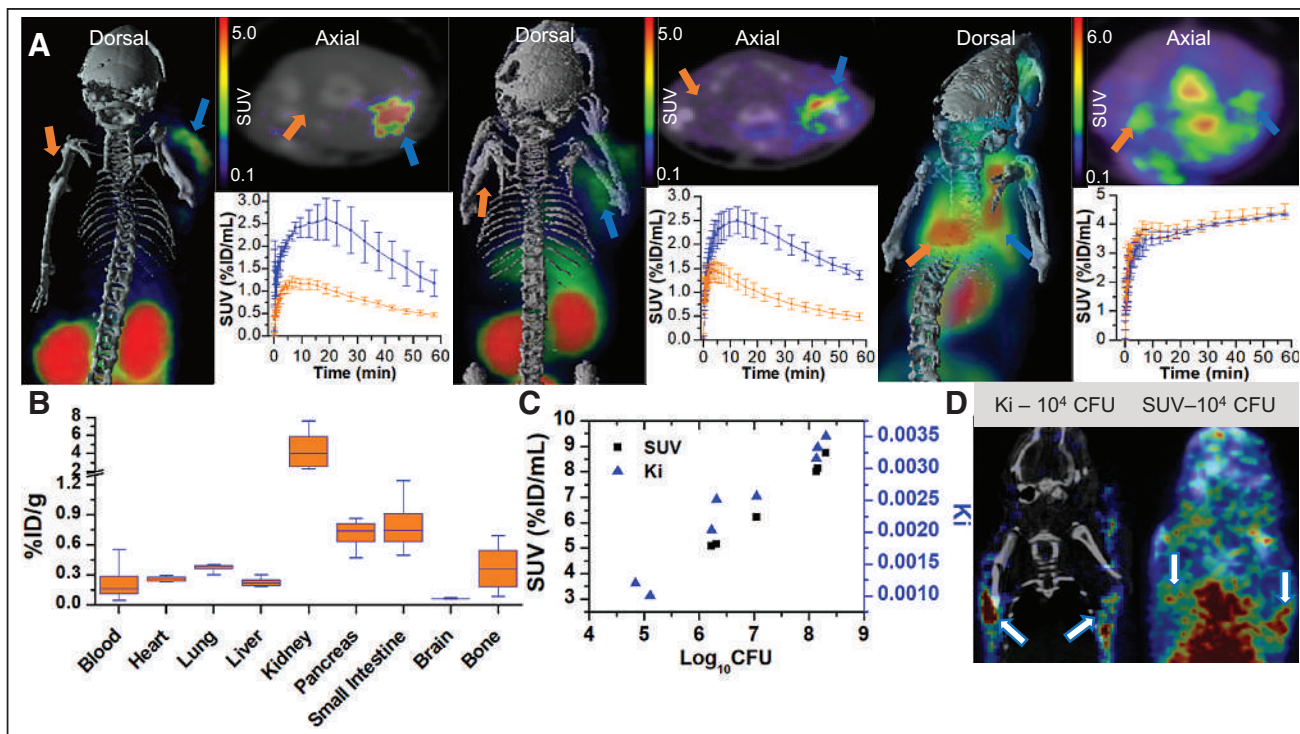


FIGURE 3. In vivo quantification of bacterial infection by ^{18}F -fluoromannitol imaging. (A) ^{18}F -fluoromannitol signal is significantly elevated in infected triceps brachii (blue arrows) but not in inflamed triceps brachii (orange arrows) in both *S. aureus* (left) and *E. coli* (middle); ^{18}F -FDG cannot differentiate infection from sterile inflammation (right) (4 each; $P < 0.001$). (B) ^{18}F -fluoromannitol ex vivo biodistribution was performed on indicated tissues of interest after imaging. Data are mean with interquartile range ($n = 4$). (C) ^{18}F -fluoromannitol imaging (SUV or net influx rate) was correlated with bacterial CFUs ex vivo to demonstrate imaging agent sensitivity. (D) ^{18}F -fluoromannitol imaging sensitivity improved approximately 20-fold using parametric imaging (left), compared with clinical standard metric of SUV (right). Arrows point to sites of histologically confirmed infection. Data are mean \pm SEM. %ID = percentage injected dose; Ki = net influx rate.

¹⁸F-Fluoromannitol Characterization In Vivo

We used a murine myositis model of musculoskeletal infection (10–12,14,20,23) to determine whether ¹⁸F-fluoromannitol can differentiate sterile inflammation from infection in vivo by inoculating the right triceps brachii with a live strain of bacteria and the left triceps brachii with a 10-times quantity of heat-killed bacteria to generate an inflammatory response. ¹⁸F-fluoromannitol accumulated specifically in the site of infection in both gram-positive and gram-negative strains (Fig. 3A). ¹⁸F-FDG was predictably unable to distinguish infection from inflammation, consistent with prior reports (10–12,14,20,23), but did serve as a valuable positive control. Dynamic imaging revealed rapid accumulation and significant differences in PET signal in as little as 5 min after ¹⁸F-fluoromannitol injection.

To quantify PET signal, we generated volumes of interest in the upper limbs of mice using CT for anatomic localization. ¹⁸F-fluoromannitol displayed a 3.5-fold increased SUV (summed frames 45–60 min after injection) compared with the contralateral site of inflammation (Supplemental Fig. 8). ¹⁸F-FDG could not show significant differences in SUV between sites of infection and inflammation. After the scans, we excised both triceps brachii to confirm the PET data using γ -counting, which confirmed the increased PET signal in the infected tissue compared with inflamed tissue (Supplemental Fig. 9). Biodistribution studies were performed in successive cohorts of mice over 3 h to determine the dosimetry of ¹⁸F-fluoromannitol (Fig. 3B; Supplemental Fig. 10). The kidneys and bladder demonstrated the highest nonspecific accumulation of ¹⁸F-fluoromannitol, consistent with PET imaging data. We also correlated static PET SUV with bacterial CFUs from excised tissue to determine the sensitivity of ¹⁸F-fluoromannitol (Fig. 3C; Supplemental Fig. 11) and found that ¹⁸F-fluoromannitol can reliably detect as little as 5 log₁₀ (CFUs/mL) of bacteria in vivo by SUV. We also investigated whether parametric mapping (21) can increase the bacterial sensitivity of ¹⁸F-fluoromannitol in vivo (as net influx rate is a quantitative measure of the rate of uptake in tissue (24)), rather than SUV (which is semiquantitative and cannot delineate signal from blood pool contamination and

tissue). Parametric imaging improved the bacterial sensitivity of ¹⁸F-fluoromannitol by roughly 20-fold (log₁₀ CFUs = 1.3; 1.7 \times 10⁶ improved to 7.0 \times 10⁵ CFUs) (Figs. 3C and 3D; Supplemental Fig. 12).

We also investigated the sensitivity of ¹⁸F-fluoromannitol compared with ¹⁸F-FDS in a mixed infection (polymicrobial) model. ¹⁸F-FDS has shown remarkable specificity for Enterobacteriaceae in vivo but has shown limited to no sensitivity toward gram-positive and other gram-negative organisms. Mice were inoculated with live *E. coli* (8.4 \times 10⁶ CFUs) and *S. aureus* (8.8 \times 10⁶ CFUs) in the right and left triceps brachii, respectively. No significant differences in SUV (P = 0.19) were observed between *E. coli* and *S. aureus* infection in the same animal (Figs. 4A and 4B) with ¹⁸F-fluoromannitol. Importantly, ¹⁸F-fluoromannitol accumulation was significantly higher than ¹⁸F-FDS accumulation in *S. aureus* infection (P < 0.001). ¹⁸F-FDS demonstrated high specificity for *E. coli*, compared with *S. aureus* (P = 0.007); however, no significant differences in *E. coli* SUV were evident between ¹⁸F-fluoromannitol and ¹⁸F-FDS (P = 0.11). Postmortem γ -counting of tissues confirmed ¹⁸F-fluoromannitol uptake in both *S. aureus* and *E. coli*, whereas ¹⁸F-FDS accumulated only in *E. coli*-infected muscle (Supplemental Fig. 13). In sum, our imaging data show that ¹⁸F-fluoromannitol accumulates in both gram-positive and gram-negative organisms and is of adequate sensitivity to serve as an in vivo broad-spectrum imaging tool for infection.

Imaging Wound Infection with ¹⁸F-Fluoromannitol PET

The emergence of carbapenem-resistant *A. baumannii* has rendered clinical management of *A. baumannii* infections difficult to impossible (25) in some cases. The urgency to improve management of *A. baumannii* infections prompted us to investigate whether ¹⁸F-fluoromannitol can detect *A. baumannii* in a laceration wound model. Mice were inoculated with *A. baumannii* (9.4 \times 10⁶ CFUs) through a small incision in the dorsal fascia and imaged using PET/CT. ¹⁸F-fluoromannitol accumulated specifically in the infected wounds of mice (Fig. 5; Supplemental Fig. 14), demonstrating nearly a 6-fold increase in SUV (7.0 log₁₀ CFUs) compared with a 10-times quantity of heat-killed bacteria in a nearby wound.

Quantifying Antimicrobial Efficacy In Vivo

The growing incidence of antimicrobial resistance in many bacterial pathogens is a serious concern because treatment failure is a major threat to global health (26). Inappropriate antibiotic use is also the primary driver of antibiotic resistance (27), which also places undue risk on patients for adverse events such as allergic reactions and *Clostridium difficile* infection. Thus, it is imperative to optimize the management of infection and use of antibiotics. We investigated whether ¹⁸F-fluoromannitol can quantify the efficacy of antibiotic therapy in vivo. Mice were inoculated with *S. aureus* in the right triceps brachii and imaged with ¹⁸F-fluoromannitol 8 h after infection, before initiation of vancomycin treatment (100 mg/kg every 8 h, intraperitoneally), and subsequently were imaged at 24 and 72 h

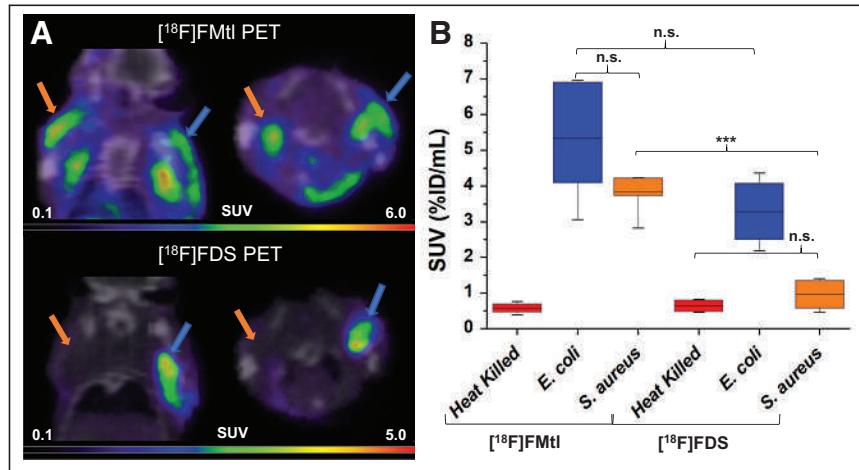


FIGURE 4. PET/CT static imaging of murine mixed myositis model of infection. (A) ¹⁸F-fluoromannitol PET signal was observed in both *S. aureus*-infected muscle (orange arrows) and *E. coli*-infected muscle (blue arrows). ¹⁸F-FDS signal is specific to *E. coli*-infected muscle and is not observed in *S. aureus* infection. (B) ¹⁸F-fluoromannitol and ¹⁸F-FDS SUV from PET scans show that both agents can detect *E. coli* with equivalent sensitivity, but ¹⁸F-fluoromannitol SUV is significantly higher than ¹⁸F-FDS SUV for *S. aureus*. *** P < 0.001. %ID = percentage injected dose; FMtl = fluoromannitol; n.s. = not statistically significant.

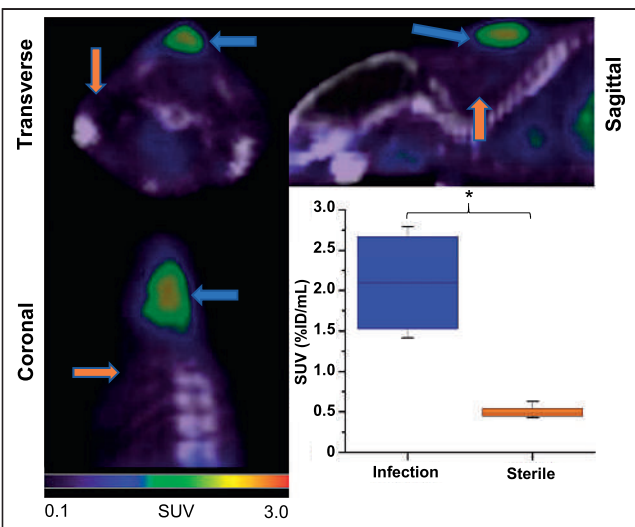


FIGURE 5. ^{18}F -fluoromannitol detects *A. baumannii* infection in wound of C57BL/6 mice (left). ^{18}F -fluoromannitol in vivo PET imaging shows significant differences in SUV in infected wound (blue arrows), compared with sterile inflammation (orange arrows) located 1 cm caudal and sinister to infected wound (right). Data are mean and range (4 animals for each group). * $P < 0.01$. %ID = percentage injected dose.

after treatment. The PET signal diminished over the course of treatment, correlating closely with CFU burden (Fig. 6A). We next investigated the accumulation of ^{18}F -fluoromannitol in a panel of bacterial isolates from infected combat wounds of military service members (Fig. 6B). ^{18}F -fluoromannitol demonstrated broad accumulation in *S. aureus* and *A. baumannii* but did not show appreciable accumulation in *P. aeruginosa*. Taken together, these findings indicate that ^{18}F -fluoromannitol can be used as an effective tool to image a variety of clinically relevant pathogens.

DISCUSSION

Mortality-associated infection disproportionately affects populations with strained access to health care (28); thus, a critical metric for any imaging agent is that it be easily disseminated. The use of ^{18}F ensures that the isotope is regularly available from cyclotron production, and the half-life (109.5 min) facilitates widespread distribution. The radiosynthesis of ^{18}F -fluoromannitol (Fig. 1) is a straightforward 3-step reaction; the first 2 steps were intentionally designed to model the radiosynthesis of ^{18}F -FDG, followed by seamless sodium borohydride reduction (29). All purifications are cartridge-based and facilitate automation on any radiosynthesizer, promoting robust access to ^{18}F -fluoromannitol.

Clinical management of infection typically commences with empiric antibiotic therapy using broad-spectrum agents, often combined with a targeted antimicrobial.

Treatment generally continues until biopsy or culture reveals the causative organism; however, treatment may continue in lieu of positive identification. The inability to rapidly delineate bacterial infection promotes unnecessary exposure to antibiotics, contributing to the rising incidence of antimicrobial resistance mechanisms and morbidities associated with antibiotic therapy (30,31). ^{18}F -fluoromannitol shows rapid and specific accumulation in bacteria *in vivo* in several clinically relevant pathogens. Despite the seeming disparity in accumulation of ^{18}F -fluoromannitol in *E. coli* compared with ^{18}F -FDS *in vitro* (Fig. 2D), no significant differences ($P = 0.11$) in tracer accumulation were observed *in vivo* in *E. coli* (Fig. 4). This important observation highlights that although *in vitro* assays play fundamentally important roles in preliminary characterization and validation, it is imperative that other characteristics, such as pharmacokinetics, not be overlooked when evaluating the candidacy of a novel radiopharmaceutical for imaging. Collectively, the minimal nonspecific accumulation and radioactive dose of ^{18}F -fluoromannitol in mammalian tissue suggest that this agent is well poised for clinical studies on anatomic localization of a variety of infections.

Imaging can realistically play a complementary role in managing several clinical applications of infection with diverse etiologies. However, the complementary role imaging will play is ultimately limited to the *in vivo* sensitivity of the agent (CFUs/mL). Several radiopharmaceuticals have been studied, including glucose (^{18}F -FDG) (32,33), sorbitol (^{18}F -FDS) (10,34), and maltose (^{18}F -fluoromaltose, ^{18}F -fluoromaltotriose) (11). ^{18}F -FDS has shown adequate sensitivity to infection in both preclinical models and human disease; however, this agent is limited to the detection of Enterobacteriales.

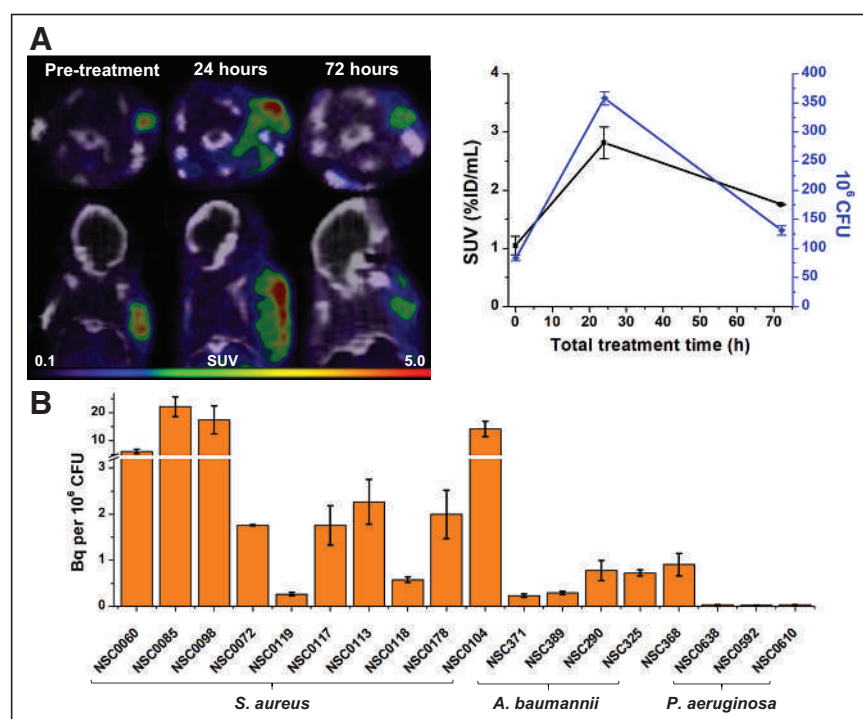


FIGURE 6. ^{18}F -fluoromannitol can quantify antimicrobial efficacy *in vivo*. (A) Mice were inoculated with clinical isolate of *S. aureus*, and antimicrobial efficacy of vancomycin was monitored over 72 h of treatment. Antimicrobial efficacy was quantified with serial PET imaging (left) and correlated with CFUs (right). Data are mean \pm SEM (3 per time point). (B) Uptake of ^{18}F -fluoromannitol in clinical isolates of *S. aureus*, *A. baumannii*, and *P. aeruginosa*. Data are mean \pm SEM (6 per strain). %ID = percentage injected dose.

Maltose-derived radiopharmaceuticals demonstrated improved strain coverage that includes *P. aeruginosa* and *S. aureus*; however, the sensitivity of these agents for clinically relevant concentrations of bacteria beyond *E. coli* remains uncertain. Other imaging agents, such as those targeting folate biosynthesis (12–14) or transpeptidases (20,23), report limited (10^8 CFUs) or unknown sensitivity. ^{18}F -fluoromannitol was able to reliably detect 10^5 CFUs *in vivo* using the clinical standard SUV, which is of sufficient sensitivity for detecting an abscess (3). Furthermore, the sensitivity of ^{18}F -fluoromannitol did not diminish between *E. coli* and *S. aureus*, suggesting that sensitivity is not dependent on a specific genus or family of bacteria.

The Centers for Disease Control and Prevention estimates that approximately 30% of prescribed antibiotics are unnecessary (27), and it is alarming that inappropriate use of antibiotics is the primary driver for the development of antibiotic resistance mechanisms. Bacterial CFUs were shown to correlate with PET SUV during vancomycin treatment using ^{18}F -fluoromannitol imaging (Fig. 6A). In addition, ^{18}F -fluoromannitol demonstrates indistinguishable accumulation in *E. coli* and *S. aureus* *in vivo*. ^{18}F -fluoromannitol is well positioned to serve as a valuable tool for diseases that are currently challenging or impossible to definitively delineate using current clinically available imaging tools, such as delineation of degenerative disk disease (sterile inflammation) from discitis osteomyelitis (infection). With the imaging tools now available, it is intriguing to envision a role in which imaging can rapidly diagnose infection (^{18}F -fluoromannitol: broad spectrum) and optimize the selection of an appropriate antibiotic for the pathogen (^{18}F -FDS: Enterobacteriales specificity). Thus, these precision medicine tools may improve management of patient care and limit or eliminate unnecessary antibiotic use.

Our study was not without limitations. ^{18}F -fluoromannitol requires active transport of mannitol mediated by the mannitol-specific phosphotransferase system in bacteria. Thus, it is possible that senescent or slow-growing bacterial populations may diminish ^{18}F -fluoromannitol sensitivity. However, recent studies have shown that mannitol and fructose stimulated bacterial metabolism and enabled aminoglycoside antibiotic sensitivity (28,35,36). Further studies may be warranted to examine whether ^{18}F -fluoromannitol can serve as a prognostic indicator for this type of therapeutic strategy. Our studies revealed limited accumulation of ^{18}F -fluoromannitol in *P. aeruginosa*, a difficult-to-manage pathogen in patients with comorbidities (37,38). This outcome is surprising because the mannitol operon is well characterized in *P. aeruginosa* (39–41). Nonetheless, this finding is consistent with other mannitol-derived and sugar alcohol-derived radiopharmaceuticals studied (19) in *P. aeruginosa* *in vitro*.

CONCLUSION

We have described a novel radiopharmaceutical, ^{18}F -fluoromannitol, for imaging infections in a diverse spectrum of pathogenic organisms, including *S. aureus*, *A. baumannii*, and *E. coli*. Production of ^{18}F -fluoromannitol is straightforward, robust, and high-yielding, thus facilitating wide accessibility. Accordingly, ^{18}F -fluoromannitol might be rapidly translated to clinical studies as a noninvasive diagnostic tool facilitating rapid delineation of infection from sterile inflammatory processes, ultimately reducing the incidence of antimicrobial resistance promoted by selection pressures derived from unnecessary use of antibiotics.

DISCLOSURE

This work is supported by NIH/NIBIB R01EB028338-01 and the Military Infectious Diseases Research Program and Defense Health Programs subcontract DoD/NMRC N3239820P0034 (Kiel Neumann). Mark Simons and Alexandria Kesterson are military service members; this work was prepared as part of their official duties. Title 17, U.S. Code, §105, provides that copyright protection under this title is not available for any work of the U.S. government. Title 17, U.S. Code, §101, defines a U.S. government work as a work prepared by a military service member or employee of the U.S. government as part of that person's official duties. The views, opinions, or findings contained in this report are those of the authors and should not be construed as an official Department of the Navy, Department of Defense, or U.S. government position, policy, or decision unless so designated by other documentation. No other potential conflict of interest relevant to this article was reported.

ACKNOWLEDGMENTS

We are grateful for the support of the University of Virginia Radiochemistry and Molecular Imaging Cores. We thank Dr. Soumen Paul for his technical assistance with PET/CT.

KEY POINTS

QUESTION: What are the limitations of ^{18}F -fluoromannitol imaging and availability?

PERTINENT FINDINGS: ^{18}F -fluoromannitol is produced using a simple nucleophilic substitution reaction that is deployable on virtually any commercially available synthesizer present in any nuclear pharmacy and is expected to be widely available for clinical use. ^{18}F -fluoromannitol PET demonstrated high sensitivity and specificity for both gram-positive and gram-negative organisms *in vivo*, and PET signal was shown to closely correlate with CFU burden.

IMPLICATIONS FOR PATIENT CARE: ^{18}F -fluoromannitol signal is not limited by bacterial genus *in vivo*, correlates with CFU burden, and can quantify antimicrobial efficacy. ^{18}F -fluoromannitol should be studied further in bacterial infections of diverse etiology in the clinical setting. The availability of this imaging tool might improve the management of deep-seated and difficult-to-manage bacterial infection.

REFERENCES

- Roth GA, Abate D, Abate KH, et al. Global, regional, and national age-sex-specific mortality for 282 causes of death in 195 countries and territories, 1980–2017: a systematic analysis for the Global Burden of Disease Study 2017. *Lancet*. 2018;392: 1736–1788.
- Stone PW. Economic burden of healthcare-associated infections: an American perspective. *Expert Rev Pharmacoecon Outcomes Res*. 2009;9:417–422.
- Ordonez AA, Sellmyer MA, Gowrishankar G, et al. Molecular imaging of bacterial infections: overcoming the barriers to clinical translation. *Sci Transl Med*. 2019;11: eaax8251.
- Antibiotic resistance threats in the United States, 2019. Centers for Disease Control and Prevention website. <https://www.cdc.gov/drugresistance/pdf/threats-report/2019-ar-threats-report-508.pdf>. Revised December 2019. Accessed January 10, 2023.
- Evans BA, Hamouda A, Amyes SGB. The rise of carbapenem-resistant *Acinetobacter baumannii*. *Curr Pharm Des*. 2013;19:223–238.
- Zapor MJ, Moran KA. Infectious diseases during wartime. *Curr Opin Infect Dis*. 2005;18:395–399.

7. Signore A, Jamar F, Israel O, Buscombe J, Martin-Comin J, Lazzeri E. Clinical indications, image acquisition and data interpretation for white blood cells and anti-granulocyte monoclonal antibody scintigraphy: an EANM procedural guideline. *Eur J Nucl Med Mol Imaging*. 2018;45:1816–1831.
8. Tsan MF. Mechanism of gallium-67 accumulation in inflammatory lesions. *J Nucl Med*. 1985;26:88–92.
9. Ning X, Seo W, Lee S, et al. PET imaging of bacterial infections with fluorine-18-labeled maltosehexaose. *Angew Chem Int Ed Engl*. 2014;53:14096–14101.
10. Weinstein EA, Ordonez AA, DeMarco VP, et al. Imaging Enterobacteriaceae infection in vivo with ¹⁸F-fluorodeoxy sorbitol positron emission tomography. *Sci Transl Med*. 2014;6:259ra146.
11. Gowrishankar G, Hardy J, Wardak M, et al. Specific imaging of bacterial infection using 6''-¹⁸F-fluoromaltotriose: a second-generation PET tracer targeting the maltodextrin transporter in bacteria. *J Nucl Med*. 2017;58:1679–1684.
12. Mutch CA, Ordonez AA, Qin H, et al. [¹¹C]para-aminobenzoic acid: a positron emission tomography tracer targeting bacteria-specific metabolism. *ACS Infect Dis*. 2018;4:1067–1072.
13. Zhang Z, Ordonez AA, Wang H, et al. Positron emission tomography imaging with 2-[¹⁸F]F-p-aminobenzoic acid detects *Staphylococcus aureus* infections and monitors drug response. *ACS Infect Dis*. 2018;4:1635–1644.
14. Sellmyer MA, Lee I, Hou C, et al. Bacterial infection imaging with [¹⁸F]fluoropropyl-trimethoprim. *Proc Natl Acad Sci USA*. 2017;114:8372–8377.
15. van Oosten M, Schäfer T, Gazendam JAC, et al. Real-time in vivo imaging of invasive- and biomaterial-associated bacterial infections using fluorescently labelled vancomycin. *Nat Commun*. 2013;4:2584–2591.
16. Jacobson GR, Lee CA, Saier MH. Purification of the mannitol-specific enzyme II of the *Escherichia coli* phosphoenolpyruvate:sugar phosphotransferase system. *J Biol Chem*. 1979;254:249–252.
17. Jacobson GR, Tanney LE, Kelly DM, Palman KB, Corn SB. Substrate and phospholipid specificity of the purified mannitol permease of *Escherichia coli*. *J Cell Biochem*. 1983;23:231–240.
18. Elferink MG, Driessens AJ, Robillard GT. Functional reconstitution of the purified phosphoenolpyruvate-dependent mannitol-specific transport system of *Escherichia coli* in phospholipid vesicles: coupling between transport and phosphorylation. *J Bacteriol*. 1990;172:7119–7125.
19. Ordonez AA, Weinstein EA, Bambarger LE, et al. A systematic approach for developing bacteria-specific imaging tracers. *J Nucl Med*. 2017;58:144–150.
20. Neumann KD, Villanueva-Meyer JE, Mutch CA, et al. Imaging active infection in vivo using D-amino acid derived PET radiotracers. *Sci Rep*. 2017;7:7903–7910.
21. Huang Q, Massey JC, Miñczuk K, Li J, Kundu BK. Non-invasive determination of blood input function to compute rate of myocardial glucose uptake from dynamic FDG PET images of rat heart in vivo: comparative study between the inferior vena cava and the left ventricular blood pool with spill over and partial volume corrections. *Phys Med Biol*. 2019;64:165010–165018.
22. Schwarz SW, Oyama R. The role of exploratory investigational new drugs for translating radiopharmaceuticals into first-in-human studies. *J Nucl Med*. 2015;56:497–500.
23. Parker MFL, Luu JM, Schulte B, et al. Sensing living bacteria in vivo using D-alanine-derived ¹¹C radiotracers. *ACS Cent Sci*. 2020;6:155–165.
24. Patlak CS, Blasberg RG. Graphical evaluation of blood-to-brain transfer constants from multiple-time uptake data generalizations. *J Cereb Blood Flow Metab*. 1985;5:584–590.
25. Dijkshoorn L, Nemec A, Seifert H. An increasing threat in hospitals: multidrug-resistant *Acinetobacter baumannii*. *Nat Rev Microbiol*. 2007;5:939–951.
26. McKenna M. Antibiotic resistance: the last resort. *Nature*. 2013;499:394–396.
27. Fleming-Dutra KE, Hersh AL, Shapiro DJ, et al. Prevalence of inappropriate antibiotic prescriptions among us ambulatory care visits, 2010–2011. *JAMA*. 2016;315:1864–1873.
28. Murima P, McKinney JD, Pethe K. Targeting bacterial central metabolism for drug development. *Chem Biol*. 2014;21:1423–1432.
29. Abdek-Akher M, Hamilton JK, Smith F. The reduction of sugars with sodium borohydride. *J Am Chem Soc*. 1951;73:4691–4692.
30. Koch-Weser J, Sidel VW, Federman EB, Kanarek P, Finer DC, Eaton AE. Adverse effects of sodium colistimethate: manifestations and specific reaction rates during 317 courses of therapy. *Ann Intern Med*. 1970;72:857–868.
31. Hartzell JD, Neff R, Ake J, et al. Nephrotoxicity associated with intravenous colistin (colistimethate sodium) treatment at a tertiary care medical center. *Clin Infect Dis*. 2009;48:1724–1728.
32. Love C, Marwin SE, Tomas MB, et al. Diagnosing infection in the failed joint replacement: a comparison of coincidence detection ¹⁸F-FDG and ¹¹¹In-labeled leukocyte/^{99m}Tc-sulfur colloid marrow imaging. *J Nucl Med*. 2004;45:1864–1871.
33. Keidar Z, Militiana D, Melamed E, Bar-Shalom R, Israel O. The diabetic foot: initial experience with ¹⁸F-FDG PET/CT. *J Nucl Med*. 2005;46:444–449.
34. Zhu W, Yao S, Xing H, et al. Biodistribution and radiation dosimetry of the Enterobacteriaceae-specific imaging probe [¹⁸F]fluorodeoxy sorbitol determined by PET/CT in healthy human volunteers. *Mol Imaging Biol*. 2016;18:782–787.
35. Allison KR, Brynildsen MP, Collins JJ. Metabolite-enabled eradication of bacterial persisters by aminoglycosides. *Nature*. 2011;473:216–220.
36. Thorsing M, Bentin T, Givskov M, Tolker-Nielsen T, Goltermann L. The bactericidal activity of β-lactam antibiotics is increased by metabolizable sugar species. *Microbiology*. 2015;161:1999–2007.
37. Malhotra S, Hayes D, Wozniak DJ. Cystic fibrosis and *Pseudomonas aeruginosa*: the host-microbe interface. *Clin Microbiol Rev*. 2019;32:e00138–e18.
38. Jones AM, Govan JR, Doherty CJ, et al. Spread of a multiresistant strain of *Pseudomonas aeruginosa* in an adult cystic fibrosis clinic. *Lancet*. 2001;358:557–558.
39. Eisenberg RC, Phibbs PV. Characterization of an inducible mannitol-binding protein from *Pseudomonas aeruginosa*. *Curr Microbiol*. 1982;7:229–234.
40. Eagon RG, Phibbs PV Jr. Kinetics of transport of glucose, fructose, and mannitol by *Pseudomonas aeruginosa*. *Can J Biochem*. 1971;49:1031–1041.
41. Phibbs PV, McCowen SM, Feary TW, Blevins WT. Mannitol and fructose catabolic pathways of *Pseudomonas aeruginosa* carbohydrate-negative mutants and pleiotropic effects of certain enzyme deficiencies. *J Bacteriol*. 1978;133:717–728.

Utility of Amino Acid PET in the Differential Diagnosis of Recurrent Brain Metastases and Treatment-Related Changes: A Meta-analysis

Timo Schlürmann¹, Birgit Waschulzik², Stephanie Combs^{3–5}, Jens Gempt⁶, Benedikt Wiestler⁷, Wolfgang Weber¹, and Igor Yakushev¹

¹Department of Nuclear Medicine, School of Medicine, Klinikum Rechts der Isar, Technical University of Munich, Munich, Germany;

²Institute of AI and Informatics in Medicine, School of Medicine, Klinikum Rechts der Isar, Technical University of Munich, Munich, Germany;

³Department of Radiation Oncology, School of Medicine, Klinikum Rechts der Isar, Technical University of Munich, Munich, Germany; ⁴Institute of Radiation Medicine at Helmholtz Zentrum München (HMGU), Oberschleißheim, Germany; ⁵Deutsches

Konsortium für Translationale Krebsforschung (DKTK), Partner Sites Munich, Freiburg, and Heidelberg; ⁶Department of

Neurosurgery, School of Medicine, Klinikum Rechts der Isar, Technical University of Munich, Munich, Germany; and ⁷Department of Neuroradiology, School of Medicine, Klinikum Rechts der Isar, Technical University of Munich, Munich, Germany

Amino acid PET is an established method to assist differential diagnosis of therapy-related changes versus recurrence in gliomas. However, its diagnostic value in brain metastases is yet to be determined. The goal of this study was to summarize evidence on the diagnostic utility of amino acid PET in recurrent brain metastases. **Methods:** The medical databases MEDLINE, EMBASE, and the Cochrane Library were screened for English-language studies with at least 10 patients who had undergone first-line treatment including radiotherapy and in whom a final diagnosis had been determined by histologic examination or imaging and clinical follow-up. Pooled estimates with 95% CIs were calculated. Heterogeneity was assessed using I^2 statistics. **Results:** Following the above criteria, 12 studies with the tracers methyl-[¹¹C]-methionine ($n = 6$), O-(2-[¹⁸F]fluoroethyl)-L-tyrosine ($n = 3$), methyl-[¹¹C]-methionine and O-(2-[¹⁸F]fluoroethyl)-L-tyrosine ($n = 1$), and 6-[¹⁸F]fluoro-L-dopa ($n = 2$), with a total of 547 lesions in 397 patients, were included. Pooled sensitivity and specificity were 82% (95% CI, 76–86) and 84% (95% CI, 79–88), respectively. Pooled positive and negative predictive values were 84% (95% CI, 77–90) and 83% (95% CI, 77–88), respectively. Positive and negative likelihood ratios, and diagnostic odds ratio were 3.8 (95% CI 3.0–4.8), 0.3 (95% CI 0.2–0.3), and 16.7 (95% CI 10.8–25.9), respectively. Heterogeneity was overall low. **Conclusion:** The present meta-analysis indicates a good accuracy of amino acid PET in the differential diagnosis of recurrent brain metastases. In particular, specificity of 84% suggests that amino acid PET may reduce the number of invasive procedures and overtreatment in patients with treatment-related changes. This study provides class IIa evidence on the utility of amino acid PET in the differential diagnosis of recurrent brain metastases.

Key Words: PET; cerebral metastases; radiation therapy; radiation necrosis; pseudoprogression

J Nucl Med 2023; 64:816–821

DOI: 10.2967/jnumed.122.264803

Brain metastases occur in 20%–40% of all tumor patients (1). The primary tumors most likely to metastasize to the brain are bronchial carcinoma (40%–50%), breast carcinoma (15%–20%), malignant melanoma (5%–20%), renal cancer (5%–10%), and cancers of the gastrointestinal tract (5%) (2). Management of patients with brain metastases usually includes surgery, radiation, and chemotherapy. Therapy is selected on an individual basis, taking into account the primary tumor and location, and number of metastases. Still, most patients with cerebral metastases receive primary, concomitant, or curative radiotherapy during the disease course. After radiation treatment, patients are followed clinically and radiographically with serial MRI. Some develop treatment-related changes (TRCs) such as radiation necrosis and pseudoprogression (3). The true incidence of TRCs is hard to estimate, with values varying widely in the literature, depending on diagnostic criteria, duration of follow-up, radiation modality, and regimen. Radiation necrosis may underlie up to half of lesions that progress radiologically after stereotactic radiosurgery (4,5). Differentiation between recurrent or progressive brain metastasis (RPBM) and TRCs is challenging. Both can manifest with similar clinical symptoms and MRI features, such as rimlike contrast enhancement, perilesional edema, and central hypointensity on T2-weighted imaging (6). For this clinical question, conventional MRI was shown to deliver a pooled sensitivity and specificity of 76% and 59%, respectively (7). As the management of patients with RPBM versus TRCs differs (4), accurate and early differential diagnosis is essential.

Originally, ¹⁸F-FDG was used to differentiate benign and low-grade tumors from high-grade tumors (8). However, the utility of ¹⁸F-FDG PET was shown to be limited by high uptake in normal gray matter and nonspecific uptake in inflammatory lesions (9). Amino acid PET takes advantage of the fact that brain malignancies often overexpress amino acid transport proteins. Common amino acid tracers include methyl-[¹¹C]-methionine (¹¹C-MET), 6-[¹⁸F]fluoro-L-dopa (¹⁸F-FDOPA), and O-(2-[¹⁸F]fluoroethyl)-L-tyrosine (¹⁸F-FET).

In recent years, several single-center studies have investigated the utility of amino acid PET in the differential diagnosis of recurrent brain metastases. The aim of the present work was to summarize existing evidence in the form of a meta-analysis.

Received Dec. 27, 2021; revision accepted Nov. 28, 2022.
For correspondence or reprints, contact Igor Yakushev (igor.yakushev@tum.de).
Published online Dec. 2, 2022.
COPYRIGHT © 2023 by the Society of Nuclear Medicine and Molecular Imaging.

MATERIALS AND METHODS

A literature search was performed in the online medical databases MEDLINE (via PubMed), EMBASE, the Cochrane Library (Cochrane Central Register of Controlled Trials), and Google Scholar. The search was limited to studies on humans. The following key words were used: *Positron Emission Tomography; PET AND recurrence, recurrent, relapse, neoplasm, metastasis, metastatic progression AND radionecrosis, radiation necrosis, radiation-induced necrosis, posttreatment necrosis, radiation injury, radionecrotic, postradiotherapy necrosis AND radiation therapy, radiation treatment, radiosurgery*. The searches were performed in various combinations, both with “AND” and “OR.” The last search was performed on December 1, 2021.

Inclusion Criteria

Studies in English with at least 10 patients who had received PET with amino acid tracers for differentiation of RPBM from TRCs after radiotherapy were included. In addition, follow-up data had to allow creation of a contingency table. Histologic examination or continuous follow-up with radiologic imaging and clinical findings served as reference standards for the final diagnosis. Due to lack of information about primary tumors and clinical outcomes at a single-subject level in most studies, a differential analysis according to the primary tumor was impossible. Figure 1 depicts a flowchart of the selection procedure.

Data Extraction

The following data were extracted from the included studies: first author, publication year, tracers, number of patients, number of lesions, number of true-positives, number of true-negatives, number of false-positives, and number of false-negatives. The calculation of the endpoints

was based on the number of lesions. Some studies in addition provided estimates from kinetic analyses (10,11), but for consistency, only estimates of tumor-to-background ratio (TBR) were considered. If studies provided both mean TBR and maximum TBR, we considered mean TBR only, as the threshold was based on mean TBR in most overviewed studies (Table 2 of Galldiks et al. (12)). To assess the quality of the selected studies, we used Quality Assessment of Diagnostic Accuracy Studies 2 (13).

Statistics

Common and random-effects bivariate models were used. Heterogeneity was assessed using I^2 statistics (the percentage of variation across studies that is due to heterogeneity rather than chance). Pooled estimates of sensitivity, specificity, and predictive values, as well as positive likelihood ratio (posLR), negative likelihood ratio (negLR), and diagnostic odds ratio (DOR) with 95% CIs, were calculated. PosLR above 3.0 were considered acceptable, above 10.0 good; NegLR below 0.3 were considered acceptable, below 0.1 good (14). DOR is used as an indicator of the effectiveness of medical tests with a binary classification. Values for DOR may range from zero to infinity; higher values indicate better test performance. DOR values above 1.0 are considered good (14). All statistical analyses were performed using the statistical software R, version 4.0.4 (15), with the meta (16) and mada (17) packages.

RESULTS

Twelve studies were included in the meta-analysis (Table 1). These were performed with the tracers ^{11}C -MET ($n = 6$), ^{18}F -FET ($n = 3$), both ^{18}F -FET and ^{11}C -MET ($n = 1$), and ^{18}F -FDOPA ($n = 2$). Although other amino acid tracers have been used in neurooncology, for example, α -[^{11}C]-methyl-L-tryptophan, they have not been applied with the above clinical question (18). Of 18 selected full-text articles (Fig. 1), six had to be excluded: one study with the tracer ^{18}F -fluciclovine (19) was too small, that is, fewer than 10 patients; one study was limited to pseudoprogression (20); and one dealt with a cost-effectiveness analysis (21). Two further studies (22,23) had to be excluded because of overlapping patient cohorts. One more study was excluded (24), because reported data did not allow creation of a contingency table.

Finally, twelve studies (10,11,25–34) with a total of 397 patients with 547 lesions were assessed (Table 1). Overall, 269 lesions (49%) were found to be RPBM.

Supplemental Table 1 summarizes the methodologic quality of the selected studies (supplemental materials are available at <http://jnm.snmjournals.org>). Overall, the study quality can be regarded as moderate. In each of the 12 included studies, the time point of tracer injection and the time period of data acquisition meet the recent practice guidelines of the European Association of Nuclear Medicine, the European Association of Neurooncology, and the working group for Response Assessment in Neurooncology

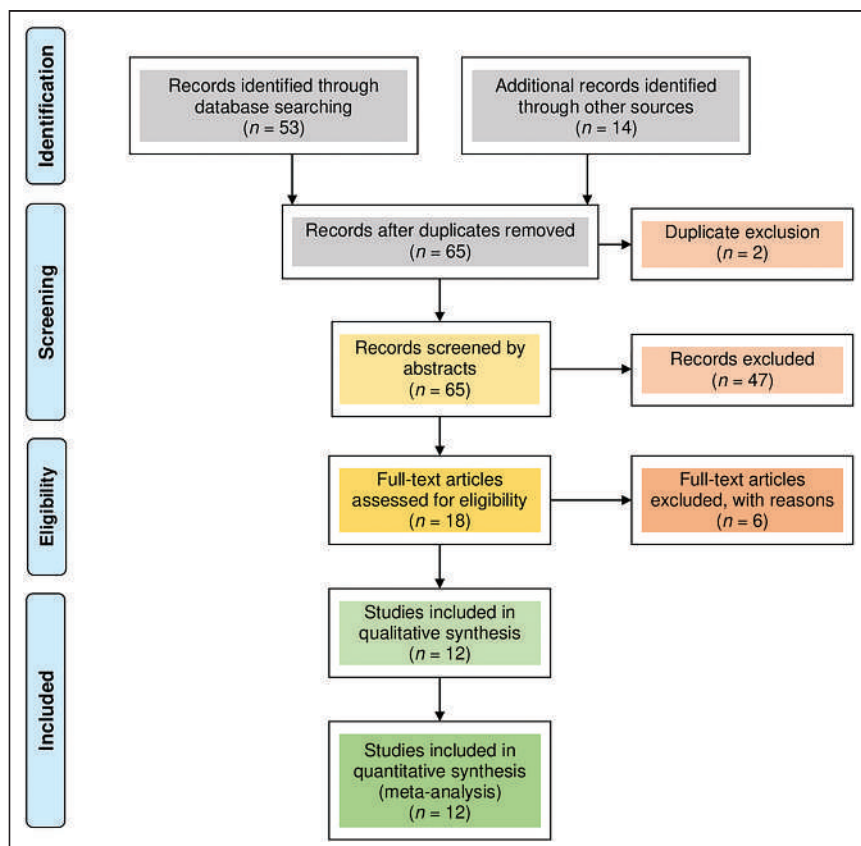


FIGURE 1. Identification of studies as PRISMA (Preferred Reporting Items for Systematic Reviews and Meta-Analyses) flow diagram.

TABLE 1
Study Characteristics

Study	Tracer	Patients (n)	Lesions (n)	Sens (%)	Spec (%)	TP (n)	TN (n)	FP (n)	FN (n)	Acc (%)	PPV (%)	NPV (%)
Tsuyuguchi et al., 2003	¹¹ C-MET	21	21	78	100	7	12	0	2	91	100	86
Terakawa et al., 2008	¹¹ C-MET	51	56	79	75	19	24	8	5	77	70	83
Minamimoto et al., 2015	¹¹ C-MET	39	42	82	86	23	12	2	5	83	92	71
Jung et al., 2017	¹¹ C-MET	48	77	71	81	36	21	5	15	74	88	58
Tomura et al., 2017	¹¹ C-MET	15	18	90	75	9	6	2	1	83	82	86
Yomo et al., 2017	¹¹ C-MET	32	37	82	75	14	15	5	3	78	74	83
Grosu et al., 2011	¹¹ C-MET, ¹⁸ F-FET	13	10	83	100	5	4	0	1	90	100	80
Romagna et al., 2016	¹⁸ F-FET	21	50	86	79	18	23	6	3	82	75	88
Ceccon et al., 2017	¹⁸ F-FET	62	76	86	88	31	35	5	5	87	86	88
Galldiks et al., 2021	¹⁸ F-FET	21	31	73	94	11	15	1	4	84	92	79
Lizarraga et al., 2014	¹⁸ F-FDOPA	32	83	81	73	26	37	14	6	76	65	86
Cicone et al., 2015	¹⁸ F-FDOPA	42	46	90	92	18	24	2	2	91	90	92

Sens = sensitivity; Spec = specificity; TP = true-positives; TN = true-negatives; FP = false-positives; FN = false-negatives; Acc = accuracy; PPV = positive predictive value; NPV = negative predictive value

with PET (35). The cutoffs and verification method (histologic confirmation vs. clinical-neuroradiologic follow-up) of the selected studies are summarized in Table 2.

As shown in Figure 2, the heterogeneity among the studies regarding sensitivity appeared to be an I^2 of 0%. Consequently, the common-effect and random-effect models provided identical results for pooled sensitivity of 0.82 (95% CI, 0.76–0.86).

The analyses of specificity are summarized in Figure 3. An I^2 of 25% means that 25% of the variability is explained by

heterogeneity among the studies. This resulted in an identical estimate for pooled specificity but a slightly different estimate for 95% CI in the common-effect and random-effect models: 0.84 (95% CI, 0.79–0.88) and 0.84 (95% CI, 0.78–0.90), respectively. Table 3 summarizes the values of DOR and likelihood ratios. DOR was 16.7 (95% CI, 10.8–25.9)—that is, good. PosLR and negLR were 3.8 (95% CI, 3.0–4.8) and 0.3 (95% CI, 0.2–0.3), respectively—that is, both within the acceptable range (14).

TABLE 2
Cutoffs and Verification Method (Histologic Confirmation vs. Clinical–Neuroradiologic Follow-up) as Percentage of Histologic Confirmation

Study	Tracer	Mean TBR cutoff	Maximum TBR cutoff	Histologic confirmation, % (lesions)*
Tsuyuguchi et al., 2003	¹¹ C-MET	1.40		52
Terakawa et al., 2008	¹¹ C-MET	1.40		54
Minamimoto et al., 2015	¹¹ C-MET		1.30	Not reported
Jung et al., 2017	¹¹ C-MET		1.61	12
Tomura et al., 2017	¹¹ C-MET		1.42	56
Yomo et al., 2017	¹¹ C-MET		1.40	41
Grosu et al., 2011	¹¹ C-MET		1.80	50
Grosu et al., 2011	¹⁸ F-FET		1.80	50
Romagna et al., 2016	¹⁸ F-FET	1.95	2.15	40
Ceccon et al., 2017	¹⁸ F-FET	1.95	2.55	34
Galldiks et al., 2021	¹⁸ F-FET	1.95		3
Lizarraga et al., 2014	¹⁸ F-FDOPA	1.70	2.02	11
Cicone et al., 2015	¹⁸ F-FDOPA		1.59	24

*Percentages, at the level of lesions (not patients).

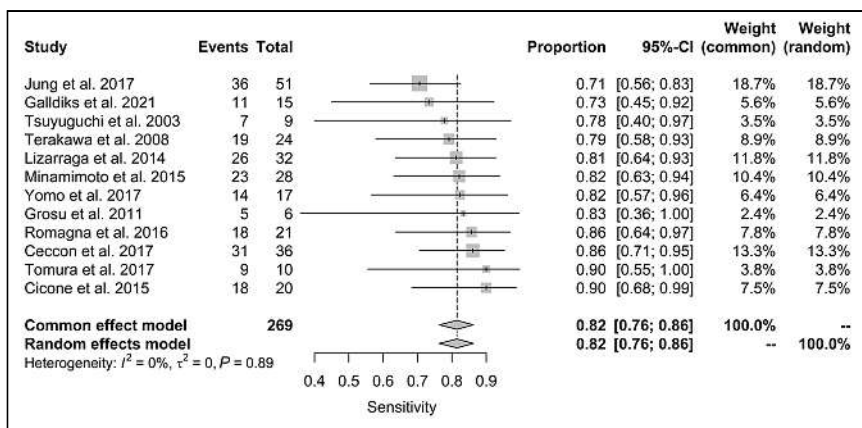


FIGURE 2. Forest plot for sensitivity. Events column lists the number of true-positives. Total column shows sum of true-positives and false-negatives. Proportion column lists reported sensitivity of individual publications and 95% CI. Weight columns indicate contribution of given study according to sample size. Area of gray squares is proportional to weight of study in the meta-analysis. Length of diamonds corresponds to corresponding CI. Vertical line represents pooled sensitivity.

Pooled diagnostic accuracy was 0.82 (95% CI, 0.78–0.85). Pooled positive and negative predictive values were 84% (95% CI, 77–90) and 83% (95% CI, 77–88), respectively. A summary receiver-operating characteristic curve as calculated using the bivariate model is shown in Supplemental Figure 1. Because the biodistribution of ¹⁸F-FDOPA differs from that of ¹¹C-MET and ¹⁸F-FET, we in addition performed the same analyses only for studies with ¹¹C-MET and ¹⁸F-FET ($n = 10$). The results did not change substantially (Supplemental Figs. 2 and 3; Supplemental Table 2). There was also no statistically significant difference between the studies with ¹¹C-MET and ¹⁸F-FET (data not shown).

DISCUSSION

To our knowledge, this is the first meta-analysis on the utility of amino acid PET in the differential diagnosis of RPBM and TRCs. It includes 12 studies with a total of 547 lesions in 397 patients. Using histologic examination or radiologic and clinical follow-up as reference, we found a pooled sensitivity and specificity of 82% and 84%,

respectively. Although values for posLR and negLR were acceptable, DOR appeared to be good.

As compared with gliomas, sensitivity of amino acid PET for differentiation of RPBM from TRCs seems to be lower. In particular, a recent meta-analysis of 39 studies with amino acid PET (36) reported a sensitivity of 85%–93% and specificity of 82%–100%, depending on the tracer, that is, ¹⁸F-FET, ¹¹C-MET, or ¹⁸F-FDOPA. Given a large variance in the amino acid transporter expression of brain metastases (37), some might primarily be PET-negative. Yet, despite a large variance in ¹⁸F-FET uptake, most (89%) newly diagnosed and untreated brain metastases were reported to be PET-positive (38). Another explanation of the lower sensitivity is the impact of systemic therapy; that is, some agents may reduce tumor vitality or amino acid transporter

expression. In this regard, it is noticeable that one of the lowest sensitivities (73%) among the included studies was in patients who had undergone immune checkpoint inhibition and targeted therapy (11). The impact of this modern, increasingly available therapy on tracer uptake warrants further studies. We found a pooled diagnostic specificity of 84%, which is well within the range of values reported for gliomas (36). That is, TRCs are more likely to be PET-negative. Similar to gliomas, however, specificity is far from perfect, as inflammatory processes such as reactive astrocytosis after radiation therapy or immunotherapy may result in tracer uptake above the level of normal brain tissue (39), in some cases leading to false-positive findings on PET (40). Pooled positive and negative predictive values were 84% and 83%, respectively. Although, from a clinical perspective, positive and negative predictive values are more helpful for decision making than conventional sensitivity and specificity, the former indices are dependent on the prevalence of a pathologic condition—that is, recurrent brain metastases in the included studies. Therefore, these results should be treated with caution.

So far, just one meta-analysis has addressed the diagnostic utility of PET in the differentiation between RPBM and TRCs (41). Yet, that work analyzed a pool of studies ($n = 15$) with ¹⁸F-FDG ($n = 6$) and amino acid tracers ($n = 9$) without a separate analysis for the latter. Among these 9 studies, only 5 fulfilled our selection criteria and were therefore included in the present work (10,31–34). Thus, the current meta-analysis includes substantially more studies and covers the amino acid tracers only, following recent recommendations of the RANO/PET group on PET imaging in patients with brain metastasis (12). Because of a low lesion-to-background ratio, that report rated ¹⁸F-FDG PET as a test with limited diagnostic accuracy (Table 3 of Gallidiks et al. (12)).

This study had certain limitations. Because brain metastases are often multifocal, and biopsy or resection is usually performed on

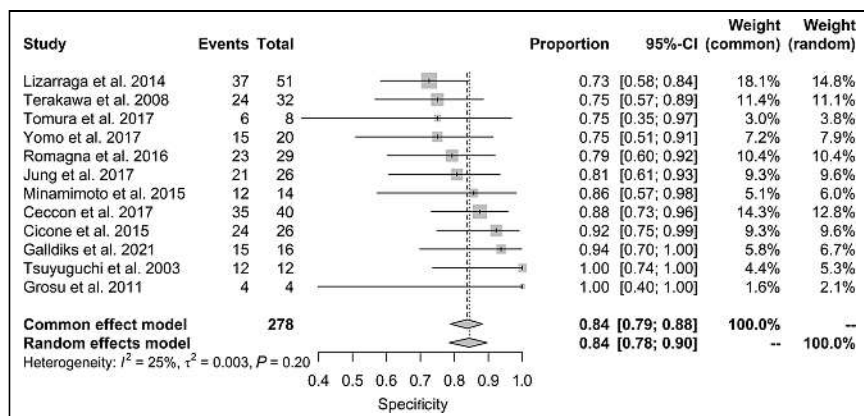


FIGURE 3. Forest plot for specificity. Events column lists the number of true-negatives. Total column shows sum of true-negatives and false-positives. Proportion column lists reported specificity of individual publications and 95% CI. Weight columns indicate contribution of given study according to sample size. Area of gray squares is proportional to weight of study in the meta-analysis. Length of diamonds corresponds to corresponding CI. Vertical line represents pooled specificity.

TABLE 3
Pooled Estimates of DOR, Positive Likelihood Ratio (posLR), and Negative Likelihood Ratio (negLR) with Corresponding 95% CIs

Study	Tracer	Value	DOR		Value	posLR		Value	negLR	
			95% CI	95% CI		95% CI	95% CI		95% CI	95% CI
Tsuyuguchi et al., 2003	¹¹ C-MET	75.00	3.16	1782.78	19.50	1.26	302.43	0.26	0.09	0.77
Terakawa et al., 2008	¹¹ C-MET	10.22	3.00	34.84	3.03	1.64	5.60	0.3	0.14	0.64
Minamimoto et al., 2015	¹¹ C-MET	21.36	4.12	110.68	4.86	1.55	15.28	0.23	0.10	0.50
Jung et al., 2017	¹¹ C-MET	9.21	3.04	27.91	3.45	1.60	7.42	0.37	0.24	0.59
Tomura et al., 2017	¹¹ C-MET	16.47	1.72	157.29	3.11	1.06	9.15	0.19	0.04	0.88
Yomo et al., 2017	¹¹ C-MET	11.68	2.55	53.35	3.08	1.45	6.53	0.26	0.10	0.70
Grosu et al., 2011	¹⁸ F-FET/ ¹¹ C-MET	33.00	1.06	1023.56	7.86	0.55	112.09	0.24	0.06	1.01
Romagna et al., 2016	¹⁸ F-FET	19.11	4.55	80.27	3.88	1.92	7.85	0.20	0.08	0.54
Ceccon et al., 2017	¹⁸ F-FET	36.97	10.32	132.37	6.35	2.88	13.97	0.17	0.08	0.37
Galldiks et al., 2021	¹⁸ F-FET	26.41	3.58	194.96	8.15	1.71	38.71	0.31	0.14	0.69
Lizarraga et al., 2014	¹⁸ F-FDOPA	10.54	3.69	30.14	2.88	1.80	4.60	0.27	0.13	0.56
Cicone et al., 2015	¹⁸ F-FDOPA	72.52	11.36	463.10	9.51	2.89	31.31	0.13	0.04	0.42
Summary*	All	16.73	10.79	25.93	3.75	2.95	4.77	0.27	0.21	0.34

*Random-effects estimates.

single lesions, radiologic and clinical criteria were used as a reference for more than two thirds of lesions. Second, the included studies varied widely regarding the follow-up duration (range, 3–23 mo). Third, most studies did not report the lesion size. Thus, it remains unclear how far the reported values of sensitivity might have been compromised by partial-volume effects in small lesions. In this respect, the maximal diameter of contrast enhancement in T1-weighted MRI (10 mm)—that is, at least double the spatial resolution (full width at half maximum) of modern PET scanners—was proposed as the minimal lesion size (29). Fourth, although we carefully checked for patient overlap, it cannot be excluded (26,28). Finally, most studies had a retrospective design.

CONCLUSION

The present meta-analysis suggests good accuracy for amino acid PET in the differential diagnosis of recurrent brain metastases. In particular, specificity of 84% indicates that amino acid PET may reduce the number of invasive procedures and overtreatment in patients with TRCs. This study provides class IIa evidence on the utility of amino acid PET in the differential diagnosis of RPBM. Further studies—preferably multicenter ones—should investigate the dependence of tracer uptake on the origin, histologic type, and molecular biomarkers of the primary tumor, as well as on the character and regime of local and systemic therapy.

DISCLOSURE

Igor Yakushev has received consultant or lecture fees from ABX-CRO, Blue Earth Diagnostics, and Piramal, as well as grants from the Alzheimer Research Initiative Germany, the German Research Foundation (DFG), and the Federal Ministry of Education

and Research Germany (BMBF). No other potential conflict of interest relevant to this article was reported.

KEY POINTS

QUESTION: How accurate is amino acid PET in the differential diagnosis of recurrent brain metastases and TRCs?

PERTINENT FINDINGS: The present study summarized, in the form of a meta-analysis, the existing evidence on the diagnostic utility of amino acid PET in recurrent brain metastases. Across 12 included studies, pooled sensitivity and specificity were 82% and 84%, respectively.

IMPLICATIONS FOR PATIENT CARE: Amino acid PET is able to assist the differential diagnosis of recurrent brain metastases versus TRCs.

REFERENCES

1. Gavrilovic IT, Posner JB. Brain metastases: epidemiology and pathophysiology. *J Neurooncol.* 2005;75:5–14.
2. Ostrom QT, Wright CH, Barnholtz-Sloan JS. Brain metastases: epidemiology. *Handb Clin Neurol.* 2018;149:27–42.
3. Dietrich J, Winter SF, Klein JP. Neuroimaging of brain tumors: pseudoprogression, pseudoresponse, and delayed effects of chemotherapy and radiation. *Semin Neurol.* 2017;37:589–596.
4. Narloch JL, Farber SH, Sammons S, et al. Biopsy of enlarging lesions after stereotactic radiosurgery for brain metastases frequently reveals radiation necrosis. *Neuro Oncol.* 2017;19:1391–1397.
5. Fujimoto D, von Eyben R, Gibbs IC, et al. Imaging changes over 18 months following stereotactic radiosurgery for brain metastases: both late radiation necrosis and tumor progression can occur. *J Neurooncol.* 2018;136:207–212.

6. Thust SC, van den Bent MJ, Smits M. Pseudoprogression of brain tumors. *J Magn Reson Imaging*. 2018;48:571–589.
7. Suh CH, Kim HS, Jung SC, Choi CG, Kim SJ. Comparison of MRI and PET as potential surrogate endpoints for treatment response after stereotactic radiosurgery in patients with brain metastasis. *AJR*. 2018;211:1332–1341.
8. Delbeke D, Meyerowitz C, Lapidus RL, et al. Optimal cutoff levels of F-18 fluorodeoxyglucose uptake in the differentiation of low-grade from high-grade brain tumors with PET. *Radiology*. 1995;195:47–52.
9. Salber D, Stoffels G, Pauleit D, et al. Differential uptake of O-(2-¹⁸F-fluoroethyl)-L-tyrosine, L-³H-methionine, and ³H-deoxyglucose in brain abscesses. *J Nucl Med*. 2007;48:2056–2062.
10. Ceccon G, Lohmann P, Stoffels G, et al. Dynamic O-(2-¹⁸F-fluoroethyl)-L-tyrosine positron emission tomography differentiates brain metastasis recurrence from radiation injury after radiotherapy. *Neuro Oncol*. 2017;19:281–288.
11. Galldiks N, Abdulla DSY, Scheffler M, et al. Treatment monitoring of immunotherapy and targeted therapy using ¹⁸F-FET PET in patients with melanoma and lung cancer brain metastases: initial experiences. *J Nucl Med*. 2021;62:464–470.
12. Galldiks N, Langen K-J, Albert NL, et al. PET imaging in patients with brain metastasis: report of the RANO/PET group. *Neuro Oncol*. 2019;21:585–595.
13. Whiting PF, Rutjes AWS, Westwood ME, et al. QUADAS-2: a revised tool for the quality assessment of diagnostic accuracy studies. *Ann Intern Med*. 2011;155:529–536.
14. Higgins JPT, Thompson SG, Deeks JJ, Altman DG. Measuring inconsistency in meta-analyses. *BMJ*. 2003;327:557–560.
15. R Core Team (2020). European Environment Agency website. <https://www.eea.europa.eu/data-and-maps/indicators/oxygen-consuming-substances-in-rivers/r-development-core-team-2006>. Accessed January 19, 2023.
16. Balduzzi S, Rücker G, Schwarzer G. How to perform a meta-analysis with R: a practical tutorial. *Evid Based Ment Health*. 2019;22:153–160.
17. Doebler P, Holling H, Sousa-Pinto B. Meta-analysis of diagnostic accuracy with mada. The Comprehensive R Archive Network website. <https://cran.r-project.org/web/packages/mada/vignettes/mada.pdf>. Accessed January 19, 2023.
18. Bosnyák E, Kamson DO, Robinette NL, Barger GR, Mittal S, Juhász C. Tryptophan PET predicts spatial and temporal patterns of post-treatment glioblastoma progression detected by contrast-enhanced MRI. *J Neurooncol*. 2016;126:317–325.
19. Parent EE, Patel D, Nye JA, et al. [¹⁸F]-fluciclovine PET discrimination of recurrent intracranial metastatic disease from radiation necrosis. *EJNMMI Res*. 2020;10:148.
20. Akhoundova D, Hiltbrunner S, Mader C, et al. ¹⁸F-FET PET for diagnosis of pseudoprogression of brain metastases in patients with non-small cell lung cancer. *Clin Nucl Med*. 2020;45:113–117.
21. Heinzel A, Müller D, Yekta-Michael SS, et al. O-(2-¹⁸F-fluoroethyl)-L-tyrosine PET for evaluation of brain metastasis recurrence after radiotherapy: an effectiveness and cost-effectiveness analysis. *Neuro Oncol*. 2017;19:1271–1278.
22. Galldiks N, Stoffels G, Filss CP, et al. Role of O-(2-¹⁸F-fluoroethyl)-L-tyrosine PET for differentiation of local recurrent brain metastasis from radiation necrosis. *J Nucl Med*. 2012;53:1367–1374.
23. Lohmann P, Stoffels G, Ceccon G, et al. Radiation injury vs. recurrent brain metastasis: combining textural feature radiomics analysis and standard parameters may increase ¹⁸F-FET PET accuracy without dynamic scans. *Eur Radiol*. 2017;27:2916–2927.
24. Okamoto S, Shiga T, Hattori N, et al. Semiquantitative analysis of C-11 methionine PET may distinguish brain tumor recurrence from radiation necrosis even in small lesions. *Ann Nucl Med*. 2011;25:213–220.
25. Tomura N, Kokubun M, Saginoya T, Mizuno Y, Kikuchi Y. Differentiation between treatment-induced necrosis and recurrent tumors in patients with metastatic brain tumors: comparison among ¹¹C-methionine-PET, FDG-PET, MR permeability imaging, and MRI-ADC-preliminary results. *AJNR*. 2017;38:1520–1527.
26. Jung T-Y, Kim I-Y, Lim S-H, et al. Optimization of diagnostic performance for differentiation of recurrence from radiation necrosis in patients with metastatic brain tumors using tumor volume-corrected ¹¹C-methionine uptake. *EJNMMI Res*. 2017;7:45.
27. Minamimoto R, Saginoya T, Kondo C, et al. Differentiation of brain tumor recurrence from post-radiotherapy necrosis with ¹¹C-methionine PET: visual assessment versus quantitative assessment. *PLoS One*. 2015;10:e0132515.
28. Yomo S, Oguchi K. Prospective study of ¹¹C-methionine PET for distinguishing between recurrent brain metastases and radiation necrosis: limitations of diagnostic accuracy and long-term results of salvage treatment. *BMC Cancer*. 2017;17:713.
29. Grosu A-L, Astner ST, Riedel E, et al. An interindividual comparison of O-(2-[¹⁸F]fluoroethyl)-L-tyrosine (FET) and L-[methyl-¹¹C]methionine (MET)-PET in patients with brain gliomas and metastases. *Int J Radiat Oncol Biol Phys*. 2011;81:1049–1058.
30. Tsuyuguchi N, Sunada I, Iwai Y, et al. Methionine positron emission tomography of recurrent metastatic brain tumor and radiation necrosis after stereotactic radiosurgery: is a differential diagnosis possible? *J Neurosurg*. 2003;98:1056–1064.
31. Romagna A, Unterrainer M, Schmid-Tannwald C, et al. Suspected recurrence of brain metastases after focused high dose radiotherapy: can [¹⁸F]FET-PET overcome diagnostic uncertainties? *Radiat Oncol*. 2016;11:139.
32. Lizarraga KJ, Allen-Auerbach M, Czernin J, et al. ¹⁸F-FDOPA PET for differentiating recurrent or progressive brain metastatic tumors from late or delayed radiation injury after radiation treatment. *J Nucl Med*. 2014;55:30–36.
33. Ciccone F, Minniti G, Romano A, et al. Accuracy of F-DOPA PET and perfusion-MRI for differentiating radionecrotic from progressive brain metastases after radiotherapy. *Eur J Nucl Med Mol Imaging*. 2015;42:103–111.
34. Terakawa Y, Tsuyuguchi N, Iwai Y, et al. Diagnostic accuracy of ¹¹C-methionine PET for differentiation of recurrent brain tumors from radiation necrosis after radiotherapy. *J Nucl Med*. 2008;49:694–699.
35. Law I, Albert NL, Arbizu J, et al. Joint EANM/EANO/RANO practice guidelines/SNMMI procedure standards for imaging of gliomas using PET with radiolabelled amino acids and [¹⁸F]FDG: version 1.0. *Eur J Nucl Med Mol Imaging*. 2019;46:540–557.
36. de Zwart PL, van Dijken BRJ, Holtman GA, et al. Diagnostic accuracy of PET tracers for the differentiation of tumor progression from treatment-related changes in high-grade glioma: a systematic review and metaanalysis. *J Nucl Med*. 2020;61:498–504.
37. Papin-Michault C, Bonnetaud C, Dufour M, et al. Study of LAT1 expression in brain metastases: towards a better understanding of the results of positron emission tomography using amino acid tracers. *PLoS One*. 2016;11:e0157139.
38. Unterrainer M, Galldiks N, Suchorska B, et al. ¹⁸F-FET PET uptake characteristics in patients with newly diagnosed and untreated brain metastasis. *J Nucl Med*. 2017;58:584–589.
39. Piroth MD, Prasath J, Willuweit A, et al. Uptake of O-(2-[¹⁸F]fluoroethyl)-L-tyrosine in reactive astrocytosis in the vicinity of cerebral gliomas. *Nucl Med Biol*. 2013;40:795–800.
40. Langen KJ, Stoffels G, Filss C, et al. Imaging of amino acid transport in brain tumours: positron emission tomography with O-(2-[¹⁸F]fluoroethyl)-L-tyrosine (FET). *Methods*. 2017;130:124–134.
41. Li H, Deng L, Bai HX, et al. Diagnostic accuracy of amino acid and FDG-PET in differentiating brain metastasis recurrence from radionecrosis after radiotherapy: a systematic review and meta-analysis. *AJNR*. 2018;39:280–288.

Tau PET Visual Reads: Research and Clinical Applications and Future Directions

David N. Soleimani-Meigooni¹ and Gil D. Rabinovici^{1,2}

¹Memory and Aging Center, Department of Neurology, University of California, San Francisco, San Francisco, California; and

²Department of Radiology and Biomedical Imaging, University of California, San Francisco, San Francisco, California

Biomarkers for tau pathology are essential to the latest Alzheimer disease (AD) research framework (1). Phosphorylated tau, the primary component of neurofibrillary tangles, is measurable in cerebrospinal fluid and plasma, but these fluid biomarkers do not capture the spatial dynamics of tau accumulation and spread (Braak staging) (2–4). Over the last decade, radiotracers that selectively bind to aggregated tau in neurofibrillary tangles have been developed, enabling diagnosis, mapping, and quantification of this pathology in living people (2,4,5). Tau PET correlates with other regional pathologic changes (synaptic loss, hypometabolism, and brain atrophy), domain-specific cognitive scores, and cognitive decline in people with AD (2). In AD clinical trials, tau PET is increasingly being used in participant selection, pretreatment staging, and measurement of treatment response (6). In the future, tau PET could become an important diagnostic and prognostic tool in clinical practice.

¹⁸F-flortaucipir is the most widely used tau PET tracer. Quantitative analysis of ¹⁸F-flortaucipir PET accurately distinguishes clinically diagnosed dementia due to AD from non-AD neurodegenerative diseases and cognitively unimpaired controls (7). Although quantitative analysis has been used primarily in research, newer visual interpretation methods may have important research and clinical applications (8,9). In a PET-to-autopsy study, majority interpretations of 5 raters applying a binary visual read algorithm (negative or positive AD tau pattern) on 64 antemortem scans showed 92% sensitivity and 80% specificity for detecting advanced tau pathology (Braak stages V–VI) at autopsy (mean PET-to-autopsy interval, 2.6 mo) (8). On the basis of these data, the U.S. Food and Drug Administration approved clinical ¹⁸F-flortaucipir PET “to estimate the density and distribution of aggregated tau neurofibrillary tangles in adult patients with cognitive impairment who are being evaluated for Alzheimer’s disease” (10). Importantly, the positive AD tau pattern excluded isolated uptake in medial and anterolateral temporal lobes, which is less specific and may represent early neurofibrillary tangle pathology in AD, age-related tau accumulation in cognitively normal adults, or off-target binding in non-AD neurodegenerative conditions (8). However, accumulation in these regions can be clinically significant, indicating Braak stage III–IV tangle pathology, which in clinicopathologic studies is often associated with mild cognitive impairment (MCI) or dementia during life (11). An alternative visual read method that

classified scans as positive on the basis of uptake in these regions showed increased sensitivity but lower specificity for MCI and mild dementia due to AD compared with the Food and Drug Administration-approved visual read method (9). Both visual read methods were developed for diagnostic purposes, and neither was intended to track disease progression or treatment response on longitudinal imaging.

Several other tau radiotracers have advanced to investigational human studies (5). 6-(fluoro-¹⁸F)-3-(1H-pyrrolo[2,3-c]pyridin-1-yl)-isoquinolin-5-amine (¹⁸F-MK-6240) has high affinity and selectivity for AD neurofibrillary tangles. Compared with ¹⁸F-flortaucipir, ¹⁸F-MK-6240 has a 2-fold higher dynamic range and less off-target binding in the choroid plexus, which may be advantageous for detecting early medial temporal neurofibrillary pathology (Braak stages I–II) and small changes in longitudinal studies or clinical trials (12,13). On the other hand, ¹⁸F-MK-6240 has more off-target binding in the meninges, which may be misinterpreted as tracer uptake in the medial and inferior temporal lobes (12).

In the March 2023 issue of *The Journal of Nuclear Medicine*, Seibyl et al. describe and evaluate an ¹⁸F-MK-6240 PET visual read method to assess the *in vivo* presence of tau pathology, measure the regional pattern and extent of tau, and classify abnormal regional patterns as either AD (temporal and extratemporal cortical tracer uptake without subcortical uptake) or non-AD neurodegeneration (subcortical tracer uptake, with some cortical uptake allowable) (14). Three expert nuclear medicine physicians applied this algorithm in masked reads of cross-sectional ¹⁸F-MK-6240 PET data from 102 participants at 60–90 min after injection, including cognitively healthy controls and patients with clinical diagnoses of MCI, AD dementia, or non-AD neurodegenerative diseases. Scans were read in gray scale, without corresponding structural neuroimaging data and with images scaled to mean activity in a cerebellar gray matter reference region. Majority visual reads were 81% sensitive and 93% specific for distinguishing patients with MCI or dementia due to AD from non-AD patients and controls. Reliability was high ($\kappa = 0.91$), with discordant reads occurring because of technical artifacts from scan processing or reconstruction, difficulty distinguishing cortical tracer retention in medial and inferior temporal lobes from nearby meningeal off-target binding, and low interrater agreement in regions of early tau accumulation (hippocampus and medial temporal lobes). Majority visual reads had higher accuracy than individual reads and higher sensitivity than various quantitative methods. The high accuracy and reliability support the plausibility of tau PET visual reads performed by experienced readers.

Received Nov. 16, 2022; revision accepted Nov. 28, 2022.

For correspondence or reprints, contact David N. Soleimani-Meigooni (david.soleimani-meigooni@ucsf.edu).

Published online Dec. 8, 2022.

COPYRIGHT © 2023 by the Society of Nuclear Medicine and Molecular Imaging.
DOI: 10.2967/jnumed.122.265017

This research represents a major advance by introducing the first systematic approach to visual interpretation of ¹⁸F-MK-6240 PET. The study also raises several important follow-up questions. First, is this an optimal ¹⁸F-MK-6240 visual read algorithm? Visual read approaches require standardization of many image visualization and classification parameters (i.e., color scale, thresholds, image scaling, target regions, and classification rules). The parameters selected for ¹⁸F-MK-6240 were notably different from those for ¹⁸F-flortaucipir. Most important was the decision to consider scans showing focal temporal uptake as AD-positive. The initial proposed criteria considered these scans negative because of concerns about inaccurate classification due to possible misinterpretation of meningeal off-target binding. However, the researchers found that visual raters could be trained to distinguish off-target binding from on-target temporal signal by applying multiple planar views, which could theoretically increase sensitivity for detecting earlier Braak stages. However, even without choroid plexus contamination, many concerns around the specificity of signal in temporal regions observed with ¹⁸F-flortaucipir also apply to ¹⁸F-MK-6240. Ultimately, PET-to-autopsy studies are needed to determine the trade-off between increased sensitivity and potentially decreased specificity associated with interpretation of isolated temporal lobe signal as consistent with AD-related tau.

Second, how will this visual read method generalize to less experienced brain PET readers? Although most readers in the present study were naïve to ¹⁸F-MK-6240, all had substantial experience with amyloid PET and other tau radiotracers. As tau radiotracers are rolled out into broader research and clinical use, the reliability of visual reads by less experienced clinicians will need to be established. Encouraging early data from the Imaging Dementia—Evidence for Amyloid Scanning (IDEAS) study found high agreement between visual reads of amyloid PET scans performed and interpreted in the community and scan classification by image quantification (15). However, unlike amyloid PET radiotracers, all of which show similar off-target binding in white matter, each tau PET tracer has unique off-target binding patterns, which can complicate visual interpretation (5,9,12,16). Novice readers may need additional radiotracer-specific training to accurately identify and discriminate off-target binding, especially near the medial temporal lobes, with the same accuracy and reproducibility as experts.

Third, should a single clinician's qualitative read be the standard for tau PET interpretation? For both ¹⁸F-MK-6240 and ¹⁸F-flortaucipir, majority visual reads show generally higher accuracy than individual visual reads, but requiring multiple expert reads for each scan is not practical (8,14). Hybrid read approaches, which incorporate both a visual read and quantitative information from the image, have been proposed to leverage the complementary strengths, and counterbalance the weaknesses, of qualitative versus quantitative approaches to image classification (17). Further research is needed to measure the effect of additional quantitative information on the accuracy and reliability of tau PET visual reads.

Fourth, will visual ratings be useful for measuring longitudinal changes in tau in individual patients? The authors propose this as a potential application of their visual read algorithm, but validation in longitudinal observational research or clinical trials is needed. The proposed region-based method may be too time-consuming for routine clinical or research purposes, and there are a variety of challenges (e.g., variable reliability of reads in different regions of interest, difficulty grading the extent of tracer binding in regions without complementary structural neuroimaging) that may impact the reliability of this method, even in the hands of expert readers. Given these challenges, quantitative approaches to measuring signal

intensity and spatial spread will likely be necessary to most precisely evaluate longitudinal changes in tau PET signal.

Lastly, how well will the visual read algorithm perform in MCI? The present study included only 21 MCI patients in the visual read test group, yet this early clinical stage represents one of the highest-priority populations for tau PET in clinical trials and future clinical practice. Patients with MCI are functionally independent and have subtle symptoms that overlap those of non-AD neurodegenerative diseases; thus, accurate and timely identification of these patients is important and may be particularly crucial for administration of future disease-modifying therapies (18). At autopsy, MCI patients have on average intermediate Braak stage III–IV neurofibrillary pathology, and the antemortem tau PET signal can be modest and subtle at this stage (8,11,19). A more sensitive visual read schema that identifies early signal in the medial temporal lobes may be particularly beneficial for detection of AD tau pathology in MCI.

Ultimately, visual reads will need to be applied to large numbers of longitudinally scanned patients who have a broad range of neurodegenerative disease diagnoses and excellent clinical characterization and amyloid biomarker data and who eventually undergo autopsy. These data will clarify the sensitivity and specificity of tau tracers to neurofibrillary tangle pathology, elucidate causes of off-target binding, and determine how longitudinal visual tracking of regional tracer uptake corresponds to pathologic progression of AD. Another area of interest is head-to-head comparisons of different tau PET ligands in the same patients, which may lead to development and validation of unified approaches to tau PET quantification and visual reads (20). Although each tau radiotracer has its idiosyncrasies, the overall spatial pattern of binding is remarkably consistent, suggesting that standardized approaches will be feasible (7). The maturation of tau PET as a powerful biomarker for diagnosis, staging, and prognosis in AD is occurring hand in hand with the emergence of novel molecular therapies that modify the course of AD pathophysiology (21). Collectively, the field seems to be at an inflection point, heralding a new era of early detection, biomarker-based diagnosis, and disease-modifying therapy.

DISCLOSURE

David Soleimani-Meigooni receives research support from the National Institute on Aging (K23-AG076960). Gil Rabinovici receives research support from National Institute on Aging, National Institute of Neurological Disorders and Stroke, the Alzheimer Association, the American College of Radiology, the Rainwater Charitable Foundation, Avid Radiopharmaceuticals, GE Healthcare, Life Molecular Imaging, and Genentech; has served as a consultant for Eli Lilly, Genentech, Roche, Merck, and Johnson & Johnson; and is an associate editor for *JAMA Neurology*. No other potential conflict of interest relevant to this article was reported.

REFERENCES

1. Jack CR, Bennett DA, Blennow K, et al. NIA-AA research framework: toward a biological definition of Alzheimer's disease. *Alzheimers Dement*. 2018;14:535–562.
2. Ossenkoppele R, Hansson O. Towards clinical application of tau PET tracers for diagnosing dementia due to Alzheimer's disease. *Alzheimers Dement*. 2021;17:1998–2008.
3. Braak H, Braak E. Neuropathological staging of Alzheimer-related changes. *Acta Neuropathol (Berl)*. 1991;82:239–259.
4. Schöll M, Lockhart SN, Schonhaut DR, et al. PET imaging of tau deposition in the aging human brain. *Neuron*. 2016;89:971–982.
5. Leuzy A, Chiotis K, Lemoine L, et al. Tau PET imaging in neurodegenerative tauopathies: still a challenge. *Mol Psychiatry*. 2019;24:1112–1134.

6. Mintun MA, Lo AC, Duggan Evans C, et al. Donanemab in early Alzheimer's disease. *N Engl J Med.* 2021;384:1691–1704.
7. Ossenkoppele R, Rabinovici GD, Smith R, et al. Discriminative accuracy of [¹⁸F]flortaucipir positron emission tomography for Alzheimer disease vs other neurodegenerative disorders. *JAMA.* 2018;320:1151–1162.
8. Fleisher AS, Pontecorvo MJ, Devous MD, et al. Positron emission tomography imaging with [¹⁸F]flortaucipir and postmortem assessment of Alzheimer disease neuropathologic changes. *JAMA Neurol.* 2020;77:829–839.
9. Sonni I, Lesman Segev OH, Baker SL, et al. Evaluation of a visual interpretation method for tau-PET with ¹⁸F-flortaucipir. *Alzheimers Dement (Amst).* 2020;12:e12133.
10. Highlights of prescribing information. TAUVID™ (flortaucipir F 18 injection), for intravenous use. Initial U.S. Approval: 2020. U.S. Food and Drug Administration website. https://www.accessdata.fda.gov/drugsatfda_docs/label/2020/212123s000lbl.pdf. Accessed December 22, 2022.
11. Hyman BT, Phelps CH, Beach TG, et al. National Institute on Aging–Alzheimer's Association guidelines for the neuropathologic assessment of Alzheimer's disease. *Alzheimers Dement.* 2012;8:1–13.
12. Gogola A, Minhas DS, Villemagne VL, et al. Direct comparison of the tau PET tracers ¹⁸F-flortaucipir and ¹⁸F-MK-6240 in human subjects. *J Nucl Med.* 2022;63:108–116.
13. Pascoal TA, Therriault J, Benedet AL, et al. ¹⁸F-MK-6240 PET for early and late detection of neurofibrillary tangles. *Brain.* 2020;143:2818–2830.
14. Seibyl JP, DuBois JM, Racine A, et al. A visual interpretation algorithm for assessing brain tauopathy with ¹⁸F MK-6240 PET. *J Nucl Med.* 2023;64:444–451.
15. Iaccarino L, La Joie R, Koeppe R, et al. rPOP: robust PET-only processing of community acquired heterogeneous amyloid-PET data. *Neuroimage.* 2022;246:118775.
16. Chapleau M, Iaccarino L, Soleimani-Meigooni D, Rabinovici GD. The role of amyloid PET in imaging neurodegenerative disorders: a review. *J Nucl Med.* 2022;63(suppl 1):13S–19S.
17. Apostolova LG, Aisen P, Eloyan A, et al. The Longitudinal Early-Onset Alzheimer's Disease Study (LEADS): framework and methodology. *Alzheimers Dement.* 2021;17:2043–2055.
18. Cummings J, Rabinovici GD, Atri A, et al. Aducanumab: appropriate use recommendations update. *J Prev Alzheimers Dis.* 2022;9:221–230.
19. Soleimani-Meigooni DN, Iaccarino L, La Joie R, et al. ¹⁸F-flortaucipir PET to autopsy comparisons in Alzheimer's disease and other neurodegenerative diseases. *Brain.* 2020;143:3477–3494.
20. Head-to-head harmonization of tau tracers in Alzheimer's disease (HEAD). Clinicaltrials.gov website. <https://clinicaltrials.gov/ct2/show/NCT05361382>. Published May 4, 2022. Updated November 9, 2022. Accessed December 16, 2022.
21. van Dyck CH, Swanson CJ, Aisen PA, et al. LeCanemab in early Alzheimer's disease. *N Engl J Med.* November 29, 2022 [Epub ahead of print].

A Multicenter Study on Observed Discrepancies Between Vendor-Stated and PET-Measured ^{90}Y Activities for Both Glass and Resin Microsphere Devices

Silvano Gnesin^{*1}, Justin K. Mikell^{*2}, Maurizio Conti³, John O. Prior⁴, Thomas Carlier⁵, Thiago V.M. Lima⁶, and Yuni K. Dewaraja⁷

¹Institute of Radiation Physics, Lausanne University Hospital, University of Lausanne, Lausanne, Switzerland; ²Department of Radiation Oncology, University of Michigan, Ann Arbor, Michigan, and Department of Radiation Oncology, Washington University, St. Louis, Missouri; ³Department of Molecular Imaging, Siemens Medical Solutions, Knoxville, Tennessee; ⁴Department of Nuclear Medicine and Molecular Imaging, Lausanne University Hospital, University of Lausanne, Lausanne, Switzerland; ⁵Nuclear Medicine Department, University Hospital of Nantes, Nantes, France; ⁶Department of Radiology and Nuclear Medicine, Luzerner Kantonsspital, Luzern, Switzerland; and ⁷Division of Nuclear Medicine, Department of Radiology, University of Michigan, Ann Arbor, Michigan

Dosimetry-guided treatment planning in selective internal radiation therapy relies on accurate and reproducible measurement of administered activity. This 4-center, 5-PET-device study compared the manufacturer-declared ^{90}Y activity in vials with quantitative ^{90}Y PET/CT assessment of the same vials. We compared ^{90}Y PET-measured activity (A_{PET}) for 56 ^{90}Y -labeled glass and 18 ^{90}Y -labeled resin microsphere vials with the calibrated activity specified by the manufacturer (A_{M}). Additionally, the same analysis was performed for 4 ^{90}Y -chloride vials. The mean $A_{\text{PET}}/A_{\text{M}}$ ratio was 0.79 ± 0.04 (range, 0.71–0.89) for glass microspheres and 1.15 ± 0.06 (range, 1.05–1.25) for resin microspheres. The mean $A_{\text{PET}}/A_{\text{M}}$ ratio for ^{90}Y -chloride vials was 1.00 ± 0.04 (range, 0.96–1.06). Thus, we found an average difference of 46% between glass and resin microsphere activity calibrations, whereas close agreement was found for chloride solutions. We expect that the reported discrepancies will promote further investigations to establish reliable and accurate patient dosimetry and dose-effect assessments.

Key Words: resin microspheres; glass microspheres; ^{90}Y ; PET/CT; activity

J Nucl Med 2023; 64:825–828

DOI: 10.2967/jnumed.122.264458

Selective internal radiation therapy (SIRT) with radioactive microspheres is an established liver-directed therapy for both primary liver cancer and liver metastases. Both ^{90}Y glass and resin microspheres are used globally; they are Food and Drug Administration-approved in the United States, and they received the CE (Conformité Européenne) mark in the European Union.

Considerable evidence of dose-effect relationships for both tumor and nontumor liver have been demonstrated for ^{90}Y SIRT (1). In particular, for glass microspheres, Garin et al. highlighted a dose-response relationship in a prospective randomized trial, which demonstrated that planned personalized dosimetry improves outcomes compared with standard single-compartment dosimetry

for locally advanced hepatocellular carcinoma (2). Another area of investigation is focused on posttreatment SIRT dosimetry, which obviates most of the difficulties linked to the hypothesis that pre-treatment imaging-based dosimetry is a robust surrogate of the actual delivered absorbed dose. In that respect, recent studies have suggested the benefit of ^{90}Y PET-based dosimetry in hepatocellular carcinoma or cholangiocarcinoma (3,4).

For reliable dosimetry-guided treatment planning and dose-effect assessment from pretherapy imaging-based absorbed dose estimates, the net administered activity of ^{90}Y microspheres should be accurately determined. Accurate assay of ^{90}Y , an almost pure β -emitter, using activity meters is challenging compared with other radionuclides commonly used in nuclear medicine procedures (5). (In this work, we adopted the term *activity meter* for the reentrant well-type ionization chamber that is calibrated to convert a measured ionization current to an activity; this device is also colloquially referred to as a dose calibrator in North America. We reserved the use of *dose* for the absorbed dose in units of Gy.) The specific geometry and material composition of the source and its container affects the spectrum of Bremsstrahlung photons, hence affecting the activity meter measurement.

^{90}Y PET imaging is also challenging because of the low true coincidence count rates associated with the low yield of positron emission (0.0032%). Despite this, there have been multiple reports demonstrating the quantification accuracy of ^{90}Y PET in phantom studies when using state-of-the-art time-of-flight scanners (6–8). It should be noted that almost all phantom studies to date have used ^{90}Y in the form of a chloride solution and not the microsphere devices themselves. Reasons may include the difficulty of suspending microspheres in a uniform distribution throughout a phantom compartment.

In this work, we used quantitative ^{90}Y PET/CT imaging to measure the ^{90}Y microsphere vial activity in air before SIRT with resin and glass microspheres at 4 institutions on 5 scanners: PET-1, a Biograph Vision 600 (Siemens Healthineers) at Lausanne University Hospital (Centre hospitalier universitaire vaudois [CHUV]); PET-2, a Discovery 690 (GE Healthcare) at CHUV; PET-3, a Biograph mCT 40 (Siemens Healthineers) at the University of Michigan; PET-4, a Biograph Vision 600 (Siemens Healthineers) at Luzerner Kantonsspital; and PET-5, a Biograph 40 mCT (Siemens Healthineers) at the University Hospital of Nantes. Additional data

Received Jun. 2, 2022; revision accepted Nov. 7, 2022.

For correspondence or reprints, contact John O. Prior (john.prior@chuv.ch).

*Contributed equally to this work.

Published online Nov. 23, 2022.

COPYRIGHT © 2023 by the Society of Nuclear Medicine and Molecular Imaging.

came from PET measurements of vials containing ^{90}Y in chloride solution and as a liquefied resin. We compared the PET-measured activity with the activity on the calibration certificate supplied by the vendor for each vial with appropriate decay correction.

MATERIALS AND METHODS

We analyzed ^{90}Y vials from 3 different manufacturers: 56 ^{90}Y -labeled glass microsphere vials (TheraSphere; Boston Scientific), 18 ^{90}Y -labeled resin microsphere vials (SIR-Spheres; Sirtex Medical), 4 vials containing ^{90}Y -chloride solution (2 from Curium and 2 from Eckert and Ziegler), and 1 vial containing a solution of dissolved ^{90}Y -labeled resin microspheres (liquefied resin). All vials were imaged in air at a single bed position centered on the 3 tomographic directions of the PET scanner to yield peak sensitivity.

Glass Microspheres

A first dataset of 43 ^{90}Y -labeled glass microsphere vials (0.7–6.3 GBq) was imaged on PET-1, with a subgroup of 8 of these vials (0.7–6.3 GBq) being additionally measured on PET-2. Another dataset of 13 glass microsphere vials (2.3–8.6 GBq) was imaged on PET-3.

Resin Microspheres

^{90}Y -labeled resin microsphere vials (3.3–4.6 GBq) were imaged on PET-1 ($n = 11$), PET-2 ($n = 1$), or PET-4 ($n = 6$).

Chloride Solution

In addition to performing acquisitions on microsphere vials, we acquired PET/CT data for vials of liquid ^{90}Y -chloride solution. Of these, 2 (0.4 and 2.5 GBq) were acquired on PET-1 and 2 (0.4 and 4.4 GBq) on PET-3.

Liquefied Resin Microspheres

The vial with the solution of dissolved ^{90}Y -labeled resin microspheres was from a prior study evaluating the reliability of measuring ^{90}Y activity using PET performed at the University Hospital of Nantes in collaboration with the French National Standard Laboratory in Paris (LNHB [Laboratoire National Henri Becquerel]–CEA [Commissariat à l'énergie atomique et aux énergies alternatives]). For this purpose, a reference activity of resin microspheres (2.95 GBq) was first dissolved (9), measured using the triple- to double-coincidence ratio method with Cherenkov counting at LNHB-CEA, and then shipped to the University Hospital of Nantes for a PET/CT acquisition on PET-5.

PET/CT Reconstruction and Quantification

Supplemental Table 1 summarizes acquisition and reconstruction parameters for the different PET/CT devices (supplemental materials are available at <http://jnm.snmjournals.org>). Manufacturer-recommended reconstruction parameters were used for ^{90}Y . Considering the measurements on PET-1 and PET-4 (the 2 Biograph Vision 600 devices), we tested both absolute and relative scatter corrections available with the manufacturer software. The relatively high noise associated with low-count ^{90}Y PET can affect the scatter correction with relative scaling, and some bias can appear in the final quantification as reported previously (6). Since the preliminary quantitative assessment showed, as expected, no significant difference between the 2 scatter methods in the low-scatter setting (in air) of the current experiment (Supplemental Tables 2 and 3), we focus on results obtained with the absolute scatter correction.

In all PET scanners used in the current study, the software enables ^{90}Y quantitation automatically from the local ^{18}F system cross-calibration, accounting for the ^{90}Y specific physical decay and positron branching ratio. The quantitative PET data were decay-corrected to the start of the PET acquisition. On the PET images, we defined cylindric (50 mm in diameter, 5 cm high) volumes of interest that encompassed the vials (diameters of 25, 35, and 25 mm for resin,

glass, and ^{90}Y -chloride, respectively), to minimize any signal loss due to partial-volume effects.

Manufacturer-Specified Activity Assessment

The manufacturer-specified calibrated activity was reported in a document shipped with the vial to the different hospitals. In this document, the manufacturer indicates the vial activity and the time of the calibration. After performing the manufacturer-specified procedure for establishing a local calibration factor, we routinely verified the activity by measuring the received vial in the local activity meter. Specifically, nominal manufacturer activity was used for resin microspheres, whereas the manufacturer-measured total activity (not nominal) was used for glass microspheres. The local versus certified manufacturer activity was found to be within 5% at all centers.

Comparison of PET-Derived Activity with Manufacturer-Specified Value

For each measurement, the total PET activity measured in the vial volume of interest (A_{PET}) was compared with the vial activity reported in the manufacturer calibration sheet (A_{M}) decay-corrected to the start of the PET acquisition, using the ratio $A_{\text{PET}}/A_{\text{M}}$. We assessed for statistical differences in $A_{\text{PET}}/A_{\text{M}}$ ratios for the same microsphere type obtained in different PET scanners by applying ANOVA and multiple-comparison tests using the MATLAB statistical toolbox (version R2021a; MathWorks). A significant difference was considered present for P values of less than 0.05.

RESULTS

Figure 1 shows a dot-plot representation of the $A_{\text{PET}}/A_{\text{M}}$ distribution across all 4 vial types and all centers. Table 1 presents the

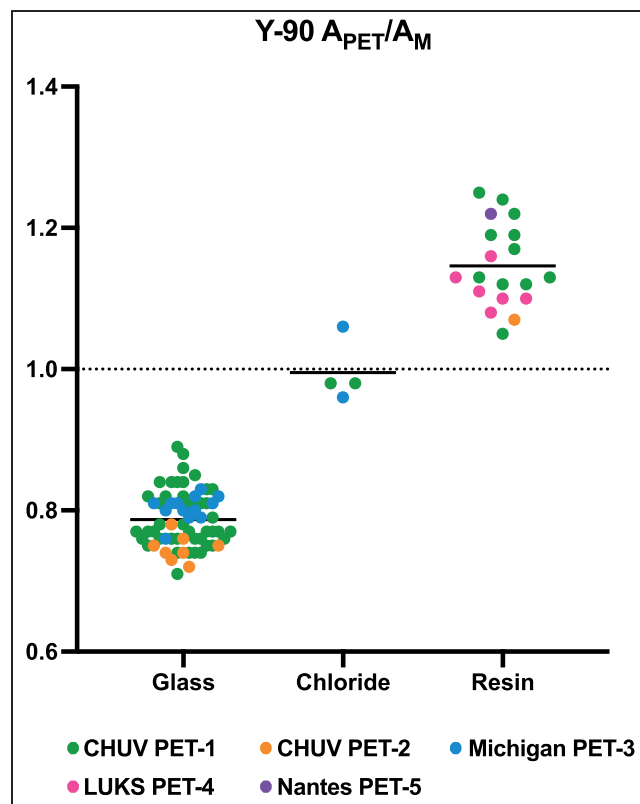


FIGURE 1. Distribution of $A_{\text{PET}}/A_{\text{M}}$ ratios for the 4 vial products tested in this study (i.e., ^{90}Y -labeled glass microspheres, ^{90}Y -chloride solution, ^{90}Y -labeled resin microspheres, and ^{90}Y -labeled liquefied resin). LUKE = Luzerner Kantonsspital, the ^{90}Y -labeled liquefied resin (Nantes PET-5, purple dot) was associated to the resin's category.

TABLE 1
Summary of A_{PET}/A_M Results

Product	Manufacturer	Vials (<i>n</i>)	Scanner	A_{PET}/A_M		
				Mean	SD	Range
Glass	Boston Scientific	43	PET-1	0.79	0.04	0.71–0.89
Glass	Boston Scientific	8	PET-2	0.74	0.02	0.72–0.78
Glass	Boston Scientific	13	PET-3	0.80	0.02	0.76–0.83
Glass	Boston Scientific	64	All	0.79	0.04	0.71–0.89
Resin	Sirtex Medical	11	PET-1	1.16	0.06	1.05–1.25
Resin	Sirtex Medical	1	PET-2	1.07		
Resin	Sirtex Medical	6	PET-4	1.11	0.03	1.08–1.16
Resin	Sirtex Medical	18	All	1.15	0.06	1.05–1.25
Resin* liquified	Sirtex Medical	1	PET-5	1.22		
Chloride	Curium	2	PET-1	0.98	0.01	0.98–0.98
Chloride*	Eckert and Ziegler	2	PET-3	1.01	0.07	0.96–1.06
Chloride	All	4	All	1.00	0.04	0.96–1.06

*Data for which relative scatter correction was applied; otherwise, absolute scatter correction was applied.
Liquification was by LNHB-CEA.

summary statistics for all measurements (full data are available in Supplemental Presentation 1). The mean A_{PET}/A_M ratio for ^{90}Y glass spheres was 0.79 ± 0.04 (range, 0.71–0.89). No statistical differences in mean A_{PET}/A_M for ^{90}Y glass spheres were found between PET-1 and PET-3 ($P = 0.43$). Statistical differences were found between PET-1 and PET-2 ($P = 0.009$) and between PET-2 and PET-3 ($P = 0.002$). The mean A_{PET}/A_M ratio for the resin spheres was 1.15 ± 0.06 (range, 1.05–1.25). In this case, no statistical difference was found between PET-1 and PET-4 ($P = 0.072$).

The mean A_{PET}/A_M measured in ^{90}Y -chloride vials was 1.00 ± 0.04 (range, 0.96–1.06) (Table 1; Supplemental Table 4). The A_{PET}/A_M measured for the liquefied resin spheres in PET-5 was 1.22 ± 0.12 , whereas good agreement was found between the LNHB-CEA reference activity and the PET activity measurements, with a ratio of 1.01.

DISCUSSION

In this study, we used PET as an independent measure of activity for ^{90}Y microsphere vials in air and compared this measure with the activity reported in the respective manufacturer's calibration sheet for ^{90}Y -labeled resin and glass microspheres and ^{90}Y in chloride solution and liquefied resin. Although we report substantial discrepancies for resin and glass microspheres, close agreement is reported for the chloride solution. Furthermore, PET measurement of the liquefied resin activity is in excellent agreement with the national metrology laboratory reference measurement, suggesting an accurate PET quantification.

For the resin spheres, we reported an average A_{PET}/A_M ratio of 1.15 ± 0.06 (i.e., A_M underestimates A_{PET} by 13%); this value is compatible with the high-purity germanium National Institute of Standards and Technology-referred results of Graves et al., who recently reported a ratio of 1.233 ± 0.030 (10). In addition, we provided original data for the glass spheres showing a trend opposite that of resin, an A_{PET}/A_M ratio of 0.79 ± 0.04 (i.e., A_M

systematically overestimating A_{PET} by 27%). Therefore, a relative difference of about 46% exists between the 2 manufacturers' ^{90}Y activity calibrations; that is, 1 Bq of ^{90}Y measured in the activity reference frame of the glass microsphere manufacturer corresponds to 1.46 Bq in that of the resin microsphere manufacturer.

Quantitative PET imaging of ^{90}Y is challenging, but it is enhanced by the state-of-the-art time-of-flight systems used in this study. However, an error in the PET-reconstructed activity may arise from a potentially inaccurate attenuation correction due to inadequate modeling of higher-density materials such as glass. The glass containers for the ^{90}Y -chloride and resin microspheres have a minimal thickness. Such a thickness will have minor effects on PET-reconstructed activity. The following observations support this claim: first, our A_{PET}/A_M for resin microspheres is consistent with prior studies (10,11) reporting that A_M is underestimated using a measurement approach different from PET; second, our A_{PET}/A_M is near unity for ^{90}Y -chloride, for which activity meter measurements are well known with a traceable standard; and third, we obtained a near-unity value for the ratio of the LNHB-CEA reference activity to the PET activity, indicating the good agreement of the 2 methods (i.e., the coincidence Cherenkov counting and the PET) in estimating the vial activity. However, the combination of a thick glass V-Vial (Wheaton Industries, Inc.) bottom and glass microspheres settling at that bottom may lead to a combined glass thickness potentially great enough to introduce bias in the attenuation correction. To estimate the potential bias, we used cone-beam CT of a glass microsphere vial to create a high-resolution (0.1 mm) model of the geometry and material used in our study. Nominal linear attenuation coefficients were then assigned, and attenuation correction factors (ACFs) were calculated along a few lines of response. We compared ACFs from the high-resolution model with ACFs calculated from the CT-derived attenuation map used in the PET reconstruction. Assuming nominal values for diameter and total number of microspheres, with a packing ratio of 0.6, we estimated the potential ACF bias along

evaluated lines of response to vary from -11% to $+13\%$. The average ACF bias was no greater than 6% , which would move our results only slightly toward unity, leaving the A_{PET}/A_M ratio at or below 0.85 . The sensitivity of attenuation correction was also tested by increasing the CT numbers above 600 Hounsfield units by 20% and then performing PET reconstruction. The resulting activity concentration image had a maximum difference of 3.6% , demonstrating minimal sensitivity to changes in Hounsfield units.

Although primary measurements from national laboratories have been reported for both devices (*12,13*), any changes from the specific source and container tied to these measurements will impact the ^{90}Y Bremsstrahlung energy spectrum and thereby the activity meter assay. One study reported a systematic bias of 4% due to likely changes in the acrylic shield used by glass microspheres (*14*). Monte Carlo simulations that model the composition and geometry of the vials, as well as the devices, might provide more insight on their impact on both the PET measurement and activity meter calibration but are beyond the scope of this work.

To the best of our knowledge, we believe this is the first report of such observed differences for ^{90}Y glass microspheres between PET and vendor-stated activity. The purpose of this study is not to fully explain the discrepancies we have observed but to share our observations that suggest a significant bias when comparing PET quantification with vendor-stated activity for both glass and resin ^{90}Y microsphere devices. Such differences would likely not affect clinical practice given the large number of patients safely and effectively treated to date with activities as stated by the vendors. However, it is important from a metrological standpoint to know the activities administered to patients; reporting true activities should enable more accurate radiobiologic modeling and dosimetry comparisons across devices and modalities. For example, our results should be considered within the context of studies reporting a lower biologic effect per Gray for glass versus resin microspheres when treating the same hepatic disease (*15*).

CONCLUSION

We have presented original data comparing quantitative PET and manufacturer-declared total activity in ^{90}Y -labeled microspheres and ^{90}Y -chloride vials. Manufacturer-declared vial activities were substantially different when measured by quantitative PET for glass (mean ratio, 0.79) and resin (mean ratio, 1.15), which showed opposite trends with a large relative difference of 46% between them. In ^{90}Y -chloride vials, PET and manufacturer-declared activities agreed closely. We expect that the reported discrepancies will promote further investigations to establish reliable and accurate patient injected-activity measurement and thus consistent dosimetry and dose–effect relation assessments.

DISCLOSURE

Yuni Dewaraja acknowledges grant funding from NIH R01 EB022075. Maurizio Conti is full-time employee of Siemens Medical Solutions USA, Inc. No other potential conflict of interest relevant to this article was reported.

ACKNOWLEDGMENTS

We thank James Hamill from Siemens Medical Solutions USA, Inc., for performing the attenuation correction sensitivity analysis,

and we thank Dr. Christophe Bobin and his team (LNHB/CEA) for providing us with the dissolved resin source.

KEY POINTS

QUESTION: How accurate are vendor-specified calibrated activities used for therapy and absorbed dose assessment in ^{90}Y SIRT?

PERTINENT FINDINGS: We compared quantitative ^{90}Y PET measurements against vendor-specified calibrated activities in both glass and resin microsphere vials across multiple centers and devices. We found a large difference between PET measurements and reported vial activities (average, -21% for glass and $+15\%$ for resin).

IMPLICATIONS FOR PATIENT CARE: Accounting for the observed differences can lead to a shift of reported administered activity and absorbed dose thresholds in dose–effect studies.

REFERENCES

1. Weber M, Lam M, Chiesa C, et al. EANM procedure guideline for the treatment of liver cancer and liver metastases with intra-arterial radioactive compounds. *Eur J Nucl Med Mol Imaging*. 2022;49:1682–1699.
2. Garin E, Tselikas L, Guiu B, et al. Personalised versus standard dosimetry approach of selective internal radiation therapy in patients with locally advanced hepatocellular carcinoma (DOSISPHERE-01): randomised, multicentre, open-label phase 2 trial. *Lancet Gastroenterol Hepatol*. 2021;6:17–29.
3. Veenstra EB, Ruiter SJS, de Haas RJ, Bokkers RPH, de Jong KP, Noordzij W. Post-treatment three-dimensional voxel-based dosimetry after yttrium-90 resin microsphere radioembolization in HCC. *EJNMMI Res*. 2022;12:9.
4. Willowson KP, Eslick EM, Bailey DL. Individualised dosimetry and safety of SIRT for intrahepatic cholangiocarcinoma. *EJNMMI Phys*. 2021;8:65.
5. Saldarriaga Vargas C, Bauwens M, Pooters INA, et al. An international multi-center investigation on the accuracy of radionuclide calibrators in nuclear medicine theranostics. *EJNMMI Phys*. 2020;7:69.
6. Carlier T, Willowson KP, Fournal E, Bailey DL, Doss M, Conti M. ^{90}Y -PET imaging: exploring limitations and accuracy under conditions of low counts and high random fraction. *Med Phys*. 2015;42:4295–4309.
7. Willowson KP, Tapner M, QUEST Investigator Team, Bailey DL. A multicentre comparison of quantitative ^{90}Y PET/CT for dosimetric purposes after radioembolization with resin microspheres: the QUEST Phantom Study. *Eur J Nucl Med Mol Imaging*. 2015;42:1202–1222.
8. Dewaraja YK, Devasia T, Kaza RK, et al. Prediction of tumor control in ^{90}Y radioembolization by logit models with PET/CT-based dose metrics. *J Nucl Med*. 2020; 61:104–111.
9. Lourenço V, Bobin C, Chisté V, et al. Primary standardization of SIR-Spheres based on the dissolution of the ^{90}Y -labeled resin microspheres. *Appl Radiat Isot*. 2015;97:170–176.
10. Graves SA, Martin M, Tiwari A, Merrick M, Sunderland J. SIR-Spheres activity measurements reveal systematic miscalibration. *J Nucl Med*. 2022;63:1131–1135.
11. Selwyn R, Micka J, DeWerd L, Nickles R, Thomadsen B. Technical note: the calibration of ^{90}Y -labeled SIR-Spheres using a nondestructive spectroscopic assay. *Med Phys*. 2008;35:1278–1279.
12. Mo L, Avci B, James D, et al. Development of activity standard for ^{90}Y microspheres. *Appl Radiat Isot*. 2005;63:193–199.
13. Coursey BM, Calhoun JM, Cessna JT. Radioassays of yttrium-90 used in nuclear medicine. *Nucl Med Biol*. 1993;20:693–699.
14. Bergeon D, Cessna J, Zimmer B. Challenges in migrating ^{90}Y calibrations to new ionization chambers: geometry, height, and impurity effects [abstract]. *J Nucl Med*. 2018;59(suppl 1):428.
15. d'Abadie P, Hesse M, Jamar F, Lhommel R, Walrand S. ^{90}Y TOF-PET based EUD reunifies patient survival prediction in resin and glass microspheres radioembolization of HCC tumours. *Phys Med Biol*. 2018;63:245010.

ATTEND THE SNMMI 2023 ANNUAL MEETING

The **SNMMI 2023 Annual Meeting** provides you with access to 130+ scientific and CE sessions, more than 1,000 scientific posters, pre-meeting categorical seminars, industry-led satellite symposia, and great networking events. Plus, you can learn about leading products and innovations in the field from more than 185 exhibiting companies. It's the can't miss opportunity for you to elevate your skills and become your clinic's expert on the latest developments, research, and clinical applications advancing precision medicine and therapy.

June 24-27
2023

SNMMI ANNUAL MEETING

EYE ON THE PATIENT

CHICAGO, ILLINOIS, USA



Register Today

WWW.SNMMI.ORG/AM2023

Virtual registration options are also available.

SNM SOCIETY OF
MI NUCLEAR MEDICINE &
MOLECULAR IMAGING



VERITON-CT®

DIGITAL SPECT/CT



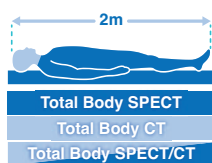
Optimization of Every Step

Spectrum Dynamics has integrated its ground-breaking BroadView Technology design into the VERITON-CT system, providing a digital platform enabling routine 3D imaging in Nuclear Medicine. The result is optimization of every step, from image acquisition to interpretation.

VERITON-CT digital SPECT/CT combines the best-in-class CZT detectors, novel system design, high resolution CT, and advanced software technology to elevate the performance of 360° digital SPECT/CT.



BroadView Technology
Proprietary swiveling detector design provides increased sensitivity for faster scans



Total Body 3D Imaging
200cm continuous coverage vertex to feet
SPECT | CT | SPECT/CT



80cm NM and CT bore
Wide Bore SPECT/CT
80cm NM and CT bore



Choice of 16/64 slice
Choice of high-resolution CT for diagnostic applications and low dose total body CTAC



TruView Console
One platform, one location for clinical care decision-making:
1. Acquisition
2. Advanced quantitative reconstruction
3. Both 3D and 4D data analysis and review

VERITON-CT Feature Application: 3D Dynamic Imaging

TruFlow for VERITON-CT offers real-time 3D in-vivo fast dynamic imaging to capture the radiopharmaceutical distribution, uptake, or clearance over time in 3D SPECT/CT parametric imaging.

TruFlow

